THE ROLE OF VOLCANISM IN THE EARLY HISTORY OF THE MOON AND MERCURY

BY
JENNIFER L. WHITTEN
B.A., ART HISTORY, THE COLLEGE OF WILLIAM AND MARY, 2009
B.S., GEOLOGY, THE COLLEGE OF WILLIAM AND MARY, 2009
SC.M., GEOLOGICAL SCIENCES, BROWN UNIVERSITY, 2011

A DISSERTATION SUBMITTED IN PARTIAL FULFILLMENT OF THE REQUIREMRENTS FOR THE DEGREE OF DOCTOR OF PHILOSOPHY IN THE DEPARTMENT OF GEOLOGICAL SCIENCES AT BROWN UNIVERSITY

PROVIDENCE, RHODE ISLAND
MAY 2014

This dissertation by Jennifer L. Whitten is accepted in its present form by the Department of Geological Sciences as satisfying the dissertation requirement for the degree of Doctor of Philosophy.

Date_____ _____
James W. Head, III, Ph.D, Advisor

Recommended to the Graduate Council

Date_____ _____
Paul C. Hess, Ph.D., Reader

Date_____ _____
Carlé M. Pieters, Ph.D., Reader

Date_____ _____
Alberto Saal, Ph.D., Reader

Date_____ _____
David T. Blewett, Ph.D., Reader

Approved by the Graduate Council

Date_____ _____
Peter M. Weber
Dean of the Graduate School

Jennifer Leigh Whitten

Planetary Geosciences Group | Department of Geological Sciences
Brown University | 324 Brook St., Box 1846 | Providence, RI 02912
(w) 401–863–3485 | (f) 401–863–3978 | (e) jennifer_whitten@brown.edu

EDUCATION

Brown University, Providence, Rhode Island
Planetary Geosciences Group, Department of Geological Sciences
PhD, Advisor: Dr. James W. Head (May 2014)

Brown University, Providence, Rhode Island
Master of Science, Geological Sciences, Advisor: Dr. James W. Head (May 2011)

The College of William and Mary, Williamsburg, Virginia
Magna Cum Laude, Phi Beta Kappa
Bachelor of Science, Geology, Advisor: Dr. Gregory Hancock (May 2009)
Bachelor of Arts, Art History (May 2009)

PROFESSIONAL EXPERIENCE

JPL Planetary Science Summer School, Io mission concept (July 2012)
Field research, Antarctic Dry Valleys (October–December 2011)
Science team member
MESSENGER Mercury Dual Imaging System (MDIS): 2011–present
Moon Mineralogy Mapper (M^3): 2009–present
NASA Planetary Volcanology Field Workshop (July 2010)
Research Assistant to Dr. James W. Head III, Brown University: 2009- present

PUBLICATIONS

Whitten, J.L., Head, J.W., Solomon, S.C., (2014) Rembrandt basin: Distinguishing between volcanic and impact-produced plains, Icarus, *in prep*.

Whitten, J.L., Head, J.W., (2014) Lunar cryptomaria II: Mineralogy and composition of ancient volcanic deposits, Icarus, *in prep*.

Whitten, J.L., Head, J.W., (2014) Lunar cryptomaria I: Characteristics, distribution and implications for ancient volcanism, Icarus, *in prep*.

Whitten, J.L., Head, J.W, Denevi, B.W., Solomon, S.C., (2014) Intercrater and intermediate plains units on Mercury: Insights into unit definition, characterization and origin using MESSENGER datasets, Icarus, *submitted*.

Whitten, J.L. and Head, J.W., (2013) Detecting volcanic resurfacing of heavily cratered terrain: Flooding simulations on the Moon using Lunar Orbiter Laser Altimeter (LOLA) data, *PSS* 85, 24–37, doi: 10.1016/j.pss.2013.05.013.

Cheek, L., Donaldson Hanna, K., Pieters, C.M., Head, J.W., and **Whitten, J.L**. (2013) The Distribution and Purity of Anorthosite across the Orientale Basin: New Perspectives from Moon Mineralogy Mapper Data, *J. Geophys. Res*. 118, doi: 10.1002/jgre.20126.

Denevi, B.W., Ernst, C.M., Meyer, H.M., Robinson, M.S., Murchie, S.L., **Whitten, J.L.**, Head, J.W., Watters, T.R., Solomon, S.C., Ostrach, L.R., Chapman, C.R., Byrne, P.K., Klimczak, C., and Peplowski, P.N., (2013) The distribution and origin of smooth plains on Mercury, *J. Geophys. Res*. 118, doi: 10.1002/jgre.20075.

Head, J.W., Chapman, C.R., Strom, R.G., Fassett, C.I., Denevi, B.W., Blewett, D.T., Ernst, C.M., Watters, T.R., Solomon, S.C., Murchie, S.L., Prockter, L.M., Chabot, N.L., Gillis-Davis, J.J., **Whitten, J.L.**, Goudge, T. A., Baker, D.M.H., Hurwitz, D.M., Ostrach, L.R., Xiao, Z., Merline, W.J., Kerber, L., Dickson, J.L., Oberst, J., Byrne, P.K., Klimczak, C. and L.R. Nittler, (2011) Flood Volcanism in the Northern High Latitudes of Mercury Revealed by MESSENGER, *Science 333*, 1853−1856, doi: 10.1126/science.1211997.

Whitten, J.L., Head, J.W., Staid, M.I., Pieters, C.M., Mustard, J.F., Clark, R., Nettles, J., Klima, R.L. and L.A. Taylor (2011) Lunar mare deposits associated with the Orientale impact basin: New insights into mineralogy, history, mode of emplacement, and relation to Orientale Basin evolution from Moon Mineralogy Mapper (M3) data from Chandrayaan-1, *Journal Geophys. Res. 116*, E00G09, doi:10.1029/2010JE003736.

Pieters, C.M., Besse, S., Boardman, J., Buratti, B., Cheek, L., Clark, R.N., Combe, J.-P., Dhingra, D., Goswami, J.N., Green, R.O., Head, J.W., Isaacson, P., Klima, R. L., Kramer, G., Lundeen, S., Malaret, E., McCord, T., Mustard, J., Nettles, J., Petro, N. C. Runyon, C., Staid, M.I., Sunshine, J., Taylor, L.A., Thaisen, K., S. Tompkins, **Whitten, J.L.** (2011) Mg-spinel lithology: A new rock type on the lunar farside, *Journal Geophys. Res. 116*, E00G08, doi:10.1029/2010JE003727.

SELECTED PRESENTATIONS AND PUBLISHED ABSTRACTS

INVITED TALKS

Brown Annual Fund Volunteer Summit, October 2013.
Title: Early Volcanism on Terrestrial Planets

International Space Development Conference, May 2013.
Title: Exploration of Lunar Volcanic Terrains: Doing Apollo Sorties with Today's Instrumentation

FIRST-AUTHORED ABSTRACTS

Whitten, J.L., Head, J.W., (2013) Determining the mineralogy of mare and cryptomare basalts: Application of the Modified Gaussian Model (MGM) to Moon Mineralogy Mapper (M^3) spectra, Lunar Sci. Forum 2013.

Whitten, J.L., Head, J.W., (2013) Ancient lunar mare volcanism: Identification, distribution, and composition of cryptomare deposits, Lunar and Planetary Science Conference XLIV, abstract 1247.

Whitten, J.L., Head, J.W., Pieters, C.M., Vaughan, W.M., (2013) Mafic anomaly in Ptolemaeus crater, Lunar and Planetary Science Conference XLIV, abstract 2461.

Whitten, J.L., Head, J.W., Zuber, M.T., Smith, D.E. and G.A. Neumann (2012) Lunar light plains and cryptomare: Analysis of compositions and distribution of early volcanic deposits, Lunar Sci. Forum 2012, abstract 592.

Whitten, J.L., J.W. Head, G.A. Neumann, M.T. Zuber and D.E. Smith (2012), Volcanic flooding experiments in impact basins and heavily cratered terrain using LOLA data: Patterns of resurfacing and crater loss, Lunar and Planetary Science Conference XLIII, abstract 1470.

Whitten, J.L., J.W. Head, S.L. Murchie, D.T. Blewett, B.W. Denevi, G.A. Neumann, M.T. Zuber, D.E. Smith and S.C. Solomon (2012), Intercrater plains on Mercury: Topographic assessment with MESSENGER data, Lunar and Planetary Science Conference XLIII, abstract 1479.

Whitten, J.L., and J.W. Head (2011) Relationship between basin formation and mare emplacement: Examining mare basalt deposits in the lunar Orientale basin, AGU 2011 Conference, abstract P31E–1734.

Whitten, J.L., Head, J.W., Zuber, M.T., Smith, D.E. and G.A. Neumann (2011) Volcanic Resurfacing of Heavily Cratered Terrain: Flooding Experiments on the Moon using Lunar Orbiter Laser Altimeter (LOLA) Data, Lunar Sci. Forum 2011, abstract 360.

Whitten, J.L., Head, J.W., Pieters, C.M., Mustard, J.F., and M^3 Team (2011) Maunder and Kopff craters: Windows into the upper lunar crust, Lunar and Planetary Science Conference XLII, abstract 2168.

Whitten, J.L., Head, J.W., Staid, M.I., Pieters, C.M., and M^3 Team (2011) Volcanism in the Orientale Basin: A comparison to other nearside basins, Lunar and Planetary Science Conference XLII, abstract 2245.

Whitten, J.L. and G. Hancock (2010), Using summit erosion rates measured with ^{10}Be to assess landscape disequilibrium in the Blue Ridge, Shenandoah National Park, Virginia, GSA Northeast and Southeast Section Annual Joint Meeting.

Whitten, J.L., Head, J.W., Staid, M., Pieters, C., Mustard, J., Taylor, L., McCord, T., Isaacson, P., Klima, R., Nettles, J., and the M^3 team (2010), Characteristics, affinities and ages of volcanic deposits associated with the Orientale basin from Chandrayaan-1 Moon Mineralogy Mapper (M^3) data: Mare Stratigraphy, Lunar and Planetary Science Conference XLI, abstract 1841.

Whitten, J.L., Head. J.W., Pieters, C., Staid, M., and M^3 team (2009), Onset and evolution of volcanism in impact basins: Morphology and distribution of volcanic vents in the lunar Orientale basin from Moon Mineralogy Mapper (M^3) data, Brown University-Vernadsky Institute Microsymposium 50.

HONORS AND AWARDS

Rhode Island Space Grant Fellow
Brown University (Summer 2011–Summer 2012; Summer 2013)
U.S. Congressional Antarctic Service Medal, United States Antarctic Program (2012).
National Association of Geoscience Teachers Outstanding Teacher Award (2011)
Phi Beta Kappa Member
The College of William and Mary (2008–present)
Chappell Research Fellowship
The College of William and Mary Research Fellowship (2008)
Dr. Ellen Stofan Research Scholarship
The College of William and Mary, Geology Dept. (2008)
VTCA/ACPA/VDOT Highway Workers' Memorial Scholar, merit scholarship (2007)

TEACHING AND OUTREACH

Sheridan Center Teaching Certificate Programs, Brown University
Certificate I: Sheridan Teaching Seminar- Reflective Teaching (2009–2010)
Certificate III: The Professional Development Seminar (2013–2014)
Certificate IV: The Teaching Consultant Program (2012–2013)
Volunteer counselor
RI Natural History Museum Space and Science Camp (Summer 2013)
Instructor
Brown University SPARK program, Providence, RI (July 2012)
Science volunteer
Vartan Gregorian Elementary School, 2nd grade science lessons (2010–present)
Teaching Assistant, Brown University (Fall 2010)
GEOL 0050: Introduction to the Geology of the Solar System.
Instructor: James Head.

PROFESSIONAL MEMBERSHIPS

Sigma Gamma Epsilon (2008–present)
Geological Society of America (2010–present)
American Geophysical Union (2011–present)
Association for Women Geoscientists (2011–present)
American Society of Civil Engineers (2014–present)

ACKNOWLEDGEMENTS

It is amazing (and overwhelming) to know that 5 years has gone by so quickly. Graduate school has been an incredible growing experience for me academically, professionally, and personally. There are many people who provided love, advice, encouragement, support, friendship, and a little bit of pressure to get me to this point.

I would like to start by thanking the professors from the Department of Geology at the College of William and Mary, because without them I would not be at Brown University pursuing a PhD. Brent Owens, Heather Macdonald, Rowan Lockwood, Chuck Bailey, and most especially Greg Hancock introduced me to the wonders of geology. It was in Greg Hancock's Surface Processes: Landscapes and Water class during a discussion of mass wasting processes that I was first introduced to planetary science. Not only did Greg introduce me to planetary science, but he was also my undergraduate thesis advisor who trusted me with hydrofluoric acid and patiently taught me how to measure isotope concentrations in rocks collected from bare bedrock summits in Shenandoah National Park.

While at Brown, I received an invaluable amount of mentoring and support from my committee members. A thank you goes to Paul Hess for constantly pushing me to think about what my spectroscopic observations reveal about lunar petrology and for thinking about volcanism on Mercury. I would like to extend a special thanks to Carlé Pieters for taking a chance on a first year graduate student and allowing me to participate on the Moon Mineralogy Mapper team. I learned so much about spectroscopy, but even more about how a mission science team works. To the rest of the professors in the department, thank you for your support the last 5 years.

I owe my advisor Jim Head a very special thank you for ushering me through graduate school. His enthusiasm for planetary science is contagious and I am happy to have had the opportunity to work with him. Jim, thank you for introducing me to the idea of comparative planetology, for giving me push when I needed it, for reining me in when I tried to take the data a little too far, and for your support and encouragement. Thank for all of the opportunities you provided me, such as going to Russia, Antarctica, and participating on the M^3 and MESSENGER science teams; these experiences have all allowed me to grow both personally and professionally. Your efforts to teach me more than just planetary science have not been lost and are much appreciated.

Thank you to the administrative staff in GeoChem and in Lincoln Field buildings (especially to Pat Davey, Lisa Noble, Anne Côté, Janet Eager, and Nancy Christy) for keeping this department working like a well-oiled machine. You all allow us to spend our time thinking about science. Without your tireless efforts I would undoubtly have missed a deadline or forgotten my poster tube in the Atlanta airport. A big thanks goes to Jeff Nettles for entertaining all of my questions about M3Tools, teaching me the ins and outs of ENVI and also for buying me a new mouse when mine went crazy and kept jumping into the corner. None of my paper figures, PowerPoint presentations, or posters would look nearly as beautiful as they do today if it were not for Jay Dickson. Over the years Jay taught me how to use Adobe Illustrator (with great success), ISIS (with some success), Photoshop (with limited success), and was always happy to entertain my deceptively simple ArcMap questions. I cannot thank you enough for all of your help over the years.

I would like to thank the graduate students of years past and present. When I first got to Brown Jim's research group included Sam Schon, Laura Kerber, Seth Kadish, Debra Hurwitz, David Hollibaugh-Baker, Alish Kress, Mark Salvatore, and Brandon Boldt, all of whom provided me with valuable support or advice over the years. Since my arrival at Brown Tim Goudge, Kat Scanlon, Lauren Jozwiak, Will Vaughan, David Weiss, James Cassanelli, and Erica Jawin have joined Jim's research group. I wish you all the best of luck in the rest of your journey through graduate school. A special thanks to Lillian Ostrach, Angela Stickle, Leah Cheek, Rebecca Greenberger, and Kerri Donaldson-Hanna for your friendship, GIF-filled e-mails, advice, edits, time, energy, cookies, and especially your cheerleading skills. Thank you goes to the members of my "thesis support group", Diane Wetzel and Julia MacDougall, for listening and providing encouragement during my ups and downs this last semester. To Mary Peterson, my roommate of three years, thank you for listening to me when I needed to talk a problem or concern out, and for watching Heavy Weights with me when I didn't.

I want to extend a special thank you to Colin Jackson. Your curious nature and willingness to discuss and understand planetary science has helped to improve my own understanding and inspire me to approach questions from a different point of view. Thank you for your love and support over the last four and a half years.

Not only have I been fortunate to have an incredible support system at Brown, but I have incredible friends from high school and college across the country. Thank you to the ladies of 903 (SarahKing, Kala, Mattie, Becca, Molly) and Jeffrey Lesky for our epic journey at William and Mary, incredible trips, for keeping me (pop) culturally aware (wobble wobble). I would like to thank Jessie Milom for always being able to pick up our

friendship right where we left off, even if it has been over a year since I last saw you. Alisa, you are the yin to my yang. Who knew that the alphabet would have such a monumental effect on our lives in second grade? Your friendship is invaluable to me. To my “fairy godmothers” (and fellow “godchildren”), your love and support means the world to me. Thank you for always being there.

I would like to take this opportunity to thank my parents, Donald and Barbara, and my younger sister Christine. Thank you for providing me with every opportunity to succeed, for being proud of me, and for telling me that I can do whatever I want. Thank you for telling me to stop doing homework and go play outside. Christine, thank you for showing me that I am not the only nerd in the family and that it is never too late to pursue your interests. Mom, Dad, Christine, your unfailing support throughout my entire life has allowed me to pursue my passions with confidence and I cannot thank you enough.

PREFACE

Geology entails the study of planetary bodies and the rocks that comprise them. Typically, the word geologist conjures images of a person hiking around outside with a rock hammer and Brunton compass in hand. However, the study of geology is not confined to Earth; many of the other planetary bodies in our solar system contain rocky surfaces as well. In order to study these other planetary bodies, a geologist must trade their rock hammer for a satellite and their Brunton compass for a computer. While we still do not understand everything about our own planet, it is important to look away from Earth to see what the other planetary bodies reveal about geologic processes in our solar system.

Volcanism is observed on all of the terrestrial planetary bodies (Mercury, Venus, Earth, the Moon, Mars, and even on the Jovian satellite Io). Volcanologic processes are expressed differently on each planet, providing unique information about the thermal evolution of a particular body. Ancient volcanic deposits on terrestrial planetary bodies preserve a record of the early stages of planetary evolution, revealing important information about both the interior evolution and the surface modification history of planetary bodies. The work presented in this dissertation has mapped ancient volcanic deposits on the Moon and Mercury and measured their physical characteristics using remote orbital datasets to understand better the distribution and flux of volcanic materials onto these planetary surfaces.

The first chapter of this dissertation focuses on characterizing how volcanic flows fill heavily cratered terrain using the latest available high-resolution Lunar Orbiter Laser Altimeter topography data. Volcanic eruptions were simulated in three different, yet

heavily cratered, geologic settings: Hertzsprung basin, the lunar central highlands, and the most heavily cratered terrain on the Moon. The burial rate of impact craters was recorded as each study area was filled with lava flows in order to understand the evolution of a crater size-frequency distribution with increased volcanic resurfacing. The results show that the shape of a crater size-frequency distribution can provide information about the pre-lava flow topography. Areal extents and map patterns can also be used to predict the volcanic deposit thickness. Additionally, this investigation into the morphologic expression of volcanism in cratered terrains indicates that the paucity of craters <64 km in diameter in the South Pole-Aitken basin can be attributed to ancient lava flows concentrated in the center of the impact basin.

The second chapter makes use of the expected morphologies for ancient volcanic deposits from the previous chapter and the latest available lunar datasets to establish the criteria necessary to distinguish obscured lunar lava flows, known as cryptomaria, from basin ejecta deposits. Eighteen regions of cryptomaria were identified and, similar to the exposed lunar mare basalts, generally cluster on the nearside with the largest deposits associated with ancient impact basins. The mapped cryptomaria increase the extent of known volcanic deposits on the Moon from ~16% to ~18% of the total surface area. A survey of the lunar farside indicates a dearth of extrusive volcanic deposits, but hydrostatic modeling suggests that mare basalts could be buried beneath a veneer of impact basin ejecta in at least one farside basin; this indicates that there could have been more volcanic eruptions across the entire lunar surface than are currently observable with available datasets.

The third chapter explores the mineralogy and composition of the identified cryptomaria to determine whether these deposits are, in fact, composed of mare basalts. Mineralogic modeling was combined with elemental analyses to assess which of the early igneous rocks could comprise cryptomare deposits. Visible to near-infrared spectra of cryptomare and exposed mare basalts from the same region overlap and are both consistent with a clinopyroxene mineralogy. The results of mineralogic modeling and compositional analyses of thorium and iron abundances indicate that the mapped cryptomare are mare basalts.

The fourth chapter focuses on identifying ancient volcanic deposits on Mercury. The Moon offered an excellent laboratory to study ancient volcanics on a planetary surface with distinct mineralogic and albedo variations, features that are lacking on Mercury. Application of the criteria and techniques developed in Chapter 2 was a useful starting place for identifying ancient volcanic deposits on Mercury. This chapter focuses on understanding the origin of the intercrater plains and determining whether the unit is dominated by basin impact deposits or volcanic processes. Ten areas from the Mariner 10 geologic maps were evaluated using MErcury Surface, Space ENvionment, GEochemistry, and Ranging (MESSENGER) data to re-characterize the intercrater plains. A geologic map covering approximately 20% of the surface was produced to understand the distribution of the intercrater plains and its relationship to younger crater ejecta deposits and smooth plains deposits. Analysis of the stratigraphic relationships between these three geomorphic units, especially the young fresh craters and smooth plains deposits, and evaluation of the basin impact ejecta origin led to the conclusion that the intercrater plains are probably dominated by volcanic processes.

The fifth chapter takes a detailed look at plains deposits on Mercury around the Rembrandt impact basin. The origin of plains within and especially around the Rembrandt basin was evaluated using available MESSENGER data. Impact scaling models suggest that basins on Mercury should produce more impact melt than lunar basins. However, little evidence of extensive impact melt deposits has been found on Mercury. The physical characteristics of the Rembrandt interior smooth plains are consistent with a volcanic origin. Evaluation of the ages, color properties, and distribution of the majority of circum-Rembrandt plains indicate that the low-albedo exterior plains are dominantly impact melt produced during the basin-formation event.

The sixth and final chapter synthesizes the results of the previous chapters, discussing how the observed lunar cryptomaria and mercurian intercrater plains correspond with the expected production of early volcanic deposits on the Moon and Mercury. A few outstanding questions related to ancient volcanic deposits are examined in some detail. The dissertation ends with an analysis of four potential landing sites, two on Mercury and two on the Moon, that would provide invaluable information about the volcanic history of these two terrestrial planetary bodies.

TABLE OF CONTENTS

Chapter 1:
Detecting volcanic resurfacing of heavily cratered terrain: Flooding simulations on the Moon using Lunar Orbiter Laser Altimeter (LOLA) data

Jennifer L. Whitten
and
James W. Head III

Department of Geological Sciences, Brown University,
324 Brook St., Box 1846, Providence, RI 02912.

Published in:
Planetary and Space Science, Vol. 85, 24-37,
doi: 10.1016/j.pss.2013.05.013 (2013)

Abstract

Early extrusive volcanism from mantle melting marks the transition from primary to secondary crust formation. Detection of secondary crust is often obscured by the high impact flux early in solar system history. To recognize the relationship between heavily cratered terrain and volcanic resurfacing, this study documents how volcanic resurfacing alters the impact cratering record and models the thickness, area, and volume of volcanic flood deposits. Lunar Orbiter Laser Altimeter (LOLA) data are used to analyze three different regions of the lunar highlands: the Hertzsprung basin; a farside heavily cratered region; and the central highlands. Lunar mare emplacement style is assumed to be similar to that of terrestrial flood basalts, involving large volumes of material extruded from dike-fed fissures over relatively short periods of time. Thus, each region was flooded at 0.5 km elevation intervals to simulate such volcanic flooding and to assess areal patterns, thickness, volumes, and emplacement history. These simulations show three primary stages of volcanic flooding: 1) Initial flooding is largely confined to individual craters and deposits are thick and localized; 2) Basalt flows breach crater rim crests and are emplaced laterally between larger craters as thin widespread deposits; and 3) Lateral spreading decreases in response to regional topographic variations and the deposits thicken and bury intermediate-sized and larger craters. Application of these techniques to the South Pole-Aitken basin shows that emplacement of ~1-2 km of cryptomaria can potentially explain the paucity of craters 20-64 km in diameter on the floor of the basin relative to the distribution in the surrounding highlands.

1. Introduction and Background

All of the terrestrial planets have experienced large-scale volcanic resurfacing at some time during their long histories (Head and Coffin, 1997). Mercury is extensively covered with smooth plains thought to be of volcanic origin (Strom et al., 1975), including those found within and around the Caloris basin (e.g., Kiefer and Murray, 1987; Murchie et al., 2008) and in the north polar region (Head et al., 2011). Almost the entire surface of Venus is thought to have been volcanically resurfaced within the last ~300-500 million years (e.g., Phillips et al., 1992; Strom et al., 1994; Ivanov and Head, 2011), and the Earth abounds with examples of large-scale volcanic eruptions, including Large Igneous Provinces (LIPs) like the Deccan Traps and continental flood basalts like the Columbia River Basalts (e.g., Coffin and Eldholm, 1994). Examples of large-scale volcanic activity on the Moon and Mars include the mare deposits in lunar basins (e.g., DeHon, 1979; Yingst and Head, 1997; Whitten et al., 2011) and the Hesperian ridged plains on Mars (e.g., Scott and Tanaka, 1986; Watters, 1993; Head et al., 2006).

As indicated by layering in the Deccan Traps, these flood basalt deposits are the result of prolonged volcanic eruptions that can take place over millions of years and include multiple eruptions (e.g., Mahoney, 1988; Tolan et al., 1989). Lengthy eruption time scales allow flood basalt deposits to attain total volumes on the order of 10^6 km^3, based on lunar and terrestrial estimates (Coffin and Eldholm, 1994; Head and Coffin, 1997). Individual flow lengths for deposits associated with flood basalts can exceed 600 km (Schaber, 1973; Coffin and Eldholm, 1994; Zimbelman, 1998). On Earth flood basalt deposits are thought to result from fissure eruptions fed by large convecting mantle plumes in the Earth's interior (e.g., Wilson, 1963; Morgan, 1971, 1981). The specific

mechanism controlling the eruption of flood basalts on the other terrestrial planetary bodies, such as the Moon, is still a highly debated topic (e.g., Solomon and Head, 1980; Hess and Parmentier, 1995; Wieczorek and Phillips, 2000; Elkins-Tanton et al., 2004; Ghods and Arkani-Hamed, 2007; Whitten et al., 2011).

Taylor (1989) classified planetary crustal formation processes into three types: 1) primary crust in which the early crust is formed from the melting of the outer part of a planet by accretional energy; 2) secondary crust, formed by partial melting of the mantle subsequent to primary crust formation (e.g., the lunar maria, seafloor basalts, and volcanic plains on Mars); and 3) tertiary crust, formed from the reworking of primary and secondary crust (e.g., continental crust on Earth, impact melt). Particularly crucial to the understanding of the early thermal evolution of planets is the onset, timing and flux of secondary crustal formation. However, detection of early volcanic deposits that mark the transition from primary to secondary crust is often obscured by the high impact flux early in solar system history. To assist in the recognition and understanding of the relationship between heavily cratered terrain developed on a primary crust and volcanic resurfacing typical of secondary crustal formation, this study documents how volcanic resurfacing alters the impact cratering record and provides guidelines to measure the thickness, area, and volume of volcanic flood deposits.

Data from the Lunar Orbiter Laser Altimeter (LOLA) instrument (Smith et al., 2010; Zuber et al., 2010) aboard the Lunar Reconnaissance Orbiter (LRO) satellite (Vondrak et al., 2010) are used to simulate lava flooding for three different regions of primary crust, including the Hertzsprung basin, a farside heavily cratered region (FHC) and the central highlands (CH; Fig. 1). Artificial flooding experiments have previously

been used to investigate volumes and thickness of volcanic deposits (Greeley and Womer, 1981; Head, 1982; Howard, 1999) and have been found to be more accurate at estimating volumes than measurements of buried and partially buried craters (DeHon, 1974, 1979). In this analysis we begin to address planetary thermal evolution by understanding the effect of volcanic flooding on pre-existing terrains, providing insight into the behavior of flood basalts on terrestrial planets. Measurements of lava volumes necessary to cover pre-existing topography and alter crater size-frequency distributions (CSFDs) are recorded to understand how to identify ancient heavily cratered volcanic deposits. In this analysis we investigate whether or not a crater population can aid in identifying ancient volcanic deposits. The techniques and results developed from these simulations are then applied to the identification of early lunar volcanic deposits.

2. Methods

The heavily cratered primary lunar crust is dominated by four major topographic elements: 1) broad regional to hemispherical variations in topography thought to be related to differences in the thickness of the anorthositic crust (e.g., Zuber et al., 1994; Wieczorek et al., 2012); 2) multi-ring impact basins that produce broad, deep, circular depressions, and annular deposits sloping away from the basin rim crest (e.g., Wilhelms, 1987; Williams and Zuber, 1998); 3) 300-600 km diameter peak-ring basins (e.g., Baker et al., 2011), and 4) inter-basin areas that have accumulated significant numbers of complex and simple craters. In order to assess this range of topographic variation, we have chosen three test areas (Fig. 1) heavily modified by impact processes, including a degraded peak-ring impact basin (Hertzsprung; ~ 3.6 x 10^5 km^2), a region dominated by

the Nectaris multi-ring basin (FHC; ~ 3.3 x 10^5 km^2) and one of the most highly cratered surfaces on the Moon (CH; ~ 2.9 x 10^5 km^2; Head et al., 2010). The three regions chosen have approximately the same total area to allow for direct comparison of their simulated flood volumes, areas and CSFDs.

LOLA data (Zuber et al., 2010; Smith et al., 2010) are used to simulate volcanic flooding and measure areal extent and volumes in the three study areas using ESRI ArcMap GIS software. LOLA gridded topographic data with a resolution of 128 pixels/ degree were flooded in 0.5 km increments to measure areal extent, CSFD, and volume of the deposits. Craters 5-20 km in diameter (including secondaries) were mapped using LOLA data to supplement the Head et al. (2010) lunar crater catalog of craters >20 km diameter. The inclusion of secondaries does not influence our results because this study focuses on the influence of volcanism on heavily cratered terrains, not the age of the surfaces used for flooding simulations. Counted craters are from the original pre-flooding surface; no fresh craters that may have impacted onto the volcanic deposit syn- or post-emplacement have been added to the crater counts.

The 100 m/pixel Lunar Reconnaissance Orbiter Camera (LROC; Robinson et al., 2010) global mosaic was used to confirm the crater mapping. Craters near the boundary of a study area were counted only if the crater center was located within the defined study area. At each flood interval the craters that were not completely flooded were counted for the CSFD of that particular flood interval; a crater is considered completely flooded when its entire rim is buried by the flood material. As a result of this method, more heavily degraded craters are buried more rapidly than similarly-sized fresh craters. Crater statistic data were plotted using the CraterStats program (Michael and Neukum, 2010).

Simulated volcanic flooding source vents were assumed to be located at the lowest elevations, consistent with general principles of magma ascent and eruption (e.g., Head and Wilson, 1992). Even if natural source vents do occur at higher elevations, the mode of emplacement suggests that the lava flooding effectively fills the lowest topography first. Two different methods of flooding were employed (Fig. 2); one method assumed that source vents were ubiquitous throughout the study region (Fig. 2a) and the terrain was flooded to specific elevations (Head, 1982). The other method begins flooding from a single source at the lowest elevation (Fig. 2b) and continues to flood terrain continuously at increasing elevations. When a crater rim is breached, the surrounding terrain is also flooded to that prescribed elevation (Fig. 2b), resulting in large increases in deposit area and thickness. Flood Landscape Analyst, an ArcMap extension written by Dongquan Zhao in 2005 (Tsinghua University, Beijing, available at http://www.esri.com/apps/products/download/) was used to simulate flooding from a single point source, calculating area and volume below the flood surface. These flooding simulations model an endmember situation where the crater locations are known pre-burial.

3. Results

3.1 Hertzsprung basin

Hertzsprung is a Nectarian aged peak-ring basin approximately 570 km in diameter (Wilhelms, 1987; Fassett et al., 2012) and located at 2.53º N, 128.99º W (Fig. 1a). This degraded basin is influenced by secondary clusters and chains, especially just inside the basin rim, from the Imbrian-aged Orientale impact basin (e.g., Wilhelms, 1987;

Whitten et al., 2011) to the southeast. In addition to the rim crest, Hertzsprung has one well-preserved basin ring (Baker et al., 2011), containing relatively unmodified smooth plains deposits on its floor.

Of the three study areas Hertzsprung has the largest range of relief (~ 10.7 km), from -1.4 km to +9.3 km (Fig. 3). Ubiquitous volcanic filling (Fig. 2a) initiates in the small deep craters on the basin floor (Fig. 3a). At first, deposit thickness increases while the areal extent remains small. Continued flooding of Hertzsprung results in the spread of volcanic deposits between the basin rings (Fig. 3b), increasing the deposit thickness and area (Fig. 6a). The high basin rim prevents large breaching events from occurring during most of the simulated flooding (Fig. 3c). However, eventually several small breaching events do occur along the basin rim (Fig. 3d) near more degraded parts of the basin rim and within superposed craters. Hertzsprung was also flooded using the second method, starting from the lowest elevation in the basin center (Fig. 2b, 3e); this was designed to simulate flooding of a basin from the most likely location of volcanic emplacement (Head and Wilson, 1992). Breaching of the interior basin ring and the basin rim permitted flood material to flow into the surrounding landscape (Fig. 3g, h). The evolution of the areal extent of volcanic flood material does not differ significantly between the ubiquitous and point source flooding models (Fig. 3a-d, e-h).

3.2 Farside heavily cratered region

The second study region is centered at 34.86º N, 153.39º W (Fig. 1c), encompasses the most heavily cratered terrain on the lunar surface (Head et al., 2010), and has a north-south regional slope, dipping towards the north pole (Fig. 1a). Many of

the craters in this region, both large and small, have flat floors and shallow depths, suggesting they have been partially filled with material, either impact-related deposits or volcanic flooding.

The FHC region (Fig. 1c) was first flooded ubiquitously with volcanic material over ~9.8 km of elevation, starting at -2.4 km elevation and filling to +7.4 km (Fig. 4). The north-south regional slope in this study area controlled the location and growth of the volcanic flood deposit. Flood simulations began in the deepest craters, and while the thickness increased the limited areal extent of the deep craters resulted in little increase in area (Fig. 6b). As the individual craters were filled "intercrater" plains formed, concentrating in the north (Fig. 4b, c). With continued flooding, the volcanic deposit spread further and further south, corresponding to higher elevations (Fig. 4c, d).

The FHC was also flooded from its deepest crater, Fowler (~145 km diameter; Fig. 4e) using the point source flooding method (Fig. 2b). In this simulated flooding model the emplacement of "intercrater" plains is much more abrupt, occurring in several stochastic areally extensive steps instead of the plains growing from small deposits and coalescing into larger continuous deposits (Fig. 6b). However, after the formation of "intercrater" plains the simulated deposits for the two flooding models evolve almost identically (Fig. 4c, d, g, h).

3.3 Nearside Central Highlands

The third study region (24.95º S, 12.99º E) contains part of the nearside central highlands (Fig. 1d) and is located in a region of high-standing topography on the lunar nearside, bordering the western edge of Nectaris basin (Fig. 1a). The inclusion of the

Nectaris basin outer rim results in a regional slope extending down from east to west. Here too there is an abundance of shallow flat-floored craters, many of which occur in the lowest lying areas of the study region. The overlap and degradation state results in coalescence of these craters into large irregular depressions. As is the case for the Orientale basin, the emplacement and ponding of impact ejecta at these radial ranges from the basin rim crest would readily serve to modify, degrade and fill these craters (e.g., Fassett et al., 2011).

In the CH study region, the total amount of relief is ~8.5 km (from -3.6 to 4.8 km; Fig. 5), the smallest range of the three study regions selected for analysis. This is likely due to the smoothing and burial effects associated with the emplacement of Nectaris basin ejecta (e.g., Fassett et al., 2011, 2012). As a result of the regional slope, the general pattern of filling moves from west to east (Fig. 5). Volcanic filling originates in the large, shallow, flat-floored craters in the region (Fig. 4a, 5a), whose morphology allows for a rapid increase in the deposit area (Fig. 6b, c). Gemma Frisius (~88 km diameter) was selected as the point source for the second flooding model (white dashed circle in Fig. 5e) because of its low elevation. Like the FHC terrain, the simulated deposits for the two flooding models evolve almost identically (Fig. 5b and f), especially after the formation of the “intercrater plains” (Fig. 5c, d, g, h).

4. Discussion

4.1 Simulated flooding measurements

Analysis of the areas (Fig. 6), volumes (Fig. 7), and CSFDs (Fig. 8) produced strikingly similar results irrespective of the flooding method used and study region

geometry. The total volume of volcanic material required to completely flood (from lowest to highest elevation) each of the study regions is on the order of 1.5-2.2 x 10^6 km^3 (Fig. 7) and total deposit thicknesses are between 8.5 and 11 km (Fig. 6, 7). The evolution of deposit area and volume with continued flooding was similar for both flooding models (Fig. 6, 7). The most significant variation occurs in the first eleven 0.5 km flooding intervals; initial point source flooding area and volume measurements stay relatively constant until the source crater is breached, at which point there is a sharp turn in the graphs (Fig. 6, 7), indicating rapidly increasing area (Fig. 6) and steadily increasing deposit volume (Fig. 7). This is expressed morphologically as lateral spreading and formation of "intercrater" plains (Fig. 3-5). The slope of the thickness and volume graphs differs between the Hertzsprung basin region and FHC and CH. The latter two have shallower slopes following the breaching event because their topography (Fig. 3- 5) is dominated by gently sloping terrain punctuated by impact craters; this geometry allows small increases in unit thickness to correspond to large increases in volume compared with Hertzsprung. In contrast, Hertzsprung basin is a large singular depression that limits the areal extent of flood deposits for a given increase in thickness.

The type of flooding simulation can influence the evolution of area and volume with increasing deposit thickness. Flooding by thickness intervals (0.5 km) produces large increases in measured area and volume in the point source flooding model. When flooding by a standard thickness interval the area and volume depend on the geometry of the topography flooded. For instance, in the point source model the only difference in the volume or area with unit thickness (Fig. 6, 7) occurs immediately after the source crater is breached when "intercrater" plains begin to develop. In the point source simulation, the

formation of “intercrater” plains occurs more abruptly because of the number and distribution of the sources. Once a certain elevation is reached all terrain in the study region below that interval is buried.

Changes in the impact CSFD as a function of the systematic flooding of each area at each interval are recorded as well. All craters >8 km were plotted in cumulative crater frequency graphs with the top (red) line in each plot representing the CSFD prior to flooding (Fig. 8). None of the CSFDs show evidence of obvious kinks (e.g., Neukum and Horn, 1976; Hiesinger et al., 2002) in the graphs because large scale resurfacing did not occur after the formation of these study areas. At the onset of simulated volcanic flooding the smallest craters are buried, which shallows the slope of the CSFD in the lowest diameter bins (Fig. 8, green). With continued volcanic activity, larger and larger craters are buried by the flood material, continuing to shallow the CSFD (Fig. 8, blue), until only a few large craters remain before complete burial.

In the Hertzsprung study region craters approximately 30-50 km in diameter are completely buried in both simulation models before all of the smallest craters (Fig. 8a and d) because many of these large craters are located on the basin floor instead of the basin exterior. Similar to the area and volume measurements, the FHC and the CH show differences in CSFDs between the two flooding simulations and Hertzsprung does not. The primary difference between the evolution of the ubiquitous and point source CSFDs for the FHC (Fig. 8b, e) and CH (Fig. 8c, f) terrains is the rate of disappearance of craters ≤20 km diameter. In the point source simulation (Fig. 8e, f) the loss of small craters does not become significant until the source crater rim is breached and “intercrater” plains

begin to form (Fig. 4e). After this event, the evolution of the CSFD shape remains almost identical in both flooding models (Fig. 8).

The geometry of the topography in a given study region can also affect the evolution of the CSFD. Compared with the other two study regions the CSFD for the CH region (Fig. 8c) shows a rapid loss of large craters, causing the collapse of the CSFD instead of just a flattening of the curve. This phenomenon can also be observed to a degree in the farside heavily cratered terrain CSFDs. It is likely that a combination of the regional slope and abundance of shallow flat-floored craters in the study area (Fig. 1c) allows craters of all sizes to be buried at similar rates. For instance, on a sloped, heavily cratered surface experiencing volcanic activity a large crater at the lowest elevations will be buried before a small crater at the highest elevations. With continued volcanic eruptions more material will be deposited, increasing unit thickness and allowing the edge of the unit to migrate upslope. In contrast, if the region were originally flat, smaller craters would be buried before larger craters because of their shallower depths and lower topographic relief.

Hiesinger et al. (2002) estimated the volumes of individual eruptive events on the Moon to be between 30 and 7700 km^3, with an average of ~775 km^3. Taking a total deposit volume and dividing it by these estimated flow volumes provides a frame-of-reference estimate of the number of individual eruptive events of this size. These lunar values suggest that 1500- 3000 individual eruptive events would be involved in the complete flooding of each of the three study regions. The Columbia River Basalt Group is estimated to have >300 individual lava flows and a total volume of ~10^5 km^3 (Tolan et al., 1989). The size of the Columbia River Basalt Group is an order of magnitude smaller

than our three study regions, suggesting that our larger flood volumes were emplaced by several thousand individual lava flows. Additionally, the total volume in each of these study areas (1.4- 2.1 x 10^6 km^3) is equivalent to approximately one-half of all the lunar mare basalt deposits which suggests that most regions are never fully flooded. This incomplete flooding is supported by the exposure of basin rims and crater central peaks in volcanically flooded regions.

The flooding simulations conducted in this study are helpful for understanding the relationship between volcanism and impact cratering. However, other variables need to be taken into consideration when applying the results of these simulations, such as the timing of the volcanic emplacement event. Early in lunar history interior temperatures were elevated and the thermal gradient was relatively large (e.g., Shearer et al., 2006), resulting in a thinner lithosphere, which would favor more efficient viscous relaxation of long wavelength topography, like large impact craters and basins (Solomon et al., 1982). Over time, for an impact occurring in a thin lithosphere, the crater would decrease in total relief as the longer wavelength topography relaxed. If volcanic deposit emplacement occurred early in lunar history such that initial crater and basin landforms were affected by viscous relaxation, then these experimental volume estimates should be considered maximum values. The modeled surfaces used in this study have preserved the most recent impact craters, produced during the later stages of early lunar thermal evolution and therefore are less likely to have undergone viscous relaxation than craters formed earlier (Solomon et al., 1982). Additionally, volcanic loads emplaced in craters in a thinner lithosphere might be expected to subside more rapidly than those craters flooded in a thicker lithosphere, making craters appear less filled.

4.2 Observed stages in flooding simulations

These flooding simulations serve as an effective tool for visualizing and understanding the thickness and volumes of volcanic material emplaced on planetary surfaces. Their utility is enhanced by the plethora of lunar data being collected and their ever-increasing resolution. Previous work analyzing the emplacement of large volumes of volcanic material on planetary surfaces (Head, 1982) relied on limb profiles and lower resolution stereo photogrammetry. From this initial work, two major stages of filling were identified. First, large quantities of volcanic material are emplaced in a confined localized area, such as a basin. The geometry of these regions leads to deposits that increase more rapidly in thicknesses than in surface area. In the second stage of filling, the inner depression or crater is breached and thin areally extensive deposits are emplaced (Head, 1982). However, from our flooding simulations presented here more detailed trends in filling can be discerned.

Stage 1 of volcanic filling is confined to larger individual craters (≥40 km) or basin floors. Volcanic material is likely to erupt in these locations because they typically represent some of the lowest elevations and thinnest crust in a given region (Head and Wilson, 1992). Deposits emplaced in this stage of flooding are up to several kilometers thick and maintain small areal extents, a result of their confinement in craters. Stage 1 flooding will continue until the source crater(s) are filled to the rim with volcanic material (Fig. 4a, e and 5a, e). Craters whose interiors are higher than their surroundings (e.g., Wargentin, Plato, Posidonius and Cassini craters) would result if volcanic flooding ceased before crater rim crests were breached at the end of stage 1.

The second stage of flooding initiates when source region crater rims are breached. After the breaching event volcanic material is emplaced laterally around and between larger craters, ≥40 km diameter, creating an "intercrater" plains unit (Fig. 4b, c, f, g and 5b, c, f, g). Stage 2 volcanic deposits are characteristically thinner than stage 1 deposits and, instead of being dominated by vertical growth, stage 2 deposits increase rapidly in surface area (Fig. 6). This stage differs only slightly between the two different flooding methods (ubiquitous and point source). In the ubiquitous model the formation of "intercrater" plains can begin as separate small patches of volcanic material, eventually coalescing into a larger plains unit. Conversely, in the point source model "intercrater" plains units are formed almost instantaneously as large continuous deposits.

Stage 3 is characterized by more areally extensive deposits as crater rims are buried and flow units coalesce (Fig. 4d, h and 5d, h). Volcanic material has covered almost the entire study region and the deposit begins to thicken, burying intermediate- and larger-sized craters. The decrease in lateral movement is in part an edge-effect dictated by the size of the area selected, but can also be attributed to containment within a basin or topographic low. In our models, stage 3 flooding accounted for 76- 89% of the total volume of material emplaced.

In certain circumstances stages 2 and 3 can occur simultaneously. For example, in sloped regions (FHC and CH; Fig. 4, 5) the low elevation areas will begin to experience stage 3, involving increased deposit thickness, before higher elevation areas in the study region. It is important to note that these simulations do not account for the production of new craters on the volcanic surfaces that would occur in a natural system. If the emplacement period is prolonged, the natural lunar volcanic deposits might appear more

similar to a mixture of stages 2 and 3 (Fig. 4b, c, f, g and 5b, c, f, g), having impact craters in various states of burial distributed across the volcanic surface. The exact morphology of the volcanic surface will depend on its age and the flux of volcanic material at that time.

The evolution of the stages of volcanic flooding differs slightly between impact basin interiors and other highly cratered terrains. In the Hertzsprung basin flooding simulations, stage 1 (Fig. 3a, e) follows the same pattern as the other two study regions. Stage 2 (Fig. 3b, f) is also similar until basin topography prevents lateral expansion and, instead, begins to produce vertical accumulation (Fig. 3c, g). This increase in deposit thickness is akin to stage 1 and will continue until the basin rim elevation is reached (Fig. 3d, h). More flooding will breach the basin rim, similar again to stage 2, and emplace volcanic material onto the terrain exterior to the basin. Depending on the geometry of the surrounding landscape, the volcanic material may experience stage 3 and begin to increase deposit thickness. Therefore, the basin filling sequence includes the same stages of flooding observed elsewhere; stages 1 and 2 are repeated in basin settings, once at the volcanic source where lava floods the source area and the basin floor, and then again, as lava continues to fill the entire basin.

4.3 Flooding lunar terrain with predetermined volumes

Thus far we have investigated the behavior of large-scale volcanic eruptions based on two different methods of volcanic flooding. In order to make a more direct comparison with deposits observed on planetary bodies, the three study regions were flooded with the volume of volcanic material that has been estimated to form a large flow

from the Columbia River flood basalts (2093 km^3; Tolan et al., 1989), a large lunar flow unit (7700 km^3; Hiesinger et al., 2002) and the entire Columbia River flood basalt system (174,356 km^3; CRFB) using the two flooding methods outlined above. The first two volumes are more akin to single eruptive events whereas the CRFB volume represents all the material emplaced in an eruptive episode. Flooding these three lunar terrains with the volume of material in the CRFB deposit produces similar map patterns for both methods (Fig. 9g-i, 10g-i), especially for the Hertzsprung basin (Fig. 9g, 10g). However, some differences are observed; point source flooding in the FHC (Fig. 10b, e, h) and CH terrains (Fig. 10c, f, i) produces thicker, rather than areally more extensive, volcanic deposits because material is concentrated around the point source vent instead of being deposited throughout topographic lows in the region (Fig. 11).

The map patterns produced by the two different flooding methods differ most significantly for the lunar flow volumes (Fig. 9a-c, 10a-c) and the CRFB flow (Fig. 9d-f, 10d-f). Ubiquitous flooding with volumes of the CRFB flow and lunar flow produce deposits contained within multiple craters that excavate deep into the crust (Fig. 9a-f). Point source map patterns for the lunar and CRFB flow clearly illustrate how the volcanic material is emplaced close to the source region; the entire volume of flooded material is contained within a single large crater (Fig. 10b, c, e, f). These contiguous deposits are in stark contrast to the map patterns observed in the ubiquitous flooding examples where small volumes of volcanic material are deposited in craters and topographic lows throughout the study regions (Fig. 9b, c, e, f).

Comparing these derived map patterns with actual lunar mare deposits results in some striking similarities. The ubiquitous flooding simulations using the large lunar and

CRFB flow volumes produce volcanic map patterns similar to those observed in Mare Australe (Fig. 12a, 9a-f). Multiple distinct mare ponds 0.5-1.1 km thick are produced from these simulated single volcanic eruptions. Mare deposit thicknesses estimated from superposed craters suggest values <1.3 km, assuming crater depth is $1/10^{th}$ crater diameter (Melosh, 1989). Mare Australe is a collection of small individual mare deposits contained in a basin structure and is most similar to the Hertzsprung ubiquitous flooding model using the large lunar flow volume (Fig. 9a), although based on our simulated map patterns, Australe was likely flooded with a greater volume of material. When the Hertzsprung study region is flooded with a volume equivalent to the entire CRFB deposit (~2.6 km total thickness), regardless of flooding method, the volcanic deposits resemble those mapped in Mare Moscoviense (Fig. 12b, 9g, 10g), with flood deposits in the basin center and between the inner ring and basin rim. Crater depth/ diameter relationships (Melosh, 1989) indicate that Mare Moscoviense has an average thickness of ~450 m. Previous measurements of flooded craters indicate Mare Moscoviense varies in thickness from ~100 m at its edges to 600 m near the center of the deposit (Morota et al., 2009). Flooding the FHC and CH terrains with a volume equivalent to the CRFBs produces map patterns similar to those observed along the western margin of Oceanus Procellarum, suggesting sloped surfaces with mare deposits between 0.7 and 1.7 km thick, locally reaching thicknesses of 6.1 km above the deepest craters (Fig. 12c, 9h-i, 10h-i). The largest craters within 100 km of the mare- highland boundary (between ~13°N and ~40°N) indicated thicknesses of <1.3 km.

Map patterns of the lunar and CRFB flow in the point source flooding simulation produce isolated volcanic deposits in large deep craters, similar to what is observed in

Campbell and Tsiolkovskiy craters on the Moon (Fig. 12d, e 10b, c, e, f). This pattern corresponds to early stages of flooding producing mare deposits on the order of 0.5- 2 km thick, depending on the crater dimensions. Thickness values can be further constrained by analysis of crater morphology. For instance, Tsiolkovskiy crater has not been filled extensively with mare lava, as evidenced by the visibility of wall terraces and the central peak (e.g., Wood, 1973). Based on our flooding simulations this morphology indicates volcanic filling <0.5 km thick. Measurements of impact crater diameters on the floor of Tsiolkovskiy indicate a mare thickness of at least ~200 m and previous estimates are ~100 m (Craddock and Greeley, 1987). The magnitude of thickness measurements determined from superposed craters is in agreement with our flooding simulations.

4.4 Applications

The results and techniques developed in this paper can be utilized in assessing many problems in planetary evolution. For example, the volcanic modification history of the lunar South Pole-Aitken (SPA) basin is highly uncertain. SPA is believed to be the oldest and largest basin on the Moon (e.g., Wilhelms et al., 1979; Wilhelms, 1987; Garrick-Bethell and Zuber, 2009). Due to its age, the basin has been heavily modified with superposed impact basins, mare basalts, basin ejecta, and smooth light plains material. Based on iron and titanium abundances (e.g., Pieters et al., 2001; Gibson et al., 2011; Petro et al., 2011), these smooth light plains are believed to be a combination of cryptomare deposits and basin ejecta deposits. Most of the mare basalt deposits within SPA are located in the superposed impact basins (e.g., Apollo and Poincaré; Fig. 13a) and surrounding topographic lows (e.g., Yingst and Head, 1997; Pieters et al., 2001). The

basin as a whole has a superposed crater density at large diameters that is indicative of its ancient age (e.g., Stuart-Alexander, 1978; Hiesinger et al., 2012). However, the basin interior is deficient in craters ~30-64 km in diameter relative to other heavily cratered lunar terrains (Head et al., 2010; Kadish et al., 2011). Could this deficiency of 30- 64 km diameter craters be due to early volcanic flooding?

Since both flooding models produce similar results, we performed a ubiquitous flooding simulation of the current SPA basin topography (Fig. 13b-d). Flooding begins at the lowest point in the region and proceeds at 0.5 km intervals, a vertical range of ~18.5 km in the defined study region. Craters ~30-64 km in diameter located in the lowest part of the basin are slowly filled from their floors and after ~3.5 km of stage 1 type flooding (Fig. 13b), the floor deposits appear similar to the actual distribution of exposed mare deposits at the present time (Fig. 13a). After another 1.0 km of flooding (Fig. 13c), stage 2 begins with “intercrater” plains-type filling, and many of the 30-64 km diameter craters have been completely obliterated. Stage 2 volcanic filling is completed after an additional 1.0 km of flooding (Fig. 13d) and, with it, the erasure of craters 30-64 km diameter in the central part of the basin. At this point, stage 1-like flooding begins again, with deposits thickening in the basin center. Continued flooding will move the boundary of the volcanic deposits to the outer parts of the basin, again initiating stage 2 “intercrater” plains-type flooding in these regions.

This simulated flooding experiment in SPA follows the same stages of filling that were observed in Hertzsprung basin. Additionally, the Hertzsprung basin simulations show a similar removal of craters 30-50 km in diameter before the smallest and largest craters. Both the pattern of fill and evolution of the CSFDs are due to the basin geometry

of these simulated flood regions. The large depression created by the basin allowed the simulated flood material to increase in thickness more rapidly that in a typical highland region, causing complete burial of larger craters before craters <30 km diameter. When the flood material began to be deposited outside the craters it ponded in an area south of the Plains South of Apollo (PSA; Petro et al., 2011) and southeast of Bose and Bhabha craters. The proximity of the first simulated volcanic materials to PSA, thought to be a region of ancient cryptomare deposits (Pieters et al., 2001; Gibson et al., 2011; Jolliff et al., 2011; Petro et al., 2011), supports the idea that these plains deposits were generated from volcanic activity. Although mare flooding in SPA did not reach elevations such as those modeled, comparison of the simulated map patterns to observations of SPA indicate that there was a significant amount of filling in the basin center. This flooding simulation readily illustrates that the emplacement of ~2 km of material could easily account for the erasure of ~30- 64 km diameter craters in the SPA basin interior.

Multiple geologic plains units have been identified on Mercury, including the intercrater and smooth plains (Strom et al., 1975; McGill and King, 1983; Trask and Guest, 1975). Smooth plains are interpreted as volcanic deposits (e.g., Strom et al., 1975; Murchie et al., 2008; Denevi et al., 2009; Head et al., 2011), but the origin of the intercrater plains is not well established. Both volcanic (e.g., Murray et al., 1974, 1975; Strom, 1977; Kiefer and Murray, 1987; Spudis and Guest, 1988) and impact ejecta deposition (e.g., Trask and Guest, 1975; Wilhelms, 1976) formation mechanisms have been proposed for the intercrater plains. The current study has important applications to understanding the formation of intercrater plains on Mercury. The characteristics of mercurian intercrater plains, including a smooth surface texture, ponding in topographic

lows and embayment of lowland terrain, can be explained by either formation mechanism. However, the creation of “intercrater” plains in our flooding experiments provides more support for a volcanic origin for these mercurian deposits because they document the manner in which volcanic activity can produce deposits with similar morphologies and distributions. Thus, these techniques and procedures can be used in specific areas of Mercury to help unravel the origin of intercrater plains at local and regional scales.

The flooding experiments conducted in this study can also be applied to detecting and characterizing cryptomare deposits on the lunar surface. Cryptomaria (Head and Wilson, 1992) are buried volcanic deposits on the Moon thought to represent some of the oldest observed volcanic activity (e.g., Hartmann and Wood, 1971; Schultz and Spudis, 1983; Bell and Hawke, 1984; Head and Wilson, 1992). Similar to the mercurian intercrater plains, cryptomaria are smooth volcanic deposits that occur outside larger craters or basins. These flooding experiments can be used to compare with remote sensing evidence for cryptomaria shapes (Whitten et al., 2013), and gravity models using GRAIL data (Zuber et al., 2013) to decipher the subsurface structure of the Moon.

5. Conclusions

The flooding simulations conducted here in three distinct regions on the Moon using LOLA data have provided insight into the character and sequence of volcanic filling in heavily cratered terrains. Based on the results of our lunar flooding simulations, a new expanded sequence of volcanic filling has been defined based on the initial geometry of a region. *Stage 1*: Deposition of material in large (>20 km diameter)

individual craters. *Stage 2*: Flooded crater rim crests are breached, allowing the development of "intercrater" plains units. *Stage 3*: Large-scale flood deposits cease spreading laterally due to regional variations in topography and begin to increase the unit thickness. Volcanically flooding large impact basins often involves a repetition of stages 1 and 2 before reaching stage 3, as lava flooding expands from the deep basin interior to the inner edge of the basin rim.

Additionally, tracking the evolution of CSFDs demonstrates that pre-existing topography has an influence in the shape of the crater distribution. Basin geometries may result in the disappearance of intermediate-sized craters (30-60 km diameter) as simulated flood material fills the basin rings and deposit thickness increases. The slope of the pre-existing surface can control the shape and evolution of the CSFD by promoting faster burial rates for large craters. Comparison of actual lunar mare basalt thicknesses with our flooding estimates indicates that our flooding simulations provide reasonable thickness values. Application of the developed techniques indicates that ancient volcanic flooding is likely to provide an explanation for the paucity of craters 30-64 km diameter in the South Pole-Aitken Basin. This work can also be applied to address other questions about the nature of the intercrater plains on Mercury, and to assist in the interpretation of the lunar GRAIL gravity data.

Acknowledgements

We gratefully acknowledge funding from the NASA Lunar Reconnaissance Orbiter (LRO) Lunar Orbiter Laser Altimeter (LOLA) experiment through grant number NNX09AM54G to JWH. Additionally, we would like to thank B.L. Jolliff, R.A DeHon and L. Wilson for providing helpful reviews that greatly improved this manuscript.

References

Baker, D.M.H., Head, J.W., Fassett, C.I., Kadish, S.J., Smith, D.E., Zuber, M.T., Neumann, G.A., 2011. The transition from complex crater to peak-ring basin on the Moon: New observations from the Lunar Orbiter Laser Altimeter (LOLA) instrument. Icarus 214. doi:10.1016/j.icarus.2011.05.030.

Bell, J.F., Hawke, B.R., 1984. Lunar dark–haloed impact craters: Origin and implications for early mare volcanism. J. Geophys. Res. 89. doi:10.1029/JB089iB08p06899.

Coffin, M.F., Eldholm, O., 1994. Large igneous provinces: Crustal structure, dimensions, and external consequences. Rev. Geophys. 32. doi: 10.1029/93RG02508.

Craddock, R.A., Greeley, R., 1987. Thickness of volume of mare Tsiolkovsky, lunar farside. Lunar Planet. Sci. Conf., 18th, Abstract 1102.

DeHon, R.A., 1974. Thickness of mare material in the Tranqillitatis and Nectaris Basins. Proc. Lunar Planet. Sci. Conf., 5th, 53-59.

DeHon, R. A., 1979. Thickness of the western mare basalts, Proc. Lunar Planet. Sci. Conf., 10th, 2935– 2955.

Denevi, B.W., Robinson, M.S., Solomon, S.C., Murchie, S.L., Blewett, D.T., Domingue, D.L., McCoy, T.J., Ernst, C.M., Head, J.W., Watters, T.R., Chabot,

N.L., 2009. The Evolution of Mercury's Crust: A Global Perspective from MESSENGER. Science 324. doi: 10.1126/science.1172226, 2009.

Elkins-Tanton, L.T., Hager, B.H., Grove, T.L., 2004. Magmatic effects of the lunar late heavy bombardment. Earth Planet. Sci. Lett. 222, 17-27.

Fassett, C.I., Head, J.W., Smith, D.E., Zuber, M.T., Neumann, G.A., 2011. Thickness of proximal ejecta from the Orientale Basin from Lunar Orbiter Laser Altimeter (LOLA) data: Implications for multi-ring basin formation, Geo. Phys. Res. Lett. 38, L17201. doi: 10.1029/2011GL048502.

Fassett, C. I., Head, J. W., Kadish, S. J., Mazarico, E., Neumann, G. A., Smith, D. E., Zuber, M.T., 2012. Lunar impact basins: Stratigraphy, sequence and ages from superposed impact crater populations measured from Lunar Orbiter Laser Altimeter (LOLA) data. J. Geophys. Res. 117, E00H06. doi:10.1029/2011JE003951.

Garrick-Bethell, I., Zuber, M.T., 2009. Elliptical structure of the lunar South Pole- Aitken basin. Icarus 204. doi: 10.1016/j.icarus.2009.05.032.

Ghods, A., Arkani-Hamed, J., 2007. Impact-induced convection as the main mechanism for formation of lunar mare basalts. J. Geophys. Res. 112, E03005. doi: 10.1029/2006JE002709.

Gibson, K.E., Jolliff, B.L., 2011. Correlation of surface FeO concentrations in the South-Pole Aitken basin interior. Lunar Planet. Sci. Conf., 42nd, Abstract# 2326.

Greeley, R., Womer, M.B., 1981. Mare basin filling on the moon: Laboratory simulations, Proc. Lunar Planet. Sci. Conf., 12th, 651-663.

Hartmann, W.K., Wood, C.A., 1971. Moon; Origin and evolution of multiring basins. The Moon 3, 3-78.

Head, J. W., 1982. Lava flooding of ancient planetary crusts: geometry, thickness, and volumes of flooded lunar impact basins. The Moon and the Planets 26. doi: 10.1007/BF00941369.

Head J. W., Coffin, M. F., 1997. Large igneous provinces: A planetary perspective, Large Igneous Provinces, in: Mahoney, J.J., Coffin, M.I. (Eds.), Large Igneous Provinces, Continental, Oceanic and Planetary Flood Volcanism, Geophysical Monograph 100. American Geophysical Union, pp. 411-438.

Head, J.W., Wilson, L., 1992. Lunar mare volcanism: Stratigraphy, eruption conditions, and the evolution of secondary crusts. Geochim. Cosmochim. Acta 55. doi: 10.1016/0016-7037(92)90183-J.

Head, J.W., Wilson, L., Dickson, J., Neukum, G., 2006. The Huygens-Hellas giant dike system on Mars: Implications for Late Noachian- Early Hesperian volcanic resurfacing and climatic evolution. Geology 34. doi: 10.1130/G22163.1.

Head, J.W., Fassett, C.I., Kadish, S.J., Smith, D.E., Zuber, M.T., Neumann, G.A., Mazarico, E., 2010. Global distribution of large lunar craters: Implications for resurfacing and impactor populations. Science 17. doi: 10.1126/science.1195050.

Head, J.W., Chapman, C.R., Strom, R.G., Fassett, C.I., Denevi, B.W., Blewett, D.T., Ernst, C.M., Watters, T.R., Solomon, S.C., Murchie, S.L., Prockter, L.M., Chabot, N.L., Gillis-Davis, J.J., Whitten, J.L., Goudge, T.A., Baker, D.M.H., Hurwitz, D.M., Ostrach, L.R., Xiao, Z., Merline, W.J., Kerber, L., Dickson, J.L., Oberst, J., Byrne, P.K., Klimczak, C., Nittler, L.R., 2011. Flood volcanism in the northern high latitudes of Mercury revealed by MESSENGER. Science 30. doi: 10.1126/science.1211997.

Hess, P.C., Parmentier, E.M., 1995. A model for the thermal and chemical evolution of the Moon's interior: Implications for the onset of mare volcanism. Earth Planet. Sci. Lett. 134, 501-514.

Hiesinger, H., Head, J.W., Wolf, U., Jaumann, R., Neukum, G., 2002. Lunar mare basalt flow units: Thickness determined from crater size-frequency distributions. GRL 29. doi: 10.1029/2002GL014847.

Hiesinger, H., van der Bogert, C.H., Pasckert, J.H., Schmedemann, N., Robinson, M.S., Jolliff, B., Petro, N., 2012. New crater size-frequency distribution measurements of the South Pole-Aitken basin. Lunar Planet. Sci. Conf., 43rd, Abstract# 2863.

Howard, A.D., 1999. Simulation of lava flow inundation on martian cratered terrains. Lunar Planet. Sci. Conf., 30th, Abstract# 1112.

Ivanov, M. A., Head, J. W., 2011. Global geological map of Venus. Planet. Space Sci. 59, 1559-1600. doi: 10.1016/j.pss.2011.07.008.

Jolliff, B.L., Gibson, K.E., Scholten, F., 2011. South Pole-Aitken basin interior: Topographic expression of mare, cryptomare, and nonmare plains units. Lunar Planet. Sci. Conf., 42nd, Abstract# 2774.

Kadish, S.J., Fassett, C.I., Head, J.W., Smith, D.E., Zuber, M.T., Neumann, G.A., Mazarico, E., 2011. A global catalog of large lunar craters (>20 km) from the Lunar Orbiter Laser Altimeter. Lunar Planet. Sci. Conf., 42nd, Abstract# 1006.

Kiefer, W.S., Murray, B.C., 1987. The formation of Mercury's smooth plains. Icarus 72. doi: 10.1016/0019-1035(87)90046-7.

Kramer, G.Y., Jolliff, B.L., Neal, C.R. 2008. Distinguishing high-alumina mare basalts using Clementine UVVIS and Lunar Prospector GRS data: Mare Moscoviense

and Mare Nectaris. J. Geophys. Res. 113, E01002. doi: 10.1029/2006JE002860.

Mahoney, J.J., 1988. Deccan Traps, in: Macdougall, J.D. (Ed.), Continental Flood Basalts. Kluwer Academic Publishers, Netherlands, pp. 151-194.

McGill, G.E., King, E.A., 1983. Geologic map of the Victoria quadrangle of Mercury. USGS, Reston, VA.

Melosh, H.J., 1989. Impact cratering: A geologic process. Oxford Univ. Press, New York.

Michael, G.G., Neukum, G., 2010. Planetary surface dating from crater size–frequency distribution measurements: Partial resurfacing events and statistical age uncertainty. Earth Planet. Sci. Lett. 294. doi: 10.1016/j.epsl.2009.12.041.

Morgan, W.J., 1971. Convection plumes in the lower mantle. Nature 230, 42-43.

Morgan, W.J., 1981. Hotspot tracks and the opening of the Atlantic and Indian oceans, in: Emiliani, C. (Eds.), The Sea, vol. 7, The Oceanic Lithosphere. Wiley-Interscience, New York, pp. 443-487.

Morota, T., Haruyama, J., Honda, C., Ohtake, M., Yokota, Y., Kimura, J., Matsunaga, T., Ogawa, Y., Hirata, N., Demura, H., Iwasaki, A., Miyamoto, H., Nakamura, R., Takeda, H., Ishihara, Y., Sasaki, S., 2009. Mare volcanism in the lunar farside Moscoviense region: Implication for lateral variation in magma production of the Moon. Geophys. Res. Letters. 36. doi; 10.1029/2009GL040472.

Murchie, S.L., Watters, T.R., Robinson, M.S., Head, J.W., Strom, R.G., Chapman, C.R., Solomon, S.C., McClintock, W.E., Prockter, L.M., Domingue, D.L., Blewett, D.T., 2008. Geology of the Caloris Basin, Mercury: A view from MESSENGER. Science 321. doi: 10.1126/science.1159261.

Murray B.C., Belton, M.J.S., Danielson, G.W., Davies, M.E., Gault, D.E., Hapke, B., O'Leary, B., Strom, R.G., Suomi, V., Trask, N., 1974. Mercury's surface: Preliminary description and interpretation from Mariner 10 pictures. Science 185. doi: 10.1126/science.185.4146.169.

Murray B.C., Strom, R.G., Trask, N.J., Gault, D.E., 1975. Surface history of Mercury: Implications for terrestrial planets. J. Geophys. Res. 80. doi: 10.1029/JB080i017p02508.

Neukum, G., Horn, P., 1976. Effects of lava flows on lunar crater populations. The Moon 15. doi: 10.1007/BF0056223.

Petro, N.E., Mest, S.C., Teich, Y., 2011. Geomorphic terrains and evidence for ancient volcanism within northeastern South Pole-Aitken basin. GSA Spec. Pap. 477, 129-140.

Phillips, R.J., Raubertas, R.F., Arvidson, R.E., Sarkar, I.C., Herrick, R.R., Izenberg, N., Grimm, R.E., 1992. Impact craters and Venus resurfacing history, J. Geophys. Res. 97. doi: 10.1029/92JE01696.

Pieters, C.M., Tompkins, S., 1999. Tsiolkovsky crater: A window into crustal processes on the lunar farside. J. Geophys. Res. 104, 21935- 21949. doi: 10.1029/1998JE001010.

Pieters, C.M., Head, J.W., Gaddis, L., Jolliff, B., Duke, M., 2001. Rock types of South Pole-Aitken basin and extent of basaltic volcanism. J. Geophys. Res. 106, 28001-28022.

Robinson, M.S., Brylow, S.M., Tschimmel, M., Humm, D., Lawrence, S.J., Thomas, P.C., Denevi, B.W., Bowman-Cisneros, E., Zerr, J., Ravine, M.A., Caplinger,

M.A., Ghaemi, F.T., Schaffner, J.A., Malin, M.C., Mahanti, P., Bartels, A., Anderson, J., Tran, T.N., Eliason, E.M., McEwen, A.S., Turtle, E., Jolliff, B.L., Hiesinger, H., 2010. Lunar Reconnaissance Orbiter Camera (LROC) instrument overview. Space Sci. Review 150, 209-241. doi: 10.1007/s11214-010-9634-2.

Schaber, G. G., 1973. Lava flows in Mare Imbrium: Geologic evaluation from Apollo orbital photography. Proc. Lunar Planet. Sci. Conf., 4th, 73– 92.

Schultz, P.H., Spudis, P., 1983. The beginning and end of lunar mare volcanism. Nature 302, 233-236. doi:10.1038/302233a0.

Scott, D.H., Tanaka, K.L., 1986. Geologic map of the western equatorial region of Mars. US Geological Survey Miscellaneous Investigations Series Map, I-1802-A, 1:15,000,000 scale.

Shearer, C.K., Hess, P.C., Wieczorek, M.A., Pritchard, M.W., Parmentier, E.M., Borg, L.E., Longhi, J., Elkins-Tanton, L.T., Neal, C.R., Antonenko, I., Canup, R.M., Halliday, A.N., Grove, T.L., Hager, B.H., Lee, D.-C., Wiechert, U., 2006. Thermal and magmatic evolution of the Moon, Reviews in Mineralogy and Geochemisty, 60, 365-518, doi: 10.2138/rmg.2006.60.4.

Smith, D.E., Zuber, M.T., Jackson, G.B., Cavanaugh, J.F., Neumann, G.A., Riris, H., Sun, X., Zellar, R.S., Coltharp, C., Connelly, J., Katz, R.B., Kleyner, I., Liiva, P., Matuszeski, A., Mazarico, E.M., McGarry, J.F., Novo-Gradac, A., Ott, M.N., Peters, C., Ramos-Izquierdo, L.A., Ramsey, L., Rowlands, D.D., Schmidt, S., Scott III, V.S., Shaw, G.B., Smith, J.C., Swinski, J., Torrence, M.H., Unger, G., Yu, A.W., Zagwodzki, T.W., 2010. The Lunar Oribiter Laser Altimeter investigation on the Lunar Reconaissance Orbiter mission. Space Sci. Review 150, 209-241.

Solomon, S.C., Head, J.W., 1980. Lunar mascon basins: lava filling, tectonics, and evolution of the lithosphere. Rev. Geophys. Space Phys. 18, 107-141.

Solomon, S.C., Comer, R.P., Head, J.W., 1982. The evolution of impact basins: Viscous relaxation of topographic relief. J. Geophys. Res. 87, 3975-3992. doi: 10.1029/JB087iB05p03975.

Spudis P. D., Guest, J.E., 1988. Stratigraphy and geologic history of Mercury, in: Vilas, F., Chapman, C.R., Matthews, M.S. (Eds.), Mercury. Univ. Ariz. Press, Tucson, pp. 336-373.

Strom, R.G., 1977. Origin and relative age of lunar and mercurian intercrater plains. Phys. Earth Planet. Interiors 15, 156-172.

Strom, R.G., Trask, N.J., Guest, J.E., 1975. Tectonism and volcanism on Mercury. J. Geophys. Res. 80, 24782507.

Strom, R.G., Schaber, G.G., Dawson, D.D., 1994. The global resurfacing of Venus. J. Geophys. Res. 99. doi: 10.1029/94JE00388.

Stuart-Alexander, D.E., 1978. Geologic map of the central far side of the Moon, USGS, Reston, VA.

Taylor, S.R., 1989. Growth of planetary crusts. Tectonophys. 161. doi: 10.1016/0040-1951(89)90151-0.

Tolan, T.L., Reidel, S., Anderson, J.L., Beeson, M.H., Fecht, K.R., Swanson, D.A., 1989. Revisions to the estimates of the areal extent and volume of the Columbia River Basalt Group. Geol. Soc. Am. Spec. Pub. 239.

Trask N.J., Guest, J.E., 1975. Preliminary geologic terrain map of Mercury. J. Geophys. Res. 80. doi: 10.1029/JB080i017p02461.

Vondrak, R., Keller, J., Chin, G., Garvin, J., 2010. Lunar Reconnaissance Orbiter (LRO): Observations for Lunar Exploration and Science. Space Sci. Rev. 150. doi:10.1007/s11214-010-9631-5.

Watters, T.R., 1993. Compressional tectonism on Mars. J. Geophys. Res. 98, 17049-17060.

Whitford-Stark, J.L., 1979. Charting the southern seas: The evolution of the lunar Mare Australe. Proc. Lunar Sci. Conf., 10th, 2975- 2994.

Whitford-Stark, J.L., Head, J.W., 1980. Stratigraphy of Oceanus Procellarum basalts: Sources and styles of emplacement. J. Geophys. Res. 85, 6579- 6609.

Whitten, J.L., Head, J.W., Staid, M.I., Pieters, C.M., Mustard, J.F., Clark, R., Nettles, J., Klima, R.L., Taylor, L., 2011. Lunar mare deposits associated with the Orientale impact basin: New insights into mineralogy, history, mode of emplacement, and relation to Orientale Basin evolution from Moon Mineralogy Mapper (M^3) data from Chandrayaan-1. J. Geophys. Res. 116. doi: 10.1029/2010JE003736.

Whitten, J.L., Head, J.W., 2013. Ancient lunar mare volcanism: Identification, distribution, and composition of cryptomare deposits. Lunar Planet. Sci. Conf., 44th, Abstract# 1247.

Wieczorek, M.A., Phillips, R.J., 2000. The "Procellarum KREEP Terrane": Implications for mare volcanism and lunar evolution. J. Geophys. Res. 105, 20,417-20,430.

Wieczorek, M.A., Neumann, G.A., Nimmo, F., Kiefer, W.S., Taylor, G.J., Melosh, H.J., Phillips, R.J., Solomon, S.C., Andrews-Hanna, J.C., Asmar, S.W., Konopliv, A.S., Lemoine, F.G., Smith, D.E., Watkins, M.M., Williams, J.G., Zuber, M.T., 2012. The crust of the Moon as seen by GRAIL, Science 8. doi: 10.1126/science.1231530.

Wilhelms D. E., 1976. Mercurian volcanism questioned. Icarus 28. doi: 10.1016/0019-1035(76)90128-7.

Wilhelms, D.E., 1987. The geologic history of the Moon, U.S. Geol. Surv., Prof. Paper 1348.

Wilhelms, D.E, Howard, K.A., Wilshire, H.G., 1979. Geologic map of the south side of the Moon. USGS, Reston, VA.

Williams, K.K., Zuber, M.T., 1998. Measurement and analysis of lunar basin depths from Clementine altimetry. Icarus 131. doi: 10.1006/icar.1997.5856.

Wilson, J.T., 1963. A possible origin of the Hawaiian Islands. Can. J. Phys. 41, 863-870.

Wood, C.A., 1973. Moon: Central peak heights and crater origins. Icarus 20, 503-506.

Yingst, R.A., Head, J.W., 1997. Volumes of lunar lava ponds in South Pole-Aitken and Orientale Basins: Implications for eruption conditions, transport mechanisms and magma source regions. J. Geophys. Res. 102. doi: 10.1029/97JE00717.

Zimbelman, J.R., 1998. Emplacement of long lava flows on planetary surfaces. J. Geophys. Res. 103. doi: 10.1029/98JB01123.

Zuber, M.T., Smith, D.E., Lemoine, F.G., Neumann, G.A., 1994. The shape and internal structure of the Moon from the Clementine Mission. Science 16. doi: 10.1126/science.266.5192.1839.

Zuber, M.T., Smith, D.E., Zellar, R.S., Neumann, G.A., Sun, X., Katz, R.B., Kleyner, I., Matuszeski, A., McGarry, J.F., Ott, M.N., Ramos-Izquierdo, L.A., Rowlands, D.D., Torrence, M.H., Zagwodzki, T.W., 2010. The Lunar Reconnaissance Orbiter Laser Ranging investigation. Space Sci. Rev. 150. doi:10.1007/s11214-009-9511-z.

Zuber, M.T., Smith, D.E., Watkins, M.M., Asmar, S.W., Konopliv, A.S., Lemoine, F.G., Melosh, H.J., Neumann, G.A., Phillips, R.J., Solomon, S.C., Wieczorek, M.A., Williams, J.G., Goossens, S.J., Kruizinga, G., Mazarico, R., Park, R.S., Yuan, D.-N., 2013. Gravity field of the Moon from the Gravity Recovery and Interior Laboratory (GRAIL) Mission. Science 339. doi: 10.1126/science.1231507.

Figure Captions

Figure 1. Location map highlighting the three study regions. a) Global map outlining location of study regions; b) Hertzsprung Basin; c) Farside cratered terrain (Head et al., 2010); d) Central Highlands. LOLA 128 pixel/degree topography data overlaying LOLA hillshade map.

Figure 2. Sketch diagrams of the different flooding models used in this study. Alternating black and striped horizontal layers represent different volcanic flooding events. Each event increases the volcanic deposit thickness by another 0.5 km elevation; the deposit thickness can vary, as indicated by the striped deposits in the right-most crater. a) Ubiquitous flooding by elevation intervals. Flooding begins at the lowest elevations throughout a region and continues from those various locations; b) Point source flooding by elevation intervals. Flooding occurs at a single point and proceeds from that point until it overflows into adjacent topography.

Figure 3. The results for the Hertzsprung basin (Fig. 1b) flooding simulations using the two different flooding methods. a) Ubiquitous flooding: 2.5 km unit thickness; b) Ubiquitous flooding: 4.0 km; c) Ubiquitous flooding: 5.5 km; d) Ubiquitous flooding: 7.0 km; e) Point source flooding: 2.5 km. White dashed line indicates location of the point source region; f) Point source flooding: 4.0 km; g) Point source flooding: 5.5 km; h) Point source flooding: 7.0 km. LOLA topographic data overlaying LOLA hillshade.

Figure 4. Results for the farside cratered terrain (Fig. 1c) flooding simulations using the two different flooding methods. a) Ubiquitous flooding: 4.0 km thickness; b) Ubiquitous flooding to 6.0 km; c) Ubiquitous flooding to 7.0 km; d) Ubiquitous flooding to 8.0 km; e) Point source flooding to 4.0 km. White dashed circle indicates location of Fowler Crater, the source crater for the point source flooding simulation; f) Point source flooding to 6.0 km; g) Point source flooding to 7.0 km; h) Point source flooding to 8.0 km.

Figure 5. Results for the Central Highlands (Fig. 1d) flooding simulations using the two different flooding methods. a) Ubiquitous flooding: 3.0 km thickness; b) Ubiquitous flooding to the 4.0 km; c) Ubiquitous flooding to 5.0 km; d) Ubiquitous flooding to 5.5 km; e) Point source flooding to 3.0 km. White dashed circle identifies location of Gemma Frisius, the 87 km diameter source crater; f) Point source flooding to 4.0 km; g) Point source flooding to 5.0 km; h) Point source flooding to 5.5 km.

Figure 6. Deposit thickness versus area graphs for the three study regions. a) Hertzsprung Basin; b) Farside cratered terrain; c) Central Highlands. Lighter colors represent values from the point source flooding method and the darker colors are the results from the ubiquitous model. Star data points correspond to each of the four images shown in Figures 3-5.

Figure 7. Thickness verses volume for the three study regions. a) Hertzsprung Basin; b) Farside cratered terrain; c) Central Highlands. Lighter colors represent values from the point source flooding method and the darker colors are the results from the ubiquitous

model. Shading indicates where volcanic fill material is contained mostly in the point source region. Star data points correspond to each of the four images shown in Figures 3-5.

Figure 8. Crater size frequency distributions (CSFDs) are arranged in columns according to the study region and by row according to the flooding method used. Each of the three CSFDs in each plot represents all craters counted (red), ~50% of craters remaining during the flooding events (green) and ~25% of craters remaining during flooding events (blue). a) Hertzsprung Basin, ubiquitous flooding showing all craters (red), remaining craters at 5.5 km (green) and 7.0 km (blue) unit thickness, respectively; b) Farside cratered terrain, ubiquitous flooding showing all countable craters (red), at 7.0 km (green) and 8.0 km (blue) unit thickness; c) Central Highlands, ubiquitous flooding showing all craters (red), and remaining craters at 5.0 km (green) and 5.5 km (blue); d) Hertzsprung Basin, point source flooding at same deposit thicknesses; e) Farside cratered terrain, point source flooding at same deposit thicknesses; f) Central Highlands, point source flooding at same deposit thicknesses.

Figure 9. Ubiquitous flooding of study regions with predefined volumes of volcanic material. Each study regions is defined by the columns and each row represents flooding with a different volume. The first row shows the three study regions flooded with 7700 km^3, a large lunar flow unit (Hiesinger et al., 2002). The second row is flooded with 2093 km^3 (one of the largest flow volumes in the Columbia River Flood Basalts) and the third row shows the three study sites flooded with the volume of material contained within the

Columbia River Flood Basalts (174,356 km^3) (Tolan et al., 1989). Elevation ranges for each study region are the same as Figures 2, 7 and 8.

Figure 10. Point source flooding of study regions with predefined volumes of volcanic material. Each study region is defined by the columns and each row represents flooding with a different volume. The first row shows the three study regions flooded with 7700 km^3, a large lunar flow unit (Hiesinger et al., 2002). The second row is flooded with 2093 km^3 (one of the largest flow volumes in the Columbia River Flood Basalts) and the third row shows the three study sites flooded with the volume of material contained within the Columbia River Flood Basalts (174,356 km^3) (Tolan et al., 1989). Elevation ranges for each study region are the same as Figures 2, 6 and 7.

Figure 11. Changes in deposit thickness with simulated flooding method. Each study region is flooded using the predetermined volume of material. Closed symbols represent thickness measurements for the point source flooding models and open symbols indicate ubiquitous model results. Colors are the same as for Figures 6 and 7.

Figure 12. Lunar examples of observed map patterns in flooding simulations. a) Australe basin (612 km diameter; e.g., Whitford-Stark, 1979); b) Mare Moscoviense (e.g., Kramer et al., 2008; Morota et al., 2009); c) western Oceanus Procellarum (e.g., Whitford-Stark and Head, 1980); d) Tsiolkovskiy crater (184 km diameter; e.g., Pieters and Tompkins, 1999). E) Campbell crater (222 km diameter). LROC 100 meters/pixel albedo map.

Figure 13. Ubiquitous flooding model applied to the South Pole-Aitken Basin. a) Sketch map of SPA with dotted lines outlining impact basins and irregular black shapes representing mare deposits; b) Simulated flooding to -5.5 km elevation / unit thickness of ~3.5 km; c) Flooding to -4.5 km elevation/ 4.5 km thickness; d) Flooding to -3.5 km elevation / 5.5 km unit thickness. LOLA 128 pixel/degree topography data overlaying LOLA hillshade map.

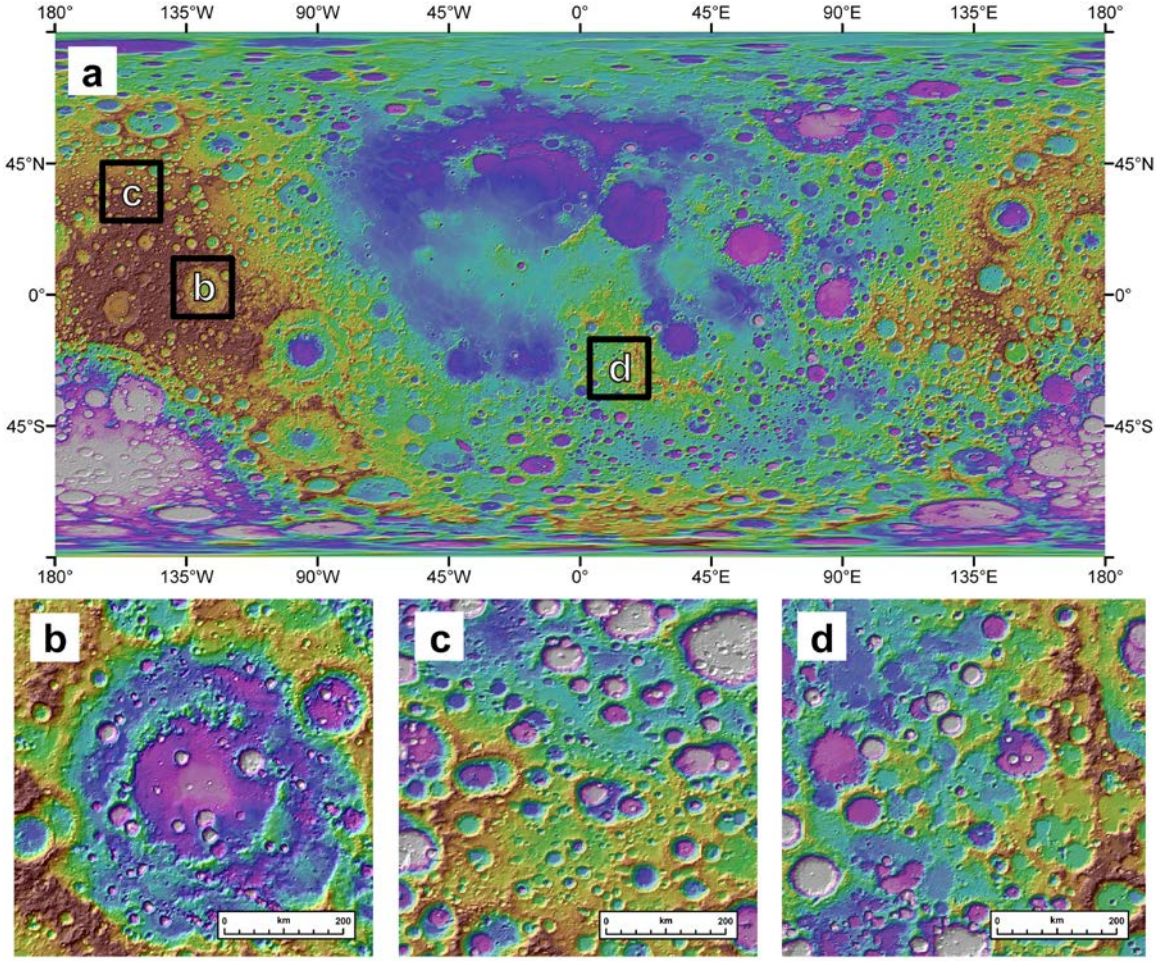

Figure 1.

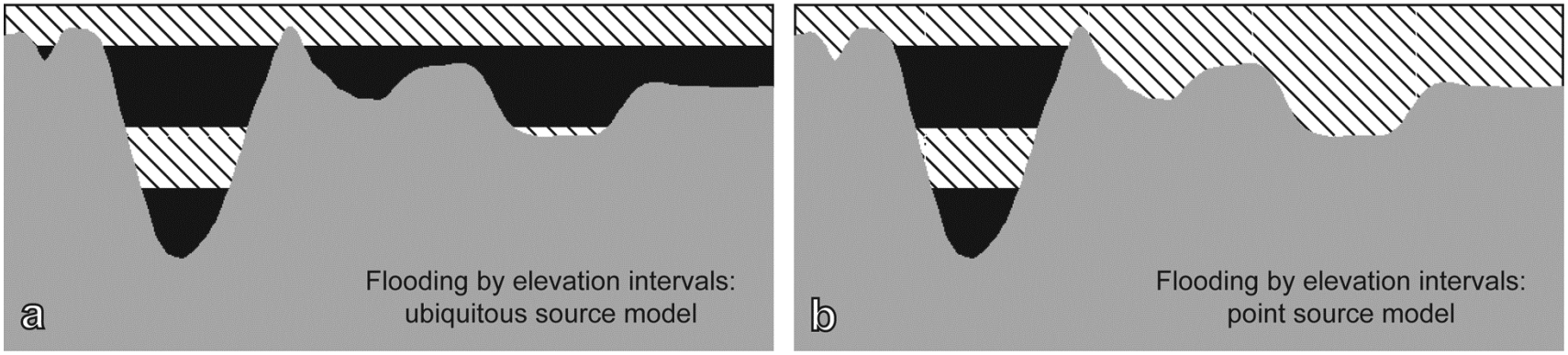
a
Flooding by elevation intervals:
ubiquitous source model
b
Flooding by elevation intervals:
point source model

Figure 2.

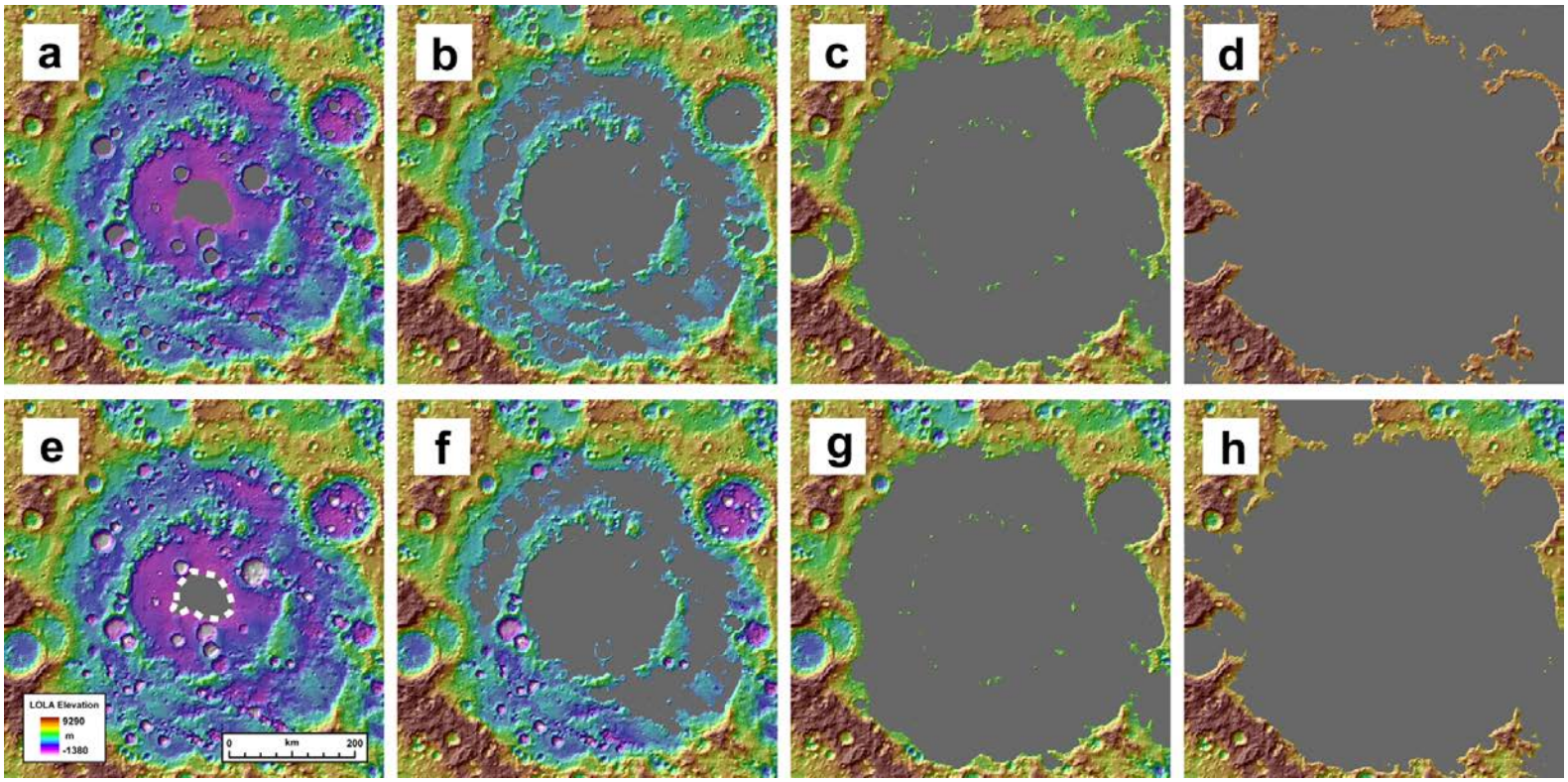

Figure 3.

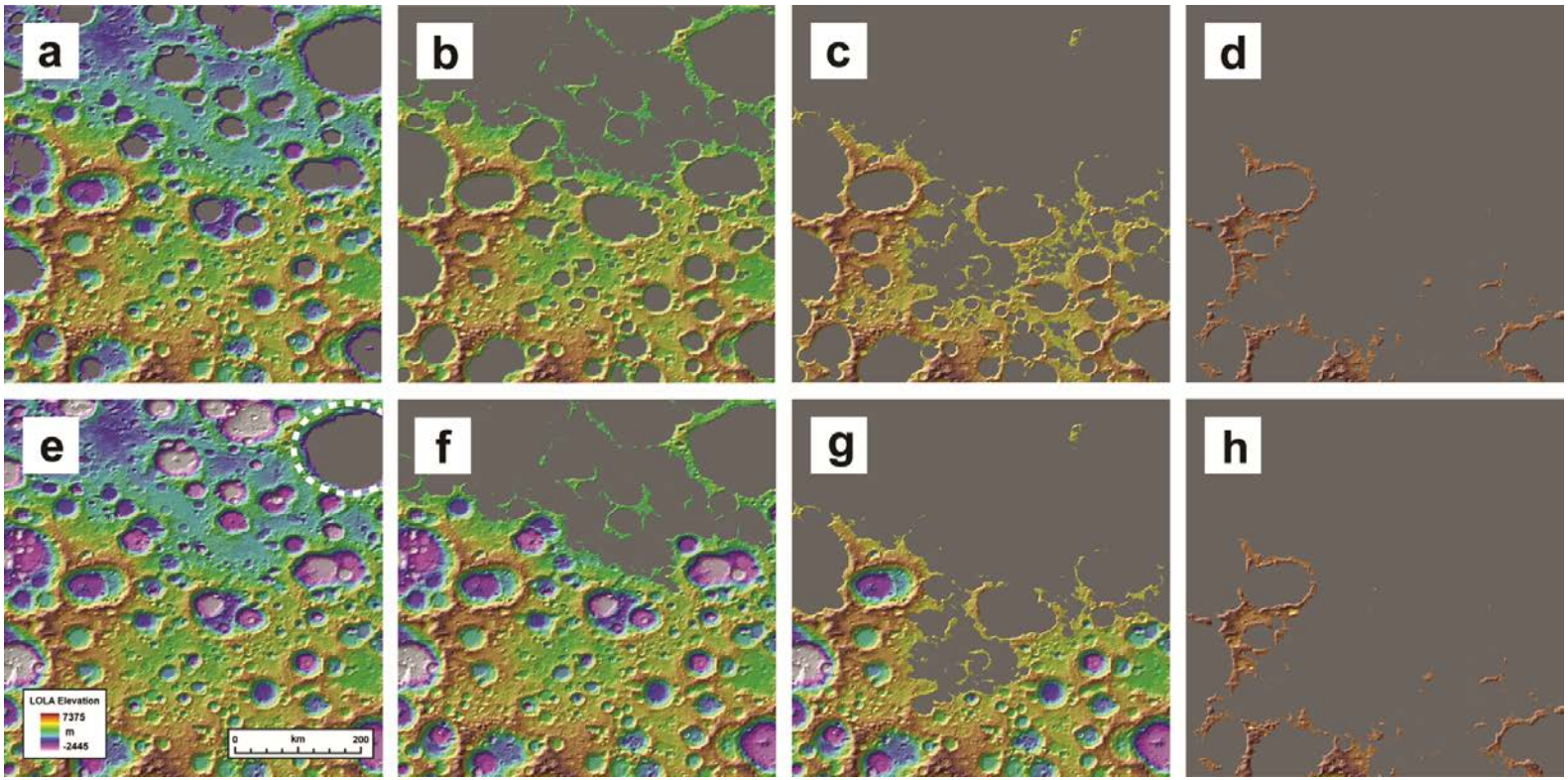

Figure 4.

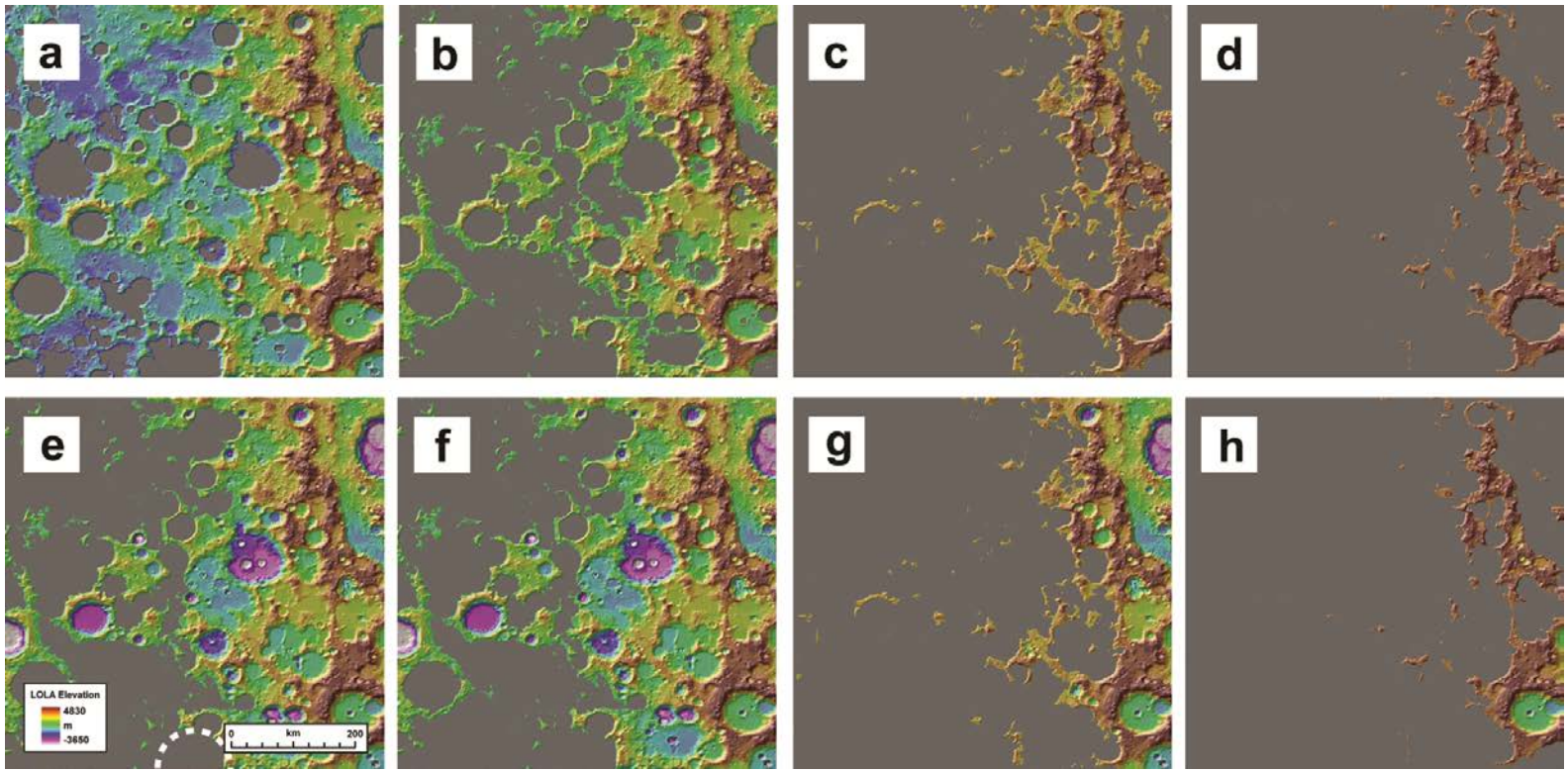

Figure 5.

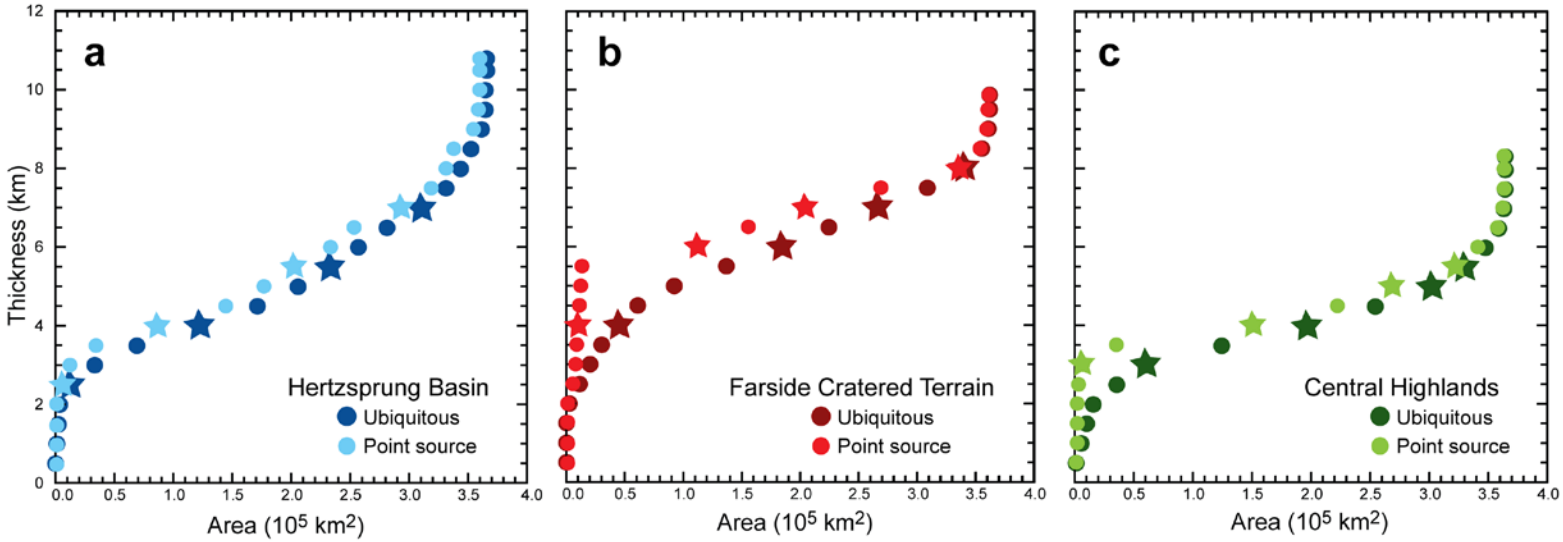
a
b
c
Thickness (km)
Area (10^5 km^2)
Hertzsprung Basin
Ubiquitous
Point source
Farside Cratered Terrain
Ubiquitous
Point source
Central Highlands
Ubiquitous
Point source

Figure 6.

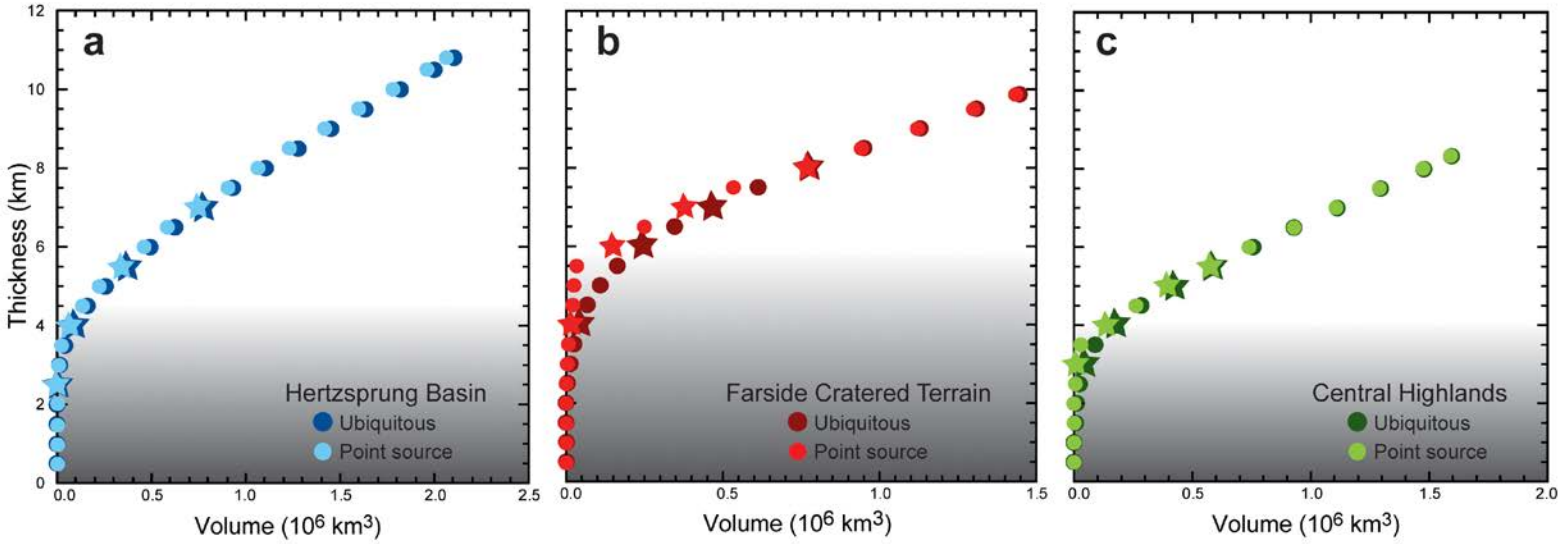
a
b
c
Thickness (km)
Volume (10^6 km^3)
Hertzsprung Basin
Ubiquitous
Point source
Farside Cratered Terrain
Ubiquitous
Point source
Central Highlands
Ubiquitous
Point source

Figure 7.

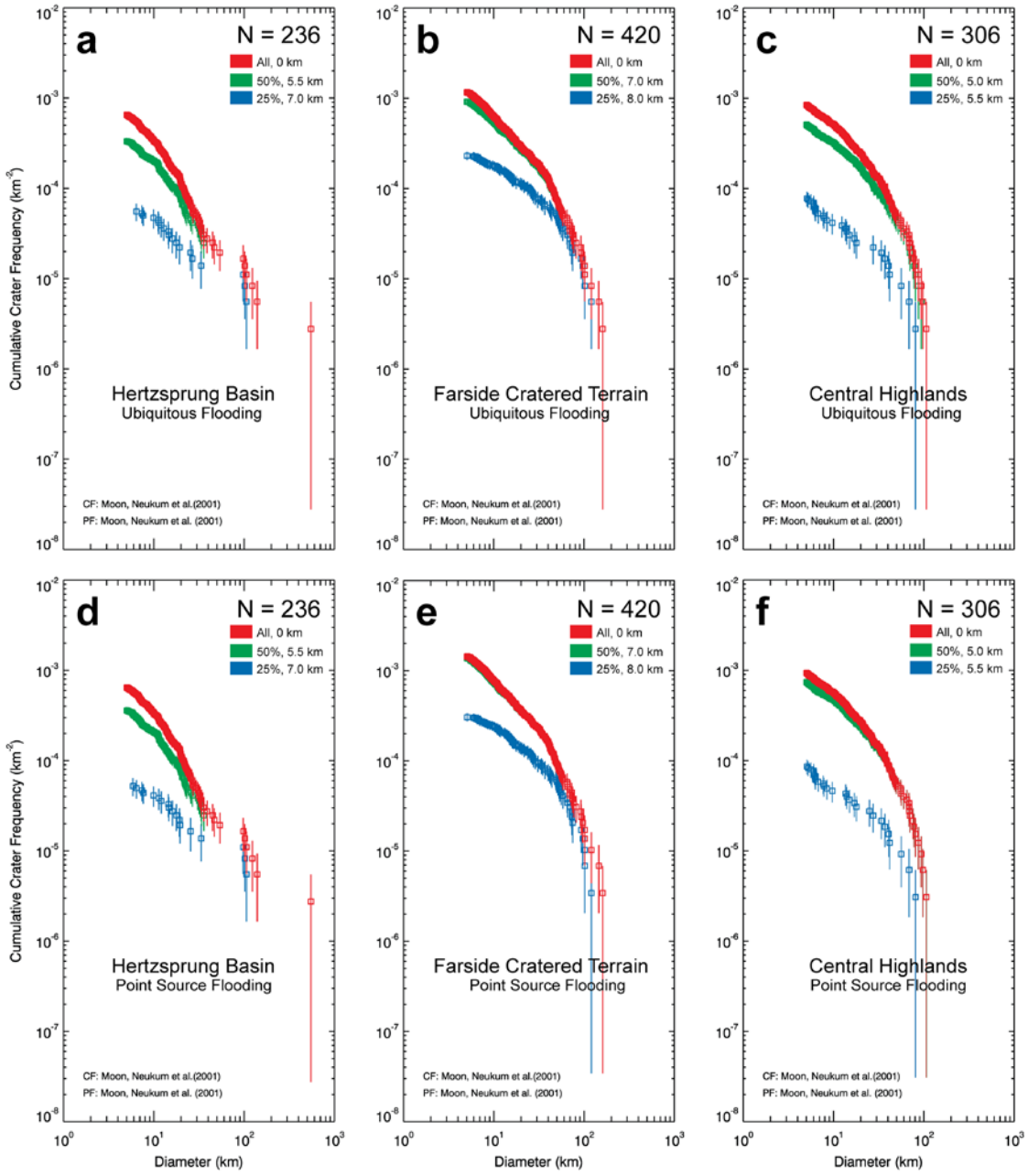
a
N = 236
All, 0 km
50%, 5.5 km
25%, 7.0 km
Hertzsprung Basin
Ubiquitous Flooding
b
N = 420
All, 0 km
50%, 7.0 km
25%, 8.0 km
Farside Cratered Terrain
Ubiquitous Flooding
c
N = 306
All, 0 km
50%, 5.0 km
25%, 5.5 km
Central Highlands
Ubiquitous Flooding
d
N = 236
All, 0 km
50%, 5.5 km
25%, 7.0 km
Hertzsprung Basin
Point Source Flooding
e
N = 420
All, 0 km
50%, 7.0 km
25%, 8.0 km
Farside Cratered Terrain
Point Source Flooding
f
N = 306
All, 0 km
50%, 5.0 km
25%, 5.5 km
Central Highlands
Point Source Flooding
CF: Moon, Neukum et al.(2001)
PF: Moon, Neukum et al. (2001)
Cumulative Crater Frequency (km-2)
Diameter (km)

Figure 8.

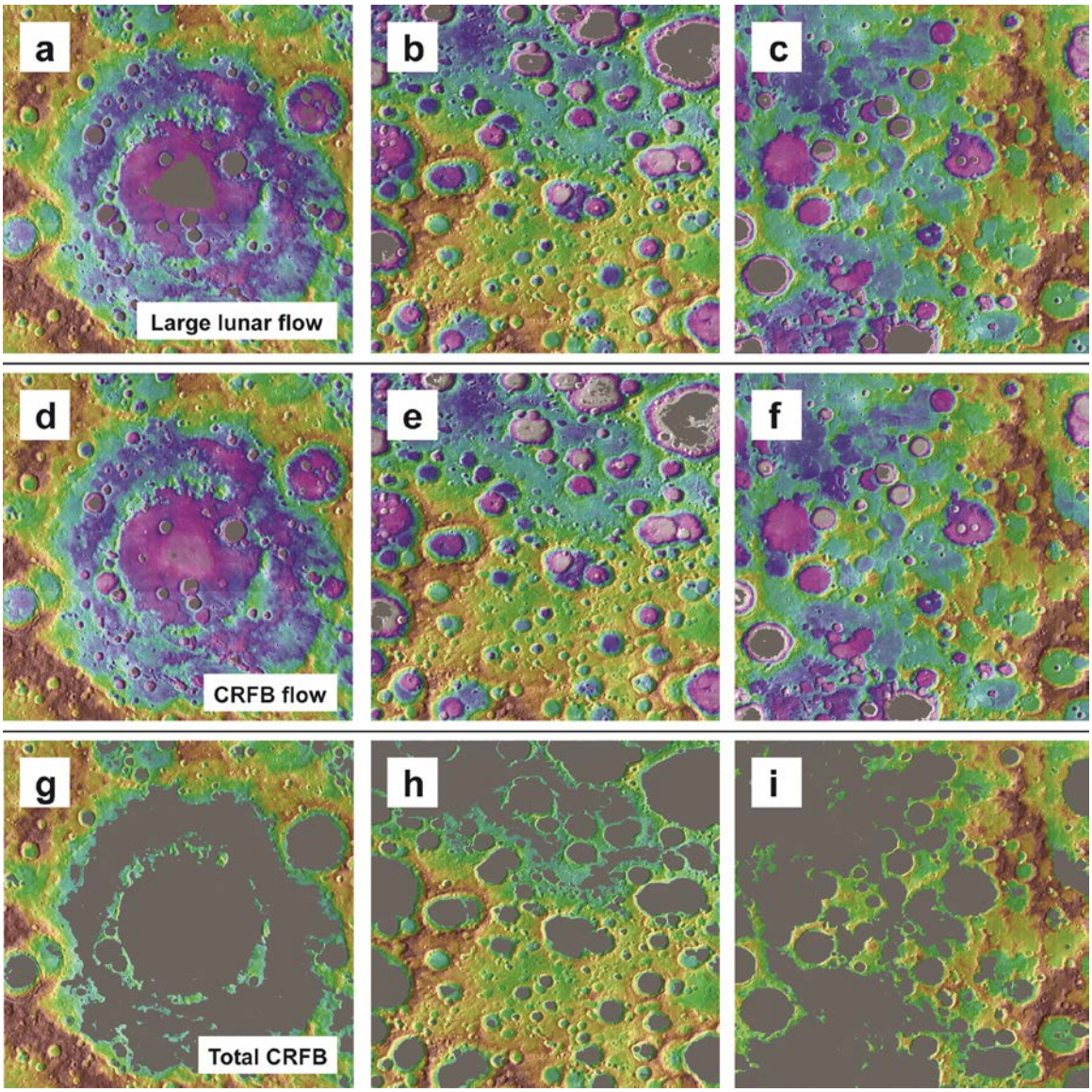

Figure 9.

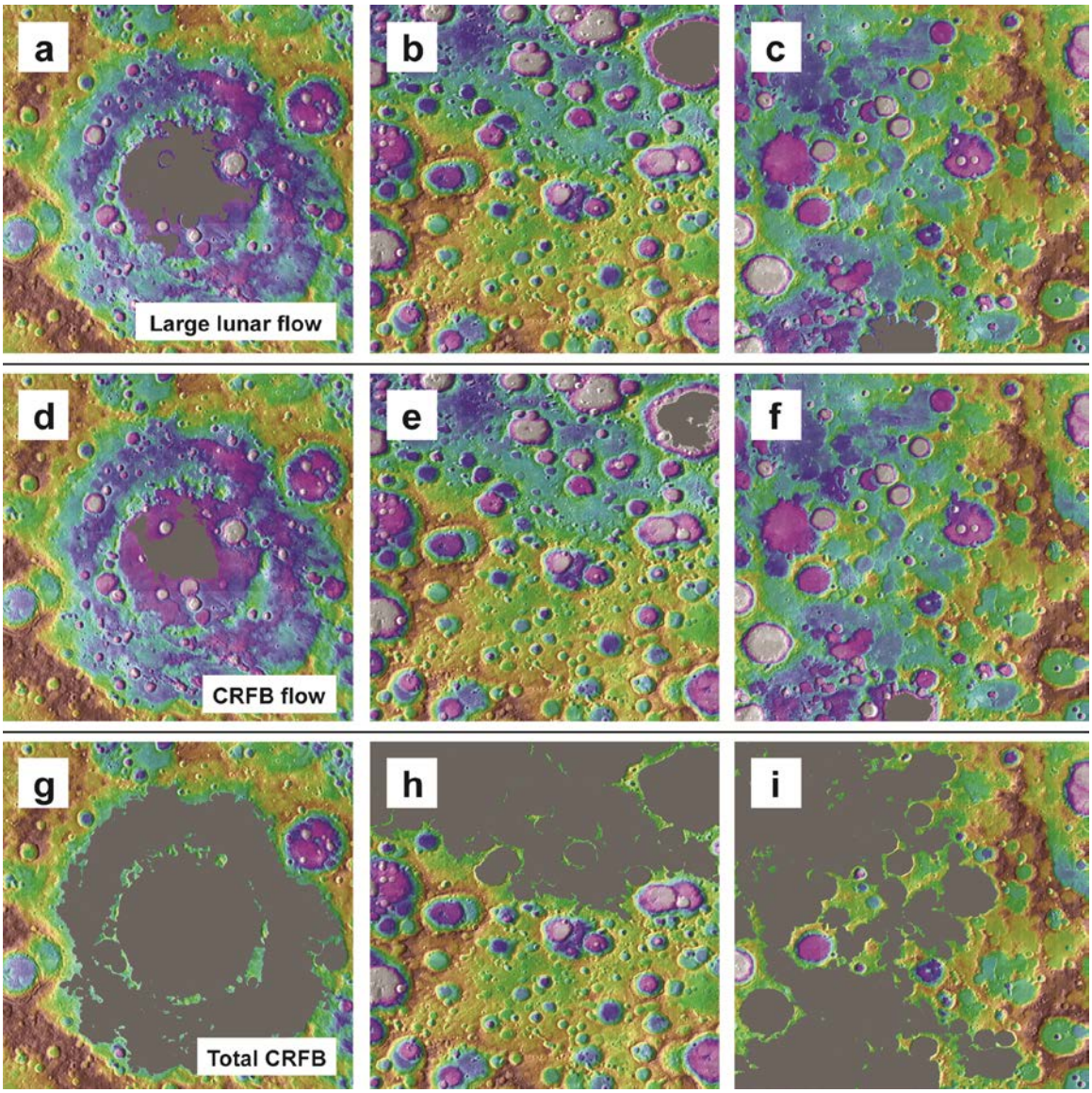

Figure 10.

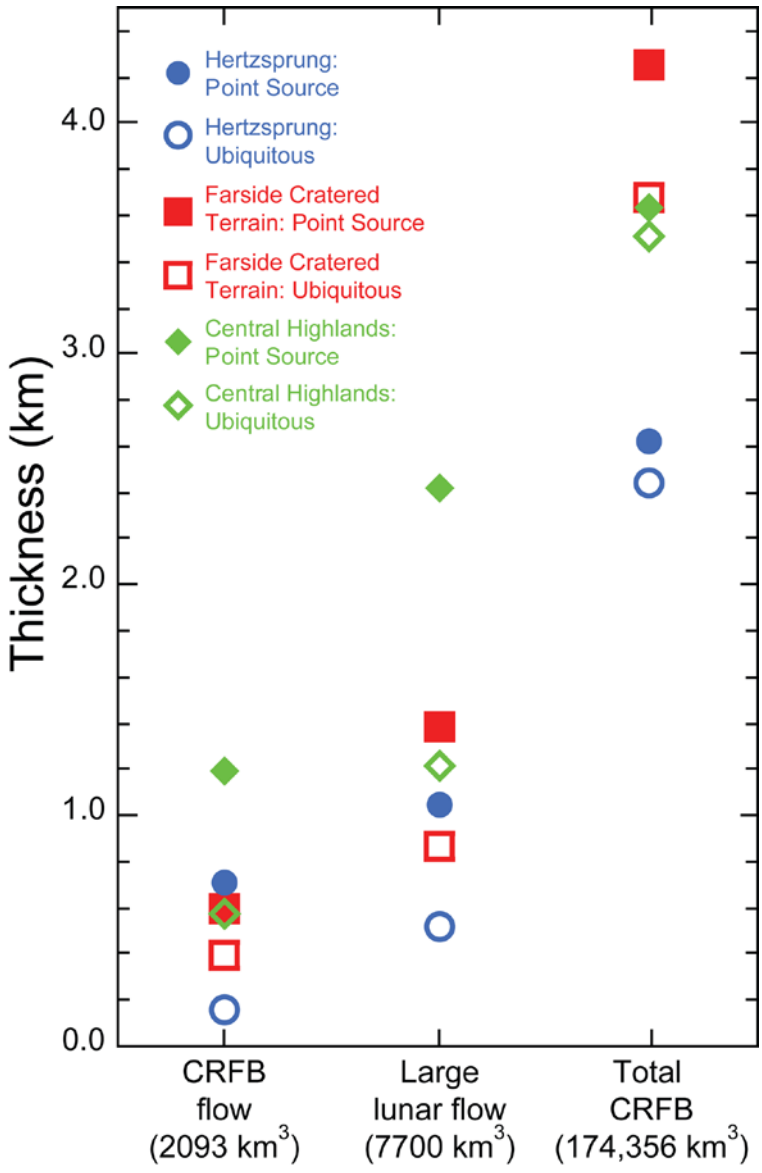
Hertzsprung:
Point Source
Hertzsprung:
Ubiquitous
Farside Cratered
Terrain: Point Source
Farside Cratered
Terrain: Ubiquitous
Central Highlands:
Point Source
Central Highlands:
Ubiquitous
Thickness (km)
4.0
3.0
2.0
1.0
0.0
CRFB
flow
(2093 km3)
Large
lunar flow
(7700 km3)
Total
CRFB
(174,356 km3)

Figure 11.

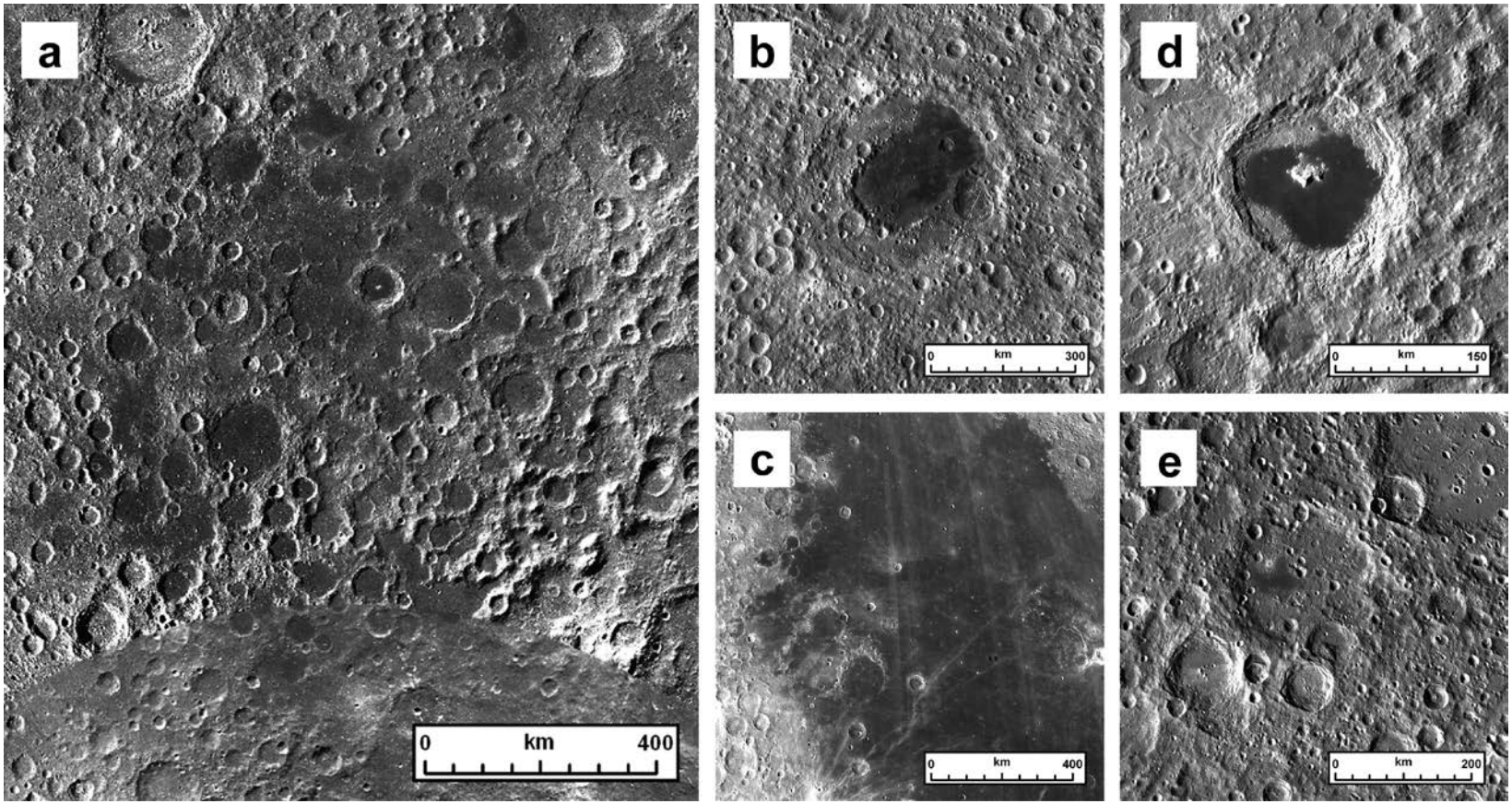

Figure 12.

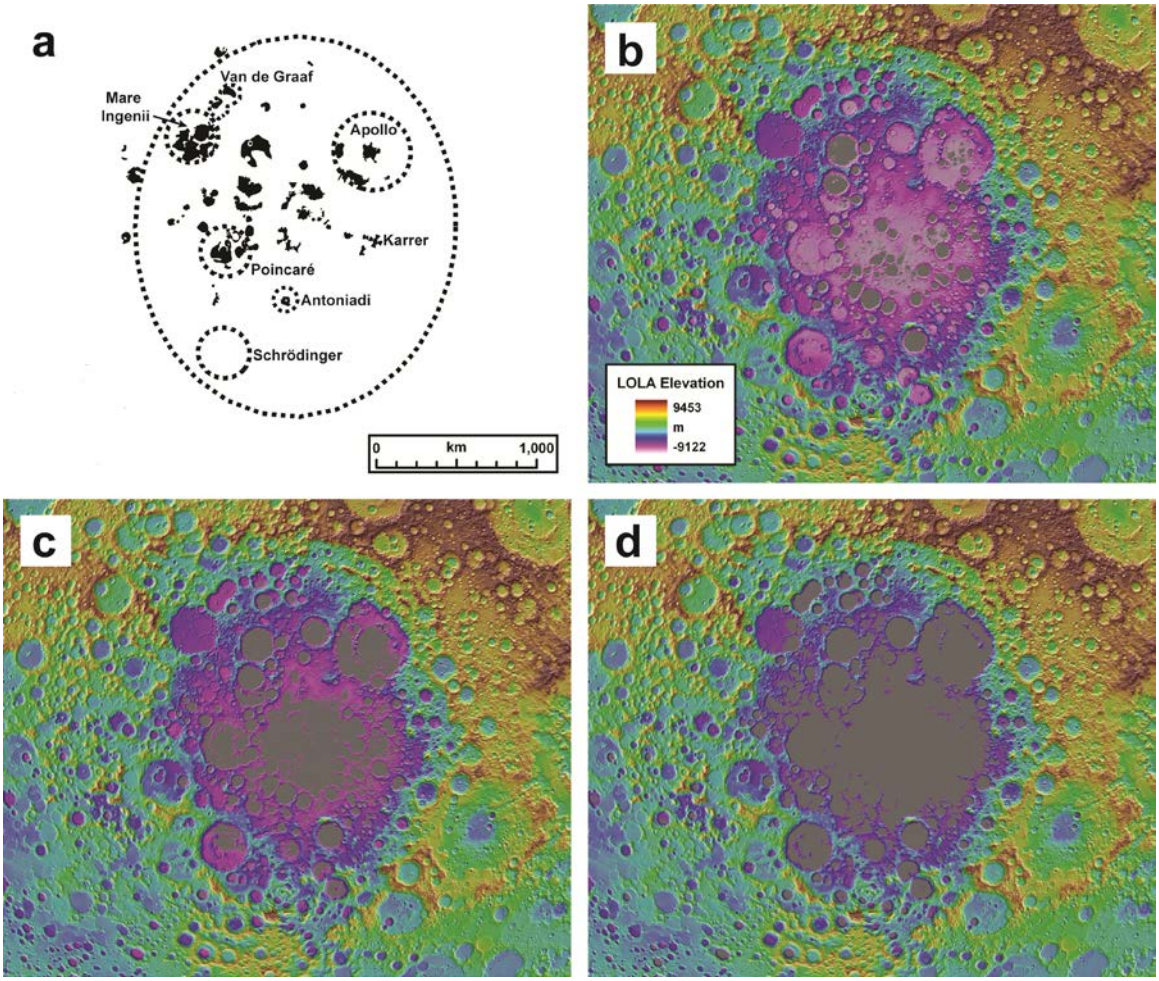
a
Van de Graaf
Mare
Ingenii
Apollo
Karrer
Poincaré
Antoniadi
Schrödinger
0
km
1,000
b
LOLA Elevation
9453
m
-9122
c
d

Figure 13.

Chapter 2:
Lunar cryptomaria, part I: Physical characteristics, Distribution, and Implications for Ancient Volcanism

Jennifer L. Whitten
and
James W. Head III

Department of Geological Sciences, Brown University,
324 Brook St., Box 1846, Providence, RI 02912.

To be submitted:
Summer 2014

Abstract

Cryptomaria, lunar volcanic deposits obscured by crater and basin impact ejecta, can provide important information about the thermal and volcanic history of the Moon. The timing of cryptomare deposition has implications for the duration and flux of mare basalt volcanism. In addition, knowing the distribution of cryptomaria can provide information about mantle convection and lunar magma ocean solidification. Here we use multiple datasets (e.g., M^3, LOLA, LROC, Diviner) to undertake a global analysis to identify the general characteristics (e.g., topography, surface roughness, rock abundance, albedo, etc.) of lunar light plains in order to better distinguish between ancient volcanic deposits (cryptomaria) and impact basin and crater ejecta deposits. Eighteen different cryptomaria regions were identified and mapped. Comparisons of light plains deposits indicate that the two deposit types (volcanic and impact-produced) cannot be distinguished from one another on the basis of topography, surface roughness, or rock abundance, but instead are best distinguished by mineralogic data. The distribution of mare volcanism does not appear to have changed substantially prior to its post-cryptomaria mare basalt distribution. There are several hypotheses explaining the distribution of mare basalts, which include the influence of crustal thickness, mantle convection, KREEP distribution, and a proposed Procellarum basin. Hydrostatic models, coupled with crustal thickness measurements from GRAIL/ LOLA, indicate that mare basalts should be observed in farside basins. The paucity of farside mare basalts means that multiple factors, such as mantle convection and crustal thickness variations, play a role in mare basalt emplacement.

1. Introduction

Ancient volcanic deposits, those emplaced prior to ~3.9 Ga during the era of large impact basin formation, did occur on the Moon. Multiple lines of evidence exist to support this very early volcanism, including the ancient (~4.35 Ga) lunar mare basalt clasts in meteorite Kalahari 009 (Terada et al., 2007), ancient basalt clasts in the lunar sample collection (e.g., Ryder and Spudis, 1980; Taylor et al., 1983), and remote chemical and mineralogical measurements (e.g., Charette et al., 1977; Ryder and Spudis, 1980; Hawke and Bell, 1981; Lawrence et al., 2008). It is difficult to directly observe any ancient volcanic deposits on the Moon because the high flux during the early impact bombardment has buried many of these deposits, known as cryptomaria (Head and Wilson, 1992), underneath a layer of crater and basin ejecta, obscuring them from view.

Volcanism has been an important process on the Moon. Documentation of the location and duration of volcanism provides information about the evolution of the lunar interior and its thermal history. Exposed maria have ages that range from 1.2 Ga to 4.2 Ga and cluster between 3.3 and 3.8 Ga, with a peak at ~3.55 Ga (Fig. 1) (e.g., Stöffler et al., 2006; Hiesinger et al., 2011), and cover ~16% of the surface area of the Moon (Head, 1976). The total volume of mare basalts is estimated to be 1×10^{7} km^3 (Head and Wilson, 1992), with individual flow volumes ranging between 30 and 7700 km^3 (Hiesinger et al., 2002). Estimates of the volcanic flux on the Moon vary as a function of time. The highest fluxes are predicted to have occurred prior to ~3.1 Ga (~10^{-2} km^3/yr), with a maximum at ~4.2 Ga (~5×10^{-2} km^3/yr) (Kirk and Stevenson, 1989). Soon afterwards, the flux of mare basalts decreased significantly, by approximately three orders of magnitude (~10^{-5} km^3/yr). Throughout the rest of lunar history the flux of mare basalt slowly decreased

until eruptions ceased altogether. Thermal evolution models (Kirk and Stevenson, 1989) are supported by flux estimates from mare basalt areas and crater retention ages (Basaltic Volcanism Study Program, 1981).

A hypothesized cataclysmic bombardment of the inner solar system (e.g., Turner et al., 1973; Tera et al., 1974a, b; Cohen et al., 2000) immediately preceded the emplacement of most observable mare basalts (Hiesinger et al., 2011). There is a gap of ~500 Ma, between the formation and differentiation of the Moon and the peak in mare basalt ages, where no significant mare basalt deposits exist. This gap in volcanic activity on the Moon could be related to either the lack of extrusive volcanic deposits or to obscuration by impact basin and crater ejecta. The formation of impact basins prior to the peak in mare basalt ages (Fig. 1) suggests that the paucity of earlier mare basalts may be due to destruction or obscuration by either impact basins and their associated ejecta, or younger mare basalt deposits. Over the last 40 years older basaltic materials, known as cryptomaria, have been identified within and adjacent to impact basins. How old are those volcanic deposits, what is their global distribution, and when did they start erupting? Analysis of cryptomaria are important for addressing these questions and for understanding whether the high flux of volcanic activity observed after the heavy bombardment also occurred earlier in lunar history. Mapping the distribution and sequence of these ancient basaltic deposits provides the first step towards understanding the duration of basaltic volcanism and whether there was a high volcanic flux prior to ~3.8 Ga.

2. Background

Cryptomaria were first defined as “covered or hidden mare deposits that are obscured from view by the emplacement of subsequent deposits of higher albedo” (Head and Wilson, 1992). Before the term cryptomaria was defined, these buried mare deposits were interpreted to have formed from superposed “ejecta deposits from large (>100 km) impact craters…” (Schultz and Spudis, 1979), such as Orientale (Belton et al., 1992; Head et al., 1993). Orientale, one of the youngest lunar impact basins, was formed ~3.7 Ga (e.g., Whitten et al., 2011); thus, the mare deposits covered with basin ejecta had to form prior to this event and are older than the exposed nearside mare basalts. Therefore, in this study the term “cryptomaria” is typically used to refer to ancient volcanic deposits that were obscured by impact basin ejecta, creating high-albedo smooth plains (Fig. 2a). On the Moon, other high-albedo light plains deposits exist that have been associated with impact-related formation mechanisms (Eggleton and Schaber, 1972; Head, 1974; Oberbeck et al., 1973, 1974) and can be easily confused with cryptomaria (Fig. 2b). These light plains are dated from the Nectarian to the Copernican periods (pIp, Cp, Np, INp, Ip, Ip1, Ip2, Ntp (Wilhelms and McCauley, 1971; Wilhelms et al., 1979; Lucchitta, 1978, Wilhelms and El-Baz, 1977; Stuart-Alexander, 1978; Scott et al., 1977)) and will hereafter be referred to as Cayley plains in order to distinguish between light plains formed by (1) obscured volcanic deposits and (2) ponding of basin or crater ejecta deposits in low-lying topography. Cayley plains are found in Ptolemaeus crater (Fig. 2b) and at the Apollo 16 landing site. Prior to the Apollo 16 mission, the landing site light plains were believed to be products of highlands volcanism (Milton, 1964; Wilhelms and McCauley, 1971).

Once the geology (both in situ and returned samples) of the light plains at the Apollo 16 site was analyzed it became obvious that these high-albedo plains were composed of brecciated material (Young et al., 1972; Muehlberger et al., 1980) produced by impact-related processes (Eggleton and Schaber, 1972; Head, 1974; Oberbeck et al., 1973, 1974). Thus, the favored interpretation for this light plains deposit became emplacement during large basin-forming impact events. Those geologic maps produced after the Apollo 16 mission (Wilhelms et al., 1979; Lucchitta, 1978, Wilhelms and El-Baz, 1977; Stuart-Alexander, 1978; Scott et al., 1977) began to interpret light plains as a combination of volcanic and impact-produced materials (Scott et al., 1977; Wilhelms and El-Baz, 1977). Eventually, all of the light plains were interpreted as basin or crater ejecta (Lucchitta, 1978; Stuart-Alexander, 1978; Wilhelms et al., 1979; Meyer et al., 2013). Now after the Apollo missions it is evident that not all high-albedo plains deposits have an impact origin. The chemistry of some high-albedo plains, such as the Apennine Bench Formation (Spudis, 1978), light plains in the Fra Mauro region (Charette et al., 1977; Hawke and Head, 1978), and around Van de Graaff (Hawke and Spudis, 1980), can be related to that of returned samples of known volcanic origin, such as high-Al basalts (Ridley, 1975), high-K Fra Mauro basalts (Shervais et al., 1985), and KREEP (Dowty et al., 1976) and KREEPy basalts (Ryder et al., 1977).

Cryptomaria are formed from the superposition of impact ejecta onto a volcanic surface. The size and distance of the crater or basin interpreted to be the source of the ejecta can be used to classify cryptomaria into different types. There are four distinct processes that can lead to obscuration of volcanic deposits, and these are classified as: (1) Copernicus-type, (2) Balmer-type, (3) Proximal basin ejecta-type, and (4) Distal basin

ejecta-type (Antonenko et al., 1995; Giguere et al., 2003; Hawke et al., 2005) (Fig. 3). The Copernicus-type cryptomaria are formed when the proximal ejecta from a single impact crater obscures a volcanic deposit. Balmer-type cryptomaria are produced from the distal ejecta deposits of multiple impact craters. The remaining two types of cryptomaria are related to basin ejecta deposits. The proximal basin ejecta-type cryptomaria are produced from the primary ejecta of an impact basin and the distal basin ejecta-type cryptomaria are formed from a mixture of basin distal ejecta and local material (Antonenko et al., 1995; Giguere et al., 2003; Hawke et al., 2005). Proximal basin ejecta-type deposits tend to be thicker and more effectively obscure volcanic deposits, compared with the distal basin ejecta-type (Fig. 3).

The generally ancient age of cryptomaria combined with the early high impact flux makes identification and mapping of cryptomaria difficult. Therefore, in order to use cryptomaria as a tool to understand the early volcanic and thermal history of the Moon, it is necessary to develop criteria to distinguish between the volcanically derived cryptomaria and impact-produced Cayley plains. Previous researchers have developed specific techniques to map cryptomaria; Schultz and Spudis (1979) proposed the existence of several cryptomare deposits based on the presence of dark-halo impact craters (DHCs). DHCs are small (<10 km in diameter) craters that formed on a high-albedo surface and excavated low-albedo basaltic material. High concentrations of DHCs on high-albedo smooth plains are indicative of a buried, areally extensive mare deposit. Other criteria, such as geochemical and mineralogic anomalies (e.g., Hawke and Bell, 1981; Antonenko et al., 1995), intermediate albedo surfaces, and Bouger gravity

anomalies (Sori et al., 2013), have also been developed to aid in the identification and mapping of cryptomaria.

In this study we build upon previous research to address several fundamental questions about cryptomaria: (1) What are the general characteristics of cryptomaria? (2) Can those identification criteria be used to distinguish cryptomaria from Cayley plains? (3) What is the distribution of cryptomaria? (4) What does that distribution tell us about ancient volcanism on the Moon?

3. Methods

A variety of lunar datasets were used to identify, map, and characterize the distribution of lunar cryptomaria. Initially analyses were carried out for those regions previously recognized as cryptomaria (Fig. 4, Table 1) (Schultz and Spudis, 1979, 1983; Hawke and Spudis, 1980; Hawke and Bell, 1981; Bell and Hawke, 1984; Hawke et al., 1993; Head et al., 1993; Antonenko et al., 1995; Blewett et al., 1995; Mustard and Head, 1996; Antonenko, 1999; Hawke et al., 2002; Giguere et al., 2003; Campbell and Hawke, 2005; Hawke et al., 2005; Lawrence et al., 2008; Hawke et al., 2013). A global mosaic (2.8 km/pixel) of Moon Mineralogy Mapper (M^3) spectral data (optical period 2c1) was used to search for non-mare regions with an anomalously pyroxene-rich regolith. Anomalously high values in this study corresponded to locations with a 1 μm integrated band depth (the area under a straight line fit between 0.789 μm and 1.308 μm) value >0.5 and associated 2 μm integrated bands depths >0.8. Several regions with large 1 and 2 μm band depth values were identified (Casatus, DeForest, Deslandres, Walther, and Zucchius

craters; Fig. 4, Table 1). Once identified, high resolution regional mosaics were made for each available M^3 optical period in order to ensure consistency when identifying a basaltic mineralogy in DHCs. Long wavelength spectral absorption features at >0.95 μm and 2>.05 μm are associated with clinopyroxene and are used to indicate the presence of mare basalt while shorter wavelength absorptions are associated with orthopyroxene in noritic lithologies (e.g., Adams, 1974). All but one study region was imaged during the 2c1 optical period; Milne was only covered during optical period 2c2. None of the regions with a pyroxene-rich soil signature identified in this study were found to contain areally extensive cryptomaria (Table 1).

Moon Mineralogy Mapper (M^3) visible to near infrared spectral data (Pieters et al., 2009), combined with Lunar Reconnaissance Orbiter Camera (LROC) WAC mosaics (100 m/pixel) (Robinson et al., 2010), were used to map the areal extent of cryptomaria in each study region. First, M^3 data were used to identify DHCs excavating basaltic material. A large concentration of DHCs on a high-albedo smooth plains deposit indicates the presence of an areally extensive cryptomare deposit. The distribution of the DHCs and the extent of the pyroxene-rich regolith (as determined from M^3 band ratio images of confirmed basaltic material) were used to mark the boundary of a given cryptomare deposit. Once the deposit extent was firmly established with M^3 mineralogical data, it was compared with LROC visible imagery to further refine the deposit boundary. Cryptomare boundaries were expanded to include all material with a similar morphology to the terrain contained within the DHC-defined deposit boundary.

After cryptomaria were identified, the deposits were analyzed using additional lunar orbital datasets, including topography (Zuber et al., 2010; Smith et al., 2010) and

surface roughness (Kreslavsky et al., 2013) from the Lunar Orbiter Laser Altimeter (LOLA), rock abundance (Bandfield et al., 2011) from the Lunar Radiometer Experiment (Diviner), and reflectance at 1489 nm (a proxy for surface albedo) using M^3, in order to determine the general physical characteristics (topography, surface roughness, rock abundance, etc.) of cryptomaria. It is important to first define the location and distribution of cryptomaria and then measure their physical characteristics because variations in these data provide information about the variation in formation process or age of the deposit. Then the physical characteristics of cryptomaria, Cayley plains, and maria were compared. In addition, as explained in detail below (section 4), there are few physical characteristics that can distinguish cryptomaria from Cayley plains (Fig. 2), other than high concentrations of DHCs or pyroxene-rich soils.

For this global study of cryptomaria we used the 237 m/pixel (128 pixel/°) LOLA digital elevation model to determine the average elevation for each cryptomare deposit, as well as the average elevation for high-albedo smooth plains (pIp, Cp, Np, INp, Ip, Ip1, Ip2, Ntp (Wilhelms and McCauley, 1971; Wilhelms et al., 1979; Lucchitta, 1978, Wilhelms and El-Baz, 1977; Stuart-Alexander, 1978; Scott et al., 1977)) and maria. Surface roughness data were provided by M. Kreslavsky. These data were converted to a roughness parameter (Kreslavsky and Head, 2012; Kreslavsky et al., 2013); three separate length scales were used to parameterize surface roughness, 0.115 km, 0.46 km, 1.84 km. Lower values of the roughness parameter indicate smoother deposits. Average rock abundance data from Diviner (Bandfield et al., 2011), in addition to surface roughness values, were derived in an effort to determine whether or not Cayley plains are rockier and more hummocky than cryptomaria. The presence of a level surface from the

obscured maria may have enabled basin ejecta to emplace more evenly across these volcanic surfaces compared with the Cayley plains in which basin ejecta many not have ponded smoothly in topographic lows. Additionally, if any light plains were emplaced by younger impact basins (Imbrium and Orientale) these deposits may contain more rocks because of the slow degradation of boulders on the Moon (Hörz et al., 1975) and could reveal information about the relative formation age. Measurements were restricted due to the dataset extent (70°N to 70°S). The average albedo of each cryptomare was determined by averaging the M^3 reflectance value at 1489 nm across the entire deposit, after applying a photometric correction relative to a sphere (M^3 SUP files).

Model ages for the Cayley plains and cryptomaria were computed to understand the temporal relationship between these two geologic units. Craters >6 km in diameter were counted on those individual cryptomare deposits with a large enough continuous areal extent (e.g., >17,500 km^2; Table 1) to provide confidence that the volcanic deposit was emplaced during a single eruptive phase (see Yingst and Head, 1997) and to ensure good statistics. To produce reliable age estimates, only deposits >17,500 km^2 were analyzed (Fig. S1). Secondary craters (oblate rims, herringbone pattern, or occurrence in crater clusters) were avoided during data collection and only craters >9 km were included in our model age calculations for cryptomaria in order to minimize accidental inclusion of secondary craters. A small superposed crater population in the South Pole-Aitken (SPA) cryptomare forced the inclusion of craters >7 km in diameter to improve the model age statistics. Craters >1.5 km in diameter were included in order to determine the model ages for Cayley plains deposits (Fig. S1); a diameter of 1.5 km was determined by identifying the smallest crater diameter bin before the size-frequency distribution began

to “roll over” due to a lack of crater identifications, a consequence of the image resolution limit (Michael and Neukum, 2010). Calculated model ages were derived using the chronology and productions functions of Neukum et al. (2001). The modeled ages are intended to provide estimates of the minimum age of the cryptomaria because, by definition, these volcanic deposits have been resurfaced by impact ejecta. Therefore, the counted crater population is related to the basin ejecta resurfacing event and not the emplacement of the cryptomaria; these cryptomaria could have been emplaced at any point before the calculated model ages. The same reasoning holds true for the Cayley plains deposits; the model ages could indicate the time of formation of the timing of their last resurfacing event.

In addition to model ages of cryptomaria, we used the most recent lunar basin stratigraphy (Fassett et al., 2012) to determine the relative ages of our mapped cryptomaria. Previous work has shown that volcanic deposits are emplaced inside of impact basins within 100-200 My of basin formation (Whitten et al., 2011). As a result, many of the cryptomare deposits located within ancient impact basins can be temporally associated with basin formation (Fig. 5; Table 2). For instance, based on the population of superposed craters Humboldtianum basin is Nectarian and Smythii is Pre-Nectarian (Fassett et al., 2012). Due to this established stratigraphic relationship Smythii ejecta would not have modified or obscured any deposits in Humboldtianum since the basin had not formed yet. Predicted basin ejecta extents were calculated (McGetchin et al., 1973; Pike, 1974; Fassett et al., 2011) to determine which basin ejecta deposits are likely to have contributed overlying high-albedo material to the mapped cryptomaria (Table 2).

For this study only basins within 3 transient crater radii, corresponding to a ~50 m thick ejecta deposit, were considered.

4. Results

4.1. Distribution of detected cryptomaria

A total of 29 possible cryptomare locations were analyzed for this study, 25 are proposed cryptomare deposits from the literature and four regions had a pyroxene-rich soil signature in M^3 data (Fig. 4a). Each location was analyzed with M^3 data to search for a high concentration of DHCs excavating basaltic materials. Of the 29 locations investigated, 18 were observed to contain cryptomaria (Fig. 4, 5; Table 1). No cryptomare was detected in the 4 regions with pyroxene-rich soils; the pyroxene absorption features are shifted to shorter wavelengths and are more indicative of a noritic composition (e.g., Adams, 1974). Several of the cryptomare locations proposed in the literature, such as Clemoedes, Korolev, Maurolycus, Mendeleev, Schrodinger, and Van de Graaff did not contain high concentrations of DHCs and, therefore, were not mapped as cryptomaria. Typically, the most areally extensive deposits are located within ancient basins (e.g., Schiller-Zucchius, Balmer, and Lomonosov-Fleming basins). This type of cryptomare deposit is known as a Distal Basin Ejecta or Balmer Type (Giguere et al., 2003; Hawke et al., 2005). The smallest cryptomaria tend to be associated with ejecta deposits from relatively young craters (e.g., Taruntius, Hercules, Aristoteles, and Glushko craters) and are classified as Copernicus-type, meaning they are young buried mare basalts that have not experienced the geologic history typically associated with cryptomaria (Giguere et al., 2003; Hawke et al., 2005).

Detected cryptomaria have a similar distribution to the observable maria; most basaltic deposits are confined to the lunar nearside within large impact basins (Fig. 5). We did not detect any large cryptomaria on the farside, with the exception of the deposits in South Pole-Aitken basin (Fig. 6n). There is one small detection on the farside, the Dewar cryptomare (Fig. 5, number 3). Dewar is not associated with an impact basin or young mare basalt deposits like the other detected cryptomaria. Additionally, Dewar is not associated with a high-albedo smooth plains deposit like most cryptomaria; the surface of Dewar is hummocky (Fig. 6c, topography). M^3 data indicate that the regolith has a high concentration of mafic material and there are ~5 DHCs (Fig. 6c, column 1, white arrows), consistent with previous studies using Clementine data (Lawrence et al., 2008). Other small deposits are located on the eastern limb of the Moon and are associated with Langemak crater (Fig. 6g) and Lacus Solitudinis (Fig. 6p).

4.2. Topography

Elevation distributions for the entire Moon, exposed maria (Fig. 7a), the Cayley plains (Fig. 7), and cryptomaria (Fig. 6, 7) were computed in order to ascertain whether topography can be used to distinguish between cryptomare and Cayley plains. The nearside mare basalts all occur within a narrow range of elevations (Fig. 7a, b), which is expected because of the hydrostatic forces and density differences between basaltic melt and the anorthositic crust controlling the total thickness of basalt erupted (Wilson and Head, 1981; Head and Wilson, 1992). Compared with the elevation frequency distributions of the other deposits, the mare distribution is narrower and shifted to lower values (shifted ~0.72 km; average elevation is –2.14 km). Both cryptomare and Cayley

plains deposits share a similar elevation frequency distribution to the entire Moon (Fig. 7a). There is a slight difference between the global distribution and the cryptomare and Cayley plains; the global distribution has one distinct elevation peak whereas both cryptomaria and Cayley plains have two distinct peaks in elevation (Fig. 7a). In fact, the distribution of elevations for cryptomare and Cayley plains are almost indistinguishable from one another (Fig. 7a, c, d). The average elevation of all Cayley plains is −1.31 km and −1.42 km for all cryptomaria. The finding that light plains in the lunar highlands, both Cayley plains and cryptomare, have the same elevation distribution indicates that elevation is not a diagnostic indicator of volcanism (Schultz and Spudis, 1979).

The variation in cryptomare topography is not strictly associated with the surrounding highland elevations. Wargentin crater (49.53°S, 299.56°E, 84.7 km in diameter), an impact crater that has been volcanically flooded to its rim, is located within the Schiller-Schickard cryptomare (Fig. 6l, column 2, white arrow) and accounts for most of the highest standing topography in all mapped cryptomaria (Fig. 7, 'Peak 1'). Langemak cryptomaria are located at the highest elevations (Fig. 6g, column 2). Conversely, the lowest lying cryptomaria are located within large impact basins such as Humboldtianum (Fig. 6f, column 2), Smythii (Fig. 6m, column 2), and South Pole-Aitken (Fig. 6n, column 2). As mentioned previously, there are two peaks in the cryptomaria elevation frequency distribution. Both of these elevation peaks (Fig. 7a) are dominated by Lomonosov-Fleming, Balmer, and Schiller-Schickard cryptomare. All three of these cryptomaria are located completely or partially within Pre-Nectarian impact basins (Lomonosov-Fleming, Balmer-Kapteyn, and Schiller-Zucchius) (Fig. 5 numbers 8, 2, 12). The cryptomare located within the centers of these Pre-Nectarian basins (e.g.,

Schiller-Zucchius basin, Schickard crater, northeast Balmer) comprise most of the larger low-elevation Peak 2, centered at approximately -2 km. The high elevation Peak 1 (centered at ~ 0 km) contains most cryptomare located in outer rings of Lomonosov-Fleming, Balmer-Kapteyn, and Schiller-Zucchius basins. The Cayley plains elevation frequency distribution also displays two peaks at approximately the same elevations as cryptomaria, though these elevations peaks are much less distinct. Cayley plains elevations are associated with the elevation of the surrounding lunar highlands; the lowest lying Cayley plains are found in South Pole-Aitken basin and the highest Cayley plains are in the southern nearside highlands and the farside highlands.

4.3. Surface roughness

Exposed maria are easily identified by surface roughness because of their smooth surface texture. Cryptomaria are not as easily distinguished on this basis. At the 1.84 km roughness baseline the average cryptomaria has a roughness parameter value of 0.78 (Fig. 8), followed by 0.74 for Cayley plains, and 0.33 for exposed maria. This means that cryptomaria and Cayley plains are equally rough at length scales on the order of 2 km while the maria are much smoother. The Langemak (Fig. 6g, column 3) and Dewar (Fig. 6c, column 3) cryptomaria are anomalously rough, but only at 1.84 km (Fig. 8a). This makes sense given the location of both cryptomare in the lunar highlands. Both Langemak and Dewar are far removed from areally extensive maria or large impact basins (Fig. 5, numbers 7 and 3), meaning that their surfaces have predominantly affected by superposed impact craters and their associated ejecta. The same is true for Lacus Solitudinis (Fig. 6p, column 3) and Milne (Fig. 6k, column 3), two other cryptomaria

with high surface roughness values. On the other hand, Humboldtianum cryptomare is anomalously smooth at the longest roughness baseline. Exposed maria have the smoothest surfaces at 0.46 km and at this baseline the Cayley plains are actually rougher than cryptomaria (Fig. 8b). However, the 0.46 km roughness for Cayley plains and cryptomare are within the uncertainties of one another, suggesting that there is no significant difference in surface roughness between these two units. There is little consistency from one roughness wavelength to the next (Fig. 8a). At 0.46 km Mendel-Rydberg has the roughest cryptomare and Taruntius the smoothest. The shortest wavelength (0.115 km) produces more scattered surface roughness values, where average cryptomaria and exposed maria are the same (Fig. 8b). Cayley plains are actually rougher at this baseline, with values of 1.05. Of all the surface roughness length scales, cryptomaria and Cayley plains are roughest at 0.46 km whereas exposed maria are roughest at 0.115 km (Fig. 8b). There is no correlation between surface roughness and rock abundance data (see below).

4.4. Rock abundance

Rock abundance values for the lunar surface were derived from measurements of surface temperature from the Diviner instrument (Bandfield et al., 2011). Estimates of rock abundance range from approximately 0–30%, depending on the geologic setting. The largest rock populations are associated with fresh impact craters. Both highland and mare regolith materials display rock abundance values <1%. In addition, rock concentrations correlate with crater age and higher rock abundances are only associated

with steeply sloped surfaces that experience mass wasting events and are not capable of building up a thick regolith (Bandfield et al., 2011).

Unsurprisingly, Diviner rock concentrations for the Cayley plains, cryptomare, and mare deposits are <1% (Fig. 9; Table 2). The Schiller-Schickard cryptomaria has the highest rock abundance at 0.45%. The lowest average rock abundances are associated with the Hercules and Mare Frigoris cryptomaria (0.27%). Rock abundances on the Cayley plains deposits and mapped cryptomare are not statistically different (Fig. 9). Measurements of exposed maria in the 18 study regions (Fig. S2) show that there is more variation in rock abundance within the exposed maria compared with cryptomaria. For instance, the exposed mare in the Lacus Solitudinis study region has the highest rock abundance (~0.64%; Table 2); this region was found to have one of the highest rock concentrations on the Moon (Greenhagen et al., 2012). The cause of this enhanced rock abundance is unrelated to cryptomaria-producing geologic processes. Formation hypotheses for this rocky terrain include an unusually high production of impact melt during the Tsiolkovskiy impact event, antipodal emplacement of impact melt from Aristarchus crater, or formation of Tsiolkovskiy from an iron-rich impactor. Any remnant iron left in the regolith may produce the unusual thermophysical properties observed (Greenhagen et al., 2012). On average, cryptomaria have lower rock concentrations than the maria, which is probably the result of a more well-developed cryptomare regolith due to the greater age of these deposits.

4.5. Average albedo (1489 nm reflectance)

When early researchers were first investigating cryptomaria, one of the distinguishing criteria was an enhanced mafic signature in the overlying regolith (e.g., Hörz, 1978; Schultz and Spudis, 1979; Antonenko et al., 1995), corresponding to an enhancement in iron (for gamma ray spectrometer data) or an increase in pyroxene absorption band depths (for VNIR spectral data). An enhancement in mafic minerals (e.g., pyroxene and olivine) produces a decrease in the average albedo of the surface. As a result, typical albedo values for cryptomaria lie between that of average highland regolith and average mare regolith. The exposed nearside maria have an average albedo (1489 nm reflectance value) of ~0.10 (Fig. 10). Average albedo values for highland plains regolith, represented by the USGS-mapped Cayley plains, is ~0.12 (Fig. 10). The average albedo of mapped cryptomaria is ~0.13, slightly higher but still statistically similar to than the USGS-defined Cayley plains (Fig. 10). In M^3 data, some of the cryptomaria regions did not have enhanced pyroxene signatures in their regolith (Fig. 6, column 1) and could only be identified by a high concentration of DHCs. The lack of detectable mafic minerals in the cryptomare regolith would allow for a higher albedo signature, similar to typical highlands, which is correlated with the thickness of superposed basin ejecta in the cryptomare deposits. Thicker ejecta deposits prevent substantial vertical mixing between the superposed ejecta and the underlying volcanic unit. When only a thin veneer of basin ejecta is emplaced both vertical and horizontal mixing can effectively mix basaltic and feldspathic compositions so that the basaltic signature dominates and the deposit has a lower average albedo than surrounding highlands. Compared with the mapped cryptomaria, many of the Cayley plains are located in the polar regions where there is less reflected light (Fig. 4b, c), producing a

lower signal-to-noise ratio; this reduced signal and resulting “noisy” spectra along with the concentration of Cayley plains at the poles could explain the albedo discrepancy.

4.6. Thickness and volume estimates

The mare surfaces that were subsequently obscured to become cryptomaria were being erupted at a time when the surface of the Moon was being continuously bombarded by bolides. Therefore, an understanding of the morphologic expression of volcanic deposits in heavily cratered terrain is critical for identification purposes. Previous studies have investigated the morphologic evolution of volcanic flooding of heavily cratered terrains by conducting simulations of volcanic filling and measuring the evolution of the volcanic deposit volume, area, crater size-frequency distribution, and thickness (Whitten and Head, 2013). Those workers showed a relationship between the areal extent and thickness of a volcanic deposit. Using this technique the areal distribution of identified cryptomaria can be compared with the simulations in order to estimate the deposit thickness.

Only cryptomaria contained within well-defined impact basins that are not labeled as Copernicus-type (Table 1) were evaluated (Table 2). The Copernicus-type cryptomaria were excluded because these young deposits are generally a small part of a much larger exposed mare deposit, which makes thickness determinations difficult. Since many cryptomaria are located within impact basins, these deposits can be compared with volcanic flooding simulations conducted within Hertzsprung basin (Whitten and Head, 2013; Fig. 3 and 6 in Chapter 1). The thinnest deposits are associated with small deposits in the basin center. As a volcanic eruption continues, more material will fill the center of

the basin until a basin ring is breached and volcanic flows can be emplaced between basin rings. Other cryptomaria have multiple small deposits spread throughout a cratered terrain; for these regions the cryptomaria deposit distribution was compared with flooding simulations in the Central Highlands and a farside heavily cratered terrain (Whitten and Head, 2013; Fig. 4–6 in Chapter 1).

By comparing the geologic setting (basin versus highlands) and areal extent of cryptomaria it was determined that the thickest deposits are Balmer, Milne, Schiller-Schickard, and Smythii (Fig. 11, numbers 2, 11, 12, 13). The thinnest cryptomaria deposits are in Langemak, Lacus Solitudinis, West Humorum, and West Procellarum (Fig. 11 numbers 7, 16, 17, 18; Table 2). As indicated by the flooding simulations (Whitten and Head, 2013), geologic setting has an influence on cryptomare deposit thickness. For instance, thick cryptomaria are associated with impact basins and thinner deposits are comprised of multiple small deposits within the lunar highlands. Magma ascent and eruptions models (Wilson and Head, 1981; Head and Wilson, 1992) support this association between geologic setting and deposit thickness. Lunar lavas preferentially erupt into lower-lying topography and produce more voluminous deposits compared with highland regions because the excess pressure required to propagate a dike to the surface is correlated with the crustal thickness. A magma body stalled below a thicker crust requires more excess pressure to erupt onto the surface compared with a region of thinner crust (Head and Wilson, 1992).

Using the above thickness estimates, the four most voluminous deposits, from largest to smallest, are: Schiller-Schickard, Lomonosov-Fleming, Balmer, and Smythii basins (Fig. 11). These basins have an estimated $1.5–4\times10^5$ km^3 of cryptomaria, a volume

that is an order of magnitude smaller than the terrestrial Columbia River basalts (1.3×10^6 km^3) (Tolan et al., 1989). All four of these cryptomaria are contained within or immediately surrounding an ancient impact basin. A large portion of the Schiller-Schickard region is also associated with the Pre-Nectarian Schiller-Zucchius basin (Fig. 6l, topography) at the southernmost extent of the cryptomare, but there are also extensive deposits to the north of the basin. Lomonosov-Fleming, Balmer, and Smythii are associated with Pre-Nectarian basins. Based on the stratigraphy of the cryptomaria and exposed mare basalts in Smythii (Fig. 6m), these are probably early basin fill deposits. The presence of more voluminous cryptomaria within basins is similar to the distribution of voluminous maria; the most areally extensive and voluminous maria are located in nearside basins, while smaller discrete deposits are distributed exterior to impact basins and throughout the highlands.

4.7. Crater size-frequency distributions

Superposed crater populations can be used to date the surface of cryptomaria. Since cryptomaria are buried volcanic deposits covered with crater or basin ejecta, this technique of using superposed craters will date the age of the crater or basin resurfacing event and not the emplacement age of the volcanic deposit. The deposition of ejecta onto the volcanic surface may have destroyed or buried any pre-existing craters on the volcanic surface. Thus, the derived model age is a minimum estimate. The size-frequency distribution of superposed craters was determined only for the largest cryptomaria. Only those regions with continuous cryptomare deposits with areas >17,500 km^2 were used in order to ensure robust statistics for age derivation. Additionally, large continuous

deposits can be assumed to have erupted in a single eruption event. The same is not necessarily true for small, areally discontinuous cryptomare deposits.

Superposed crater populations from six cryptomaria (Balmer, Lomonosov-Fleming, Marginis, Schiller-Schickard, Smythii, and South Pole-Aitken) indicate that the deposits were all emplaced before ~3.8 Ga (Fig. 12; Table 2). Lomonosov-Fleming cryptomare has the oldest calculated resurfacing age of 4.0 Ga, followed by Smythii, South Pole-Aitken and Marginis, Balmer, and Schiller-Schickard (Fig. 12; Table 2). It is worth noting that, as expected, the resurfacing age of the Schiller-Schickard region matches well with age estimates of the Orientale impact event (~3.7 Ga) (e.g., Whitten et al., 2011).

Cryptomaria were emplaced between the formation of their confining basin and the basin ejecta resurfacing ages presented above; the volcanic deposits had to erupt into the basin after its formation, but prior to the emplacement of the superposed impact ejecta. Many cryptomaria are confined to Nectarian and Pre-Nectarian impact basins, which formed after the solidification of the anorthositic crust at ~4.4 Ga (Nemchin et al., 2009; Meyer et al., 2010; Elkins-Tanton et al., 2011). Therefore, cryptomaria must have been emplaced between 3.8 (Fig. 12; Table 2) and 4.4 Ga. Over a period of 600 Ma, approximately 9.6×10^5 km^3 (total estimated volume of dated cryptomaria) of basaltic material (Chapter 3) was extruded onto the surface of the Moon. This produces a flux of ~1.6×10^3 km^3/Ma. If the total volume of all cryptomaria is used (1.1×10^6 km^3) then a surface volcanic flux of ~1.8×10^3 km^3/Ma is predicted. This flux estimate is approximately an order of magnitude smaller than that estimated based on unit thicknesses and crater retention ages (Basaltic Volcanism Study Project, 1981). The

cryptomare analyzed in this study needed to have erupted within a ~100 Ma period in order to produce eruption rates of ~10^{-2} km^3.

Ages for the Cayley plains (Fig. 12; Table 3) are, on average, younger than the cryptomaria; the average Cayley plains age is 3.75 ±0.01 Ga (Table 3) and the youngest cryptomaria age is 3.77 +0.05/-0.07 Ga (Table 2). Some individual Cayley plains count areas are older than the cryptomaria, especially those Cayley plains deposits in the "North" study area (Fig. 12). The age spread in the "North" study region is 3.73 to 3.95 Ga, with an average age of 3.80 Ga. Cayley plains within the "Farside" study region have ages between 3.68 and 3.83 Ga and a slightly lower average age of 3.77 Ga. Lastly, the youngest Cayley plains (average age 3.68 Ga) are located in the central highlands count region, with individual deposit ages between 3.62 and 3.83 Ga (Table 3). These Cayley plains crater retention ages correspond to the latest model ages determined for the Orientale-formation event, ~3.65 Ga (Whitten et al., 2011), suggesting that Orientale basin ejecta may have produced these light plains. In addition, the young ages for individual Cayley plains deposits may also be explained by ejecta emplaced by smaller craters (>50 km in diameter) local to the dated deposits.

4.8. Basin ejecta

The distribution of basin ejecta deposits was calculated using the models developed by McGetchin et al. (1973) and Pike (1974) (Fig. 13). Transient crater diameter estimates were taken from Petro and Pieters (2008). The amount of possible impact basin ejecta at each cryptomare site was evaluated based on the lunar basin stratigraphy from Fassett et al. (2012), cryptomaria proximity to the basin impact event,

the type of cryptomaria (Copernicus-types were excluded) (Table 1), and the crater retention ages (Fig. 12; Table 2). Craters with observed topographic rims >300 km in diameter were included in these calculations (Fig. 5, blue circles). Using the criteria listed above, the most destructive impact basin event was the Smythii formation event (Table 2). The Smythii impact has the potential to deposit >50 m of basin ejecta on the Australe, Balmer, Langemak, Lomonosov-Fleming, Marginis, Milne, and Lacus Solitudinis cryptomaria due to the magnitude of the basin-forming event and the proximity of these cryptomaria (Fig 13z). Other important cryptomare-forming basin impact events are Crisium, Imbrium, and Orientale. These three basins have the potential to affect 3–4 cryptomare deposits (Fig. 13f, k, t; Table 2). Those basins with the smallest effect on cryptomaria formation include Apollo, Humorum, Mendel-Rydberg, and Planck basins (Fig. 13b, j, p, u). The cryptomaria least affected by basin impact deposits are the young Copernicus-type deposits (e.g., Taruntius, Hercules, and Mare Frigoris); these cryptomaria were formed much later in lunar history by craters <100 km in diameter.

5. Discussion

5.1. Cryptomaria distribution

Detected cryptomaria increase the area of the Moon covered with mare basalt (Chapter 3), from 16.3% to 18.1%, and share the same distribution as the exposed mare deposits (Fig. 5). For instance, mapped cryptomaria have increased the concentration of mare basalt on the eastern nearside of the Moon. The areal extent of maria in the eastern hemisphere is 12.4%, but when the areal extent of cryptomaria is included the total areal coverage increases to 15.1%. Including cryptomaria in surface area calculations for the

western hemisphere increases only 1%, from 19.9% to 20.9%. The concentration of most extrusive volcanic deposits on the nearside, both exposed maria (<3.8 Ga) and cryptomaria (>3.8 Ga), indicates that the process responsible for magma ascent and eruption was active early in lunar history. Theories explaining the concentration of mare basalts on the nearside include crustal thickness variations (e.g., Solomon, 1975; Head and Wilson, 1992), degree-1 mantle convection (e.g., Zhong et al., 2000), concentration of KREEP (the residual materials of magma ocean solidification that are enriched in potassium, rare earth elements, and phosphorus, as well as uranium and thorium) materials on the nearside (e.g., Haskin, 1998; Lawrence et al., 1998; Wieczorek and Phillips, 2000), and the proposed Procellarum impact basin (Cadogan, 1974; Whitaker, 1981; Wilhelms, 1987; Nakamura et al., 2012):

The nearside/ farside crustal thickness dichotomy mirrors the distribution of mare basalt deposits, suggestive of a relationship between crustal thickness and mare basalt distribution. Melts from mare basalt source regions ascend through the mantle/ crust and stall when a level of neutral buoyancy is reached. The melt bodies remain in the neutral buoyancy zone until excess pressures, such as volume changes from an injection of new magma or crystallization of some of the melt, cause an eruption onto the surface. In regions of thinner crust (e.g., impact basins and craters) smaller excess pressures are needed to overcome the density difference between the magma and the anorthositic crust and, thus, mare basalts tend to erupt in these locations (Head and Wilson, 1992). On a more local scale, crustal thickness variations have been shown to have influenced the eruption of mare basalts in the Orientale basin (Whitten et al., 2011). The basin is located on the western limb of the Moon and straddles the thin nearside crust and the thicker

farside crust. Mare deposits within Orientale are dated between ~1.7 and ~3.7 Ga (e.g., Greeley et al., 1993; Whitten et al., 2011), spanning a large period of time and, yet, incompletely filling Orientale basin. This ~2 Gy duration of mare basalt activity suggests that the extrusion and emplacement of maria was restricted by something other than the thermal state of the lunar mantle; based on the location of Orientale and the pattern of mare fill from nearside to farside basins, it is probable that crustal thickness variations played a role in the extrusion of mare magmas.

While the association of mare basalts with thinner crust has been proposed as a major control on mare basalt distribution, it is important to note the exceptions to this observation. There is not a direct correlation between mare emplacement and topography; the South Pole-Aitken basin has a paucity of mare basalts, especially for the basin's size and depth. This observation suggests that the eruption of mare basalts may have been controlled by a geologic process, such as mantle convection. Dense, ilmenite-rich cumulates crystallized during solidification of the last 5–10% of the lunar magma ocean liquids (e.g., Zhong et al., 2000; Parmentier et al., 2002). The density disparity between low-density early cumulates and the dense late-stage ilmenite-rich cumulates resulted in a gravitational instability that led to mantle overturn (e.g., Ringwood and Kesson, 1976; Hess and Parmentier, 1995). The wavelength of the instability controls the mantle convection, such that at longer lengthscales degree-1 mantle convection dominates. This overturn and subsequent degree-1 mantle convection has been cited as a possible process for concentrating mare basalt volcanism on the lunar nearside (e.g., Zhong et al., 2000; Parmentier et al., 2002).

There is also an association between mare basalts and the distribution of KREEP. KREEP materials are concentrated on the nearside (e.g., Haskin, 1998; Lawrence et al., 1998) in the Procellarum KREEP Terrane (Jolliff et al., 2000) and have been associated with mare basalt genesis. The high concentration of radiogenic elements (e.g., U, Th) is thought to provide additional heat for extensive and prolonged melting on the nearside (e.g., Wieczorek and Phillips, 2000). Several different models have been proposed to explain the observed distribution of KREEP, from impact modification and distribution (e.g., Arkani-Hamed and Pentecost, 2001) to asymmetric crystallization of the lunar magma ocean (e.g., Warren and Wasson, 1979). Models indicate that the concentration of KREEP beneath the nearside induces melting almost immediately and continues into the present, though to a much lesser extent (Wieczorek and Phillips, 2000). There are several issues with this model of mare basalt petrogenesis, including the density barrier that a less-dense KREEP liquid layer creates for the ascent of mare basalt magmas, a lithosphere heated by a thick KREEP layer would not be strong enough to support the observed mascon basins, and the model cannot reproduce the observed geochemical and isotopic characteristics of the magnesian suite (Hess and Parmentier, 2001). These difficulties with the model prevent an adequate explanation for the production and eruption of both cryptomaria and maria magmas.

The formation of a giant basin, known colloquially as the Procellarum basin, was proposed to explain the distribution of KREEP material and the nearside/ farside crustal asymmetry (Cadogan, 1974). If present, Procellarum is the oldest basin on the Moon. Due to its proposed age (~4.2-4.3 Ga (e.g., Taylor et al., 1983 and references therein)) and the calculated ages of the Apollo and Luna samples, it is likely that this depression

was filled with early volcanic deposits. Age estimates, both from isotopic studies and the superposed crater population, indicate that several types of volcanic deposits were erupting onto and within the lunar surface as early as 4.35 Ga. The Procellarum basin likely created a large amount of heat, as well as a large topographic depression, encouraging production and eruption of volcanic deposits. Depending on the depth to which a basin 3200 km in diameter (Wilhelms, 1987) excavated, the Procellarum basin may have tapped into the mantle and mixed together urKREEP (the residual liquid of the lunar magma ocean) and mantle cumulates (Nyquist and Shih, 1992). Many researchers proposed that the early volcanic deposits in the Procellarum basin were KREEP volcanics (e.g., Cadogan, 1974; Wilhelms, 1987). Others suggest that the basin triggered the production of aluminous mare basalts (Nyquist and Shih, 1992) or mare-type volcanism (Taylor et al., 1983).

The present study indicates that the largest cryptomaria are contained within ancient impact basins (e.g., Schiller-Zucchius, Lomonosov-Fleming, Balmer-Kapteyn; Fig. 5), similar to the largest exposed mare deposits. This geologic-tectonic setting suggests that even early in lunar history impact basins have been effective at facilitating the eruption of volcanic deposits onto the lunar surface, by creating a large cavity in the crust and removing a portion of the low-density anorthositic crust. The distribution of cryptomaria and maria on the Moon provides support for eruption models controlled by either crustal thickness or mantle convection patterns, or both.

5.2. Farside basin smooth plains

There is a dearth of cryptomaria and maria on the lunar farside (Fig. 5). The deposits that are present are small and contained within large basins and craters. Dewar and South Pole-Aitken are the only farside cryptomaria (deposits between 135°E and 135°W). Exposed mare basalts are found in Moscoviense basin, Campbell crater, Freundlich-Sharonov (Lacus Luxuriae), Kohlschütter crater, and around the periphery and within South-Pole Aitken basin. Several farside basins, such as Mendeleev (325 km; 5.37°N, 141.17°E), Korolev (423 km; 4.19°S, 202.59°E) (Fig. 14a), and Hertzsprung (536 km; 1.37°N, 231.34°E) (Fig. 14b), are almost completely filled with high-albedo smooth plains, presumed to be Cayley plains. Larger and much older basins, such as Freundlich-Sharonov basin (600 km in diameter (Wilhelms, 1987); 19.18°N, 175.41°E) (Fig. 14c), are barely filled with any material, mare, or Cayley plains (Fig. 14, 15a). In fact, ~7 km of vertical relief is preserved in Freundlich-Sharonov basin. If the plains deposits within Mendeleev, Korolev and Hertzsprung basins were all impact-derived then other similarly-aged farside basins, such as Freundlich-Sharonov, would be filled with similar amounts of basin ejecta (McGetchin et al., 1973; Pike, 1974). However, this is not the case. Both Mendeleev and Korolev basin were investigated for the presence of cryptomare (Table 1), by searching for DHCs and pyroxene-rich soils, neither of which were detected in these two basins. Perhaps some of the farside basins do have cryptomaria, but these ancient volcanic deposits are buried by thick layers of ejecta that cannot be penetrated by DHCs.

A hydrostatic model of magma ascent and eruption (Wilson and Head, 1981) was used to determine the expected depth of a hypothetical mare basalt fill in Mendeleev basin (equation 46 from Wilson and Head (1981)):

$$D_{bf} = \frac{\rho_h D_h + \rho_m D_m - \rho_l D_m}{\rho_l} \quad (1)$$

where D_{bf} is the crustal thickness of the basin fill, D_h is the crustal thickness, D_m is the depth below the crust-mantle boundary, and ρ_l, ρ_h, and ρ_m are the liquid, crustal, and mantle densities. Crustal thickness, crustal density (2550 kg/m^3), and mantle density (3220 kg/m^3) values were taken from the latest GRAIL results (Wieczorek et al., 2013). Measurements of the nearby mare-filled Kohlschütter crater (Fig. 15a) were used to determine the value of D_m, the depth of the basaltic source region, by rearranging equation 1. Kohlschütter crater formed after Mendeleev, meaning that the source region of the Kohlschütter mare basalts was potentially deeper than any volcanic deposits in Mendeleev; thermal evolution models indicate that over time mantle melting increases with depth (Wieczorek et al., 2000). Thus the D_m determined from Kohlschütter crater represents a maximum depth of the basalt source for Mendeleev basin. The crustal thickness of Kohlschütter crater, D_f, was measured from the lunar crustal thickness models of Wieczorek et al. (2013). Depth/diameter relationships (Kalynn et al., 2013) combined with topographic profiles (Fig. 15b) provided an estimate for the amount of mare basalt fill in Kohlschütter (~2.6 km). After solving for D_m, the same method was applied to Mendeleev basin using the depth/diameter relationships from Williams and Zuber (1998).

The model results indicate that in Mendeleev basin there is the potential for volcanic deposits ~7.4 km thick (red dashed line, Fig. 15b) or there may not be any volcanic deposits (blue dashed line, Fig. 15b), depending on the assumed magma composition. The depth of Mendeleev basin is estimated to be ~5 km (Williams and Zuber, 1998), indicating that there is ~1.1 km of fill in the basin interior. According to

ejecta emplacement models, the amount of basin ejecta fill is on the order of 0.5 km (McGetchin et al., 1973; Pike, 1974), leaving 0.6 km basin fill of unknown composition. The hydrostatic model of magma ascent and eruption suggests that a magma density of ~3000 km/m^3 could produce a basaltic deposit consistent with observations, depending on the depth of the source region. A decrease in the depth of the basalt source region (D_m) reduces the amount of calculated volcanic fill possible in the basin, requiring lower-density magmas to produce the observed deposit.

Hydrostatic calculations suggest that some amount of mare was emplaced in Mendeleev before being covered up by impact deposits. This result assumes that the magma source region depth was the same for both younger craters (i.e., Kohlschütter crater) and older impact basins (i.e., Mendeleev basin). The source depth of mare basalts is expected to increase with time (e.g., Wieczorek and Phillips, 2000), which produces even thicker volcanic fill deposits. However, in the hydrostatic model used, crustal thickness has a stronger control on the predicted basin or crater fill compared with magma source depth (Table 4). If Mendeleev is filled with 0.5 km of basin ejecta overlying cryptomaria then superposed craters >5 km in diameter (e.g., Harden (15 km), Fischer (30 km), Benedict (14 km), and Richards (17 km) craters) should have basaltic low-albedo ejecta. This is not the case (Fig. 16), which implies that Mendeleev is completely filled with feldspathic impact basin ejecta. The lack of mineral absorption features (Fig. 16b) could imply an Mg-rich magma composition, but hydrostatic calculations indicate that lower density magmas are expected to erupt and form thicker deposits (Fig. 15b), which is not consistent with observations. The model assumptions about crustal density, mantle density, the derived mantle depth may not have been

representative of the conditions present early in lunar history. Perhaps these variables were such that basaltic eruptions were not possible on the farside at that time in lunar history. Based on this analysis of Mendeleev basin and other observations of limited farside basalt fill (e.g., Lacus Luxuriae in Freundlich-Sharonov basin), both mantle convection patterns and crustal thickness variations are still plausible mechanisms for controlling the eruption of basalts.

6. Conclusions

The distribution of mare basalt volcanism does not appear to have changed from its inception >4.35 Ga. A specific analysis of cryptomare mineralogy is discussed in a companion paper (Chapter 3) and concludes that cryptomaria are most consistent with the presence of obscured or buried mare basalts. In this study, cryptomaria were mapped using M^3 spectral data and then these identified cryptomaria (Fig. 5) were analyzed to quantify the general characteristics of these ancient volcanic deposits (e.g., topography, surface roughness, rock abundance, albedo, etc.) to better identify them and to understand what they reveal about early lunar mare volcanism:

(1) The oldest cryptomare is in either the Balmer or Lomonosov-Fleming study region based on basin ages, morphology/ preservation, and exposed mare ages (Table 2). Older (Fig. 12) and areally extensive (Fig. 11) cryptomaria are associated with impact basins.

(2) Lacus Solitudinis and Milne are the youngest cryptomaria that are not classified as Copernicus-type (Table 1).

(3) The best criterion to distinguish between Cayley plains and cryptomaria is a high concentration of DHCs excavating basaltic material. Mapped cryptomaria and the USGS-map-defined Cayley plains cannot be distinguished from one another using topography, surface roughness, rock abundance, or average albedo.

(4) The distribution of cryptomaria, combined with hydrostatic calculations, and the lack of mafic mineral absorption features in light plains within farside basins suggests that volcanic eruptions onto the lunar surface have the potential to be controlled by mantle convection processes and/ or crustal thickness variations.

Acknowledgements

We thank M. Kreslavsky for kindly sharing surface roughness data he derived from LOLA topography for our analysis.

References

Adams, J.B., 1974. Visible and near-infrared diffuse reflectance spectra of pyroxenes as applied to remote sensing of solid objects in the solar system. Journal of Geophysical Research 79, 4829–4836.

Antonenko, I., 1999. Global estimates of cryptomare deposits: Implications for lunar volcanism. Lunar Planet. Sci. Conf., 30th, Abstract 1703.

Antonenko, I., Head, J.W., Mustard, J.F., Hawke, B.R., 1995. Criteria for the detection of lunar cryptomaria. Earth, Moon and Planets 69, 141–172.

Arkani-Hamed, J., Pentecost, A., 2001. On the source of the lunar mare basalt. Journal of Geophysical Research 106, 14691–14700.

Bandfield, J. L., R. R. Ghent, A. R. Vasavada, D. A. Paige, S. J. Lawrence, and M. S. Robinson, 2011. Lunar surface rock abundance and regolith fines temperatures derived from LRO Diviner Radiometer data. Journal of Geophysical Research 116, E00H02, doi: 10.1029/2011JE003866.

Basaltic Volcanism Study Project, 1981. Basaltic Volcanism on the Terrestrial Planets. Pergamon Press, New York, 1286 pp.

Bell, J.F., Hawke, B.R., 1984. Lunar dark-haloed impact craters: Origin and implications for early mare volcanism. Journal of Geophysical Research 89, 6899-6910.

Belton, M.J.S., Head, J.W., Pieters, C.M., Greeley, R., McEwen, A.S., Neukum, G., Klaasen, K.P., Anger, C.D., Carr, M.H., Chapman, C.R., Davies, M.E., Fanale, F.P., Gierasch, P.J., Greenberg, R., Ingersoll, A.P., Johnson, T., Paczkowski, Pilcher, C.B., Veverka, J., 1992. Lunar impact basins and crustal heterogeneity: New western limb and far side data from Galileo. Science 255, 570–576.

Blewett, D.T., Hawke, B.R., Lucey, P.G., Taylor, G.J., 1995. Remote sensing and geological studies of the Schiller-Schickard region of the Moon, J. Geophys. Res. 100, 16959–16977.

Cadogan, P.H., 1974. Oldest and largest lunar basin? Nature 250, 315–316.

Campbell, B.A., Hawke, B.R., 2005. Radar mapping of lunar cryptomaria east of Orientale basin. Journal of Geophysical Research 110, E09002, doi: 10.1029/2005JE002425.

Charette, M.P., Taylor, S.R., Adams, J.B., McCord, T.B., 1977. The detection of soils of Fra Mauro basalt and anorthositic gabbro composition in the lunar highlands by remote spectral reflectance techniques. Proceedings of the Lunar and Planetary Science Conference, 8th, 1049–1061.

Cohen, B.A., Swindle, T.D., Kring, D.A., 2000. Support for the Lunar Cataclysm Hypothesis from Lunar Meteorite Impact Melt Ages. Science 290, 1754–1756, doi: 10.1126/science.290.5497.1754.

Dowty, E., Keil, K., Prinz, M., Gros, J., Takahashi, H., 1976. Meteorite-free Apollo 15 crystalline KREEP. Proc. Lunar Planet. Sci. Conf. 7, 1833–1844.

Eggleton, R.E., Schaber, G.G., 1972. Cayley Formation interpreted as basin ejecta. In: Apollo 16 Preliminary Science Report. Special Publication SP-315, NASA, Washington, D.C., pp. 29–7 to 29–16.

Elkins-Tanton, L.T., Burgess, S., Yin, Q.-Z., 2011. The lunar magma ocean: Reconciling the solidification process with lunar petrology and geochronology. Earth and Planetary Science Letters 304, 326–336, doi: 10.1016/j.epsl.2011.02.004.

Fassett, C.I., Head, J.W., Smith, D.E., Zuber, M.T., Neumann, G.A., 2011. Thickness of proximal ejecta from the Orientale Basin from Lunar Orbiter Laser Altimeter (LOLA) data: Implications for multi-ring basin formation. Geophysical Research Letters 38, L17201, doi: 10.1029/2011GL048502.

Fassett, C.I., Head, J.W., Kadish, S.J., Mazarico, E., Neumann, G.A., Smith, D.E., Zuber, M.T., 2012. Lunar impact basins: Stratigraphy, sequence and ages from superposed impact crater populations measured from Lunar Orbiter Laser Altimeter (LOLA) data. Journal of Geophysical Research 117, E00H06, doi: 10.1029/2011JE003951.

Giguere, T.A., Hawke, B.R., Blewett, D.T., Bussey, D.B.J., Lucey, P.G., Smith, G.A., Spudis, P.D., Taylor, G.J., 2003. Remote sensing studies of the Lomonosov-Fleming region of the Moon. Journal of Geophysical Research 108, 5118, doi: 10.1029/2003JE002069.

Greeley, R., Kadel, S.D., Williams, D.A., Gaddis, L.R., Head, J.W., McEwan, A.S., Murchie, S.L., Magel, E., Neukum, G., Pieters, C.M., Sunshine, J.M., Wagner, R., Belton, M.J.S., 1993. Galileo imaging observations of lunar maria and related

deposits. Journal of Geophysical Research 98, 17183–17205, doi:10.1029/93JE01000.

Greenhagen, B.T., Bandfield, J.L., Hayne, P.O., Lucey, P.G., Donaldson Hanna, K.L., Cheek, L.C., Siegler, M.A., Petro, N.E., Paige, D.A., 2012. Investigating potential sources of enhanced rock abundances near Tsiolkovskiy Crater. EPSC Abstracts 7, Abstract 712.

Haskin, L.A., 1998. The Imbrium impact event and the thorium distribution at the lunar highlands surface. Journal of Geophysical Research 103, 1679–1689.

Hawke, B.R., Spudis, P.D., 1980. Geochemical anomalies on the eastern limb and farside of the moon. Proceedings of the Conference on the Lunar Highlands Crust, Papike, J.J., Merrill, R.B. (eds.), 467–481.

Hawke, B.R., Bell, J.F., 1981. Remote sensing studies of lunar dark-halo impact craters: Preliminary results and implications for early volcanism. Proceedings of the Lunar and Planetary Science Conference, 12B, 665–678.

Hawke, B.R., Peterson, C.A., Lucey, P.G., Taylor, G.J., Blewett, D.T., Campbell, B.A., Coombs, C.R., Spudis, P.D., 1993. Remote sensing studies of the terrain northwest of Humorum Basin. Geophysical Research Letters 20, 419–422.

Hawke, B.R., Giguere, T.A., Blewett, D.T., Lucey, P.G., Smith, G.A., Taylor, G.J., Spudis, P.D., 2002. Igneous activity in the southern highlands of the Moon. Journal of Geophysical Research 107, 5122, doi: 10.1029/2000JE001494.

Hawke, B.R., Gillis, J.J., Giguere, T.A., Blewett, D.T., Lawrence, D.J., Lucey, P.G., Smith, G.A., Spudis, P.D., Taylor, G.J., 2005. Remote sensing and geologic

setting of the Balmer-Kapteyn region of the Moon. Journal of Geophysical Research 110, E06004, doi: 10.1029/2004JE002383.

Hawke, B.R., Giguere, T.A., Gaddis, L.R., Gustafson, J.O., Lawrence, D.J., Stopar, J.D., Peterson, C.A., Bell III, J.F., Robinson, M.S., and the LROC Science Team, 2013. Cryptomare and pyroclastic deposits on the northern east side of the Moon. Lunar and Planetary Science Conference 44th, Abstract 1883.

Head, J.W., 1974. Stratigraphy of the Descartes region (Apollo 16): Implications for the origin of samples. Moon 11, 77–99.

Head, J.W., 1976. Lunar volcanism in space and time. Rev. Geophys. Space Phys. 14, 265–300 .

Head, J.W., Wilson, L., 1992. Lunar mare volcanism: Stratigraphy, eruption conditions, and the evolution of secondary crusts. Geochimica et Cosmochimica Acta 56, 2155–2175.

Head, J.W., Murchie, S., Mustard, J.F., Pieters, C.M., Neukum, G., McEwan, A., Greeley, R., Nagel, E., Bleton, M.J.S., 1993. Lunar impact basins: New data for the western limb and far side (Orientale and South Pole-Aitken basins) from the first Galileo flyby. Journal of Geophysical Research 98, 17149–17181.

Head, J.W., Fassett, C.I., Kadish, S.J., Smith, D.E., Zuber, M.T., Neumann, G.A., Mazarico, E., 2010. Global distribution of large lunar craters: Implications for resurfacing and impactor populations. Science 329, 15044–1507. doi:10.1126/science.1195050.

Hess, P.C., Parmentier, E.M., 1995. A model of the thermal and chemical evolution of the Moon's interior: implications for the onset of mare volcanism. Earth and Planetary Science Letters 134, 501–514.

Hess, P.C., Parmentier, E.M., 2001. Thermal evolution of a thicker KREEP liquid layer, J. Geophys. Res. 106, 28023–28032. doi:10.1029/2000JE001416.

Hiesinger, H., Head, J.W., Wolf, U., Jaumann, R., Neukum, G., 2002. Lunar mare basalt flow units: Thicknesses determined from crater size-frequency distributions. Geophys. Lett. 29, 89-1–89-4. doi:10.1029/2002GL014847.

Hiesinger, H., Head, J.W., Wolf, U., Jaumann, R., Neukum, G., 2011. Ages and stratigraphy of lunar mare basalts: A synthesis. Geological Society of America Special Paper 477, 1–51.

Hiesinger, H., van der Bogert, C.H., Pasckert, J.H., Schmedemann, N., Robinson, M.S., Jolliff, B., Petro, N., 2012. New crater size-frequency distribution measurements of the South Pole-Aitken basin. Lunar and Planetary Science Conference, 43rd, Abstract 2863.

Hörz, F., 1978. How thick are lunar mare basalts? Proceedings of the Lunar and Planetary Science Conference, 9th, 3311–3331.

Hörz, F., Schneider, E., Gault, D.E., Hartung, J.B., Brownlee, D.E., 1975. Catastrophic rupture of lunar rocks: A Monte Carlo simulation. The Moon 13, 235–258.

Housen, K.R., Schmidt, R.M., Holsapple, K.A., 1983. Crater ejecta scaling laws: Fundamental forms based on dimensional analysis. Journal of Geophysical Research 88, 2485–2499.

Jolliff, B.L., Gillis, J.J., Haskin, L.A., Korotev, R.L., Wieczorek, M.A., 2000. Major lunar crustal terranes: Surface expressions and crust-mantle origins. Journal of Geophysical Research 105, 4197–4216.

Kirk, R.L., Stevenson, D.J., 1989. The competition between thermal contraction and differentiation in the stress history of the Moon. J. Geophys. Res. 94, 12133–12144.

Kreslavsky, M.A., Head, J.W., 2012. New observational evidence of global seismic effects of basin-forming impacts on the Moon from Lunar Reconnaissance Orbiter Lunar Orbiter Laser Altimeter data. Journal of Geophysical Research 117, E00H24, doi: 10.1029/2011JE003975.

Kreslavsky, M.A., Head, J.W., Neumann, G.A., Rosenburg, M.A., Aharonson, O., Smith, D.E., Zuber, M.T., 2013. Lunar topographic roughness maps from Lunar Orbiter Laster Altimeter (LOLA) data: Scale dependence and correlation with geologic features. Icarus 226, 52–66, doi: /10.1016/j.icarus.2013.04.027.

Lawrence, D.J., Feldman, W.C., Barraclough, B.L., Binder, A.B., Elphic, R.C., Maurice, S., Thomsen, D.R., 1998. Global elemental maps of the Moon: The Lunar Prospector gamma-ray spectrometer. Science 281, 1484–1489, doi: 10.1126/science.281.5382.1484.

Lawrence, S.J., Hawke, B.R., Gillis-Davis, J.J., Taylor, G.J., Lawrence, D.J., Cahill, J.T., Hagerty, J.J., Lucey, P.G., Smith, G.A., Keil, K., 2008. Composition and origin of the Dewar geochemical anomaly. Journal of Geophysical Research 113, E02001, doi: 10.1029/2007JE002904.

Lucchitta, B.K., 1978. Geologic map of the north side of the Moon, US Geo. Survey Map I-1062, Reston, VA.

McGetchin, T.R., Settle, M., Head, J.W., 1973. Radial thickness variation in impact crater ejecta: Implications for lunar basin deposits. Earth and Planetary Science Letters 20, 226–236.

Meyer, J., Elkins-Tanton, L.T., Wisdom, J., 2010. Coupled thermal-orbital evolution of the early Moon. Icarus 208, 1–10.

Meyer, H.M., Denevi, B.W., Boyd, A.K., Robinson, M.S., 2013. The distribution and origin of lunar light plains around Orientale basin. Lunar Planet Sci. 44, abstract 1539.

Michael, G.G., Neukum, G., 2010. Planetary surface dating from crater size-frequency distribution measurements: Partial resurfacing events and statistical age uncertainty. Earth Planet. Sci. Lett. 294, 223–229. doi:10.1016/j.epsl.2009.12041.

Milton, D.J., 1964. Stratigraphy of the terra part of the Theophilus quadrangle. Astrogeol. Studies Ann. Prog. Rept., July 1963 to July 1964, pt. A, Open-file Report, U.S. Geological Survey, Denver, Colo., pp. 17–27.

Muehlberger, W.R., Hörz, F., Sevier, J.R., Ulrich, G.E., 1980. Mission objectives for geological exploration of the Apollo 16 landing site. In: Papike, J.J., Merrill, R.B. (Eds.). Proceedings of the Conference on the Lunar Highlands Crust, Pergamon, New York, pp. 1–49.

Mustard, J.F., Head, J.W., 1996. Buried stratigraphic relationships along the southwestern shores of Oceanus Procellarum: Impliations for early lunar volcanism. Journal of Geophysical Research 101, E02001, 18913–18925.

Nakamura, R., Yamamoto, S., Matsunaga, T., Ishihara, Y., Morota, T., Hiroi, T., Takeda, H., Ogawa, Y., Yokota, Y., Hirata, N., Ohtake, M., Saiki, K. (2012) Compositional evidence for an impact origin of the Moon's Procellarum basin. Nature Geoscience 5, 775–778, doi: 10.1038/ngeo1614.

Nemchin, A., Timms, N., Pidgeon, R., Geisler, T., Reddy, S., Meyer, C., 2009. Timing of crystallization of the lunar magma ocean constrained by the oldest zircon. Nature Geoscience 2, 133–136, doi: 10.1038/NGEO417.

Neukum, G., Ivanov, B.A., Hartmann, W.K., 2001. Cratering records in the inner solar system in relation to the lunar reference system. Space Science Reviews 96, 55–86.

Norman, M.D., 2009. The lunar cataclysm: Reality or "mythconception"? Elements 5, 23–28, doi: 10.2113/gselements.5.1.23.

Nyquist, L.E., Shih, C.-Y., 1992. The isotopic record of lunar volcanism. Geochimica et Cosmochimica Acta 56, 2213–2234.

Oberbeck, V.R., Hörz, F., Morrison, R.H., Quaide, W.L., 1973. Emplacement of the Cayley Formation. NASA Tech. Memo. 62, 38 pp.

Oberbeck, V.R., Morrison, R.H., Hörz, F., Quaide, W.L., Gault, D.E., 1974. Smooth plains and continuous deposits of craters and basins. Proc. Lunar Sci. Conf. 5th, 111–136.

Parmentier, E.M., Zhong, S., Zuber, M.T., 2002. Gravitational differentiation due to initial chemical stratification: origin of lunar asymmetry by the creep of dense KREEP? Earth and Planetary Science Letters 201, 473–480.

Petro, N.E., Pieters, C.M., 2008. The lunar-wide effects of basin ejecta distribution on the early megaregolith. Meteoritics and Planetary Science 43, doi: 10.1111/j.1945-5100.2008.tb01025.x.

Pieters, C.M., Boardman, J., Buratti, B., Chatterjee, A., Clark, R., Glavich, T., Green, R., Head, J., Isaacson, P., Malaret, E., McCord, T., Mustard, J., Petro, N., Runyon, C., Staid, M., Sunshine, J., Taylor, L., Tompkins, S., Varanasi, P., White, M., 2009. The Moon Mineralogy Mapper (M^3) on Chandrayaan-1. Current Science 96, 500–505.

Pike, R.J., 1974. Ejecta from large craters on the Moon: Comments on the geometric model of McGetchin et al. Earth and Planetary Science Letters 23, 265–274.

Ridley, W.I., 1975. On high-alumina mare basalts. Proc. Lunar Planet. Sci. Conf. 6, 131–145.

Ringwood, A.E., Kesson, S.E., 1976. A dynamic model for mare basalt petrogenesis. Proceedings of the Lunar and Planetary Science Conference, 7th, 1697–1722.

Robinson, M.S., Brylow, S.M., Tschimmel, M., Humm, D., Lawrence, S.J., Thomas, P.C., Denevi, B.W., Bowman-Cisneros, E., Zerr, J., Ravine, M.A., Caplinger, M.A., Ghaemi, F.T., Schaffner, J.A., Malin, M.C., Mahanti, P., Vartels, Al., Anderson, J., Tran, T.N., Eliason, E.M., McEwen, A.S., Turtle, E., Jolliff, B.L., Hiesinger, H., 2010. Lunar Reconnaissance Orbiter Camera (LROC) Instrument Overview. Space Science Reviews 150, 81–124. doi: 10.1007/s11214-010-9634-2.

Ryder, G., Spudis, P.D., 1980. Volcanic rocks in the lunar highlands. Proceedings of the Conference on the Lunar Highlands Crust, 353–375.

Ryder, G., Stoeser, D.B., Wood, J.A., 1977. Apollo 17 KREEPy basalt: A rock type intermediate between mare and KREEP basalts. Earth Planet. Sci. Lett 35, 1–13.

Schultz, P.H., Spudis, P.D., 1979. Evidence for ancient mare volcanism. Proceedings of the Lunar and Planetary Science Conference 10th, 2899–2918.

Schultz, P.H., Spudis, P.D., 1983. The beginning and end of lunar mare volcanism. Nature 302, 233–236.

Scott, D.H., McCauley, J.F., West, M.N., 1977. Geologic map of the west side of the Moon. US Geo. Survey Map I-1034, Reston, VA.

Shervais, J.W., Taylor, L.A., Laul, J.C., Shih, C-Y., Nyquist, L.E., 1985. Very high potassium (VHK) basalts: Complications in lunar mare basalt petrogenesis. Proc. Lunar Planet. Sci. Conf. 16, J. Geophys. Res. 90, D3–D18.

Smith, D.E., M. T. Zuber, G. B. Jackson, J. F. Cavanaugh, G. A. Neumann, H. Riris, X. Sun, R. S. Zellar, C. Coltharp, J. Connelly, R. B. Katz, I. Kleyner, P. Liiva, A. Matuszeski, E. M. Mazarico, J. F. McGarry, A. Novo-Gradac, M. N. Ott, C. Peters, L. A. Ramos-Izquierdo, L. Ramsey, D. D. Rowlands, S. Schmidt, V. S. Scott III, G. B. Shaw, J. C. Smith, J. Swinski, M. H. Torrence, G. Unger, A. W. Yu, T. W. Zagwodzki, 2010. The Lunar Oribiter Laser Altimeter investigation on the Lunar Reconaissance Orbiter mission. Space Science Reviews, 150, 209–241.

Solomon, S.C., 1975. Mare volcanism and lunar crustal structure. Proceedings of the Lunar and Planetary Science Conference, 6th, 1021–1042.

Sori, M.M., Zuber, M.T., Head, J.W., Kiefer, W.S., 2013. GRAIL search for cryptomaria, Lunar and Planetary Science Conference, 44th, abstract 2755.

Spudis, P.D., 1978. Composition and origin of the Apennine Bench Formation. Proceedings of the Lunar and Planetary Science Conference, 9th, 3379–3394.

Stöffler, D., Ryder, G., 2001. Stratigraphy of isotope ages of lunar geologic units: Chronological standard for the inner solar system. In: Chronology and Evolution of Mars. Kallenbach, R., Geiss, J., Hartmann, W.K. (eds.) Kluwer, 9–54 pp.

Stöffler, D., Ryder, G., Ivanov, B.A., Artemieva, N.A., Cintala, M.J., Grieve, R.A.F., 2006. Cratering history and lunar chronology. Reviews in Mineralogy and Geochemistry 60, 519–596.

Stuart-Alexander, D.E., 1978. Geologic map of the central far side of the Moon. US Geo. Survey, Map I-1047, Reston, VA.

Taylor, L.A., Shervais, J.W., Hunter, R.H., Shih, C.-Y., Bansal, B.M., Wooden, J., Nyquist, L.E., Laul, L.C., 1983. Pre-4.2 AE mare-basalt volcanism in the lunar highlands. Earth and Planetary Science Letters 66, 337–47.

Tera, F., Papanastassiou, D.A., Wasserburg, G.J., 1974a. The lunar time scale and a summary of isotopic evidence for a terminal lunar cataclysm. Lunar Planet Sci. Conf. 5, abstract 1289.

Tera, F., Papanastassiou, D.A., Wasserburg, G.J., 1974b. Isotopic evidence for a terminal lunar cataclysm. Earth Planet. Lett. 22, 1–21.

Terada, K., Anand, M., Sokol, A.K., Bischoff, A., Sano, Y., 2007. Cryptomare magmatism 4.35 Gyr ago recorded in lunar meteorite Kalahari 009. Nature 450, doi: 10.1038/nature06356.

Tolan, T.L., Reidel, S., Anderson, J.L., Beeson, M.H., Fecht, K.R., Swanson, D.A., 1989. Revisions to the estimates of the areal extent and volume of the Columbia River Basalt Group. Geological Society of America Special Paper 239, 1–20.

Turner, G., Cadogan, P.H., Yonge, C.J., 1973. Argon selenochronology. Proceedings of the Lunar and Planetary Science Conference, 4th, 1889–1914.

Warren, P.H., Wasson, J.T., 1980. Early lunar petrogenesis, oceanic and extraoceanic. Proceedings of the Conference on the Lunar Highlands Crust, 81–99.

Whitaker, E.A., 1981. The lunar Procellarum basin. Proceedings of the Lunar and Planetary Science Conference., 12th, 105–111.

Whitten, J.L., Head, J. W., Staid, M., Pieters, C. M., Mustard, J., Clark, R., Nettles, J., Klima, R. L., Taylor, L., 2011. Lunar mare deposits associated with the Orientale impact basin: New insights into mineralogy, history, mode of emplacement, and relation to Orientale Basin evolution from Moon Mineralogy Mapper (M^3) data from Chandrayaan-1. Journal of Geophysical Research 116, E00G09, doi: 10.1029/2010JE003736.

Whitten, J.L., Head, J.W., 2013. Detecting volcanic resurfacing of heavily cratered terrain: Flooding simulations on the Moon using Lunar Orbiter Laser Altimeter (LOLA) data. Planetary and Space Science 85, 24–37, doi: 10.1016/j.pss.2013.05.013.

Wieczorek, M.A., Phillips, 2000. The “Procellarum KREEP Terrane”: Implications for mare volcanism and lunar evolution. Journal of Geophysical Research 105, 20417–20430.

Wieczorek, M.A., Neumann, G.A., Minno, F., Kiefer, W.S., Taylor, G.J., Melosh, H.J., Phillips, R.J., Solomon, S.C., Andrews-Hanna, J.C., Asmar, S.W., Konopliv, A.S., Lemoine, F.G., Smith, D.E., Watkins, M.M., Williams, J.G., Zuber, M.T., 2013. The crust of the Moon as seen by GRAIL. Science 339, 671–674, doi: 10.1126/science.1231530.

Wilhelms, D.E., 1987. The geologic history of the Moon. US Geologic Survey Special Paper 1348, pp. 302.

Wilhelms, D.E., McCauley, J.F., 1971. Geologic map of the near side of the Moon. US Geo. Survey Map I-703, Reston, VA.

Wilhelms, D.E., El-Baz, F., 1977. Geologic map of the east side of the Moon. US Geo. Survey Map I-948, Reston, VA.

Wilhelms, D.E., Howard, K.A., Wilshire, H.G., 1979. Geologic map of the south side of the Moon. US Geo. Survey Map I-1162, Reston, VA.

Wilhelms, D.E. (1987) The Geologic History of the Moon. US Geological Survey Special Paper 1348, 302 pp.

Williams, K.K., Zuber, M.T., 1998. Measurement and analysis of lunar basin depths from Clementine Altimerty. Icarus 131, 107–122, doi: 10.1006/icar.1997.5856.

Wilson, L., Head, J.W., 1981. Ascent and eruption of basaltic magma on the Earth and Moon. Journal of Geophysical Research 86, doi: 10.1029/JB086iB04p02971.

Yingst, R. A. and J. W. Head, Volumes of lunar lava ponds in South Pole-Aitken and Orientale Basins: Implications for eruption conditions, transport mechanisms and magma source regions, Journal of Geophysical Research 102, 10909–10931, 1997.

Young, J.W., Mattingly, T.K., Duke, C.M., 1972. Crew observations. In: Apollo 16 Preliminary Science Report. Special Publication SP-315, NASA, Washington D.C., pp. 5-1 to 5-6.

Zhong, S., Parmentier, E.M., Zuber, M.T., 2000. A dynamic origin for the global asymmetry of lunar mare basalts. Earth an Planetary Science Letters 177, 131–140.

Zuber, M.T., Smith, D.E., Zellar, R.S., Neumann, G.A., Sun, X., Katz, R.B., Kleyner, I., Matuszeski, A., McGarry, J.F., Ott, M.N., Ramos-Izquierdo, L.A., Rowlands, D.A. Torrence, M.H., Zagwodzki, T.W., 2010. The Lunar Reconnaissance Orbiter Laser Ranging Investigation. Space Science Reviews 150, 63–80. doi: 10.1007/s11214-009-9511-z.

Table 1. Evaluations of proposed cryptomaria.

Region	Observed Cryptomaria	Latitude[1]	Longitude[1]	Area (km^2)	Type of cryptomare deposit[2]
Australe	Y	-46.91	96.83	2.70E+04	Balmer/ Distal basin ejecta-type
Balmer	Y	-18.74	68.78	6.06E+04	Balmer-type
Bel'kovich	N	61.53	90.15		
Casatus	N	-72.70	102.85		
Cleomedes	N	27.60	55.50		
De Forest	N	-76.94	196.67		
Deslandres/ Walther	N	-32.72	-2.43		
Dewar	Y	-1.44	166.41	4.78E+03	Balmer-type
Mare Frigoris	Y	53.45	19.39	7.62E+03	Copernicus-type
Hercules	Y	44.89	42.39	1.20E+04	Copernicus-type
Humboldtianum	Y	59.37	73.99	9.11E+03	Balmer/ Distal basin ejecta-type
Korolev	N	-4.19	-157.41		
Langemak	Y	-8.02	116.42	3.33E+04	Copernicus/ Distal basin ejecta-type
Lomonosov-Fleming	Y	19.30	106.90	1.13E+05	Balmer/ Distal basin ejecta-type
Marginis	Y	10.42	92.74	2.51E+04	Balmer-type
Maurolycus	N	-41.77	13.92		
Mendeleev	N	5.38	141.17		
Mendel-Rydberg	Y	-48.30	-94.21	6.17E+03	Distal basin ejecta-type
Milne	Y	-30.67	112.90	1.18E+04	Balmer-type
Schiller-Schickard	Y	-48.92	-51.75	1.32E+05	Distal basin ejecta-type
Schrödinger	N	-74.73	132.93		
Smythii	Y	-1.94	85.12	3.88E+04	Distal basin ejecta-type
SPA	Y	-49.37	-157.95	2.96E+04	Balmer/ Distal basin ejecta-type
Taruntius	Y	5.10	45.23	2.29E+03	Copernicus-type
Lacus Solitudinis	Y	-26.47	113.96	2.04E+04	Balmer/ Distal basin ejecta-type
Van de Graaff	N	-27.04	172.01		
W. Humorum	Y	-21.52	-56.87	3.23E+03	Copernican-type/ Distal basin ejecta-type
W. Procellarum	Y	7.37	-71.44	1.67E+04	Copernican/ Distal basin ejecta-type
Zucchius	N	-61.38	-50.65		

[1]Center latitude and longitude of the proposed cryptomare region investigated in this study.
[2]These deposit types were developed in *Giguere et al.* (2003) and *Hawke et al.* (2005).

Table 2. Identified cryptomaria characteristics.

Region[1]	Avg. Topo. (m)	Surface Roughness			Rock abundance (% rocks)	Avg. Albedo	Model age (crater SFD)	Superposed basin ejecta	Associated impact basin[2]	Estimated thickness (km)[2]	Flooding style[3,4]
		0.115 km	0.46 km	1.84 km							
Australe (1)	-1952	0.86	0.90	0.61	0.29	0.12	-	Planck, Smythii	-	0.5 - 1	U
Balmer (2)	-987	0.95	1.07	0.79	0.33	0.14	3.84 +0.05/-0.07	Serenitatis, Smythii, Nectaris	Balmer-Kapteyn	≤3	B
Dewar (3)	542	0.93	0.95	1.21	0.37	0.13	-	Freundlich-Sharonov	Keeler-Heaviside	≤1	P
Mare Frigoris (4)	-2413	0.89	0.99	0.69	0.27	0.12	-	-	-	-	-
Hercules (5)	-1789	0.86	0.95	0.63	0.27	0.14	-	-	-	-	-
Humboldtianum (6)	-3645	1.04	0.84	0.41	0.30	0.14	-	Imbrium	s	<0.5	U
Langemak (7)	1627	1.08	1.16	1.23	0.36	0.15	-	Smythii	-	<0.5	U
Lomonosov-Fleming (8)	-947	0.98	0.96	0.80	0.39	0.15	4.01 +0.02/-0.03	Smythii, Crisium	s	≤2	P
Marginis (9)	-1928	0.87	0.87	0.58	0.38	0.12	3.88 +0.06/-0.12	Smythii, Crisium	-	-	-
Mendel-Rydberg (10)	-1765	1.21	1.25	0.82	0.37	0.15	-	Orientale	s	≤1	P
Milne (11)	-1036	0.93	1.06	1.06	0.36	0.14	-	Smythii	-	≤3	
Schiller-Schickard (12)	-666	1.06	1.09	0.68	0.45	0.14	3.77 +0.05/-0.07	Orientale, Mendel-Rydberg, Humorum, Nubium	Schiller-Zucchius	≤3	U
Smythii (13)	-3119	0.88	0.95	0.74	0.35	0.12	3.90 +0.05/-0.07	Serenitatis, Crisium	s	3.5 - 4	U
South Pole-Aitken (14)	-4666	0.83	0.96	0.77	0.30	0.11	3.88 +0.06/-0.10	Apollo	s	≤1.5	U
Taruntius (15)	-1793	0.81	0.97	0.85	0.31	0.10	-	-	-	-	-
Lacus Solitudinis (16)	-1036	0.93	1.06	1.06	0.36	0.14	-	Smythii	-	≤0.5	
W. Humorum (17)	-557	1.06	1.12	0.76	0.37	0.15	-	Orientale, Imbrium, Nubium	Humorum	≤0.5	U
W. Procellarum (18)	-1606	0.94	1.08	0.66	0.34	0.12	-	Orientale, Imbrium	-	≤0.5	-

[1]Numbers in parentheses correspond to the numbered deposits in Fig. 4.
[2]The letter 's' means that the name of the region is the same as the containing basin. No 's' or a '-' means that the cryptomaria is not in an obvious impact basin and, instead, could be in a topographic low or smaller crater.
[3]These table columns were determined using information from *Whitten et al.*, 2013.
[4]Abbreviations for the flooding method used to determine unit thickness. U = ubiquitous, P = point, B = both.

Table 3. Calculated ages for Cayley plains deposits.

Region	Age	Errors	Area (km^2)	Number of craters
		Central Highlands		
CH1	3.72	+0.03 -0.04	1.20E+04	34
CH2	3.62	+0.03 -0.04	2.82E+04	49
CH3	3.63	+0.04 -0.05	1.29E+04	25
CH4	3.75	+0.04 -0.06	3.45E+03	12
CH5	3.74	+0.06 -0.11	2.14E+03	6
CH6	3.83	+0.03 -0.04	5.50E+03	27
All CH	3.68	+0.02 -0.02	6.42E+04	153
		Farside		
F1	3.73	+0.03 -0.03	1.57E+04	44
F2	3.68	+0.05 -0.08	5.52E+03	10
F3	3.83	+0.02 -0.02	2.48E+04	71
All F	3.77	+0.01 -0.02	4.61E+04	125
		North		
N1	3.95	+0.02 -0.02	7.12E+03	66
N2	3.76	+0.02 -0.02	2.49E+04	85
N3	3.89	+0.02 -0.03	8.55E+03	39
N4	3.73	+0.03 -0.03	2.33E+04	46
All N	3.80	+0.01 -0.01	6.39E+04	236
All Cayley plains	3.75	+0.01 -0.01	1.74E+05	514

Table 4. Comparison of the influence of crustal thickness and mantle depth variations on basin fill thicknesses.[a]

Crustal thickness (km)	Mantle depth (km)	Basin fill (km)
40	55	-0.93[b]
42	55	0.77
44	55	2.47
46	55	4.17
48	55	5.87
50	55	7.57
Calculated mantle depth (km)	**Crustal thickness (km)**	**Basin fill (km)**
50	44	2.11
52	44	2.25
54	44	2.40
56	44	2.55
58	44	2.69
60	44	2.84

[a]Calculations are made assuming ρ_l= 3000 kg/m^3, ρ_c= 2550 kg/m^3, ρ_m= 3220 km/m^3.
[b]Negative values indicate that no eruption occurred.

Figure Captions

Figure 1. Histogram of the ages of surficial mare deposits. The start of mare basalt emplacement appears to occur abruptly at ~3.8 Ga and slowly trails off over the next 2.5 Gy. Most of the mare basalts were erupted during a peak of volcanic activity ~3.6 Ga. These are all model ages derived from crater size-frequency distribution. Vertical blue band represents isotope ages for impact basins derived from returned lunar samples: Orientale = 3.72–3.85, Imbrium = 3.77–3.91, Crisium = 3.84–3.89, Serenitatis = 3.87–3.98, and Nectaris = 3.85–4.10 . 'N' represents the number of ages included in the histogram. Mare basalt age data is from Hiesinger et al. (2011) and Whitten et al. (2011) and basin ages are from Stöffler et al. (2006).

Figure 2. Comparison of volcanic and impact-produced light plains deposits on the Moon. (a) Cryptomare in Balmer-Kapteyn basin. (b) Light plains deposits in Ptolemaeus crater (bottom left) and Hipparchus crater (top right), hereafter referred to as Cayley plains, that are hypothesized to have been produced by ejecta ponding in topographic lows during the Imbrium impact event. Linear features oriented northwest–southeast superposed on these crater rims were sculpted by Imbrium ejecta. White dashed lines denote the location of cryptomare and Cayley plains deposits. LROC WAC 100 m/pixel base map.

Figure 3. Diagram of the four distinct types of cryptomaria (Copernicus-type, Balmer-type, proximal basin ejecta-type, and distal basin ejecta-type) that are formed by different processes. Cross-section (top row) and bird's eye (bottom row) diagrams of each

formation process. Maria are indicated by dark grey, high-albedo ejecta are shown in light grey, impact crater rims (>20 km) are delineated by black circles, and cryptomaria are shown as hatched shapes. Highland regions are shown in white.

Figure 4. Proposed cryptomare locations superposed on the distribution of light plains deposits. (a) Detected cryptomaria are represented by red circles and those cryptomaria we were unable to positively identify are indicated by red ×'s. (b) North pole. (c) South pole. Exposed mare basalts are shown in black and light plains deposits (pIp, Cp, Np, INp, Ip, Ip1, Ip2, Ntp (Wilhelms and McCauley, 1971; Wilhelms et al., 1979; Lucchitta, 1978, Wilhelms and El-Baz, 1977; Stuart-Alexander, 1978; Scott et al., 1977)) are shown in yellow. LOLA 128 pixel/° hillshade mosaic.

Figure 5. The distribution of the cryptomaria deposits (orange) confirmed in this study. This figure shows how the cryptomaria increase the areal coverage of basalts more extensively in the eastern hemisphere (a 2.6% increase in areal coverage of basalts), compared to the western hemisphere (a 1.0% increase). Numbers correspond to the identified cryptomaria listed in Table 2. Maria are shown in grey (Wilhelms and McCauley, 1971; Scott et al., 1977; Wilhelms and El-Baz, 1977; Lucchitta, 1978; Stuart-Alexander, 1978; Wilhelms et al., 1979) and basins are shown in blue (Wilhelms and El-Baz, 1977; Maxwell and Andre, 1981; Head et al., 2010). See Fig. 6 for a detailed view of each cryptomare region.

Figure 6. Individual mapped cryptomare deposits in (from left to right) M^3 mafic color composite (R: 1 μm integrated band depth, G: 2 μm integrated band depth, B: reflectance at 1489 nm; column 1), LOLA topography (blue is low-lying topography and orange-brown is high-standing topography; column 2), surface roughness at 1.84 km (black is smooth and white is rough; column 3), and M^3 1489 nm surface reflectance (column 4). (a) Australe. (b) Balmer. (c) Dewar. (d) Mare Frigoris. (e) Hercules. (f) Humboldtianum. (g) Langemak. (h) Lomonosov-Fleming. (i) Marginis. (j) Mendel-Rydberg. (k) Milne. (l) Schiller-Schickard. (m) Smythii. (n) South Pole-Aitken. (o) Taruntius. (p) Lacus Solitudinis. (q) West Humorum. (r) West Procellarum. Orange outlines delineate the extent of cryptomare deposits. In the M^3 color composite yellow and orange colors indicate the presence of pyroxene and blue denotes the location of feldspathic materials. (c) White arrows point to dark-halo craters superposed on Dewar cryptomare (M^3 color composite). (l) White arrow points to Wargentin (84 km in diameter), an impact crater filled to its rim with mare (LOLA topography).

Figure 7. Elevation distribution of all mapped maria (blue), cryptomaria (orange), light plains (green), and the entire Moon (black). The global and Cayley plains elevation values have a similar distribution to the cryptomaria; the maria have a distinct elevation distribution, with both a narrower and lower range in elevation values. Maria and light plains distributions mapped in USGS maps (Wilhelms and McCauley, 1971; Scott et al., 1977; Wilhelms and El-Baz, 1977; Lucchitta, 1978; Stuart-Alexander, 1978; Wilhelms et al., 1979). “Peak 1” encompasses the highest cryptomare elevations, especially those deposits in the exterior rings of Pre-Nectarian/ Nectarian impact basins. “Peak 2”

elevations are generally associated with the innermost cryptomaria in Pre-Nectarian/ Nectarian impact basins. Altimetry from LOLA 128 pixel/° dataset.

Figure 8. Measured LOLA surface roughness at all three lengthscales (0.115, 0.46, and 1.84 km). (a) Surface roughness values at 0.115 km (red), 0.46 km (yellow), and 1.84 km (purple) for each individual cryptomare study region. Cryptomaria are numbered according to Table 2. (b) Average surface roughness at the three different baselines for cryptomaria (orange), Cayley plains (green), and maria (blue).

Figure 9. The average rock concentrations for lunar cryptomaria (orange) and associated exposed mare (blue), average Cayley plains (green), and average maria (blue) are all <1%. Dewar (3) and Milne (11) cryptomare do not have exposed maria in the study area and thus do not have a blue data column. The number of the cryptomaria (abscissa) corresponds to the deposit name in Table 2. Letter A is the average rock abundance for all of the Cayley plains and letter B is the average value for all exposed maria.

Figure 10. Albedo of the cryptomaria (orange), Cayley plains (green), and maria (blue) measured using $M^3$1489 nm reflectance values. The average cryptomare 1489 nm reflectance value is indicated by the dashed dark orange line; this average cryptomare albedo value is within error of the measured albedo for the Cayley plains. The maria have a lower average albedo than either the Cayley plains or cryptomaria. The number of the cryptomaria (abscissa) corresponds to the deposit name in Table 2. Letter A is the

average rock abundance for all of the Cayley plains and letter B is the average value for all exposed maria.

Figure 11. Thickness, area, and volume of cryptomaria. Thickness estimates (bottom graph) (Table 2) were produced by comparing the areal distribution or map pattern of mapped cryptomaria with simulated volcanic flooding events (Whitten and Head, 2013). See text for a more detailed description of how cryptomaria thicknesses were estimated. Copernicus-type (numbers 4, 5, 15; Table 1) and non-basin associated (number 9) cryptomare deposit thicknesses could not be estimated. The numbers on the abscissa correspond to a cryptomare deposit name from Table 2. Area (top graph, orange bars) and volume (top graph, hollow dark orange bars) measurements of cryptomaria. Volume is derived by multiplying the estimated thickness by the measured cryptomare area.

Figure 12. Model ages determined for large continuous cryptomaria (orange symbols; Table 2) and the Cayley plains (green symbols; Fig. S1, Table 3). Cryptomare data are labeled by number (Fig. 4, Table 2). The diamond symbols represent the model age for each individual Cayley plains deposit measured (blue outlines in Fig. S1b-d) and the triangles represent the average age for all deposits within a defined count region (north, farside, or central highland). The green square is the average model age for all measured Cayley plains. See Tables 2 and 3 for specific model ages and associated errors. The histogram (light grey) of exposed mare basalt ages (Fig. 1) is superposed for comparison and the blue field represents the range of predicated basin ages for Nectaris, Serenitatis, Crisium, Imbrium, and Orientale (from Fig. 1).

Figure 13. The predicted ejecta distribution for impact basins on the Moon. Only basins with estimated transient crater diameters (Petro and Pieters, 2008) were included. The area marked in red corresponds to the predicted ejecta distribution; grey regions are not affected by the ejecta deposit. Impact basin rims are denoted by blue ovals and the location of the impact basin is indicated by the yellow star. Cryptomaria are in black.

Figure 14. Three farside impact basins with varying amounts of light plains filling their interiors. (a) Korolev basin (423 km in diameter) is almost completely filled with light plains. (b) Hertzsprung basin (536 km in diameter) is also almost completely filled with light plains material in its interior, though more of the central ring is preserved above the basin fill. Hertzsprung rim and fill material was modified by secondary crater chains from the Orientale impact event (chains are oriented southeast–northwest). (c) The Freundlich-Sharonov basin (600 km in diameter) interior appears largely unfilled, due to the elevation difference between the basin rim-crest and the basin interior. Small mare deposits are located in the basin center (Lacus Luxuriae and interior to Buys Ballot crater; white outlines).

Figure 15. (a) Mendeleev basin (325 km in diameter) and Kohlschütter crater (56 km in diameter) on the lunar farside. Dotted line represents the profile location in part (b). Mendeleev basin is filled in with high albedo plains material and Kohlschütter crater is filled with mare basalts. LOLA 128 pixels/° data overlaying LROC WAC 100 m/pixel map. (b) Topographic profile of Mendeleev basin and Kohlschütter crater. The predicted

crater depths are indicated by the dashed half circles (Williams and Zuber, 1998; Kalynn et al., 2013). The dashed horizontal lines labeled with density values are the calculated volcanic fill thickness in Mendeleev, assuming that the source region for the magma was located at a similar depth to that determined for Kohlschütter crater (red: 2800 kg/m^3, orange: 2900 kg/m^3, green: 3000 kg/m^3, blue: 3100 kg/m^3). Kohlschütter fill is mare basalt (black) and Mendeleev basin is filled with at least 0.5 km of basin ejecta (dark yellow). The composition of the remaining material below (hatched pattern) is undetermined.

Figure 16. Mendeleev basin on the farside of the Moon. (a) Mendeleev basin is filled with light plains. The basin floor is outlined in black. LROC 1000 m/pixel mosaic. (b) There are no mafic mineral signatures (pyroxene or olivine) on the floor of Mendeleev; in this color composite pyroxene materials would appear orange or yellow. M^3 mafic color composite (R: 1 μm integrated band depth, G: 2 μm integrated band depth, B: reflectance at 1489 nm) composed of data from the 2c1 optical period. Vertical stripping is from calibration effects and does not represent real mineralogic variations. Black vertical strip is missing data. Lambert azimuthal equidistant projection centered on Mendeleev basin.

Figure S1. Location of regions analyzed for crater size-frequency determinations of the Cayley plains. a) Global view of the different count regions (blue polygons): b) Central highlands count area. c) Farside count area. d) North count area. Individual deposits measured are shown outlined in blue. Red circles are the craters included in age determinations and yellow circles are counted craters that were not included because they

have secondary crater or collapse pit morphologies. The light plains deposits not identified as cryptomaria are in yellow (from the USGS geologic maps) (Wilhelms and McCauley, 1971; Scott et al., 1977; Wilhelms and El-Baz, 1977; Lucchitta, 1978; Stuart-Alexander, 1978; Wilhelms et al., 1979).

Figure S2. Distribution of maria (diagonal hatch region) and cryptomaria (black) in study regions. (a) Australe. (b) Balmer. (c) Dewar. (d) Frigoris. (e) Hercules. (f) Humboldtianum. (g) Langemak. (h) Lomonosov-Fleming. (i) Marginis. (j) Mendel-Rydberg. (k) Schiller-Schickard. (l) Smythii. (m) South Pole-Aitken. (n) Taruntius. (o) Lacus Solitudinis and Milne. Milne cryptomaria are the two southernmost deposits in the center of the image. (p) West Humorum. (q) West Proceallarum. Horizontal black bars in the bottom right corner represent 100 km scale bars. Dewar and Milne do not have associated maria. Cryptomaria at Frigoris (d), Hercules (e), Taruntius (n) are created by the superposition of fresh crater ejecta on much larger mare deposits.

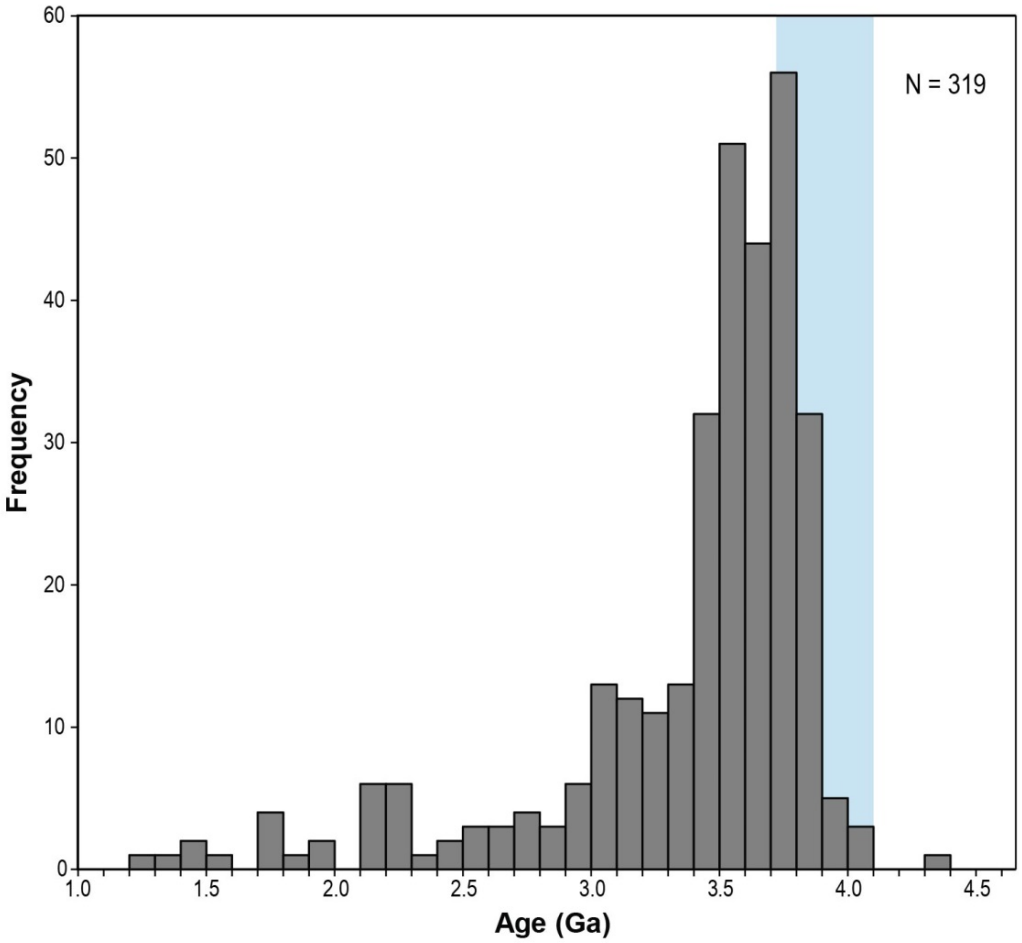

Figure 1.

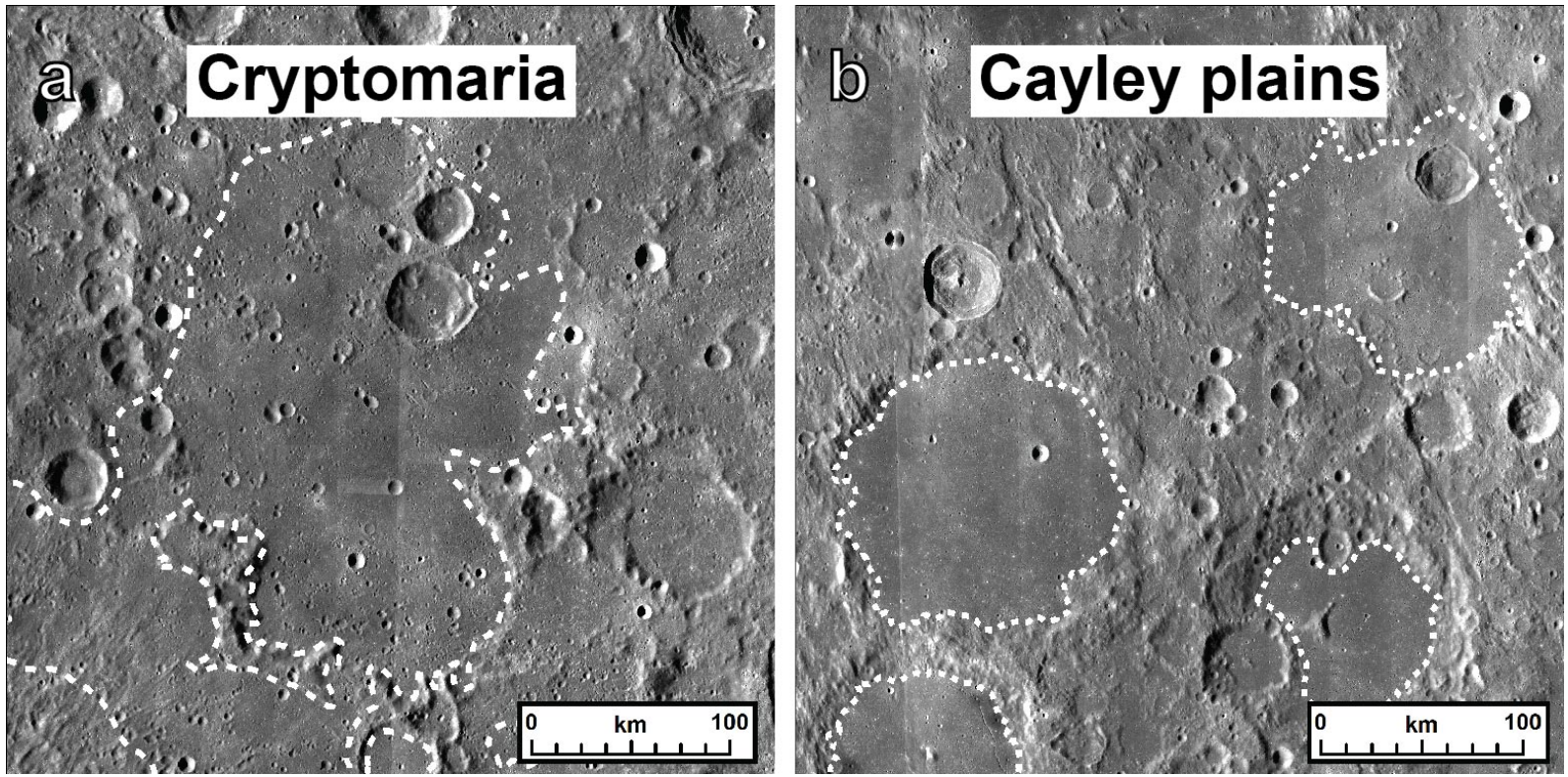

Figure 2.

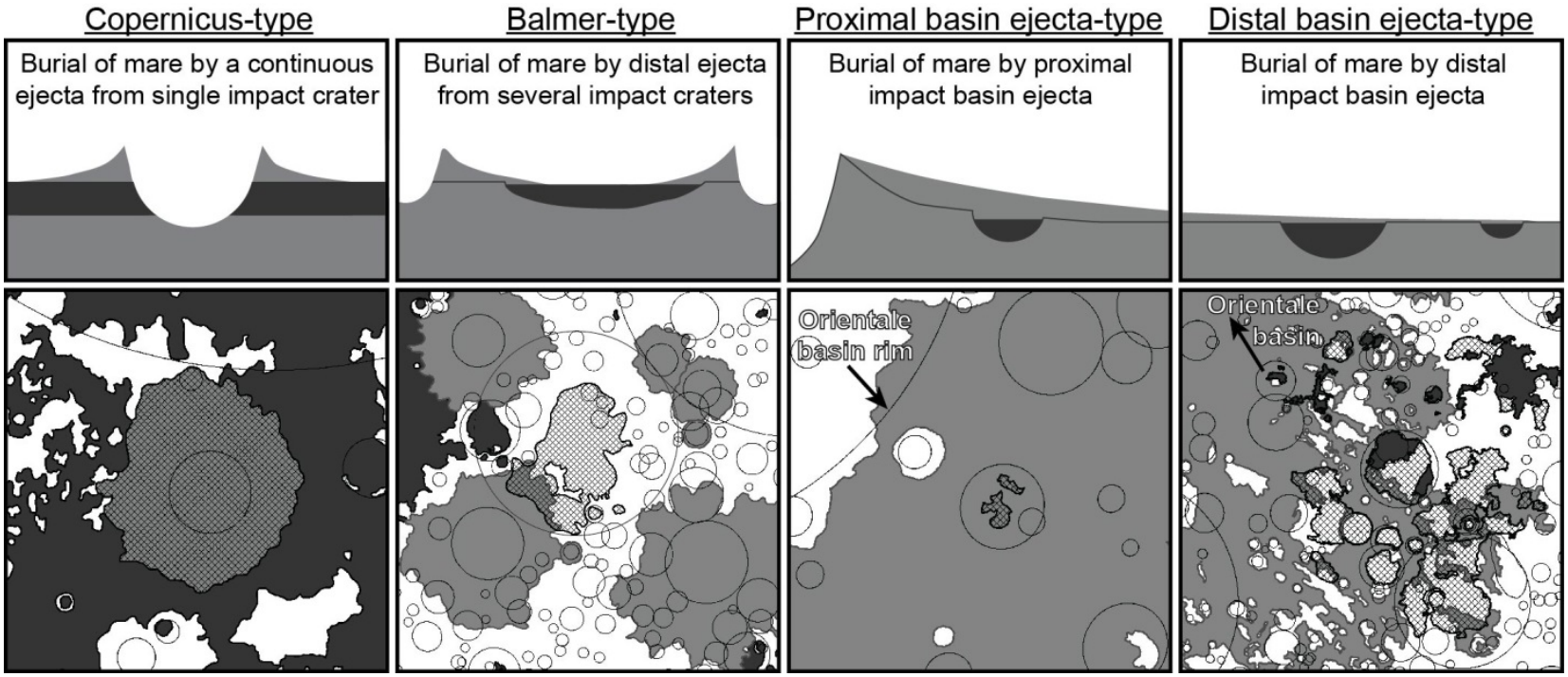
Copernicus-type
Balmer-type
Proximal basin ejecta-type
Distal basin ejecta-type
Burial of mare by a continuous ejecta from single impact crater
Burial of mare by distal ejecta from several impact craters
Burial of mare by proximal impact basin ejecta
Burial of mare by distal impact basin ejecta
Orientale basin rim
Orientale basin

Figure 3.

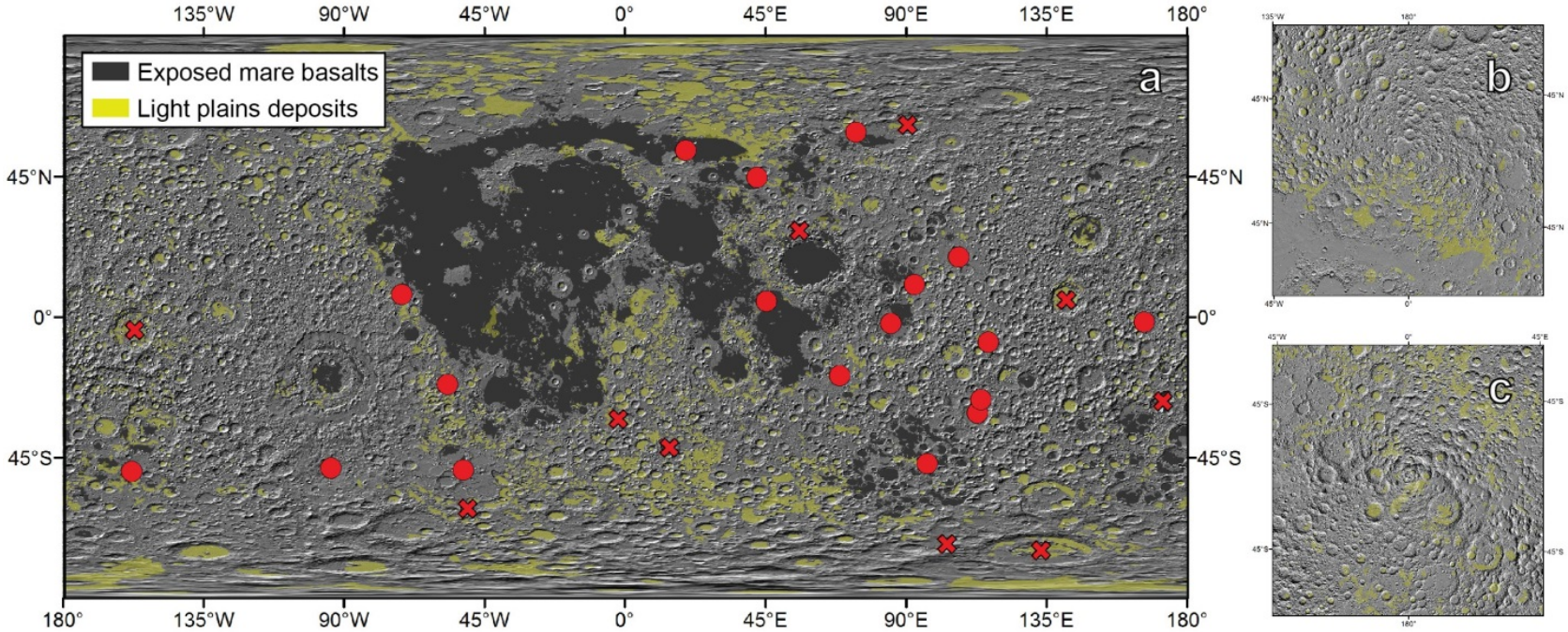
Exposed mare basalts
Light plains deposits
a
b
c
135°W
90°W
45°W
0°
45°E
90°E
135°E
180°
45°N
0°
45°S

Figure 4.

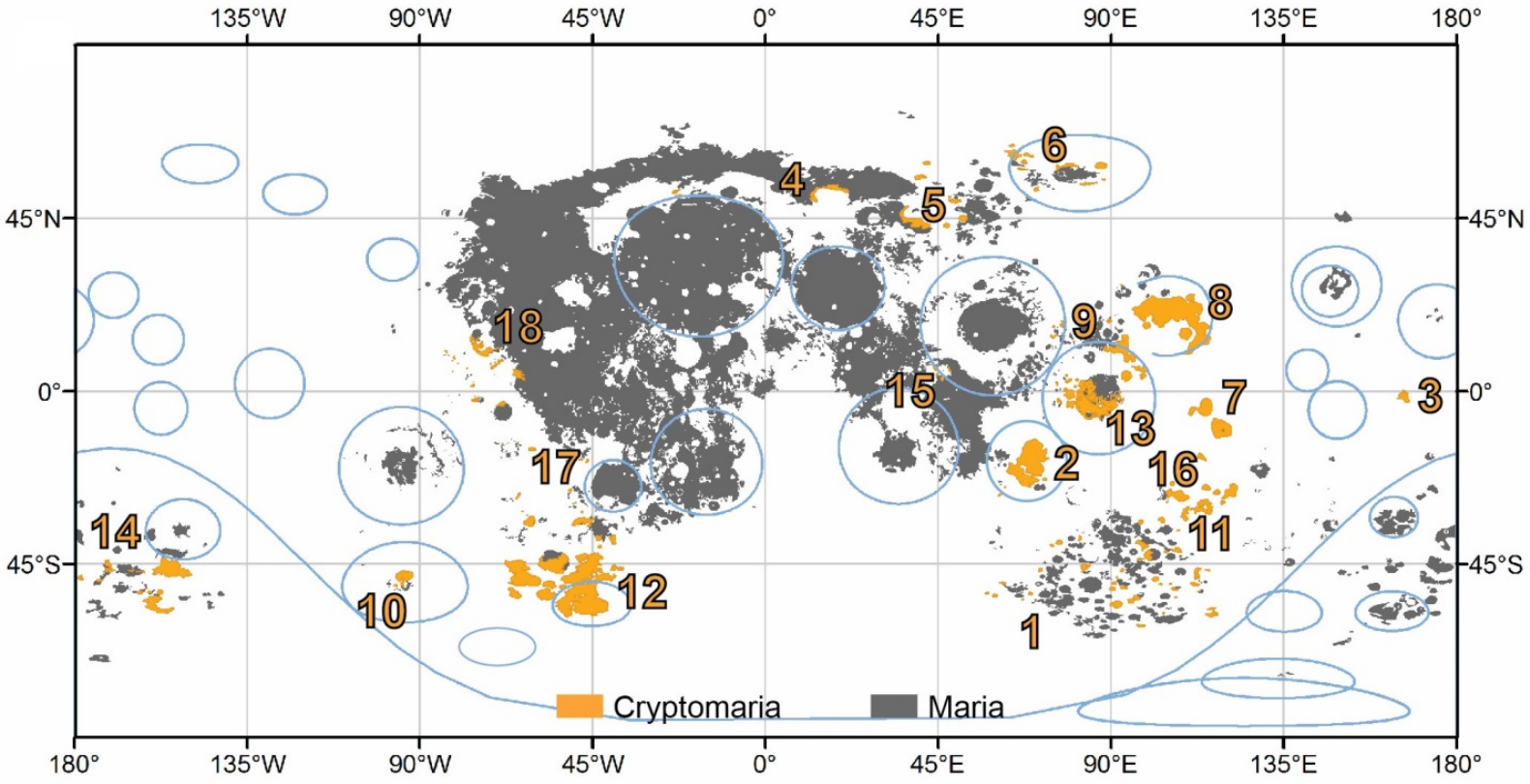
135°W
90°W
45°W
0°
45°E
90°E
135°E
180°
45°N
0°
45°S
1
2
3
4
5
6
7
8
9
10
11
12
13
14
15
16
17
18
Cryptomaria
Maria

Figure 5.

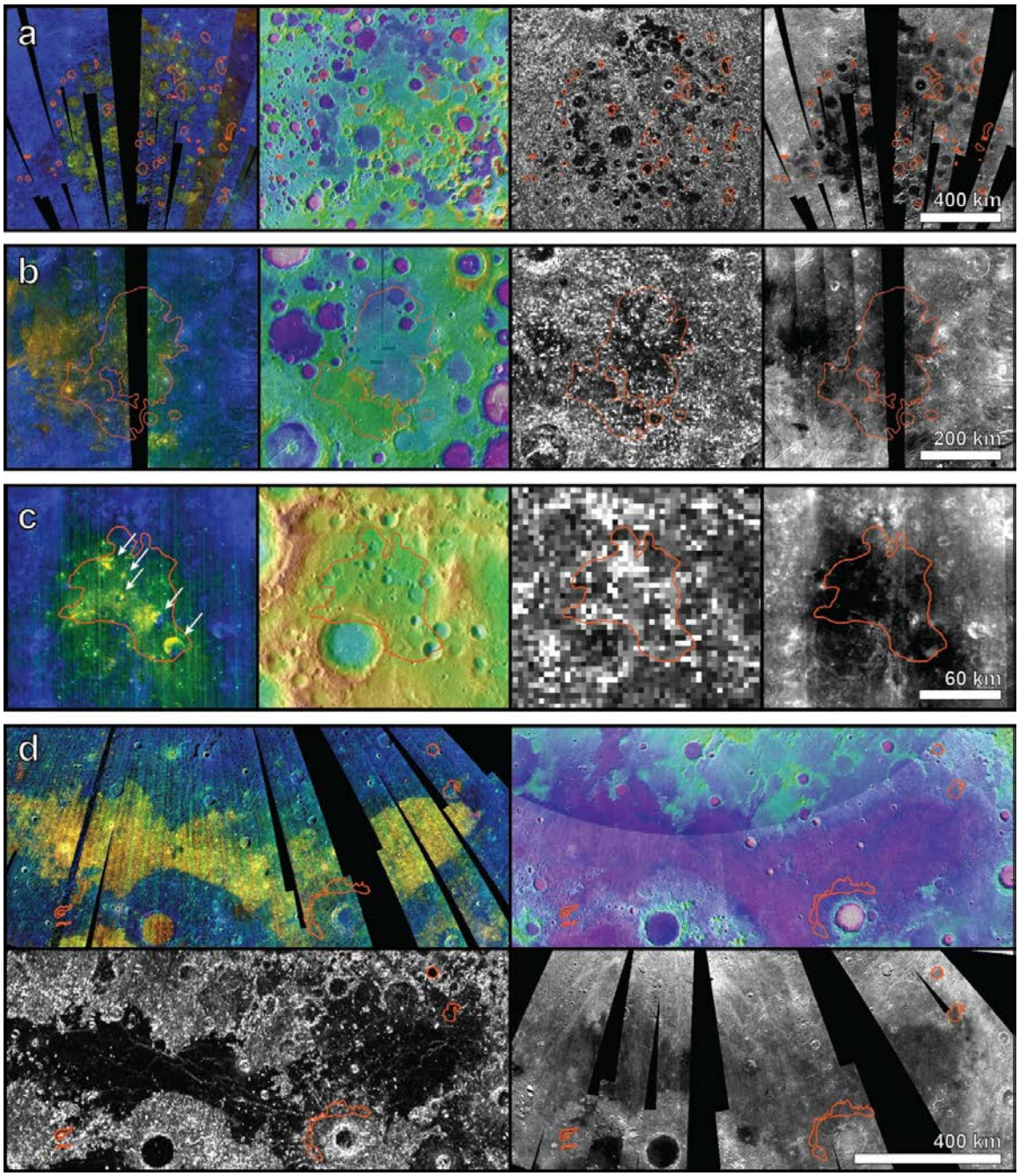

Figure 6.

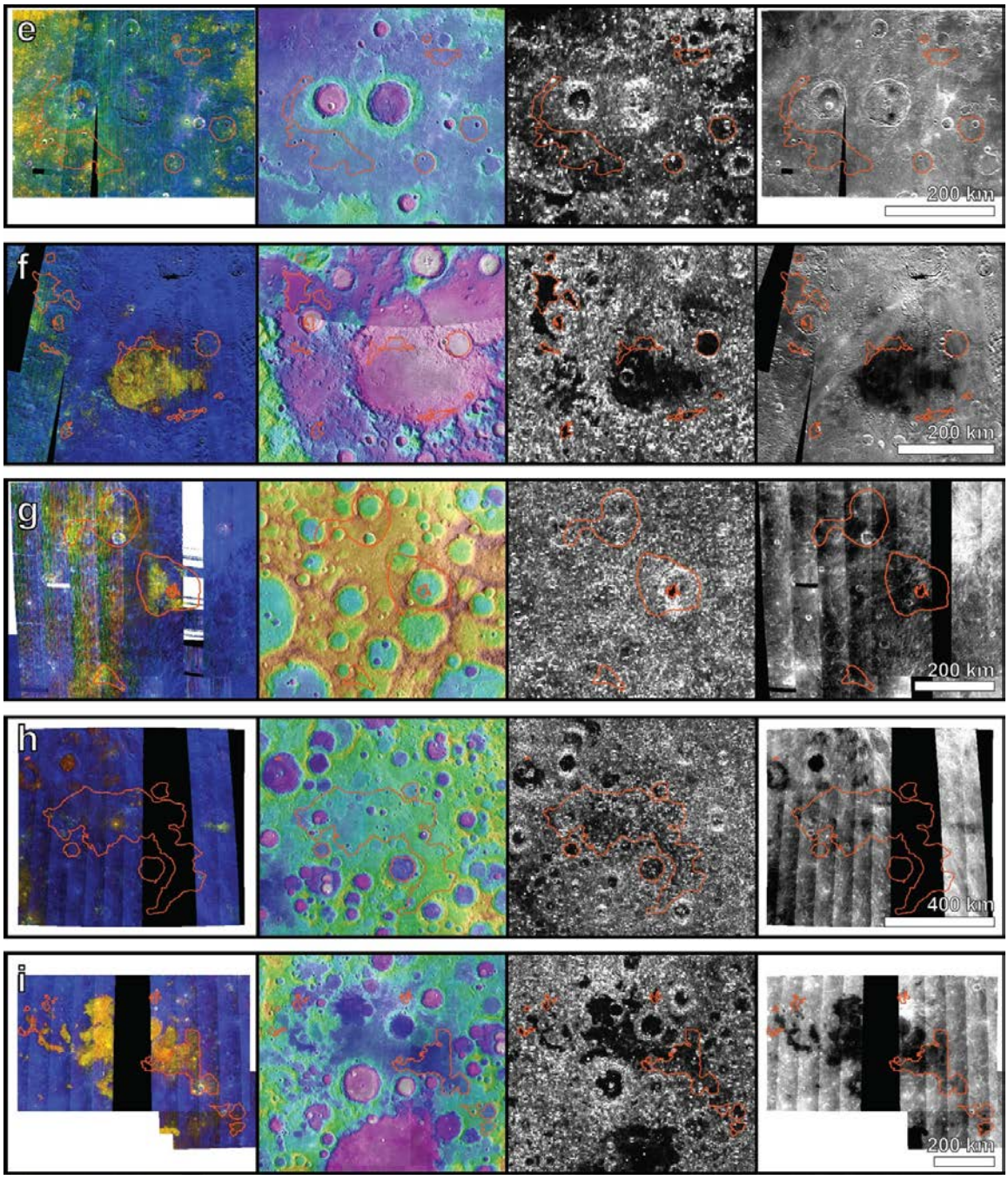

Figure 6. continued

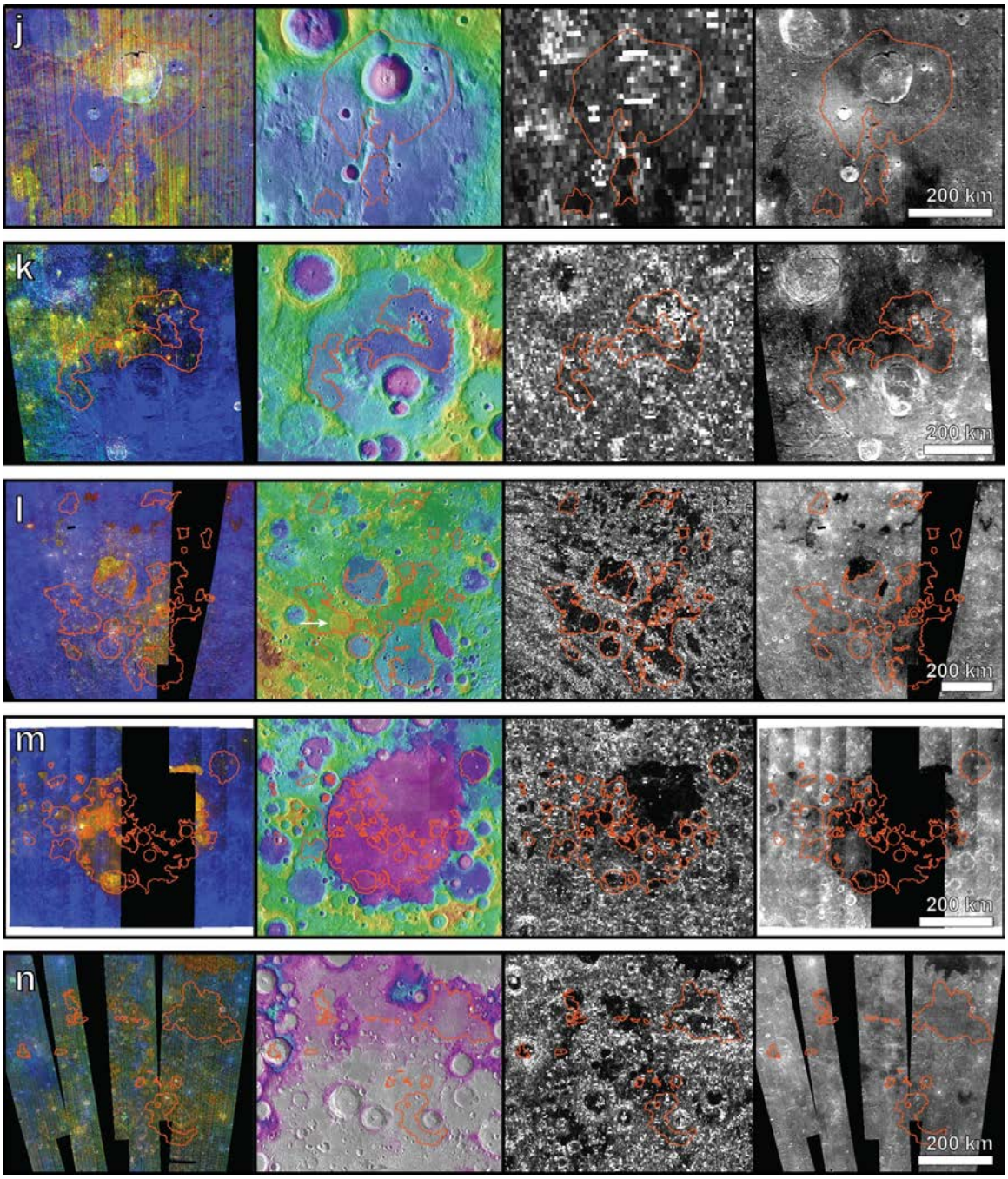

Figure 6. continued

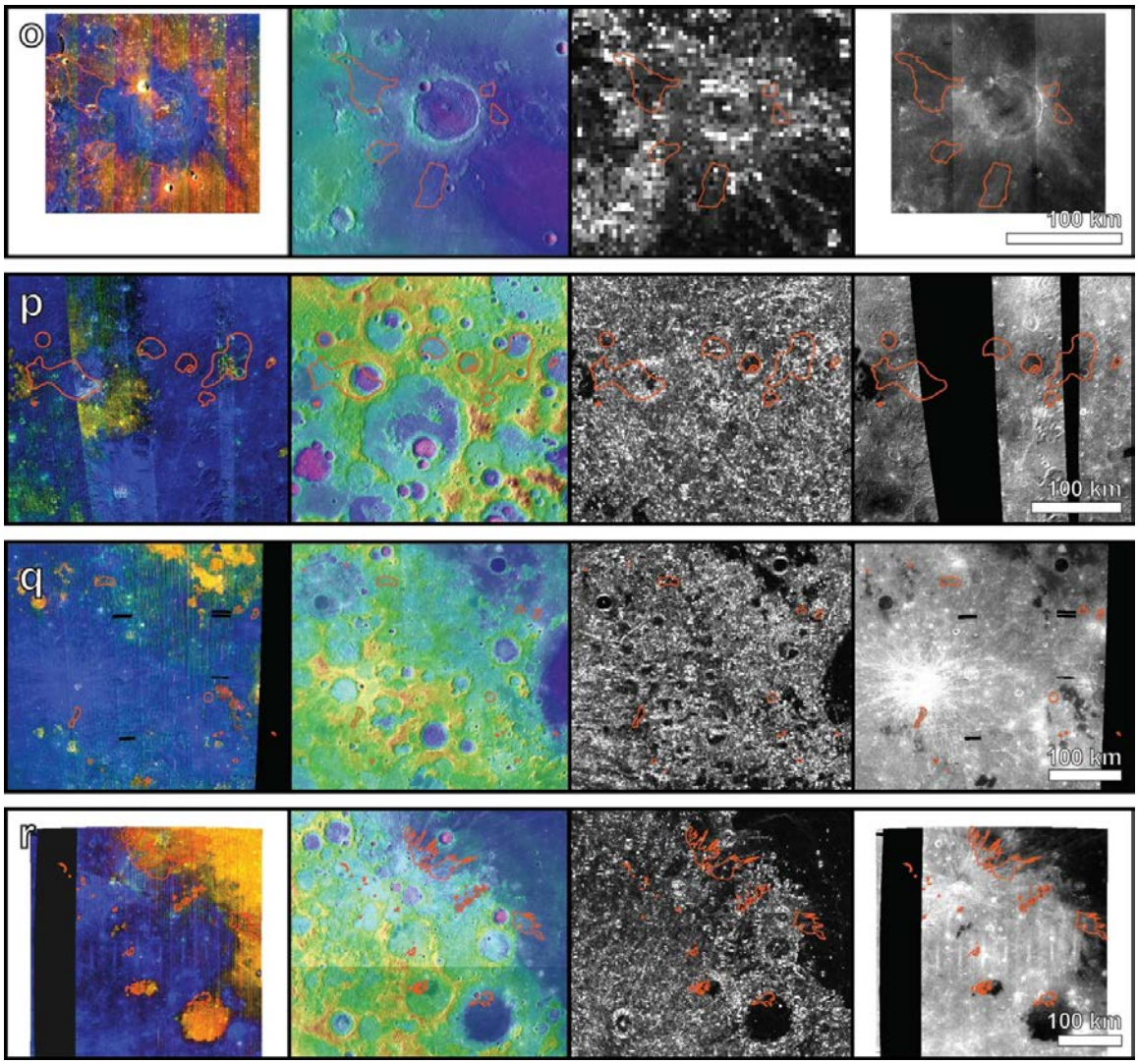

Figure 6. continued

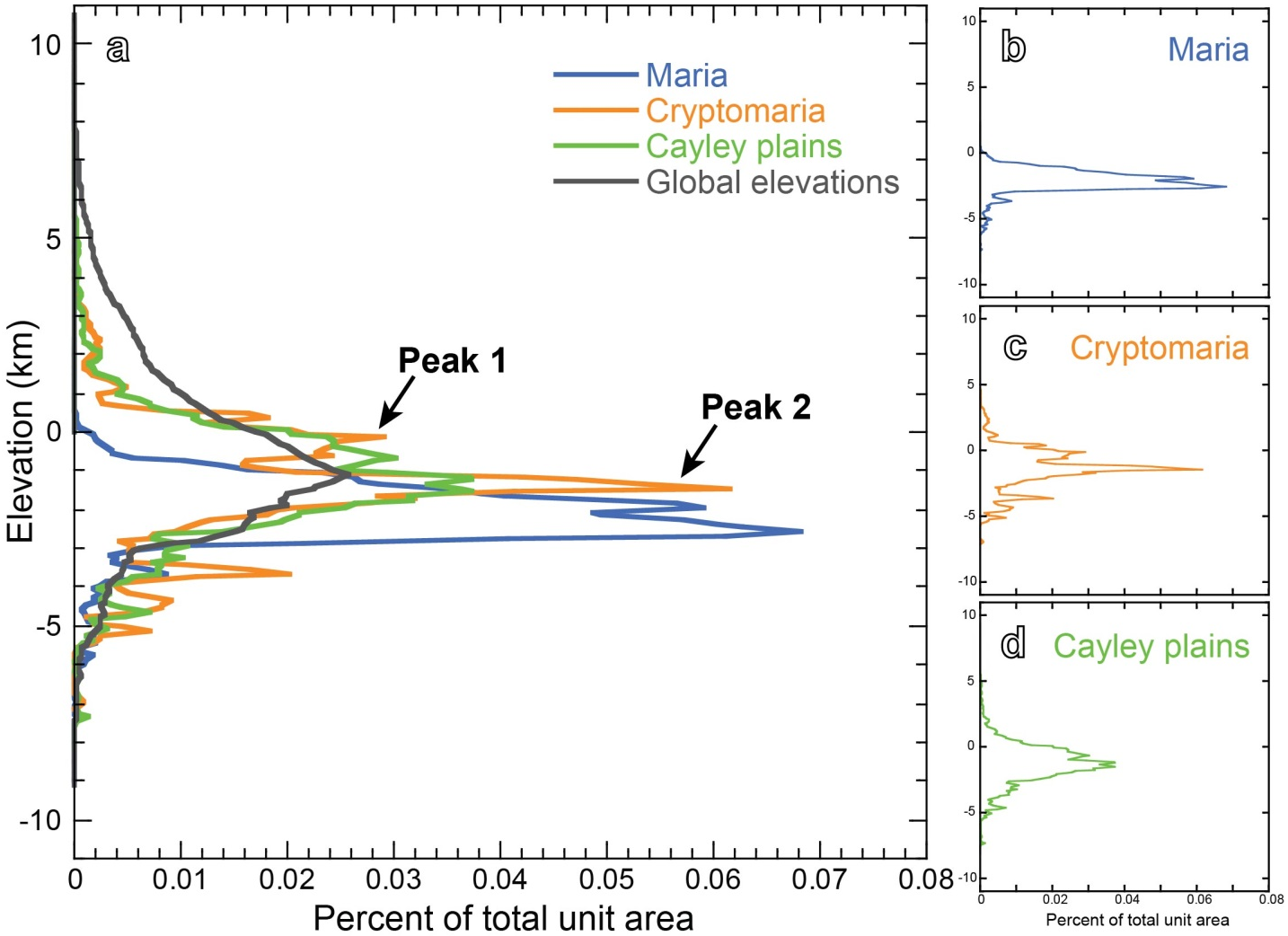
a
Maria
Cryptomaria
Cayley plains
Global elevations
Peak 1
Peak 2
Elevation (km)
10
5
0
-5
-10
0
0.01
0.02
0.03
0.04
0.05
0.06
0.07
0.08
Percent of total unit area
b
Maria
c
Cryptomaria
d
Cayley plains
0.02
0.04
0.06
0.08
Percent of total unit area

Figure 7.

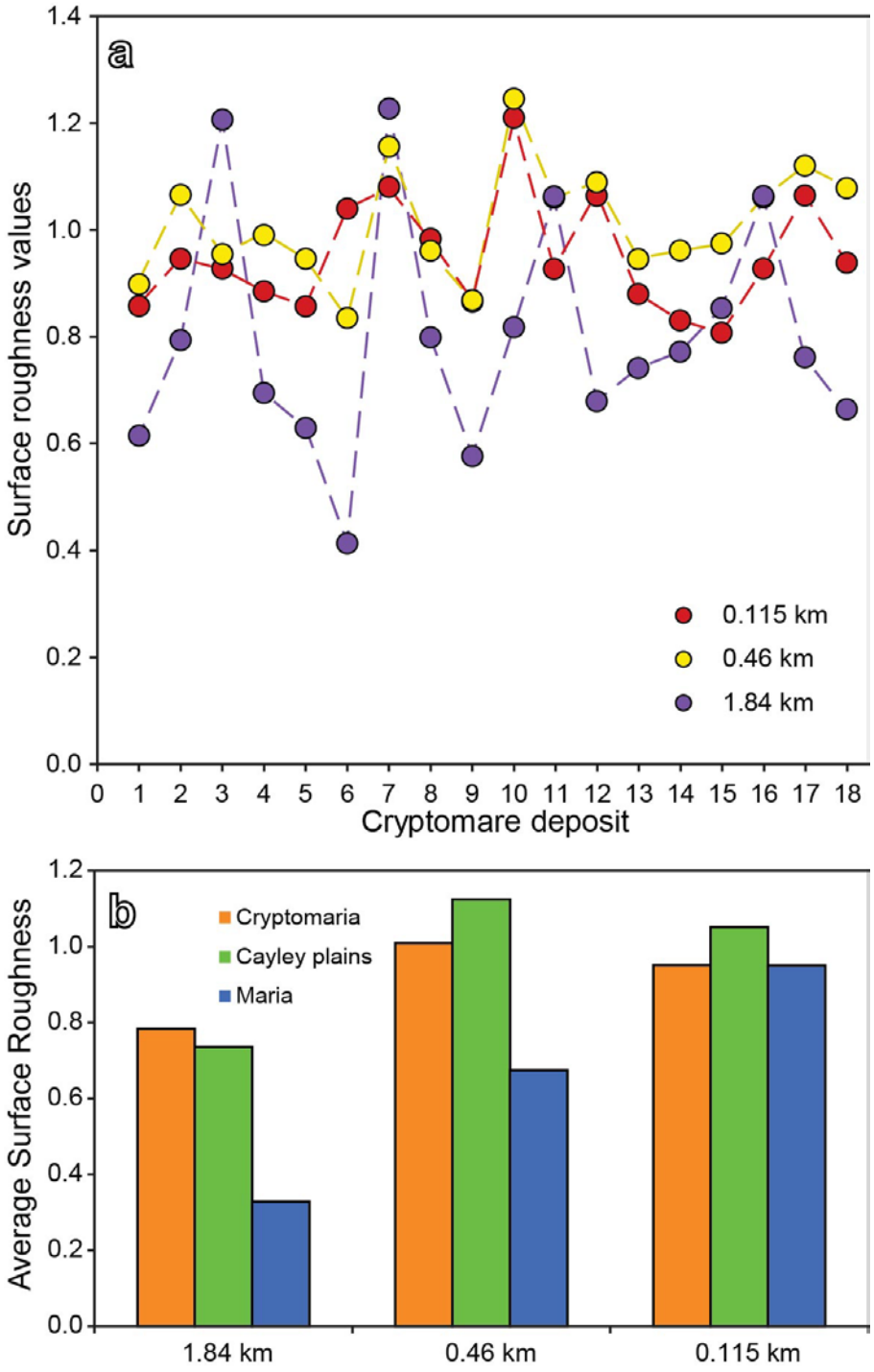
a
Surface roughness values
Cryptomare deposit
0.115 km
0.46 km
1.84 km
b
Average Surface Roughness
Cryptomaria
Cayley plains
Maria
1.84 km
0.46 km
0.115 km

Figure 8.

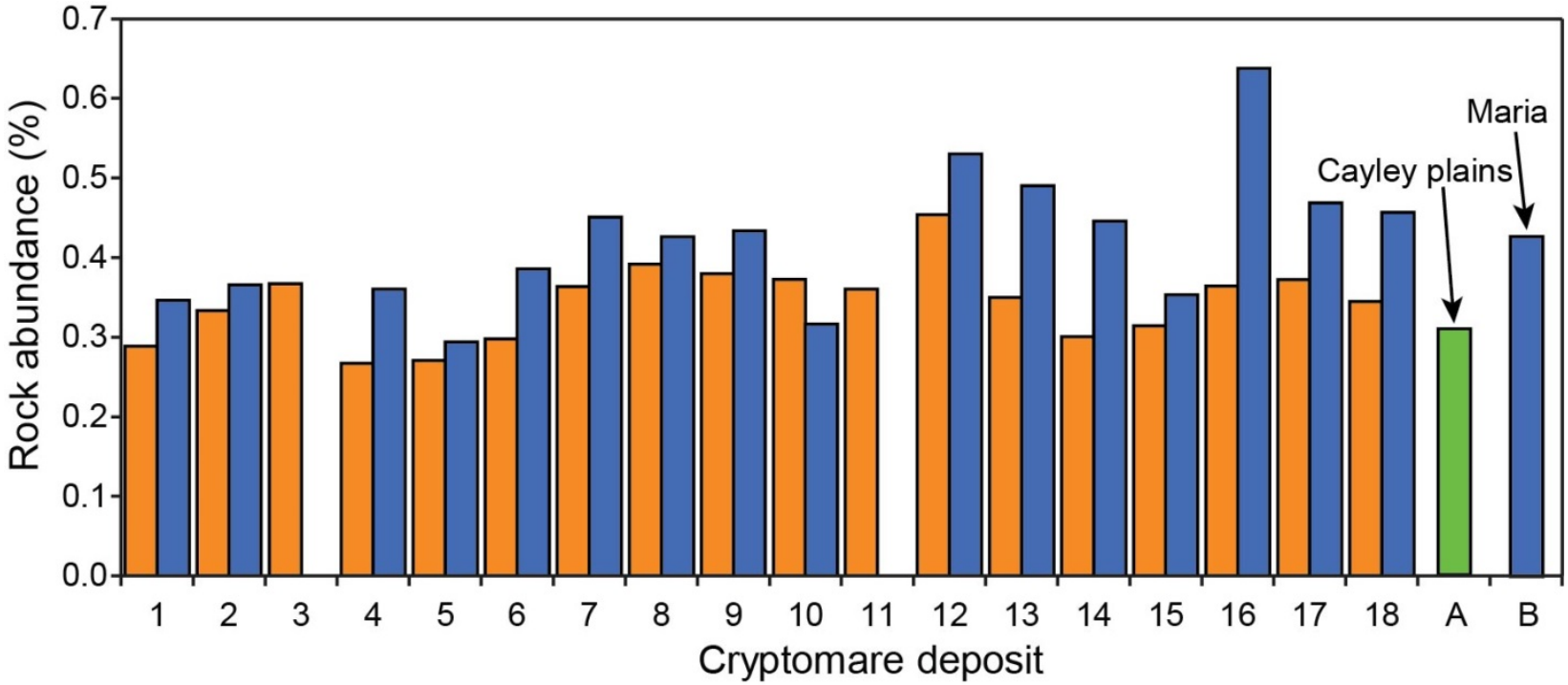
Rock abundance (%)
0.0
0.1
0.2
0.3
0.4
0.5
0.6
0.7
1
2
3
4
5
6
7
8
9
10
11
12
13
14
15
16
17
18
A
B
Cryptomare deposit
Cayley plains
Maria

Figure 9.

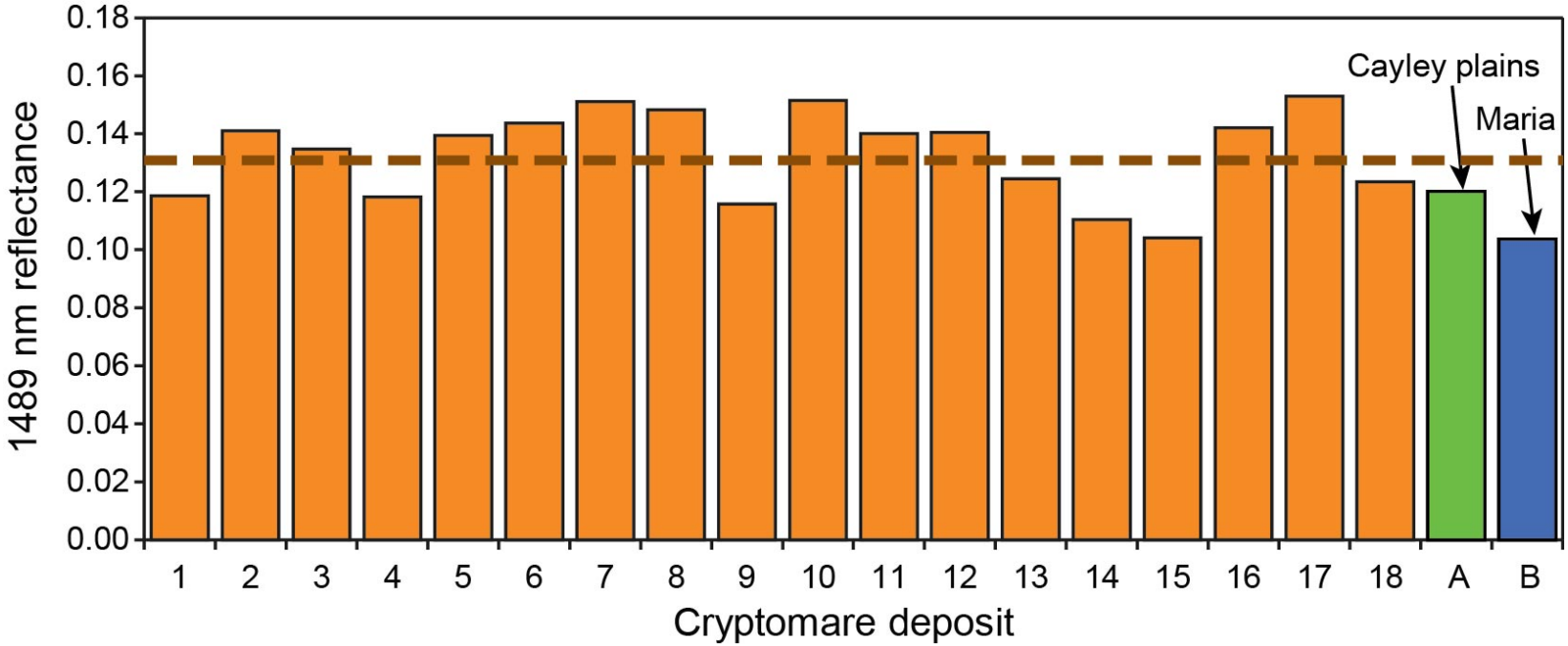
0.18
0.16
0.14
0.12
0.10
0.08
0.06
0.04
0.02
0.00
1489 nm reflectance
Cayley plains
Maria
1
2
3
4
5
6
7
8
9
10
11
12
13
14
15
16
17
18
A
B
Cryptomare deposit

Figure 10.

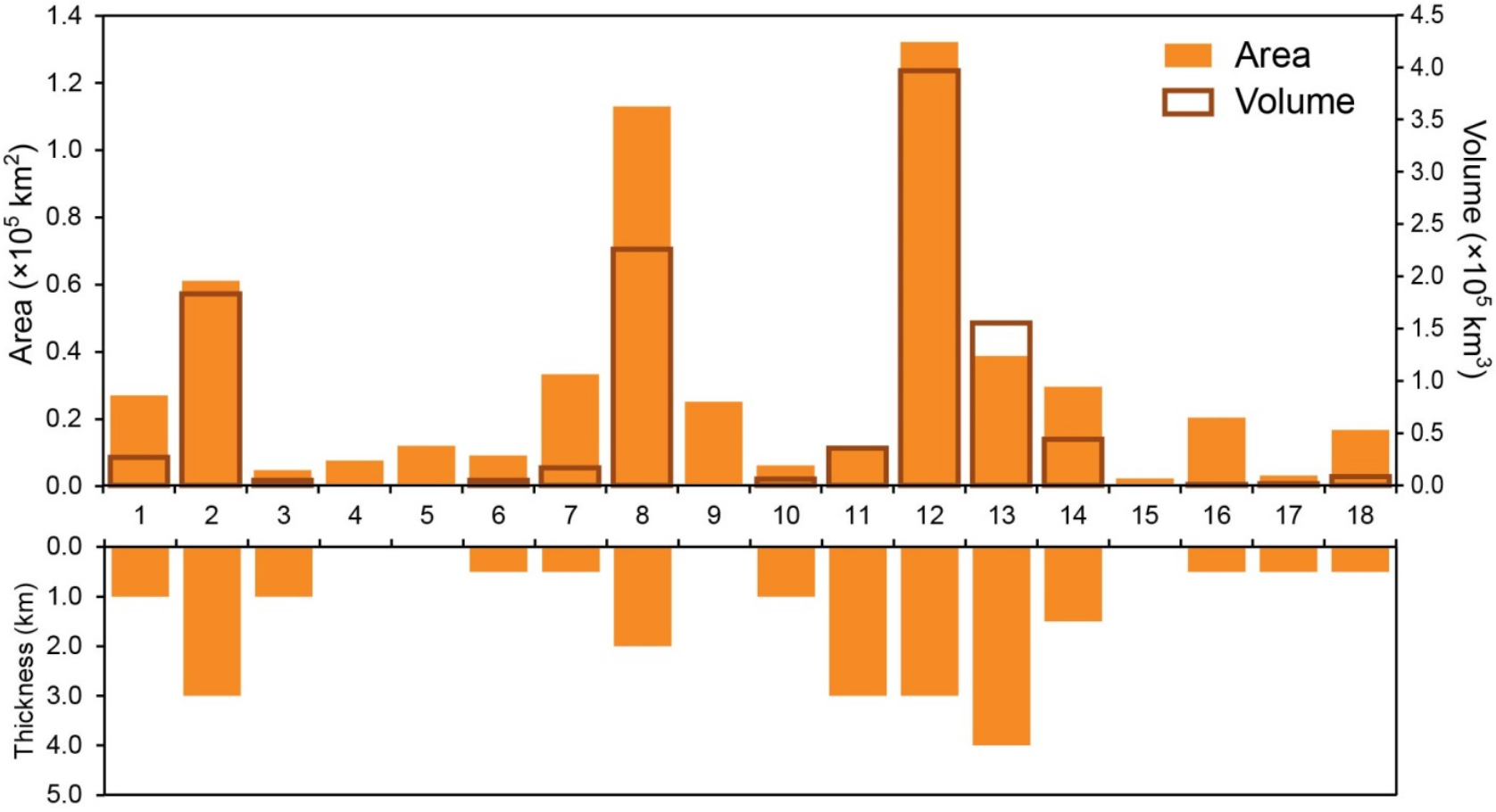
Area
Volume
Area (×10^5 km^2)
Volume (×10^5 km^3)
Thickness (km)
1.4
1.2
1.0
0.8
0.6
0.4
0.2
0.0
4.5
4.0
3.5
3.0
2.5
2.0
1.5
1.0
0.5
0.0
1 2 3 4 5 6 7 8 9 10 11 12 13 14 15 16 17 18
0.0
1.0
2.0
3.0
4.0
5.0

Figure 11.

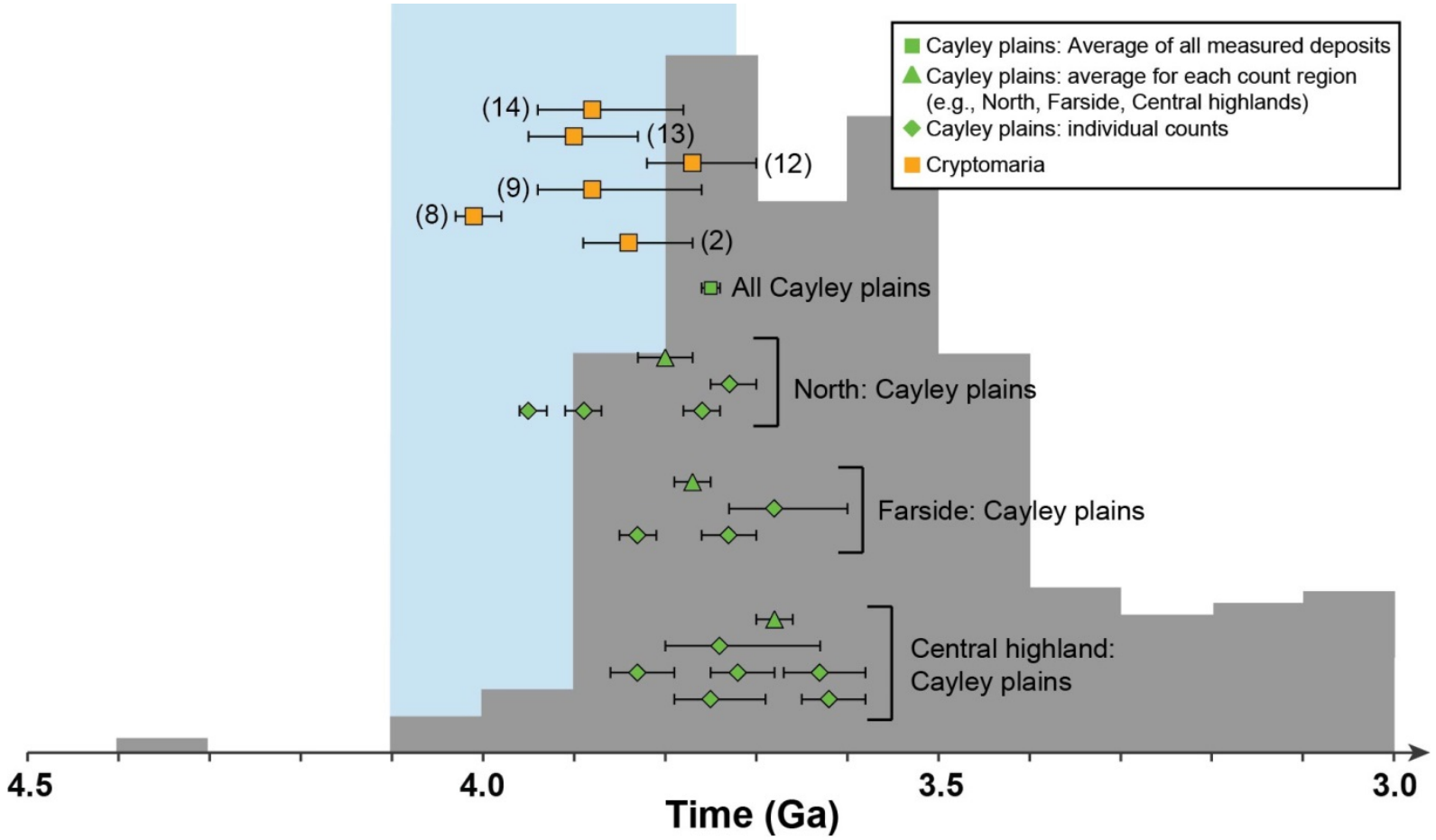
Cayley plains: Average of all measured deposits
Cayley plains: average for each count region (e.g., North, Farside, Central highlands)
Cayley plains: individual counts
Cryptomaria
(14)
(13)
(12)
(9)
(8)
(2)
All Cayley plains
North: Cayley plains
Farside: Cayley plains
Central highland: Cayley plains
4.5
4.0
3.5
3.0
Time (Ga)

Figure 12.

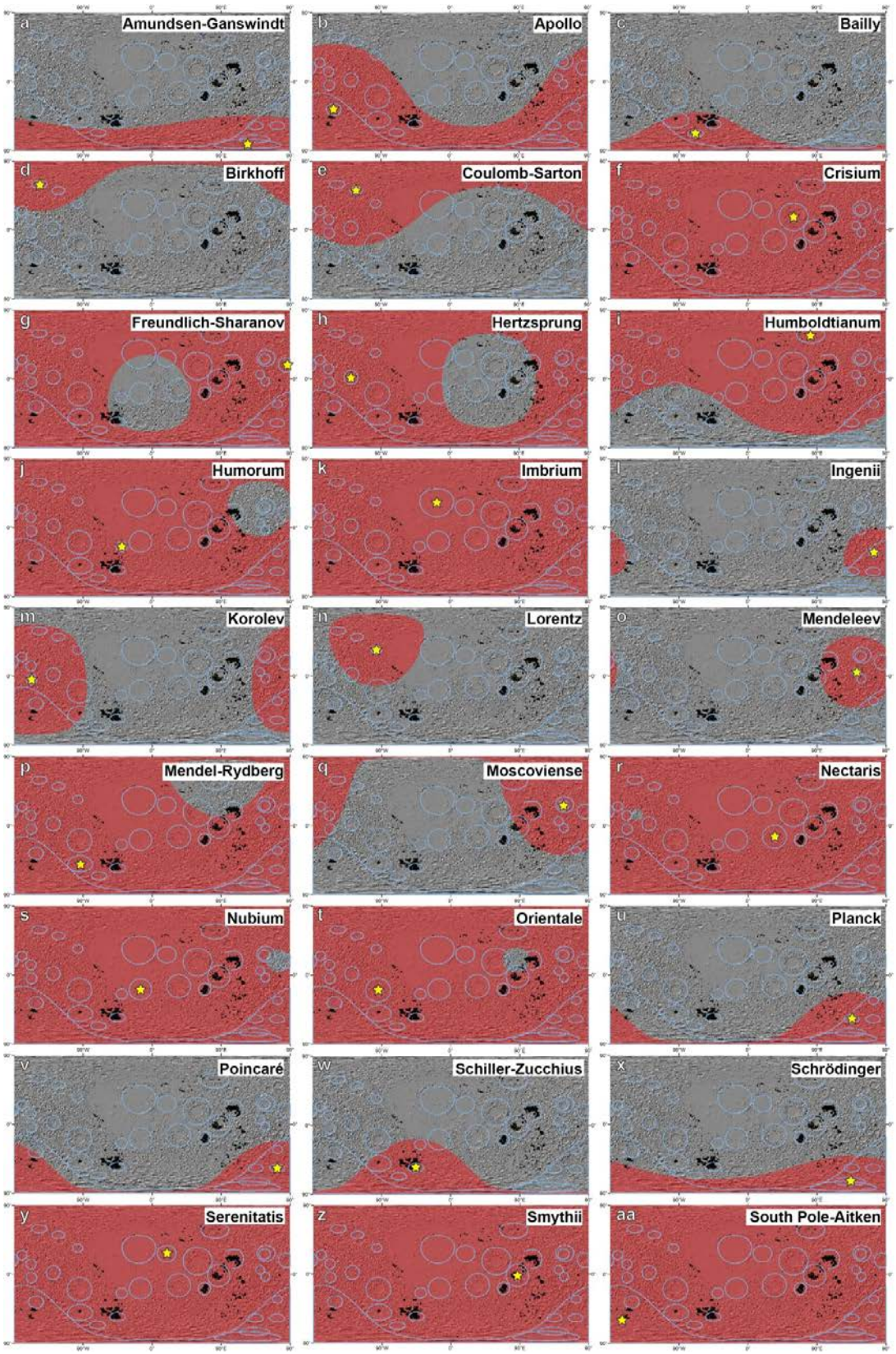
a
Amundsen-Ganswindt
b
Apollo
c
Bailly
d
Birkhoff
e
Coulomb-Sarton
f
Crisium
g
Freundlich-Sharanov
h
Hertzsprung
i
Humboldtianum
j
Humorum
k
Imbrium
l
Ingenii
m
Korolev
n
Lorentz
o
Mendeleev
p
Mendel-Rydberg
q
Moscoviense
r
Nectaris
s
Nubium
t
Orientale
u
Planck
v
Poincaré
w
Schiller-Zucchius
x
Schrödinger
y
Serenitatis
z
Smythii
aa
South Pole-Aitken

Figure 13.

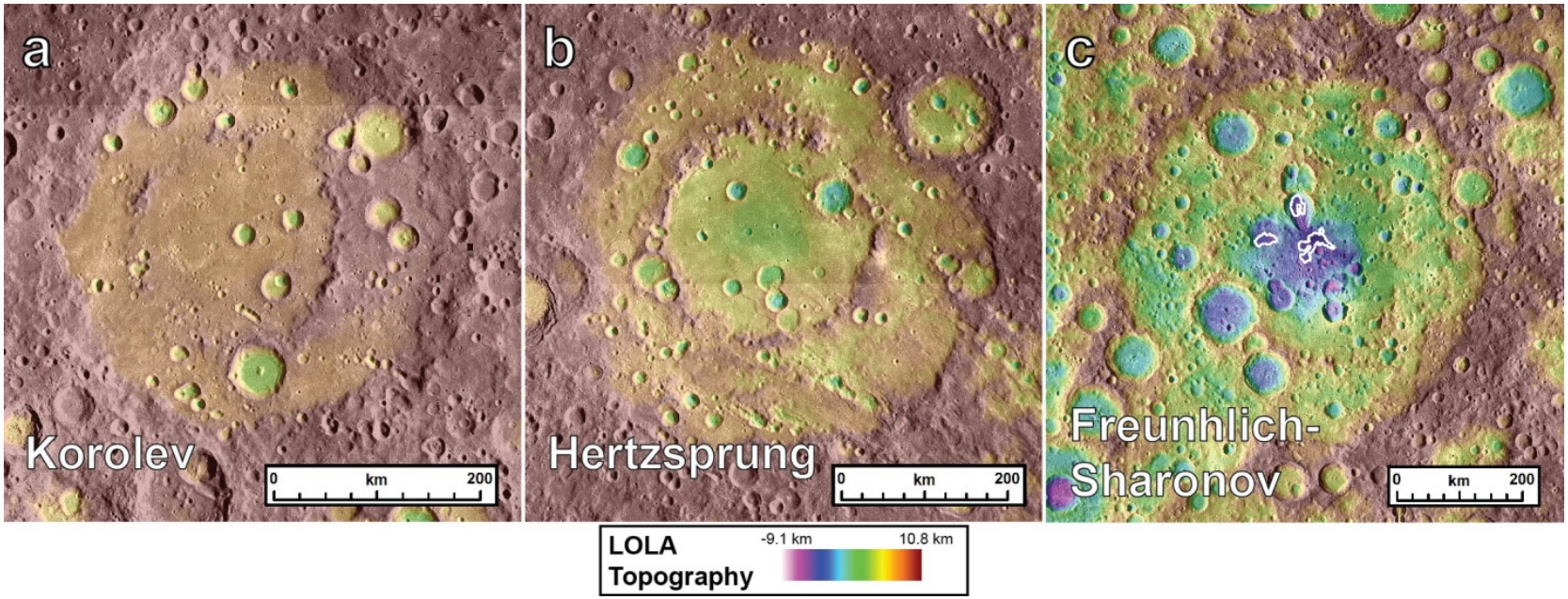
a
Korolev
0 km 200
b
Hertzsprung
0 km 200
c
Freunhlich-
Sharonov
0 km 200
LOLA
Topography
-9.1 km
10.8 km

Figure 14.

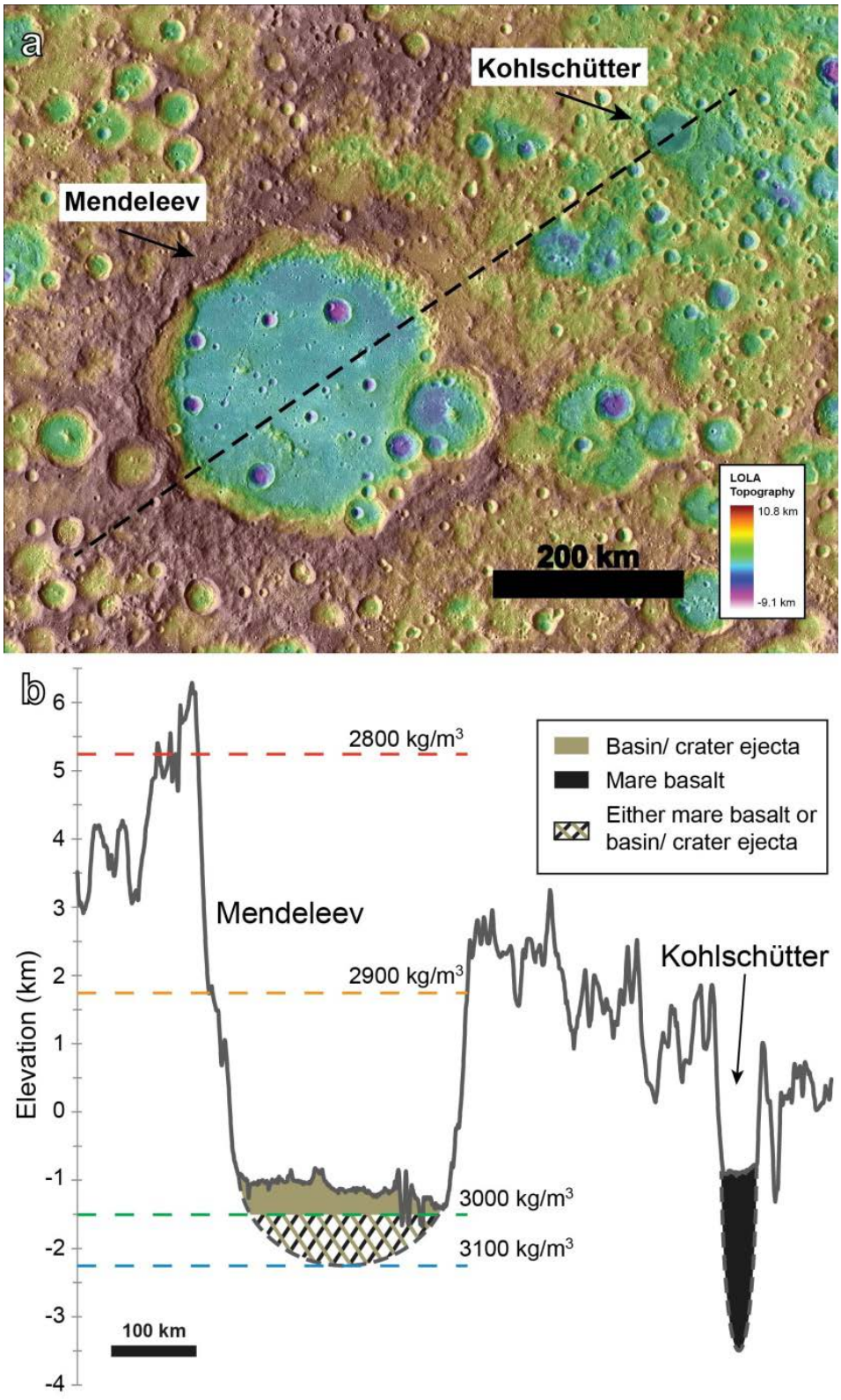
a
Kohlschütter
Mendeleev
LOLA Topography
10.8 km
-9.1 km
200 km
b
2800 kg/m3
2900 kg/m3
3000 kg/m3
3100 kg/m3
Basin/ crater ejecta
Mare basalt
Either mare basalt or basin/ crater ejecta
Mendeleev
Kohlschütter
Elevation (km)
6
5
4
3
2
1
0
-1
-2
-3
-4
100 km

Figure 15.

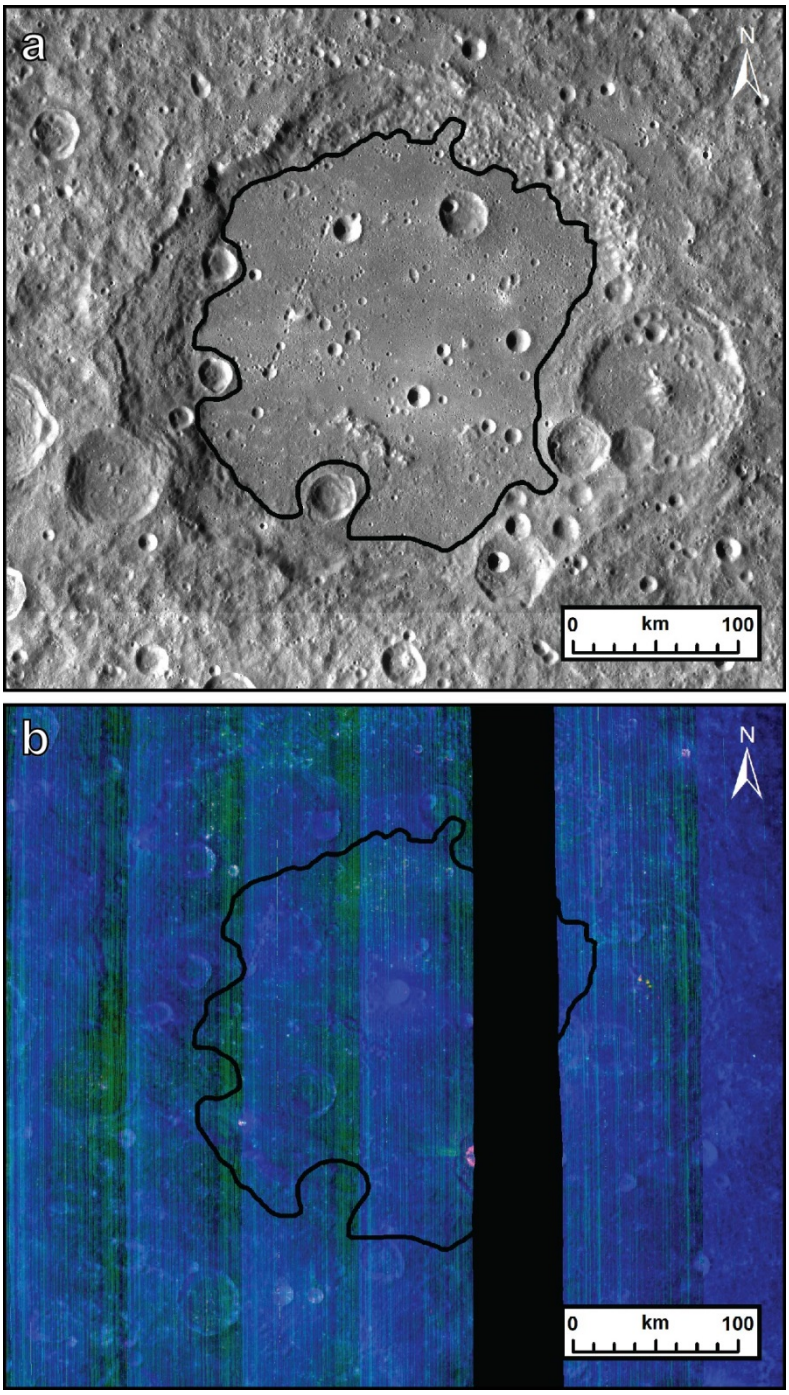

Figure 16.

Supplimental Figures

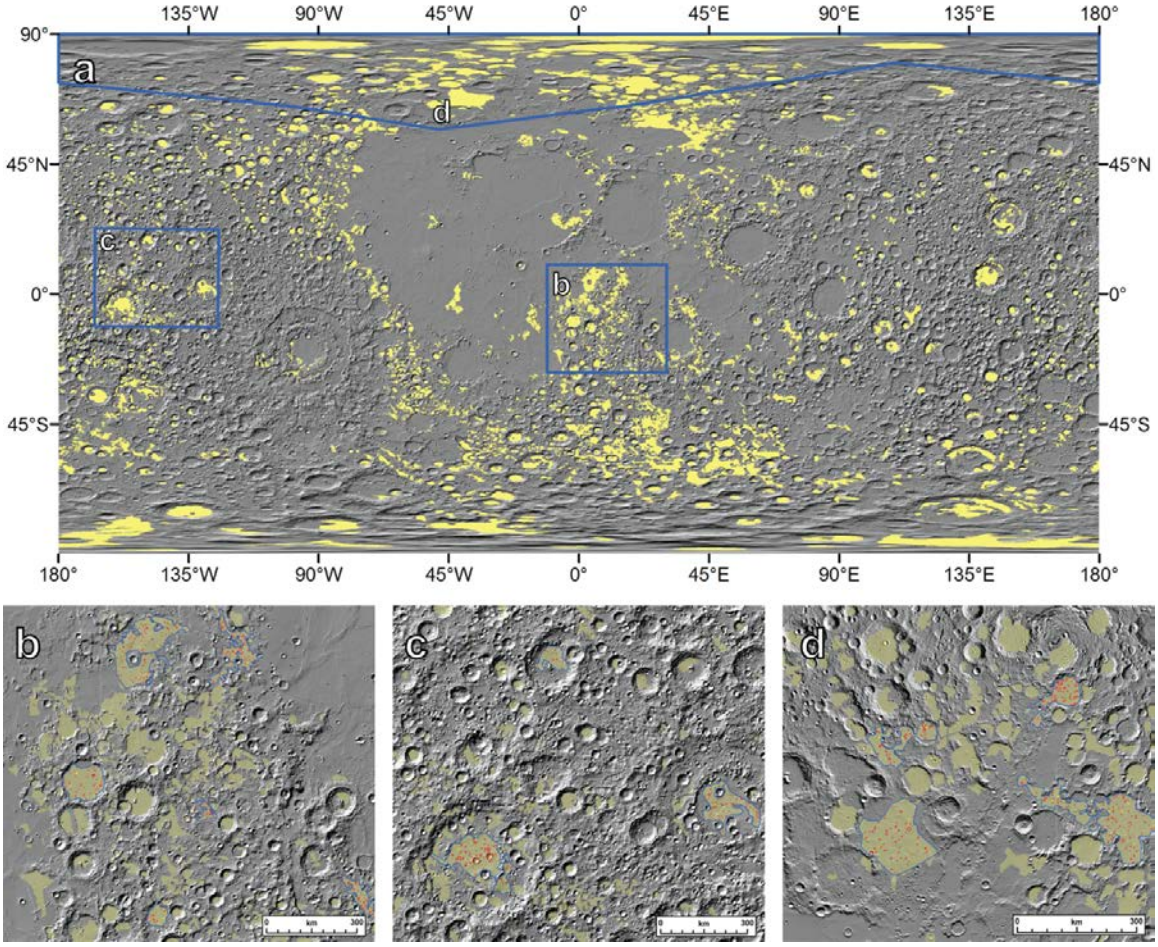

Figure S1.

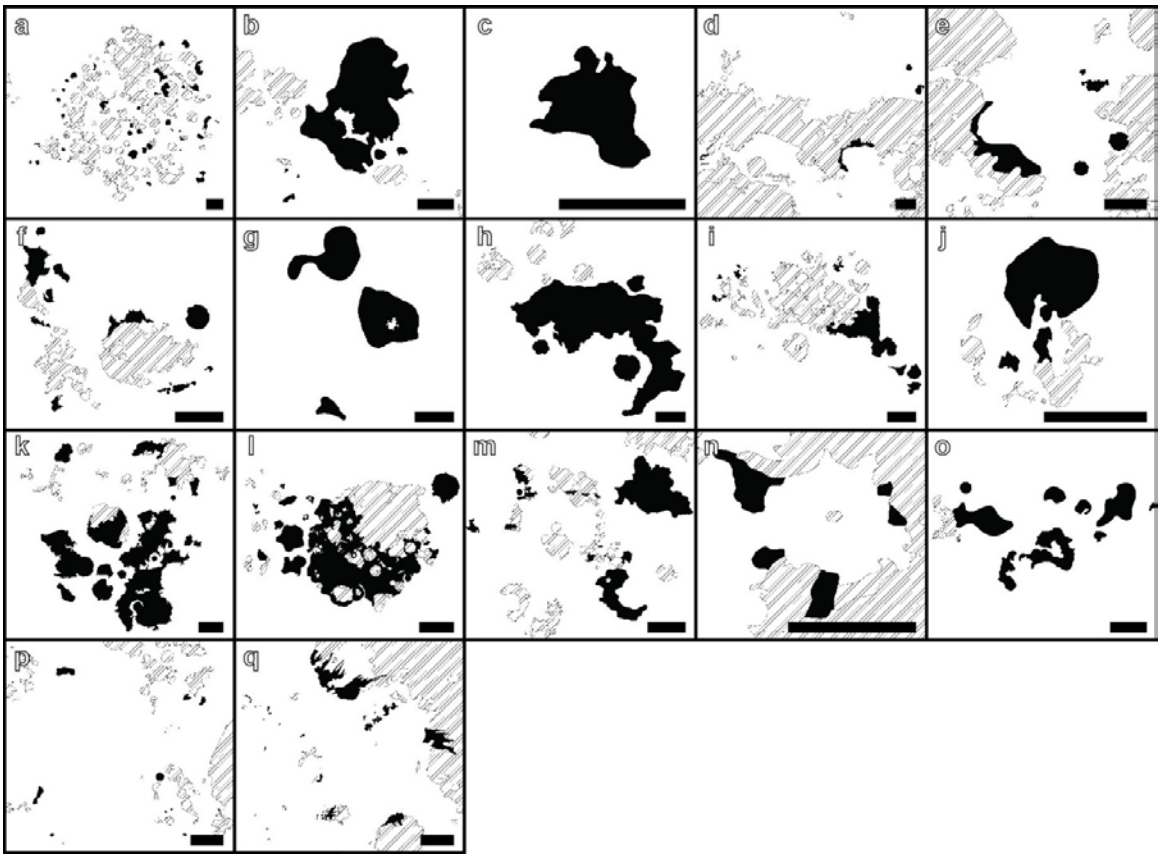

Figure S2.

Chapter 3:
Lunar cryptomaria, part II:
Mineralogy and composition of ancient volcanic deposits

Jennifer L. Whitten
and
James W. Head III

Department of Geological Sciences, Brown University,
324 Brook St., Box 1846, Providence, RI 02912.

To be submitted:
Summer 2014

Abstract

Ancient lunar volcanic deposits, known as cryptomaria, have been detected by remote telescopic and orbital measurements since the 1970s. Cryptomaria are most easily identified by the presence of dark-halo impact craters and are associated with a mare basalt mineralogy, which is indicated by two absorptions near 1 μm and 2 μm in the visible to near-infrared (VNIR) wavelengths. However, there are many early igneous lithologies that have been identified in the Apollo sample collection that have a similar VNIR spectral signal, implying a mineralogy dominated by pyroxene. In this study we use high resolution Moon Mineralogy Mapper (M^3) VNIR spectral data and the Modified Gaussian Model (MGM) to determine cryptomare mineralogy as well as Lunar Prospector (LP) FeO and Th compositional measurements to evaluate which ancient igneous rocks (low-Ti mare basalt, high-Ti mare basalt, Mg-suite rocks, dunite, high-Al mare basalt, KREEP basalt) are consistent with observations. In addition, spectra from different M^3 optical periods were compared to determine how the MGM-derived absorption band centers vary with the dataset. Band center differences between optical periods are on the order of ~6±4 nm and ~25±10 nm for the 1 μm and 2 μm features, respectively. Cryptomare mineralogies are dominated by clinopyroxene and are consistent with measurements from locally exposed mare basalts. Significant mineralogic variation is observed for a few cryptomaria (e.g., Schiller-Schickard, West Humorum), hinting at heterogeneous mantle source regions. LP measurements support a mare basalt rock type when regolith mixing is taken into account. Of the ancient igneous rocks investigated, cryptomare are most consistent with low-Ti mare basalts.

1. Introduction and background

Ancient lunar volcanic deposits, known as cryptomaria (Head and Wilson, 1992), have been identified beneath basin ejecta deposits (Schultz and Spudis, 1979, 1983; Hawke and Spudis, 1980; Hawke and Bell, 1981; Bell and Hawke, 1984; Hawke et al., 1993; Head et al., 1993; Antonenko et al., 1995; Blewett et al., 1995; Mustard and Head, 1996; Antonenko, 1999; Hawke et al., 2002; Giguere et al., 2003; Campbell and Hawke, 2005; Hawke et al., 2005; Lawrence et al., 2008; Hawke et al., 2013). The assigned name of these ancient volcanic deposits, cryptomare, implies something about the composition of these materials. Namely, that these ancient volcanic deposits are mare basalts. However, mare basalts are not the only ancient igneous lithology that was produced on the Moon during its earliest geologic history. Samples returned from the Apollo missions indicate that a diverse suite of ancient rock types, including ferroan anorthosites, KREEP basalts, high-Al mare basalts, and Mg-suite rocks such as troctolites, dunites, norites, and gabbros (e.g., Warren and Wasson, 1977) formed as the lunar magma ocean finished crystallizing and shortly thereafter. The primary lunar crust is dominated by ferroan anorthosites (Smith et al., 1970; Wood et al., 1970), while extrusive KREEP basalts and intrusive Mg-suite rocks are derived from melts of the lunar mantle (Warren and Wasson, 1977). The few dated samples of Mg-suite rocks and KREEP basalts indicate ancient ages >3.8 Ga (Ryder and Spudis, 1980; Nyquist and Shih, 1992; Stöffler et al., 2006). There is no indication that these lithologies continued to be produced after 3.8 Ga. The paucity of Mg-suite and KREEP basalt samples could be a preservation effect, since much of the lunar nearside has been resurfaced over the last 3.8 Ga by mare basalts (Hiesinger et al., 2011), or it could be due to a cessation of their formation process.

Whatever the cause of the paucity of the Mg-suite and KREEP basalts, mare basalts quickly became the dominant igneous rock type for the remainder of the Moon's volcanic history.

Cryptomaria were first identified by the presence of dark-halo impact craters (Schultz and Spudis, 1979, 1983), which are small craters, <10 km in diameter, that excavate low albedo material from beneath higher-albedo surface material. Initially, the dark-halo crater compositions were reported as basaltic, with some deposits being enriched in magnesium and KREEP (Schultz and Spudis, 1979). Further geochemical and visible to near-infrared (VNIR) spectral analyses suggested that the composition of dark-halo craters was consistent with mare basalt material (Maxwell and Andre, 1981; Hawke and Spudis, 1980; Hawke and Bell, 1981; Bell and Hawke, 1984; Blewett et al., 1995; Giguere et al., 2003; Hawke et al., 2005; Lawrence et al., 2008). Geochemical analyses of cryptomaria utilized measurements of elemental ratios, such as Mg/Al and Mg/Si, and elemental abundances (thorium and iron) from gamma ray and x-ray spectrometer data (Hawke and Spudis, 1980; Maxwell and Andre, 1981; Lawrence et al., 2008). Measurements of elemental abundances over regions with a high concentration of dark-halo craters were compared with mare basalts and KREEP-rich basalts in order to ascertain the composition of the buried volcanic material. These geochemical surface measurements of dark-halo craters were interpreted to indicate the presence of Mg-rich basalts, mare basalts, or KREEP-rich basalts.

More recent telescopic and remote spectral measurements of dark-halo craters are consistent with a mare basalt composition. These dark-halo VNIR spectral measurements are dominated by two pyroxene absorption features centered near 1 μm and 2 μm. The

center wavelength of the absorption bands provide information about the composition of the pyroxene; longer wavelength 1 μm and 2 μm absorption features are associated with Fe- and Ca-rich pyroxenes (Adams, 1974; Cloutis and Gaffey, 1991). Therefore, many spectral studies of dark-halo craters have focused on measuring the position of the two absorption band centers and comparing those values to the composition of known lunar samples (e.g., Bell and Hawke, 1984). Previous studies have found that dark-halo VNIR spectra have long wavelength absorption features that are consistent with clinopyroxene (Ca-rich pyroxene). Spectral analyses have been combined with other compositional datasets, such as Clementine and Lunar Prospector FeO and TiO_2 distribution maps, to further refine the compositional parameter space; the results remain consistent with dark-halo craters excavating mare basalts from below an overlying feldspathic unit.

Deconvolving the composition of ancient volcanic materials has important implications for the thermal history of the Moon. Analysis of mare basalt ages and their distribution provide information about mantle dynamics, including the timing of magma ocean overturn and the formation of mare basalt source regions in the mantle. Cryptomaria composition is also important for determining the composition of magmas melting within and being erupted from the mantle. For instance, Mg-rich mantle melts may have been produced early in lunar history, intruding into the anorthositic crust, and it is only after mantle overturn (e.g., Hess and Parmentier, 1995) that the mare basalt source regions were established and able to melt. The frequency distribution of mare basalt crater retention ages (Hiesinger et al., 2011) shows a peak in the flux of volcanic activity around ~3.6 Ga. Returned samples tell the story of a much more compositionally and temporally diverse volcanic history compared to the mare basalt deposits. During the first

500 My, the Moon was simultaneously producing mare basalts, KREEP basalts, and Mg-suite rocks. Soon afterwards, around 3.6 Ga, there was either a substantial increase in the eruption of mare basalts or a decrease in the production of parental melts for KREEP basalts and Mg-suite rocks or both processes occurred simultaneously.

The mineralogy and composition of identified ancient volcanic deposits is important for understanding the early volcanic history of the Moon and the relationship between the different ancient volcanic lithologies. Therefore, we have undertaken a study of the mineralogy of dark-halo craters identified in Chapter 2 (Whitten and Head, 2014) using Moon Mineralogy Mapper VNIR spectral data, as well as an analysis of elemental data for the mapped cryptomare deposits. The purpose of this investigation is to: (1) determine the mineralogy of mapped cryptomare deposits to ascertain if some or all of the deposits are mare basalts, (2) investigate the mineralogical variations both within a cryptomare region and also between cryptomare regions, (3) measure the compositional characteristics (Th and FeO) of all identified cryptomare to further characterize their compositions, and (4) understand how calculated mineralogies compare with ancient volcanic lithologies from the Apollo sample collection. Despite the fact that the Mg-suite is interpreted as intrusive, the Mg-suite lithologies (e.g., troctolite, norite) are included in this analysis in order to make as few assumptions as possible about the mineralogy and composition of cryptomaria; at some time during early lunar history conditions may have been such that the eruption of Mg-suite parental magmas was possible (e.g., Prissel et al., 2013).

2. Methods

2.1. Collection of VNIR spectra

All of the visible and near-infrared (VNIR) spectra used in this study were collected from the Moon Mineralogy Mapper (M^3) dataset. M^3 was a VNIR imaging spectrometer aboard the Chandrayaan-1 spacecraft that collected mineralogic information about the Moon's surface in 85 bands, from approximately 0.4 μm to 3.0 μm, at a spatial resolution of 140 to 280 m/pixel depending on the spacecraft altitude (Pieters et al., 2009; Green et al., 2011). All spectra examined in this study were collected from M^3 mosaics composed of individual data strips (Table A1) and have a spatial resolution of 140 m/pixel and each pixel has an associated 85-band spectrum. Average reflectance spectra (3×3 pixels) are collected from dark-halo craters located within 18 mapped cryptomare locations and any associated exposed mare basalt deposits (Fig. 1a) (Chapter 2). Cryptomare units contain between 1 and 40 individual volcanic deposits (Table A2), therefore, for each deposit multiple spectra were collected from dark-halo craters (Fig. 1c, d) and averaged together to produce a diagnostic spectrum for that particular volcanic deposit. Thus, each cryptomare region has multiple spectral measurements (Tables 1, 2, A2). A ground truth correction derived from laboratory spectra of feldspathic lunar soils was applied to the M^3 sampled spectra. This correction improves the accuracy of the position of the M^3 1 μm absorption feature and is relevant for spectral analyses involving the determination of pyroxene and olivine compositions based on their respective 1 μm band positions (Isaacson et al., 2013). Most of the data were collected from a single optical period of M^3 data (2c1). However, not all of the cryptomare deposits were imaged during optical period 2c1 and, as a result, spectra were collected from other optical periods (i.e., 1b and 2c2), where available. In order to quantify the spectral differences

optical periods, we compared the Modified Gaussian Model (MGM)-derived 1 μm and 2 μm absorption band centers from the same sample location in two different optical periods. Australe, Dewar, Langemak, and Lomonosov-Fleming dark-halo crater spectra were used for the optical period 2c1-2c2 comparisons while spectra from Frigoris, Mendel-Rydberg, Schiller-Schickard, Taruntius, West Humorum, and West Procellarum were used for the optical period 2c1-1b comparisons.

2.2. Continuum removal

The spectral slope (continuum) was removed prior to calculating the absorption band centers using MGM. Lunar spectra have a characteristic red-sloped continuum that is, in part, a product of space weathering processes (e.g., Pieters et al., 1993). In order to accurately model the wavelength position of mineral absorption bands the spectral continuum must be removed (e.g., Sunshine et al., 1990; Hiroi et al., 2000). M^3 spectra were fit with a two-part linear continuum in wavelength space; one part of the continuum was fit over the 1 μm absorption band and the second part was fit over the 2 μm absorption band. Three tie points were selected for continuum removal (Fig. 2). Once selected, the reflectance values for the wavelength immediately long and short of the tie point, in addition to the reflectance of the selected tie point, were averaged together to determine the reflectance value of the tie point. Tie point 1 (Fig. 2) was fixed at 0.75 μm, while tie point 2 and 3 were allowed to vary. The last two continuum tie points were selected from within a wavelength range using the convex hull method. For each spectrum tie points were chosen as follows: tie point 2 was confined to wavelengths between 1.329 μm and 1.778 μm and tie point 3 was assigned to be longer than 2.776

μm. A straight line was then fit between the reflectance values of tie points 1 and 2 and between tie points 2 and 3. In order to produce a single, continuum-removed reflectance spectrum, the reflectance values across shorter wavelengths of each spectrum were divided by the linear fit over the 1 μm absorption and the reflectance values across longer wavelengths were divided by the 2 μm linear fit. This spectrum was then input into the Modified Gaussian Model in order to calculate the absorption band centers.

2.3. Mineralogical analysis

The mineralogy of the cryptomare deposits was determined using the Modified Gaussian Model (MGM), an inverse model that deconvolves an individual spectrum into a continuum and a series of modified Gaussian curves approximating electronic absorption features observed within minerals (Sunshine et al., 1990). The MGM was included in a script that automated the continuum removal process and the MGM absorption fitting routine. In total 514 spectra were processed to determine the mineralogy of the mapped cryptomare deposits (Table 1, 2). All collected spectra are dominated by a pyroxene absorption signature with strong 1 μm and 2 μm features. Orthopyroxenes (low-Ca pyroxene), associated with noritic lunar rocks, have short wavelength 1 μm and 2 μm absorptions features near 0.9 μm and 1.9 μm (Adams, 1974; Cloutis and Gaffey, 1991; Klima et al., 2007); clinopyroxenes (high-Ca pyroxene) have 1 μm and 2 μm absorptions features at wavelengths longer than 0.95 μm and 2.05 μm (Adams, 1974; Cloutis and Gaffey, 1991; Klima et al., 2011), which dominate the spectral signatures of mare basalts. In order to determine the dominant pyroxene signature in the cryptomare deposits, the M^3 spectra (0.541–2.976 μm) were modeled

assuming that only a single pyroxene composition is present. The presence of two pyroxenes of distinct compositions would produce wider absorption features. Even if the M^3 instrument measured compositionally zoned or two distinct pyroxenes on the lunar surface, MGM can still be used to determine the average pyroxene composition of those units (Sunshine and Pieters, 1993) and aid in detecting variations within or between cryptomare deposits. Thus, continuum-removed spectra were processed using the MGM using only four absorption features. Three modified Gaussian bands were used to approximate the pyroxene crystal field bands at 1 μm, 1.2 μm, and 2 μm. The fourth band (0.35 μm) was used to describe the metal-oxygen charge transfer absorption in the visible part of the spectrum (Fig. 3, blue Gaussians). Gaussian band centers can be assigned to wavelengths outside of the spectrum wavelengths so that partial absorption features, such as the one at 0.35 μm, can still be modeled. Since the spectral continuum is removed prior to MGM processing the slope parameter in the model is held constant to ensure a flat continuum for each spectrum (Fig. 3, red horizontal line). This type of modeling is sufficient to: (1) search for variations in pyroxene composition within a particular cryptomare region, and (2) to identify differences in pyroxene composition between all of the mapped cryptomare units. The calculated 1 μm and 2 μm band centers were compared with band positions for a suite of low- and high-Ca synthetic pyroxenes (Klima et al., 2007, 2011) to characterize the mineralogy of the cryptomare deposits.

2.4. Compositional analysis

In addition to mineralogical analyses, the mapped cryptomare were analyzed using Lunar Prospector gamma ray spectrometer (LP GRS) Th (ppm) and FeO (wt %)

data (Lawrence et al., 1998). Both of these datasets have the highest available LP GRS resolution at 0.5°/pixel (~15 km/pixel). The FeO and Th values were employed to estimate better the lithology of the mapped cryptomare deposits. LP pixels contained within the mapped cryptomaria boundaries were used to calculate the average value for the entire deposit; the LP pixels are too large to measure the composition of individual dark-halo craters. While VNIR spectral data provide information about the spectrally dominant mineralogy, LP Th measurements can provide information about the abundance of incompatible elements in the rock and will help to distinguish between lithologies with a high abundance of incompatible elements, such as the Mg-suite (<5 ppm) (Wieczorek et al., 2006) and KREEP basalts (5–15 ppm, but the Apollo 15 extrusive KREEP basalts are 10–11 ppm) (Lucey et al., 2006; Wieczorek et al., 2006), and those rock types with a lower concentration of incompatible elements (i.e., mare basalts, <1 ppm on average) (Korotev, 1998). FeO measurements can also provide more precise estimates of the iron content than the VNIR spectral data and will be useful for distinguishing between iron- and magnesium-rich rocks.

3. Results

3.1. Optical period comparison

Data from the three different M^3 optical periods (1b, 2c1, 2c2) analyzed in this study do produce different calculated band center positions for the 1 μm and 2 μm absorption features (Figure 4, Table 3). Optical period 2c1 was used initially to analyze spectra collected from dark-halo craters in cryptomaria and fresh craters within exposed maria from the same study region (i.e., sampling spectra in Schiller-Schickard

cryptomaria and exposed maria). For instance, In order to estimate the uncertainty in the calculated band centers from optical period 2c1, it was necessary to determine the potential variability in the band center calculations due to differences in the M^3 observations (illumination, spacecraft geometry, etc.). The 1.2 μm absorption feature shows the least amount of variation between optical periods, approximately 2 nm (Table 3). In addition, the difference between optical periods 1b and 2c1 and 2c2 and 2c1 was almost identical at 1.9 nm and 1.8 nm, respectively. The standard deviation in these values was <1 nm. Band center variations in the 1 μm region are slightly larger, with an average value of 6 nm. Optical periods 1b and 2c1 showed a larger discrepancy in the calculated band center values, 8.1 nm, compared to 2c2 and 2c1, 3.5 nm. The 2 μm absorption band had, by far, the most variable calculated band center values; the average band center difference between optical periods is 25.4 nm, with the difference between 2c2 and 2c1 slightly larger than for the 1b-2c1 comparison. However, the standard deviation for the 2 μm band center values is only 9.8 nm.

There are more dark-halo units with the same M^3 spectral coverage in optical periods 1b and 2c1 than in optical periods 2c2 and 2c1 (Fig. 4, compare left column with right column). The variation in calculated band centers observed between 2c2 and 2c1 appears random as there are no clear systematic trends observed for the 1.0 μm, 1.2 μm, or 2.0 μm absorption features (cf. Fig. 4a, b, c). For the 1 μm and 1.2 μm absorption features the data are evenly distributed around a 1:1 line, but for the 2 μm absorption band center 2c2 either produces short wavelength band centers or 2c1 measurements result in long wavelength band centers. However, these observed relationships could be due to the paucity of overlapping data points for 2c2 and 2c1. The abundance of

overlapping data in optical periods 1b and 2c1 enables a more robust comparison of the calculated band centers. Similar to the 2c2-2c1 comparisons, the 1.2 μm band center does not show any systematic variation between 1b and 2c1 (Fig. 4d). Conversely, the 1 μm and 2 μm absorptions do show systematic variations. If optical period 2c1 is taken as the baseline dataset, then the wavelengths of the 1 μm band centers calculated for the 1b data are too short (Fig. 4b). The reverse is true for the calculated 2 μm band centers (Fig. 4f); the 1b 2 μm calculated using the MGM are located at longer wavelengths compared with the 2c1 data.

The temperature of the M^3 instrument was above its ideal operating temperature for most of the mission. During the "hot" optical periods such as 2c1 and part of 2c2 temperatures exceeded 160 K (Green et al., 2011). "Cold" optical periods occurred when the instrument was below 160 K and include optical periods 1b and part of 2c2. Variations in detector temperatures affect the shape of spectra as evidenced by the need to generate two different ground truth corrections, one for "hot" and one for "cold" data (e.g., Isaacson et al., 2011). "Hot" data deviated more from the laboratory-measured spectra compared to the "cold" data. The application of the ground truth correction brought the 1 μm band position of "hot" and "cold" spectra closer together, such that at lower latitudes they are almost identical. It is only at higher latitudes that a deviation in the shape of spectra occurs. Therefore, smaller spectral variations are expected in the 1 μm region due to the applied ground truth corrections and the lack of significant thermal effects at wavelengths <~1.5 μm. In fact, smaller variations in the position of the 1 μm are observed (Fig. 4; Table 3). The 2 μm variations between optical periods are much more substantial and are difficult to attribute to one variable. A comparison of the MGM-

derived 2 μm positions suggests that there is no correlation between detector temperatures (Fig. 4e, f). Optical period 2c1 is "hot" and 2c2 is both "hot" and "cold". In the 2c1-2c2 comparison (Fig. 4e), 2c1 is either producing long wavelength band centers, or 2c2 band centers are too short. On the other hand, the 2b1-1b comparison (Fig. 4f) suggests that 2c1 produces short wavelength absorptions, or 1b values occur at longer wavelengths. Thus, the "hot" 2c1 data produce MGM 2 μm absorptions that occur at both long and short wavelengths. These data indicate that M^3 spectra can be used to distinguish between the presence of low- versus high-Ca pyroxene. Identification of specific pyroxene compositions, especially distinguishing between different high-Ca pyroxene species, using the wavelength position of the 2 μm band center is difficult.

3.2. Modified Gaussian Model mineralogies

The calculated mineralogies of the 517 measured cryptomare and exposed mare deposits all overlap substantially with one another (Fig. 5). Cryptomare and exposed mare display a spread in band center values, from 0.95–1.00 μm and 2.05–2.30 μm. However, all of the M^3 remote measurements overlap with well-characterized synthetic clinopyroxene samples measured in the laboratory (Fig. 5, 6). In 83% of study regions there is no clear distinction between the MGM-derived band center values for cryptomare and exposed mare units (Fig. 6). However, there are a few cryptomare regions that do show some distinction between the cryptomare and exposed mare mineralogies (Fig. 6g, h, i). For the deposits in Lacus Solitudinis (Fig. 6g) the cryptomare typically have longer wavelength 1 μm and 2 μm absorption features compared to the exposed mare. The reverse is true for the Langemak (Fig. 6h) and Lomonosov-Fleming (Fig. 6i) regions;

cryptomare have shorter wavelength 1 μm and 2 μm absorption bands. However, there is still substantial overlap between the cryptomare and exposed mare around Lacus Solitudinis and Lomonosov-Fleming.

Frigoris, Hercules, and Tarunitus are "young" cryptomare deposits, formed from the continuous ejecta deposits of Eratosthenian- and Copernican-aged craters overlying maria (Wilhelms and McCauley, 1971; Giguere et al., 2003) compared to the basin events that formed the larger cryptomaria (Whitten and Head, 2014). These two study regions are not associated with ancient Pre-Nectarian and Nectarian basins. Instead, these cryptomare units are produced when feldspathic ejecta from a young impact crater superposes exposed mare deposits. This formation mechanism for "young" (Giguere et al., 2003) cryptomaria thus assumes that the exposed mare deposits should have the same composition as the dark-halo craters from cryptomare deposits. MGM-derived 1 μm and 2 μm band centers support this formation hypothesis. Hercules is a clear example of the overlap in MGM-derived band center values between cryptomare and exposed mare compositions (Fig. 6e).

A few study regions show large variations in the mineralogy of both the cryptomare and exposed mare deposits (Fig. 6m, q), on the order of 0.015–0.045 μm and 0.115–0.225 μm for the 1 μm and 2 μm absorption bands, respectively. The short wavelength end of the calculated absorption bands centers corresponds to low-Ca pigeonites and the longer wavelength end of the trend corresponds to low-Ca augites. These mineralogic variations in the pyroxene composition are probably not related to the evolution of the magma source region over time because the same trend is observed for both old (cryptomare) and young (mare) volcanic deposits. In order to be detected in M^3

spectra, the different pyroxene compositions need to be generated by a process that is active over spatial scales of hundreds of meters. A heterogeneous source region for the magmas erupted in the Schiller-Schickard and West Humorum regions may provide a possible explanation for the observed pyroxene variations.

Other study regions do not display significant mineralogic differences (Fig. 6n, o), with <0.025 μm and <0.07 μm variation for the wavelength position of the 1 μm and 2 μm absorption bands, respectively. Many study regions have rather large data clouds with no distinct mineral trends; the numerous observations from Australe produce a large data cloud with <0.05 μm variation in the calculated position of the 1 μm absorption band, but 0.1 μm variation in the 2 μm absorption band (Fig. 6a). Most of the observed mineralogic variation is in the 2 μm absorption band. For all processed spectra, both cryptomare and exposed mare, the wavelength position of the 1 μm absorption band has a much narrower range of calculated values. This observed variation is consistent with the measured band center variations between the different M^3 optical periods (Table 3, Fig. 4) and also with laboratory measurements of synthetic and natural samples (Cloutis and Gaffey, 1991; Klima et al., 2007, 2011). Terrestrial and synthetic pyroxenes have ~170 nm variation in the position of the 1 μm band and ~525 nm of variation in the 2 μm absorption band between ortho- and clinopyroxenes. Of the three crystal field absorptions modeled, the 2 μm band has the largest uncertainty between the different M^3 optical periods, ±25.3 nm which is the error value assigned to each data point. The uncertainty associated with the 1 μm absorption feature is only ±5.8 nm, five times smaller. The variability and uncertainties in the calculated band center values also coincide with the change in spectral resolution from the 1 μm region to the 2 μm region. Between ~730 nm and

~1550 nm the M^3 imaging spectrometer has a spectral resolution of 20 nm. At longer wavelengths, from 1580–2500 nm the spectral resolution decreases to 40 nm (Green et al., 2011). Thus, there are more data points available in the 1 μm region to constrain the position of the absorption feature compared with the 2 μm region.

Many of the calculated band center values plot to the left of the synthetic pyroxene trend (Fig. 4b, g, h, i, j, n, p, q, r). Typically, when data plot off of the pyroxene trend it indicates that more than one mineral phase is present (Adams, 1974). The presence of other minerals may play a role in the band center results from this study because lunar rocks contain many minerals including olivine, plagioclase, and other minor phases (e.g., ilmenite and spinel) that could influence the shape of the spectrum. For instance, plagioclase has a distinct mineral absorption at 1.25 μm (e.g., Conel and Nash, 1970), overlapping with the 1.2 μm pyroxene absorption (e.g., Sunshine et al., 1990; Klima et al., 2008). While both the plagioclase and pyroxene absorption features at ~1.2 μm are observable with trace amounts of Fe, pyroxene tends to dominate the spectrum and can completely mask the plagioclase absorption. As little as 5–10 wt % pyroxene is needed to remove all evidence of crystalline plagioclase in a VNIR spectrum (Cheek et al., 2013). Currently, it is difficult to distinguish between a pyroxene spectrum with a strong 1.2 μm absorption and a spectrum of a plagioclase-pyroxene mixture; the geologic setting (e.g., volcanic lava flow versus crater central peak) of most spectral detections usually provides enough evidence to interpret the spectrum.

However, it is more likely that residual thermal effects in the M^3 dataset are influencing the position of the 2 μm absorption band center. A first-order thermal correction was applied to the M^3 data by deriving temperature and emissivity from the

spectra and removing the thermal component from near infrared wavelengths (Clark et al., 2011). This thermal correction did improve the shape of the M^3 spectra at infrared wavelengths, but in order to completely correct for thermal effects a more complex model incorporating local topographic scattering effects must be developed and applied to the spectra (McCord et al., 2011; Bandfield et al., 2014). Despite the incomplete removal of thermal emission from the M^3 spectra, we chose to model the entire M^3 wavelength range (540–2976 nm). A shorter wavelength could be chosen as tie point 3 for the continuum removal process (Section 2.2.) to partially combat the thermal effects in the infrared part of the spectrum, but there is no way to ensure that this technique would move the position of the 2 μm absorption band center closer to its original expected value. Therefore, to avoid adding this uncertainty into the band center values the entire wavelength range of the spectra were processed. Regardless of the exact wavelength position of the 2 μm absorption band center, all of the cryptomare spectra indicate a clinopyroxene-dominant mineralogy, consistent with a mare basalt composition.

3.3. Compositional data

To further constrain the possible rock types of the mapped cryptomare regions (Fig. 1a) the Th (ppm) and FeO (wt. %) abundances were estimated using the LP GRS data (Fig. 7). The comparatively low resolution of the LP data requires that the average value for the entire mapped cryptomare deposit be used in the derivation of these compositional values. Thus, the reported values are averages of material exposed by dark-halo craters and the feldspathic material superposed on the cryptomare deposit. For all cryptomaria, thorium abundances fall between 1.0 and 4.4 ppm (Fig. 7), with a group

average value of 1.6 ppm. The Frigoris cryptomare has the largest Th concentration at 4.4 ppm, followed by West Procellarum (3.0 ppm), Hercules (2.5 ppm), and West Humorum (1.9 ppm). All of these cryptomare are located on the edge of the Procellarum KREEP Terrane (PKT) (Jolliff et al., 2000) which suggests that these Th values are affected by the concentration of incompatible elements found in this region of the Moon and may not reflect the actual amount of Th in the cryptomare deposit. Of the cryptomare not associated with the PKT, only Dewar and South Pole-Aitken have Th values >2 ppm. The South Pole-Aitken Terrane (SPAT) (Jolliff et al., 2000), which encompasses the South Pole-Aitken cryptomare, is also enriched in Th. The remaining cryptomare have Th values between 1.0 and 1.4 ppm.

Cryptomare FeO values are between 5.4 and 12.4 wt %, with an average of 8.4 wt %. The highest FeO values are generally associated with cryptomare adjacent to areally extensive mare basalt deposits. Frigoris, Hercules, Taruntius, and West Procellarum all have >9.5 wt % FeO. However, other cryptomare, namely Smythii and South Pole-Aitken, also have high FeO values. In the case of Smythii the high FeO is due to its close proximity to extensive mare basalt deposits contained within the impact basin. As mentioned previously, the South Pole-Aitken cryptomare are within the SPAT, which has an FeO enrichment. The remaining cryptomare generally have between 6–9 wt % FeO. Dewar has the lowest average FeO value, 5.4 wt %, which may be a function of its isolated location on the farside. Over lunar history, the small deposit on the farside was probably covered with a substantial layer of feldspathic material due to impact gardening. Compared with the compositional measurements of lunar rocks, cryptomare average Th and FeO values are dominantly associated with the Mg-norite and Mg-gabbronorite

values (Fig. 7). However, it is important to remember that these values are mixtures of the underlying cryptomare and the overlying feldspathic ejecta. The influence of ejecta may bias the Th and FeO values to overlap with the Mg-norites as feldspathic materials typically contain some amount of noritic material, however we have not identified orthopyroxene (the composition of pyroxene dominant in norites) in the cryptomare regions.

The average FeO content of Schiller-Schickard is rather low, 7.8 wt % (Fig. 7). However, the range in FeO varies from ~5 to 10 wt % FeO. These FeO variations can be correlated with the albedo of the surface, where higher FeO values correspond to lower albedo materials. The reverse is also true, where high albedo surfaces have lower FeO values. This albedo-FeO correlation suggests that the regions with high FeO and low albedo have only a thin layer of basin or crater ejecta superposing the deposit. The albedo and FeO variations are consistent with the Schiller-Schickard region being resurfaced by the Orientale impact event, with the northwestern deposits having the highest albedo and lowest FeO values and the southeastern parts of the cryptomare deposit having lower albedo and higher FeO.

4. Comparison with other ancient igneous rocks

All cryptomare and exposed mare deposit rock types correspond to clinopyroxene-dominated mineralogies (Fig. 5, 6). A clinopyroxene-rich mineralogy is typically associated with mare basalts while orthopyroxene-rich geologic materials, with pyroxene absorption band centers at shorter wavelengths, denote a noritic composition. A comparison with other ancient volcanic rocks types reinforces this interpretation (Fig. 8).

Reflectance Experiment Laboratory (RELAB) spectra of Apollo samples (Fig. 8a), such as a low-Ti basalt (15058,276), a high-Ti basalt (70017), a dunite (72415,64), a norite (72255,74), a troctolite (76535,17), a high-Al mare basalt (14301,49), and a KREEP basalt (14310,152) were processed using the same methods as described above for the M^3 spectra, including the continuum removal process. Lunar samples that are not dominated by pyroxene were processed to determine how the automated MGM would fit the spectra of these samples and to test the robustness of the automated MGM and the defined pyroxene absorption bands. If any M^3 spectra of dunite or troctolite were input into the model it would be easy to differentiate these lithologies from pyroxene-dominated basalts and norites. As expected, the calculated positions of the 1 μm and 2 μm band centers show greater variability than the cryptomare or exposed mare deposits. In addition, all of these ancient lunar rock types plot off of the synthetic pyroxene trend indicating the complex mineralogy of these rock samples.

For instance, the band center results from the dunite sample are far removed from the synthetic pyroxene trend (Fig. 8b). This is expected given that this sample is dominated by olivine and the automated MGM input parameters are optimized for pyroxene spectra. Olivine has three individual absorption features that comprise its 1 μm absorption band (e.g., Burns, 1970), which cannot be modeled accurately with only the two bands assigned to the 1 μm region in our MGM model. The high-Ti basalt spectrum was also poorly fit by the parameters used in our automated MGM model which, again, makes sense given the presence of opaque ilmenite (the Ti-bearing mineral phase in the rock) and its distinct spectral signature in the visible to near-infrared, being dark and rather featureless (Loeffler et al., 1975; Riner et al., 2009; Isaacson et al., 2011). The

abundance of olivine and plagioclase in the troctolite sample resulted in MGM-derived band centers that are fairly consistent with the synthetic pyroxene trend. A closer inspection of the troctolite spectrum (Fig. 8a) shows that the continuum removal process would actually shift the 2 μm band center to longer wavelengths which moves the position of the troctolite sample closer to the synthetic pyroxene trend. In this case, the combination of the olivine and plagioclase absorption shifts the calculated 1 μm band center to shorter wavelengths. As expected, the Apollo norite 72255,74 plots near the orthopyroxene suite. Its slight offset may be explained by a combination of the continuum removal process and the wavelength range of the spectrum, shifting the 2 μm band center to shorter wavelengths. The high-Al mare basalt and KREEP basalt spectra have low spectral contrast, but appear well fit by the model (Fig. 8a). Both rock types are slightly offset from the synthetic orthopyroxene mineral trend, which can also be attributed to the continuum removal process shifting the wavelength position of the 2 μm absorption band center or the low spectral contrast. Since the high-Al and KREEP spectra are rather flat the automated MGM may have had trouble uniquely fitting the 2 μm absorption band.

Of all the ancient lunar volcanic rocks, the low-Ti basalt sample plots closest to the synthetic pyroxene trend and also, corresponds to the position of the M^3 cryptomare and exposed mare spectra on the trend. Again, the low-Ti data plot to the left of the synthetic pyroxene trend, which is due to the limited wavelength range of the spectrum and the continuum removal process creating a shorter wavelength 2 μm absorption band center. The mineralogy of this low-Ti Apollo sample is consistent with a mare basalt

composition, having pyroxene (~63%; ~4% orthopyroxene, 58% clinopyroxene), plagioclase (~30%), opaque minerals (~5%), and trace olivine (Isaacson et al., 2011).

Over geologic time there is significant regolith mixing with the uppermost millimeters of the lunar surface (McEwen et al., 1997), overturning more rapidly than deeper parts of the lunar regolith (Gault et al., 1974). The upper microns of the regolith, corresponding to the optical surface viewed by spectrometers, is overturned within ~10^4 years. At a depth of ~10 cm the turnover rate is on the order of 0.5 Ga (Shoemaker et al., 1970; Gault et al., 1974; McEwen et al., 1997). Thus, the amount of mixing between the basaltic ejecta deposits of dark-halo impact craters and the underlying feldspathic basin ejecta will depend on the thickness of the dark-halo ejecta deposits. Lateral mixing is also an important process that contributes to homogenization of the lunar regolith (Li and Mustard, 2000). The combination of vertical and lateral mixing diminishes the compositional and spectral signatures of dark-halo craters. Measurements of mare soils collected during the Apollo program indicate there is less Fe and more Al present compared to the corresponding mare basaltic rocks, providing observational evidence for feldspathic highlands contamination in lunar basaltic soils (Korotev, 1998). The observed offset between the LP FeO and Th estimated for cryptomare and the measured FeO and Th values for lunar mare basalts can be explained by regolith mixing (Fig. 7). The LP data collected for the cryptomaria are averages of the whole deposit (green circles), dark-halo craters and basin ejecta deposits, which are more offset from expected mare basalt values compared to the LP Th/ Clementine FeO data (orange circles). The Clementine dataset has a higher spatial resolution (100–200 m/pixel) than Lunar Prospector FeO measurements (~15 km/ pixel) allowing for the FeO content of individual DHCs to be

estimated, instead of averaging the entire mapped cryptomare deposit. Previous researchers have come to the same conclusion, that regolith mixing has artificially decreased the Th and FeO measurements of cryptomare deposits (Giguere et al., 2003; Hawke et al., 2005; Lawrence et al., 2008).

The geologic setting of each of these ancient lunar rock types (Fig. 8a) varies and can provide further information to determine the dominant lithology of cryptomaria. Both high-Ti and low-Ti mare basalts are typically located in large impact basins or within Oceanus Procellarum. The majority of returned samples that have a KREEP basalt composition are actually impact melt rocks associated with the Imbrium impact (Haskin, 1998; Jolliff et al., 2000). However, there are a few samples from the Apollo 15 and 17 missions that are believed to be extrusive based on a primary igneous texture, the lack of lithic clasts and siderophile elements indicative of meteorite impacts, and evidence for a two-stage cooling process (e.g., 15404, 15358, 15382, 15386, 15434) (Ryder, 1987). It is difficult to infer a geologic setting for many of these samples since they are typically only small hand sample fragments. However, the fact that the KREEP samples were collected in basin settings at the Apollo 15 and 17 sample sites as well as suggestions from geologic mappers (Cadogan, 1974; Hawke and Head, 1977; Wilhelms, 1987) indicate that many of the extrusive KREEP basalts may have formed early basin fill deposits. The density of KREEP and high-Al mare basalts is similar to the latest estimates of the average crustal density (Wieczorek et al., 2013), which would allow these mantle melts to propagate and erupt onto the surface if located within hydrostatically favorable locations such as impact basins (Solomon, 1975). The high aluminum content of the KREEP and high-Al mare basalts and their occurrence in Apollo 14 Fra Mauro breccias argues for a

similar geologic provenance (Nyquist and Shih, 1992). The identification of troctolite-rich lithologies is confined to crater central peaks (Pieters and Tompkins, 1999; Tompkins and Pieters, 1999). During an impact, the crater central peaks are thought to expose the deepest-seated crustal materials (Ullrich et al., 1977; Melosh, 1989). The fact that troctolite-rich materials are only exposed in crater central peaks suggests that they occur dominantly as intrusive igneous deposits in the lunar crust. Dunite and olivine-rich rocks are also excavated from the crust (Pieters, 1982; Tompkins and Pieters, 1999) and possibly from the mantle during impact basin events (Yamamoto et al., 2010).

The presence of troctolite and dunite lithologies in central peaks and the lack of detections outside of impact craters imply that these rocks occur primarily as plutons and are usually of limited areal extent; this observation is inconsistent with the geologic settings of mapped cryptomaria (Fig. 1). The most areally extensive cryptomaria are associated with ancient impact basins, such as Schiller-Zucchius and Lomonosov-Fleming, while the remaining deposits are associated with other smaller impact structures. Cryptomare detections are made through the mineralogy of dark-halo craters, which are superposed on smooth plains. There is no positive detection of cryptomare that is associated with the walls or central peak of a large impact crater or basin. Based on orbital detections of early lunar volcanic rock-types, the lithologies that are expected to erupt as voluminous deposits on the lunar surface are mare basalts, either high- or low-Ti magmas, KREEP basalts, and high-Al mare basalts. The observed distribution of these four basaltic lithologies is consistent with the geologic setting of the mapped cryptomare (Fig. 1).

Despite the diverse suite of lithologies possible based on the observed cryptomare geologic settings the composition and mineralogic data provide further constraints to determine whether high-Ti, low-Ti, KREEP, or high-Al basalts are the dominant rock type. Several lines of evidence suggest that the cryptomaria analyzed in this study correspond to a low-Ti mare basalt mineralogy: (1) dominance of clinopyroxene in the M^3 spectra (Fig. 5, 6), (2) the overlap of MGM-derived absorption band positions for cryptomare and exposed mare basalts (Fig. 5, 6), (3) mixing analyses/ turnover rates for the lunar regolith explains the low FeO values measured for the cryptomare deposits, and (4) the low Th values consistent with mare basalts (Fig. 7).

1. Conclusions

M^3 and LP data have been used to determine which ancient lunar rock type is consistent with the observed mineralogic and compositional characteristics of mapped cryptomare deposits. The MGM was used to estimate the position of the 1 μm and 2 μm absorption features observed in the M^3 cryptomare spectra. In addition, different M^3 optical period data sets have been compared to determine how the model-derived mineralogies vary due to spacecraft temperature, altitude, geometry, etc. We find that:

(1) Residual thermal effects in the M^3 spectra influence the MGM-calculated position of the 2 μm absorption band. The model-derived 2 μm band position is estimated at shorter wavelengths than expected based on laboratory measurements of natural and synthetic pyroxenes.

(2) The derived pyroxene mineralogies of cryptomare are generally consistent with exposed mare basalts in the same local region (e.g., Australe, Smythii, and

South-Pole Aitken). In addition, in most cryptomaria there is little observable variation in the model-derived pyroxene mineralogy.

(3) The LP measurements were measured over large areas meaning these values represent an average of the ejecta of dark-halo craters and the superposed feldspathic basin ejecta deposits. Therefore, the anomalously low values that suggest Mg-rich lithologies can actually be explained by regolith mixing processes.

(4) There are a few cryptomare regions (e.g., Schiller-Schickard, West Humorum) with significant variation in the calculated pyroxene mineralogies, especially in the position of the 2 μm absorption band. This observed variation cannot all be attributed to thermal effects because all of the collected cryptomare spectra contain residual thermal energy and neither Schiller-Schickard or West Humorum are associated with thermal anomalies on the surface; both cryptomare are located at similar mid-latitudes away from the lunar poles and the equator. Compositional heterogeneities in the magma source region may be able to account for the observed pyroxene variations.

(5) Of the ancient igneous rocks considered (low-Ti mare basalts, high-Ti mare basalts, Mg-suite rocks, dunite, high-Al mare basalts, KREEP basalts), only the mare basalts have absorption band centers and FeO and Th concentrations consistent with the sampled cryptomare spectra and are expected to have been erupted as areally extensive volcanic deposits. Therefore, the cryptomare deposits analyzed in this study are consistent with a low-Ti mare basalt mineralogy.

References

Adams, J.B., 1974. Visible and near-infrared diffuse reflectance spectra of pyroxenes as applied to remote sensing of solid objects in the solar system. J. Geophys. Res. 79, 4829–4836.

Antonenko, I., 1999. Global estimates of cryptomare deposits: Implications for lunar volcanism. Lunar Planet. Sci. Conf. 30, abstract 1703.

Antonenko, I., Head, J.W., Mustard, J.F., Hawke, B.R., 1995. Criteria for the detection of lunar cryptomaria. Earth, Moon and Planets 69, 141–172.

Bandfield, J.L., Hayne, P.O., Paige, D.A., 2014. What is the surface temperature of the Moon? Lunar Planet. Sci. Conf. 45, abstract 1519.

Bell, J.F., Hawke, B.R., 1984. Lunar dark-haloed impact craters: Origin and implications for early mare volcanism, J. Geophys. Res. 89, 6899–6910.

Blewett, D.T., Hawke, B.R., Lucey, P.G., Taylor, G.J., 1995. Remote sensing and geological studies of the Schiller-Schickard region of the Moon, J. Geophys. Res. 100, 16959–16977.

Burns, R.G., 1970. Crystal field spectra and evidence of cation ordering in olivine minerals. Am. Mineral. 55, 1608–1632.

Cadogan, P.H., 1974. Oldest and largest lunar basin? Nature 250, 315–316.

Campbell, B.A., Hawke, B.R., 2005. Radar mapping of lunar cryptomaria east of Orientale basin. Journal of Geophysical Research 110, E09002, doi:10.1029/2005JE002425.

Cheek, L.C., Donaldson Hanna, K.L., Pieters, C.M., Head, J.W., Whitten, J.L., 2013. The distribution and purity of anorthosite across the Orientale basin: New perspectives

from Moon Mineralogy Mapper data. J. Geophys. Res. 118, 1–16. doi:10.1002/jgre.20126.

Clark, R.N., Pieters, C.M., Green, R.O., Boardman, J.W., Petro, N.E., 2011. Thermal removal from near-infrared imaging spectroscopy data of the Moon. J. Geophys. Res. 116, E00G16. doi:10.1029/2010JE003751.

Cloutis, E.D., Gaffey, M.J., 1991. Pyroxene spectroscopy revisited: Spectral-compositional correlations and relationship to geochemistry. J. Geophys. Res. 96, 22809–22826.

Conel, J.E., Nash, D.B., 1970. Spectral reflectance and albedo of Apollo 11 lunar samples: Effects of irradiation and vitrification and com- parison with telescopic observation. Proc. Lunar Sci. Conf., 11, 2013–2023.

Gault, D.E., Hörz, F., Brownlee, D.E., Hartung, J.B., 1974. Mixing of the lunar regolith, Proc. Lunar Sci. Conf., 5, 2365–2386.

Green, R.O., Pieters, C., Mouroulis, P., Eastwood, M., Boardman, J., Glavich, T., Isaacson, P., Annadurai, M., Besse, S., Barr, D., Buratti, B., Cate, D., Chatterjee, A., Clark, R., Cheek, L., Combe, J., Dhingra, D., Essandoh, V., Geier, S., Goswami, J.N., Green, R., Haemmerle, V., Head, J., Hovland, L., Hyman, S., Klima, R., Koch, T., Kramer, G., Kumar, A.S.K., Lee, K., Lundeen, S., Malaret, E., McCord, T., McLaughlin, S., Mustard, J., Nettles, J., Petro, N., Plourde, K., Racho, C., Rodriquez, J., Runyon, C., Sellar, G., Smith, C., Sobel, H., Staid, M., Sunshine, J., Taylor, L., Thaisen, K., Tompkins, S., Tseng, H., Vane, G., Varanasi, P., White, M., Wilson, D., 2011. The Moon Mineralogy Mapper (M^3) imaging spectrometer for lunar science: Instrument description, calibration, on-

orbit measurements, science data calibration and on-orbit validation. J. Geophys. Res. Planets 116, E00G19. doi:10.1029/2011JE003797.

Giguere, T.A., Hawke, B.R., Blewett, D.T., Bussey, D.B.J., Lucey, P.G., Smith, G.A., Spudis, P.D., Taylor, G.J., 2003. Remote sensing studies of the Lomonosov-Fleming region of the Moon, J. Geophys. Res. 108, 5118. doi:10.1029/2003JE002069.

Haskin, L.A., 1998. The Imbrium impact event and the thorium distribution at the lunar highlands surface. J. Geophys. Res. 103, 1679–1689.

Hawke, B.R., Head, J.W., 1977. Pre-Imbrium history of the Fra Mauro region and Apollo 14 sample provenance. Proc. Lunar Planet. Sci. Conf. 8, 2741–2761.

Hawke, B.R., Spudis, P.D., 1980. Geochemical anomalies on the eastern limb and farside of the moon. Proceedings of the Conference on Lunar Highlands Crust, 467–481.

Hawke, B.R., Bell, J.F., 1981. Remote sensing studies of lunar dark-halo impact craters: Preliminary results and implications for early volcanism, Proceedings of the Lunar and Planetary Science Conference 12B, 665–678.

Hawke, B.R., Peterson, C.A., Lucey, P.G., Taylor, G.J., Blewett, D.T., Campbell, B.A., Coombs, C.R., Spudis, P.D., 1993. Remote sensing studies of the terrain northwest of Humorum Basin. Geophysical Research Letters 20, 419–422.

Hawke, B.R., Giguere, T.A., Blewett, D.T., Lucey, P.G., Smith, G.A., Taylor, G.J., Spudis, P.D., 2002. Igneous activity in the southern highlands of the Moon. Journal of Geophysical Research 107, 5122, doi:10.1029/2000JE001494.

Hawke, B.R., Blewett, D.T., Bussey, D.B.J., Giguere, T.A., Lawrence, D.J., Lucey, P.G., Smith, G.A., Spudis, P.D., Taylor, G.J., 2003. Geochemical anomalies in the lunar highlands. Lunar Planet. Sci. Conf. 34, abstract 1198.

Hawke, B.R., Gillis, J.J., Giguere, T.A., Blewett, D.T., Lawrence, D.J., Lucey, P.G., Smith, G.A., Spudis, P.D., Taylor, G.J., 2005. Remote sensing and geologic setting of the Balmer-Kapteyn region of the Moon. J. Geophys. Res. 110, E06004. doi:10.1029/2004JE002383.

Head, J.W., Wilson, L., 1992. Lunar mare volcanism: Stratigraphy, eruption conditions, and the evolution of secondary crusts. Geochim. Cosmochim. Acta 56, 2155–2175. doi:10.1016/0016-7037(92)90183-J.

Hawke, B.R., Giguere, T.A., Gaddis, L.R., Gustafson, J.O., Lawrence, D.J., Stopar, J.D., Peterson, C.A., Bell III, J.F., Robinson, M.S., and the LROC Science Team, 2013. Cryptomare and pyroclastic deposits on the northern east side of the Moon. Lunar Planet. Sci. Conf. 44, abstract 1883.

Head, J.W., Murchie, S., Mustard, J.F., Pieters, C.M., Neukum, G., McEwen, A., Greeley, R., Nagel, E., Bleton, M.J.S., 1993. Lunar impact basins: New data for the western limb and far side (Orientale and South Pole-Aitken basins) from the first Galileo flyby. Journal of Geophysical Research 98, 17149–17181.

Hess, P.C., Parmentier, E.M., 1995. A model for the thermal and chemical evolution of the Moon's interior: Implications for the onset of mare volcanism. Earth Planet. Sci. Lett. 134, 501–514.

Hiesinger, H., Head, J.W., Wolf, U., Jaumann, R., Neukum, G., 2011. Ages and stratigraphy of lunar mare basalts: A synthesis. Geological Society of America Special Paper 477, 1–51.

Hiroi, T., Pieters, C.M., Noble, S.K., 2000. Improved scheme of Modified Gaussian deconvolution for reflectance spectra of lunar soils. Lunar Planet. Sci. Conf. 31, abstract 1548.

Isaacson, P.J., Basu Sarbadhikari, A., Pieers, C.M., Klima, R.L., Hiroi, T., Liu, Y., Taylor, L.A., 2011. The lunar rock and mineral characterization consortium: Deconstruction and integrated mineralogical, petrologic, and spectroscopic analyses of mare basalts. Met. Planet. Sci. 46, 228–251. doi:10.1111/j.1945-5100.2010.01148.x.

Isaacson, P.J., Petro, N.E., Pieters, C.M., Besse, S., Boardman, J.W., Clark, R.N., Green, R.O., Lundeen, S., Malaret, E., McLaughlin, S., Sunshine, J.M., Taylor, L.A., 2013. Development, importance, and effect of a ground truth correction for Moon Mineralogy Mapper reflectance data set. J. Geophys. Res., Planets 118, 369–381. doi:10.1002/jgre.20048.

Jolliff, B.L., Gillis, J.J., Haskin, L.A., Korotev, R.L., Wieczorek, M.A., 2000. Major lunar crustal terranes: Surface expressions and crust-mantle origins. J. Geophys. Res. 105, 4197–4216.

Klima, R.L., Pieters, C.M., Dyar, M.D., 2007. Spectroscopy of synthetic Mg-Fe pyroxenes I: Sping-allowed and spin-forbidden crystal field bands in the visible and near-infrared. Meteorit. Planet. Sci. 42, 235–253.

Klima, R.L., Pieters, C.M., Dyar, M.D., 2008. Characterization of the 1.2 μm M1 pyroxene band: Extracting cooling history from near-IR spectra of pyroxenes and pyroxene-dominated rocks. Meteorit. Planet. Sci. 43, 1591–1604.

Klima, R.L., Dyar, M.D., Pieters, C.M., 2011. Near-infrared spectra of clinopyroxenes: Effects of calcium content and crystal structure. Meteorit. Planet. Sci. 46, 379–395. doi:10.1111/j.1945-5100.2010.01158.x.

Korotev, R.L., 1998. Concentrations of radioactive elements in lunar materials. J. Geophys. Res. 103, 1691–1701.

Lawrence, D.J., Feldman, W.C., Barraclough, B.L., Binder, A.B., Elphic, R.C., Maurice, S., Thomsen, D.R., 1998. Global elemental maps of the Moon: The Lunar Prospector gamma-ray spectrometer. Science 281, 1484–1489. doi:10.1126/science.281.5382.1484.

Lawrence, S.J., Hawke, B.R., Gillis-Davis, J.J., Taylor, G.J., Lawrence, D.J., Cahill, J.T., Hagerty, J.J., Lucey, P.G., Smith, G.A., Keil, K., 2008. Composition and origin of the Dewar geochemical anomaly. J. Geophys. Res. 113, E02001, doi:10.1029/2007JE002904.

Li, L., Mustard, J.F., 2000. Compositional gradients across mare-highlands contacts: Importance and geological implication of lateral transport. J. Geophys. Res. 105, 20431–20450.

Loeffler, B.M., Burns, R.G., Tossell, J.A., 1975. Metal-to-metal charge transfer transitions: Interpretation of visible-region spectra of the moon and lunar materials. Proc. Lunar Planet. Sci. Conf. 6, 2663–2676.

Lucey, P.G., Taylor, G.J., Malaret, E., 1995. Abundance and distribution of iron on the Moon. Science 268, 1150–1153.

Lucey, P., Korotev, R.L., Gillis, J.J., Taylor, L.A., Lawrence, D., Campbell, B.A., Elphic, R., Feldman, W., Hood, L.L., Hunten, D., Mendillo, M., Noble, S., Papike, J.J., Reedy, R.C., Lawson, S., Prettyman, T., Gasnault, O., Maurice, S., 2006. Understanding the lunar surface and space-Moon interactions. Rev. Mineral. Geochem. 60, 83–219. doi:10.2138/rmg.2006.60.2.

Maxwell, T.A., Andre, C.G., 1981. The Balmer basin: Regional geology and geochemistry of an ancient lunar impact basin, Proceedings of the Lunar and Planetary Science Conference 12, 715–725.

McCord, T.B., Adams, J.B., 1973. Progress in remote optical analysis of lunar surface composition. The Moon 7, 453–474.

McCord, T.B., Taylor, L.A., Combe, J.-P., Kramer, G., Pieters, C.M., Sunshine, J.M., Clark, R.N., 2011. Sources and physical processes responsible for OH/H_2O in the lunar soil as revealed by the Moon Mineralogy Mapper (M^3). J. Geophys. Res. 116, E00G05. doi:10.1029/2010JE003711.

McEwen, A.S., Moore, J.M., Shoemaker, E.M., 1997. The Phanerozoic impact cratering rate: Evidence from the farside of the Moon. J. Geophys. Res. 107, 9231–9242.

Melosh, H.J., 1989. Impact Cratering: A Geologic Process. Oxford Univ. Press, Oxford, UK, 245 pp.

Mustard, J.F., Head, J.W., 1996. Buried stratigraphic relationships along the southwestern shores of Oceanus Procellarum: Impliations for early lunar volcanism. Journal of Geophysical Research 101, E02001, 18913–18925.

Nyquist, L.E., Shih, C.-Y., 1992. The isotopic record of lunar volcanism. Geochim. Cosmochim. Acta 56, 2213–2234.

Pieters, C.M., 1982. Copernicus crater central peak: Lunar mountain of unique composition. Science 215, 59–61.

Pieters, C.M., Rode, O., Basu, A., 1993. Optical effects of space weathering: The role of the finest fraction. J. Geophys. Res. 98, 20817–20824.

Pieters, C.M., Tompkins, S., 1999. Tsiolkovsky crater: A window into crustal processes on the lunar farside. J. Geophys. Res. 104, 21935–21949.

Pieters, C.M., Goswami, J.N., Clark, R.N., Annadurai, M., Boardman, J., Buratti, B., Combe, J.-P., Dyar, M.D., Green, R., Head, J.W., Hibbits, C., Hicks, M., Isaacson, P., Klima, R., Kramer, G., Kumar, S., Livo, E., Lundeen, S., Malaret, E., McCord, T., Mustard, J., Nettles, J., Petro, N., Runyon, C., Staid, M., Sunshine, J., Taylor, L.A., Tompkins, S., Varanasi, P., (2009) Character and spatial distribution of OH/ H_2O on the surface of the Moon as seen by M^3 on Chandrayaan-1, Science 326, 568–572. doi:10.1126/science.1178658.

Prissel, T.C., Parman, S.W., Head, J.W., Wilson, L., 2013. Mg-suite plutons: Implications for mantle-derived primitive magma source depths on the Moon. Lunar Planet. Sci. Conf. 44, abstract 3041.

Riner, M.A., Lucey, P.G., Desch, S.J., McCubbin, F.M., 2009. Nature of opaque components on Mercury: Insights into a Mercurian magma ocean. Geophys. Res. Lett. 36, L02201. doi:10.1029/2008GL036128.

Ryder, G., 1987. Petrologic evidence for nonlinear cooling rates and a volcanic origin for Apollo 15 KREEP basalts. J. Geophys. Res. 92, E331–E339.

Ryder, G., Spudis, P., 1980. Volcanic rocks in the lunar highlands. Proc. Conf. Lunar Highlands Crust, 353–375.

Schultz, P.H., Spudis, P.D., 1979. Evidence for ancient mare volcanism. Proceedings of the Lunar and Planetary Science Conference 10th, 2899–2918.

Schultz, P.H., Spudis, P.D., 1983. The beginning and end of lunar mare volcanism. Nature 302, 233–236.

Shoemaker, E.M., Hait, M.H., Swann, G.A., Schleicher, D.L., Schaber, G.G., Sutton, R.L., Dahlem, D.H., Goddard, E.N., Waters, A.C., 1970. Origin of the lunar regolith at Tranquillity Base. Proc. Apollo 11 Lunar Sci. Conf. 3: 2399–2412.

Smith, J.V., Anderson, A.T., Newton, R.C., Olsen, E.J., Wyllie, P.J., Crewe, A.V., Isaacson, M.S., Johnson, D., 1970. Petrologic history of the moon inferred from petrography, mineralogy, and petrogenesis of Apollo 11 rocks. Proc. Apollo 11 Lunar Sci. Conf., 897–925.

Stöffler, D., Ryder, G., Ivanov, B.A., Artemieva, N.A., Cintala, M.J., Grieve, R.A.F., 2006. Cratering history and lunar chronology. Rev. Min. Geochem. 60, 519–596.

Sunshine, J.M., Pieters, C.M., Pratt, S.F., 1990. Deconvolution of mineral absorption bands: An improved approach. J. Geophys. Res. 95, 6955–6966.

Sunshine, J.M., Pieters, C.M., 1993. Estimating model abundances from the spectra of natural and laboratory pyroxene mixtures using the Modified Gaussian Model. J. Geophys. Res. 98, 9075–9087.

Taylor, L.A., Shervais, J.W., Hunter, R.H., Shih, C.-Y., Bansal, B.M., Wooden, J., Nyquist, L.E., Laul, L.C., 1983. Pre-4.2 AE mare-basalt volcanism in the lunar highlands. Earth Planet. Sci. Lett. 66, 33–47.

Terada, K., Anand, M., Sokol, A.K., Bischoff, A., Sano, Y., 2007. Cryptomare magmatism 4.35 Gyr ago recorded in lunar meteorite Kalahari 009. Nature 450, 849–852. doi:10.1038/nature06356.

Tompkins, S., Pieters, C.M., 1999. Mineralogy of the lunar crust: Results from Clementine. Met. Planet. Sci. 34, 25–41.

Ullrich, G.W., Roddy, D.J., Simmons, G., 1977. Numerical simulation of a 20-ton TNT detonation on the Earth's surface, in Impact and Explosion Cratering, D.J. Roddy, R.O. Pepin, R.B. Merrill, (Eds.), Pergamon Press, New York, p. 959.

Warren, P.H., Wasson, J.T., 1977. Pristine nonmare rocks and the nature of the lunar crust. Proc. Lunar Planet. Sci. Conf. 8, 2215–2235.

Whitten, J.L., Head, J.W., 2014. Lunar cryptomaria, part I: Physical characteristics, distribution, and implications for ancient volcanism. Icarus, in preparation.

Wieczorek, M.A., Jolliff, B.L., Khan, A., Pritchard, M.E., Weiss, B.P., Williams, J.G., Hood, L.L., Righter, K., Neal, C.R., Shearer, C.K., McCallum, I.S., Tompkins, S., Hawke, B.R., Peterson, C., Gillis, J.J., Bussey, B., 2006. The constitution and structure of the lunar interior. Rev. Mineral. Geochem. 60, 221–364. doi:10.2138/rmg.2006.60.3.

Wieczorek, M.A., Neumann, G.A., Nimmo, F., Kiefer, W.S., Talor, G.J., Melosh, H.J., Phillips, R.J., Solomon, S.C., Andrews-Hanna, J.C., Asmar, S.W., Konopliv, A.S., Lemoine, F.G., Smith, D.E., Watkins, M.M., Williams, J.G., Zuber, M.T., 2013. The crust of the Moon as seen by GRAIL. Science 339, 671–675. doi:10.1126/science.1231530.

Wilhelms, D.E., 1987. The geologic history of the Moon. US Geological Survey Professional Paper 1348.

Wilhelms, D.E., McCauley, J.F., 1971. Geologic map of the near side of the Moon. US Geo. Survey Map I-703, Reston, VA.

Wood, J.A., Dickey Jr., J.S., Marvin, U.B., Powell, B.N., 1970. Lunar anorthosites and a geophysical model of the moon. Proc. Apollo 11 Lunar Sci. Conf., 965–988.

Yamamoto, S., Nakamura, R., Matsunaga, T., Ogawa, Y., Ishihara, Y., Morota T., Hirata, N., Ohtake, M., Hiroi, T., Yokota, Y., Haruyama, J., 2010. Possible mantle origin of olivine around lunar impact basins detected by SELENE. Nature Geoscience 3, 533–536. doi:10.1038/NGEO897.

Table 1. M^3 cryptomare spectra calculated band centers and RMS values.

Cryptomare Deposit	Pond ID	# of spectra	OP2c1 Band Center 1 μm	OP2c1 Band Center 2 μm	OP2c1 Band Center RMS	OP	# of spectra	Band Center 1 μm	Band Center 2 μm	Band Center RMS
Australe	0	2	963	2160	0.011	-	-	-	-	-
Australe	1	1	956	2180	0.013	-	-	-	-	-
Australe	2	3	974	2177	0.010	-	-	-	-	-
Australe	3	1	972	2172	0.010	-	-	-	-	-
Australe	4	2	965	2140	0.011	-	-	-	-	-
Australe	5	1	964	2159	0.012	-	-	-	-	-
Australe	6	2	966	2120	0.013	-	-	-	-	-
Australe	7	2	968	2159	0.008	-	-	-	-	-
Australe	8	3	981	2200	0.009	-	-	-	-	-
Australe	9	1	980	2201	0.010	-	-	-	-	-
Australe	10	1	974	2163	0.011	-	-	-	-	-
Australe	11	1	977	2219	0.011	-	-	-	-	-
Australe	12	1	967	2147	0.013	-	-	-	-	-
Australe	13	3	955	2143	0.014	-	-	-	-	-
Australe	15	2	963	2163	0.011	2c2	2	970	2163	0.011
Australe	16	1	965	2141	0.017	-	-	-	-	-
Australe	17	1	958	2170	0.013	-	-	-	-	-
Australe	18	1	966	2167	0.011	-	-	-	-	-
Australe	19	1	968	2177	0.014	-	-	-	-	-
Australe	20	2	964	2156	0.012	-	-	-	-	-
Australe	21	1	968	2182	0.012	-	-	-	-	-
Australe	22	1	964	2134	0.017	-	-	-	-	-
Australe	23	1	962	2171	0.011	-	-	-	-	-
Australe	24	2	957	2142	0.015	-	-	-	-	-
Australe	25	2	964	2178	0.010	-	-	-	-	-
Australe	27	2	970	2156	0.009	-	-	-	-	-
Australe	28	1	965	2161	0.010	-	-	-	-	-
Australe	29	2	961	2159	0.011	-	-	-	-	-
Australe	31	2	962	2146	0.009	-	-	-	-	-

Australe	32	1	959	2186	0.012	2c2	1	962	2170	0.010
Australe	33	2	967	2142	0.012	2c2	2	973	2106	0.009
Australe	34	2	974	2149	0.009	-	-	-	-	-
Australe	35	-	-	-	-	2c2	2	970	2123	0.010
Australe	36	-	-	-	-	2c2	1	964	2133	0.012
Australe	37	-	-	-	-	2c2	2	967	2096	0.008
Australe	38	-	-	-	-	2c2	2	975	2123	0.009
Australe	39	-	-	-	-	2c2	1	984	2162	0.010
Balmer	0, 1, 2	4	988	2178	0.005	-	-	-	-	-
Balmer	3	4	967	2146	0.007	-	-	-	-	-
Balmer	4	3	967	2161	0.006	-	-	-	-	-
Balmer	5	8	972	2138	0.008	-	-	-	-	-
Dewar	1	2	989	2205	0.006	2c2	2	988	2228	0.007
Frigoris	0	3	965	2143	0.010	1b	4	962	2161	0.008
Frigoris	1	5	959	2161	0.011	1b	5	964	2142	0.008
Frigoris	2	3	971	2167	0.008	1b	4	964	2196	0.010
Frigoris	3	2	973	2193	0.010	1b	1	966	2235	0.010
Frigoris	5	2	973	2212	0.011	-	-	-	-	-
Hercules	0	4	959	2098	0.008	-	-	-	-	-
Hercules	1	4	967	2157	0.009	-	-	-	-	-
Hercules	2	4	967	2148	0.008	-	-	-	-	-
Hercules	3	4	968	2133	0.008	-	-	-	-	-
Hercules	4	5	968	2144	0.008	-	-	-	-	-
Humboldtianum	0	1	972	2115	0.007	-	-	-	-	-
Humboldtianum	1	3	974	2144	0.007	-	-	-	-	-
Humboldtianum	2	5	972	2147	0.008	-	-	-	-	-
Humboldtianum	3	6	971	2156	0.009	-	-	-	-	-
Humboldtianum	4	4	979	2179	0.009	-	-	-	-	-
Humboldtianum	5	2	977	2150	0.010	-	-	-	-	-
Humboldtianum	6	3	969	2158	0.008	-	-	-	-	-
Humboldtianum	7	3	966	2116	0.011	-	-	-	-	-
Humboldtianum	8	2	962	2148	0.010	-	-	-	-	-
Humboldtianum	9	4	966	2159	0.011	-	-	-	-	-

Humboldtianum	10	2	957	2106	0.010	-	-	-	-	-
Humboldtianum	11	2	957	2059	0.009	-	-	-	-	-
Langemak	0	2	976	2167	0.007	2c2	4	975	2162	0.006
Langemak	1	-	-	-	-	2c2	2	984	2165	0.006
Langemak	0	2	964	2110	0.007	2c2	3	968	2127	0.006
Lomonosov-Fleming	1	2	982	2185	0.007	-	-	-	-	-
Lomonosov-Fleming	2	4	984	2198	0.009	2c2	9	980	2156	0.007
Lomonosov-Fleming	3	-	-	-	-	2c2	2	985	2184	0.008
Lomonosov-Fleming	4	-	-	-	-	2c2	2	990	2192	0.007
Marginis	1	1	982	2172	0.007	-	-	-	-	-
Marginis	2	1	986	2168	0.008	-	-	-	-	-
Marginis	6	3	980	2160	0.008	-	-	-	-	-
Marginis	7	3	982	2175	0.009	-	-	-	-	-
Marginis	10	2	985	2191	0.008	-	-	-	-	-
Marginis	8	2	991	2186	0.007	-	-	-	-	-
Marginis	9	3	988	2216	0.006	-	-	-	-	-
Mendel-Rydberg	0	3	980	2179	0.005	1b	3	977	2212	0.010
Mendel-Rydberg	1	4	978	2171	0.010	1b	3	981	2206	0.011
Mendel-Rydberg	2	5	979	2178	0.009	1b	5	972	2207	0.007
Milne	0	-	-	-	-	2c2	5	987	2211	0.006
Milne	1	-	-	-	-	2c2	4	981	2190	0.006
Schiller-Schickard	0	4	975	2175	0.009	1b	4	961	2196	0.010
Schiller-Schickard	1	4	977	2190	0.008	1b	4	977	2216	0.012
Schiller-Schickard	2	-	-	-	-	1b	4	972	2196	0.009
Schiller-Schickard	3	-	-	-	-	1b	3	960	2077	0.007
Schiller-Schickard	4	-	-	-	-	1b	4	975	2194	0.008
Schiller-Schickard	5	4	983	2207	0.008	1b	4	970	2212	0.006
Schiller-Schickard	6	3	978	2160	0.007	1b	3	955	2144	0.006
Schiller-Schickard	7	4	972	2156	0.007	1b	3	982	2190	0.009
Schiller-Schickard	8	3	968	2151	0.008	1b	3	969	2192	0.010
Schiller-Schickard	9	3	971	2092	0.009	1b	4	969	2210	0.010
Schiller-Schickard	10	7	974	2171	0.009	1b	8	970	2184	0.010
Schiller-Schickard	11	7	971	2157	0.009	1b	7	969	2204	0.010

Schiller-Schickard	12	3	966	2153	0.008	-	-	-	-	-
Schiller-Schickard	13	3	968	2169	0.008	1b	4	958	2123	0.009
Smythii	1	2	986	2167	0.008	-	-	-	-	-
Smythii	2	4	982	2170	0.007	-	-	-	-	-
Smythii	3	2	989	2171	0.007	-	-	-	-	-
Smythii	4	2	985	2171	0.008	-	-	-	-	-
Smythii	5	1	989	2148	0.013	-	-	-	-	-
Smythii	7	2	980	2156	0.007	-	-	-	-	-
Smythii	8	1	982	2166	0.007	-	-	-	-	-
Smythii	9	4	977	2168	0.007	-	-	-	-	-
Smythii	10	5	980	2156	0.008	-	-	-	-	-
Smythii	13	1	983	2165	0.008	-	-	-	-	-
Smythii	14	3	979	2164	0.006	-	-	-	-	-
South Pole-Aitken	0	3	977	2142	0.012	-	-	-	-	-
South Pole-Aitken	1	2	970	2162	0.012	-	-	-	-	-
South Pole-Aitken	2	2	974	2190	0.010	-	-	-	-	-
South Pole-Aitken	3	1	978	2143	0.014	-	-	-	-	-
South Pole-Aitken	4	2	971	2152	0.011	-	-	-	-	-
South Pole-Aitken	5	1	965	2169	0.009	-	-	-	-	-
South Pole-Aitken	6	2	969	2159	0.011	-	-	-	-	-
South Pole-Aitken	7	3	973	2151	0.010	-	-	-	-	-
South Pole-Aitken	8	2	969	2170	0.011	-	-	-	-	-
South Pole-Aitken	9	3	964	2148	0.009	-	-	-	-	-
South Pole-Aitken	10	3	967	2154	0.011	-	-	-	-	-
South Pole-Aitken	11	4	973	2182	0.008	-	-	-	-	-
South Pole-Aitken	12	1	968	2167	0.011	-	-	-	-	-
South Pole-Aitken	13	4	966	2191	0.009	-	-	-	-	-
Taruntius	0	2	989	2208	0.008	1b	2	976	2206	0.009
Taruntius	1	3	990	2196	0.007	1b	3	973	2221	0.005
Taruntius	2	3	985	2184	0.007	1b	2	976	2209	0.007
Taruntius	3	3	981	2167	0.008	1b	3	974	2198	0.006
Taruntius	4	2	982	2181	0.007	1b	2	973	2213	0.006
Taruntius	5	-	-	-	-	1b	4	970	2212	0.006

Taruntius	6	-	-	-	-	1b	3	955	2144	0.009
Taruntius	8	-	-	-	-	1b	3	969	2192	0.010
Taruntius	9	-	-	-	-	1b	4	969	2210	0.010
Taruntius	10	-	-	-	-	1b	8	970	2184	0.010
Taruntius	11	-	-	-	-	1b	7	969	2204	0.010
Taruntius	13	-	-	-	-	1b	4	958	2123	0.009
Lacus Solitudinis	5	2	985	2198	0.007	-	-	-	-	-
Lacus Solitudinis	2	2	987	2200	0.006	-	-	-	-	-
Lacus Solitudinis	3	3	985	2191	0.007	-	-	-	-	-
Lacus Solitudinis	4	2	985	2176	0.007	-	-	-	-	-
Lacus Solitudinis	8	4	980	2194	0.007	-	-	-	-	-
Lacus Solitudinis	9	2	989	2202	0.009	-	-	-	-	-
West Humorum	2	1	986	2197	0.009	-	-	-	-	-
West Humorum	3	2	980	2175	0.007	1b	2	972	2217	0.007
West Humorum	5	3	983	2190	0.009	1b	3	975	2205	0.008
West Humorum	11	3	987	2176	0.006	1b	3	981	2224	0.007
West Humorum	6	2	974	2163	0.008	-	-	-	-	-
West Humorum	9	1	989	2216	0.010	-	-	-	-	-
West Humorum	12	4	969	2085	0.006	-	-	-	-	-
West Humorum	4	-	-	-	-	1b	1	984	2226	0.006
West Procellarum	12	3	993	2210	0.010	1b	3	983	2230	0.009
West Procellarum	5, 13, 20	4	979	2137	0.008	1b	4	969	2162	0.009
West Procellarum	21	1	976	2152	0.008	-	-	-	-	-
West Procellarum	23	2	987	2184	0.009	1b	5	978	2206	0.008
West Procellarum	24	2	992	2189	0.009	1b	3	988	2198	0.008
West Procellarum	25	2	998	2194	0.009	1b	2	988	2204	0.008
West Procellarum	26	3	985	2143	0.009	1b	2	976	2192	0.009
West Procellarum	28	1	983	2186	0.008	1b	1	981	2196	0.008
West Procellarum	30	3	988	2199	0.009	1b	3	981	2212	0.009
West Procellarum	31	1	991	2212	0.007	1b	2	975	2210	0.007
West Procellarum	34	2	987	2184	0.008	1b	2	987	2207	0.006
West Procellarum	35	1	982	2158	0.008	1b	2	980	2200	0.007
West Procellarum	36	1	988	2157	0.009	1b	2	977	2171	0.008

West Procellarum	37	2	951	2107	0.007	1b	2	974	2186	0.008
West Procellarum	22	-	-	-	-	1b	1	982	2196	0.007
West Procellarum	27	-	-	-	-	1b	1	985	2216	0.007

Table 2. M^3 mare spectra calculated band centers and RMS values.

Mare Deposit	Pond ID	OP2c1 Band Center				OP	Band Center			
		# of spectra	1 μm	2 μm	RMS		# of spectra	1 μm	2 μm	RMS
Australe	0	3	974	2168	0.010	-	-	-	-	-
Australe	1	4	969	2178	0.011	-	-	-	-	-
Australe	2	3	971	2164	0.010	-	-	-	-	-
Australe	3	4	969	2176	0.009	-	-	-	-	-
Australe	4	3	963	2167	0.015	-	-	-	-	-
Australe	6	3	976	2185	0.010	-	-	-	-	-
Australe	7	2	972	2206	0.017	-	-	-	-	-
Australe	8	2	975	2207	0.014	-	-	-	-	-
Australe	10	1	958	2174	0.010	-	-	-	-	-
Australe	11	1	972	2139	0.015	-	-	-	-	-
Australe	12	1	963	2179	0.014	-	-	-	-	-
Australe	14	2	971	2173	0.013	-	-	-	-	-
Australe	15	2	971	2152	0.011	-	-	-	-	-
Australe	16	4	967	2166	0.010	-	-	-	-	-
Australe	17	1	965	2196	0.011	-	-	-	-	-
Australe	18	2	965	2159	0.012	-	-	-	-	-
Australe	19	2	966	2144	0.013	-	-	-	-	-
Australe	23	3	968	2168	0.013	-	-	-	-	-
Australe	24	2	955	2145	0.013	-	-	-	-	-
Australe	25	2	957	2180	0.014	-	-	-	-	-
Australe	26	1	953	2147	0.019	-	-	-	-	-
Australe	27	4	969	2163	0.012	-	-	-	-	-
Australe	28	1	981	2214	0.012	-	-	-	-	-
Australe	29	1	969	2179	0.011	-	-	-	-	-
Australe	30	3	975	2186	0.009	-	-	-	-	-
Australe	31	3	974	2188	0.015	-	-	-	-	-
Australe	32	2	959	2140	0.018	-	-	-	-	-
Australe	33	3	968	2178	0.013	-	-	-	-	-
Australe	34	3	965	2162	0.014	-	-	-	-	-

Australe	38	2	939	2211	0.018	-	-	-	-	-
Australe	36	2	963	2174	0.016	-	-	-	-	-
Australe	35	2	961	2167	0.015	-	-	-	-	-
Australe	41	3	973	2170	0.018	-	-	-	-	-
Australe	42	2	975	2181	0.011	2c2	2	979	2172	0.010
Australe	46	2	970	2186	0.012	2c2	3	968	2164	0.009
Australe	47	3	967	2158	0.011	-	-	-	-	-
Australe	48	4	973	2181	0.012	-	-	-	-	-
Australe	49	3	964	2179	0.012	-	-	-	-	-
Australe	50	1	954	2143	0.014	-	-	-	-	-
Australe	51	2	967	2171	0.014	-	-	-	-	-
Australe	52	2	969	2231	0.014	-	-	-	-	-
Australe	54	4	961	2178	0.013	2c2	3	969	2147	0.009
Australe	55	3	965	2169	0.012	-		-	-	-
Australe	56	1	965	2161	0.015	-		-	-	-
Australe	57	1	987	2144	0.015	2c2	1	960	2156	0.013
Australe	58	1	977	2166	0.012	2c2	1	971	2127	0.012
Australe	59	1	959	2223	0.017	2c2	1	962	2112	0.011
Australe	66	3	973	2170	0.009	-	-	-	-	-
Australe	67	3	970	2162	0.010	2c2	3	973	2169	0.008
Australe	68	2	973	2152	0.011	2c2	2	980	2144	0.009
Australe	69	3	975	2165	0.008	-	-	-	-	-
Australe	70	1	978	2185	0.011	-	-	-	-	-
Australe	72	4	972	2160	0.010	-	-	-	-	-
Australe	74	4	970	2179	0.010	-	-	-	-	-
Australe	75	1	959	2162	0.012	-	-	-	-	-
Australe	76	3	971	2157	0.011	-	-	-	-	-
Australe	77	7	972	2161	0.012	-	-	-	-	-
Australe	78	1	972	2148	0.010	-	-	-	-	-
Australe	79	3	971	2164	0.010	-	-	-	-	-
Australe	83	1	982	2129	0.011	-	-	-	-	-
Australe	84	1	975	2157	0.011	-	-	-	-	-
Australe	85	1	978	2189	0.010	-	-	-	-	-

Australe	87	2	963	2155	0.016	-	-	-	-	-
Australe	44	-	-	-	-	2c2	2	974	2156	0.008
Australe	53	-	-	-	-	2c2	2	970	2140	0.012
Australe	61	-	-	-	-	2c2	1	969	2157	0.009
Balmer	0	4	985	2181	0.008	-	-	-	-	-
Balmer	1, 2, 14	7	977	2170	0.009	-	-	-	-	-
Balmer	3	3	977	2143	0.007	-	-	-	-	-
Balmer	4	7	971	2164	0.007	-	-	-	-	-
Balmer	5	6	978	2160	0.007	-	-	-	-	-
Balmer	6	1	980	2129	0.010	-	-	-	-	-
Balmer	8	2	976	2140	0.008	-	-	-	-	-
Balmer	7	1	986	2171	0.006	-	-	-	-	-
Balmer	12	3	976	2154	0.008	-	-	-	-	-
Balmer	13	6	990	2182	0.008	-	-	-	-	-
Frigoris	A	5	973	2187	0.013	1b	5	973	2195	0.012
Frigoris	B	6	969	2177	0.011	1b	6	968	2182	0.014
Hercules	4	4	967	2169	0.009	-	-	-	-	-
Hercules	1	4	967	2144	0.009	-	-	-	-	-
Hercules	0	3	967	2141	0.009	-	-	-	-	-
Hercules	3	3	967	2122	0.009	-	-	-	-	-
Hercules	A	5	967	2134	0.009	-	-	-	-	-
Hercules	B	3	971	2150	0.008	-	-	-	-	-
Humboldtianum	0	7	973	2157	0.010	-	-	-	-	-
Humboldtianum	1	3	968	2139	0.009	-	-	-	-	-
Humboldtianum	3	2	966	2143	0.009	-	-	-	-	-
Humboldtianum	2	5	967	2138	0.008	-	-	-	-	-
Humboldtianum	4	8	967	2157	0.008	-	-	-	-	-
Humboldtianum	5	5	967	2166	0.010	-	-	-	-	-
Humboldtianum	6	2	978	2167	0.008	-	-	-	-	-
Langemak	0	2	989	2177	0.009	-	-	-	-	-
Lomonosov-Fleming	1	5	989	2203	0.006	-	-	-	-	-
Lomonosov-Fleming	0	5	986	2219	0.009	-	-	-	-	-
Lomonosov-Fleming	3	2	987	2210	0.008	-	-	-	-	-

Lomonosov-Fleming	5	4	985	2195	0.008	-	-	-	-	-
Lomonosov-Fleming	4	3	984	2188	0.008	-	-	-	-	-
Marginis	0	2	988	2156	0.008	-	-	-	-	-
Marginis	1	1	993	2194	0.006	-	-	-	-	-
Marginis	5	4	981	2165	0.007	-	-	-	-	-
Marginis	2	5	975	2145	0.009	-	-	-	-	-
Marginis	3	4	980	2147	0.009	-	-	-	-	-
Marginis	4	4	985	2198	0.009	-	-	-	-	-
Marginis	6	5	979	2161	0.010	-	-	-	-	-
Marginis	7	1	988	2157	0.009	-	-	-	-	-
Marginis	8	2	984	2169	0.007	-	-	-	-	-
Marginis	9	1	982	2139	0.008	-	-	-	-	-
Marginis	11	3	987	2172	0.007	-	-	-	-	-
Marginis	13	3	983	2163	0.006	-	-	-	-	-
Marginis	14	1	981	2178	0.007	-	-	-	-	-
Marginis	15	8	978	2169	0.010	-	-	-	-	-
Marginis	16	2	983	2180	0.006	-	-	-	-	-
Marginis	17	1	980	2156	0.008	-	-	-	-	-
Marginis	18	2	977	2141	0.008	-	-	-	-	-
Marginis	21	2	983	2157	0.007	-	-	-	-	-
Marginis	22	3	985	2169	0.007	-	-	-	-	-
Marginis	23	2	978	2183	0.008	-	-	-	-	-
Mendel-Rydberg	0	3	980	2163	0.008	1b	5	990	2215	0.009
Mendel-Rydberg	1	2	966	2205	0.009	1b	2	1002	2184	0.010
Mendel-Rydberg	2	6	979	2199	0.009	1b	6	980	2221	0.009
Mendel-Rydberg	3	5	983	2186	0.008	1b	5	981	2201	0.010
Mendel-Rydberg	4	1	982	2184	0.008	1b	1	992	2229	0.008
Mendel-Rydberg	5	4	982	2168	0.010	1b	4	973	2196	0.010
Schiller-Schickard	A	5	982	2181	0.007	1b	5	976	2187	0.013
Schiller-Schickard	B	5	987	2246	0.007	1b	6	979	2290	0.007
Schiller-Schickard	C	5	964	2078	0.009	1b	8	963	2100	0.011
Schiller-Schickard	D	4	975	2187	0.008	1b	6	973	2209	0.010
Schiller-Schickard	E	6	968	2115	0.009	1b	8	962	2129	0.009

Schiller-Schickard	F	5	982	2216	0.008	-	-	-	-	-
Schiller-Schickard	G	5	979	2238	0.009	-	-	-	-	-
Schiller-Schickard	H	6	981	2219	0.009	1b	7	978	2255	0.007
Schiller-Schickard	I	4	977	2146	0.007	1b	6	971	2166	0.008
Schiller-Schickard	J	6	975	2159	0.008	1b	6	967	2147	0.013
Schiller-Schickard	K	6	981	2192	0.008	-	-	-	-	-
Smythii	1	4	979	2147	0.012	-	-	-	-	-
Smythii	12, 13	1	976	2149	0.008	-	-	-	-	-
Smythii	15	4	980	2148	0.011	-	-	-	-	-
Smythii	18	2	983	2140	0.008	-	-	-	-	-
Smythii	20	5	982	2169	0.011	-	-	-	-	-
Smythii	23	3	981	2149	0.010	-	-	-	-	-
Smythii	24	4	988	2163	0.010	-	-	-	-	-
Smythii	26	6	988	2166	0.008	-	-	-	-	-
Smythii	27	8	985	2165	0.009	-	-	-	-	-
Smythii	28	1	986	2179	0.009	-	-	-	-	-
Smythii	30	2	985	2154	0.008	-	-	-	-	-
Smythii	35	2	976	2142	0.008	-	-	-	-	-
Smythii	36	3	985	2153	0.008	-	-	-	-	-
Smythii	37	4	976	2152	0.008	-	-	-	-	-
Smythii	38	4	979	2134	0.007	-	-	-	-	-
Smythii	40	3	975	2140	0.008	-	-	-	-	-
Smythii	41	1	983	2204	0.008	-	-	-	-	-
Smythii	42	2	980	2140	0.009	-	-	-	-	-
South Pole-Aitken	0	5	980	2183	0.010	-	-	-	-	-
South Pole-Aitken	4	4	974	2136	0.011	-	-	-	-	-
South Pole-Aitken	5	2	981	2175	0.012	-	-	-	-	-
South Pole-Aitken	6	2	976	2166	0.010	-	-	-	-	-
South Pole-Aitken	8	1	968	2124	0.015	-	-	-	-	-
South Pole-Aitken	9	3	976	2141	0.012	-	-	-	-	-
South Pole-Aitken	10	2	975	2167	0.010	-	-	-	-	-
South Pole-Aitken	11	3	974	2165	0.010	-	-	-	-	-
South Pole-Aitken	12	2	961	2155	0.010	-	-	-	-	-

South Pole-Aitken	13	2	976	2182	0.012	-	-	-	-	-
South Pole-Aitken	14	2	977	2156	0.011	-	-	-	-	-
South Pole-Aitken	15	3	968	2172	0.011	-	-	-	-	-
South Pole-Aitken	16	2	968	2148	0.012	-	-	-	-	-
South Pole-Aitken	17	3	976	2153	0.009	-	-	-	-	-
South Pole-Aitken	18	2	977	2174	0.009	-	-	-	-	-
South Pole-Aitken	19	3	975	2163	0.012	-	-	-	-	-
South Pole-Aitken	20	3	973	2144	0.010	-	-	-	-	-
South Pole-Aitken	21	2	982	2181	0.012	-	-	-	-	-
South Pole-Aitken	22	2	974	2173	0.010	-	-	-	-	-
South Pole-Aitken	23	3	977	2171	0.010	-	-	-	-	-
South Pole-Aitken	24	3	970	2167	0.009	-	-	-	-	-
South Pole-Aitken	25	2	959	2151	0.009	-	-	-	-	-
South Pole-Aitken	26	4	973	2138	0.011	-	-	-	-	-
South Pole-Aitken	28	2	978	2182	0.011	-	-	-	-	-
South Pole-Aitken	29	4	972	2131	0.014	-	-	-	-	-
South Pole-Aitken	30	3	968	2172	0.014	-	-	-	-	-
South Pole-Aitken	31	2	969	2179	0.012	-	-	-	-	-
Taruntius	0	8	981	2175	0.009	1b	8	970	2180	0.008
Taruntius	1	1	1001	2219	0.008	1b	1	977	2261	0.008
Lacus Solitudinis	0	5	979	2169	0.010	-	-	-	-	-
Lacus Solitudinis	57	4	985	2181	0.008	-	-	-	-	-
Lacus Solitudinis	59	5	978	2188	0.010	-	-	-	-	-
Lacus Solitudinis	56	2	974	2170	0.009	-	-	-	-	-
Lacus Solitudinis	36	3	976	2185	0.008	-	-	-	-	-
Lacus Solitudinis	16	3	973	2137	0.010	-	-	-	-	-
Lacus Solitudinis	12	2	977	2148	0.011	-	-	-	-	-
Lacus Solitudinis	14	2	983	2167	0.008	-	-	-	-	-
West Humorum	0	1	998	2193	0.007	1b	1	985	2223	0.007
West Humorum	2	1	984	2217	0.007	1b	1	986	2232	0.007
West Humorum	3	3	987	2188	0.011	1b	3	980	2204	0.009
West Humorum	4	1	996	2206	0.009	1b	1	988	2224	0.006
West Humorum	5	2	992	2195	0.008	1b	2	990	2208	0.007

West Humorum	6	3	991	2186	0.008	1b	3	984	2202	0.008
West Humorum	7	2	989	2166	0.010	1b	2	979	2183	0.009
West Humorum	17	1	998	2185	0.008	1b	1	977	2207	0.008
West Humorum	9	-	-	-	-	1b	1	1004	2222	0.009
West Humorum	10	2	999	2205	0.007	1b	1	986	2238	0.007
West Humorum	14	2	996	2189	0.008	1b	2	986	2221	0.008
West Humorum	15	1	995	2204	0.010	1b	1	988	2219	0.008
West Humorum	16	2	993	2213	0.007	1b	2	981	2228	0.007
West Humorum	18	1	989	2190	0.010	1b	1	988	2204	0.009
West Humorum	19	3	991	2196	0.009	1b	3	983	2210	0.008
West Humorum	21	1	988	2171	0.010	1b	1	987	2188	0.011
West Humorum	22	3	971	2115	0.008	1b	3	964	2144	0.010
West Humorum	25	3	976	2127	0.007	1b	3	961	2157	0.009
West Humorum	26	1	985	2153	0.007	1b	1	976	2166	0.010
West Humorum	27	1	970	2109	0.009	1b	1	963	2106	0.010
West Humorum	28	2	988	2277	0.007	1b	2	966	2310	0.007
West Humorum	29	-	-	-	-	1b	1	991	2291	0.008
West Humorum	30	3	985	2255	0.008	1b	3	977	2280	0.008
West Humorum	32	1	986	2207	0.007	1b	1	977	2266	0.008
West Humorum	33	3	987	2217	0.007	1b	3	978	2241	0.007
West Humorum	37	-	-	-	-	1b	4	975	2232	0.008
West Humorum	38	-	-	-	-	1b	1	978	2220	0.010
West Humorum	40	1	972	2205	0.007	1b	1	970	2220	0.008
West Humorum	41	2	990	2206	0.009	1b	2	981	2228	0.007
West Humorum	48	3	981	2180	0.008	1b	3	971	2200	0.009
West Humorum	31	3	991	2181	0.009	-	-	-	-	-
West Humorum	34	3	984	2173	0.009	-	-	-	-	-
West Humorum	35	1	990	2185	0.011	-	-	-	-	-
West Humorum	36	1	1000	2253	0.008	-	-	-	-	-
West Humorum	42	2	995	2223	0.014	-	-	-	-	-
West Humorum	43	2	990	2176	0.011	-	-	-	-	-
West Humorum	44	1	955	2054	0.010	-	-	-	-	-
West Humorum	45	3	990	2177	0.009	-	-	-	-	-

West Humorum	46	3	983	2149	0.012	-	-	-	-	-
West Humorum	47	1	987	2165	0.011	-	-	-	-	-
West Humorum	49	1	983	2116	0.013	-	-	-	-	-
West Procellarum	0	1	1003	2221	0.009	1b	1	1012	2254	0.010
West Procellarum	6	2	994	2183	0.010	-	-	-	-	-
West Procellarum	7	2	989	2196	0.010	1b	2	977	2191	0.008
West Procellarum	9	1	981	2191	0.007	1b	1	970	2189	0.009
West Procellarum	10	5	990	2208	0.011	1b	5	983	2215	0.010
West Procellarum	11	2	993	2199	0.008	1b	2	985	2210	0.007
West Procellarum	13	2	985	2149	0.010	1b	2	974	2157	0.009
West Procellarum	14	-	-	-	-	1b	3	959	2145	0.008
West Procellarum	16	-	-	-	-	1b	1	986	2203	0.008
West Procellarum	15	-	-	-	-	1b	1	985	2217	0.007
West Procellarum	17	-	-	-	-	1b	3	976	2184	0.007
West Procellarum	18	5	987	2199	0.011	1b	5	982	2204	0.011
West Procellarum	20	3	994	2192	0.012	1b	3	978	2186	0.009
West Procellarum	21	-	-	-	-	1b	1	995	2182	0.009

Table 3. Average difference in calculated 1.0, 1.2, and 2.0 μm absorption features between the different M^3 optical periods (1b verses 2c1; 2c2 verses 2c1).

Optical Period		Band center difference (nm)
1.0 μm	1b, 2c1	8.1
	2c2, 2c1	3.5
	Average	5.8
	Std. Deviation	4.0
1.2 μm	1b, 2c1	1.9
	2c2, 2c1	1.8
	Average	1.9
	Std. Deviation	0.8
2.0 μm	1b, 2c1	24.3
	2c2, 2c1	26.3
	Average	25.3
	Std. Deviation	9.8

Figure Captions

Figure 1. Moon Mineralogy Mapper (M^3) data of mapped cryptomare and the dark-halo craters used to identify the mafic deposits. (a) Color composite global OP2c1 M^3 dataset (R: 1 μm integrated band depth, G: 2 μm integrated band depth, B: 1489 nm reflectance). Pyroxene-rich deposits appear yellow and orange, while anorthosite-rich material is blue. The locations of cryptomare deposits are indicated by white polygons. Dashed white box denotes the location of (b). Lunar Orbiter Laser Altimeter 128 pixel/° hillshade map overlain by M^3 data. (b) Detailed view of the Balmer cryptomare (white polygons), showing the location of individual dark-halo craters sampled to determine the deposit mineralogy. Dashed white box shows the location of parts (c) and (d). (c) 4.5 km diameter dark-halo crater. Low-albedo ejected material is excavated from below a high-albedo surface material. M^3 1489 nm reflectance image. (d) M^3 color composite (R: 1 μm integrated band depth, G: 2 μm integrated band depth, B: 1489 nm reflectance) of the same dark-halo crater showing that the crater walls and ejecta deposit are composed of pyroxene-rich materials.

Figure 2. Automated continuum removal for M^3 spectra. (a) Original OP2c1 M^3 spectra collected from dark-halo craters in the Balmer cryptomare. Numbers indicate the 3 tie points used to remove the continuum over the 1 μm and 2 μm absorption features. Tie point 1 is fixed at 750 nm while tie points 2 and 3 are allowed to vary. Grey region highlights the wavelength range used to calculate the position of tie point 2. (b) Continuum removed spectra.

Figure 3. Two examples of the Modified Gaussian Model (MGM) fitting process (Sunshine et al., 1990). (a) Example 1 showing the initial conditions of the model. The orange '+' outline the input spectrum, the red horizontal line is the continuum, the blue Gaussians represent the modeled pyroxene absorption features, the modeled spectrum in black, and the residual in pink. (b) Model result for example 1. The residual (pink line) shows that the MGM has iteratively positioned and sized the Gaussians to best fit the input spectrum (orange '+'). (c) Example 2 of the initial conditions of the MGM. The 4 blue Gaussians and the black model spectrum are the same for both examples and represent the initial conditions chosen for the automated MGM developed in this study to process 100s of spectra at a time. (d) Model result for example 2. The ordinate is compressed in (b) and (d) in order to show the position of the fitted Gaussians and residual values.

Figure 4. Comparison of calculated band centers (1 μm, 1.2 μm, and 2 μm) from three different M^3 optical periods, 1b, 2c1, and 2c2. Spectra collected from the same location in two datasets were processed using the MGM to compare calculated absorption band centers. The observed variation in band centers between M^3 optical periods can be used to estimate the error of these measurements. Data collected during optical period 2c1 have the largest areal extent and cover at least a portion of all mapped cryptomaria. Thus, these data are considered as the baseline from which 1b and 2c2 values will be compared. (a) Calculated 1 μm band centers in OP2c1 verses OP2c2; (b) Calculated 1 μm band centers in OP2c1 verses OP1b; (c) Calculated 1.2 μm band centers in OP2c1 verses OP2c2; (d) Calculated 1.2 μm band centers in OP2c1 verses OP1b; (e) Calculated 2 μm

band centers in OP2c1 verses OP2c2; (f) Calculated 2 μm band centers in OP2c1 verses OP1b.

Figure 5. Plot of the position of the 1 μm and 2 μm absorption features (McCord and Adams, 1973) for all cryptomare (orange circles) and exposed mare deposits (blue diamonds). The data are overlain on laboratory measurements of a suite of well-characterized synthetic pyroxenes (Klima et al., 2007, 2011). All collected spectra, cryptomare and mare, coincide with the synthetic clinopyroxene 1 μm and 2 μm absorption positions. The location of the data cloud at the lowermost portion of the clinopyroxene trend is consistent with pigeonite (Klima et al., 2011). Error bars are the average differences in calculated band centers between the different M^3 optical periods (Fig. 4; Table 3). All data are from OP2c1, except for the Milne cryptomare (OP2c2) because it was not imaged during OP2c1.

Figure 6. Wavelength positions of the 1 μm and 2 μm absorption features for each individual study region. Cryptomare (dark-halo craters; orange circles) and exposed mare (blue diamonds) from each study region are plotted against a suite of synthetic pyroxenes (Klima et al., 2007, 2011). (a) Australe. (b) Balmer. (c) Dewar. (d) Frigoris. (e) Hercules. (f) Humboldtianum. (g) Lacus Solitudinis. (h) Langemak. (i) Lomonosov-Fleming. (j) Marginis. (k) Mendel-Rydberg. (l) Milne. (m) Schiller-Schickard. (n) Smythii. (o) South-Pole Aitken. (p) Taruntius. (q) West Humorum. (r) West Procellarum.

Figure 7. FeO verses Th values for identified cryptomare (Fig. 1). Average Lunar Prospector Th (ppm) and FeO (wt %) for the entire mapped cryptomare deposit are plotted in green circles. FeO values of dark-halo craters derived from Clementine data (Lucey et al., 1995) and Lunar Prospector Th values measured in previous studies (Giguere et al., 2003; Hawke et al., 2003; Hawke et al., 2005; Lawrence et al., 2008) are shown in orange circles. Black horizontal lines connect circles identifying the minimum and maximum values measured for a single cryptomare deposit. Black symbols superposed on circles indicate a specific cryptomare in order to show how the Lunar Prospector FeO values of the entire deposit compare with Clementine FeO values of dark-halo craters: upright triangle = Dewar, square = Balmer, diamond = Schiller-Schickard, upside down triangle = Lomonosov-Fleming. As expected, the Th values are consistent between the data collected in this study (green circles) and data from previous studies (orange circles). The Lunar Prospector FeO values are low, as would be expected for a basaltic deposit that has been covered and mixed with feldspathic material. After Figure 2.5 from Lucey et al. (2006).

Figure 8. Sample spectra for ancient volcanic rocks on the Moon. (a) RELAB spectra of 7 different volcanic lithologies re-sampled to M^3 wavelengths: a low-Ti basalt (15058,276; LR-CMP-152), a high-Ti basalt (70017; LR-CMP-156), olivine clasts from a dunite (72415,64; LS-CMP-003), a norite (72255,74; LS-JBA-212), a troctolite (76535,17; LS-JBA-245), a high-Al basalt (14301,49; LS-JBA-093), and a KREEP basalt (14310,152; LS-JBA-095). Spectra were measured only to 2.5 μm. (b) 2 μm verses 1 μm

plot showing the calculated band positions of the ancient volcanic rocks, using the same method applied to the M^3 orbital spectra.

Figure A1. Locations of the individual cryptomare and mare ponds in the 18 different study regions. a) Australe cryptomare. b) Balmer cryptomare. c) Dewar cryptomare. d) Australe mare. e) Balmer mare. f) No Dewar exposed mare was detected. g) Frigoris cryptomare. h) Hercules cryptomare. i) Frigoris mare. j) Hercules mare. k) Humboldtianum cryptomare. l) Langemak cryptomare. m) Lomonosov-Fleming cryptomare. n) Humboldtianum mare. o) Langemak mare. p) Lomonosov-Fleming mare. q) Marginis cryptomare. r) Mendel-Rydberg cryptomare. s) Milne cryptomare. t) Marginis mare. u) Mendel-Rydberg mare. v) No Milne exposed mare was detected. w) Schiller-Schickard cryptomare. x) Smythii cryptomare. y) South Pole-Aitken cryptomare. z) Schiller-Schickard mare. aa) Smythii mare. bb) South Pole-Aitken mare. cc) Taruntius cryptomare. dd) Lacus Solitudinis cryptomare. ee) West Humorum cryptomare. ff) Taruntius mare. gg) Lacus Solitudinis mare. hh) West Humorum mare. ii) West Procellarum cryptomare. jj) West Procellarum mare.

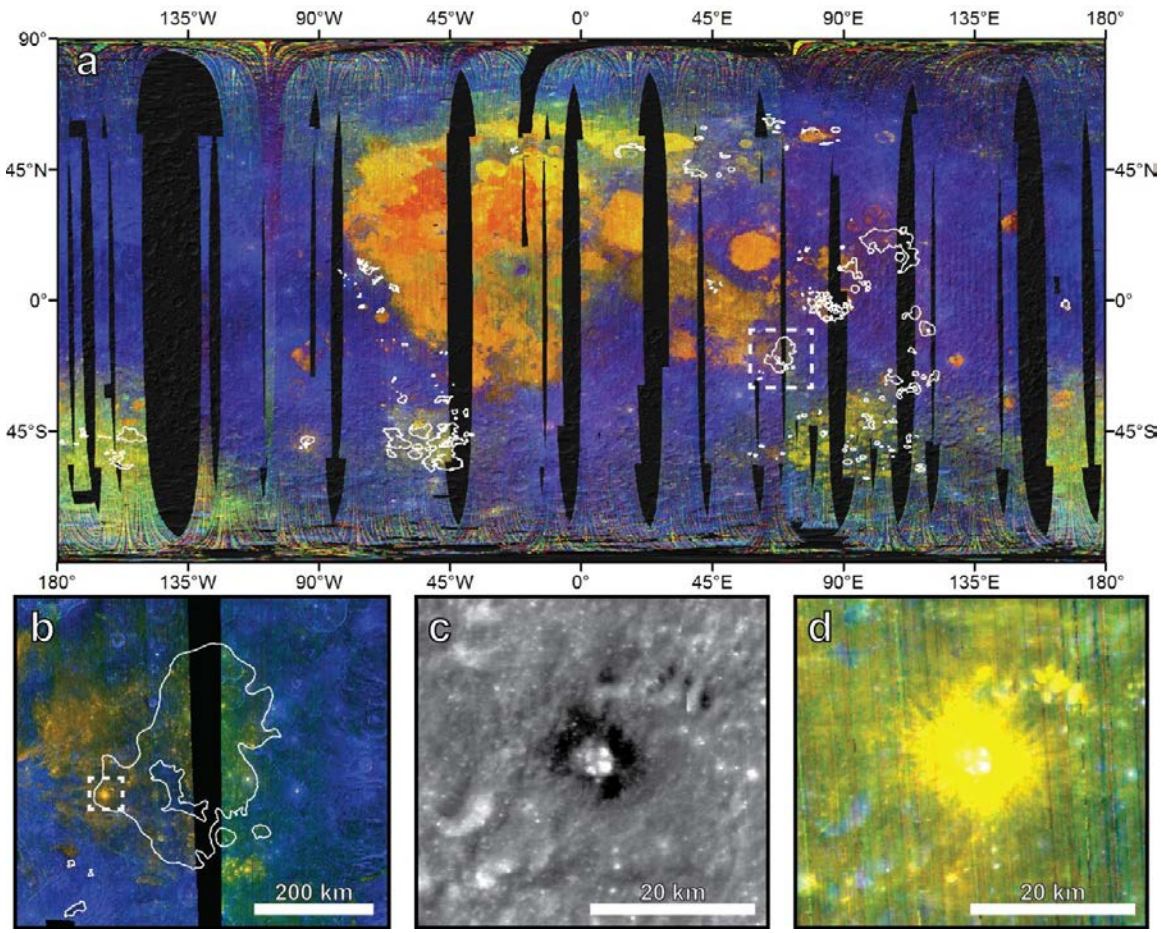
a
135°W
90°W
45°W
0°
45°E
90°E
135°E
180°
90°
45°N
0°
45°S
b
200 km
c
20 km
d
20 km

Figure 1.

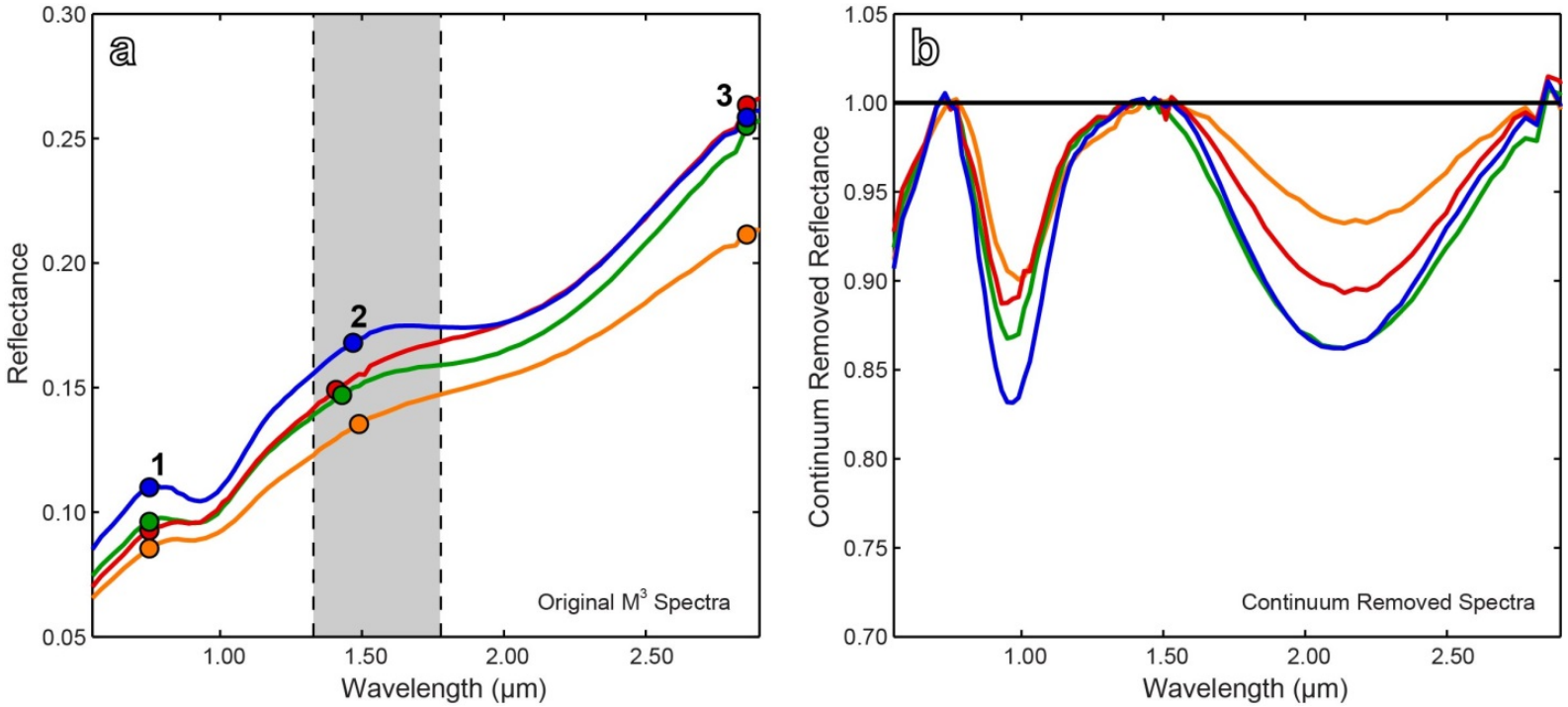
a
b
1
2
3
Reflectance
Wavelength (μm)
Original M3 Spectra
Continuum Removed Reflectance
Continuum Removed Spectra
0.30
0.25
0.20
0.15
0.10
0.05
1.05
1.00
0.95
0.90
0.85
0.80
0.75
0.70
1.00
1.50
2.00
2.50

Figure 2.

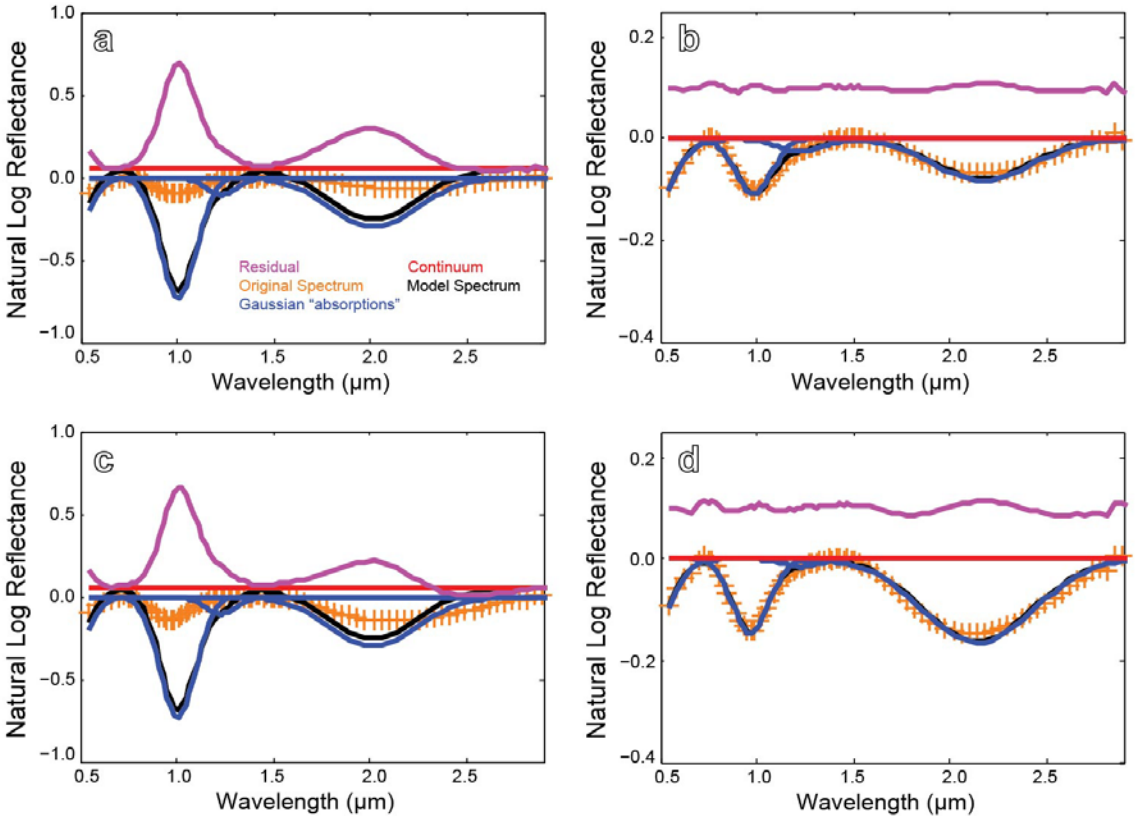
a
b
c
d
Natural Log Reflectance
Wavelength (μm)
Residual
Original Spectrum
Gaussian "absorptions"
Continuum
Model Spectrum

Figure 3.

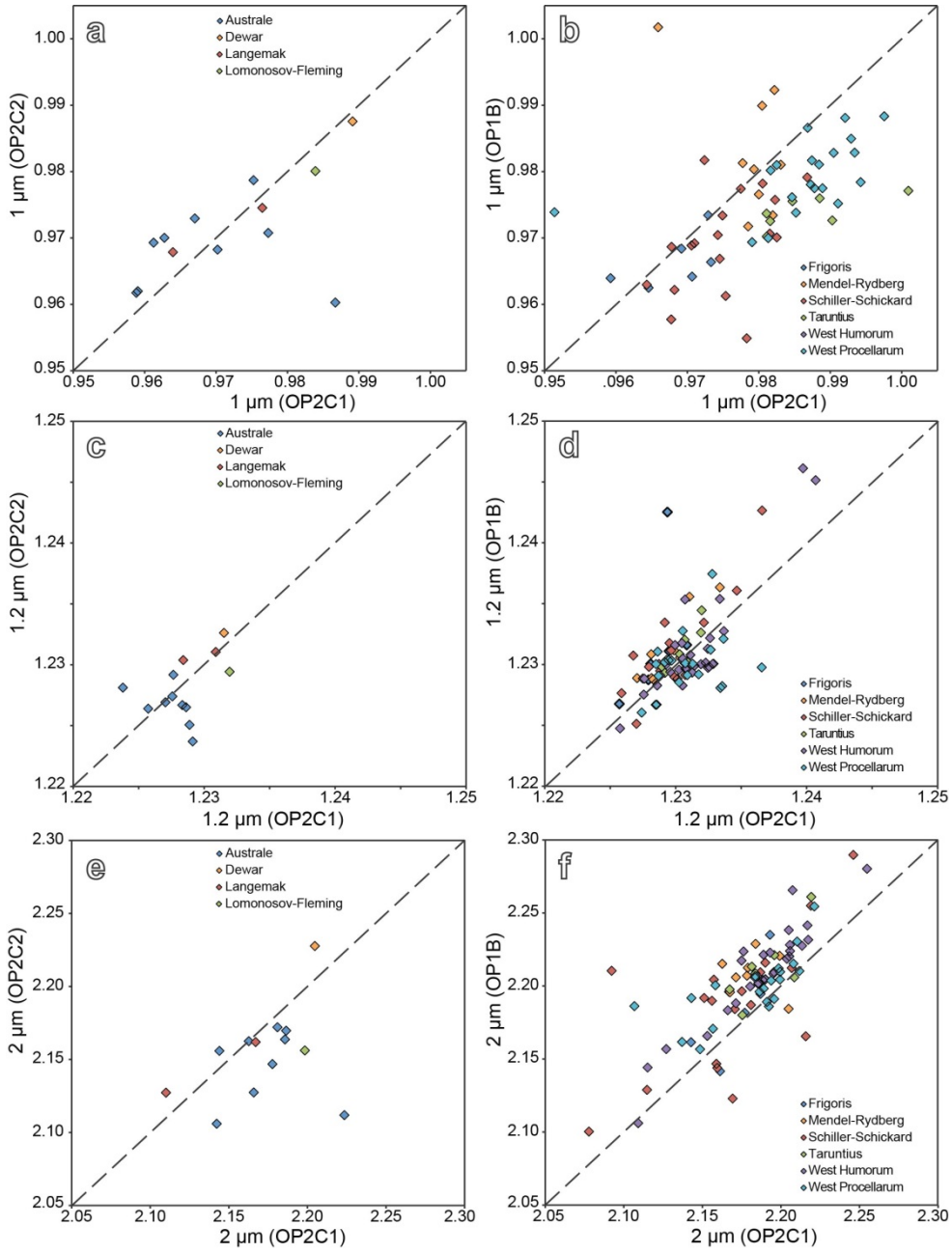
a
Australe
Dewar
Langemak
Lomonosov-Fleming
1 µm (OP2C2)
1 µm (OP2C1)
b
Frigoris
Mendel-Rydberg
Schiller-Schickard
Taruntius
West Humorum
West Procellarum
1 µm (OP1B)
1 µm (OP2C1)
c
1.2 µm (OP2C2)
1.2 µm (OP2C1)
d
1.2 µm (OP1B)
1.2 µm (OP2C1)
e
2 µm (OP2C2)
2 µm (OP2C1)
f
2 µm (OP1B)
2 µm (OP2C1)

Figure 4.

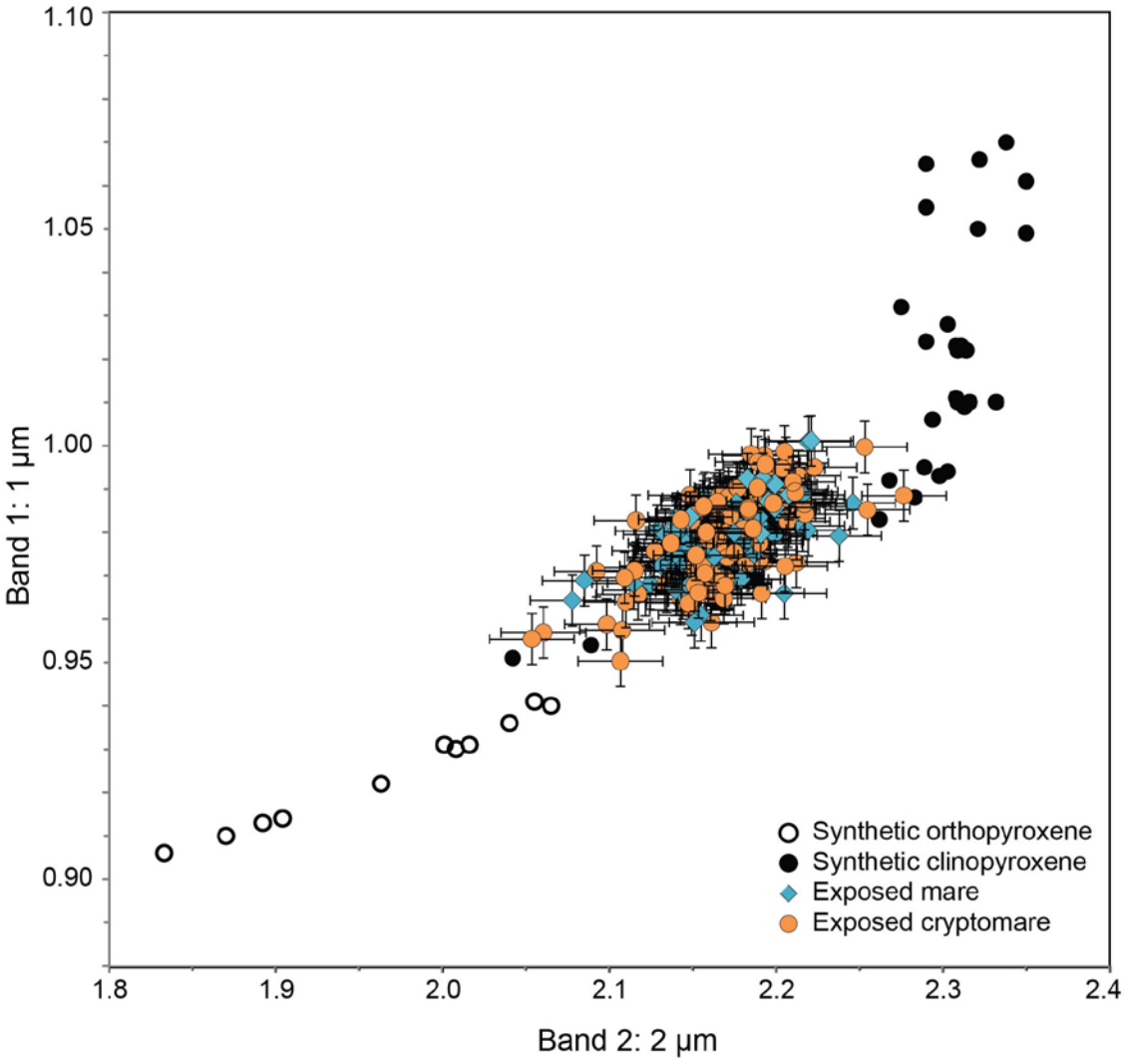
1.10
1.05
1.00
0.95
0.90
Band 1: 1 µm
1.8
1.9
2.0
2.1
2.2
2.3
2.4
Band 2: 2 µm
Synthetic orthopyroxene
Synthetic clinopyroxene
Exposed mare
Exposed cryptomare

Figure 5.

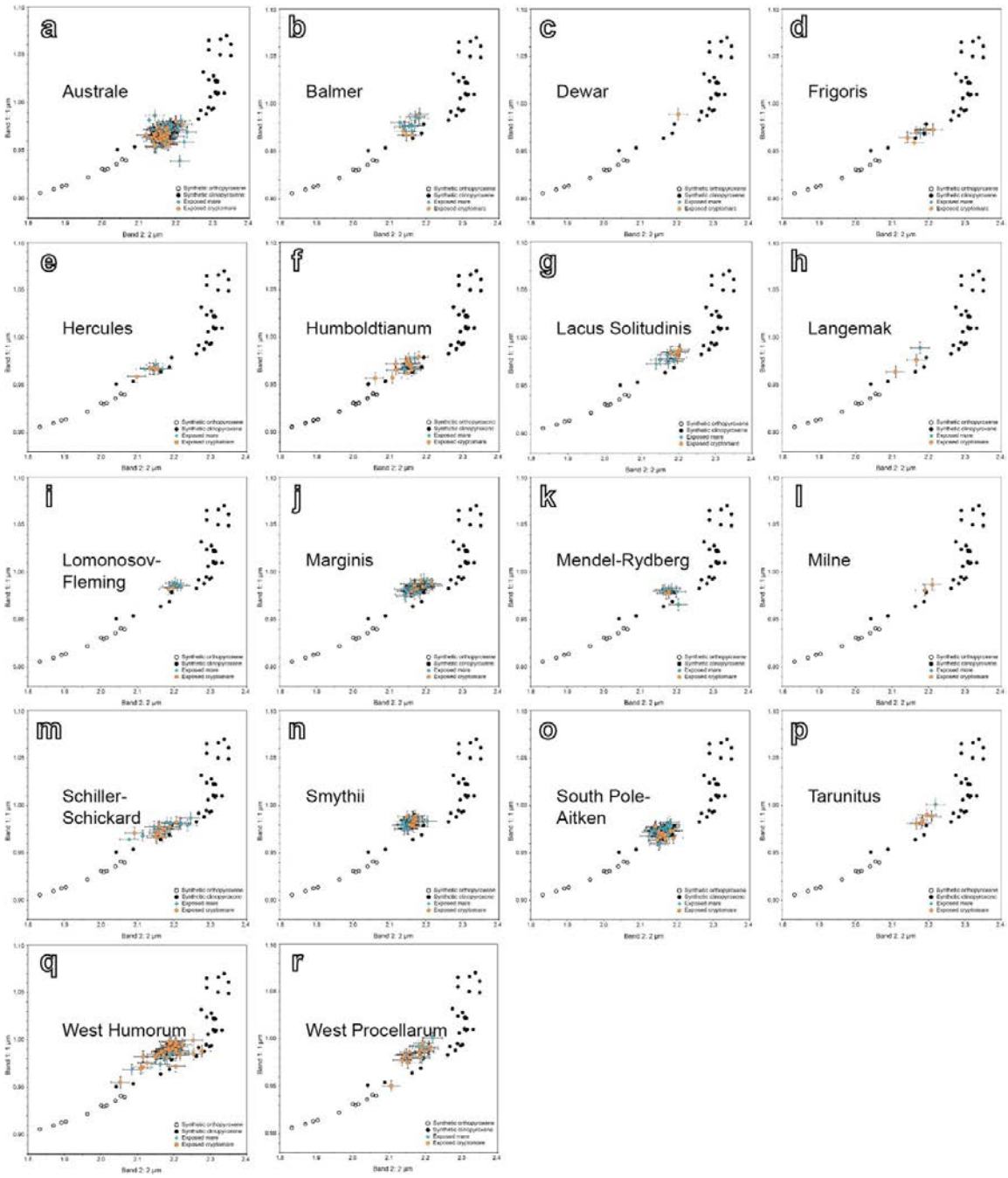
a
Australe
b
Balmer
c
Dewar
d
Frigoris
e
Hercules
f
Humboldtianum
g
Lacus Solitudinis
h
Langemak
i
Lomonosov-Fleming
j
Marginis
k
Mendel-Rydberg
l
Milne
m
Schiller-Schickard
n
Smythii
o
South Pole-Aitken
p
Tarunitus
q
West Humorum
r
West Procellarum

Figure 6.

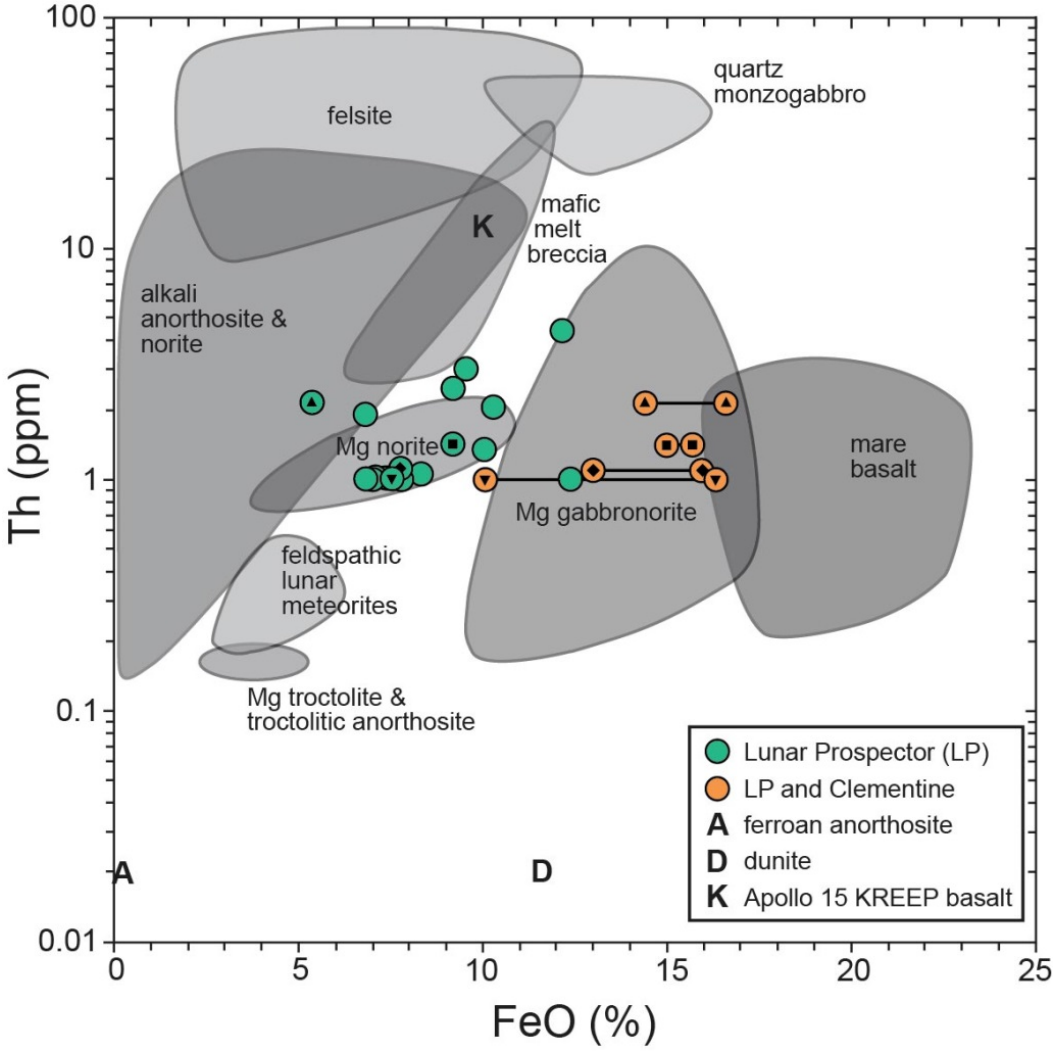
100
10
1
0.1
0.01
Th (ppm)
0
5
10
15
20
25
FeO (%)
felsite
quartz
monzogabbro
mafic
melt
breccia
K
alkali
anorthosite &
norite
Mg norite
mare
basalt
Mg gabbronorite
feldspathic
lunar
meteorites
Mg troctolite &
troctolitic anorthosite
A
D
Lunar Prospector (LP)
LP and Clementine
A ferroan anorthosite
D dunite
K Apollo 15 KREEP basalt

Figure 7.

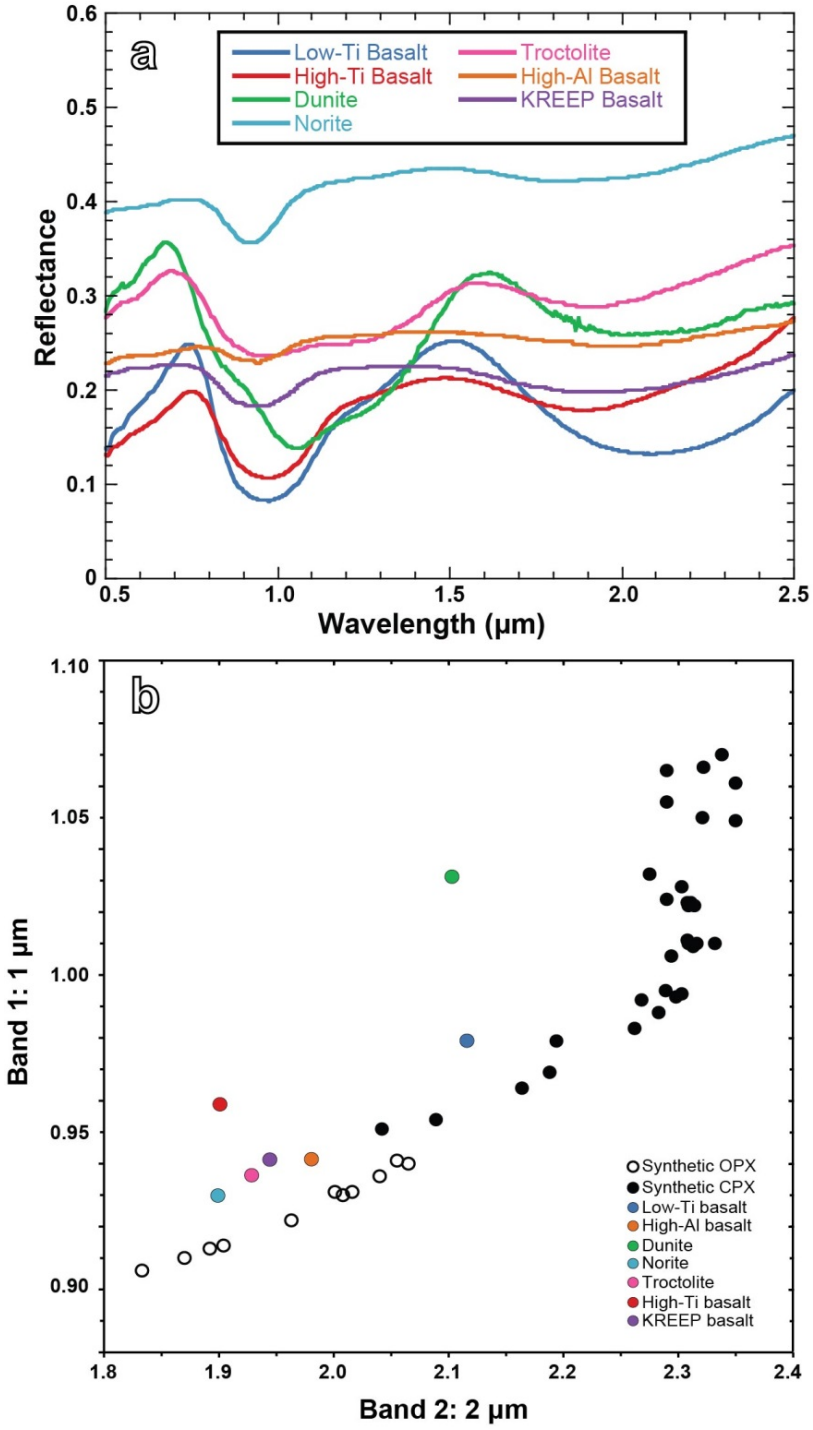
a
Low-Ti Basalt
High-Ti Basalt
Dunite
Norite
Troctolite
High-Al Basalt
KREEP Basalt
Reflectance
Wavelength (μm)
b
Band 1: 1 μm
Band 2: 2 μm
Synthetic OPX
Synthetic CPX
Low-Ti basalt
High-Al basalt
Dunite
Norite
Troctolite
High-Ti basalt
KREEP basalt

Figure 8.

Appendix

Table A1. M^3 optical period and strip numbers used for each study region mosaic.

Study region	Optical Period	Image strip ID			
Australe	2c1	M3G20090529T013507	M3G20090529T100749	M3G20090529T183825	M3G20090529T230608
		M3G20090530T030925	M3G20090530T073724	M3G20090530T160828	M3G20090530T201123
		M3G20090531T132341	M3G20090531T133050	M3G20090531T172712	M3G20090531T215442
		M3G20090601T021112	M3G20090601T061442	M3G20090601T062753	M3G20090601T104211
		M3G20090601T145212	M3G20090602T074711	M3G20090602T121452	M3G20090602T163012
		M3G20090602T203342	M3G20090603T010112	M3G20090603T050442	M3G20090603T134223
		M3G20090603T174502	M3G20090603T221232	M3G20090604T064302	M3G20090604T104552
		M3G20090604T151322	M3G20090604T191631	M3G20090604T234352	M3G20090605T034701
		M3G20090605T081431			
	2c2	M3G20090626T142653	M3G20090626T142733	M3G20090626T182943	M3G20090627T031213
		M3G20090627T071503	M3G20090627T114223	M3G20090627T154523	M3G20090627T201242
Balmer	2c1	M3G20090602T074711	M3G20090602T121452	M3G20090602T163012	M3G20090602T203342
		M3G20090603T010112	M3G20090603T050442	M3G20090603T134223	M3G20090603T174502
		M3G20090603T221232	M3G20090604T023806	M3G20090604T064302	
Dewar	2c1	M3G20090623T012541	M3G20090623T052831	M3G20090623T095551	M3G20090623T135841
		M3G20090623T142528			
	2c2	M3G20090720T003411	M3G20090720T043741	M3G20090720T090521	M3G20090720T173631
		M3G20090720T214000			
Frigoris	2c1	M3G20090605T081431	M3G20090605T085558	M3G20090605T170055	M3G20090605T212253
		M3G20090606T010302	M3G20090606T053022	M3G20090607T025544	M3G20090607T070124
		M3G20090607T073505	M3G20090607T153144	M3G20090607T201038	M3G20090608T000122
		M3G20090608T042049	M3G20090608T083142	M3G20090608T125102	M3G20090609T060742
		M3G20090609T101951	M3G20090609T183254	M3G20090609T230815	M3G20090610T070604
		M3G20090610T113334	M3G20090610T162800	M3G20090610T200344	M3G20090611T001830

		M3G20090611T043527	M3G20090611T090220	M3G20090612T060502	M3G20090612T101600
		M3G20090612T143522	M3G20090612T183813	M3G20090613T032520	M3G20090612T230542
	1b	M3G20090202T103351	M3G20090202T122051	M3G20090202T123639	M3G20090202T142951
		M3G20090202T161651	M3G20090202T182612	M3G20090202T201251	M3G20090202T222211
		M3G20090203T041059	M3G20090203T061431	M3G20090203T080104	M3G20090203T135512
		M3G20090203T160452	M3G20090203T175131	M3G20090203T200051	M3G20090204T094731
		M3G20090204T113444	M3G20090204T134332	M3G20090204T152951	M3G20090204T173931
		M3G20090204T192552	M3G20090204T233457	M3G20090205T013151	M3G20090205T031811
		M3G20090205T071411	M3G20090205T092400	M3G20090205T111013	M3G20090205T131953
		M3G20090205T150614	M3G20090205T171614	M3G20090205T190233	M3G20090205T211213
		M3G20090205T225833	M3G20090206T010833	M3G20090206T025453	M3G20090206T030351
		M3G20090206T050433	M3G20090206T050647	M3G20090206T065053	M3G20090206T084850
		M3G20090206T105850	M3G20090206T124510	M3G20090206T145451	M3G20090206T164110
		M3G20090206T185050	M3G20090206T185403	M3G20090206T203710	M3G20090206T222411
		M3G20090207T003331	M3G20090207T061610	M3G20090207T082530	M3G20090207T083836
		M3G20090207T101751	M3G20090207T121011	M3G20090207T141950	M3G20090207T142313
		M3G20090207T161103	M3G20090207T181550	M3G20090207T200231	M3G20090207T221151
		M3G20090207T235830	M3G20090208T001912	M3G20090208T020750	M3G20090208T021836
		M3G20090208T035432	M3G20090208T075032	M3G20090208T080838	M3G20090208T100012
		M3G20090208T114652	M3G20090208T135610	M3G20090208T160125	M3G20090208T175211
		M3G20090208T194335	M3G20090208T214811	M3G20090208T233940	M3G20090209T014431
		M3G20090209T033051	M3G20090209T054031	M3G20090209T072710	M3G20090209T212512
		M3G20090209T233432	M3G20090210T012132		
	Hercules	2c1	M3G20090604T234352	M3G20090605T040250	M3G20090605T081431	M3G20090605T085558
		M3G20090605T170055	M3G20090605T212253	M3G20090606T010302	M3G20090604T104552
		M3G20090604T151322	M3G20090604T195758	M3G20090604T234352	M3G20090605T040250
		M3G20090605T081431	M3G20090605T085558	M3G20090605T170055	M3G20090605T212253
		M3G20090606T010302	M3G20090606T053022	M3G20090607T025544	

Humboldtianum	2c1	M3G20090531T215442	M3G20090601T021112	M3G20090601T064032	M3G20090601T104211
		M3G20090601T145212	M3G20090601T193005	M3G20090601T235923	M3G20090602T082937
		M3G20090602T124100	M3G20090602T164851	M3G20090602T203342	M3G20090603T010112
		M3G20090603T050442	M3G20090603T134223	M3G20090603T174502	M3G20090604T023806
		M3G20090604T064302			
Langemak	2c1	M3G20090529T183825	M3G20090529T230608	M3G20090530T030925	M3G20090530T073724
		M3G20090530T160828	M3G20090530T201123		
	2c2	M3G20090626T142653	M3G20090626T182943	M3G20090626T190019	M3G20090626T190203
		M3G20090626T190233	M3G20090627T031213	M3G20090627T071503	M3G20090627T114223
		M3G20090627T154523	M3G20090627T201242		
Lomonosov-Fleming	2c1	M3G20090530T160828	M3G20090530T201123	M3G20090531T133050	M3G20090531T134207
		M3G20090531T172712	M3G20090531T215442	M3G20090601T021112	M3G20090601T064032
		M3G20090601T104211	M3G20090601T145212	M3G20090601T193005	
	2c2	M3G20090626T190524	M3G20090627T031213	M3G20090627T071503	M3G20090627T114223
		M3G20090627T154523	M3G20090627T163233	M3G20090627T201242	
Marginis	2c1	M3G20090601T021112	M3G20090601T064032	M3G20090601T104211	M3G20090601T145212
		M3G20090601T193005	M3G20090602T074711	M3G20090602T121452	M3G20090602T124100
		M3G20090602T163012	M3G20090602T164851	M3G20090602T203342	M3G20090603T010112
		M3G20090531T172712	M3G20090531T215442	M3G20090601T021112	M3G20090601T064032
		M3G20090601T104211	M3G20090601T145212	M3G20090601T193005	
Mendel-Rydberg	2c1	M3G20090520T065048	M3G20090520T111838	M3G20090614T043933	M3G20090614T045922
		M3G20090614T090712	M3G20090614T131003	M3G20090614T173733	M3G20090615T062313
		M3G20090615T102602	M3G20090615T145333	M3G20090615T185632	M3G20090615T232402
		M3G20090616T032653	M3G20090616T075432	M3G20090616T115723	M3G20090617T005342
		M3G20090617T045633			
	1b	M3G20090211T171539	M3G20090211T185152	M3G20090211T203852	M3G20090211T231038
		M3G20090212T011737	M3G20090212T024412	M3G20090212T044205	M3G20090212T064032
		M3G20090212T082712	M3G20090212T104932	M3G20090212T122313	M3G20090212T143253

		M3G20090212T162141	M3G20090212T184721	M3G20090212T203719	M3G20090212T222453
		M3G20090213T001153	M3G20090213T022112	M3G20090213T040732	M3G20090213T061652
		M3G20090213T080353	M3G20090213T101313	M3G20090213T115953	M3G20090213T140913
		M3G20090213T180532	M3G20090213T195213		
Milne	2c2	M3G20090626T142733	M3G20090626T182943	M3G20090627T031213	M3G20090627T071503
		M3G20090627T114223	M3G20090627T154523	M3G20090627T201242	
Schiller-Schickard	2c1	M3G20090610T070604	M3G20090610T113334	M3G20090610T154042	M3G20090610T200344
		M3G20090611T000633	M3G20090611T001830	M3G20090611T043402	M3G20090611T043527
		M3G20090611T083653	M3G20090612T013733	M3G20090612T060502	M3G20090612T101600
		M3G20090612T143522	M3G20090612T183813	M3G20090612T230542	M3G20090613T030843
		M3G20090613T032520	M3G20090613T073612	M3G20090613T113913	M3G20090613T160643
		M3G20090613T161036	M3G20090613T200943	M3G20090614T003642	M3G20090614T043933
		M3G20090614T045922	M3G20090614T090712	M3G20090614T131003	
	1b	M3G20090207T124241	M3G20090207T142313	M3G20090207T165529	M3G20090207T183846
		M3G20090207T204327	M3G20090207T210337	M3G20090207T221151	M3G20090207T225624
		M3G20090208T001912	M3G20090208T021836	M3G20090208T061844	M3G20090208T080838
		M3G20090208T101739	M3G20090208T121842	M3G20090208T143051	M3G20090208T160125
		M3G20090208T175211	M3G20090208T201331	M3G20090208T214811	M3G20090209T000934
		M3G20090209T014431	M3G20090209T022618	M3G20090209T033051	M3G20090209T042503
		M3G20090209T062002	M3G20090209T212512	M3G20090209T233432	M3G20090210T014535
		M3G20090210T033052	M3G20090210T035959	M3G20090210T051732	M3G20090210T060351
		M3G20090210T072652	M3G20090210T080318	M3G20090210T094056	M3G20090210T112252
		M3G20090210T151912	M3G20090210T155054	M3G20090210T171205	M3G20090210T191512
		M3G20090210T210152	M3G20090210T231132	M3G20090210T233730	M3G20090211T011239
		M3G20090211T032906	M3G20090211T034215	M3G20090211T045412	M3G20090211T053806
		M3G20090211T070332	M3G20090211T085804		
Smythii	2c1	M3G20090601T062753	M3G20090601T064032	M3G20090601T104211	M3G20090601T145212
		M3G20090601T193005	M3G20090602T074711	M3G20090602T121452	M3G20090602T163012

		M3G20090602T164851	M3G20090602T203342	M3G20090603T010112	M3G20090531T172712
		M3G20090531T215442	M3G20090601T021112	M3G20090601T064032	M3G20090601T104211
		M3G20090601T145212	M3G20090601T193005		
South Pole-Aitken	2c1	M3G20090620T051312	M3G20090620T094042	M3G20090620T134543	M3G20090620T181042
		M3G20090621T022743	M3G20090621T025007	M3G20090621T065503	M3G20090621T193712
		M3G20090622T041041	M3G20090622T082242		
Taruntius	2c1	M3G20090604T191631	M3G20090604T234352	M3G20090605T040250	M3G20090605T081431
	1b	M3G20090201T224531	M3G20090202T003211	M3G20090202T005641	M3G20090202T024131
		M3G20090202T042831	M3G20090202T064453	M3G20090202T083314	
Lacus Solitudinis	2c1	M3G20090528T083319	M3G20090528T130108	M3G20090528T213152	M3G20090529T015004
		M3G20090529T060422	M3G20090529T061013	M3G20090529T100749	M3G20090529T143509
		M3G20090529T183825	M3G20090529T230608	M3G20090530T030925	M3G20090530T073724
		M3G20090530T160828	M3G20090530T201123	M3G20090531T132341	M3G20090531T133050
		M3G20090531T172712	M3G20090531T215442	M3G20090602T074711	M3G20090602T121452
		M3G20090623T135841	M3G20090623T142528	M3G20090623T182551	
West Humorun	2c1	M3G20090610T200344	M3G20090611T001830	M3G20090611T043527	M3G20090611T083653
		M3G20090611T090220	M3G20090612T013733	M3G20090612T060502	M3G20090612T101600
		M3G20090612T143522	M3G20090612T183813	M3G20090612T230542	M3G20090613T030843
		M3G20090613T032520	M3G20090613T073612	M3G20090613T113913	M3G20090613T120320
		M3G20090613T160643	M3G20090613T161036	M3G20090613T200943	M3G20090614T003642
		M3G20090614T043933	M3G20090614T045922	M3G20090614T090712	M3G20090614T131003
		M3G20090614T173733			
	1b	M3G20090207T142313	M3G20090207T165529	M3G20090207T183846	M3G20090207T204327
		M3G20090207T221151	M3G20090207T225624	M3G20090208T001912	M3G20090208T021836
		M3G20090208T061844	M3G20090208T080838	M3G20090208T101739	M3G20090208T121842
		M3G20090208T135610	M3G20090208T143051	M3G20090208T160125	M3G20090208T175211
		M3G20090208T201331	M3G20090208T214811	M3G20090209T000934	M3G20090209T014431
		M3G20090209T022618	M3G20090209T033051	M3G20090209T042503	M3G20090209T054031

		M3G20090209T062002	M3G20090209T212512	M3G20090209T233432	M3G20090210T014535
		M3G20090210T033052	M3G20090210T051732	M3G20090210T072652	M3G20090210T094056
		M3G20090210T112252	M3G20090210T132052	M3G20090210T151912	M3G20090210T171205
		M3G20090210T191512	M3G20090210T210152	M3G20090210T231132	M3G20090210T233730
		M3G20090211T011239	M3G20090211T030946	M3G20090211T032906	M3G20090211T045412
		M3G20090211T070332	M3G20090211T105952	M3G20090211T171539	M3G20090211T185152
		M3G20090211T203852	M3G20090211T231038		
West Procellarum	2c1	M3G20090613T073612	M3G20090613T120320	M3G20090613T161036	M3G20090613T200943
		M3G20090614T003642	M3G20090614T045922	M3G20090614T090712	M3G20090614T131003
		M3G20090614T173733	M3G20090614T175501	M3G20090615T062313	
	1b	M3G20090210T093444	M3G20090210T094056	M3G20090210T112252	M3G20090210T132052
		M3G20090210T151912	M3G20090210T171205	M3G20090210T191512	M3G20090210T210152
		M3G20090210T231132	M3G20090211T011239	M3G20090211T030946	M3G20090211T045412
		M3G20090211T070332	M3G20090211T085804	M3G20090211T105952	M3G20090211T185152
		M3G20090211T203852	M3G20090211T224812	M3G20090212T003453	M3G20090212T024412
		M3G20090212T044205			

Table A2. Location information for the dark-halo spectra (from all optical periods).

#	Location	Types	Pond	Longitude	Latitude
1	Australe	Cryptomare	0	91.624	-55.373
2	Australe	Cryptomare	0	90.493	-55.507
3	Australe	Cryptomare	1	95.689	-54.631
4	Australe	Cryptomare	2	83.112	-45.361
5	Australe	Cryptomare	2	82.618	-45.187
6	Australe	Cryptomare	2	82.769	-46.107
7	Australe	Cryptomare	3	82.090	-38.419
8	Australe	Cryptomare	4	75.823	-39.528
9	Australe	Cryptomare	4	75.663	-39.564
10	Australe	Cryptomare	5	74.623	-40.416
11	Australe	Cryptomare	6	71.218	-46.438
12	Australe	Cryptomare	6	71.295	-46.498
13	Australe	Cryptomare	7	68.736	-52.653
14	Australe	Cryptomare	7	68.807	-52.459
15	Australe	Cryptomare	8	62.360	-49.929
16	Australe	Cryptomare	8	62.598	-49.984
17	Australe	Cryptomare	8	62.632	-50.108
18	Australe	Cryptomare	9	61.185	-49.915
19	Australe	Cryptomare	10	59.296	-53.389
20	Australe	Cryptomare	11	57.373	-52.759
21	Australe	Cryptomare	12	67.014	-54.280
22	Australe	Cryptomare	13	97.716	-61.027
23	Australe	Cryptomare	13	98.911	-61.018
24	Australe	Cryptomare	13	98.567	-61.060
25	Australe	Cryptomare	15	106.558	-51.730
26	Australe	Cryptomare	15	106.943	-51.594
27	Australe	Cryptomare	16	103.290	-50.110
28	Australe	Cryptomare	17	105.680	-50.378
29	Australe	Cryptomare	18	101.564	-48.734
30	Australe	Cryptomare	19	93.538	-50.945
31	Australe	Cryptomare	20	91.087	-50.280
32	Australe	Cryptomare	20	91.468	-50.522
33	Australe	Cryptomare	21	90.970	-51.446
34	Australe	Cryptomare	22	96.636	-53.926
35	Australe	Cryptomare	23	91.536	-48.659
36	Australe	Cryptomare	24	93.226	-46.638
37	Australe	Cryptomare	24	92.794	-46.817
38	Australe	Cryptomare	25	99.679	-42.543
39	Australe	Cryptomare	25	100.303	-43.781
40	Australe	Cryptomare	27	98.771	-40.068

41	Australe	Cryptomare	27	96.961	-39.315
42	Australe	Cryptomare	28	104.379	-41.536
43	Australe	Cryptomare	29	106.992	-41.751
44	Australe	Cryptomare	29	108.054	-41.808
45	Australe	Cryptomare	31	103.001	-33.131
46	Australe	Cryptomare	31	103.162	-33.007
47	Australe	Cryptomare	32	115.479	-58.276
48	Australe	Cryptomare	33	115.599	-46.693
49	Australe	Cryptomare	33	115.206	-46.405
50	Australe	Cryptomare	34	97.731	-33.697
51	Australe	Cryptomare	34	98.608	-33.948
52	Australe	Mare	0	96.759	-42.203
53	Australe	Mare	0	95.825	-41.585
54	Australe	Mare	0	95.186	-42.082
55	Australe	Mare	1	76.772	-43.923
56	Australe	Mare	1	75.746	-44.122
57	Australe	Mare	1	75.613	-43.304
58	Australe	Mare	1	76.309	-43.095
59	Australe	Mare	2	79.482	-39.258
60	Australe	Mare	2	79.460	-38.768
61	Australe	Mare	2	78.996	-38.577
62	Australe	Mare	3	80.934	-40.443
63	Australe	Mare	3	81.271	-40.308
64	Australe	Mare	3	81.606	-40.487
65	Australe	Mare	3	80.121	-40.819
66	Australe	Mare	4	77.855	-52.403
67	Australe	Mare	4	77.807	-51.897
68	Australe	Mare	4	77.412	-50.987
69	Australe	Mare	6	84.495	-49.425
70	Australe	Mare	6	82.599	-50.103
71	Australe	Mare	6	84.843	-51.843
72	Australe	Mare	7	72.223	-48.292
73	Australe	Mare	7	72.232	-48.005
74	Australe	Mare	8	72.165	-50.068
75	Australe	Mare	8	71.878	-50.604
76	Australe	Mare	10	66.860	-49.970
77	Australe	Mare	11	81.325	-42.750
78	Australe	Mare	12	82.324	-44.264
79	Australe	Mare	14	82.827	-47.239
80	Australe	Mare	14	83.596	-47.381
81	Australe	Mare	15	71.098	-43.370
82	Australe	Mare	15	71.194	-43.501
83	Australe	Mare	16	75.024	-49.658

84	Australe	Mare	16	75.404	-47.453
85	Australe	Mare	16	76.250	-46.668
86	Australe	Mare	16	74.595	-46.020
87	Australe	Mare	17	72.952	-44.886
88	Australe	Mare	18	78.147	-41.243
89	Australe	Mare	18	78.371	-42.195
90	Australe	Mare	19	70.694	-41.241
91	Australe	Mare	19	70.549	-41.500
92	Australe	Mare	23	83.397	-54.649
93	Australe	Mare	23	83.375	-54.418
94	Australe	Mare	23	81.994	-54.764
95	Australe	Mare	24	76.207	-53.695
96	Australe	Mare	24	77.020	-53.920
97	Australe	Mare	25	74.640	-57.570
98	Australe	Mare	25	76.181	-57.436
99	Australe	Mare	26	78.545	-57.830
100	Australe	Mare	27	75.688	-52.901
101	Australe	Mare	27	71.950	-53.681
102	Australe	Mare	27	78.141	-53.413
103	Australe	Mare	27	76.725	-56.024
104	Australe	Mare	28	64.885	-50.406
105	Australe	Mare	29	67.042	-53.337
106	Australe	Mare	30	65.370	-51.670
107	Australe	Mare	30	66.861	-51.896
108	Australe	Mare	30	62.629	-50.641
109	Australe	Mare	31	90.110	-58.402
110	Australe	Mare	31	92.069	-58.568
111	Australe	Mare	31	90.890	-59.415
112	Australe	Mare	32	93.079	-60.256
113	Australe	Mare	32	92.363	-60.182
114	Australe	Mare	33	96.736	-59.495
115	Australe	Mare	33	95.781	-58.961
116	Australe	Mare	33	95.877	-58.687
117	Australe	Mare	34	80.672	-58.591
118	Australe	Mare	34	82.161	-58.619
119	Australe	Mare	34	81.499	-59.152
120	Australe	Mare	35	80.570	-60.483
121	Australe	Mare	35	81.929	-60.587
122	Australe	Mare	36	83.691	-59.533
123	Australe	Mare	36	83.690	-60.096
124	Australe	Mare	38	81.425	-59.728
125	Australe	Mare	38	80.634	-59.465
126	Australe	Mare	41	85.347	-63.047

127	Australe	Mare	41	83.484	-63.174
128	Australe	Mare	41	85.642	-63.853
129	Australe	Mare	42	105.427	-42.709
130	Australe	Mare	42	105.204	-43.136
131	Australe	Mare	46	107.434	-47.532
132	Australe	Mare	46	107.199	-46.792
133	Australe	Mare	47	102.026	-44.940
134	Australe	Mare	47	102.880	-45.379
135	Australe	Mare	47	101.372	-46.360
136	Australe	Mare	48	104.263	-53.826
137	Australe	Mare	48	103.629	-52.769
138	Australe	Mare	48	105.478	-53.489
139	Australe	Mare	48	105.536	-53.502
140	Australe	Mare	49	104.342	-54.907
141	Australe	Mare	49	103.916	-55.766
142	Australe	Mare	49	102.401	-55.639
143	Australe	Mare	50	101.583	-55.139
144	Australe	Mare	51	97.202	-52.885
145	Australe	Mare	51	97.461	-52.972
146	Australe	Mare	52	104.904	-56.487
147	Australe	Mare	52	105.590	-56.656
148	Australe	Mare	54	105.424	-58.543
149	Australe	Mare	54	105.878	-59.265
150	Australe	Mare	54	103.591	-59.001
151	Australe	Mare	54	99.364	-56.711
152	Australe	Mare	55	94.608	-50.627
153	Australe	Mare	55	93.823	-50.388
154	Australe	Mare	55	92.867	-49.767
155	Australe	Mare	56	95.402	-49.113
156	Australe	Mare	57	108.063	-51.340
157	Australe	Mare	58	114.699	-49.852
158	Australe	Mare	59	113.862	-52.128
159	Australe	Mare	66	101.808	-43.646
160	Australe	Mare	66	101.964	-41.485
161	Australe	Mare	66	100.454	-41.238
162	Australe	Mare	67	105.870	-38.873
163	Australe	Mare	67	105.741	-38.543
164	Australe	Mare	67	105.809	-39.743
165	Australe	Mare	68	107.063	-37.231
166	Australe	Mare	68	107.482	-38.442
167	Australe	Mare	69	104.502	-37.225
168	Australe	Mare	69	105.162	-36.335
169	Australe	Mare	69	103.023	-35.763

170	Australe	Mare	70	84.454	-35.566
171	Australe	Mare	72	100.135	-36.707
172	Australe	Mare	72	100.373	-36.767
173	Australe	Mare	72	99.120	-36.505
174	Australe	Mare	72	99.342	-36.038
175	Australe	Mare	74	95.805	-46.657
176	Australe	Mare	74	95.797	-47.878
177	Australe	Mare	74	99.056	-45.435
178	Australe	Mare	74	97.486	-48.508
179	Australe	Mare	75	99.140	-50.698
180	Australe	Mare	76	92.441	-36.556
181	Australe	Mare	76	93.807	-35.804
182	Australe	Mare	76	92.200	-36.563
183	Australe	Mare	77	96.250	-34.666
184	Australe	Mare	77	94.413	-33.762
185	Australe	Mare	77	92.311	-32.556
186	Australe	Mare	77	97.611	-37.024
187	Australe	Mare	77	98.498	-38.717
188	Australe	Mare	77	99.932	-39.509
189	Australe	Mare	77	103.541	-39.785
190	Australe	Mare	78	94.563	-38.753
191	Australe	Mare	79	93.759	-38.483
192	Australe	Mare	79	93.795	-38.836
193	Australe	Mare	79	91.159	-41.788
194	Australe	Mare	83	84.358	-37.545
195	Australe	Mare	84	82.313	-37.225
196	Australe	Mare	82	84.439	-39.727
197	Australe	Mare	84	85.132	-61.743
198	Australe	Mare	84	85.024	-61.384
199	Balmer	Cryptomare	0,1,2	61.283	-24.282
200	Balmer	Cryptomare	0,1,2	61.320	-24.422
201	Balmer	Cryptomare	0,1,2	60.763	-27.132
202	Balmer	Cryptomare	0,1,2	60.829	-27.182
203	Balmer	Cryptomare	3	70.664	-23.406
204	Balmer	Cryptomare	4	72.900	-22.798
205	Balmer	Cryptomare	4	72.464	-22.758
206	Balmer	Cryptomare	4	72.494	-22.675
207	Balmer	Cryptomare	5	68.359	-20.156
208	Balmer	Cryptomare	5	64.991	-20.065
209	Balmer	Cryptomare	5	63.596	-20.739
210	Balmer	Cryptomare	5	71.993	-20.088
211	Balmer	Cryptomare	5	72.214	-18.190
212	Balmer	Cryptomare	5	70.903	-19.866

213	Balmer	Mare	0	60.639	-23.382
214	Balmer	Mare	0	60.899	-23.416
215	Balmer	Mare	0	61.188	-23.765
216	Balmer	Mare	0	61.604	-23.671
217	Balmer	Mare	1,2	81.616	-29.902
218	Balmer	Mare	1,2	80.612	-29.555
219	Balmer	Mare	1,2	79.668	-29.838
220	Balmer	Mare	1,2	79.669	-29.143
221	Balmer	Mare	1,2	79.401	-29.009
222	Balmer	Mare	1,2	79.112	-29.150
223	Balmer	Mare	1,2	78.914	-29.113
224	Balmer	Mare	3	62.223	-18.868
225	Balmer	Mare	3	62.549	-19.164
226	Balmer	Mare	3	62.404	-19.164
227	Balmer	Mare	4	70.638	-24.721
228	Balmer	Mare	4	70.702	-24.474
229	Balmer	Mare	4	71.064	-24.809
230	Balmer	Mare	4	70.818	-25.444
231	Balmer	Mare	4	71.410	-25.398
232	Balmer	Mare	4	71.500	-25.047
233	Balmer	Mare	4	71.877	-25.031
234	Balmer	Mare	5	61.867	-15.762
235	Balmer	Mare	5	63.044	-16.464
236	Balmer	Mare	5	62.533	-17.053
237	Balmer	Mare	5	60.496	-17.155
238	Balmer	Mare	5	60.533	-16.666
239	Balmer	Mare	5	62.622	-17.610
240	Balmer	Mare	6	60.814	-17.853
241	Balmer	Mare	7	59.776	-19.934
242	Balmer	Mare	8	60.874	-19.112
243	Balmer	Mare	8	60.699	-19.266
244	Balmer	Mare	12	79.066	-25.338
245	Balmer	Mare	12	78.943	-25.501
246	Balmer	Mare	12	80.111	-24.910
247	Balmer	Mare	13	82.346	-25.703
248	Balmer	Mare	13	82.813	-25.592
249	Balmer	Mare	13	82.870	-26.005
250	Balmer	Mare	13	82.842	-26.043
251	Balmer	Mare	13	83.307	-25.838
252	Balmer	Mare	13	83.367	-25.898
253	Dewar	Cryptomare	0	165.233	-1.631
254	Dewar	Cryptomare	0	165.511	-1.793
255	Dewar	Cryptomare	0	166.951	-1.869

256	Dewar	Cryptomare	0	167.388	-2.443
257	Frigoris	Cryptomare	0	41.903	59.560
258	Frigoris	Cryptomare	0	42.227	59.237
259	Frigoris	Cryptomare	0	42.592	59.387
260	Frigoris	Cryptomare	1	41.552	55.589
261	Frigoris	Cryptomare	1	41.640	55.707
262	Frigoris	Cryptomare	1	40.077	55.863
263	Frigoris	Cryptomare	1	39.474	55.652
264	Frigoris	Cryptomare	1	39.377	55.579
265	Frigoris	Cryptomare	2	13.304	49.377
266	Frigoris	Cryptomare	2	13.049	50.276
267	Frigoris	Cryptomare	2	12.467	52.074
268	Frigoris	Cryptomare	3	-22.278	52.439
269	Frigoris	Cryptomare	3	-22.601	52.388
270	Frigoris	Cryptomare	5	-22.573	50.856
271	Frigoris	Cryptomare	5	-23.019	50.827
272	Frigoris	Mare	A	-36.248	55.428
273	Frigoris	Mare	A	-35.960	56.662
274	Frigoris	Mare	A	-37.437	55.796
275	Frigoris	Mare	A	-47.726	50.456
276	Frigoris	Mare	A	-47.872	49.721
277	Frigoris	Mare	B	7.547	57.410
278	Frigoris	Mare	B	2.662	57.382
279	Frigoris	Mare	B	-45.632	55.424
280	Frigoris	Mare	B	-29.732	59.411
281	Frigoris	Mare	B	36.388	53.764
282	Frigoris	Mare	B	29.105	54.485
283	Hercules	Cryptomare	0	47.786	50.597
284	Hercules	Cryptomare	0	47.912	50.700
285	Hercules	Cryptomare	0	48.004	50.648
286	Hercules	Cryptomare	0	47.819	50.557
287	Hercules	Cryptomare	1	51.119	45.296
288	Hercules	Cryptomare	1	52.659	45.093
289	Hercules	Cryptomare	1	52.511	44.756
290	Hercules	Cryptomare	1	52.576	44.622
291	Hercules	Cryptomare	2	49.748	49.793
292	Hercules	Cryptomare	2	50.102	49.608
293	Hercules	Cryptomare	2	48.530	49.111
294	Hercules	Cryptomare	2	48.052	49.723
295	Hercules	Cryptomare	3	47.217	43.319
296	Hercules	Cryptomare	3	47.375	43.084
297	Hercules	Cryptomare	3	47.369	42.857
298	Hercules	Cryptomare	3	47.038	42.950

299	Hercules	Cryptomare	4	37.319	44.813
300	Hercules	Cryptomare	4	36.713	44.990
301	Hercules	Cryptomare	4	35.920	45.608
302	Hercules	Cryptomare	4	36.058	47.169
303	Hercules	Cryptomare	4	37.367	48.082
304	Hercules	Mare	0	49.620	50.544
305	Hercules	Mare	0	49.344	50.529
306	Hercules	Mare	0	50.042	50.587
307	Hercules	Mare	1	53.293	50.787
308	Hercules	Mare	1	51.668	51.044
309	Hercules	Mare	1	50.927	50.841
310	Hercules	Mare	1	48.967	51.230
311	Hercules	Mare	3	53.221	49.661
312	Hercules	Mare	3	53.346	49.708
313	Hercules	Mare	3	53.398	49.917
314	Hercules	Mare	4	38.731	47.243
315	Hercules	Mare	4	38.744	47.074
316	Hercules	Mare	4	38.444	46.985
317	Hercules	Mare	4	38.768	46.629
318	Humboldtianum	Cryptomare	0	83.464	54.299
319	Humboldtianum	Cryptomare	1	82.948	53.922
320	Humboldtianum	Cryptomare	1	82.777	53.815
321	Humboldtianum	Cryptomare	1	82.056	53.842
322	Humboldtianum	Cryptomare	2	86.119	54.321
323	Humboldtianum	Cryptomare	2	85.123	54.072
324	Humboldtianum	Cryptomare	2	85.085	54.002
325	Humboldtianum	Cryptomare	2	84.760	54.158
326	Humboldtianum	Cryptomare	2	83.882	53.950
327	Humboldtianum	Cryptomare	3	75.842	58.792
328	Humboldtianum	Cryptomare	3	76.915	58.364
329	Humboldtianum	Cryptomare	3	79.195	58.488
330	Humboldtianum	Cryptomare	3	79.366	58.983
331	Humboldtianum	Cryptomare	3	80.005	59.348
332	Humboldtianum	Cryptomare	3	80.100	58.844
333	Humboldtianum	Cryptomare	4	87.474	58.968
334	Humboldtianum	Cryptomare	4	88.851	58.712
335	Humboldtianum	Cryptomare	4	88.042	58.039
336	Humboldtianum	Cryptomare	4	86.673	58.222
337	Humboldtianum	Cryptomare	5	88.233	55.005
338	Humboldtianum	Cryptomare	5	88.334	55.151
339	Humboldtianum	Cryptomare	6	70.292	52.369
340	Humboldtianum	Cryptomare	6	70.655	52.657
341	Humboldtianum	Cryptomare	6	70.744	52.944

342	Humboldtianum	Cryptomare	7	68.140	57.747
343	Humboldtianum	Cryptomare	7	68.143	57.668
344	Humboldtianum	Cryptomare	7	66.483	57.914
345	Humboldtianum	Cryptomare	8	66.984	59.477
346	Humboldtianum	Cryptomare	8	67.669	59.331
347	Humboldtianum	Cryptomare	9	64.110	60.801
348	Humboldtianum	Cryptomare	9	65.278	61.271
349	Humboldtianum	Cryptomare	9	64.110	62.158
350	Humboldtianum	Cryptomare	9	66.357	61.500
351	Humboldtianum	Cryptomare	10	68.718	61.385
352	Humboldtianum	Cryptomare	10	69.060	61.258
353	Humboldtianum	Cryptomare	11	64.553	63.900
354	Humboldtianum	Cryptomare	11	64.722	64.283
355	Humboldtianum	Mare	0	78.784	58.017
356	Humboldtianum	Mare	0	78.510	56.684
357	Humboldtianum	Mare	0	77.816	56.556
358	Humboldtianum	Mare	0	79.448	55.600
359	Humboldtianum	Mare	0	83.002	56.430
360	Humboldtianum	Mare	0	85.046	56.469
361	Humboldtianum	Mare	0	82.449	55.190
362	Humboldtianum	Mare	1	80.675	54.553
363	Humboldtianum	Mare	1	80.669	54.480
364	Humboldtianum	Mare	1	80.446	54.393
365	Humboldtianum	Mare	2	71.885	54.266
366	Humboldtianum	Mare	2	71.978	54.032
367	Humboldtianum	Mare	2	72.525	53.999
368	Humboldtianum	Mare	2	73.878	53.710
369	Humboldtianum	Mare	2	73.708	53.147
370	Humboldtianum	Mare	3	74.757	52.739
371	Humboldtianum	Mare	3	74.804	52.801
372	Humboldtianum	Mare	4	69.232	57.145
373	Humboldtianum	Mare	4	70.301	57.397
374	Humboldtianum	Mare	4	68.622	56.158
375	Humboldtianum	Mare	4	68.189	55.188
376	Humboldtianum	Mare	4	70.863	56.766
377	Humboldtianum	Mare	4	69.502	54.505
378	Humboldtianum	Mare	4	69.642	54.424
379	Humboldtianum	Mare	4	70.410	53.636
380	Humboldtianum	Mare	5	64.763	60.245
381	Humboldtianum	Mare	5	64.121	59.958
382	Humboldtianum	Mare	5	64.193	59.246
383	Humboldtianum	Mare	5	64.693	58.816
384	Humboldtianum	Mare	5	66.098	59.125

385	Humboldtianum	Mare	6	85.620	52.042
386	Humboldtianum	Mare	6	85.739	52.134
387	Langemak	Cryptomare	0	115.239	-5.758
388	Langemak	Cryptomare	0	116.062	-4.249
389	Langemak	Cryptomare	2	117.766	-11.930
390	Langemak	Cryptomare	2	118.451	-11.596
391	Langemak	Mare	0	119.417	-10.364
392	Langemak	Mare	0	118.907	-9.983
393	Lomonosov-Fleming	Cryptomare	1	99.239	16.447
394	Lomonosov-Fleming	Cryptomare	1	98.481	17.059
395	Lomonosov-Fleming	Cryptomare	2	107.116	22.647
396	Lomonosov-Fleming	Cryptomare	2	104.961	20.369
397	Lomonosov-Fleming	Cryptomare	2	96.626	21.083
398	Lomonosov-Fleming	Cryptomare	2	108.038	22.851
399	Lomonosov-Fleming	Mare	0	98.936	28.219
400	Lomonosov-Fleming	Mare	0	98.735	27.431
401	Lomonosov-Fleming	Mare	0	98.001	27.466
402	Lomonosov-Fleming	Mare	0	98.434	28.244
403	Lomonosov-Fleming	Mare	0	98.353	26.665
404	Lomonosov-Fleming	Mare	1	94.617	25.200
405	Lomonosov-Fleming	Mare	1	94.642	24.521
406	Lomonosov-Fleming	Mare	1	92.358	24.314
407	Lomonosov-Fleming	Mare	1	94.141	26.522
408	Lomonosov-Fleming	Mare	1	92.209	25.571
409	Lomonosov-Fleming	Mare	3	99.754	24.519
410	Lomonosov-Fleming	Mare	3	99.294	25.152
411	Lomonosov-Fleming	Mare	4	97.662	30.021
412	Lomonosov-Fleming	Mare	4	99.197	30.079
413	Lomonosov-Fleming	Mare	4	99.868	30.711
414	Lomonosov-Fleming	Mare	5	105.179	25.250
415	Lomonosov-Fleming	Mare	5	105.257	25.903
416	Lomonosov-Fleming	Mare	5	103.127	25.752
417	Lomonosov-Fleming	Mare	5	103.715	25.263
418	Marginis	Cryptomare	1	77.175	17.202
419	Marginis	Cryptomare	2	77.036	18.136
420	Marginis	Cryptomare	6	89.427	17.577
421	Marginis	Cryptomare	6	89.676	17.745
422	Marginis	Cryptomare	6	89.356	18.159
423	Marginis	Cryptomare	7	90.493	10.758
424	Marginis	Cryptomare	7	93.912	11.555
425	Marginis	Cryptomare	7	94.449	7.861
426	Marginis	Cryptomare	8	98.960	6.073
427	Marginis	Cryptomare	8	98.348	5.212

428	Marginis	Cryptomare	9	98.212	4.211
429	Marginis	Cryptomare	9	98.295	4.217
430	Marginis	Cryptomare	9	98.850	3.652
431	Marginis	Cryptomare	10	97.215	5.757
432	Marginis	Cryptomare	10	95.892	6.324
433	Marginis	Mare	0	75.948	16.542
434	Marginis	Mare	0	76.006	16.657
435	Marginis	Mare	1	77.595	15.983
436	Marginis	Mare	2	79.274	14.444
437	Marginis	Mare	2	79.468	15.208
438	Marginis	Mare	2	80.012	13.904
439	Marginis	Mare	2	80.095	13.480
440	Marginis	Mare	2	79.542	13.652
441	Marginis	Mare	3	80.538	12.982
442	Marginis	Mare	3	80.320	12.367
443	Marginis	Mare	3	80.424	12.243
444	Marginis	Mare	3	80.166	12.111
445	Marginis	Mare	4	78.008	14.464
446	Marginis	Mare	4	77.214	13.433
447	Marginis	Mare	4	76.785	13.520
448	Marginis	Mare	4	77.896	12.803
449	Marginis	Mare	5	77.503	16.684
450	Marginis	Mare	5	78.036	15.999
451	Marginis	Mare	5	78.189	15.978
452	Marginis	Mare	5	78.103	16.074
453	Marginis	Mare	6	84.579	9.741
454	Marginis	Mare	6	83.207	8.724
455	Marginis	Mare	6	83.809	8.513
456	Marginis	Mare	6	84.626	7.722
457	Marginis	Mare	6	84.818	7.451
458	Marginis	Mare	7	80.266	8.567
459	Marginis	Mare	8	76.700	7.510
460	Marginis	Mare	8	76.795	7.503
461	Marginis	Mare	9	74.790	11.680
462	Marginis	Mare	11	91.250	19.716
463	Marginis	Mare	11	91.021	19.781
464	Marginis	Mare	11	90.984	19.431
465	Marginis	Mare	13	92.268	17.779
466	Marginis	Mare	13	92.874	17.540
467	Marginis	Mare	13	92.781	17.218
468	Marginis	Mare	14	83.077	18.294
469	Marginis	Mare	15	90.157	15.339
470	Marginis	Mare	15	89.147	15.355

471	Marginis	Mare	15	90.643	12.694
472	Marginis	Mare	15	90.093	12.032
473	Marginis	Mare	15	84.877	11.923
474	Marginis	Mare	15	84.365	13.026
475	Marginis	Mare	15	82.872	15.588
476	Marginis	Mare	15	83.147	17.533
477	Marginis	Mare	16	78.044	16.836
478	Marginis	Mare	16	78.156	16.863
479	Marginis	Mare	17	80.875	15.106
480	Marginis	Mare	18	82.468	13.017
481	Marginis	Mare	18	82.749	13.095
482	Marginis	Mare	21	75.478	11.607
483	Marginis	Mare	21	75.485	11.550
484	Marginis	Mare	22	89.725	19.004
485	Marginis	Mare	22	89.838	19.059
486	Marginis	Mare	22	89.886	18.996
487	Marginis	Mare	23	91.636	16.010
488	Marginis	Mare	23	91.752	15.917
489	Mendel-Rydberg	Cryptomare	0	-95.974	-50.766
490	Mendel-Rydberg	Cryptomare	0	-96.083	-50.534
491	Mendel-Rydberg	Cryptomare	0	-96.581	-50.701
492	Mendel-Rydberg	Cryptomare	1	-94.480	-49.759
493	Mendel-Rydberg	Cryptomare	1	-94.449	-49.908
494	Mendel-Rydberg	Cryptomare	1	-94.320	-50.431
495	Mendel-Rydberg	Cryptomare	1	-92.518	-47.575
496	Mendel-Rydberg	Cryptomare	2	-94.464	-47.016
497	Mendel-Rydberg	Cryptomare	2	-95.289	-49.638
498	Mendel-Rydberg	Cryptomare	2	-96.029	-48.082
499	Mendel-Rydberg	Cryptomare	2	-93.036	-46.498
500	Mendel-Rydberg	Mare	0	-104.714	-45.431
501	Mendel-Rydberg	Mare	0	-104.606	-45.303
502	Mendel-Rydberg	Mare	0	-104.783	-45.306
503	Mendel-Rydberg	Mare	1	-94.619	-51.910
504	Mendel-Rydberg	Mare	1	-94.752	-51.751
505	Mendel-Rydberg	Mare	2	-92.654	-50.453
506	Mendel-Rydberg	Mare	2	-93.083	-51.272
507	Mendel-Rydberg	Mare	2	-94.911	-50.800
508	Mendel-Rydberg	Mare	2	-92.468	-50.075
509	Mendel-Rydberg	Mare	2	-94.553	-51.428
510	Mendel-Rydberg	Mare	2	-93.850	-51.410
511	Mendel-Rydberg	Mare	3	-98.259	-50.225
512	Mendel-Rydberg	Mare	3	-97.969	-50.885
513	Mendel-Rydberg	Mare	3	-97.953	-51.061

514	Mendel-Rydberg	Mare	3	-98.346	-49.989
515	Mendel-Rydberg	Mare	3	-97.723	-50.170
516	Mendel-Rydberg	Mare	4	-97.859	-49.286
517	Mendel-Rydberg	Mare	5	-95.516	-51.649
518	Mendel-Rydberg	Mare	5	-95.239	-51.923
519	Mendel-Rydberg	Mare	5	-96.574	-51.785
520	Mendel-Rydberg	Mare	5	-96.354	-51.565
521	Milne	Cryptomare	0	115.470	-29.774
522	Milne	Cryptomare	0	114.706	-31.466
523	Schiller-Schickard	Cryptomare	0	-53.821	-44.169
524	Schiller-Schickard	Cryptomare	0	-53.213	-44.060
525	Schiller-Schickard	Cryptomare	0	-52.578	-43.486
526	Schiller-Schickard	Cryptomare	0	-55.329	-44.902
527	Schiller-Schickard	Cryptomare	1	-55.163	-50.708
528	Schiller-Schickard	Cryptomare	1	-55.476	-50.465
529	Schiller-Schickard	Cryptomare	1	-56.820	-50.416
530	Schiller-Schickard	Cryptomare	1	-56.399	-49.579
531	Schiller-Schickard	Cryptomare	5	-46.089	-33.892
532	Schiller-Schickard	Cryptomare	5	-49.493	-34.785
533	Schiller-Schickard	Cryptomare	5	-49.742	-34.049
534	Schiller-Schickard	Cryptomare	5	-48.519	-33.688
535	Schiller-Schickard	Cryptomare	6	-60.339	-34.013
536	Schiller-Schickard	Cryptomare	6	-60.366	-33.370
537	Schiller-Schickard	Cryptomare	6	-60.801	-34.683
538	Schiller-Schickard	Cryptomare	7	-58.021	-51.712
539	Schiller-Schickard	Cryptomare	7	-57.224	-51.642
540	Schiller-Schickard	Cryptomare	7	-57.652	-53.637
541	Schiller-Schickard	Cryptomare	7	-55.990	-52.198
542	Schiller-Schickard	Cryptomare	8	-37.134	-46.158
543	Schiller-Schickard	Cryptomare	8	-37.671	-46.249
544	Schiller-Schickard	Cryptomare	8	-37.035	-46.086
545	Schiller-Schickard	Cryptomare	9	-64.868	-53.282
546	Schiller-Schickard	Cryptomare	9	-64.900	-52.319
547	Schiller-Schickard	Cryptomare	9	-65.268	-51.756
548	Schiller-Schickard	Cryptomare	10	-65.971	-48.845
549	Schiller-Schickard	Cryptomare	10	-63.408	-45.579
550	Schiller-Schickard	Cryptomare	10	-63.809	-44.033
551	Schiller-Schickard	Cryptomare	10	-67.540	-44.531
552	Schiller-Schickard	Cryptomare	10	-60.507	-50.368
553	Schiller-Schickard	Cryptomare	10	-59.535	-50.181
554	Schiller-Schickard	Cryptomare	10	-64.670	-48.030
555	Schiller-Schickard	Cryptomare	11	-48.347	-52.578
556	Schiller-Schickard	Cryptomare	11	-45.509	-45.563

557	Schiller-Schickard	Cryptomare	11	-48.193	-42.798
558	Schiller-Schickard	Cryptomare	11	-52.071	-56.493
559	Schiller-Schickard	Cryptomare	11	-47.062	-48.127
560	Schiller-Schickard	Cryptomare	11	-49.685	-51.014
561	Schiller-Schickard	Cryptomare	11	-50.751	-50.109
562	Schiller-Schickard	Cryptomare	12	-53.112	-50.685
563	Schiller-Schickard	Cryptomare	12	-51.912	-51.027
564	Schiller-Schickard	Cryptomare	12	-52.617	-51.142
565	Schiller-Schickard	Cryptomare	13	-45.767	-48.563
566	Schiller-Schickard	Cryptomare	13	-46.288	-49.115
567	Schiller-Schickard	Cryptomare	13	-46.613	-48.924
568	Schiller-Schickard	Mare	A	-67.786	-36.151
569	Schiller-Schickard	Mare	A	-68.394	-35.686
570	Schiller-Schickard	Mare	A	-68.097	-35.881
571	Schiller-Schickard	Mare	A	-68.265	-35.966
572	Schiller-Schickard	Mare	A	-67.450	-36.152
573	Schiller-Schickard	Mare	B	-57.462	-33.657
574	Schiller-Schickard	Mare	B	-58.214	-33.072
575	Schiller-Schickard	Mare	B	-56.949	-33.337
576	Schiller-Schickard	Mare	B	-58.030	-33.524
577	Schiller-Schickard	Mare	B	-57.296	-33.515
578	Schiller-Schickard	Mare	C	-60.249	-34.307
579	Schiller-Schickard	Mare	C	-60.131	-34.529
580	Schiller-Schickard	Mare	C	-60.397	-34.438
581	Schiller-Schickard	Mare	C	-60.299	-34.513
582	Schiller-Schickard	Mare	C	-60.232	-34.511
583	Schiller-Schickard	Mare	D	-45.882	-35.302
584	Schiller-Schickard	Mare	D	-45.480	-34.736
585	Schiller-Schickard	Mare	D	-45.496	-35.505
586	Schiller-Schickard	Mare	D	-45.851	-35.522
587	Schiller-Schickard	Mare	E	-64.054	-38.729
588	Schiller-Schickard	Mare	E	-63.261	-37.697
589	Schiller-Schickard	Mare	E	-62.844	-36.158
590	Schiller-Schickard	Mare	E	-63.616	-37.128
591	Schiller-Schickard	Mare	E	-63.111	-38.849
592	Schiller-Schickard	Mare	E	-63.810	-39.254
593	Schiller-Schickard	Mare	F	-54.790	-37.312
594	Schiller-Schickard	Mare	F	-54.579	-37.452
595	Schiller-Schickard	Mare	F	-55.551	-37.364
596	Schiller-Schickard	Mare	F	-54.590	-37.262
597	Schiller-Schickard	Mare	F	-55.048	-37.638
598	Schiller-Schickard	Mare	G	-50.732	-38.391
599	Schiller-Schickard	Mare	G	-51.875	-38.262

600	Schiller-Schickard	Mare	G	-50.992	-37.670
601	Schiller-Schickard	Mare	G	-51.035	-37.583
602	Schiller-Schickard	Mare	G	-51.645	-38.087
603	Schiller-Schickard	Mare	H	-45.931	-35.942
604	Schiller-Schickard	Mare	H	-46.766	-37.085
605	Schiller-Schickard	Mare	H	-47.890	-37.123
606	Schiller-Schickard	Mare	H	-48.173	-37.189
607	Schiller-Schickard	Mare	H	-47.088	-37.053
608	Schiller-Schickard	Mare	H	-46.332	-36.624
609	Schiller-Schickard	Mare	I	-35.485	-36.813
610	Schiller-Schickard	Mare	I	-35.643	-36.216
611	Schiller-Schickard	Mare	I	-35.106	-36.503
612	Schiller-Schickard	Mare	I	-35.052	-36.656
613	Schiller-Schickard	Mare	J	-55.826	-41.621
614	Schiller-Schickard	Mare	J	-55.199	-42.860
615	Schiller-Schickard	Mare	J	-57.786	-43.404
616	Schiller-Schickard	Mare	J	-54.760	-42.069
617	Schiller-Schickard	Mare	J	-56.604	-43.047
618	Schiller-Schickard	Mare	J	-54.735	-42.931
619	Schiller-Schickard	Mare	K	-52.057	-46.501
620	Schiller-Schickard	Mare	K	-51.152	-45.359
621	Schiller-Schickard	Mare	K	-51.522	-44.967
622	Schiller-Schickard	Mare	K	-52.868	-46.140
623	Schiller-Schickard	Mare	K	-51.608	-45.435
624	Schiller-Schickard	Mare	K	-51.623	-45.557
625	Smythii	Cryptomare	1	81.008	2.576
626	Smythii	Cryptomare	1	81.087	2.896
627	Smythii	Cryptomare	2	78.321	2.485
628	Smythii	Cryptomare	2	79.082	2.547
629	Smythii	Cryptomare	2	79.154	2.700
630	Smythii	Cryptomare	2	79.157	2.328
631	Smythii	Cryptomare	3	80.797	1.023
632	Smythii	Cryptomare	3	80.672	0.899
633	Smythii	Cryptomare	4	94.693	4.390
634	Smythii	Cryptomare	4	94.674	4.342
635	Smythii	Cryptomare	5	92.154	-0.027
636	Smythii	Cryptomare	7	76.728	-2.429
637	Smythii	Cryptomare	7	76.223	-2.326
638	Smythii	Cryptomare	8	78.692	-3.133
639	Smythii	Cryptomare	9	79.126	-0.229
640	Smythii	Cryptomare	9	78.839	-0.599
641	Smythii	Cryptomare	9	79.552	-0.585
642	Smythii	Cryptomare	9	79.526	-1.641

643	Smythii	Cryptomare	10	83.041	-3.374
644	Smythii	Cryptomare	10	82.161	-2.933
645	Smythii	Cryptomare	10	81.331	-0.518
646	Smythii	Cryptomare	10	81.575	-0.003
647	Smythii	Cryptomare	10	81.598	0.149
648	Smythii	Cryptomare	13	75.818	2.129
649	Smythii	Mare	1	83.911	-6.266
650	Smythii	Mare	1	83.657	-6.165
651	Smythii	Mare	1	83.718	-6.031
652	Smythii	Mare	1	83.528	-5.697
653	Smythii	Mare	12, 13	81.271	-4.492
654	Smythii	Mare	15	84.757	-2.177
655	Smythii	Mare	15	84.587	-2.491
656	Smythii	Mare	15	84.461	-2.809
657	Smythii	Mare	15	84.688	-2.768
658	Smythii	Mare	18	84.256	2.037
659	Smythii	Mare	18	84.311	1.987
660	Smythii	Mare	20	82.782	-0.732
661	Smythii	Mare	20	83.028	-0.321
662	Smythii	Mare	20	83.456	-0.681
663	Smythii	Mare	20	83.568	-1.411
664	Smythii	Mare	20	83.559	-1.093
665	Smythii	Mare	23	84.513	0.694
666	Smythii	Mare	23	84.781	0.739
667	Smythii	Mare	23	84.716	1.102
668	Smythii	Mare	24	92.058	-1.197
669	Smythii	Mare	24	91.870	-0.954
670	Smythii	Mare	24	91.988	-0.719
671	Smythii	Mare	24	91.994	-0.544
672	Smythii	Mare	26	92.016	-2.348
673	Smythii	Mare	26	91.900	-2.685
674	Smythii	Mare	26	92.036	-2.606
675	Smythii	Mare	26	92.577	-2.386
676	Smythii	Mare	26	93.037	-3.283
677	Smythii	Mare	26	92.836	-3.377
678	Smythii	Mare	27	89.223	3.825
679	Smythii	Mare	27	89.989	3.940
680	Smythii	Mare	27	90.111	3.631
681	Smythii	Mare	27	91.620	3.641
682	Smythii	Mare	27	91.963	3.240
683	Smythii	Mare	27	91.531	2.714
684	Smythii	Mare	27	91.668	0.484
685	Smythii	Mare	27	91.871	0.971

686	Smythii	Mare	28	84.773	-0.648
687	Smythii	Mare	30	81.599	-2.329
688	Smythii	Mare	30	81.421	-2.129
689	Smythii	Mare	35	77.558	3.299
690	Smythii	Mare	35	78.159	3.262
691	Smythii	Mare	36	76.700	0.390
692	Smythii	Mare	36	76.756	0.389
693	Smythii	Mare	36	76.697	0.763
694	Smythii	Mare	37	76.036	0.388
695	Smythii	Mare	37	76.217	0.434
696	Smythii	Mare	37	76.040	0.084
697	Smythii	Mare	37	75.853	-0.030
698	Smythii	Mare	38	75.345	4.759
699	Smythii	Mare	38	75.173	4.569
700	Smythii	Mare	38	75.625	4.207
701	Smythii	Mare	38	75.668	4.129
702	Smythii	Mare	40	75.082	-3.633
703	Smythii	Mare	40	74.865	-3.253
704	Smythii	Mare	40	75.186	-2.792
705	Smythii	Mare	41	76.456	-3.885
706	Smythii	Mare	42	81.862	-5.486
707	Smythii	Mare	42	81.894	-5.497
708	South Pole-Aitken	Cryptomare	0	-171.002	-45.683
709	South Pole-Aitken	Cryptomare	0	-171.470	-45.118
710	South Pole-Aitken	Cryptomare	0	-171.801	-44.739
711	South Pole-Aitken	Cryptomare	1	-171.936	-46.325
712	South Pole-Aitken	Cryptomare	1	-171.798	-46.407
713	South Pole-Aitken	Cryptomare	2	-171.437	-46.729
714	South Pole-Aitken	Cryptomare	2	-171.123	-46.745
715	South Pole-Aitken	Cryptomare	3	-173.351	-49.211
716	South Pole-Aitken	Cryptomare	4	-165.421	-46.673
717	South Pole-Aitken	Cryptomare	4	-164.835	-46.642
718	South Pole-Aitken	Cryptomare	5	-163.199	-46.984
719	South Pole-Aitken	Cryptomare	6	-161.865	-47.048
720	South Pole-Aitken	Cryptomare	6	-161.866	-47.171
721	South Pole-Aitken	Cryptomare	7	-178.973	-48.793
722	South Pole-Aitken	Cryptomare	7	-178.149	-48.643
723	South Pole-Aitken	Cryptomare	7	-178.254	-48.941
724	South Pole-Aitken	Cryptomare	8	-161.397	-51.351
725	South Pole-Aitken	Cryptomare	8	-161.295	-51.399
726	South Pole-Aitken	Cryptomare	9	-162.958	-52.748
727	South Pole-Aitken	Cryptomare	9	-163.468	-52.702
728	South Pole-Aitken	Cryptomare	9	-162.910	-52.503

729	South Pole-Aitken	Cryptomare	10	-160.779	-52.324
730	South Pole-Aitken	Cryptomare	10	-160.455	-52.130
731	South Pole-Aitken	Cryptomare	10	-159.837	-52.647
732	South Pole-Aitken	Cryptomare	11	-150.604	-47.955
733	South Pole-Aitken	Cryptomare	11	-157.603	-46.863
734	South Pole-Aitken	Cryptomare	11	-156.000	-45.975
735	South Pole-Aitken	Cryptomare	11	-154.946	-44.693
736	South Pole-Aitken	Cryptomare	12	-157.656	-52.180
737	South Pole-Aitken	Cryptomare	13	-158.969	-53.723
738	South Pole-Aitken	Cryptomare	13	-160.473	-55.629
739	South Pole-Aitken	Cryptomare	13	-157.621	-57.431
740	South Pole-Aitken	Cryptomare	13	-155.311	-57.070
741	South Pole-Aitken	Mare	0	-150.245	-35.195
742	South Pole-Aitken	Mare	0	-151.958	-35.414
743	South Pole-Aitken	Mare	0	-152.881	-35.885
744	South Pole-Aitken	Mare	0	-152.826	-37.062
745	South Pole-Aitken	Mare	0	-150.465	-35.995
746	South Pole-Aitken	Mare	4	-158.988	-35.508
747	South Pole-Aitken	Mare	4	-158.858	-35.961
748	South Pole-Aitken	Mare	4	-158.679	-37.037
749	South Pole-Aitken	Mare	4	-159.558	-37.598
750	South Pole-Aitken	Mare	5	-166.344	-51.533
751	South Pole-Aitken	Mare	5	-166.076	-51.918
752	South Pole-Aitken	Mare	6	-164.052	-51.641
753	South Pole-Aitken	Mare	6	-163.215	-51.785
754	South Pole-Aitken	Mare	8	-159.041	-40.641
755	South Pole-Aitken	Mare	9	-157.181	-41.185
756	South Pole-Aitken	Mare	9	-152.162	-41.412
757	South Pole-Aitken	Mare	9	-151.933	-41.364
758	South Pole-Aitken	Mare	10	-161.851	-50.685
759	South Pole-Aitken	Mare	10	-161.700	-50.645
760	South Pole-Aitken	Mare	11	-161.363	-50.010
761	South Pole-Aitken	Mare	11	-161.168	-49.542
762	South Pole-Aitken	Mare	11	-161.729	-49.549
763	South Pole-Aitken	Mare	12	-161.648	-48.731
764	South Pole-Aitken	Mare	12	-161.466	-48.699
765	South Pole-Aitken	Mare	13	-170.522	-44.443
766	South Pole-Aitken	Mare	13	-171.234	-44.144
767	South Pole-Aitken	Mare	14	-171.048	-46.178
768	South Pole-Aitken	Mare	14	-170.749	-46.408
769	South Pole-Aitken	Mare	15	-170.144	-46.972
770	South Pole-Aitken	Mare	15	-170.060	-46.942
771	South Pole-Aitken	Mare	15	-170.897	-46.920

772	South Pole-Aitken	Mare	16	-172.688	-48.639
773	South Pole-Aitken	Mare	16	-172.399	-47.842
774	South Pole-Aitken	Mare	17	-166.285	-45.419
775	South Pole-Aitken	Mare	17	-163.542	-45.124
776	South Pole-Aitken	Mare	17	-163.306	-46.638
777	South Pole-Aitken	Mare	18	-161.859	-47.780
778	South Pole-Aitken	Mare	18	-161.798	-47.729
779	South Pole-Aitken	Mare	19	-152.923	-53.295
780	South Pole-Aitken	Mare	19	-151.937	-53.872
781	South Pole-Aitken	Mare	19	-151.106	-52.670
782	South Pole-Aitken	Mare	20	-175.288	-37.212
783	South Pole-Aitken	Mare	20	-175.331	-37.942
784	South Pole-Aitken	Mare	20	-175.502	-38.354
785	South Pole-Aitken	Mare	21	-161.867	-53.247
786	South Pole-Aitken	Mare	21	-161.727	-53.196
787	South Pole-Aitken	Mare	22	-162.567	-51.960
788	South Pole-Aitken	Mare	22	-162.393	-51.926
789	South Pole-Aitken	Mare	23	-162.570	-51.409
790	South Pole-Aitken	Mare	23	-163.004	-51.374
791	South Pole-Aitken	Mare	23	-162.138	-51.141
792	South Pole-Aitken	Mare	24	-161.929	-52.228
793	South Pole-Aitken	Mare	24	-162.247	-52.478
794	South Pole-Aitken	Mare	24	-162.120	-52.390
795	South Pole-Aitken	Mare	25	-160.132	-54.385
796	South Pole-Aitken	Mare	25	-160.077	-54.406
797	South Pole-Aitken	Mare	26	-159.662	-52.033
798	South Pole-Aitken	Mare	26	-158.856	-52.675
799	South Pole-Aitken	Mare	26	-159.294	-52.746
800	South Pole-Aitken	Mare	26	-159.298	-53.106
801	South Pole-Aitken	Mare	28	-159.017	-51.191
802	South Pole-Aitken	Mare	28	-158.757	-51.269
803	South Pole-Aitken	Mare	29	-173.353	-56.275
804	South Pole-Aitken	Mare	29	-175.185	-54.677
805	South Pole-Aitken	Mare	29	-174.016	-54.573
806	South Pole-Aitken	Mare	29	-173.698	-54.500
807	South Pole-Aitken	Mare	30	-171.635	-58.366
808	South Pole-Aitken	Mare	30	-171.354	-57.868
809	South Pole-Aitken	Mare	30	-169.249	-57.703
810	South Pole-Aitken	Mare	31	-169.278	-56.283
811	South Pole-Aitken	Mare	31	-169.458	-56.544
812	Taruntius	Cryptomare	0	46.477	3.929
813	Taruntius	Cryptomare	0	45.936	3.093
814	Taruntius	Cryptomare	1	47.555	6.017

815	Taruntius	Cryptomare	1	47.709	6.001
816	Taruntius	Cryptomare	1	47.663	6.108
817	Taruntius	Cryptomare	2	47.956	5.425
818	Taruntius	Cryptomare	2	48.051	5.512
819	Taruntius	Cryptomare	2	47.795	5.351
820	Taruntius	Cryptomare	3	44.417	5.714
821	Taruntius	Cryptomare	3	43.753	6.959
822	Taruntius	Cryptomare	3	45.060	6.356
823	Taruntius	Cryptomare	4	44.564	4.313
824	Taruntius	Cryptomare	4	44.344	4.450
825	Taruntius	Mare	0	47.370	3.617
826	Taruntius	Mare	0	47.587	3.351
827	Taruntius	Mare	0	44.389	7.797
828	Taruntius	Mare	0	45.575	7.045
829	Taruntius	Mare	0	45.603	7.509
830	Taruntius	Mare	0	47.948	8.120
831	Taruntius	Mare	0	48.910	6.372
832	Taruntius	Mare	0	46.633	3.315
833	Taruntius	Mare	1	46.309	5.388
834	Lacus Solidutidinis	Cryptomare	2	115.163	-25.816
835	Lacus Solidutidinis	Cryptomare	2	115.525	-24.722
836	Lacus Solidutidinis	Cryptomare	3	122.362	-25.849
837	Lacus Solidutidinis	Cryptomare	3	121.529	-27.041
838	Lacus Solidutidinis	Cryptomare	3	119.804	-27.669
839	Lacus Solidutidinis	Cryptomare	4	119.197	-28.687
840	Lacus Solidutidinis	Cryptomare	4	119.111	-29.451
841	Lacus Solidutidinis	Cryptomare	5	118.267	-26.015
842	Lacus Solidutidinis	Cryptomare	5	118.185	-26.796
843	Lacus Solidutidinis	Cryptomare	8	105.364	-25.860
844	Lacus Solidutidinis	Cryptomare	8	104.891	-26.459
845	Lacus Solidutidinis	Cryptomare	8	104.859	-27.399
846	Lacus Solidutidinis	Cryptomare	8	104.995	-27.582
847	Lacus Solidutidinis	Cryptomare	9	124.245	-26.568
848	Lacus Solidutidinis	Cryptomare	9	124.678	-26.131
849	Lacus Solidutidinis	Mare	12	127.758	-26.120
850	Lacus Solidutidinis	Mare	12	127.789	-26.170
851	Lacus Solidutidinis	Mare	14	128.675	-26.040
852	Lacus Solidutidinis	Mare	14	128.551	-25.777
853	Lacus Solidutidinis	Mare	16	125.354	-33.400
854	Lacus Solidutidinis	Mare	16	126.056	-33.044
855	Lacus Solidutidinis	Mare	16	126.422	-33.389
856	Lacus Solidutidinis	Mare	36	146.838	-17.988
857	Lacus Solidutidinis	Mare	36	147.749	-17.802

858	Lacus Solidutidinis	Mare	36	147.859	-17.106
859	Lacus Solidutidinis	Mare	56	103.290	-26.638
860	Lacus Solidutidinis	Mare	56	103.316	-26.543
861	Lacus Solidutidinis	Mare	57	103.196	-24.591
862	Lacus Solidutidinis	Mare	57	102.707	-25.089
863	Lacus Solidutidinis	Mare	57	102.905	-25.345
864	Lacus Solidutidinis	Mare	57	103.287	-25.224
865	Lacus Solidutidinis	Mare	59	103.709	-25.773
866	Lacus Solidutidinis	Mare	59	103.942	-26.022
867	Lacus Solidutidinis	Mare	59	103.879	-27.170
868	Lacus Solidutidinis	Mare	59	104.249	-27.458
869	Lacus Solidutidinis	Mare	59	104.311	-27.839
870	West Humorum	Cryptomare	2	-64.461	-27.481
871	West Humorum	Cryptomare	3	-60.074	-15.347
872	West Humorum	Cryptomare	3	-61.426	-15.090
873	West Humorum	Cryptomare	5	-46.775	-18.429
874	West Humorum	Cryptomare	5	-46.573	-17.888
875	West Humorum	Cryptomare	5	-46.433	-18.260
876	West Humorum	Cryptomare	6	-48.058	-17.607
877	West Humorum	Cryptomare	6	-48.060	-17.882
878	West Humorum	Cryptomare	9	-49.479	-28.989
879	West Humorum	Cryptomare	11	-47.926	-31.449
880	West Humorum	Cryptomare	11	-47.889	-31.369
881	West Humorum	Cryptomare	11	-47.929	-31.535
882	West Humorum	Cryptomare	12	-50.551	-25.769
883	West Humorum	Cryptomare	12	-50.571	-25.666
884	West Humorum	Cryptomare	12	-50.674	-25.789
885	West Humorum	Cryptomare	12	-50.918	-26.026
886	West Humorum	Mare	0	-68.689	-17.323
887	West Humorum	Mare	2	-66.144	-15.776
888	West Humorum	Mare	3	-67.229	-16.753
889	West Humorum	Mare	3	-66.852	-17.140
890	West Humorum	Mare	3	-66.932	-16.597
891	West Humorum	Mare	4	-65.788	-17.528
892	West Humorum	Mare	5	-67.426	-15.370
893	West Humorum	Mare	5	-67.424	-15.724
894	West Humorum	Mare	6	-68.719	-14.617
895	West Humorum	Mare	6	-68.598	-15.660
896	West Humorum	Mare	6	-68.553	-14.143
897	West Humorum	Mare	7	-70.026	-13.511
898	West Humorum	Mare	7	-69.380	-13.715
899	West Humorum	Mare	10	-66.318	-17.704
900	West Humorum	Mare	10	-66.230	-17.669

901	West Humorum	Mare	14	-64.735	-16.765
902	West Humorum	Mare	14	-64.802	-16.916
903	West Humorum	Mare	15	-65.394	-15.659
904	West Humorum	Mare	16	-66.809	-13.419
905	West Humorum	Mare	16	-66.713	-13.425
906	West Humorum	Mare	17	-65.368	-13.015
907	West Humorum	Mare	18	-67.416	-13.722
908	West Humorum	Mare	19	-64.738	-13.633
909	West Humorum	Mare	19	-65.255	-14.192
910	West Humorum	Mare	19	-63.937	-14.148
911	West Humorum	Mare	21	-68.490	-27.997
912	West Humorum	Mare	22	-67.940	-28.542
913	West Humorum	Mare	22	-67.814	-28.240
914	West Humorum	Mare	22	-68.259	-28.485
915	West Humorum	Mare	25	-65.870	-27.941
916	West Humorum	Mare	25	-65.998	-28.184
917	West Humorum	Mare	25	-66.158	-27.858
918	West Humorum	Mare	26	-66.530	-28.287
919	West Humorum	Mare	27	-65.637	-28.736
920	West Humorum	Mare	28	-47.344	-26.248
921	West Humorum	Mare	28	-47.460	-26.319
922	West Humorum	Mare	30	-47.701	-26.586
923	West Humorum	Mare	30	-47.961	-26.025
924	West Humorum	Mare	30	-48.078	-27.108
925	West Humorum	Mare	31	-49.205	-29.972
926	West Humorum	Mare	31	-49.819	-29.801
927	West Humorum	Mare	31	-49.328	-29.944
928	West Humorum	Mare	32	-46.809	-30.377
929	West Humorum	Mare	33	-46.664	-30.099
930	West Humorum	Mare	33	-46.411	-30.192
931	West Humorum	Mare	33	-47.141	-29.223
932	West Humorum	Mare	34	-50.762	-29.551
933	West Humorum	Mare	34	-50.548	-30.355
934	West Humorum	Mare	34	-50.914	-29.902
935	West Humorum	Mare	35	-52.895	-25.908
936	West Humorum	Mare	36	-51.298	-27.239
937	West Humorum	Mare	40	-45.707	-26.183
938	West Humorum	Mare	41	-36.856	-33.430
939	West Humorum	Mare	41	-36.855	-33.429
940	West Humorum	Mare	42	-50.373	-13.957
941	West Humorum	Mare	42	-49.717	-13.994
942	West Humorum	Mare	43	-52.179	-17.369
943	West Humorum	Mare	43	-52.154	-15.745

944	West Humorum	Mare	44	-51.461	-19.114
945	West Humorum	Mare	45	-51.516	-17.945
946	West Humorum	Mare	45	-51.714	-17.863
947	West Humorum	Mare	45	-51.375	-17.965
948	West Humorum	Mare	46	-50.948	-15.559
949	West Humorum	Mare	46	-50.138	-15.958
950	West Humorum	Mare	46	-51.688	-15.066
951	West Humorum	Mare	47	-49.467	-15.236
952	West Humorum	Mare	48	-47.203	-16.723
953	West Humorum	Mare	48	-47.202	-17.118
954	West Humorum	Mare	48	-47.497	-17.019
955	West Humorum	Mare	49	-33.262	-29.465
956	West Procelllarum	Cryptomare	5, 13, 20	-74.924	-2.001
957	West Procelllarum	Cryptomare	5, 13, 20	-75.387	-2.786
958	West Procelllarum	Cryptomare	5, 13, 20	-75.857	-2.226
959	West Procelllarum	Cryptomare	5, 13, 20	-75.130	-1.849
960	West Procelllarum	Cryptomare	12	-67.404	-3.554
961	West Procelllarum	Cryptomare	12	-68.113	-2.835
962	West Procelllarum	Cryptomare	12	-67.111	-3.331
963	West Procelllarum	Cryptomare	21	-77.813	5.863
964	West Procelllarum	Cryptomare	23	-64.173	4.900
965	West Procelllarum	Cryptomare	23	-64.498	4.607
966	West Procelllarum	Cryptomare	24	-71.510	6.012
967	West Procelllarum	Cryptomare	24	-70.847	6.266
968	West Procelllarum	Cryptomare	25	-70.698	6.731
969	West Procelllarum	Cryptomare	25	-70.598	6.612
970	West Procelllarum	Cryptomare	26	-69.424	7.820
971	West Procelllarum	Cryptomare	26	-68.736	7.942
972	West Procelllarum	Cryptomare	26	-69.315	7.277
973	West Procelllarum	Cryptomare	28	-70.463	7.561
974	West Procelllarum	Cryptomare	30	-71.813	9.605
975	West Procelllarum	Cryptomare	30	-75.243	12.092
976	West Procelllarum	Cryptomare	30	-74.478	10.687
977	West Procelllarum	Cryptomare	31	-76.799	13.332
978	West Procelllarum	Cryptomare	34	-81.043	8.470
979	West Procelllarum	Cryptomare	34	-80.791	8.395
980	West Procelllarum	Cryptomare	35	-81.452	7.957
981	West Procelllarum	Cryptomare	36	-79.908	7.346
982	West Procelllarum	Cryptomare	37	-81.141	8.869
983	West Procelllarum	Cryptomare	37	-80.917	9.002
984	West Procelllarum	Mare	0	-81.629	-2.819
985	West Procelllarum	Mare	6	-77.554	3.822
986	West Procelllarum	Mare	6	-77.701	3.511

987	West Procelllarum	Mare	7	-76.877	4.022
988	West Procelllarum	Mare	7	-76.713	4.105
989	West Procelllarum	Mare	9	-75.775	3.611
990	West Procelllarum	Mare	10	-67.752	-4.441
991	West Procelllarum	Mare	10	-67.748	-5.649
992	West Procelllarum	Mare	10	-66.179	-5.395
993	West Procelllarum	Mare	10	-67.852	-7.318
994	West Procelllarum	Mare	10	-70.125	-4.576
995	West Procelllarum	Mare	11	-66.429	1.942
996	West Procelllarum	Mare	11	-66.314	1.534
997	West Procelllarum	Mare	13	-68.753	9.071
998	West Procelllarum	Mare	13	-68.645	9.213
999	West Procelllarum	Mare	18	-68.053	13.133
1000	West Procelllarum	Mare	18	-62.798	8.082
1001	West Procelllarum	Mare	18	-63.084	6.710
1002	West Procelllarum	Mare	18	-62.714	8.858
1003	West Procelllarum	Mare	18	-67.259	12.677
1004	West Procelllarum	Mare	20	-74.029	-2.236
1005	West Procelllarum	Mare	20	-73.827	-1.894
1006	West Procelllarum	Mare	20	-73.557	-2.283

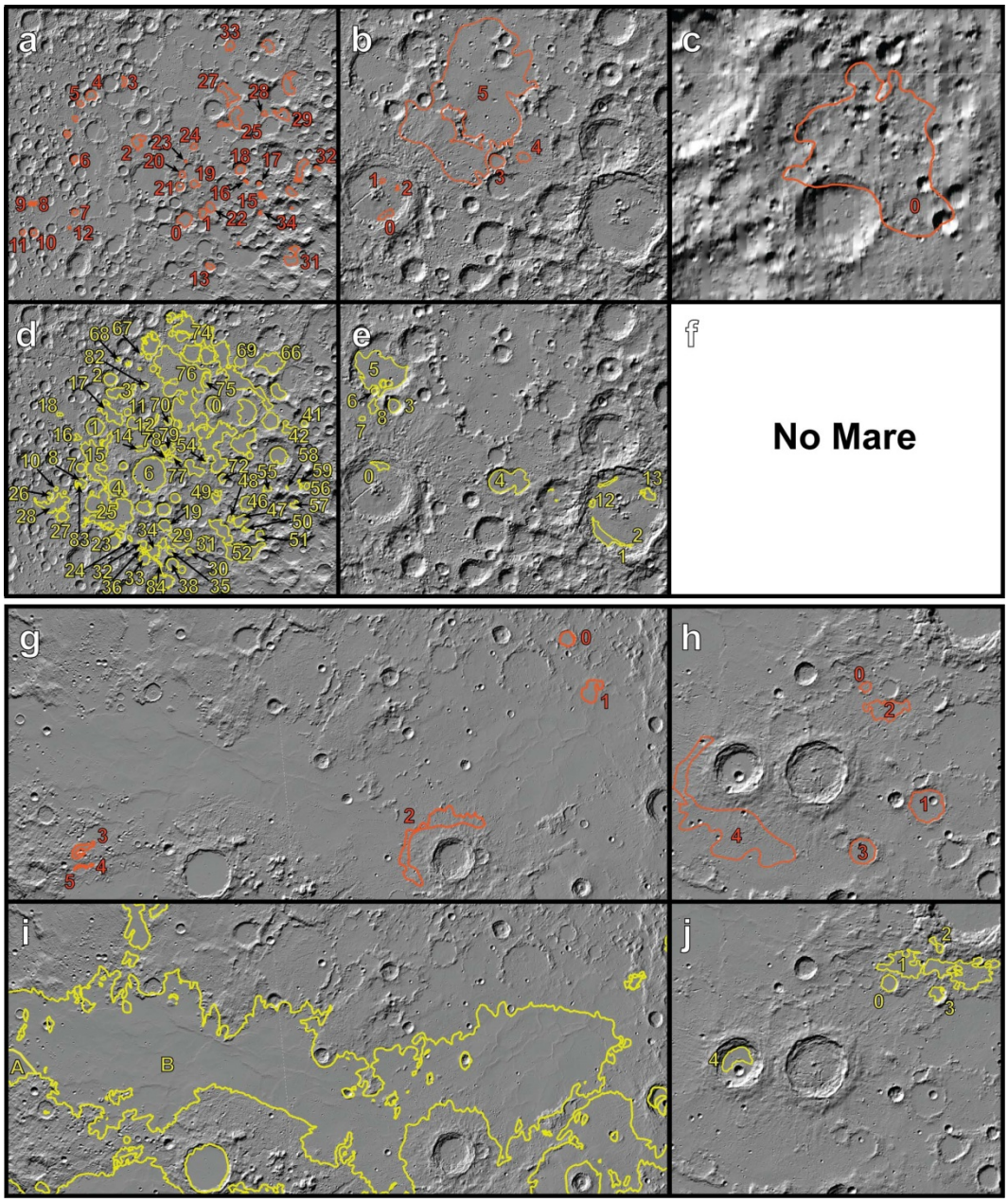

Figure A1.

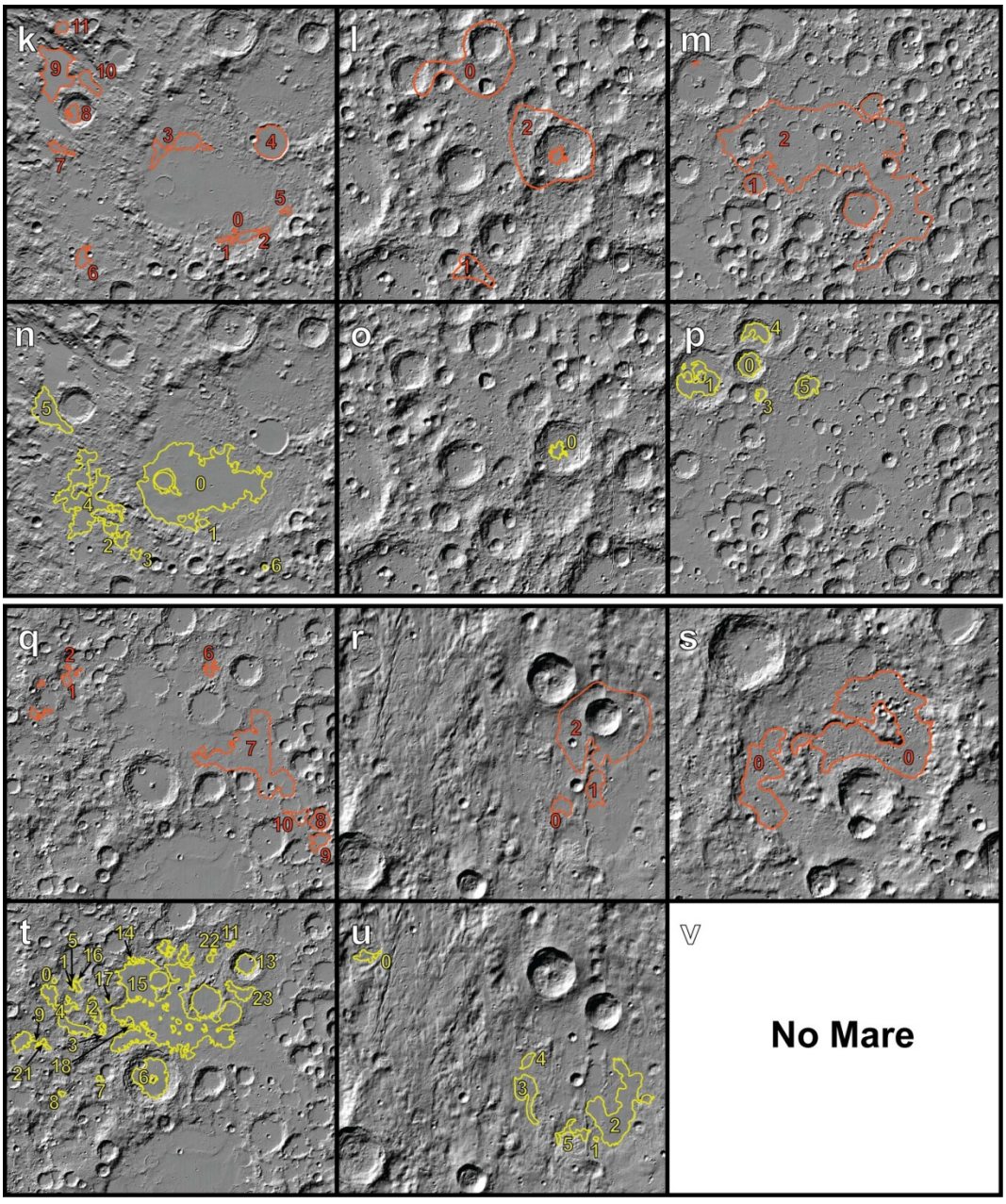

Figure A1. continued

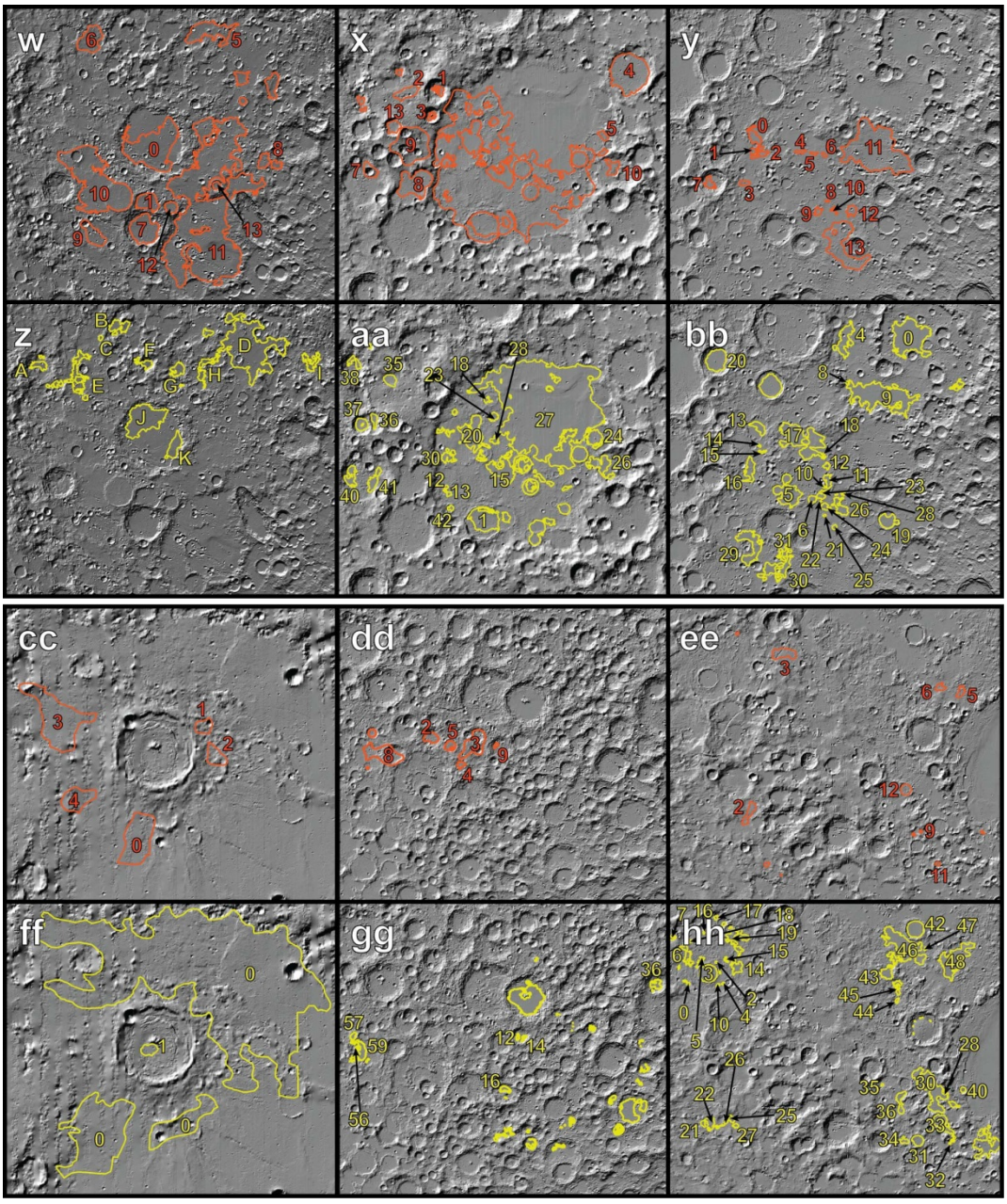

Figure A1. continued

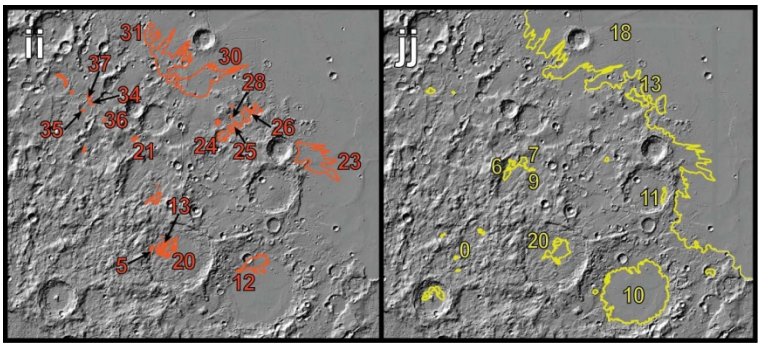

Figure A1. continued

Chapter 4:
Intercrater plains on Mercury: Insights into unit definition, characterization, and origin from MESSENGER datasets

Jennifer L. Whitten[a,],
James W. Head[a], Brett W. Denevi[b], and Sean C. Solomon[c,d]

[a]Department of Geological Sciences, Brown University, Providence, RI 02912, USA
[b]The Johns Hopkins University Applied Physics Laboratory, Laurel, MD 20723, USA
[c]Department of Terrestrial Magnetism, Carnegie Institution of Washington, Washington, DC 20015, USA
[d]Lamont-Doherty Earth Observatory, Columbia University, Palisades, NY 10964, USA

Submitted to:
Icarus, March 2013

Abstract

Orbital observations by the MErcury Surface, Space ENvironment, GEochemistry, and Ranging (MESSENGER) spacecraft are used to re-evaluate the nature and origin of the oldest mapped plains deposits on Mercury, the intercrater and intermediate plains units defined by Mariner 10 investigators. Despite the large areal extent of these plains, which comprise approximately one-third of the planetary surface area viewed by Mariner 10, their formation mechanism was not well constrained by Mariner 10 imaging. One hypothesis attributed plains formation to ponding of fluidized impact ejecta to create relatively smooth surfaces. Another hypothesis was that these plains are of volcanic origin. To assess the origin of these older plains and the contribution of early volcanism to resurfacing on Mercury, we have used MESSENGER data to analyze the morphology, spectral properties, impact crater statistics, and topography of Mariner 10 type-areas of intercrater and intermediate plains. On the basis of new criteria for the identification of intercrater and intermediate plains derived from these observations, we have remapped 18% of the surface of Mercury. We find that the intercrater plains are a highly textured unit with an abundance of secondary craters, whereas the intermediate plains are composed of both intercrater and smooth plains. We suggest that the term “intermediate plains” not be used to map the surface of Mercury henceforth, but rather this unit should be subdivided into its constituent intercrater and smooth plains units. We argue that a substantial percentage of the intercrater plains are composed of volcanic materials on the basis of (1) examples of areas where ejecta from a small number of superposed craters have transformed smooth plains deposits of volcanic origin into a unit indistinguishable from intercrater plains; (2) the range in ages of intercrater plains deposits as interpreted

from crater size-frequency distributions; and (3) the near-global distribution of intercrater plains compared with the uneven distribution of impact basins and their associated ejecta deposits.

1. Introduction

The first spacecraft images of Mercury were obtained by Mariner 10 (M10) during three flybys in 1974–1975. M10 imaged approximately 40% of the planet's surface (Fig. 1), ~55% of which was covered with several different plains deposits. The earliest geological interpretation of images from the first M10 flyby (Murray et al., 1974) included a regional map showing three distinct geologic units: plains material, hilly and lineated terrain, and heavily cratered terrain. The intercrater plains unit shortly thereafter was identified as a subdivision of this "heavily cratered terrain" marked by level to gently rolling, densely cratered surfaces between craters >30 km in diameter (Trask and Guest, 1975; Trask, 1976). From geologic maps (Trask and Guest, 1975; Schaber and McCauley, 1980; DeHon et al., 1981; Guest and Greeley, 1983; McGill and King, 1983; Grolier and Boyce, 1984; Spudis and Prosser, 1984; Trask and Dzurisin, 1984; King and Scott, 1990; Strom et al., 1990) constructed from M10 images, it is clear that the intercrater plains are the most widespread unit on the portion of the planet imaged by that spacecraft. A distinguishing characteristic of the intercrater plains is their high density of small, superposed craters 5–15 km in diameter (Trask and Guest, 1975; Strom, 1977; Leake, 1981). According to Trask and Guest (1975), the majority of these small craters are likely to be secondary impact craters formed from material ejected from larger craters (>30 km in diameter) within the heavily cratered terrain. The superposition of these secondary craters was invoked as evidence that the majority of the intercrater plains are older than the heavily cratered terrain (Trask and Guest, 1975). This observed stratigraphic relationship and inferred relative age, combined with the unit extent and crater size-frequency distributions, led to the hypothesis that the intercrater plains are

remnants of a volcanic surface that partially predated a period of heavy bombardment of the terrestrial planets (Murray et al., 1975; Trask and Guest, 1975).

The findings from the Apollo 16 mission to the Moon, however, called into question a volcanic origin for plains units on Mercury. Before the Apollo 16 mission, the high-reflectance Cayley plains on which the Apollo 16 astronauts landed were thought to be products of highland volcanism (Milton, 1964; Wilhelms and McCauley, 1971). During the mission (Young et al., 1972) and thereafter (Hodges et al., 1973; Muehlberger et al., 1980), however, the abundance of brecciated material in returned samples (Gast et al., 1973) indicated that these light plains were produced by impact-related processes involving some combination of local, regional, and basin-related material (Eggleton and Schaber, 1972; Head, 1974; Oberbeck et al., 1974). This discovery from the Moon, along with the lack of distinct contrasts in reflectance between surrounding morphologic units on Mercury (Hapke et al., 1975; Rava and Hapke, 1987) and the muted morphology of local wrinkle ridges there (e.g., Strom et al., 1975), prompted some researchers to explore the idea that the intercrater plains on Mercury were emplaced as fluidized ejecta from basin impacts (Wilhelms, 1976; Oberbeck et al., 1977). The surface morphology and albedo relationships on Mercury matched Cayley plains material more closely than those of the volcanic lunar mare deposits.

The dominant formation mechanism for the intercrater plains on Mercury continues to be debated, with ideas for the unit's formation focused on two hypotheses: (1) formation as volcanic flows (Murray et al., 1974, 1975; Strom, 1977; Kiefer and Murray, 1987; Spudis and Guest, 1988) and (2) formation by the emplacement of fluidized impact ejecta, an origin similar to that hypothesized for the Cayley plains on the

Moon (Trask and Guest, 1975; Wilhelms, 1976; Oberbeck et al., 1977). Another plains unit, the intermediate plains defined in some geological maps constructed from M10 images (Schaber and McCauley, 1980; Guest and Greeley, 1983; McGill and King, 1983; Grolier and Boyce, 1984; Spudis and Prosser, 1984; Trask and Dzurisin, 1984; King and Scott, 1990; Strom et al., 1990), shares many of the same characteristics as the intercrater plains (except that it is less densely cratered), including an uncertain formation origin.

Widespread resurfacing occurred early in Mercury's geologic history, as evidenced by a deficit of craters 20–100 km in diameter compared with the lunar highlands, and at least a portion of that resurfacing is thought to have occurred by the emplacement of intercrater plains (Fassett et al., 2011; Strom et al., 2011; Marchi et al., 2013). The global distribution of these ancient intercrater plains has a substantial influence on the interpretation of the geologic history of Mercury. If most or all of the intercrater plains are volcanic in origin, then volcanism played a substantial role on Mercury during its earliest history. However, if most of these deposits are impact-related, then a different thermal evolution is implied, perhaps more like that of the Moon, for which the onset of major mare volcanism occurred near the end of the late heavy bombardment of the inner solar system and partially flooded an earlier crust (Taylor, 1989) of distinctly different composition (e.g., Shearer et al., 2006).

To address these issues, we use observations from the MErcury Surface, Space ENvironment, GEochemistry, and Ranging (MESSENGER) spacecraft, in orbit about Mercury since March 2011, to assess several type areas of intercrater and intermediate plains units defined during geologic mapping from M10 images, and we revisit the interpretations of these areas. In the sections that follow we utilize the high-resolution

image and topography data provided by the MESSENGER mission, together with the M10 geologic maps, to define more clearly the intermediate and intercrater plains units in order to understand their origin and role in the geologic history of Mercury and to provide criteria for future mapping. Considerable uncertainty remains regarding the influence and extent of volcanic activity early in Mercury's history, so the confident identification of volcanic units can provide important information about the volcanic flux and thermal history and its relationship to the thermal history of other planetary bodies (e.g., Head and Solomon, 1981). A goal of this analysis is to provide new insights into the definition and distinction of the intercrater and intermediate plains and their origins and to formulate improved guidelines for the definition and use of these unit terms for future analyses with MESSENGER data and in planning for the upcoming BepiColombo mission of the European Space Agency and the Japan Aerospace Exploration Agency (Benkhoff et al., 2010).

2. Methods

To characterize intercrater and intermediate plains, we have examined the M10 geologic unit definitions and used MESSENGER data to reassess and refine these definitions further. Ten different areas located between 0° and 180°E longitude (Fig. 1 and Table 1) and previously mapped with M10 data (Fig. 3, column 4) (Schaber and McCauley, 1980; Guest and Greeley, 1983; McGill and King, 1983; Grolier and Boyce, 1984; Spudis and Prosser, 1984; Trask and Dzurisin, 1984) were chosen for analysis. To facilitate comparison, half of the study regions selected for our reanalysis were originally mapped from M10 images predominantly as intermediate plains, and the other half were

mapped predominantly as intercrater plains. These 10 regions were chosen on the basis of the size and continuity of the geologic unit, and all have approximately the same area (~ 130,000 km^2). For each of the 10 study regions we analyzed images acquired by the MESSENGER Mercury Dual Imaging System (MDIS; Hawkins et al., 2007) and topographic maps and profiles derived from Mercury Laser Altimeter (MLA; Cavanaugh et al., 2007) observations (Fig. 3, columns 1 and 2).

The size-frequency distributions of impact craters were determined for each study region (Fig. 1) to estimate relative ages. MDIS images (Hawkins et al., 2007) were used to identify all visible craters, including embayed craters, greater than ~6 km in diameter (Strom et al., 2008). Including secondary craters in counts can cause a surface to appear older than it actually is because secondary craters on Mercury can have diameters as large as 10 km (e.g., Strom et al., 2008); craters <10 km in diameter were included in this study only if they did not display one of the morphologic characteristics of secondary craters, including an oblate rim, a herringbone pattern, or a location within a chain or cluster. To compare the areal density of impact craters and relative ages of the geologic units, we report values of $N(10)$ and $N(20)$ for each study area, where $N(D)$ is the number of craters with diameter $\geq D$ (in km) per 10^6 km^2 area within a given region. The standard deviation (σ) for each value of N(D) is taken to be equal to the square root of the number of craters per diameter bin per area, i.e., $\sigma = [\sqrt{N(D)}/A]\times 10^6 km^2$, where A is the unit area in km^2 (Crater Analysis Techniques Working Group, 1979).

MDIS images have also been used to characterize the morphology of these 10 study areas. Both a 250 m/pixel base map and individual MDIS wide-angle camera (WAC) and narrow-angle camera (NAC) images with resolutions <250 m/pixel were

obtained where available. M10 unit definitions were employed to evaluate the observed morphologies and determine if MESSENGER data support the original unit classification. M10 geologic units were compared with MDIS color image products, such as the global color unit map of Denevi et al. (2009), to determine if there is a correlation between morphologic and color boundaries and also if there are observable color differences within and between the morphologic units. The topography of the intercrater and intermediate plains study regions was characterized with individual MLA profiles, an MLA gridded data product (Zuber et al., 2012), and digital terrain models derived from stereo photogrammetric analysis (Edmundson et al., 2011; Becker et al., 2012) of MDIS images.

3. Results

3.1. Intercrater plains

3.1.1. Morphology

Most of the intercrater plains regions mapped from M10 images have a highly textured surface that appears substantially rougher in the higher-resolution MDIS images (Fig. 3, compare column 1, MESSENGER, and column 5, M10). This surface texture is created by small secondary craters (<10 km in diameter), which are degraded and partially filled with smooth material (Fig. 3a). Larger craters in the study regions are all but completely filled with smooth material, and their rims are almost totally obscured (e.g., Fig. 3a, f, k). Some of these craters would be impossible to identify were it not for the difference in texture between their smooth resurfaced interiors and the highly sculpted crater exterior. Fresh crater chains or secondary clusters are easily identified around

younger impact craters, and older crater chains can be identified by the alignment of degraded, filled secondary craters (Fig. 3u). Some study regions have isolated, irregular smooth patches intermixed with the heavily textured surface, and other study regions have parallel lobate scarps (e.g., Strom et al., 1975) that are typically associated with smoother geologic materials (i.e., Fig. 3u).

3.1.2. Topography

Topographic data, generally unavailable from M10, provide important information on the regional elevations of the intercrater plains study areas (Fig. 3, column 2). Three (ICP1, ICP2 and ICP3) of the five intercrater plains study regions are covered by MLA data; for all five study areas there are stereographic data. General agreement between the two topographic datasets in areas of overlap provides confidence that stereo photogrammetry may be used to compare and characterize the intercrater (and intermediate) plains study regions in areas where MLA data are not available. The intercrater plains occur at a variety of elevations, from -0.8 km to 0.5 km relative to a datum of 2440 km radius, according to the average elevation of each intercrater plains study region.

The intercrater plains are more varied in local relief than might be expected for a volcanic plains unit. As shown by Whitten and Head (2013b), heavily cratered terrain on the Moon that has been flooded by volcanic deposits tends to show a narrow range of elevations. In some settings, intercrater plains are seen on highland plateaus and in topographic depressions within close proximity (Fig. 3l). Many of the most abrupt variations in local topography within the intercrater plains are controlled by impact crater

ejecta deposits and degraded crater remnants. The modest relief in ICP1 is controlled by large, partially filled impact structures (Chong-Gauguin basin; Fassett et al., 2012), except for the low-lying southern portion of this study area. The 1.0 km elevation change across ICP2 (Fig. 3g) is gradual and is consistent with the lack of any fresh impacts >30 km diameter. In ICP3 the high relief (~1.6 km; Fig. 3l) is produced by the location of the study area on the edge of a plateau east of Budh Planitia, which accounts for the observed increase in topography northward (Fig. 1). There are several depressions formed from older impact structures in the southern portion of ICP3, but they are not part of the intercrater plains. ICP4 is on the western edge of a large, high-standing plateau that extends from 45°N to 45°S and 315°E to 0°E (Fig. 1b), creating ~2.8 km of relief (Fig. 3q) within the study region. The southwestern topographic low is related to an overlap of the "probable" ~830-km-diameter Andal-Coleridge basin (Fassett et al., 2012) with this study region (Fig. 1). ICP5 has a similar geometry; it lies partly on another high-standing plateau to the east-southeast of Tolstoj basin (Fig. 1) and has a relief of ~1.5 km (Fig. 3v); the low-lying topography in ICP5 contains no known major impact structures. The variation in the topography of intercrater plains could be the result of modification by superposed impact craters or changes to long-wavelength topography after plains emplacement (e.g., Zuber et al., 2012; Klimczak et al., 2013).

3.1.3. MDIS color units

Intercrater plains mapped from M10 images are represented in each of the MDIS color units defined by Denevi et al. (2009; Fig. 3, column 3), except for the low-reflectance blue plains (LBP). The majority of ICP3 and ICP5 were not mapped with the

flyby MDIS color data owing to poor illumination geometry or lack of coverage. Those regions that do overlap with the MESSENGER MDIS color flyby data are composed of multiple color units, including the high-reflectance red plains (HRP) and intermediate plains (IP), and low-reflectance material (LRM) (Fig. 3, column 3; Table 1), where red and blue denote more and less steeply increasing spectral reflectance from visible to near-infrared wavelengths, respectively. The HRP and IP units were mapped together by Denevi et al. (2009) and are therefore reported together in this paper. Texture differences can be used to distinguish the morphologically smooth HRP/IP unit from the other color units, but there is no consistent textural difference between LRM and geologic materials within other color units. Approximately 50% of both ICP2 and ICP4 are composed of HRP/IP, occurring either as interior material in impact basins and large craters or as a plains-like deposit outside of impact features. The remaining mapped area in ICP2 is composed of ~29% LRM, typically as widespread plains-like units. The remaining area in ICP4 was not mapped by Denevi et al. (2009). ICP1 is mostly composed of LRM material, with minor amounts of HRP/IP. There is no morphologic evidence for flow-like embayments between the different color units in the intercrater plains.

3.1.4. Crater statistics

Cumulative crater size-frequency distributions (SFDs) were computed for each of the five intercrater plains study regions (Fig. 4a-e). The superposed craters range in size from 6 km in diameter to several hundred kilometers in diameter. For most of the ICP study regions, the SFDs have a similar slope and density of impact craters, especially those <30 km in diameter, except for ICP1 and ICP5 (see below). Collectively, the crater

SFDs for intercrater plains overlap and have a slightly higher crater density at a given diameter than intermediate plains study regions (Fig. 4k).

As expected for Mercury, the steep slopes of the crater SFDs at diameters <10 km (Fig. 4a, e, f, i, j) are believed to be the result of secondary cratering (Strom et al., 2008; Xiao et al., 2014), an interpretation supported by the abundant secondary craters visible (Fig. 3, left column). Several of the crater SFDs have a steep roll-off for the bins at the largest crater diameters (ICP2, ICP4 and ICP5; Fig. 4b, d and e), consistent with the finding of others that Mercury is deficient in craters 20–100 km diameter relative to the Moon (Fassett et al., 2011). ICP1 has a lower density of craters 12–20 km diameter, a result that could be the result of resurfacing from Chong-Gauguin basin (~330 km in diameter), located in the northwest corner of the study region. The *N*(10) values for the intercrater plains study regions vary between 154±34 and 370±53, and *N*(20) values are between 62±22 and 162±35 (Table 1). These ranges correspond to Tolstojan to pre-Tolstojan ages (Fig. 5; Spudis and Guest, 1988).

The intercrater plains study regions were analyzed for spatial relationships between the locations of small secondary craters and the proximity of fresh impact craters. Nearby fresh impact craters could cause intercrater plains regions to be artificially aged by an abundance of secondary craters. To assess this possibility, the relationship between crater diameter and maximum distance of secondary craters (Gault et al., 1975) was extrapolated linearly to determine the maximum distance of secondary craters for 23 fresh impact craters adjacent to our study regions. We found no relationship between proximity of relatively fresh impact craters and the steepness of the upturn observed in the crater SFDs. Such a lack of a relationship is in part a result of our attempt

to exclude secondary craters from the crater counts; fresh secondary craters are much easier to identify and exclude from crater counts than degraded ones. Thus, the upturns observed in SFDs likely result from the inclusion of morphologically degraded secondary craters which, at this size range, are difficult to distinguish from degraded primary craters.

3.1.5. Intercrater plains: Summary

To summarize, intercrater plains are densely cratered at diameters <10 km in diameter, and this extensive cratering has created a highly textured surface. Despite the surface roughness, several broad morphologic features that might be the result of volcanism are distinguishable, such as large infilled craters (e.g., Fig. 3a, k, u), but no specific volcanic features (e.g., vents, flow fronts) were identified. The resolution of the MESSENGER dataset enabled the identification of these characteristic features, which are useful criteria for further mapping of intercrater plains and provide a sharper view of the surface than did M10 data (Fig. 3, column 5). The intercrater plains as defined and mapped do not have any clear relation with topography (Fig. 3, column 2). This unit covers high-standing plateaus and continues into topographic depressions. The intercrater deposits identified from M10 images are not composed of a single color unit (Denevi et al., 2009). Different regions of the intercrater plains have some of the reddest (HRP/IP) and bluest (LRM) spectral reflectance, as well as the highest (HRP/IP) and lowest (LRM) reflectance values, suggesting that whatever their origin(s), the intercrater plains have a range of color unit variations. We confirm the pre-Tolstojan and Tolstojan age estimates of these intercrater plains regions (Fig. 5).

3.2. Intermediate plains

3.2.1. Morphology

Most of the intermediate plains regions are composed of many moderately cratered smooth plains-like deposits (Fig. 6a, k, p) with some highly textured regions (Fig. 6f, u). The highly textured surfaces result from a combination of sculpted ejecta and small secondary craters and appear similar to the intercrater plains. Recent crater chains (Fig. 6a) and, in a few study regions, parallel lobate ridges (Fig. 6k) are observed. In the smoother regions there is evidence for buried craters (typically <25 km diameter), such as partially buried rims and wrinkle ridge rings (Fig. 6p). Such circular patterns of wrinkle ridges are believed to have been formed by compressional stresses localized by a shallowly buried crater rim crest (Guest and Fielder, 1968; Cruikshank et al., 1973; Watters, 1993; Freed et al., 2012; Watters et al., 2012) and are typically observed in volcanic terrains (e.g., Lambert R on the Moon and Mercury's northern smooth plains; Head et al., 2011). Impact-degraded craters are identified by filled interiors and disrupted crater rims that have been modified by ejecta from later impact events. A lunar example of an impact-modified crater is the Ptolemaeus crater, which was filled with Imbrium ejecta and had its rim scoured by Imbrium ejecta. Larger craters in intermediate plains are partially infilled (e.g., Fig. 6f, u), and the more degraded craters have lost most of their rim elevation.

3.2.2. Topography

IP1 is located within the Beethoven basin, and its surface slopes down toward the center of the basin (Fig. 6b). IP2 (Fig. 1) has a ridge through its center and slopes toward the northern smooth plains and Suisei Planitia to the south (total relief is ~2.0 km). Stereographic data show that IP3 (Fig. 1) has a large north–south trending trough (~175 km wide) with a total relief of ~1.2 km in the study area. The topography in IP4 (Fig. 6q) is generally low-lying, partially the result of an unnamed ~245-km-diameter crater in the northern part of the study region (Fig. 1). IP5 (Fig. 6v) is located within a heavily cratered region containing highly undulating crater topography (i.e., crater rims and depressions). MLA and stereographic data indicate that the morphologically smooth regions of the intermediate plains are located at lower elevations than the rougher textured material (intercrater plains). Similar to the case for intercrater plains, much of the observed topographic variability of intermediate plains could be the result of impact crater morphology (fresh or degraded) or changes to long-wavelength topography subsequent to plains emplacement (e.g., Zuber et al., 2012; Klimczak et al., 2013).

3.2.3. MDIS color units

Several of the selected intermediate plains study regions were mapped using the MESSENGER flyby color data (Denevi et al., 2009), including IP1, IP3, and IP4. IP2 and IP5 were not mapped owing to poor viewing conditions (Fig. 6, column 3; Table 1). The three regions of intermediate plains mapped are >50% HRP/IP, and the remaining area was unmapped. In contrast to the M10 intercrater plains, which are characterized by a wide variety of color units, the intermediate plains appear to have generally similar MDIS color characteristics; the unit is dominated by HRP/ IP material. This HRP/IP color

signature has also been correlated with the presence of smooth plains units identified by their morphology and interpreted to be of volcanic origin (e.g., Robinson et al., 2008; Denevi et al., 2009; Head et al., 2011). The agreement in MDIS color characteristics between the M10-defined intermediate plains and M10- and MESSENGER-defined smooth plains material is consistent with the observation of many small patches of smooth plains deposits within the M10-mapped intermediate plains (Fig. 6, column 1).

3.2.4. Crater statistics

As is the case with the intercrater plains, the intermediate plains study regions have an abundance of secondary craters, as indicated by the sharp upturn in crater SFDs at diameters <10 km (Fig. 4f-j). In IP2 and IP3 there is small break in slope at 10 km before the crater SFD levels out at the smallest crater diameters, likely due to incomplete counting in the smallest-diameter bins. Most of these crater SFDs cluster together on a cumulative plot (Fig. 4k). IP1 (Fig. 4f) is an outlier crater SFD, having a different shape to its distribution and a lower overall density of craters at all sizes. IP2 and IP3 are almost uniformly cratered across their surfaces and show a crater SFD more typical for intermediate plains (Fig. 4g, h). IP4 and IP5 show distributions (Fig. 4i, j) potentially indicative of resurfacing, an inference supported by embayed and partially buried craters in IP4 (Fig. 6p). The $N(10)$ values for the intermediate plains study regions have a larger range, from 77±24 to 361±53, than the intercrater plains study regions (Table 1). Calculated $N(20)$ values are between 31±15 and 115±30 and correspond to Calorian through pre-Tolstojan ages (Spudis and Guest, 1988). From the $N(20)$ values, IP1 is associated with the Calorian time period, along with many other smooth plains deposits

(Spudis and Guest, 1988). The *N*(10) and *N*(20) values for the four remaining intermediate plains regions correspond to the pre-Tolstojan time period (Fig. 5).

3.2.5. Intermediate plains: Summary

On the basis of high-resolution MESSENGER datasets, the intermediate plains unit defined at M10 resolution appears in the study regions examined here to be a combination of older intercrater plains units and younger smooth plains deposits, rather than a distinctive geologic unit. Fresh crater chains, lobate scarps, and buried craters are observed in this map unit (Fig. 6k). No volcanic landforms (e.g., vents, flow fronts) were detected within the unit. Many of the smooth plains associated with the M10-mapped intermediate plains are topographically lower than some of the other more heavily cratered parts (i.e., IP5; Fig. 6u, v). With the exception of IP1, all of these intermediate plains regions have crater size-frequency distributions that overlap with those for the intercrater plains (Fig. 4k) and correspond to pre-Tolstojan and Tolstojan times (Fig. 5; Table 1).

4. Discussion

4.1. Summary of intercrater and intermediate plains units

The intercrater and intermediate plains units require more stringent identification criteria than were used previously in order to avoid confusion. M10 mapping efforts indicated that the intercrater plains covered a third of the imaged surface of Mercury (e.g., Strom, 1977; Kiefer and Murray, 1987), and MESSENGER data support the conclusion of widespread intercrater plains deposits. Comparisons of the MESSENGER

and M10 image data (Fig. 3) show that the higher resolution and variety of the MESSENGER datasets have enabled a more detailed definition and analysis of the intercrater plains. However, in contrast to areas of smooth plains (Denevi et al., 2013a), the new MESSENGER data reveal no specific color or topographic characterization for intercrater plains that might permit distinction from surrounding units similarly older than smooth plains. MDIS color data show that the intercrater plains have variable color characteristics; all but the LBP color unit of Denevi et al. (2009) can be found in intercrater plains areas. There is no evident relation between topography and the distribution of intercrater plains; intercrater plains can be found in topographic lows, atop the highest plateaus on Mercury, and at elevations and slopes in between. According to our analysis of MESSENGER data, in support of the findings of M10 mappers, the intercrater plains can be most readily distinguished by a more densely cratered surface than that of the smooth plains (Fig. 3, column 1) and crater density values corresponding to the Tolstojan to pre-Tolstojan periods.

A comparison of MESSENGER (Fig. 6, column 1) and M10 (Fig. 6, column 5) images shows why ambiguity over the definition of the intermediate plains persisted. The lower resolution and illumination geometries of M10 data “smoothes away” some of the texture created by secondary impact craters (Fig. 6k, o, p and t), confusing unit identification. Our analysis indicates that intermediate plains mapped from M10 images are a combination of highly textured material and small pockets of smooth plains material (Fig. 6, column 1). The intermediate plains are composed primarily of the HRP/IP MDIS color unit, and in several study regions (i.e., IP3) the HRP/IP unit corresponds to the location of low-lying smooth plains deposits. In addition, the M10 intermediate plains

map unit has an abundance of secondary craters <10 km in diameter (i.e., upturn at 10 km; Fig. 4), sharing this defining quality of the intercrater plains. The majority of the M10 intermediate plains are dated as pre-Tolstojan (Fig. 5) on the basis of crater density values, suggesting that these deposits formed early in the geologic history of Mercury.

On the basis of this analysis, we propose that the definition of intercrater plains should include a highly textured surface morphology (Fig. 3a, f, k and p) with few smooth patches. The units we mapped had a high crater density, $N(10)$ >~225, and an upturn in their crater SFDs at diameters <10 km that is attributed to an abundance of secondary craters. Intermediate plains should be analyzed in detail and subdivided into either intercrater or smooth plains units; the highly textured regions with the abundance of secondary craters (as indicated by the upturn in the crater SFDs, Fig. 4) should be included in the intercrater plains unit, and patches of smooth plains material >750 km^2 (partially infilling craters ~50 km in diameter or greater) should be grouped with other smooth plains deposits. These proposed geologic unit definitions require the reclassification of several study regions, as described below.

IP1 is located in the center of Beethoven basin (Figs. 1, 6, 8), and on the basis of morphology, MDIS color, and crater size-frequency distribution it should be reclassified as smooth plains material (Denevi et al., 2013a). The $N(20)$ value of 31±15 for IP1 is comparable to smooth plains $N(20)$ values, which range from 10±10 to 45±12 (Fig. 5; Table 1; Denevi et al., 2013a). Other intermediate plains regions, including IP3 and IP4 (Figs. 1, 6, 8), should also be reclassified as smooth plains. The morphology of these two study regions is smooth with some small regions having a more intercrater-plains-like texture, again with smoother areas located at lower elevations. Low $N(10)$ values,

corresponding to a lower density of secondary craters, for IP3 and IP4 are closer to smooth plains values than to intercrater plains *N*(10) values (Table 1). The low *N*(10) value is in contrast to the higher *N*(20) values, suggestive of a pre-Tolstojan age. This apparent contradiction in crater density values may indicate an extended interval of volcanic eruptions, as detailed below (section 4.4.). The prevalence of the HRP/IP MDIS color unit (Denevi et al., 2009) in these two regions, coupled with the latest mapping of smooth plains deposits (Denevi et al., 2013a), supports such a reclassification of IP3 and IP4. IP5 (Figs. 1, 6, 8) shows the same general characteristics as IP3 and IP4. The morphology of the unit indicates that IP5 is likely to be an older smooth plains deposit. IP2, in contrast, should be mapped as intercrater plains, on the basis of its heavily cratered texture (Fig. 6, column 1) and intercrater plains-like crater size-frequency distribution (Table 1). The *N*(10) and *N*(20) values for IP2 are among the highest values for all of the study areas.

In addition to the reclassification of intermediate plains, there is one intercrater plains study region (ICP5) that, according to our interpretation of the *N*(10) crater density values (Table 1), should be labeled as smooth plains. However, the interpretation as smooth plains is not supported by the morphology of the study area. ICP5, located to the east of Tolstoj basin (Fig. 1), includes regions of smooth plains that embay older intercrater plains deposits. This interpretation of the local stratigraphy is supported by the topography data, with smooth plains located in low-lying areas and the older intercrater plains areas having higher elevations (Fig. 3v). The surface of ICP5 is covered with ancient northwest–southeast-trending secondary crater chains from Valmiki crater (~210 km diameter) and younger secondary craters from Sophocles crater (~142 km diameter).

The calculated $N(10)$ value of 154±34 is consistent with other smooth plains values, as is the $N(20)$ of 62±22 (Table 1). It appears as though the recent secondary impact modification has roughened the surface sufficiently to characterize ICP5 as intercrater plains; the conflict between the morphologic interpretation and the $N(10)$ and $N(20)$ values that are similar to those of smooth plains deposits indicate that, in this particular location, secondary crater production has outpaced that of primary impacts.

4.2. Discussion of criteria to distinguish intercrater plains formation processes

As noted above, two hypotheses have been proposed to explain the formation mechanism for intercrater plains, volcanism (Murray et al., 1974, 1975; Strom, 1977; Kiefer and Murray, 1987; Spudis and Guest, 1988) and emplacement as fluidized ejecta from large impacts (Wilhelms, 1976; Oberbeck et al., 1977). Here we discuss the identification criteria (Table 2) that may be useful in distinguishing between these hypotheses for specific intercrater plains deposits.

The Mariner 10 science team interpreted the intercrater plains to be mostly volcanic deposits, on the basis of the extensive areal distribution of the deposits (e.g., Murray et al., 1975) as a major piece of evidence. Mapped intercrater plains deposits are widespread across the surface of Mercury (Trask and Guest, 1975; Schaber and McCauley, 1980; Guest and Greeley, 1983; McGill and King, 1983; Grolier and Boyce, 1984; Spudis and Prosser, 1984; Trask and Dzurisin, 1984; King and Scott, 1990; Strom et al., 1990), implying that the formation process was active on essentially a global scale. The extensive nature of volcanic smooth plains, especially the northern smooth plains and Caloris (Fassett et al., 2009; Head et al., 2011; Denevi et al., 2013a), coupled with

models of magma ascent and eruption (Wilson and Head, 2008), suggests that flood basalt volcanism was the dominant eruption style for smooth plains on Mercury and may have been for intercrater plains as well.

Additionally, M10 data and the acquired MDIS global coverage of Mercury have revealed a deficit of craters 20–100 km in diameter compared with the Moon (e.g., Strom, 1977; Strom et al., 2008; Fassett et al., 2011), interpreted to be the result of volcanic plains formation during the period of heavy bombardment of the inner solar system. Basins >300 km in diameter on Mercury have an asymmetric distribution, with the majority of large basins occurring in the western hemisphere (Fassett et al., 2012). This asymmetric distribution of basins implies an asymmetric distribution of remaining impact basin deposits, and thus could indicate that older basins have been modified beyond recognition by volcanism instead of later impact events.

Volcanic deposits might be expected to have distinct compositional boundaries coincident with morphologic boundaries, in a manner similar to the smooth plains deposits (Robinson and Lucey, 1997; Robinson et al., 2008; Denevi et al., 2009; 2013a). Volcanic deposits might also contain volcanic vents or other diagnostic landforms (e.g., Head et al., 2009a, 2009b; Byrne et al., 2013; Hurwitz et al., 2013).

MESSENGER Gamma-Ray Spectrometer (GRS) measurements of the surface abundances of the radioactive elements Th, K, and U indicate that Mercury's interior heat production may have been four times higher ~4 billion years ago than at present (Peplowski et al., 2011). Such greater heat production could have supported partial melting of the mantle and widespread source regions for volcanic activity during the period of heavy bombardment. Additionally, the lack of a low-density anorthositic crust

and the low abundances of iron and titanium in volcanic materials on Mercury (Nittler et al., 2011) may have prevented the generation of magmas higher in density than average crustal material, in contrast to the situation on the Moon (e.g., Head and Wilson, 1992) and favorable to early surface eruptions.

Under the fluidized ejecta hypothesis, impact melt or impact ejecta and locally excavated material ponded in topographic lows and produced plains that were later covered with myriad secondary craters. Instead of forming large continuous deposits, such material was more likely to form discrete smaller deposits similar to the Imbrian smooth plains (Wilhelms and McCauley, 1971; Oberbeck et al., 1977; Meyer et al., 2013) that are concentrated in isolated patches around the lunar nearside basins. Regional heterogeneity in the color properties of intercrater plains might be expected if the unit were produced from impact-related processes, depending on the lateral and vertical heterogeneity of Mercury's crust (Denevi et al., 2009) and the depth of excavation of individual impacts. On the other hand, lunar light plains do not show major variations in color properties relative to background highlands; exceptions are subtle differences related to cryptomaria (e.g., Hawke and Spudis, 1980; Antonenko et al., 1995; Whitten and Head, 2013a). The heterogeneous MDIS color properties of intercrater plains could also result from mixing of crustal materials by the ~4 Gy of impacts after plains emplacement.

Cratering models for the terrestrial planets (e.g., Richardson, 2009) suggest that the lunar highlands are saturated (meaning that for each new crater formed another crater of similar diameter is destroyed). Mercury (Fassett et al., 2011) shows a size distribution of large craters (>128 km in diameter) similar to that of the Moon, providing support for

an impact-related origin for some intercrater plains deposits. Regardless of the dominant formation process, the intercrater plains have been extensively modified by primary and secondary impact cratering.

4.3. Geologic mapping

Analysis of the plains units identified in the M10 geologic maps with MESSENGER data suggests that surface morphology provides good criteria for the definition and identification of smooth plains, but poor criteria for the intercrater plains (i.e., the lack of color contrasts and extensive topographic variation) other than high values of crater density. A regional assessment and a remapping of these major units were completed over a broad study region spanning 18% of the surface of Mercury; the resulting map is shown in Fig. 7. This remapping exercise provides a basis for assessing the candidate modes of origin for intercrater and intermediate plains.

4.3.1. Definition of map units

Crater materials. Crater rims, central peaks, and ejecta deposits were mapped for all observable craters > 20 km in diameter. Buried craters were not mapped because their original morphology has been obscured by plains deposits. Digital terrain models from stereo photogrammetry and MDIS image data were used to determine the extent of crater ejecta blankets. Only the continuous ejecta deposit was mapped for most craters because its morphology is more readily distinguished for each individual crater. Determining the extent of the secondary crater field for individual impacts becomes more difficult with increasing crater degradation. Impact craters and their associated ejecta deposits obscure

the underlying material, making plains unit identification difficult in certain situations; these impacts could have superposed either smooth or intercrater plains deposits. Therefore for Fig. 7 we mapped only the uppermost surface unit.

Smooth plains. Analysis of MESSENGER data has not substantially changed the definition of the smooth plains deposits from the original unit definition developed by the M10 team. Smooth plains are level to gently sloped over distances of 100–200 km, and they have a low density of superposed craters (e.g., Trask and Guest, 1975; Denevi et al., 2013a). These deposits can be expansive, such as the Caloris exterior plains (e.g., Trask and Guest, 1975; Denevi et al., 2013a) and the northern smooth plains (Head et al., 2011), and they can be small in area, contained within craters tens of kilometers in diameter. Smooth plains of volcanic origin are characterized by regionally smooth deposits; the presence of kipukas; sharp and distinctive color boundaries; an association with volcanic vents; the presence of partially buried impact craters, ghost craters, and wrinkle ridges at expected rim and peak ring locations; and burial of crater terraces by smooth plains (e.g., Head et al., 2008, 2009a, 2011; Denevi et al., 2013a).

Intercrater plains. The intercrater plains constitute a morphologic unit that can still be characterized by an extremely textured surface, caused by the high density of craters <10 km in diameter (Fig. 8). The areas mapped are plains regions between craters >20 km in diameter; the elevation of areas of intercrater plains varies by ~5 km, but the slope of the mapped plains regions is generally <2.0°. Thus, locally the intercrater plains are nearly level deposits, but regionally the plains are a more gently rolling or undulating unit. As mapped, the intercrater plains include a wide variety of heavily cratered surface morphologies, from regions with fresh and distinct secondary impact craters (Fig. 8a) to

regions with muted surface textures where the secondary craters are degraded and have merged together (Fig. 8b-e). Secondary craters and chains tend to be in distributions radial to their primary crater (Fig. 8a, c).

4.3.2. Application to geologic mapping

On the basis of these definitions of plains units, the geological map in Fig. 7 was constructed. The mapped area (13.5×10^6 km^2) spans a substantial part of the western hemisphere of Mercury (180°E to 270°E and 80°N to 30°S). The map includes 7 of 10 of our study regions, in order to compare with previous geologic maps and to ensure that map patterns are not controlled by impact basin structures or long-wavelength topography that may have postdated plains formation (Zuber et al., 2012). The most current global tectonic maps (e.g., Byrne et al., 2014) indicate no major long-wavelength topographic undulations in our mapped region. The fractional areas occupied by the three units defined above are ~30% smooth plains, ~33% intercrater plains, and ~33% crater materials. The remaining area (~4%) is covered by hummocky Caloris interior units (Caloris Montes, Nervo Formation, and the Odin Formation) that do not meet the unit definitions described above and were therefore not mapped in this study.

The location of the map region to the east of Caloris is responsible for the nearly equivalent proportions of intercrater and smooth plains (Fig. 7). There is a high concentration of smooth plains deposits at 170°E longitude, within and around the Caloris basin, compared with other regions of Mercury (Denevi et al., 2013a). Approximately 78% of the mapped smooth plains area is contained in 15 large continuous deposits >15,000 km^2 in area; the remaining 23% of the smooth plains area

(Fig. 7) consists of small (<15,000 km^2) deposits located within and adjacent to craters 20 to 200 km in diameter. The smooth plains deposits generally collocate with topographic lows; these areas are typically, but not exclusively, associated with impact structures.

All of the study areas previously mapped as intercrater plains on the basis of M10 data (Fig. 3) are still classified as intercrater plains in this map, except for ICP5. In contrast, the M10-defined intermediate plains (Fig. 6) are all reclassified because of our revision of unit definitions. Of the three intermediate plains study areas contained in the map (Fig. 7), one has been reclassified as entirely smooth plains (IP1), another is mostly intercrater plains material (IP2), and the last is dominated by smooth plains material (IP4).

4.4. Implications of geologic mapping

The region selected for mapping (Figs. 1, 7) provides insights into the dominant formation process of the intercrater plains. The improved resolution and coverage of MESSENGER MDIS data have permitted detailed analysis of the additive effect of secondary craters on smooth plains. Secondary crater fields are extensive and can heavily modify the surface proximal to the impact crater. Young, volcanically emplaced smooth plains, such as the northern smooth plains (Head et al., 2011), can quickly develop an intercrater plains-like texture if there are multiple near-contemporaneous impacts within a small area (Fig. 9). This evolution from a smooth-plains to an intercrater-plains morphology can occur with as few as two young, nearby impact craters. For instance, the overlapping ejecta deposits of Gaudí and Stieglitz craters (Fig. 9a) create an intercrater plains texture (Fig. 9b) on part of the volcanically emplaced northern smooth plains.

When the full region is assessed it is obvious that the area shown in Fig. 9b is a recently modified part of a larger smooth plains deposit.

This same effect is observed at larger scales as well (Fig. 9c, d). The northwestern boundary of Sobkou Planitia has been altered by Strindberg and Ahmad Baba craters (Fig. 9c). Intercrater plains and the smooth plains in this area have a gradational contact. The intercrater plains dominate in the northern portion of Fig. 9c and then eventually grade into smooth plains in the south. As in the area in Figs. 9a and 9b, the superposition of secondary craters from relatively young impact craters was able to produce intercrater plains from smooth plains.

It is easy to identify a buildup of secondary craters on extensive volcanic surfaces (e.g., 9a, b), but it becomes more difficult to map out crater materials when an impact occurs on a heavily cratered surface, such as the intercrater plains, because secondary crater fields readily blend into the surrounding terrain. The two examples of Fig. 9 suggest that smooth volcanic plains could have formed throughout the geologic history of Mercury and later been heavily modified by nearby impact craters. During the early history of Mercury, when cratering rates were relatively high (e.g., Strom and Neukum, 1988; Marchi et al., 2009, 2013; Le Feuvre and Wieczorek, 2008), it would have been possible to convert a deposit of smooth volcanic plains into intercrater plains within a geologically short interval, making the identification of ancient volcanic deposits challenging from modern images.

That intercrater plains are typically found on gently undulating terrain is consistent with a volcanic origin. Typically, clearly identified smooth plains deposits on Mercury (e.g., Denevi et al., 2013a) are areally extensive, with gently rolling to level

surfaces. Some such surfaces, however, have been modified by long-wavelength topographic change (e.g., Zuber et al., 2012; Klimczak et al., 2013; Byrne et al., 2014). The topographic signature associated with impact-produced deposits, such as the lunar Imbrian plains, in contrast, is more variable in that elevations do not cluster around a single elevation as they would with a more nearly horizontal original surface (Schultz and Spudis, 1979). However, the intercrater plains texture is observed both on the flanks of high-standing plateaus and in topographic depressions across the surface of Mercury (e.g., ICP4, ICP5, IP3). This observation suggests that the intercrater plains formation process must be able to act over an elevation range of several kilometers (a finding that would support an origin by emplacement of impact ejecta onto topography more nearly similar to that found today), or that the plains formed horizontal surfaces (a finding that would support an origin either as volcanic deposits or fluidized ejecta) that were subsequently modified by uplift, subsidence, or tilting (Oberst et al., 2010; Zuber et al., 2012; Klimczak et al., 2013) and secondary cratering.

Predicted extents of continuous ejecta deposits on Mercury (Gault et al., 1975; Melosh, 1989) suggest that the influence of the ejecta deposit does not extend outward of the crater rim by more than two crater radii, less than on the Moon because of Mercury's higher surface gravitational acceleration. By this rule of thumb, intercrater plains are observed to be more widely distributed than the lateral extent of continuous basin ejecta deposits and thus cannot all be impact-produced deposits (cf. Wilhelms, 1976). Analysis of the distribution of high-albedo smooth plains around the lunar Orientale basin has shown that the majority of smooth plains occur at approximately two to four basin radii outward of the Cordillera Ring (Meyer et al., 2013). These observations support the idea

that secondary basin ejecta materials should be considered as candidate source material for intercrater plains, but it is important to keep in mind the differences (i.e., surface gravitational acceleration, impact velocity, target rheology) between the Moon and Mercury that could affect cratering efficiency on these two planetary bodies. The higher gravitational acceleration at the surface of Mercury is believed to have a substantial influence on the lower total extent of ejecta deposits compared with the Moon (e.g., Gault et al., 1975). Therefore, on Mercury, basin secondary ejecta deposits are likely to pond in terrain nearer to the basin rim than 2–4 basin radii. Even if basin secondary ejecta proves to be a substantial component (~20%; Meyer et al., 2013) of the material at 1.3–2.6 basin radii (scaling the lunar values by 0.65; Gault et al., 1975), the deposits formed are typically small and discontinuous, making it difficult to resurface large portions of the mercurian crust. Small, well-preserved basins such as Raditladi (258 km in diameter) and Rachmaninoff (306 km in diameter) do not have observable areally extensive plains deposits associated with their ejecta deposits. In addition, if discrete plains deposits did form on Mercury in this manner, then such deposits should be observed around young basins on Mercury similar in age to the lunar Orientale basin (~3.7 Ga; Le Feuvre and Wieczorek, 2011). Such deposits are not observed around young basins such as Rembrandt (Whitten et al., 2014).

A comparison of the distribution of intercrater plains on Mercury with the asymmetric distribution of known impact basins (Fassett et al., 2012) supports the interpretation that the formation mechanism for intercrater plains could be dominated by volcanic processes. However, at least a portion of the intercrater plains areas in this study are within approximately one basin radius of the nearest identified impact basin structure,

indicating that basin ejecta is present at these sites, at least as a component of an impact-gardened regolith that also includes locally derived material (e.g., Oberbeck et al., 1974). For either plains emplacement mechanism, the number of craters with diameters >20 km (~7390 craters; Fassett et al., 2011) has been sufficient to produce the morphology (i.e., the rough texture produced by secondary impacts) observed across intercrater plains today.

A comparison of the crater density values and the smooth morphology of individual study regions lends support to the idea that volcanic activity on Mercury was widespread early in the planet's history (Fig. 5). From our analysis, an $N(10)$ value of ~225 can be used to distinguish between smooth and intercrater plains deposits. On the other hand, $N(20)$ crater density values have more overlap for regions that are morphologically classified as either smooth or intercrater plains. For example, IP3 and IP4 have high $N(20)$ values, suggesting these regions are pre-Tolstojan in age. However, the MDIS color data and the dominant smooth morphology of IP3 and IP4 indicate that these are regions of smooth plains. This apparent contradiction can be resolved by an extended interval of eruptions of smooth plains lavas. The large $N(20)$ values, which include embayed craters in IP3 and IP4, represent the crater density on an ancient surface by this argument, whereas the $N(10)$ values record the age of the younger smooth plains. Craters >20 km in diameter are less likely to be buried by a volcanic eruption, having crater rim heights of ~0.66 km or more (Pike, 1988), and, therefore, can remain intact and observable even though the surrounding terrain and smaller craters are buried (e.g., Whitten and Head, 2013b). Craters <10 km in diameter, in contrast, have rim heights <0.47 km (Pike, 1988), implying that lava flows at least 0.5 km thick would bury these

smaller craters. This relationship between crater density and regional morphology is consistent with the view that early smooth plains on Mercury were emplaced volcanically and able to resurface the regions between large craters across large areas (Whitten and Head, 2013b). The variation in $N(10)$ for the identified smooth plains regions (i.e., ICP5, IP1, IP3, IP4, IP5) suggests variability in ages, an observation likely to be the result of differences in time of emplacement.

The spread in crater size-frequency distributions (Fig. 4) may not span the entire duration of volcanic activity and, instead, part of this variation may be the result of a variable preservation state of the intercrater plains deposits. Intercrater plains regions more heavily modified by volcanic resurfacing or basin ejecta deposition might have a lower crater density than well-preserved deposits and contribute to a spread in crater size-frequency distributions. Estimates of the timing of intercrater plains formation can be made by examining the crater size-frequency distributions for each of the study regions. Crater statistics for all of the regions defined as intercrater plains in our analysis (i.e., ICP1, ICP2, ICP3, ICP4, IP2) cluster together (Fig. 4k) and have $N(20)$ values of ~70–160 (Table 1). Whereas the crater size-frequency distributions are similar among the intercrater plains study regions, the cratering statistics are not identical, suggesting some variability in the unit ages. One recent estimate for the absolute age of a region with the highest observed crater density on Mercury is ~4.0–4.1 Ga (Marchi et al., 2013), providing evidence that ancient terrains can be preserved for billions of years on Mercury.

On the basis of the evidence outlined above, especially the rate at which smooth volcanic plains can be transformed into intercrater plains, we conclude that the intercrater

plains could have formed as a series of areally extensive volcanic flows that were modified by superposed primary and secondary impacts. Stratigraphic relationships between the intercrater plains and superposed impact craters suggest that this unit was deposited over an extended period of time during the period of heavy bombardment, an inference supported by crater size-frequency distributions (Fig. 5, Table 1). This interpretation of intercrater plains formation differs from the proposal that such units were emplaced largely as impact deposits (e.g., Wilhelms, 1976; Oberbeck et al., 1977). The continual emplacement of volcanic flows and subsequent modification would result in a continuum of cratered deposits; the oldest deposits are the most densely cratered and highly textured (Fig. 8e) whereas the youngest plains deposits have an abundance of secondary craters but are not as modified as the older deposits (Fig. 8a). Other evidence presented in previous studies, including a paucity of craters <100 km diameter (e.g., Strom, 1977; Strom et al., 2011; Fassett et al., 2011) and the near-global distribution of the intercrater plains (Trask and Guest, 1975; Spudis and Prosser, 1984; Denevi et al., 2009; Fig. 7), supports the interpretation that the intercrater plains were formed by the modification of early volcanic deposits during the period of heavy bombardment.

More data are needed to fully understand the origin of the intercrater plains unit. Since much of the surface of Mercury has been affected by impact processes it would be helpful to know the composition of the material excavated by craters tens of kilometers in diameter superposed on the mapped intercrater plains to determine the composition at depth (e.g., Denevi et al., 2013b). If the excavated compositions of these craters are similar to the HRP/IP color unit typical of the smooth plains or if the crater material has compositions distinct from the surrounding terrain, such information would provide

strong evidence for a volcanic origin. If the excavated materials have a compositional signature similar to that of the impacted surface, such information would lend more support to an impact-related formation hypothesis. High-resolution spectral datasets from MESSENGER's Mercury Atmospheric and Surface Composition Spectrometer (MASCS) (McClintock and Lankton, 2007) and the MErcury Radiometer and Thermal Infrared Spectrometer (MERTIS) instrument (Hiesinger et al., 2010) on the BepiColombo Mercury Planetary Orbiter (Benkhoff et al., 2010) can be utilized to identify mineralogically distinct intercrater plains regolith by employing spectral classification (e.g., Helbert et al., 2013; Izenberg et al., 2014) or spectral mixing models. Analysis of global topography, particularly with regional slopes removed (e.g., Head et al., 2002), would aid in analyzing elevation across the intercrater plains by highlighting variations that might be typical of volcanic flooding (e.g., Whitten and Head, 2013b). Lastly, a high-resolution global topographic dataset, especially at lower latitudes where intercrater plains are mapped, would enable analysis of the surface roughness of all intercrater plains regions, potentially enabling identification of subunits (e.g., Kreslavsky and Head, 2000; Kreslavsky et al., 2013; Yang et al., 2013).

5. Conclusions

High-resolution MESSENGER data acquired at optimal viewing geometries for morphologic mapping studies have enabled a more detailed analysis of the intercrater and intermediate plains units defined for Mercury's surface during the mapping and data analysis that followed the Mariner 10 flybys. The lower resolution of M10 images and lack of systematic topographic measurements caused some features (e.g., crater and basin

rims, degraded and subdued craters) to be included in "plains." MESSENGER datasets indicate that the plains units are most easily identified and mapped on the basis of morphology and areal density of impact craters. Intercrater plains are highly textured, sculpted by impact ejecta, and covered with secondary craters in a variety of states of degradation. Crater size-frequency distributions indicate that the intercrater plains are ancient and are consistently older than the smooth plains. MDIS color data indicate that the intercrater plains are characterized by a wide variety of spectral units. From this analysis, we interpret the intermediate plains to be composed mainly of intercrater plains with patches of smooth plains material and, therefore, we suggest that the intermediate plains unit should be subdivided into these two units and that each should then be mapped separately. The removal of the intermediate plains makes the distinction between the smooth plains and the intercrater plains clearer than in earlier maps and analyses.

Our work supports a volcanic origin for a substantial percentage of the intercrater plains (Fig. 7). The basis for this conclusion includes (1) the ability of ejecta from a small number of superposed craters to transform known smooth plains deposits of volcanic origin into a unit indistinguishable from intercrater plains; (2) the variety of ancient ages for intercrater plains deposits as interpreted from crater size-frequency distributions; and (3) the near-global distribution of intercrater plains (between craters ≥30 km in diameter) compared with the uneven distribution of impact basins and their associated ejecta deposits. Several conditions early in Mercury's history also support a volcanic origin for intercrater plains including the lack of a low-density anorthositic crust (Nittler et al., 2011), the extensive nature of young volcanic deposits (e.g., Denevi et al., 2013a), and

the paucity of craters <100 km diameter (e.g., Strom, 1977; Fassett et al., 2011; Marchi et al., 2013).

Nonetheless, an impact origin is still a possibility for some intercrater plains. For example, MESSENGER data have revealed several local intercrater plains deposits that are interpreted to be impact related (Denevi et al., 2013b). These case studies indicate the importance of interpreting each individual deposit with care and seeking characteristics (Table 2) that would support either a volcanic or impact-related origin.

Despite the difficulty in ascertaining the origin of a specific occurrence of intercrater plains, this work provides useful criteria for distinguishing the different plains units on Mercury. The unit definitions described in this study, especially for the intercrater plains, can be used to produce consistent geological maps of Mercury and aid in the interpretation of specific examples of intercrater plains. Additionally, spectral information from MASCS, elemental information from MESSENGER's GRS and X-Ray Spectrometer, and data from the future BepiColombo mission (e.g., the MERTIS instrument) can be used to further define unit boundaries and identify mineralogically or compositionally distinct intercrater plains material. An ability to identify and map the distribution of more rigorously defined intercrater and smooth plains will aid in unraveling the geological stratigraphy of Mercury. Once the intercrater plains have been fully mapped, subtle variations in morphology, spectral properties, and topography can be investigated to define deposits of varying age and, more broadly, sharpen our understanding of the geologic history of Mercury.

Acknowledgements

We gratefully acknowledge funding from the MESSENGER project, which is supported by the NASA Discovery Program under contracts NASW-00002 to the Carnegie Institution of Washington and NAS5-97271 to The Johns Hopkins University Applied Physics Laboratory.

References

Antonenko, I., Head, J.W., Mustard, J.F., Hawke, B.R., 1995. Criteria for the detection of lunar cryptomaria. Earth Moon Planets 69, 141–172.

Becker, K.J., Weller, L.A., Edmundson, K.L., Becker, T.L., Robinson, M.S., Enns, A.C., Solomon, S.C., 2012. Global controlled mosaic of Mercury from MESSENGER orbital images. Lunar Planet. Sci. 43, abstract 2654.

Benkhoff, J., van Casteren, J., Hayakawa, H., Fujimoto, M., Laakso, H., Novara, M., Ferri, P., Middleton, H.R., Ziethe, R., 2010. BepiColombo – Comprehensive exploration of Mercury: Mission overview and science goals. Planet. Space Sci. 58, 2–20. doi:10.1016/j.pss.2009.09.020.

Byrne, P.K., Klimczak, C., Williams, D.A., Hurwitz, D.M., Solomon, S.C., Head, J.W., Preusker, F., Oberst, J., 2013. An assemblage of lava flow features on Mercury. J. Geophys. Res. Planets 118, 1303–1322. doi:10.1002/jgre.20052.

Byrne, P.K., Klimczak, C., Şengör, A.M.C., Solomon, S.C., Watters, T.R., Hauck II, S.A., 2014. Mercury's global contraction much greater than earlier estimates. Nature Geosci., in press. doi:10.1038/NGE02097.

Cavanaugh, J.F., Smith, J.C., Sun, X., Bartels, A.E., Ramos-Izquierdo, L., Krebs, D.J., McGarry, J. F., Trunzo, R., Novo-Fradac, A.M., Britt, J.L., Karsh, J., Katz, R.B., Lukemire, A.T., Szymkiewicz, R., Berry, D. L., Swinski, J.P., Neumann, G.A, Zuber, M.T., Smith, D.E., 2007. The Mercury Laser Altimeter instrument for the MESSENGER mission. Space Sci. Rev. 131, 451–479. doi:10.1007/s11214-007-9273-4.

Crater Analysis Techniques Working Group, 1979. Standard techniques for presentation and analysis of crater size-frequency data. Icarus 37, 467–474.

Cruikshank, D.P., Hartmann, W.K., Wood, C.A., 1973. Moon: 'Ghost' craters formed during mare filling. Moon 7, 440–452.

DeHon, R.A., Scott, D.H., Underwood, J.R., 1981. Geologic map of the Kuiper (H-6) Quadrangle of Mercury. Map I-1233, Misc. Investigations Ser., U.S. Geological Survey, Denver, Colo.

Denevi, B.W., Robinson, M.S., Solomon, S.C., Murchie, S.L., Blewett, D.T., Domingue, D.L., McCoy, T.J., Ernst, C.M., Head, J.W., Watters, T.R., Chabot, N.L., 2009. The evolution of Mercury's crust: A global perspective from MESSENGER. Science 324, 613–618. doi:10.1126/science.1172226.

Denevi, B.W., Ernst, C.M., Meyer, H.M., Robinson, M.S., Murchie, S.L., Whitten, J.L., Head, J.W., Watters, T.R., Solomon, S.C., Ostrach, L.R., Chapman, C.R., Byrne, P.K., Klimczak, C., Peplowski, P.N., 2013a. The distribution and origin of smooth plains on Mercury. J. Geophys. Res. Planets 118, 891–907. doi:10.1002/jgre.20075.

Denevi, B.W., Ernst, C.M., Whitten, J.L., Head, J.W., Murchie, S.L., Watters, T.R., Byrne, P.K., Blewett, D.T., Solomon, S.C., Fassett, C.I., 2013b. The volcanic origin of a region of intercrater plains. Lunar. Planet. Sci. 44, abstract 1218.

Edmundson, K.L., Weller, L.A., Becker, K.J., Becker, T.L., Rosiek, M.R., Robinson, M.S., Solomon, S.C., 2011. Preliminary photogrammetric control of MESSENGER orbital images of Mercury. Abstracts with Programs 43 (5), paper 100-6, p. 267, Geological Society of America, Boulder, Colo.

Eggleton, R.E., Schaber, G.G., 1972. Cayley Formation interpreted as basin ejecta. In: Apollo 16 Preliminary Science Report. Special Publication SP-315, NASA, Washington, D.C., pp. 29-7 to 29-16.

Fassett, C.I., Head, J.W., Blewett, D.T., Chapman, C.R., Dickson, J.L., Murchie, S.L., Solomon, S.C., Watters, T.R., 2009. Caloris impact basin: Exterior geomorphology, stratigraphy, morphometry, radial sculpture, and smooth plains deposits. Earth Planet. Sci. Lett. 285, 297–308. doi:10.1016/j.epsl.2009.05.022.

Fassett, C.I., Kadish, S.J., Head, J.W., Solomon, S.C., Strom, R.G., 2011. The global population of large craters on Mercury and comparison with the Moon. Geophys. Res. Lett. 38, L10202. doi:10.1029/2011GL047294.

Fassett, C.I., Head, J.W., Baker, D.M.H., Zuber, M.T., Smith, D.E., Neumann, G.A., Solomon, S.C., Klimczak, C., Strom, R.G., Chapman, C.R., Prockter, L.M., Phillips, R.J., Oberst, J., Preusker, F., 2012. Large impact basins on Mercury: Global distribution, characteristics, and modification history from MESSENGER orbital data. J. Geophys. Res. 117, E00L08. doi:10.1029/2012JE004154.

Freed, A. M., Blair, D.M., Watters, T.R., Klimczak, C., Byrne, P.K., Solomon, S.C., Zuber, M.T., Melosh, H.J., 2012. On the origin of graben and ridges within and near volcanically buried craters and basins in Mercury's northern plains. J. Geophys. Res. 117, E00L06. doi:10.1029/2012JE004119.

Gast, P.W., Phinney, W.C., Duke, M.B., Jackson, E.K., Hubbard, N.J., Butler, P., Laughon, R.B., Agrell, S.O., Bass, M.N., Brett, R., Carrier, W.D., Clanton, U.S., Eaton, A.L., Head, J., Heiken, G.H., Horz, F., Lofgren, G.E., McKay, D.S., Morrison, D.A., Muehlberger, W.R., Nagle, J.S., Reid, A.M., Ridley, W.I., Simonds, C., Stuart-Alexander, D., Warner, J.L., Williams, R.J., Wilshire, H., Bansal, B.M., Brannon, J.A., Landry, A.M., Rhodes, J.M., Rodgers, K.V., Wainwright, J.E., Bennett, L., Clark, R.S., Keith, J.E., O'Kelley, G.D., Perkins, R.W., Rancitelli, L.A., Portenier, W.R., Robbins, M.K., Schonfeld, E., Gibson, E.K., Lewis, C.F., Moore, C.B., Moore, D.R., 1973. The Apollo 16 lunar samples: Petrographic and chemical description. Science 179, 23–34.

Gault, D.E., Guest, J.E., Murray, J.B., Dzurisin, D., Malin, M.C., 1975. Some comparisons of impact craters on Mercury and the Moon. J. Geophys. Res. 80, 2444–2460.

Grolier, M. J., Boyce, J.M., 1984. Geologic map of the Borealis region (H-1) of Mercury. Map I-1660, Misc. Investigations Ser., U.S. Geological Survey, Denver, Colo.

Guest, J.E., Fielder, G., 1968. Lunar ring structures and the nature of the maria. Planet. Space Sci. 16, 665–673.

Guest, J.E., Greeley, R., 1983. Geologic map of the Shakespeare (H-3) Quadrangle of Mercury. Map I-1408, Misc. Investigations Ser., U.S. Geological Survey, Denver, Colo.

Hapke, B., Danielson, G.E., Klaasen, K., Wilson, L., 1975. Photometric observations of Mercury from Mariner 10. J. Geophys. Res. 80, 2431–2443.

Hawke, B.R., Spudis, P.D., 1980. Geochemical anomalies on the eastern limb and farside of the moon. In: Papike, J.J., Merrill, R.B. (Eds.). Proceedings of the Conference on the Lunar Highlands Crust. Pergamon, New York, pp. 467–481.

Hawkins III, S.E., Boldt, J.D., Darlington, E.H., Espiritu, R., Gold, R.E., Gotwols, B., Grey, M.P., Hash, C.D., Hayes, J.R., Jaskulek, S.E., Kardian, C.J., Keller, M.R., Malaret, E.R., Murchie, S.L., Murphy, P.K., Peacock, K., Prockter, L.M., Reiter, R.A., Robinson, M.A., Schaefer, E.D., Shelton, R.G., Sterner, R.E., Taylor, H.W., Watters, T.R., Williams, B.D., 2007. The Mercury Dual Imaging System on the MESSENGER spacecraft. Space Sci. Rev. 131, 247–338. doi:10.1007/s11214-007-9266-3.

Head, J.W., 1974. Stratigraphy of the Descartes region (Apollo 16): Implications for the origin of samples. Moon 11, 77–99.

Head, J.W., Solomon, S.C., 1981. Tectonic evolution of the terrestrial planets. Science 213, 62–76.

Head, J.W., Wilson, L., 1992. Lunar mare volcanism: Stratigraphy, eruption conditions, and the evolution of secondary crusts. Geochim. Cosmochim. Acta 56, 2155–2175. doi:10.1016/0016-7037(92)90183-J.

Head, J.W., Kreslavksy, M.A., Pratt, S., 2002. Northern lowlands of Mars: Evidence for

widespread volcanic flooding and tectonic deformation in the Hesperian Period. J. Geophys. Res. 107(E1), doi:10.1029/2000JE001445.

Head, J.W., Murchie, S.L., Prockter, L.M., Robinson, M.S., Solomon, S.C., Strom, R.G., Chapman, C.R., Watters, T.R., McClintock, W.E., Blewett, D.T., Gillis-Davis, J.J., 2008. Volcanism on Mercury: Evidence from the first MESSENGER flyby. Science 321, 69–72. doi:10.1126/science.1159256.

Head, J.W., Murchie, S.L., Prockter, L.M., Solomon, S.C., Chapman, C.R., Strom, R.G., Watters, T.R., Blewett, D.T., Gillis-Davis, J.J., Fassett, C.I., Dickson, J.L., Morgan, G.A., Kerber, L., 2009a. Volcanism on Mercury: Evidence from the first MESSENGER flyby for extrusive and explosive activity and the volcanic origin of plains. Earth Planet. Sci. Lett. 285, 222–242. doi:10.1016/j.epsl.2009.03.007.

Head, J.W., Murchie, S.L., Prockter, L.M., Solomon, S.C., Chapman, C.R., Strom, R.G., Watters, T.R., Blewett, D.T., Gillis-Davis, J.J., Fassett, C.I., Dickson, J.L., Morgan, G.A., Kerber, L., 2009b. Evidence for intrusive activity on Mercury from the first MESSENGER flyby. Earth Planet. Sci. Lett. 285, 251–262. doi:10.1016/j.epsl.2009.03.008.

Head, J.W., Chapman, C.R., Strom, R.G., Fassett, C.I., Denevi, B.W., Blewett, D.T., Ernst, C.M., Watters, T.R., Solomon, S.C., Murchie, S.L., Prockter, L.M., Chabot, N.L., Gillis-Davis, J.J., Whitten, J.L., Goudge, T.A., Baker, D.M.H., Hurwitz, D.M., Ostrach, L.R., Xiao, Z., Merline, W.J., Kerber, L., Dickson, J.L., Oberst, J., Byrne, P.K., Klimczak, C., Nittler, L.R., 2011. Flood volcanism in the northern high latitudes of Mercury revealed by MESSENGER. Science 333, 1853–1856. doi:10.1126/science.1211997.

Helbert, J., D'Amore, M., Izenberg, N.R., Domingue, D.L., Head, J.W., D'Incecco, P., Maturilli, A., Holsclaw, G.M., McClintock, W.E., Solomon, S.C., 2013. Surface units on Mercury revealed by unsupervised classification of MESSENGER spectral reflectance data from the first year in orbit. J. Geophys. Res. Planets, submitted.

Hiesinger, H., Helbert, J., MERTIS Co-I Team, 2010. The Mercury Radiometer and Thermal Infrared Spectrometer (MERTIS) for the BepiColombo mission. Planet. Space Sci. 58, 144–165. doi:10.1016/j.pss.2008.09.019.

Hodges, C.A., Muehlberger, W.R., Ulrich, G.E., 1973. Geologic setting of Apollo 16. Proc. Lunar Sci. Conf. 4th, 1–25.

Hurwitz, D.M., Head, J.W., Byrne, P.K., Xiao, Z., Solomon, S.C., Zuber, M.T., Smith, D.E., Neumann, G.A., 2013. Investigating the origin of candidate lava channels on Mercury with MESSENGER data: Theory and observations. J. Geophys. Res. Planets 118, 471–486. doi:10.1029/2012JE004103.

Izenberg, NR., Klima, R.L., Murchie, S.L., Blewett, D.T., Holsclaw, G.M., McClintock, W.E., Malaret, E., Mauceri, C., Vilas, F., Sprague, A.L., Helbert, J., Domingue, D.L., Head III, J.W., Goudge, T.A., Solomon, S.C., Hibbitts, C.A., Dyar, M.D., 2014. The low-iron, reduced surface of Mercury as seen in spectral reflectance by MESSENGER. Icarus 228, 364–374.

Kiefer, W.S., Murray, B.C., 1987. The formation of Mercury's smooth plains. Icarus 72, 477–491.

King, J.S., Scott, D.H., 1990. Geologic map of the Beethoven (H-7) Quadrangle of Mercury. Map I-2048, Misc. Investigations Ser., U.S. Geological Survey, Denver,

Colo.

Klimczak, C., C. M. Ernst, P. K. Byrne, S. C. Solomon, T. R. Watters, S. L. Murchie, F. Preusker, J. A. Balcerski, 2013. Insights into the subsurface structure of the Caloris basin, Mercury, from assessments of mechanical layering and changes in long-wavelength topography. J. Geophys. Res. Planets 118, 2030–2044. doi:10.1002/jgre.20157.

Kreslavsky, M.A., Head, J.W., 2000. Kilometer-scale roughness of Mars: Results from MOLA data analysis. J. Geophys. Res. 105, 26695–26711. doi:10.1029/2000JE001259.

Kreslavsky, M.A., Head, J.W., Neumann, G.A., Rosenburg, M.A., Aharonson, O., Smith, D.E., Zuber, M.T., 2013. Lunar topographic roughness maps from Lunar Orbiter Laser Altimeter (LOLA) data: Scale dependence and correlation with geologic features and units. Icarus 226. 52–66. doi:10.1016/j.icarus.2013.04.027.

Le Feuvre, M., Wieczorek, M.A., 2008. Nonuniform cratering of the terrestrial planets. Icarus 197, 291–306. doi:10.1016/j.icarus.2008.04.011.

Le Feuvre, M., Wieczorek, M.A., 2011. Nonuniform cratering of the Moon and a revised crater chronology of the inner Solar System. Icarus 214, 1–20. doi:10.1016/j.icarus.2011.03.010.

Leake, M.A., 1981. The intercrater plains of Mercury and the Moon: Their nature, origin, and role in terrestrial planet evolution. Ph.D. thesis, Univ. Arizona, Tucson, Ariz.

Marchi, S., Mottola, S., Cremonese, G., Massironi, M., Martellato, E., 2009. A new chronology for the Moon and Mercury. Astron. J. 137, 4936–4948. doi:10.1088/0004-6256/137/6/4936.

Marchi, S., Chapman, C.R., Fassett, C.I., Head, J.W., Bottke, W.F., Strom, R.G., 2013. Global resurfacing of Mercury 4.0-4.1 billion years ago by heavy bombardment and volcanism. Nature 499, 59–61. doi:10.1038/nature12280.

McClintock, W.E., Lankton, M.R., 2007. The Mercury Atmospheric and Surface Composition Spectrometer for the MESSENGER mission. Space. Sci. Rev. 131, 481–521. doi:10.1007/s11214-007-9264-5.

McGill, G.E., King, E.A., 1983. Geologic map of the Victoria (H-2) Quadrangle of Mercury. Map I-1409, Misc. Investigations Ser., U.S. Geological Survey, Denver, Colo.

Melosh, H.J., 1989. Impact Cratering: A Geologic Process. Oxford Univ. Press, Oxford, UK, 245 pp.

Meyer, H.M., Denevi, B.W., Boyd, A.K., Robinson, M.S., 2013. The distribution and origin of lunar light plains around Orientale basin. Lunar Planet Sci. 44, abstract 1539.

Milton, D.J., 1964. Stratigraphy of the terra part of the Theophilus quadrangle. Astrogeol. Studies Ann. Prog. Rept., July 1963 to July 1964, pt. A, Open-file Report, U.S. Geological Survey, Denver, Colo., pp. 17–27.

Muehlberger, W.R., Hörz, F., Sevier, J.R., Ulrich, G.E., 1980. Mission objectives for geological exploration of the Apollo 16 landing site. In: Papike, J.J., Merrill, R.B. (Eds.). Proceedings of the Conference on the Lunar Highlands Crust, Pergamon, New York, pp. 1–49.

Murray, B.C., Belton, M.J.S., Danielson, G. E., Davies, M.E., Gault, D.E., Hapke, B., O'Leary, B., Strom, R.G., Suomi, V., Trask, N., 1974. Mercury's surface:

Preliminary description and interpretation from Mariner 10 pictures. Science 185, 169–179. doi:10.1126/science.185.4146.169.

Murray, B. C., Strom, R. G., Trask, N. J., Gault, D.E., 1975. Surface history of Mercury: Implications for terrestrial planets. J. Geophys. Res. 80, 2508–2514. doi:10.1029/JB080i017p02508.

Nittler, L.R., Starr, R.D., Weider, S.Z., McCoy, T.J., Boynton, W.V., Ebel, D.S., Ernst, C.M., Evans, L.G., Goldsten, J.O., Hamara, D.K., Lawrence, D.J., McNutt Jr., R.L., Schlemm II, C.E., Solomon, S.C., Sprague, A.L., 2011. The major-element composition of Mercury's surface from MESSENGER X-ray spectrometry. Science 333, 1847–1850. doi:10.1126/science.1211567.

Oberbeck, V.R., Morrison, R.H., Hörz, F., Quaide, W.L., Gault, D.E., 1974. Smooth plains and continuous deposits of craters and basins. Proc. Lunar Sci. Conf. 5th, 111–136.

Oberbeck, V.R., Quaide, W.L., Arvidson, R.E., Aggarwal, H.R., 1977.Comparative studies of lunar, martian, and mercurian craters and plains. J. Geophys. Res. 82, 1681–1698.

Oberst, J., Preusker, F., Phillips, R.J., Watters, T.R., Head, J.W., Zuber, M.T., Solomon, S.C., 2010. The morphology of Mercury's Caloris basin as seen in MESSENGER stereo topographic models. Icarus 209, 230–238. doi:10.1016/j.icarus.2010.03.009.

Peplowski, P.N., Evans, L.G., Hauck, S.A., McCoy, T.J., Boynton, W.V., Gillis-Davis, J.J., Ebel, D.S., Goldsten, J.O., Hamara, D.K., Lawrence, D.J., McNutt Jr., R.L., Nittler, L.R., Solomon, S.C., Rhodes, E.A., Sprague, A.L., Starr, R.D., Stockstill-

Cahill, K.R., 2011. Radioactive elements on Mercury's surface from MESSENGER: Implications for the planet's formation and evolution. Science 333, 1850–1852. doi:10.1126/science.1211576.

Pike R.J., 1988. Geomorphology of impact craters on Mercury. In: Vilas, F., Chapman, C.R., Matthews, M.S. (Eds.). Mercury. Univ. Ariz. Press, Tucson, Ariz., pp. 165–273.

Rava, B., Hapke, B., 1987. An analysis of the Mariner 10 color ratio map of Mercury. Icarus 71, 397–429. doi:10.1016/0019-1035(87)90037-6.

Richardson, J.E., 2009. Cratering saturation and equilibrium: A new model looks at an old problem. Icarus 204, 697–715.

Robinson, M.S., Lucey, P.G., 1997. Recalibrated Mariner 10 color mosaics: Implications for Mercurian volcanism. Science 275, 197–200. doi:10.1126/science.275.5297.197.

Robinson, M.S., Murchie, S.L., Blewett, D.T., Domingue, D.L., Hawkins, S.E., Head, J.W., Holsclaw, G.M., McClintock, W.E., McCoy, T.J., McNutt Jr., R.L., Prockter, L.M., Solomon, S.C., Watters, T.R., 2008. Reflectance and color variations on Mercury: Regolith processes and compositional heterogeneity. Science 321, 66–69.

Schaber, G.G., McCauley, J.F., 1980. Geologic map of the Tolstoj (H-8) Quadrangle of Mercury. Map I-1199, Misc. Investigations Ser., U.S. Geological Survey, Denver, Colo.

Schultz, P.H., Spudis, P.D., 1979. Evidence for ancient mare volcanism. Proc. Lunar Planet. Sci. Conf. 10th, 2899–2918.

Shearer, C.K., Hess, P.C., Wieczorek, M.A., Pritchard, M.E., Parmentier, E.M., Borg, L.E., Longhi, J., Elkins-Tanton, L.T., Neal, C.R., Antonenko, I., Canup, R.M., Halliday, A.N., Grove, T.L., Hager, B.H., Lee, D-C., Wichert, U., 2006. Thermal and magmatic evolution of the Moon. Rev. Mineral. Geochem. 60, 365–518.

Spudis P.D., Guest, J.E., 1988. Stratigraphy and geologic history of Mercury. In: Vilas, F., Chapman, C.R., Matthews, M.S. (Eds.). Mercury. Univ. Ariz. Press, Tucson, Ariz., pp. 118–164.

Spudis, P.D., Prosser, J.G., 1984. Geologic map of the Michaelangelo (H-12) Quadrangle of Mercury. Map I-1659, Misc. Investigations Ser., U.S. Geological Survey, Denver, Colo.

Strom, R.G., 1977. Origin and relative age of lunar and mercurian intercrater plains. Phys. Earth Planet. Inter. 15, 156–172.

Strom, R.G., Neukum, G., 1988. The cratering record on Mercury and the origin of impacting objects. In: Vilas, F., Chapman, C.R., Matthews, M.S. (Eds.). Mercury. Univ. Ariz. Press, Tucson, Ariz., pp. 336–373.

Strom, R.G., Trask, N.J, Guest, J.E., 1975. Tectonism and volcanism on Mercury. J. Geophys. Res. 80, 2478–2507.

Strom, R.G., Malin, M.C., Leake, M.A., 1990. Geologic map of the Bach (H-15) Quadrangle of Mercury. Map I-2015, Misc. Investigations Ser., U.S. Geological Survey, Denver, Colo.

Strom, R.G., Chapman, C.R., Merline, W.J., Solomon, S.C., Head, J.W., 2008. Mercury cratering record viewed from MESSENGER's first flyby. Science 321, 79–81. doi:10.1126/science.1159317.

Strom, R.G., Banks, M.E., Chapman, C.R., Fassett, C.I., Forde, J.A., Head, J.W., Merline, W.J., Prockter, L.M., Solomon, S.C., 2011. Mercury crater statistics from MESSENGER flybys: Implications for stratigraphy and resurfacing history. Planet. Space Sci. 59, 1960–1967. doi:10.1016/j.pss.2011.03.018.

Taylor, S.R., 1989. Growth of planetary crusts. Tectonophysics 161, 147–156.

Trask, N.J., 1976. Cratering history of the heavily cratered terrain on Mercury. Geologica Romana 15, 471–476.

Trask, N.J., Dzurisin, D., 1984. Geologic map of the Discovery (H-11) Quadrangle of Mercury. Map I-1658, Misc. Investigations Ser., U.S. Geological Survey, Denver, Colo.

Trask, N.J., Guest, J.E., 1975. Preliminary geologic terrain map of Mercury. J. Geophys. Res. 80, 2461–2477. doi:10.1029/JB080i017p02461.

Watters, T.R., 1993. Compressional tectonism on Mars. J. Geophys. Res. 98, 17049–17060. doi:10.1029/93JE01138.

Watters, T. R., Solomon, S.C., Klimczak, C., Freed, A.M., Head, J.W., Ernst, C.M., Blair, D.M., Goudge, T.A., Byrne, P.K., 2012. Extension and contraction within volcanically buried impact craters and basins on Mercury. Geology 40, 1123–1126.

Whitten J.L., Head, J.W., 2013a. Ancient lunar mare volcanism: Identification, distribution, and composition of cryptomare deposits. Lunar Planet. Sci. 44, abstract 1247.

Whitten, J.L., Head, J.W., 2013b. Detecting volcanic resurfacing of heavily cratered terrain: Flooding simulations on the Moon using Lunar Orbiter Laser Altimeter (LOLA) data. Planet. Space Sci. 85, 24–37. doi:10.1016/j.pss.2013.05.013.

Whitten, J.L., Head, J.W., Helbert, J., Solomon, S.C., 2014. Rembrandt basin: Distinguishing between volcanic and impact-produced smooth plains deposits on Mercury. Lunar Planet. Sci. 45, abstract 1289.

Wilhelms, D. E., 1976. Mercurian volcanism questioned. Icarus 28, 551–558. doi:10.1016/0019-1035(76)90128-7.

Wilhelms, D.E., McCauley, J., 1971. Geological map of the near side of the Moon. Map I-703. Misc. Investigations Ser., U.S. Geological Survey, Denver, Colo.

Wilson, L., Head, J.W., 2008. Volcanism on Mercury: A new model for the history of magma ascent and eruption. Geophys. Res. Lett. 35, L23205. doi:10.1029/2008GL035620.

Xiao, Z., Strom, R.G., Chapman, C.R., Head, J.W., Klimczak, C., Ostrach, L.R., Helbert, J., D'Incecco, P., 2014. Comparisons of fresh complex impact craters on Mercury and the Moon: Implications for controlling factors in impact crater excavation. Icarus 228, 260–275.

Yang, D., Zuber, M.T., Head, J.W., Solomon, S.C., 2013. Distribution of topographic slope and roughness in Mercury's northern hemisphere. Lunar Planet. Sci. 44, abstract 2347.

Young, J.W., Mattingly, T.K., Duke, C.M., 1972. Crew observations. In: Apollo 16 Preliminary Science Report. Special Publication SP-315, NASA, Washington D.C., pp. 5-1 to 5-6.

Zuber, M.T., Smith, D.E., Phillips, R.J., Solomon, S.C., Neumann, G.A., Hauck, S.A., Peale, S.J., Barnouin, O.S., Head, J.W., Johnson, C.L., Lemoine, F.G., Mazarico, E., Sun, X., Torrence, M.H., Freed, A.M., Klimczak, C., Margot, J.-L., Oberst, J., Perry, M.E., McNutt Jr., R.L., Balcerski, J.A., Michel, N., Talpe, M.J., Yang, D., 2012. Topography of the northern hemisphere of Mercury from MESSENGER laser altimetry. Science 336, 217–220. doi:10.1126/science.1218805.

Table 1. Locations of areas of intercrater plains and intermediate plains included in this study.

Study regions	Latitude[a]	Longitude[a]	Area (km^2)	Color unit coverage	*N*(10)	*N*(20)
ICP1	52.25	-98.89	1.30×10^5	LRM: 78.5% HRP/IP: 14.1% LBP: 0.02% unmapped: 7.4%	169±36	62±22
ICP2	35.49	-107.89	1.30×10^5	HRP/IP: 52.9% LRM: 29.2% unmapped: 17.9%	323±50	162±35
ICP3	12.80	-132.76	1.30×10^5	HRP/IP: 15.2% unmapped: 84.8%	370±53	162±35
ICP4	-30.09	-46.43	1.30×10^5	HRP/IP: 55.9% unmapped: 44.1%	300±48	131±32
ICP5	-16.26	-150.51	1.30×10^5	LRM: 15.7% unmapped: 84.3%	154±34	62±22
IP1	-22.00	-126.85	1.30×10^5	HRP/IP: 59.9% unmapped: 40.1%	77±24	31±15
IP2	73.77	-148.97	1.30×10^5	unmapped: 100%	361±53	115±30
IP3	33.00	-30.16	1.30×10^5	HRP/IP: 60.2% unmapped: 39.8%	223±41	100±28
IP4	-2.17	-126.14	1.30×10^5	HRP/IP: 83.0% unmapped: 17.0%	177±37	108±29
IP5	-55.86	-130.84	1.30×10^5	unmapped: 100%	223±41	92±27

[a]Latitude and longitude values are the coordinates for the center of the study regions.

Table 2. Lines of evidence that would support a volcanic or impact origin for the intercrater plains.

Volcanic	Impact
1. Widespread distribution	1. Smaller discrete deposits associated with craters or basins
2. Continuous, areally extensive deposits (~10^5 to 10^6 km^2)[a]	2. Concentration around large basins and craters
3. Paucity of craters <100 km in diameter[b]	3. Spectral characteristics similar to those of surrounding terrain
4. No areal association with impact basins	4. Proportionally more melt in craters on Mercury then the Moon[c]
5. Spatial density and distribution of large basins (>500 km diameter)[d]	5. Abundance of primary craters, coupled with cratering models indicating surface saturation for craters >128 km in diameter[e]
6. Distinct compositional boundaries within or at margins of deposits[f]	
7. Volcanic landforms (e.g., ghost craters, sinuous rilles, rimless depressions)[g]	
8. Interior heat production and thermal history[h]	

[a] Head et al. (2011); Denevi et al. (2013b).
[b] e.g., Strom (1977); Strom et al. (2011); Fassett et al. (2011).
[c] e.g., O'Keefe and Ahrens (1977); Cintala (1992).
[d] Fassett et al. (2012).
[e] Richardson (2009).
[f] Robinson et al. (2008); Denevi et al. (2009).
[g] e.g., Head et al. (2008, 2009a, 2009b).
[h] Peplowski et al. (2011).

Figure captions

Figure 1. Map of the study locations in this analysis. Red polygons represent the areas dominated by intercrater plains (ICP), and blue polygons denote the areas dominated by intermediate plains (IP); the numbers are specific identifiers used for reference in the text. The darkened area indicates the part of Mercury that was not imaged by M10. Identified basins (Fassett et al., 2012) are outlined in white. The white dashed box outlines the region mapped in Fig. 8. Overlaid on the MDIS 250 m/pixel mosaic is a model of global topography derived by stereo photogrammetry (Edmundson et al., 2011; Becker et al., 2012). Simple cylindrical projection.

Figure 2. Example of a Mariner 10 image of intercrater plains (ICP), as defined by Trask and Guest (1975). The lobate scarp Santa Maria Rupes cuts across these intercrater plains from the northwest to southeast. The image is approximately 200 km across; north is up. Mariner 10 frame 27448.

Figure 3. Subsets of the intercrater plains (ICP) study regions identified in Figure 1. Column 1: MDIS 250 m/pixel mosaic or WAC and NAC images. North is up (white arrow). Column 2: topography data from stereo photogrammetry (~2.6 km/pixel) overlaid on MDIS data. Column 3: color units mapped by Denevi et al. (2009). White areas are unmapped. Column 4: M10 geologic map. Column 5: M10 images. (a) is from images EW0226880104G, EW0226837761G and EW0226795417G. (f) is from images EW0226964416G, EW0226922188G, and EW0226879730G. (k), (p), and (u) are from

the 250 m/pixel MDIS base map. All images and maps are in stereographic projections centered on the given study region (see Table 1 for coordinates).

Figure 4. (a-j) Cumulative crater size-frequency distributions for the intercrater and intermediate plains study regions. Insets are expanded views of the size-frequency distributions for craters between 5 and 20 km diameter. Grey regions indicate portions of the crater size-frequency distribution strongly affected by secondary craters, as evidenced by the break in slope near 10 km diameter (dashed line). For several study regions, this break in slope is less obvious because we attempted to avoid secondary craters in constructing these plots. Nonetheless, it is clear that avoiding secondary craters in this size range is difficult for Mercury and poses a challenge for determining crater size-frequency distributions at smaller diameters (Strom et al., 2008). Some of the distributions have shallow slopes at the smallest diameters because not all of these smallest craters (~6 km diameter) were counted. The number *n* of craters counted in each study region is indicated. (k) Average crater size-frequency distributions for the intercrater and intermediate plains study regions and their associated errors. Red and blue areas span the range of values for individual study areas.

Figure 5. Crater density values *N*(10) (top) and *N*(20) (bottom) for the ICP and IP study regions of this paper, as well as for different plains areas (Spudis and Guest, 1988; Denevi et al., 2013) and basins (Spudis and Guest, 1988; Fassett et al., 2009) on Mercury. The plots show that *N*(10) and *N*(20) values provide consistent estimates of relative age. Values for intercrater and intermediate plains indicate that these units are Tolstojan to

pre-Tolstojan in age. Errors in *N* are large for several study regions, which implies that many of the study areas could have formed at any time during the Pre-Tolstojan and Tolstojan periods. Spudis and Guest (1988) did not report *N*(10) values. The figure is modeled from Figure 26 of Spudis and Guest (1988), so the abscissa is aligned with corresponding lunar stratigraphic systems (Pre-Nectarian, Nectarian, and Imbrian periods), for which absolute ages are known or may be estimated. Data points are arbitrarily spaced evenly within each time period.

Figure 6. Subsets of the intermediate plains (IP) study regions identified in Fig. 1. Column 1: MDIS 250 m/pixel mosaic or WAC and NAC images. North is up (white arrow). Column 2: topography data from stereo photogrammetry (~2.6 km/pixel) overlaid on MDIS data. Column 3: color units mapped by Denevi et al. (2009). White color indicates unmapped region. Column 4: M10 geologic map. Column 5: M10 images. (a) is from the 250 m/pixel MDIS base map. (f) is from images EW0214589955G, EW0214589935G, EW0214676881G, and EW0214633400G. (k) is from images EW0213025967G, and EW0213025938. (p) is from images EN0226963098M, EN0226920771M, EN0226920672M, and EN0226920674M. (u) is from image EN0227550741M. All images and maps are in stereographic projections centered on the given study region (see Table 1 for coordinates).

Figure 7. Geologic map constructed with the unit identification criteria developed in this study. The region shown is located to the east of the Caloris impact basin (Fig. 1); many of the smooth plains deposits in the western portion of this region are circum-Caloris

deposits. An MDIS close-up image of each study region (column 1, Figs. 3 and 6) is included to the right of the sketch map; north is up in each image and all scale bars (white) are 60 km in length. The MDIS images are in stereographic projections centered on the given study region. The locations of these images on the map are indicated by red (intercrater plains) and blue (intermediate plains) outline. Caloris interior deposits that were not mapped into one of the three units defined in this study are shown in black. The geologic map is in a Lambert azimuthal equal-area projection centered on the map region.

Figure 8. Examples of the different morphologies included in the intercrater plains map unit. (a) Superposed secondary craters from relatively recent impacts. Secondary craters have sharp and easily identifable crater rims and can occur in chains. (b) Older secondary craters and chains with flat floors. Some crater rims blend in with the background hummocky texture. (c and d) Mixtures of degraded and fresh craters. In (c) there are more fresh craters and degraded craters are more easily distinguishable. In (d) the degraded craters are difficult to identify individually and thus contribute more to forming a hummocky textured surface. (e) Areas with no obvious secondary craters or chains. Superposed secondary craters are indistinguishable from one another and blend together to form a hummocky texture. All images are from the MDIS 250 m/pixel base map. Lambert azimuthal equal-area projection, centered on the map region in Fig. 7.

Figure 9. Two examples of the transformation of smooth plains to intercrater plains by secondary cratering. (a) An area of northern smooth plains (Head et al., 2011) that includes the relatively young craters Gaudí (81 km diameter, left) and Stieglitz (100 km

diameter, right). Black box outlines the area of panel (b). (b) Close-up of the overlapping ejecta deposits from Gaudí and Stieglitz craters. The overlapping secondary craters from Gaudí and Stieglitz produced intercrater plains texture on the northern smooth plains. (c) An area surrounding two fresh impact craters, Strindberg (189 km diameter, left) and Ahmad Baba (126 km diameter, top), in the northwestern region of Sobkou Planitia, a basin-hosted smooth plains deposit. Superposition of ejecta deposits from the large craters has created an extensive intercrater plains deposit. The white dashed line shows the approximate boundary between the smooth and intercrater plains regions, and the black box outlines the area of panel (d). (d) An intercrater plains deposit created from the overlapping ejecta deposits of Strindberg and Ahmad Baba craters. These regions of intercrater plains (b and d) were created from the modification of smooth plains by the superposed ejecta deposits of only two craters each, emphasizing the rapidity with which intercrater plains can be formed.

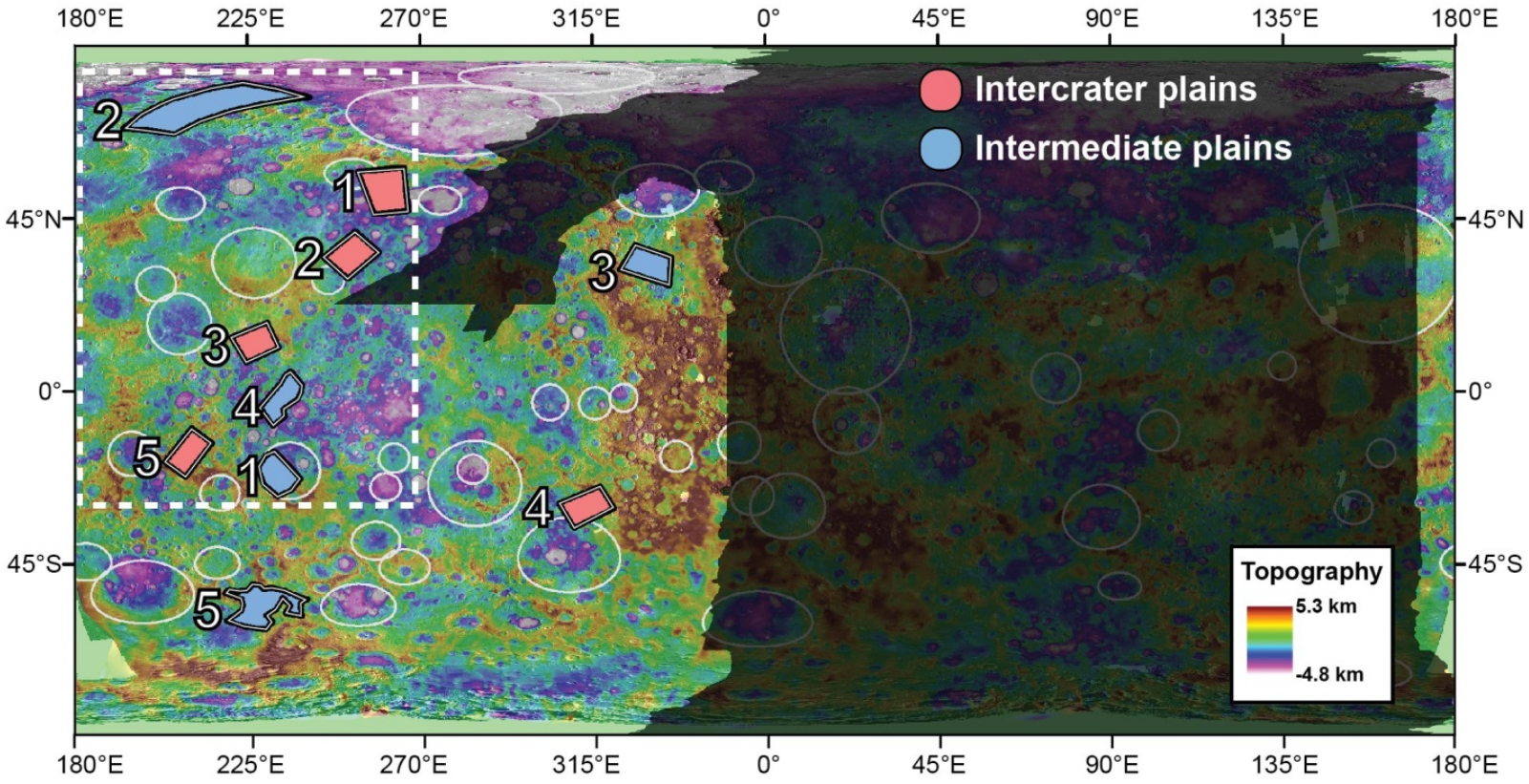
180°E
225°E
270°E
315°E
0°
45°E
90°E
135°E
180°E
45°N
0°
45°S
Intercrater plains
Intermediate plains
Topography
5.3 km
-4.8 km
1
2
3
4
5

Figure 1.

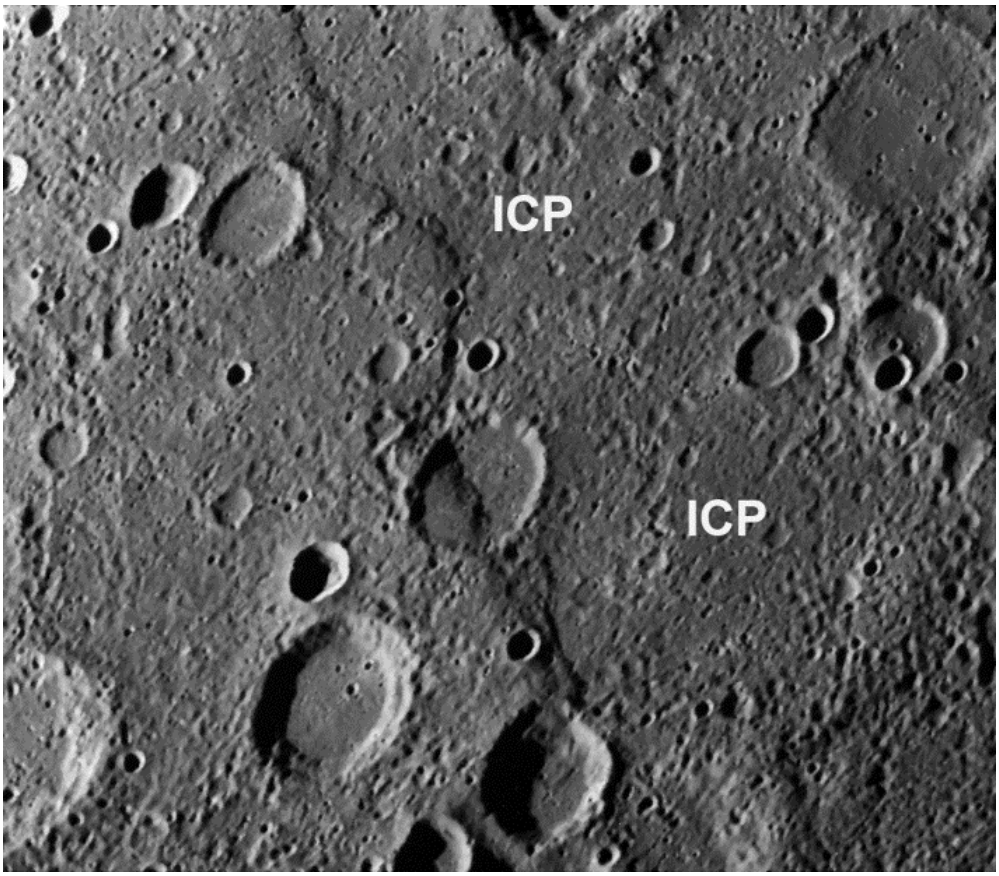

Figure 2.

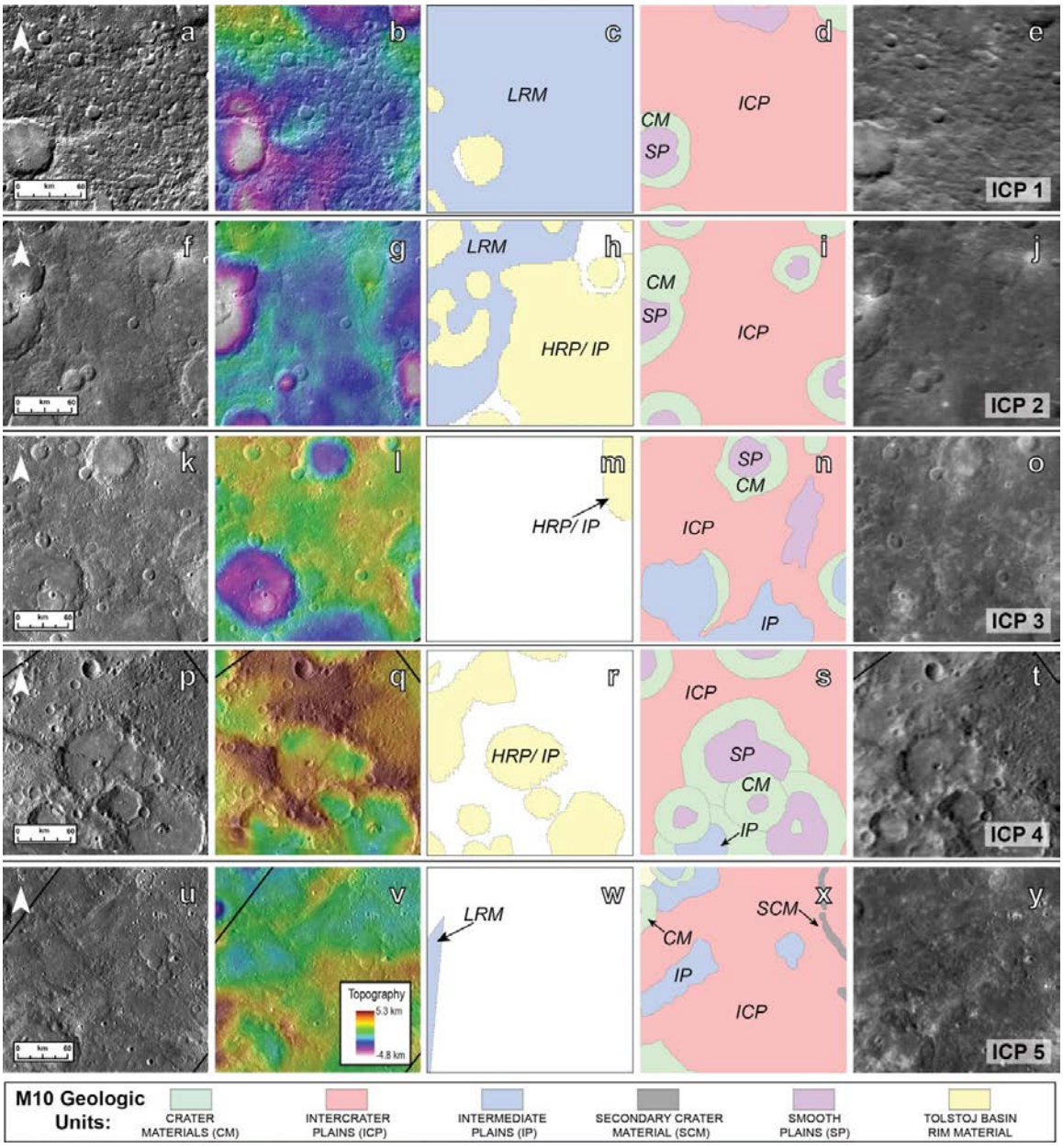
a
b
c
LRM
d
ICP
CM
SP
e
ICP 1
f
g
LRM
h
HRP/ IP
i
CM
SP
ICP
j
ICP 2
k
l
m
HRP/ IP
SP
CM
n
ICP
IP
o
ICP 3
p
q
r
HRP/ IP
ICP
s
SP
CM
IP
t
ICP 4
u
v
Topography
5.3 km
-4.8 km
w
LRM
SCM
x
CM
IP
ICP
y
ICP 5
M10 Geologic Units:
CRATER MATERIALS (CM)
INTERCRATER PLAINS (ICP)
INTERMEDIATE PLAINS (IP)
SECONDARY CRATER MATERIAL (SCM)
SMOOTH PLAINS (SP)
TOLSTOJ BASIN RIM MATERIAL

Figure 3.

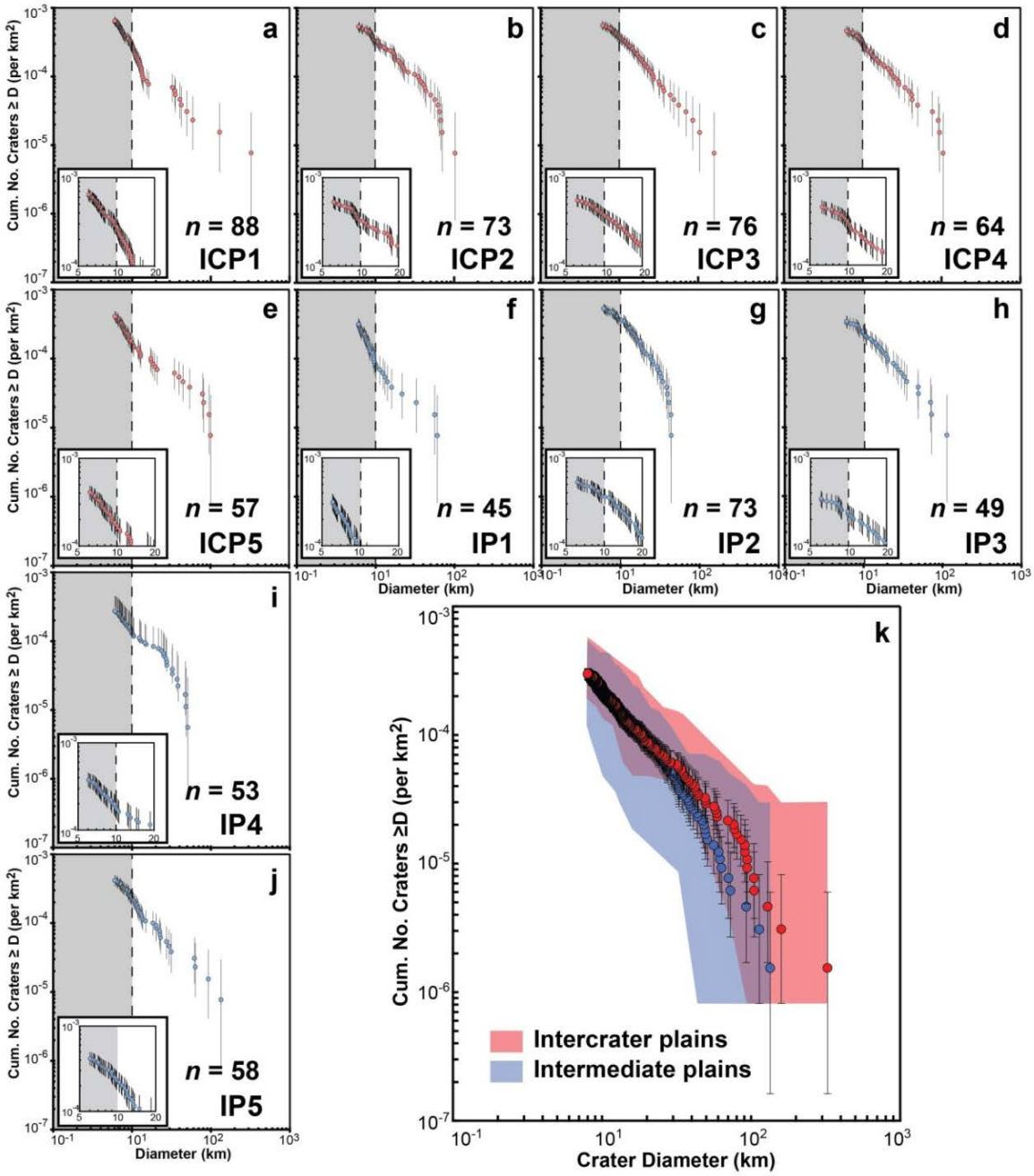
a
n = 88
ICP1
b
n = 73
ICP2
c
n = 76
ICP3
d
n = 64
ICP4
e
n = 57
ICP5
f
n = 45
IP1
g
n = 73
IP2
h
n = 49
IP3
i
n = 53
IP4
j
n = 58
IP5
k
Cum. No. Craters ≥ D (per km²)
Cum. No. Craters ≥D (per km²)
Diameter (km)
Crater Diameter (km)
Intercrater plains
Intermediate plains

Figure 4.

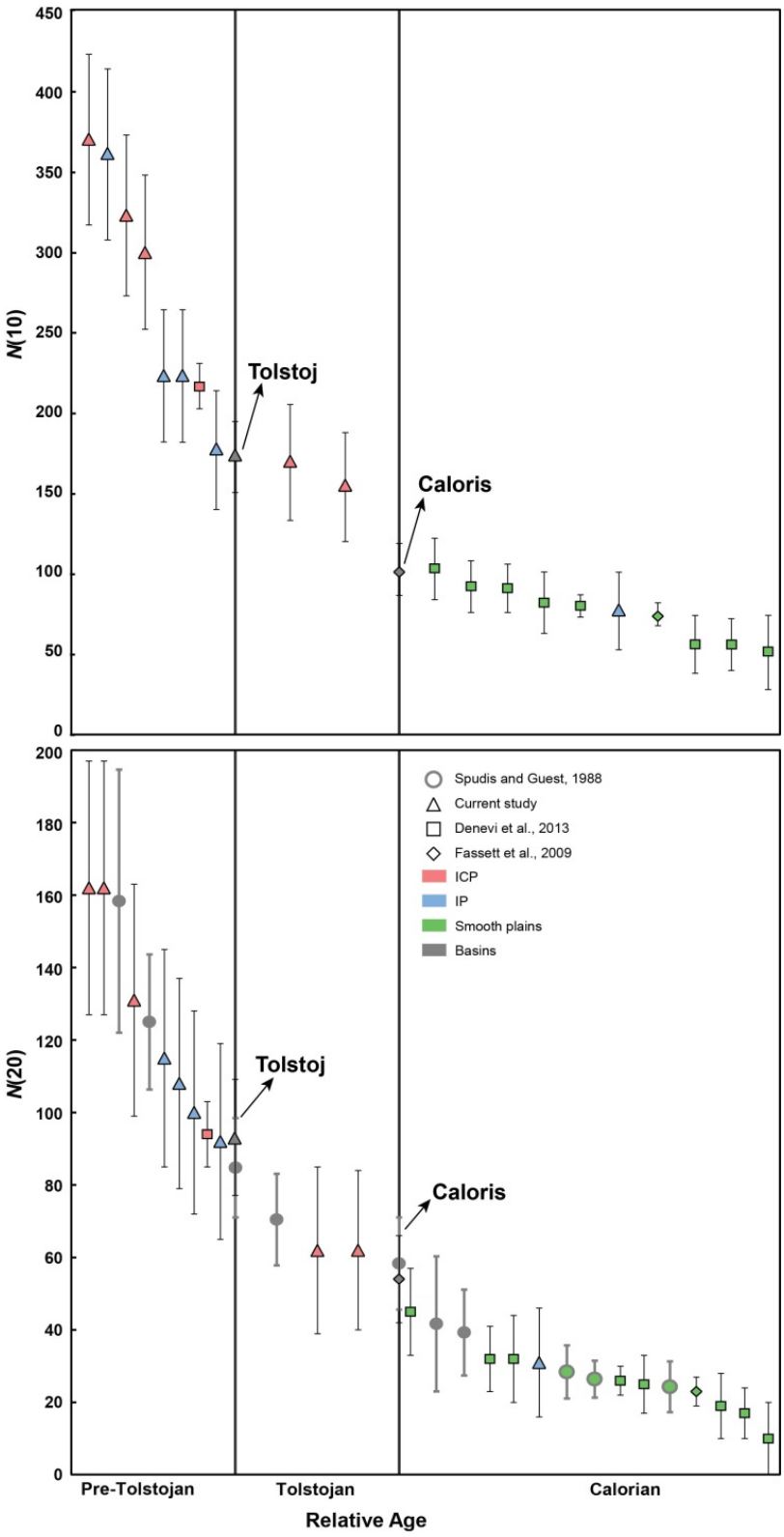
N(10)
N(20)
Tolstoj
Caloris
Spudis and Guest, 1988
Current study
Denevi et al., 2013
Fassett et al., 2009
ICP
IP
Smooth plains
Basins
Pre-Tolstojan
Tolstojan
Calorian
Relative Age

Figure 5.

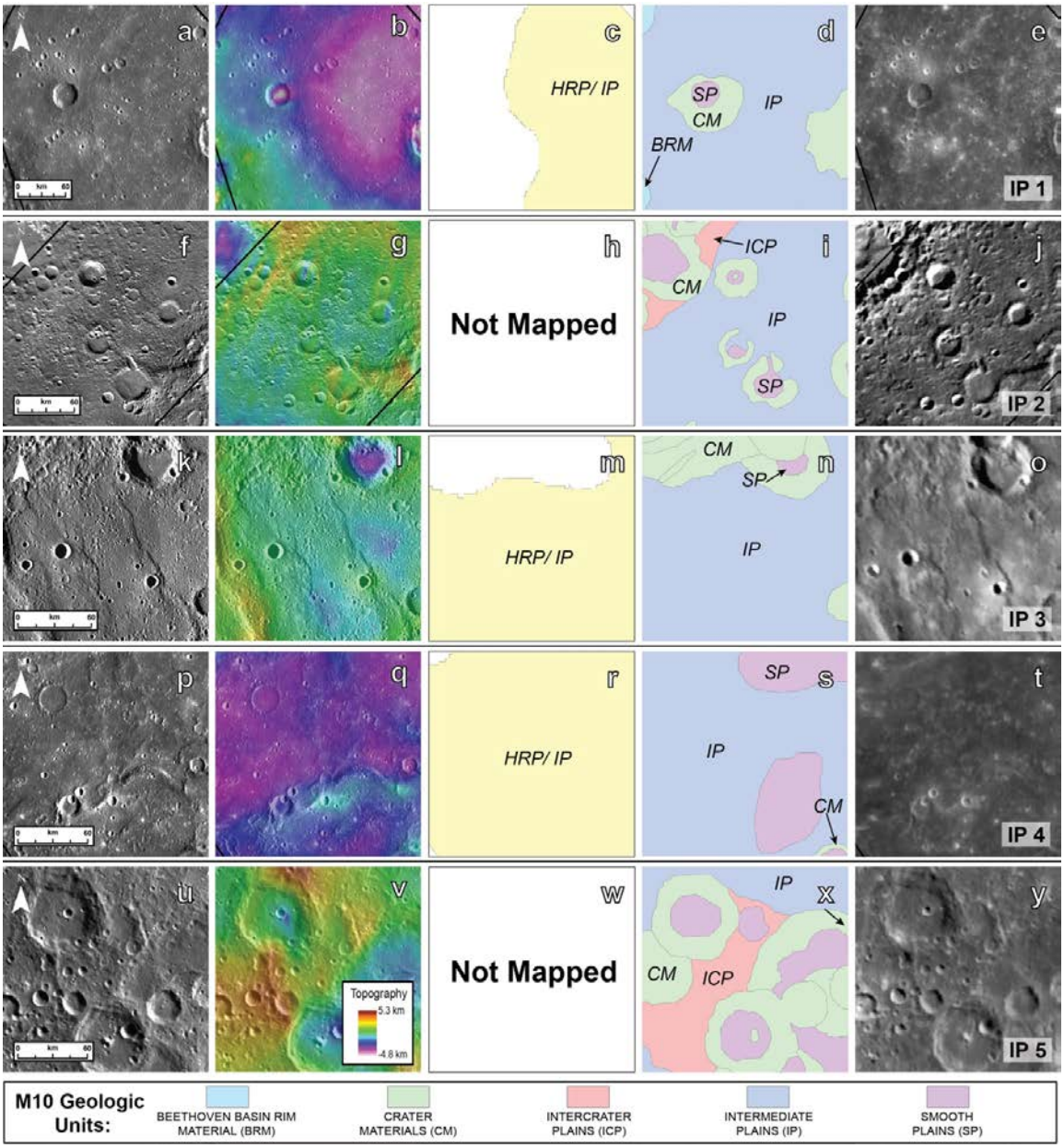
a
b
c
HRP/ IP
d
SP
IP
CM
BRM
e
IP 1
f
g
h
Not Mapped
ICP
i
CM
IP
SP
j
IP 2
k
l
m
HRP/ IP
CM
SP
n
IP
o
IP 3
p
q
r
HRP/ IP
SP
s
IP
CM
t
IP 4
ü
v
Topography
5.3 km
-4.8 km
w
Not Mapped
IP
x
CM
ICP
y
IP 5
M10 Geologic Units:
BEETHOVEN BASIN RIM MATERIAL (BRM)
CRATER MATERIALS (CM)
INTERCRATER PLAINS (ICP)
INTERMEDIATE PLAINS (IP)
SMOOTH PLAINS (SP)

Figure 6.

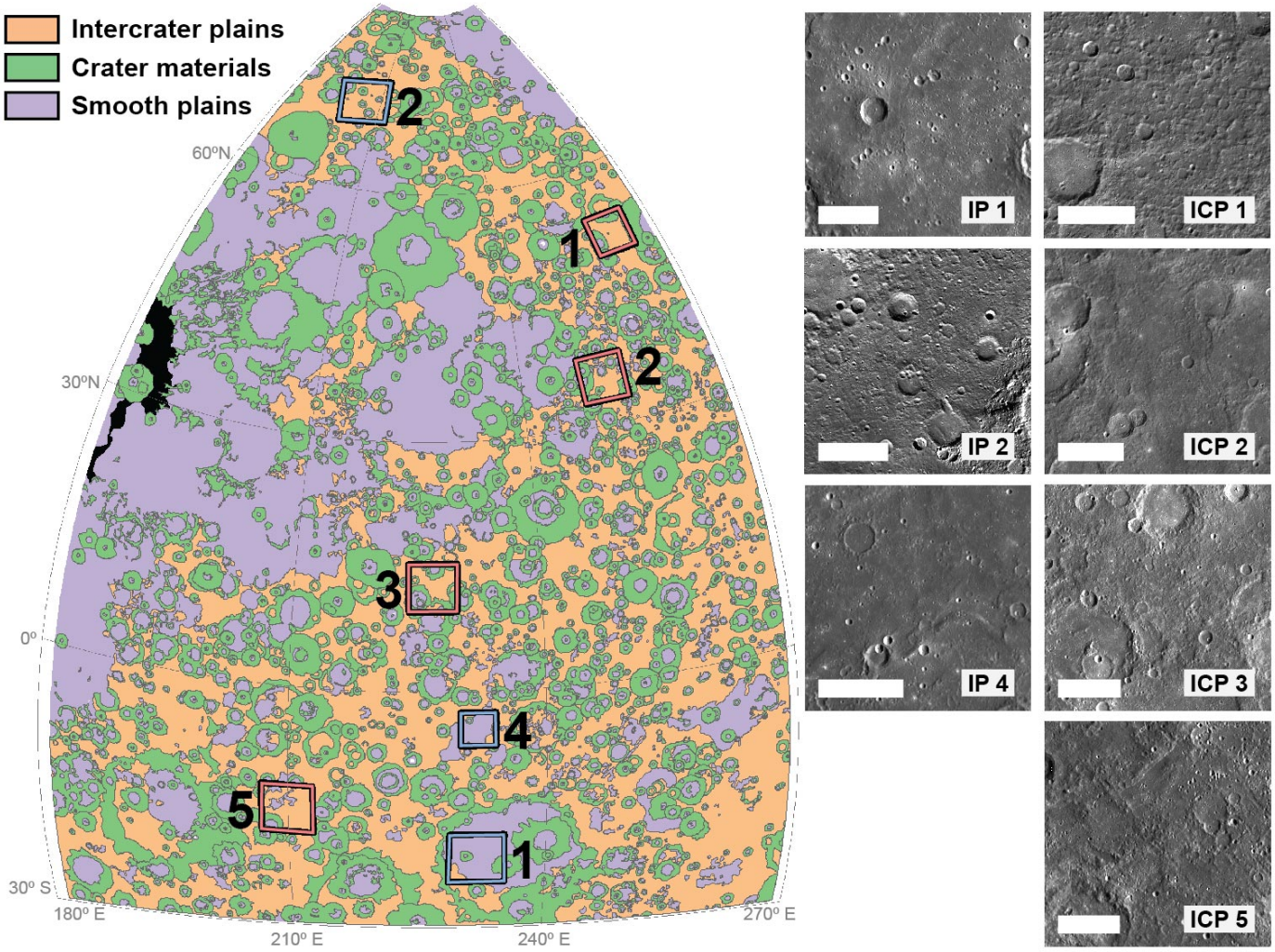
Intercrater plains
Crater materials
Smooth plains
60ºN
30ºN
0º
30º S
180º E
210º E
240º E
270º E
1
2
3
4
5
IP 1
ICP 1
IP 2
ICP 2
IP 4
ICP 3
ICP 5

Figure 7.

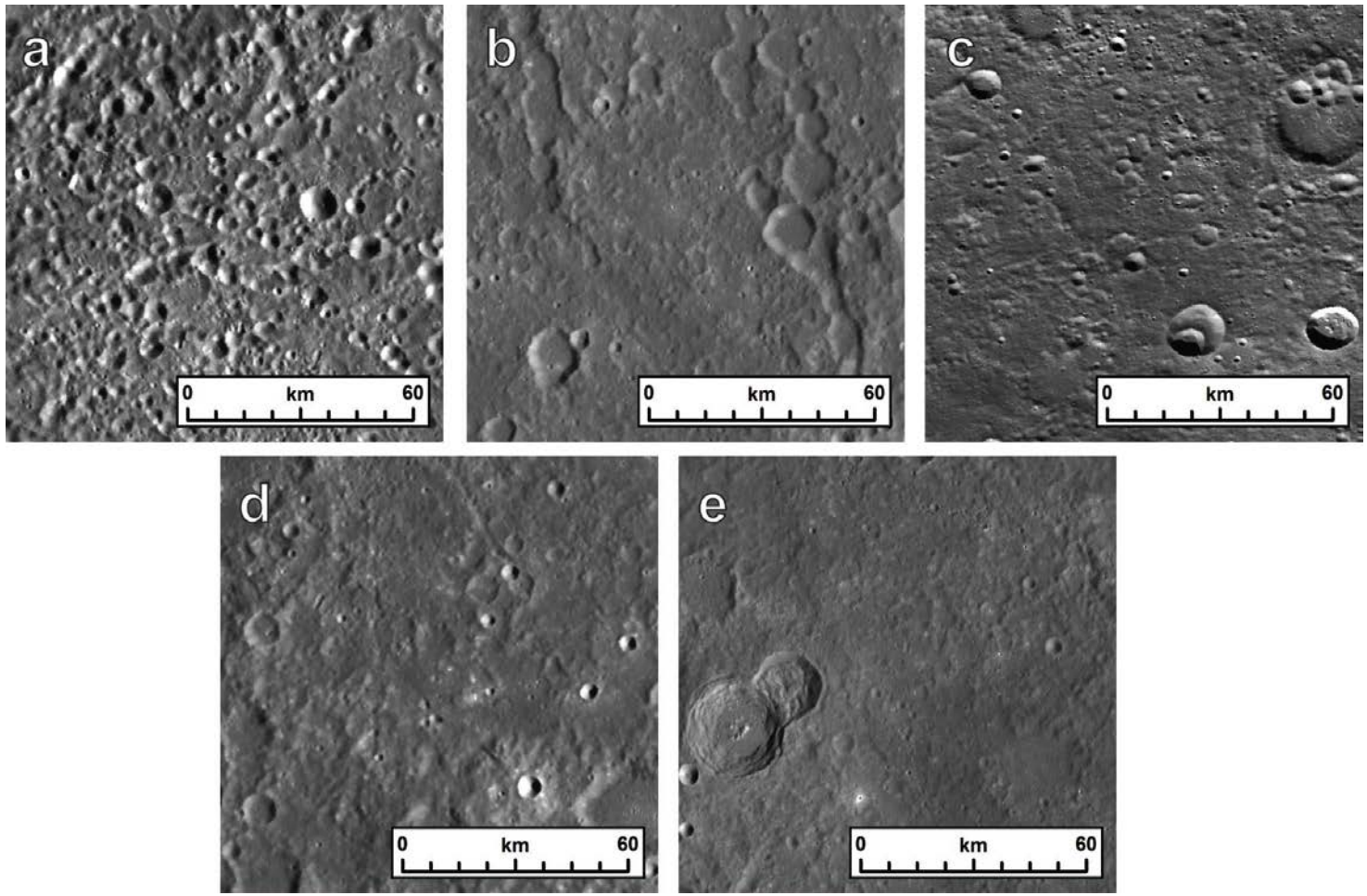

Figure 8.

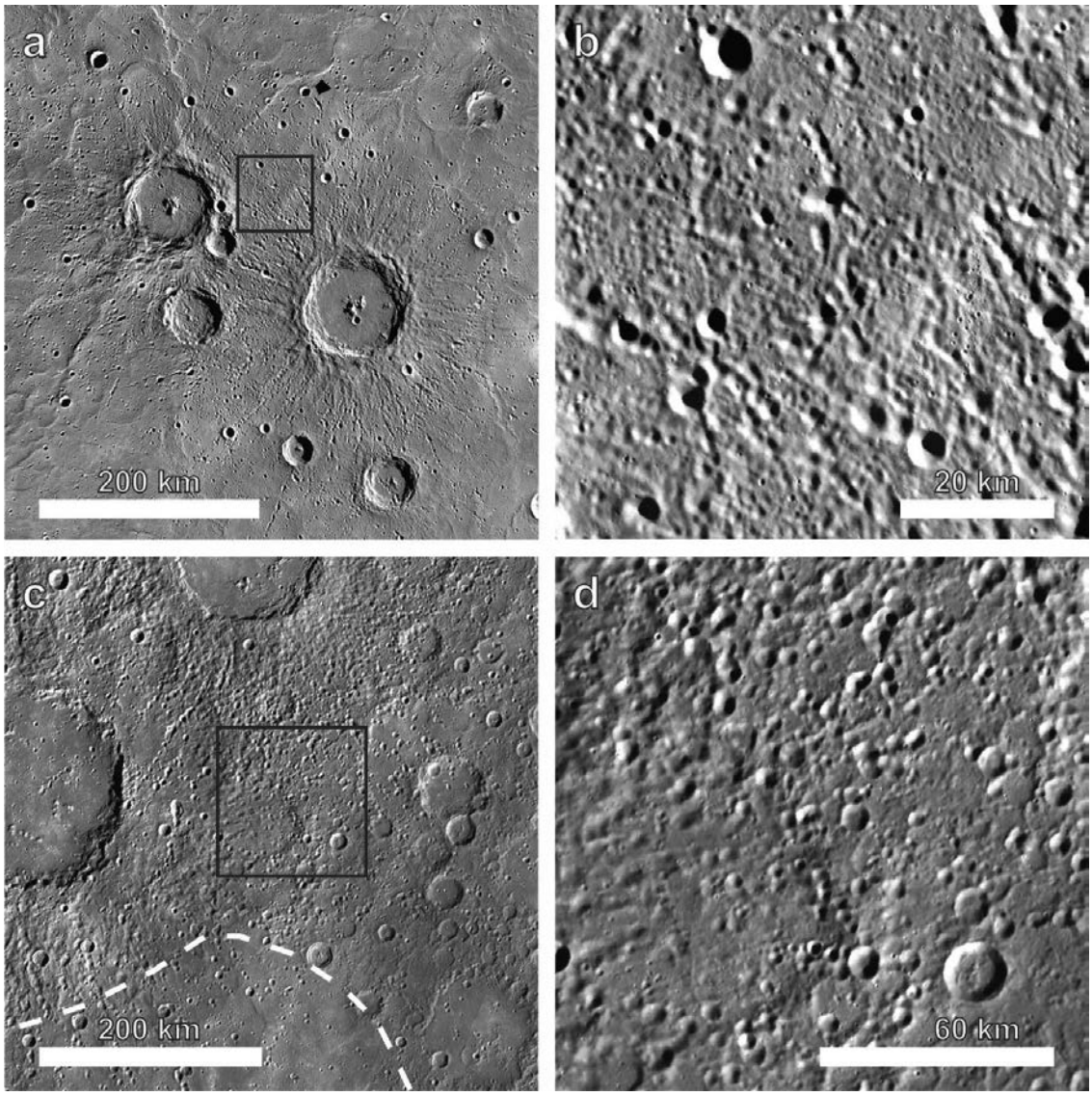

Figure 9.

Chapter 5:
Rembrandt basin:
Distinguishing between volcanic and impact-produced plains

Jennifer L. Whitten[a],
James W. Head[a] and Sean C. Solomon[b,c]

[a]Department of Geological Sciences, Brown University, Providence, RI 02912, USA
[b]Department of Terrestrial Magnetism, Carnegie Institution of Washington, Washington, DC 20015, USA
[c]Lamont-Doherty Earth Observatory, Columbia University, Palisades, NY 10964, USA

To be submitted:
Summer 2014

Abstract

The surface of Mercury has been heavily modified since the formation of the planet's original crust. The process responsible for such widespread resurfacing has been heavily debated, producing two primary hypotheses: resurfacing by impact basin ejecta, or by volcanic activity. In order to better understand the role that impact basins play in resurfacing on Mercury, we used MESSENGER Mercury Dual Imaging System (MDIS) data to map the distribution of plains deposits within and around the relatively young Rembrandt impact basin (~720 km in diameter). There are three different Rembrandt plains units: (1) high-albedo interior plains, (2) high-albedo exterior plains, and (3) low-albedo exterior plains. The morphology, crater size-frequency distribution, and $N(20)$ crater density were analyzed for each deposit. Observations of the two high-albedo plains deposits are consistent with previous studies of volcanically produced smooth plains deposits on Mercury. The low-albedo exterior plains are substantially older than the other high-albedo plains and comparable in age to the Rembrandt basin impact event. Owing to age and albedo relationships with basin materials, the low-albedo plains are interpreted as basin impact melt deposits. The large areal extent of the low-albedo plains suggests that basin impact melt deposits may have played an important role in resurfacing Mercury, especially during the early geologic history of the planet when impact rates were higher.

1. Introduction

The process controlling the formation of smooth plains deposits on the terrestrial planetary bodies has been strongly debated, with two major formation hypotheses: (1) formation as volcanic flows (Murray et al., 1974b, 1975; Strom, 1977; Kiefer and Murray, 1987; Spudis and Guest, 1988) and (2) formation by the emplacement of fluidized impact ejecta, an origin similar to that hypothesized for the Cayley plains on the Moon (Trask and Guest, 1975; Wilhelms, 1976; Oberbeck et al., 1977). For the Moon it is now generally accepted that low-albedo smooth plains (lunar maria) are produced from volcanic eruptions. Persuasive evidence has been presented by many of the high-albedo smooth plains surrounding large impact basins, especially Orientale and Imbrium, are the result of cratering processes. However, on Mercury such distinct albedo and morphologic relationships do not exist.

Most scientists involved in the geological mapping of Mercury from Mariner 10 data interpreted the smooth plains deposits to be of volcanic origin on the basis of their textural similarity to the lunar maria, stratigraphic relationships with smaller flooded craters in basin interiors, their location within many large impact craters and basins, the large volume of smooth plains deposits contained within topographic depressions, and spectral and albedo variations between the smooth plains and the surrounding terrain (e.g., Hapke et al., 1975; Strom et al., 1975). Reanalysis of the Mariner 10 color data led Robinson and Lucey (1997) to conclude that the locations of boundaries between distinct color units provided further evidence for an effusive volcanic origin of smooth plains, as well as for some pyroclastic activity. Nonetheless, considerable uncertainty remained about the volcanic origin of smooth plains, and it was thought that perhaps Mariner 10

resolution (mostly ~1 km) was insufficient to resolve diagnostic volcanic landforms such as volcanic edifices and vents (Milkovich et al., 2002). MESSENGER data provided further support for a volcanic origin for smooth plains (Murchie et al., 2008; Head et al., 2008, 2009a, 2011; Denevi et al., 2013a), including both such large-scale deposits as the northern smooth plains and small smooth plains deposits within individual craters ≤200 km diameter (Head et al., 2009a, 2011).

However, impact melt scaling laws (e.g., Cintala and Grieve, 1998) indicate that more impact melt should be produced on Mercury compared with the Moon. Impact melt production is dominated by the magnitude of an impact event which, in turn, is controlled by the impactor density, size and velocity, and the target density. Predicted impact velocities for the terrestrial planets indicate that Mercury has the highest average velocity, 42.5 km/s compared with 19.4 km/s for the Moon (Le Feuvre and Wieczorek, 2008). Expected melt volumes for basin-sized impact events are on the order of $>10^5 km^3$ (Cintala and Grieve, 1998; Abramov et al., 2012). The proportion of impact melt retained within the impact craters and basins increases with larger transient crater diameters, so that large impact basins could contain >60% of the impact melt produced. This percent suggests that approximately 10^4 km^3 of impact melt could be deposited exterior to the basin, a volume comparable to that of Mare Orientale on the Moon (Whitten et al., 2011); such a large volume of melt should be observable around the youngest mercurian impact basins.

Several young impact basins contain extensive smooth plains both within and exterior to the basin rim. While the interior deposits are generally thought to be volcanic, the basin exterior plains have a more ambiguous origin. For instance, Caloris (~1550 km

in diameter; Fassett et al., 2012) has extensive smooth plains deposits interior and exterior to the entire basin (Denevi et al., 2013a). The Caloris interior smooth plains have spectral properties consistent with the high reflectance plains (HRP) color unit (Denevi et al., 2009), which has been linked to a volcanic origin. The morphology, tectonics, and superposed crater population of the interior smooth plains are also consistent with a volcanic origin (e.g., Murchie et al., 2008; Watters et al., 2009b). On the other hand, the low-reflectance, color properties (Rava and Hapke, 1987; Robinson et al., 2008; Denevi et al., 2009), morphology, and stratigraphic relationship between the exterior plains and the Caloris rim, most especially the hummocky Odin formation, are consistent with the exterior smooth plains deposits that are associated with the impact basin formation (Fassett et al., 2009; Denevi et al., 2013). However, the size-frequency distribution of superposed impact craters indicates that emplacement of the Caloris exterior smooth plains occurred well after the basin-forming event (Strom et al., 2008; Fassett et al., 2009; Denevi et al., 2013). Either the crater size-frequency distributions do indicate real differences in the ages of the Caloris smooth plains, or one of several things has to be true: (1) the variations in the crater populations are not statistically significant, (2) the physical strength of the Caloris exterior plains is different from the interior plains leading to variations in crater diameter for the same-sized projectile, or (3) the rim of Caloris experienced self-secondary cratering which artificially increased the age of the basin impact event (Denevi et al., 2013).

Rembrandt basin (~720 km in diameter; Fassett et al., 2012) has similar morphologic units, interior and exterior plains deposits that can be used to evaluate these different possibilities and elucidate the distribution of impact basin ejecta on Mercury.

Rembrandt was discovered during the MErcury Surface, Space ENvironment, GEochemistry, and Ranging (MESSENGER) spacecraft's second flyby of Mercury (Watters et al., 2009a) in the southern hemisphere (32.89°S, 87.87°E). It is the second largest, well-preserved impact basin on Mercury that formed at approximately the same time as Caloris (Watters et al., 2009a). While Rembrandt is noteworthy for its successive phases of contractional and extensional deformation, the interior and exterior plains deposits provide an interesting case study for better understanding the distribution of basin ejecta deposits and the relationship between basin formation the emplacement of volcanic deposits on Mercury.

Similar to Caloris, the color properties of the Rembrandt basin plains vary between the basin interior deposits and the exterior plains deposits. Unsupervised cluster analyses conducted with MESSENGER's Mercury Atmospheric and Surface Composition Spectrometer (MASCS) data support the observation of different MDIS color units interior and exterior to Rembrandt basin (Helbert et al., 2013). The MASCS unsupervised cluster analysis results suggest that the Rembrandt interior plains are similar to the northern smooth plains while the exterior plains are similar to the surrounding terrain. Supervised classification of MASCS data from 300–1450 nm (Izenberg et al., 2013) also observed that the plains around Rembrandt have a spectral signature distinct from the interior plains. These color identifications support the hypothesis that the interior and exterior plains have different formation processes.

Analysis of the spectrally distinct interior and exterior plains deposits associated with Rembrandt basin will be useful for understanding the relationship between impact basins and their associated ejecta deposits on Mercury. The plains around Rembrandt will

be analyzed to determine whether impact basins on Mercury have extensive exterior impact melt deposits or whether the plains are dominantly volcanic in origin. The majority of circum-Caloris smooth plains are thought to have been formed volcanically (Fassett et al., 2009; Denevi et al., 2013); however, there are lingering questions about whether a certain circum-Caloris unit (the Odin formation) is impact basin ejecta. This study will specifically address the following questions: (1) Are there different types of smooth plains deposits around Rembrandt basin? and (2) What is the formation mechanism responsible for the emplacement of these plains deposits? Through this research, we hope to use the Rembrandt deposits to address larger outstanding questions regarding what the distribution of different plains reveals about the relationship between impact basins and volcanism or, conversely, what the Rembrandt plains deposits divulge about the generation of basin impact melt on Mercury.

2. Methods

The primary data for this study are images derived from the MESSENGER Mercury Dual Imaging System (MDIS) instrument (Hawkins et al., 2007). Other supplemental datasets include stereo photogrammetric topography data (Gaskell et al., 2008; Edmundson et al., 2011; Becker et al., 2012) derived from MDIS images and the MDIS color data. A region approximately 1700 km × 1400 km in size, centered over Rembrandt basin, was selected for detailed mapping of plains deposits. Smooth plains, referred to as high-albedo plains in this study, were mapped according to the identification criteria developed previously (e.g., Trask and Guest, 1975; Denevi et al., 2013), which includes surfaces that are sparsely cratered, are flat to gently undulating,

and have a smooth surface texture. Other plains deposits were noted in this region and were most easily identified by a lower albedo, a greater population of superposed craters, and in turn a rougher texture compared with the high-albedo smooth plains. Initially, in order to distinguish between high and low-albedo smooth plains, only an MDIS albedo mosaic (750 nm) was used for mapping. Then, a high incidence angle map of the same region was used to ensure that all smooth plains deposits had been mapped. Images taken at a high incidence angle, having longer shadows, effectively capture the morphology of a surface. Subtle features, such as wrinkle ridges and smooth textures, are easier to identify using images with a high incidence angle. The high incidence map was most useful when mapping the low-albedo plains; the lower surface albedo of this unit made it difficult to discern the morphology in some locations. Only the most areally extensive smooth plains deposits, those >20 km in horizontal extent, were included in the mapping.

The average reflectance of each areally extensive plains deposit was measured using an MDIS 8-band color mosaic (~670 m/ pixel). The 1000 nm band, the longest MDIS wavelength, was chosen for analysis because MDIS color units (Deveni et al., 2009) have the largest variation in surface reflectance at longer wavelengths due to variations in spectral slope. To ensure that the albedo values derived from the Rembrandt plains units can be compared with MDIS color units, the average reflectance values for representative MDIS color units were also measured (Table 1). Low-reflectance material (LRM) is the darkest MDIS color unit followed by low-reflectance blue plains (LBP), intermediate plains (IP), and high reflectance-red plains (HRP). Tolstoj rim and surrounding plains materials, plains south of Caloris, and the rims of Neruda and Atget craters are representative areas of LRM. The circum-Caloris plains and the region around

Neruda crater were measured to derive an average LBP value while the Borealis plains, Caloris interior, and the Firdousi-Faulkner plains were used to derive average reflectance for the HRP unit.

To estimate the ages and determine the stratigraphic relationships between the different plains units within and surrounding Rembrandt basin we measured the superposed crater populations. A MDIS 250 m/pixel image mosaic was used to identify all superposed craters >5 km in diameter (Strom et al., 2008). Obvious secondary craters (e.g., oblate rim, herringbone pattern, location in a chain or cluster) were excluded from our counts because these craters can make a planetary surface appear artificially older. Crater size-frequency distributions and crater density values (Table 2) were determined for each exposure of plains (Fig. 1) to determine stratigraphic relationships. In order to compare the areal density of impact craters and relative ages of the geologic units, $N(20)$ values are calculated for each study region, where $N(D)$ is the number of craters with diameter $\geq D$ (in km) per 10^6 km^2 area within a study region. Confidence intervals for each data point are reported as 1σ, which are estimated as the square root of the number of craters per diameter bin (Crater Analysis Techniques Working Group, 1979).

Embayed craters were used to estimate the volume of each exterior plains unit. To be considered embayed, a crater (a) must be almost completely filled with smooth plains so that only its rim is visible, or (b) lacks an identifiable secondary crater field and its proximal ejecta deposits appear to be truncated. One to two embayed craters were identified in each plains deposit (deposits 1–5, Fig. 1b) between 8 and 40 km in diameter (Table 3). Morphologic relationships derived by Pike (1988) were used to estimate the expected rim heights of these embayed craters. It was assumed that these craters were

morphologically fresh at the time of embayment and that the predicted crater rim height accurately estimated the buried crater rim height. If the impact craters were degraded prior to embayment then the Pike (1988) relationships will overestimate the rim height. Stereo photogrammetric topographic data (Gaskell et al., 2008; Edmundson et al., 2011; Becker et al., 2012) were used to produce topographic profiles across the selected embayed craters in order to determine current rim heights. The predicted and actual rim heights were then compared to produce an estimate of the plains deposit thickness. If more than one embayed crater was identified in a plains unit, then the estimated thickness of the plains was determined by averaging the two thickness estimates.

3. Plains identification and mapping

Many plains deposits can be identified around Rembrandt basin, most of which are not contained within impact structures. Three different plains units were identified during geologic mapping, (1) the high-albedo interior plains, (2) the high-albedo exterior plains, and (3) the low-albedo exterior plains. The low-albedo exterior plains predominate, covering 24.6% of the map region. In total the high-albedo plains cover 20.6% of the map area, with the exterior plains comprising 11.8% and the interior plains 8.8% of the surface area. Similar to many other basins on Mercury, Rembrandt is filled with high-albedo smooth plains, as noted previously (Watters et al., 2009; Denevi et al., 2009, 2013). Almost half of the high-albedo exterior plains (47%) are contained within impact craters >35 km in diameter. The remaining high-albedo exterior plains are associated with topographic lows (Fig. 2). All high-albedo plains have a smooth surface texture and a low abundance of superposed craters (Fig. 1c, d).

Low-albedo plains are predominantly confined to the Rembrandt basin exterior as large areally extensive deposits. The albedo of this unit varies across the map area, but is consistently lower than that of the high-albedo plains (Fig. 1c, d, and e). The topographic distribution of the low-albedo plains is markedly different from the high-albedo plains. Low-albedo plains are not confined to topographic lows; instead, each deposit of low-albedo plains traverses high and low-standing topography (Fig. 2). For instance, units 4 and 5 (Fig. 1b) overlap with Enterprise Rupes and thus have rapid and substantial changes in topography, on the order of 1.7 km and 2.8 km. Compared with the high-albedo plains, the low-albedo plains have a larger superposed crater population and appear to be more modified by impact and tectonic processes. For instance, the low-albedo plains are heavily modified by wrinkle ridges and lobate scarps, especially to the northeast of the basin (Fig. 3a). This dense region of wrinkle ridges and lobate scarps coincides with the most well-preserved exposures of Rembrandt basin sculpture (Fig. 3b), lineated terrain oriented radial to the basin center. Low-albedo plains do not show any evidence of basin ejecta modification. Instead, the low-albedo plains fill in the topographically low regions within this lineated terrain, so that only the sculpture “rims” are visible above the plains (arrows, Fig. 3b).

4. Surface reflectance values

Average albedo values for each of the areally extensive plains units (Fig. 1b) were derived using MDIS color data at 1000 nm. The LRM, LBP, IP, and HRP units have surface reflectance values of 0.071, 0.081, 0.096, and 0.116, respectively (Fig. 4; Table 1). Both the interior and exterior reflectance plains around Rembrandt basin have average

reflectance values of 0.110 and 0.101, consistent with the MDIS HRP unit (Table 1). The Rembrandt low-albedo plains 1000 nm surface reflectance of 0.088 is much lower than either of the high-albedo plains. Reflectance measurements of a hummocky plains deposit in the northern interior of the basin (Fig. 1a, f), believed to represent original basin materials, have a surface reflectance of 0.082. The hummocky basin unit and the low-albedo exterior plains have values that are most consistent with the MDIS LBP unit. Rembrandt exterior low-albedo plains have a comparatively higher albedo than the other LBP units, but this is contamination due to deposition of bright fresh crater ejecta onto the eastern deposits of low-albedo plains (i.e., unit 2; Fig. 1b) (Fig. 6a).

5. Crater statistics

Size-frequency distributions of superposed crater populations were determined for each of the plains units mapped within and around Rembrandt basin (Fig. 5). A cumulative frequency plot shows the Rembrandt interior high-albedo plains, the exterior high-albedo plains, and the exterior low-albedo plains (Fig. 5a). The superposed crater populations of all of the low-albedo plains (units 2–5, Fig. 1) were combined to improve statistics because these plains have similar morphologies, suggesting the low-albedo plains represent a single geologic unit. A cumulative size-frequency plot of the individual low-albedo plains displays a similar density of craters in each diameter bin (Fig. 5b), confirming that these plains were deposited contemporaneously and can in fact be analyzed as a single unit. The low-albedo exterior plains have a higher density of superposed craters compared with both of the high-albedo units (Fig. 5a), indicating that the low-albedo exterior plains are older than either high-albedo plains unit. Of the two

high-albedo units, the exterior plains are younger than the interior plains. Thus, plains emplacement began with the low-albedo exterior plains, followed by the interior high-albedo plains. The exterior high-albedo plains were the last to be emplaced, according to the superposed crater populations.

The crater size-frequency distributions for the low-albedo exterior plains and the high-albedo interior plains overlap at diameters >45 km (Fig. 5a). The lower frequency of craters >45 km in diameter on the low-albedo exterior plains could be due to obscuration and destruction by later impact events. Fresh impact craters, including Amaral (~109 km in diameter, 26.5°S 117.9°E) and two unnamed craters (17.3°S 110.4°E, 23.3°S 112.2°E), obscure much of the terrain northeast of Rembrandt basin (Fig. 6). Due to the high density of craters in various states of degradation it is difficult to map plains deposits to the northeast of Rembrandt. A high density of relatively more degraded craters obscures the original stratigraphy to the west, and HRP smooth plains (Denevi et al., 2013) cover much of the terrain south of Rembrandt basin. *R*-plots (see Crater Analysis Techniques Working Group, 1978) of the superposed crater populations (Fig. 5c, d) show a characteristic flat Population 2 shape indicative of the post-heavy bombardment crater population (Strom et al., 2005).

Crater density values were also computed for the plains units within and around Rembrandt basin (Fig. 7, Table 2). The rim-crest of Rembrandt basin has an $N(20)$ of 58±16. This crater density is comparable to the $N(20)$ values determined for the low-albedo plains, which vary from 29±21 to 63±16. The similarity and overlap in the cumulative size-frequency of the low-albedo plains indicates that these deposits formed near-contemporaneously and can be considered as one unit, therefore, the $N(20)$ value for

the combined low-albedo plains is 53±13. Similar to the crater size-frequency distributions, *N*(20) values for the high-albedo plains, the interior and exterior deposits, are 38±13 and 11±8, respectively (Table 2). Denevi et al. (2013) reported an *N*(20) value of 45±12 for the Rembrandt interior plains, which is in agreement with our calculated value. The exterior high-albedo plains has a low *N*(20) value. However, despite a low *N*(20) the exterior high-albedo plains are comparable to other smooth plains, including the Rudaki plains (*N*(20)=10±10) and the plains south of Rachmaninoff basin (*N*(20)=17±7 (Table 2) (Denevi et al., 2013).

6. Estimated Volumes

The volume of the exterior plains was estimated using morphologic measurements of embayed craters to derive thickness estimates (Fig. 8). Embayed craters that appeared to have sharper rims were preferentially selected for this analysis to ensure that the calculated plains thicknesses were not over-predicted. All of the exterior plains deposits, both high and low-albedo deposits, were estimated to be between 0.39 and 0.57 km thick. Two embayed craters were measured for all of the exterior plains deposits except for unit 5 (Fig. 1b), which only had one identifiable embayed crater in the map area. Stereo photogrammetric topographic profiles were measured to ascertain the current rim height of the selected embayed craters. This current rim height estimate was subtracted from the predicted rim height (Pike, 1988) to determine the plains thickness (Fig. 8a). When two embayed craters were present within a given plains deposit the thickness estimates were averaged together. The embayed craters measured in the exterior high-albedo smooth plains produce a deposit thickness of 0.39 km (unit 1; Fig. 1b, Table 3). Thickness

estimates for the low-albedo exterior plains are, 0.45, 0.36, 0.57, and 0.39 km respectively; the low-albedo exterior plains had an average thickness of 0.44 km (Table 3).

The thickness estimates and measurements of areal extent were then used to calculate the volume of each exterior plains deposit (Table 3). Unit 2 (Fig. 1b) is the most areally extensive plains deposit, comparable in extent to the smooth plains in Beethoven basin (~630 km in diameter) (Denevi et al., 2013). The high-albedo exterior plains and the low-albedo plains unit 4 are similar in area. The remaining exterior plains have a smaller areal extent. Most plains deposits are on the order of 10^4 km^3 except unit 2, the largest low-albedo plains unit located in the northeastern portion of the Rembrandt basin exterior, which is 1.1×10^5 km^3. Low-albedo plains units 3–5 (Fig. 1b) have volumes between 2.0 and 5.4×10^4 km^3. Combined, the low-albedo exterior plains are 2.06×10^5 km^3, volumetrically similar to the Stillwater Complex igneous intrusion (~2.3×10^5 km^3; Bonini, 1982). Unit 1, the one deposit of high-albedo exterior plains, has an estimated volume of 3.54×10^4 km^3.

7. Discussion

7.1. Distribution of the exterior plains

Three different plains units have been identified in and around Rembrandt basin on Mercury: (1) high-albedo interior plains, (2) high-albedo exterior plains, and (3) low-albedo exterior plains. The high-albedo interior plains have a smooth surface morphology (Fig. 1d) with a low density of superposed impact craters (Fig. 5, 7; Table 2). A comparison of Rembrandt crater rim and high-albedo interior $N(20)$ values, 58±16

(Watters et al., 2009) and 38±13, indicates that these plains were emplaced after the basin formation event. High-albedo smooth plains, similar to that observed for these Rembrandt interior plains, have been associated with a volcanic origin as a result of flooding and embayment relationships and distinct color contrasts with surrounding terrain (Murchie et al., 2008; Denevi et al., 2013). The combination of the low crater density, the high-albedo, and sharp morphologic and albedo boundaries of these interior plains provides strong evidence of a volcanic origin.

The high-albedo exterior plains share the same morphologic, albedo (Fig. 1c), and stratigraphic (Fig. 5, 7; Table 2) properties as the high-albedo interior plains. However, the high-albedo exterior plains are substantially younger than the high-albedo interior plains (Fig. 5, 7; Table 2). *N*(20) values for the interior (38±13) and exterior (11±8) high-albedo do not overlap, suggesting that these plains were not formed contemporaneously and were probably not produced from the same mantle melting event. The distribution of the high-albedo exterior plains is controlled by topography as almost all deposits are confined in topographic lows throughout the map region. This concentration in topographic lows, combined with a smooth to gently undulating surface, indicates that the high-albedo exterior plains were not significantly modified post-emplacement and that the terrain has not been substantially modified by tectonic activity since plains emplacement. Based on the evidence presented, the high-albedo exterior plains are volcanic in origin. This conclusion is supported by previous studies of smooth plains deposits on Mercury (Denevi et al., 2009, 2013).

The measured characteristics of the low-albedo plains are more ambiguous than either of the high-albedo plains deposits. Low-albedo plains are more textured than the

high-albedo plains due to the higher density of superposed craters (Fig. 5, 7; Table 2). Both of these observations indicate that the low-albedo plains are older than either high-albedo plains unit. In fact, the low-albedo plains are comparable in age to the Rembrandt basin formation event; Rembrandt basin has an $N(20)$ value of 58±16 (Watters et al., 2009) which substantially overlaps with the average value for the low-albedo plains, $N(20)$ = 53±13 (Table 2). The distribution of the low-albedo plains is not controlled by the current topography around Rembrandt basin. All five low-albedo units contain high and low-lying topography, including relief variations between 1.3 km and 2.8 km. Units 4 and 5 have rapid changes in topography owing to the presence of Enterprise Rupes (Fig. 2); however, not all of the relief changes over such a short distance. The large topographic variations (Fig. 2) and the tectonic modification (Fig. 3a) of the low-albedo plains indicate that these plains were modified post-emplacement. These observations do not elucidate the formation mechanism responsible for the deposition of the low-albedo plains. The two prevailing formation hypotheses for plains deposits on Mercury are related to impact-ejecta deposition (Trask and Guest, 1975; Wilhelms, 1976; Oberbeck et al., 1977) and volcanism (Murray et al., 1974b, 1975; Strom, 1977; Kiefer and Murray, 1987; Spudis and Guest, 1988). Below we review in detail the evidence of and against each formation process for the low-albedo plains.

7.2. Low-albedo plains: Impact or volcanic origin?

Ejecta scaling laws indicate that the continuous ejecta deposits and secondary crater fields for impact craters and basins on Mercury were emplaced much closer to the rim crest compared with lunar impact features (Gault et al., 1975; Melosh, 1989). The

higher gravitational acceleration at the surface of Mercury could have led to more well-preserved impact ejecta deposits because these deposits would be more areally extensive close to basin and crater rims compared with the Moon. Smooth lunar basin ejecta deposits, referred to as either the Cayley formation or light plains, are formed from secondary craters (e.g., Oberbeck et al., 1973), typically as discrete small deposits 2–4 basin radii outward from the basin rim crest (Meyer et al., 2013). Scaling these lunar values to Mercury (Gault et al., 1975), the smooth ejecta deposits would be expected within 1.3–2.6 basin radii. For Rembrandt basin, the secondary ejecta-produced smooth plains deposits would be expected in an annulus between 470 km and 935 km from the basin rim. The majority of mapped low-albedo deposits are actually interior to this annulus (hatched area in Fig. 9). Owing to the discrepancy between the predicted location of impact-produced smooth plains deposits and the low-albedo exterior plains, the low-albedo exterior plains do not appear to originate from this secondary cratering process. However, the close proximity of the low-albedo exterior plains suggests that these plains deposits may be impact melt.

Impact melt deposits are found to occur on impact crater rims on Mercury (Hawke and Cintala, 1977), similar to results for the Moon (e.g., Hawke and Head, 1977). The distance between the low-albedo plains and the Rembrandt rim-crest and their location varies azimuthally around the basin (Fig. 9). There are no low-albedo plains in the northwest quadrant of the map area. Low-albedo plains on the southeast half are closest to the rim (to the right of the 45°–255° line, Fig. 9). The remaining low-albedo plains, located in the northwest half of the map region, are within ~200 km of the basin rim. If the low-albedo plains are impact melt then the observed distribution may provide

information about the impact event, as oblique impacts are expected to produce asymmetric ejecta deposits (e.g., Howard and Wilshire, 1975). Larger impact features on Mercury, such as the small young impact basins Raditladi (258 km in diameter) and Rachmaninoff (306 km in diameter) (Prockter et al., 2010; Marchi et al., 2011), have smooth plains deposits interpreted as exterior impact melt deposits adjacent to the basin rim-crest (Fig. 10). The exterior smooth plains around Raditladi (Fig. 10a) and Rachmaninoff (Fig. 10b) are preferentially distributed around the basins with the most areally extensive plains concentrated in the northwest and southwest, respectively. Rachmaninoff is the larger of the two basins and has substantially more areally extensive impact melt. Both of these basins are less than half the size of Rembrandt and, thus, cannot be used for a direct volumetric comparison. However, the location of impact melt deposits on the basin rim of Raditladi and Rachmaninoff indicates that the close proximity of the Rembrandt low-albedo plains to the basin rim-crest provides evidence of an impact melt origin.

To estimate the volume of impact melt expected from a basin impact event the size of Rembrandt, we used the methods of Cintala and Grieve (1998). Other volume estimation methods (Abramov et al., 2012) produced values of similar magnitude to the results presented here. The volume of total impact melt produced is approximated by the equation:

$$V_m = c \cdot D_{tc}^{d}$$

where V_m is the volume of impact melt produced, D_{tc} is the diameter of the transient cavity, and c and d are constants dependent on the impactor properties (e.g., composition and velocity, Cintala and Grieve, 1998). The transient crater diameter was estimated using the equations of Schmidt and Housen (1987), where the transient crater diameter is

dependent on the projectile density, projectile diameter, target density, impact velocity, and surface gravitational acceleration of the planetary body in question:

$$D_{tc} = 1.16 \cdot \left(\frac{\rho_p}{\rho_t}\right)^{\frac{1}{3}} \cdot d_p^{0.78} \cdot v_i^{0.44} \cdot g^{-0.22}$$

For simplicity, the density of the target (ρ_t) and projectile (ρ_p) were taken as equal (Roberts and Barnouin, 2012; Ernst et al., 2010). The impact velocity (v_i) was assumed to be 42.5 km/s, the average value for Mercury (Le Feuvre and Wieczorek, 2008). The projectile diameter (d_p), ~42.4 km in diameter, was estimated using equation 7a from Cintala and Grieve (1998). From these equations, the diameter of transient cavity of Rembrandt basin was determined to be ~385 km which produces a volume of impact melt of ~1.5×10^6 km^3. The total amount of melt estimated to remain in the impact cavity is approximately 64% (Cintala and Grieve, 1998). Therefore, ~5.39×10^5 km^3 of impact melt should be ejected from Rembrandt basin and emplaced in the surrounding terrain. This estimate of the ejected impact melt is only 2.6 times greater than our estimate for the volume of low-albedo exterior plains, 2.06×10^5 km^3.

Extensive volcanic deposits occur across the surface of Mercury. The northern smooth plains (Head et al., 2011) and the circum-Caloris plains (Fassett et al., 2009, Denevi et al., 2013) are some of the largest identified volcanic deposits. However, the areal extent and implied volumes of young volcanic plains vary substantially as there are volcanic deposits in smaller impact craters (high-albedo exterior plains, Fig. 1b). Superposed crater populations on these surfaces indicate they are some of the youngest deposits on Mercury. Typically, identified young volcanic deposits have been associated with high-albedos (Robinson and Lucey, 1997; Robinson et al., 2008; Denevi et al., 2009) and smooth flat to gently undulating surfaces (Trask and Guest, 1975; Denevi et

al., 2013). The low-albedo plains surrounding Rembrandt basin do not have a high-albedo and are not smooth. Young volcanic flows are associated with high-albedos (Denevi et al., 2009, 2013), but proposed older volcanic deposits, such as the intercrater plains do not have high-albedos (Whitten et al., 2014). The color properties of intercrater plains are more similar to the global average than to the young volcanic plains. Analyses of the intercrater plains imply that the color properties of volcanic deposits change over time on Mercury, mostly through reworking by impact processes. Additionally, the Rembrandt low-albedo plains cover a range of elevations (Fig. 2).

Embayed craters within smooth plains also provide evidence for a volcanic origin. The morphology of embayed craters can vary. In some cases, these craters have breached rim-crests where the crater has been filled with material of similar composition and texture to the surrounding terrain. Elsewhere, a crater may be unfilled but its ejecta deposits are not superposed on the surrounding terrain and are instead truncated or embayed (e.g., Murchie et al., 2008). In the low-albedo plains surrounding Rembrandt basin there are many embayed craters present (Fig. 8b-j). However, it is difficult to place all of these craters within a stratigraphic framework with the basin sculpture (Fig. 11a, b) and the low-albedo plains. For instance, if the low-albedo plains were composed of impact melt then these embayed craters would have had to form prior to the basin impact event and their crater rims should show evidence of basin ejecta sculpture, based on their proximity to the basin.

Several craters adjacent to the Rembrandt basin rim-crest have sculpted rims (craters A and B in Fig. 11b), but are filled with high-albedo plains material (Fig. 1b). On the western side of Rembrandt there is another crater filled with low-albedo material that

has basin sculpture on the part of its rim nearest to the basin (Fig. 1a, b). This second example provides evidence that the crater was pre-Rembrandt and the low-albedo plains were emplaced afterwards. There are a few examples of craters that may be embayed by low-albedo plains and show no evidence of basin sculpture on their rims (Fig. 11c, d). For one of these craters, it may lack basin sculpture because it is too far from Rembrandt's rim. Since this crater is located just outside of the furthest extent of basin sculpture it is impossible to place it within the stratigraphic sequence of events. Within some of the Rembrandt secondary crater chains there are small superposed craters (Fig. 11e) that may be embayed. This would suggest that Rembrandt basin formed, then these small craters occurred on material within the secondary chain that was then embayed by low-albedo plains. However, at current image resolutions it is difficult to determine unequivocally whether these small impact craters are embayed. Is this because the basin ejecta are not ejected such far distances? On the Moon, large (Ptolemaeus, 153 km in diameter) and small (Flammarion U, 11 km in diameter) impact craters show evidence of Imbrium basin sculpture on their rims (Fig. 11f) as far away as 820 km from the basin rim. Scaling that distance to Mercury (Gault et al., 1975), basin sculpture is expected to occur at distances up to 530 km from the basin rim-crest, which coincides with the interior boundary of the secondary crater zone from Fig. 9. However, there is no morphologic evidence to suggest that basin sculpture on Mercury extends to those theoretical distances. Therefore, there is no unequivocal evidence for embayed craters in the low-albedo plains that were formed post-basin, but prior to emplacement of low-albedo plains.

Based on the evidence presented above we interpret the low-albedo plains to have an impact origin, specifically an impact melt origin. Low-albedo plains occur closer to the Rembrandt basin rim than is expected for impact basin secondary deposits, such as the lunar Cayley formation (Fig. 9). In addition, the low-albedo plains do not fit the expected morphology of secondary crater-produced smooth plains deposits (small discrete deposits confined to topographic lows and impact craters) (Meyer et al., 2013). The similarity in the measured and calculated exterior impact melt volumes, the location of the low-albedo plains near the basin rim-crest, the overlapping basin rim and low-albedo plains $N(20)$ values, and the similar albedo properties between the low-albedo plains and the basin interior materials provided strong evidence for an impact origin. Image resolutions (>250 m/pixel) of the currently available MESSENGER data are unable to provide unambiguous evidence that the low-albedo plains contain embayed craters with sculpted rims. Thus, with the currently available data it appears that the circum-Rembrandt low-albedo plains are impact melt deposits from the basin formation event. This is the first identification of basin impact melt deposits on Mercury and has important implications for the resurfacing history of the planet.

7.3. Comparison of Rembrandt and Caloris exterior smooth plains

The Caloris and Rembrandt impact basins formed at approximately the same time (Watters et al., 2009) and are the largest well-preserved basins on Mercury. Both Rembrandt and Caloris have interior smooth plains composed of the high reflectance red plains (HRP) MDIS color unit and low-albedo exterior deposits classified as either low-reflectance blue plains (LBP) or low-reflectance material (LRM) (Denevi et al., 2009).

For Caloris specifically, the MDIS color variations between interior and exterior smooth plains deposits are consistent with a formation model where the exterior deposits are associated with basin formation and the interior smooth plains have a distinct origin. However, it was found that this hypothesis is inconsistent with crater density values derived for the Caloris basin rim ($N(20)= 54\pm12$), interior ($N(20)= 23\pm4$), and exterior ($N(20)=25\pm9$) smooth plains deposits (Fassett et al., 2009); the large contrast in crater density between the Caloris basin event and the exterior plains indicates that these units did not form contemporaneously. As a result of this temporal difference, several workers have interpreted crater size-frequency distributions and crater density values to mean that both the exterior and interior plains are volcanic in origin (e.g., Fassett et al., 2009; Denevi et al., 2013) despite the observed MDIS color variations.

The same cannot be said for Rembrandt basin and its plains deposits. While the MDIS color relationships are similar to those observed at Caloris (HRP interior plains, LBP exterior plains), the size-frequency distributions of craters are not. Like Caloris, Rembrandt interior and exterior smooth plains show distinct color variations, with HRP interior plains and exterior plains composed of HRP, LBP, and LRM materials. The majority of the plains surrounding Rembrandt are LBP and LRM, similar to the original basin materials (Ernst et al., 2010). The high-albedo exterior plains consistent with the HRP color unit are much smaller than the low-albedo plains deposits. Additionally, the largest deposit of high-albedo plains is confined to the north of the basin (Fig. 1b). Crater size-frequency distributions and crater density values for the interior and exterior plains do not show the same temporal relationship as the Caloris data. The crater populations for the Rembrandt plains do not necessarily support a volcanic origin for all of the exterior

plains units (Figs. 4, 6). The two high-albedo plains units, Rembrandt interior and exterior high-albedo plains (yellow symbols, Figs. 6), have significantly lower *N*(20) values compared with the basin (purple circle, Fig. 7). A volcanic origin for these two high-albedo plains is consistent with the crater density values, the smooth and level morphology of the unit, and the MDIS HRP color unit assignment. On the other hand, the *N*(20) value for the Rembrandt low-albedo exterior plains does not differ significantly from the Rembrandt basin rim *N*(20) value (Fig. 7; Table 2). The near-contemporaneous ages implied from the *N*(20) crater density values, combined with the similarity in MDIS color properties between the exterior low-albedo plains and Rembrandt rim, tend to suggest an impact origin.

The results of this study confirm that the plains around Caloris and Rembrandt basins were not formed by the same geologic process. Rembrandt low-albedo exterior plains are impact melt deposits while the Caloris plains are all likely volcanic in origin. The volcanic interpretation of the exterior deposits around Caloris is dominated by the young ages calculated for the plains. For Rembrandt, the exterior plains are similar in age to the basin formation event and share similar MDIS color properties with the original basin materials. Thus, the two largest well-preserved impact basins on Mercury provide conflicting information about the distribution of impact ejecta. Rembrandt basin indicates that there should be large deposits of impact melt on Mercury close to basin rim crests and Caloris does not appear to have any preserved impact melt deposits. This lack of impact melt around Caloris could be due to later resurfacing of impact deposits, however. The oldest deposits on Mercury, known as the intercrater plains, are believed to have formed as a series of smooth volcanic plains deposits that were emplaced during the early

geologic history of Mercury (Chapter 4); however, this discovery of areally extensive basin impact melt deposits provides another important mechanism for large-scale resurfacing events. The fact that Mercury is saturated with craters >128 km in diameter (Fassett et al., 2011) implies that the surface has been completely modified by impact craters and their associated ejecta deposits.

8. Conclusion

MESSENGER image data have been used to map the distribution of plains deposits within and around the Rembrandt impact basin on Mercury and to determine the origin of those identified plains. Additionally, this analysis of plains deposits around the young and well-preserved Rembrandt basin has provided information about basin ejecta deposits and the relationship between basin formation and emplacement of volcanic deposits. We find that:

(1) Three different types of plains exist within and around Rembrandt basin, the high-albedo interior plains, high-albedo exterior plains, and low-albedo exterior plains. The low-albedo exterior plains have the greatest areal extent.

(2) Both the high-albedo interior and exterior plains are interpreted as volcanic in origin based on their high-albedo, sparse superposed crater populations, and smooth surface textures.

(3) The Rembrandt low-albedo exterior plains are interpreted as basin impact melt. This plains deposit has a high density of superposed craters and a low surface reflectance; these characteristics are shared with Rembrandt rim materials and are also consistent with ejecta deposits around other impact basins such as

Tolstoj (e.g., Denevi et al., 2009). Additionally, the distribution of the low-albedo plains immediately adjacent to the Rembrandt basin rim supports an impact melt origin.

(4) The presence of embayed craters with circum-basin plains materials would provide strong evidence for a volcanic origin if positively identified. However, because Rembrandt basin is located in the southern hemisphere of Mercury there is a paucity of high resolution images available to determine whether embayed craters exist within the low-albedo plains.

(5) The morphology and distribution of Rembrandt low-albedo plains indicates that basin impact deposits were volumetrically and areally extensive enough to resurface large portions of the planet. This has important implications for global resurfacing and the formation of intercrater plains.

(6) The MErcury Radiometer and Thermal Infrared Spectrometer (MERTIS) instrument (Hiesinger et al., 2010) on the BepiColombo Mercury Planetary Orbiter (Benkhoff et al., 2010) will provide further data on the mineralogy and composition of the different plains deposits on Mercury and thus aid in the determination their formation process.

Acknowledgements

We gratefully acknowledge funding from the MESSENGER project, which is supported by the NASA Discovery Program under contracts NASW-00002 to the Carnegie Institution of Washington and NAS5-97271 to The Johns Hopkins University Applied Physics Laboratory.

References

Abramov, O., Wong, S.M., Kring, D.A., 2012. Differential melt scaling for oblique impacts on terrestrial planets. Icarus 218, 906–916. doi: 10.1016/j.icarus.2011.12.022.

Becker, K.J., Weller, L.A., Edmundson, K.L., Becker, T.L., Robinson, M.S., Enns, A.C., Solomon, S.C., 2012. Global controlled mosaic of Mercury from MESSENGER orbital images. Lunar Planet. Sci. 43, abstract 2654.

Benkhoff, J., van Casteren, J., Hayakawa, H., Fujimoto, M., Laakso, H., Novara, M., Ferri, P., Middleton, H.R., Ziethe, R., 2010. BepiColombo – Comprehensive exploration of Mercury: Mission overview and science goals. Planet. Space Sci. 58, 2–20. doi:10.1016/j.pss.2009.09.020.

Bonini, W.E.,1982. The size of the Stillwater complex: An estimate from gravity data. In: Walker, D., McCallum, I.S. (Eds.), Workshop on Magmatic Processes of Early Planetary Crusts: Magma Oceans and Stratiform Layered Intrusions. Lunar and Planetary Institute, Houston, TX, pp. 53–55.

Cintala, M.J., Grieve, R.A.F., 1998. Scaling impact melting and crater dimensions: Implications for the lunar cratering record. Meteor. Planet. Sci. 33, 889–912.

Crater Analysis Techniques Working Group, 1979. Standard techniques for presentation and analysis of crater size-frequency data. Icarus 37, 467–474.

Denevi, B.W., Robinson, M.S., Solomon, S.C., Murchie, S.L., Blewett, D.T., Domingue, D.L., McCoy, T.J., Ernst, C.M., Head, J.W., Watters, T.R., Chabot, N.L., 2009. The evolution of Mercury's crust: A global perspective from MESSENGER. Science 324, 613–618. doi: 10.1126/science.1172226.

Denevi, B.W., Ernst, C.M., Meyer, H.M., Robinson, M.S., Murchie, S.L., Whitten, J.L., Head, J.W., Watters, T.R., Solomon, S.C., Ostrach, L.R., Chapman, C.R., Burne, P.K., Klimczak, C., Peplowski, P.N., 2013. The distribution and origin of smooth plains on Mercury. J. Geophys. Res. Planets 118, 891–907. doi: 10.1002/jgre.20075.

Edmundson, K.L., Weller, L.A., Becker, K.J., Becker, T.L., Rosiek, M.R., Robinson, M.S., Solomon, S.C., 2011. Preliminary photogrammetric control of MESSENGER orbital images of Mercury. Abstracts with Programs 43 (5), paper 100-6, p. 267, Geological Society of America, Boulder, Colo.

Ernst, C.M., Murchie, S.L., Barnouin, O.S., Robinson, M.S., Denevi, B.W., Blewett, D.T., Head, J.W., Izenberg, N.R., Solomon, S.C., Roberts, J.H., 2010. Exposure of spectrally distinct material by impact crater on Mercury: Implications for global stratigraphy. Icarus 209, 210–223.

Fassett, C.I., Head, J.W., Blewett, D.T., Chapman, C.R., Dickson, J.L., Murchie, S.L., Solomon, S.C., Watters, T.R., 2009. Caloris impact basin: Exterior geomorphology, stratigraphy, morphometry, radial sculpture, and smooth plains deposits. Earth Planet. Sci. Lett. 285, 297–308. doi: 10.1016/j.epsl.2009.05.022.

Fassett, C.I., Kadish, S.J., Head, J.W., Solomon, S.C., Strom, R.G., 2011. The global population of large craters on Mercury and comparison with the Moon. Geophys. Res. Lett. 38, L10202. doi:10.1029/2011GL047294.

Fassett, C.I., Head, J.W., Baker, D.M.H., Zuber, M.T., Smith, D.E., Neumann, G.A., Solomon, S.C., Klimczak, C., Strom, R.G., Chapman, C.R., Prockter, L.M., Phillips, R.J., Oberst, J., Preusker, F., 2012. Large impact basins on Mercury: Global distribution, characteristics, and modification history from MESSENGER orbital data. J. Geophys. Res. 117, E00L08. doi: 10.1029/2012JE004154.

Gaskell, R.W., Gillis-Davis, J., Sprague, A.L., 2008. Topography of Mercury from imaging data. AAS, Division Planet. Sci. Meet. 40, abstract 51.05.

Gault, D.E., Guest, J.E., Murray, J.B., Dzurisin, D., Malin, M.C., 1975. Some comparisons of impact craters on Mercury and the Moon. J. Geophys. Res. 80, 2444–2460.

Hapke, B., Danielson, G.E., Klaasen, K., Wilson, L., 1975. Photometric observations of Mercury from Mariner 10. J. Geophys. Res. 80, 2431–2443.

Hawke, B. R. and Cintala, M. J. 1977, Impact Melts on Mercury and the Moon, Bulletin of the American Astronomical Society, Vol. 9, p531 (abstract).

Hawke, B.R., Head, J.W., 1977. Impact melt on lunar crater rims. In: Roddy, D.J., Pepin, R.O., Merrill, R.B., (Eds.). Impact and Explosion Cratering. Pergamon Press, New York, NY, pp. 815–841.

Hawkins III, S.E., Boldt, J.D., Darlington, E.H., Espiritu, R., Gold, R.E., Gotwols, B., Grey, M.P., Hash, C.D., Hayes, J.R., Jaskulek, S.E., Kardian, C.J., Keller, M.R., Malaret, E.R., Murchie, S.L., Murphy, P.K., Peacock, K., Prockter, L.M., Reiter,

R.A., Robinson, M.A., Schaefer, E.D., Shelton, R.G., Sterner, R.E., Taylor, H.W., Watters, T.R., Williams, B.D., 2007. The Mercury Dual Imaging System on the MESSENGER spacecraft. Space Sci. Rev. 131, 247–338. doi: 10.1007/s11214-007-9266-3.

Head, J.W., Chapman, C.R., Domingue, D.L., Hawkins, S.E., McClintock, W.E., Murchie, S.L., Prockter, L.M., Robinson, M.S., Strom, R.G., Watters, T.R., 2007. The geology of Mercury: The view prior to MESSENGER mission. Space Sci. Rev. 131, 41–84. doi: 10.1007/s11214-007-9263-6.

Head, J.W., Murchie, S.L., Prockter, L.M., Robinson, M.S., Solomon, S.C., Strom, R.G., Chapman, C.R., Watters, T.R., McClintock, W.E., Blewett, D.T., Gillis-Davis, J.J., 2008. Volcanism on Mercury: Evidence from the first MESSENGER flyby. Science 321, 69–72. doi: 10.1126/science.1159256.

Head, J.W., Murchie, S.L., Prockter, L.M., Solomon, S.C., Chapman, C.R., Strom, R.G., Watters, T.R., Blewett, D.T., Gillis-Davis, J.J., Fassett, C.I., Dickson, J.L., Morgan, G.A., Kerber, L., 2009a. Volcanism on Mercury: Evidence from the first MESSENGER flyby for extrusive and explosive activity and the volcanic origin of plains. Earth Planet. Sci. Lett. 285, 227–242. doi: 10.1016/j.epsl.2009.03.007.

Head, J.W., Chapman, C.R., Strom, R.G., Fassett, C.I., Denevi, B.W., Blewett, D.T., Ernst, C.M., Watters, T.R., Solomon, S.C., Murchie, S.L., Prockter, L.M., Chabot, N.L., Gillis-Davis, J.J., Whitten, J.L., Goudge, T.A., Baker, D.M.H., Hurwitz, D.M., Ostrach, L.R., Xiao, Z., Merline, W.J., Kerber, L., Dickson, J.L., Oberst, J., Byrne, P.K., Klimczak, C., Nittler, L.R., 2011. Flood volcanism in the northern high latitudes of Mercury revealed by MESSENGER. Science 333, 1853–1856.

doi: 10.1126/science.1211997.

Helbert, J., D'Amore, M., Head, J.W., Byrne, P.K., Holsclaw, G.M., Izenberg, N.R., McClintock, W.E., Solomon, S.C., 2013. A comparison of the spectral properties of the Caloris and Rembrandt impact basins. Lunar Planet. Sci. 44, abstract 1496.

Hiesinger, H., Helbert, J., MERTIS Co-I Team, 2010. The Mercury Radiometer and Thermal Infrared Spectrometer (MERTIS) for the BepiColombo mission. Planet. Space Sci. 58, 144–165. doi:10.1016/j.pss.2008.09.019.

Howard, K.A., Wilshire, H.G., 1975. Flows of impact melt at lunar craters. J. Res. U.S. Geol. Survey 3, 237–251.

Izenberg, N.R., Klima, R.L., Murchie, S.L., Blewett, D.T., Holsclaw, G.M., McClintock, W.E., Malaret, E., Mauceri, C., Vilas, F., Sprague, A.L., Helbert, J., Domingue, D., Head III, J.W., Goudge, T.A., Solomon, S.C., Hibbitts, C., Dyar, M.D., 2014. The low-iron, reduced surface of Mercury as seen in spectral reflectance by MESSENGER. *Icarus* 228, 364–374. doi: 10.1016/j.icarus.2013.10.023.

Kiefer, W.S., Murray, B.C., 1987. The formation of Mercury's smooth plains. Icarus 72, 477–491.

Le Feuvre, M., Wieczorek, M.A., 2008. Nonuniform cratering of the terrestrial planets. Icarus 197, 291–306. doi: 10.1016/j.icarus.2008.04.011.

Marchi, S., Massironi, M., Cremonese, G., Martellato, E., Giacomini, L., Prockter, L., 2011. The effects of the target material properties and layering on the crater chronology: The case of Raditladi and Rachmaninoff basins on Mercury. Planet. Space Sci. 59, 1968–1980. doi: 10.1016/j.pss.2011.06.007.

Melosh, H.J., 1989. Impact Cratering: A Geologic Process. Oxford Univ. Press, Oxford,

UK, 245 pp.

Meyer, H.M., Denevi, B.W., Boyd, A.K., Robinson, M.S., 2013. The distribution and origin of lunar light plains around Orientale basin. Lunar Planet Sci. 44, abstract 1539.

Milkovich, S.M., Head, J.W., Wilson, L., 2002. Identification of mercurian volcanism: Resolution effects and implications for MESSENGER. Meteorit. Planet. Sci. 37, 1209–1222.

Murchie, S.L., Watters, T.R., Robinson, M.S., Head, J.W., Strom, R.G., Chapman, C.R., Solomon, S.C., McClintock, W.E., Prockter, L.M., Domingue, D.L., Blewett, D.T., 2008. Geology of the Caloris Basin, Mercury: A view from MESSENGER. Science 321, 73–76. doi: 10.1126/science.1159261.

Murray, B.C., Belton, M.J.S., Danielson, G. E., Davies, M.E., Gault, D.E., Hapke, B., O'Leary, B., Strom, R.G., Suomi, V., Trask, N., 1974b. Mercury's surface: Preliminary description and interpretation from Mariner 10 pictures. Science 185, 169–179. doi: 10.1126/science.185.4146.169.

Murray, B. C., Strom, R. G., Trask, N. J., Gault, D.E., 1975. Surface history of Mercury: Implications for terrestrial planets. J. Geophys. Res. 80, 2508–2514. doi: 10.1029/JB080i017p02508.

Oberbeck, V.R., Hörz, F., Morrison, R.H., Quaide, W.L., 1973. Emplacement of the Cayley formation. NASA Technical Memorandum X-62,302, pp. 51.

Oberbeck, V.R., Quaide, W.L., Arvidson, R.E., Aggarwal, H.R., 1977. Comparative studies of lunar, martian, and mercurian craters and plains. J. Geophys. Res. 82, 1681–1698.

Prockter, L.M., Ernst, C.M., Denevi, B.W., Chapman, C.R., Head III, J.W., Fassett, C.I., Merline, W.J., Solomon, S.C., Watters, T.R., Strom, R.G., Cremonese, G., Marchi, S., Massironi, M., 2010. Evidence for young volcanism on Mercury from the third MESSENGER flyby. Science 329, 668–671. doi: 10.1126/science.1188186.

Rava, B., Hapke, B., 1987. An analysis of the Mariner 10 color ratio map of Mercury. Icarus 71, 397–429.

Roberts, J.H., Barnouin, O.S., 2012. The effect of the Caloris impact on the mantle dynamics and volcanism of Mercury. J. Geophys. Res. 117, E02007. doi: 10.1029/2011JE003876.

Robinson, M.S., Lucey, P.G., 1997. Recalibrated Mariner 10 color mosaics: Implications for Mercurian volcanism. Science 275, 197–200. doi: 10.1126/science.275.5297.197.

Robinson, M.S., Murchie, S.L., Blewett, D.T., Domingue, D.L., Hawkins, S.E., Head, J.W., Holsclaw, G.M., McClintock, W.E., McCoy, T.J., McNutt Jr., R.L., Prockter, L.M., Solomon, S.C., Watters, T.R., 2008. Reflectance and color variations on Mercury: Regolith processes and compositional heterogeneity. Science 321, 66–69.

Schmidt, R.M., Housen, K.R., 1987. Some recent advances in the scaling of impact and explosion cratering. Int. J. Impact Engin. 5, 543–560.

Spudis P. D., Guest, J. E., 1988. Stratigraphy and geologic history of Mercury. In: Vilas, F., Chapman, C.R., Matthews, M.S. (Eds.). Mercury. Univ. Ariz. Press, Tucson, Ariz., pp. 336–373.

Strom, R.G., 1977. Origin and relative age of lunar and mercurian intercrater plains. Phys. Earth Planet. Inter. 15, 156–172.

Strom, R.G., Trask, N.J, Guest, J.E., 1975. Tectonism and volcanism on Mercury. J. Geophys. Res. 80, 2478–2507.

Strom, R.G., Malhotra, R., Ito, T., Yoshida, F., Kring, D.A., 2005. The origin of planetary impactors in the inner solar system. Science 309, 1847–1850. doi:10.1126/science.1113544.

Strom, R.G., Chapman, C.R., Merline, W.J., Solomon, S.C., Head, J.W., 2008. Mercury cratering record viewed from MESSENGER's first flyby. Science 321, 79–81. doi:10.1126/science.1159317.

Trask, N.J., Guest, J.E., 1975. Preliminary geologic terrain map of Mercury. J. Geophys. Res. 80, 2461–2477. doi: 10.1029/JB080i017p02461.

Watters, T.R., Head, J.W., Solomon, S.C., Robinson, M.S., Chapman, C.R., Denevi, B.W., Fassett, C.I., Murchie, S.L., Strom, R.G., 2009a. Evolution of the Rembrandt impact basin on Mercury. Science 324, 618–621. doi: 10.1126/science.1172109.

Watters, T.R., Murchie, S.L., Robinson, M.S., Solomon, S.C., Denevi, B.W., André, S.L., Head, J.W., 2009b. Emplacement and tectonic deformation of smooth plains in the Caloris basin, Mercury. Earth Planet. Sci. Lett. 285, 309–319. doi: 10.1016/j.epsl.2009.03.040.

Whitten, J.L., Head, J.W., Staid, M.I., Pieters, C.M., Mustard, J., Clark, R., Nettles, J., Klima, R.L., Taylor, L., 2011. Lunar mare deposits associated with the Orientale impact basin: New insights into mineralogy, history, mode of emplacement, and

relation to Orientale Basin evolution from Moon Mineralogy Mapper (M^3) data from Chandrayaan-1. J. Geophys. Res. 116, E00G09. doi: 10.1029/2010JE003736.

Whitten, J.W., Head, J.W., Denevi, B.W., Solomon, S.C., 2014. Intercrater plains on Mercury: Insights into unit definition, characterization, and origin from MESSENGER datasets, in preparation.

Wilhelms, D. E., 1976. Mercurian volcanism questioned. Icarus 28, 551–558. doi: 10.1016/0019-1035(76)90128-7.

Table 1. 1000 nm surface reflectance for global MDIS color units and Rembrandt plains deposits.

Unit	1000 nm reflectance
Low-reflectance material	
Tolstoj rim	0.071
Neruda	0.065
Atget	0.075
Tolstoj plains	0.074
South Caloris plains	0.072
Average LRM	0.071
Low-reflectance blue plains	
circum-Caloris	0.085
circum-Nerdua	0.077
Average LBP	0.081
High-reflectance red plains	
Borealis plains	0.119
Caloris interior	0.107
Firdousi-Faulkner plains	0.123
Average HRP	0.116
Intermediate plains	
Global average	0.096
Rembrandt plains	
Unit 1	0.101
Rembrandt interior	0.110
Hummocky plains	0.082
Unit 2	0.084
Unit 3	0.082
Unit 4	0.095
Unit 5	0.091
Average low-albedo plains	0.088

Table 2. Crater density ages for Rembrandt, Caloris, and smooth plains deposits.

Unit[a]	***N*(20)**	***N*(10)**	**Source**
	Rembrandt deposits		
All high-albedo	11±8	44±15	this study
(1) High-albedo	11±11	22±16	this study
All low-albedo	53±13	217±15	this study
(2) Low-albedo	63±16	121±22	this study
(3) Low-albedo	29±21	88±36	this study
(4) Low-albedo	42±21	116±35	this study
(5) Low-albedo	58±34	117±48	this study
Rim	58±16	-	*Watters et al*, 2009
Interior	38±13	110±23	this study
Interior	45±12	103±19	*Denevi et al.*, 2013
	Caloris deposits		
Rim	54±12	-	*Watters et al*, 2009
South of Caloris	32±9	92±16	*Denevi et al.*, 2013
Caloris interior	26±4	80±7	*Denevi et al.*, 2013
West of Caloris	25±8	91±15	*Denevi et al.*, 2013
East of Caloris	19±9	56±16	*Denevi et al.*, 2013
Caloris basin	58±13	-	*Spudis and Guest*, 1988
Caloris floor	39±12	-	*Spudis and Guest*, 1988
	Tolstoj basin		
Ejecta deposit	93±16	173±22	*Whitten et al.*, 2014
	Smooth plains		
Shakespeare Quad. (H-3)	28±7	-	*Spudis and Guest*, 1988
Tolstoj Quad. (H-8)	26±5	-	*Spudis and Guest*, 1988
H-3 and H-8 Quads.	24±7	-	*Spudis and Guest*, 1988
Rudaki plains	10±10	51±23	*Denevi et al.*, 2013
South of Rachmaninoff	17±7	58±13	*Denevi et al.*, 2013

[a]Numbers listed next to certain units denote their location in Fig. 1b.

Table 3. Variables necessary for calculating the volumes of the plains exterior to Rembrandt basin.

	Embayed crater parameters			***Plains unit parameters***		
	Diameter (km)	**Estimated rim height (km)[a]**	**Measured rim height (km)**	**Area (km^2)**	**Thickness (km)**	**Volume (km^3)**
Unit 1[b]	-	-	-	9.09×10^4	0.39	3.54×10^4
Crater 1	14.1	0.54	0.23	-	-	-
Crater 2	38.4	0.89	0.42	-	-	-
Unit 2	-	-	-	2.40×10^5	0.45	1.08×10^5
Crater 1	8.3	0.37	0.06	-	-	-
Crater 2	33.4	0.83	0.31	-	-	-
Unit 3	-	-	-	6.81×10^4	0.36	2.45×10^4
Crater 1	21.3	0.66	0.13	-	-	-
Crater 2	29.1	0.77	0.58	-	-	-
Unit 4	-	-	-	9.49×10^4	0.57	5.41×10^4
Crater 1	34.2	0.84	0.32	-	-	-
Crater 2	39.7	0.89	0.27	-	-	-
Unit 5	-	-	-	5.15×10^4	0.39	2.01×10^4
Crater 1	33.9	0.83	0.51	-	-	-

[a]Rim heights estimated using the morphologic relationships developed in Pike (1988).
[b]Unit numbers correspond to the plains labeled in Fig. 1b.

Figure Captions

Figure 1. (a) Rembrandt basin (~720 km in diameter; Fassett et al., 2012) on Mercury. (b) Plains map units both interior and exterior to the basin. High-albedo plains are mapped in orange and low-albedo plains are mapped in blue. Numbers on the mapped plains are associated with the crater statistics listed in Table 1. (c-e) Type examples of the mapped plains deposits in part (b). (c) The exterior high-albedo plains are brighter than surrounding geologic materials and have a smooth surface texture with few superposed impact craters. (d) Interior high-albedo plains have a morphology and superposed crater population similar to that of the exterior high-albedo plains. (e) Low-albedo exterior plains appe ar darker than the surrounding terrain and have a higher density of superposed craters (see Figs. 2 and 4). The surface of low-albedo plains is more textured than either type of high-albedo plains deposit. (f) Northern interior of Rembrandt basin. The hummocky low-albedo material (dashed white outline) within the basin rim is thought to represent original basin materials (Watters et al., 2009). MDIS 250 m/pixel mosaic. Lambert azimuthal equal area projection centered on Rembrandt basin.

Figure 2. Topograhpy of the largest exterior mapped deposits of high (black outline) and low-albedo plains (white outline). The high-albedo plains are confined to topographic lows that are not associated with impact basins. Several small high-albedo plains deposits are found in the topogrpahic low assciated with the large lobate scarp, Enterprise Rupes, directly west of the basin. However, the low-albedo plains are not confined to a specific topographic range. Instead, low-albedo plains occur across steep topographic gradients such as unit 4 and the northern section of unit 2 (Fig. 1b). Dashed black circle denotes the

rim-crest of Rembrandt basin. North is up. Stereo photogrammetric topography data overlaying the MDIS 250 m/pixel mosaic. Lambert azimuthal equal area projection.

Figure 3. Tectonic landforms and basin sculpture to the northeast of the Rembrandt basin rim. (a) Wrinkle ridges and lobate scarps within the low-albedo plains. (b) Rembrandt basin sculpture filled in with low-albedo plains. Arrows incidate the location of the high-standing remains of the lineations produced from the Rembrandt basin sculpture. A large wrinkle ridge traverses the scene perpendicular to the basin sculpture. The white outline in (a) and (b) dispays the location of low-albedo plains unit 2 (Fig 1b). MDIS 250 m/pixel high incidence angle image mosaic. Lambert azimuthal equal area projection.

Figure 4. Surface reflectance values for different MDIS color units and Rembrandt plains deposits. Rembrandt high-albedo plains are consistent with HRP surface reflectance values and the Rembrandt low-albedo plains are most similar to the LBP MDIS color unit. The surface reflectance of the Rembrandt hummocky unit (Fig. 1f) is also most consistent with LBP deposits. The stars represent the average surface reflectance value for each unit. Surface reflectance values and the specific measured areas are listed in Table 1. The measured Rembrandt plains are defined in Fig. 1.

Figure 5. Crater size-frequency distributions for the plains units within and around Rembrandt basin. (a) Cumulative crater size-frequency plot showing the density of craters on the Rembrandt exterior low-albedo plains, the exterior high-albedo plains, and the interior high-albedo plains mapped in Fig. 1. The combined crater size-frequency

distribution for the exterior low-albedo smooth plains (blue diamonds) has a higher crater density, implying an older age for this unit compared to the high-albedo plains. (b) Cumulative crater size-frequency plot of each individual low-albedo plains unit showing that all of the low-albedo plains have a similar density of superposed craters and can, therefore, be combined into one unit as displayed in part (a). (c) *R*-plot of the Rembrandt combined low-albedo, high-albedo, and interior plains (same data displayed in (a)). (d) *R*-plot of all of low-albedo plains units. Both *R*-plots have the characteristic Population 2 shallow slope. Arrows are shown for bins containing a single crater.

Figure 6. Several fresh impact craters superposing the terrain to the east of Rembrandt basin. Craters are designated by white arrows. (a) View of the terrain east of Rembrandt basin showing the abundance of relatively young impact craters. Labeled white arrows indicate the location of the craters shown in (b-d). Orange and blue shapes indicate the high-albedo and low-albedo plains in Fig. 1b. The black line represents the boundary of the map area (see Fig. 1). MDIS 250 m/ pixel mosaic. Lambert azimuthal equal area projection. (b) Unnamed crater located at 17.3°S, 110.4°E. (c) Unnamed crater located at 23.3°S, 112.2°E. (d) Amaral crater (~109 km in diameter, 26.5°S 117.9°E). MDIS 250 m/ pixel mosaic. Stereographic projection centered on each of the craters.

Figure 7. Crater density values *N*(20) for Rembrandt and Caloris basins and associated smooth plains units. Other plains areas (green triangles and diamonds; Spudis and Guest, 1988) and Tolstoj basin (orange circle; Whitten et al., *in preparation*) are included for reference. The plot shows that while the circum-Caloris plains are not related to the

basin-forming event, at least one plains unit (low-albedo plains) is contemporaneous with the Rembrandt impact event. Similar to Caloris, Rembrandt exterior high-albedo plains deposits are not associated with the basin-forming event. However, the exterior low-albedo plains (blue diamond) have a similar $N(20)$ value to Rembrandt basin, indicating that the formation of the exterior low-albedo plains is related to Rembrandt basin impact event.

Figure 8. Sketch of the measurements required and the embayed craters used to estimate plains thickness. (a) Cross section of an embayed crater. The "predicted rim height" was calculated using the morphologic relationships quantified in Pike (1988). "Measured rim height" was determined by taking topographic profiles across each embayed crater. The difference between these two measurements is the plains thickness estimate. (b) Embayed crater 14.14 km in diameter, located in unit 1. (c) 38.38 km, unit 1. (d) 8.31 km, unit 2. (e) 33.40 km, unit 2. (f) 21.26 km, unit 3. (g) 29.12 km, unit 3. (h) 34.19 km, unit 4. (i) 38.66 km, unit 4. (j) 33.87 km, unit 5. MDIS 250 m/ pixel mosaic. Stereographic projection.

Figure 9. Diagram examining the possibility that the low-albedo smooth plains are basin ejecta deposits. The geologic map of the distribution of plains deposits is overlain by a hatched area representing the region predicted to contain smooth plains deposits (Gault et al., 1975; Meyer et al., 2013) produced from secondary impacts (Oberbeck et al., 1977). The inner boundary of the torus is 470 km from the basin rim and its outer edge is 935 km away. Most of the mapped low-albedo plains are not contained within this torus and,

instead, are located just within the expected zone of secondary impact-produced smooth plains. In addition, there is a superposed reference frame to investigate the azimuthal distribution of the low-albedo plains (0° = North, 90° = East, 180° = South, 270° = West). Using this reference system, the majority of the low-albedo plains are located between 45° and 225°, on the southeast half of the basin; these deposits are also the closest to the basin rim-crest (black dashed circle). Lambert azimuthal equal area projection.

Figure 10. Other impact basins on Mercury with smooth plains deposits (grey) interpreted to be impact melt ponds, near the rim-crest. (a) Raditladi basin (~258 km in diameter). (b) Rachmaninoff basin (~306 km in diameter). Similar to the low-albedo plains around Rembrandt, the largest impact melt deposits around Raditladi and Rachmaninoff show a preferential distribution. The impact melt ponds around Raditladi are concentrated in the northwest and those surrounding Rachmaninoff are focused in the southwest. Rachmaninoff, the larger of the two basins, has more areally extensive exterior impact melt deposits. MDIS 250 m/pixel monochrome mosaic. Stereographic projection centered over each basin.

Figure 11. Basin sculpture surrounding Rembrandt basin on Mercury (a) and possible embayed craters (c-e), and Imbrium basin sculpture on the Moon (f). (a) Rembrandt basin with regions affected by basin sculpture (yellow lines) and the low-albedo plains (blue regions) outlined. Most of the preserved basin sculpture is in the southwest and northeast regions of Rembrandt basin. MDIS 250 m/pixel 750 nm mosaic. (b) Region northeast of

Rembrandt basin with the most well-preserved basin sculpture oriented southwest–northeast. Craters labeled A and B show evidence of basin sculpture on their rims. The box labeled ‘c’, which indicates the location of part c, denotes an embayed crater without basin sculpture that is located well within the region expected to be affected by basin ejecta. White outline defines the region of the low-albedo exterior plains unit 2 and the white dashed line marks the Rembrandt basin rim. MDIS 250 m/pixel high incidence angle mosaic. (c) A 33 km diameter crater that is embayed by low-albedo plains. The crater rim does not appear to have been affected by basin sculpture, especially to the degree observed on the Moon (f), but there may be some sculpture on its southwest rim. White arrows show the location of the crater rim. (d) A 66 km diameter crater embayed by low-albedo plains and without basin sculpture on its rim. However, it is too far from the basin rim to have been modified by basin sculpture and therefore cannot aid in determine the relative stratigraphy of the low-albedo plains. (e) Three craters <5 km in diameter within a basin secondary chain that may be embayed by low-albedo plains. The image resolution is not sufficient to definitely determine if these small craters have been embayed. (f) Impact craters, including Ptolemaeus and Flammarion U (labeled), in the lunar central highlands with Imbrium basin sculpture (oriented northwest–southeast) on their crater rims. Those craters that formed after the Imbrium basin impact event do not have lineations on their crater rims from the basin ejecta. Lunar Reconnaissance Orbiter Camera 100 m/pixel mosaic. Stereographic projections centered on Rembrandt (a-e) and Ptolemaeus (f).

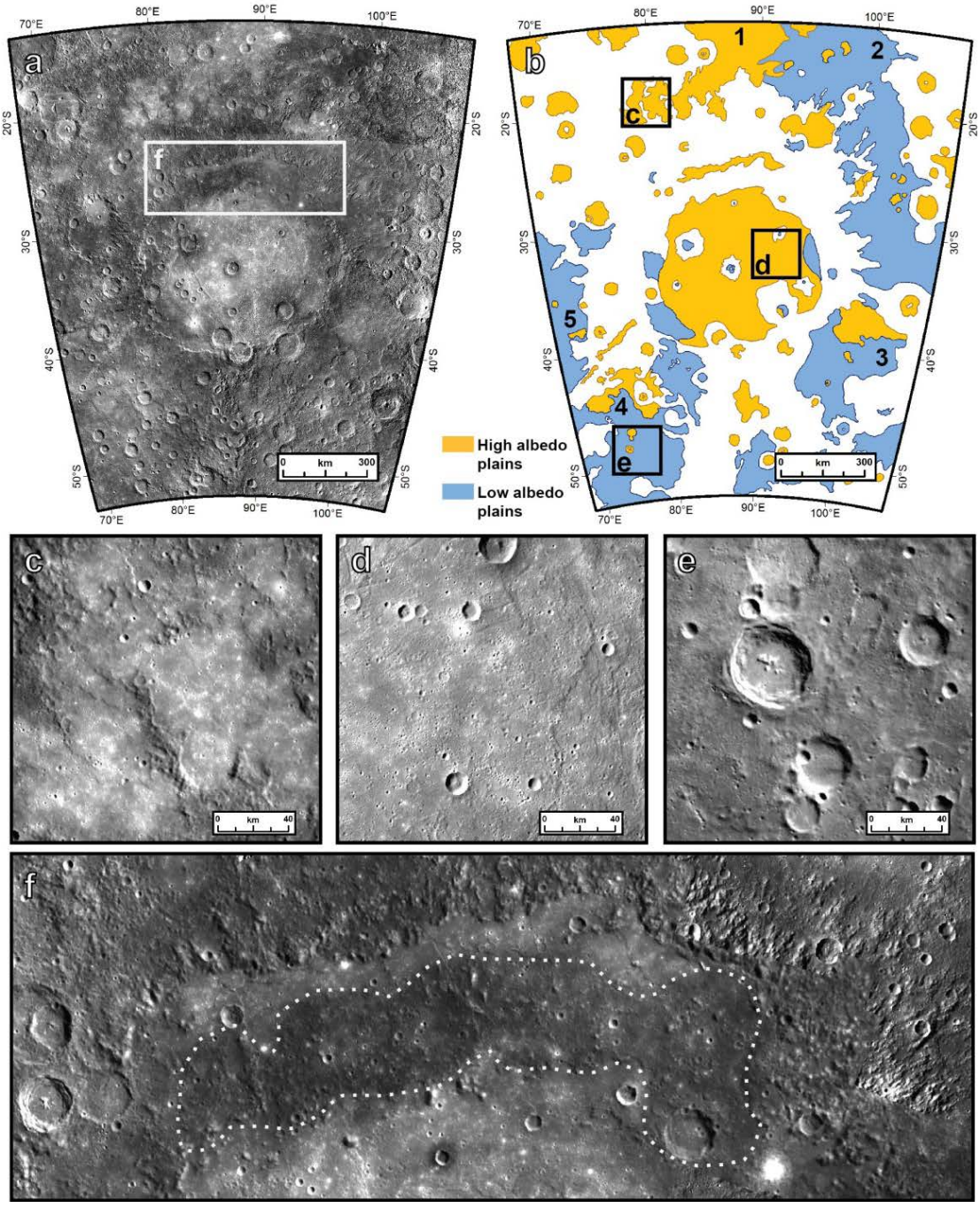
a
b
c
d
e
f
1
2
3
4
5
High albedo plains
Low albedo plains
70°E
80°E
90°E
100°E
20°S
30°S
40°S
50°S
0 km 300
0 km 40

Figure 1.

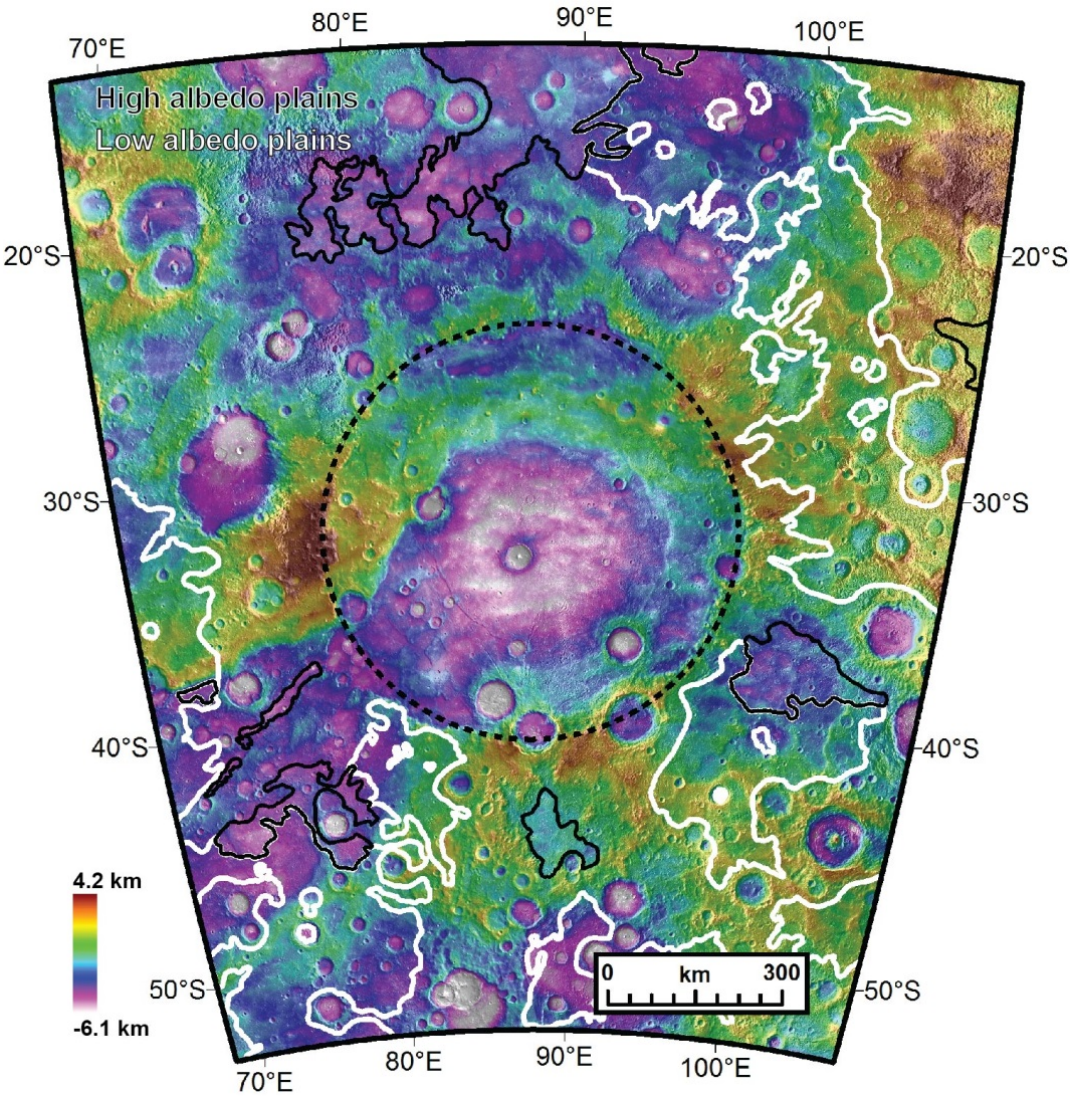
70°E
80°E
90°E
100°E
High albedo plains
Low albedo plains
20°S
30°S
40°S
50°S
4.2 km
-6.1 km
0
km
300

Figure 2.

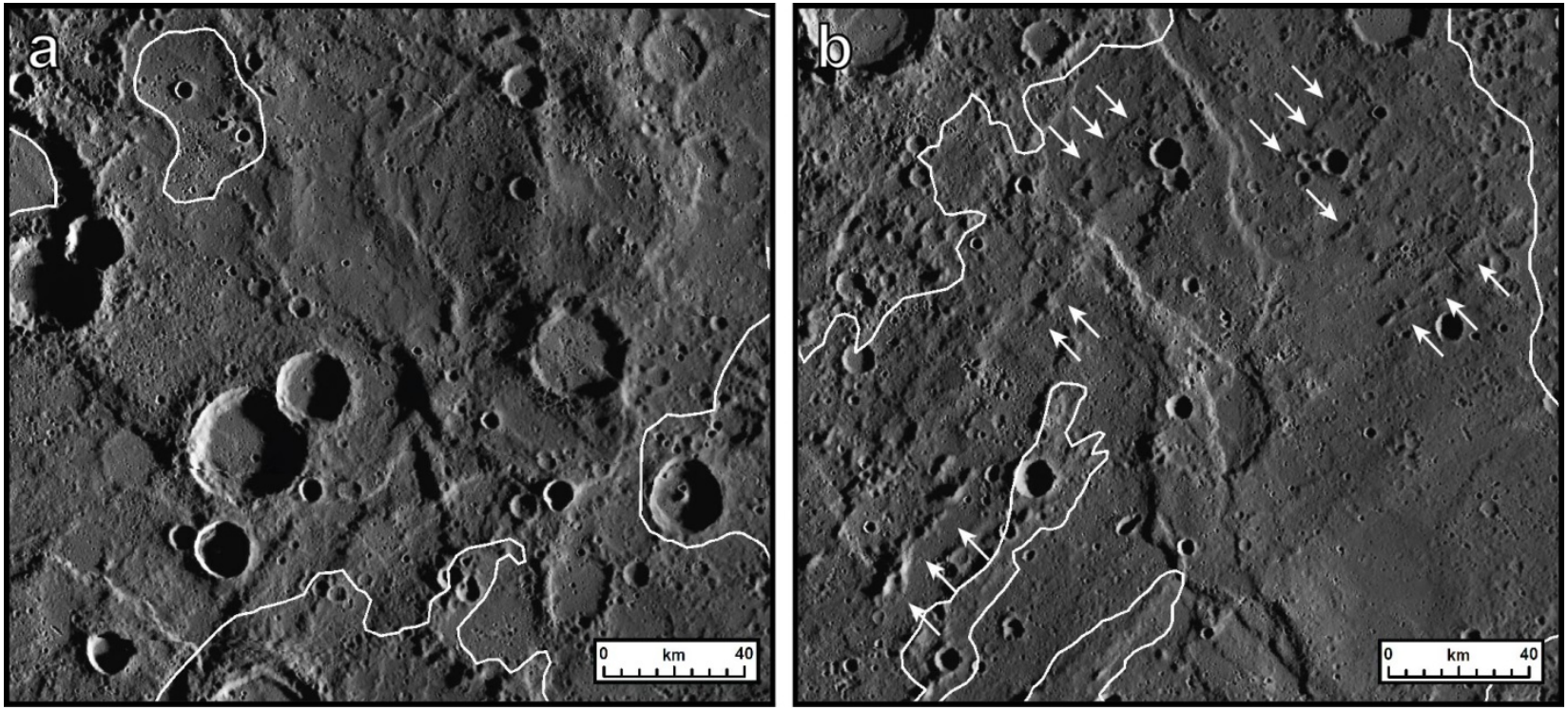

Figure 3.

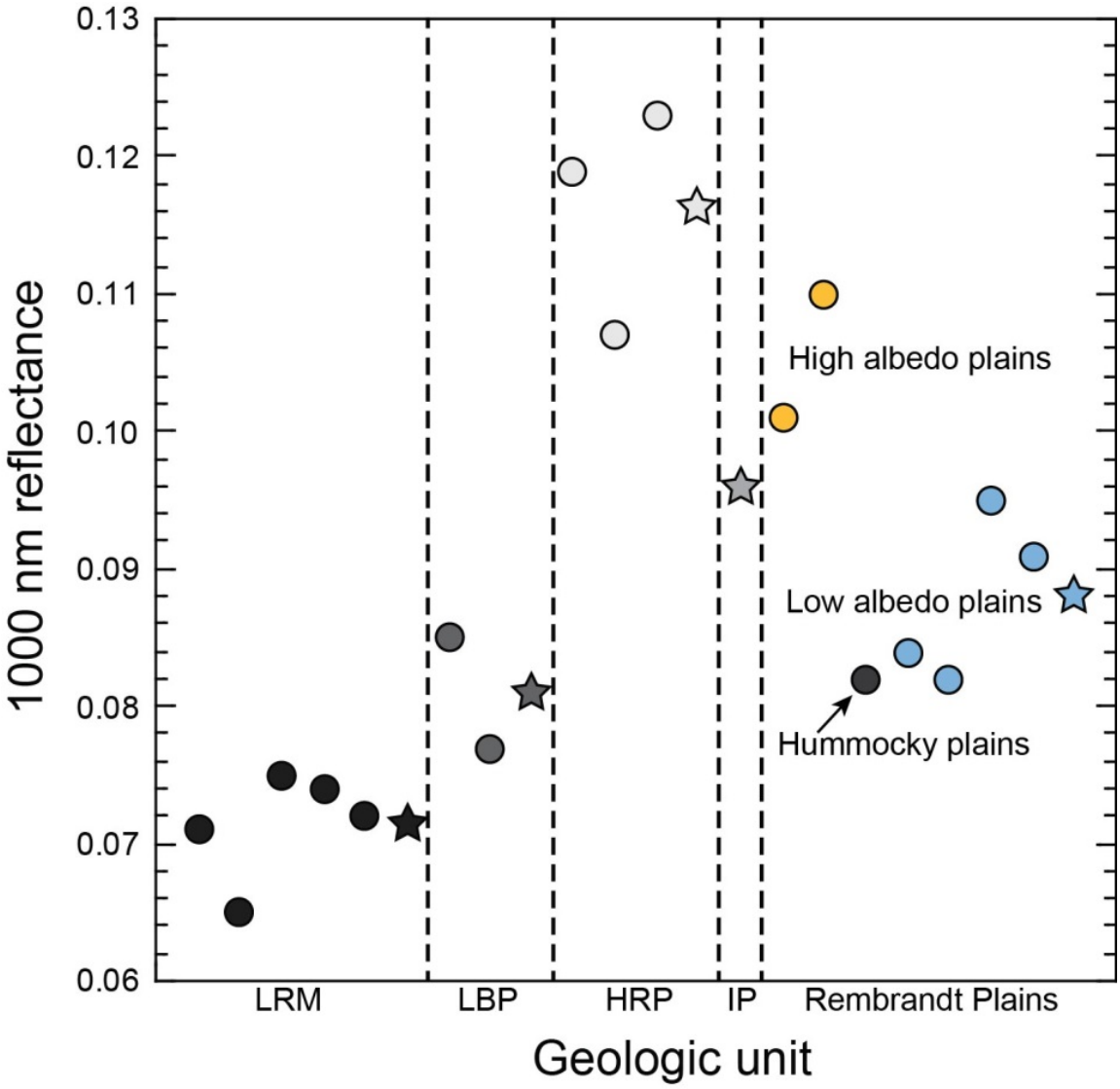
0.13
0.12
0.11
0.10
0.09
0.08
0.07
0.06
1000 nm reflectance
High albedo plains
Low albedo plains
Hummocky plains
LRM
LBP
HRP
IP
Rembrandt Plains
Geologic unit

Figure 4.

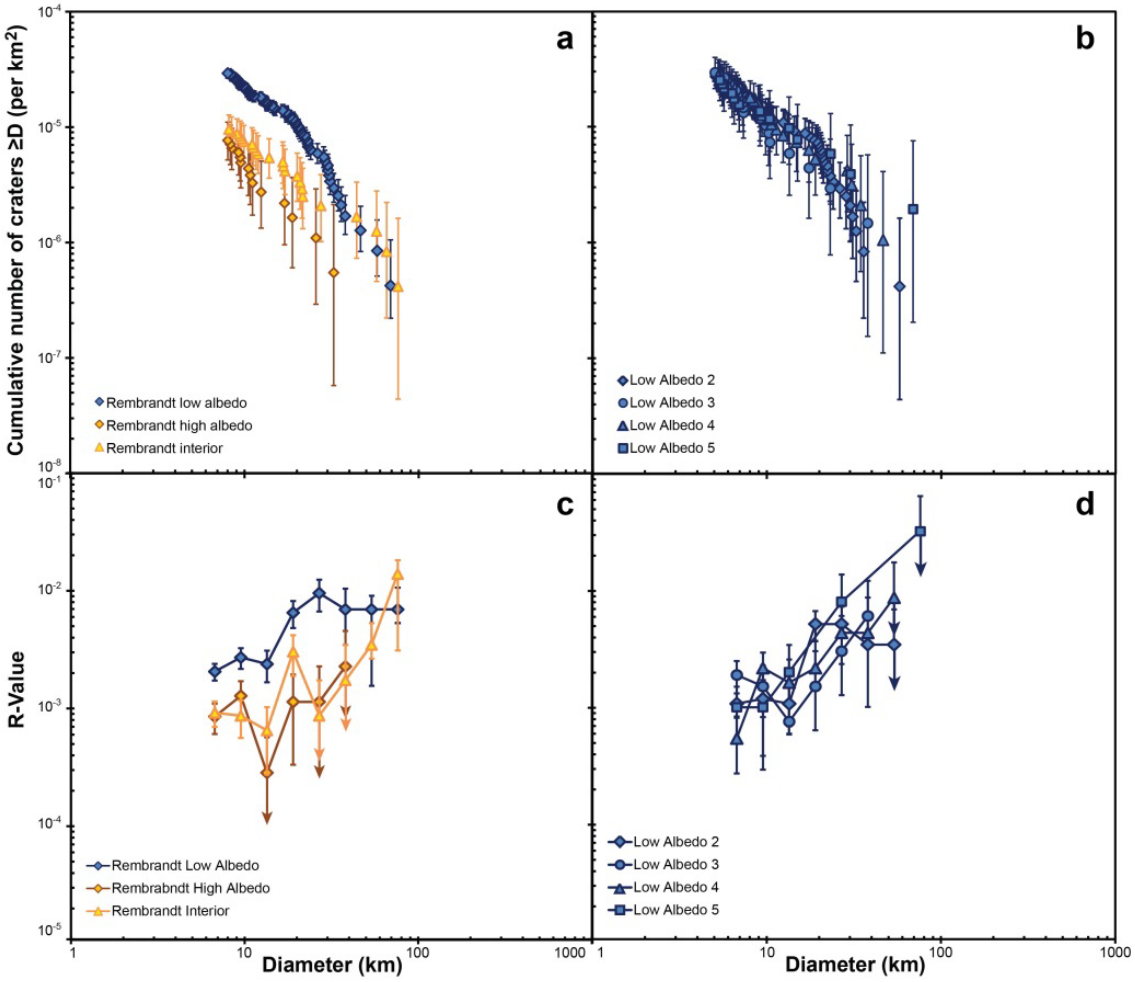
a
b
c
d
Cumulative number of craters ≥D (per km²)
R-Value
Diameter (km)
Diameter (km)
Rembrandt low albedo
Rembrandt high albedo
Rembrandt interior
Low Albedo 2
Low Albedo 3
Low Albedo 4
Low Albedo 5
Rembrandt Low Albedo
Rembrabndt High Albedo
Rembrandt Interior
Low Albedo 2
Low Albedo 3
Low Albedo 4
Low Albedo 5

Figure 5.

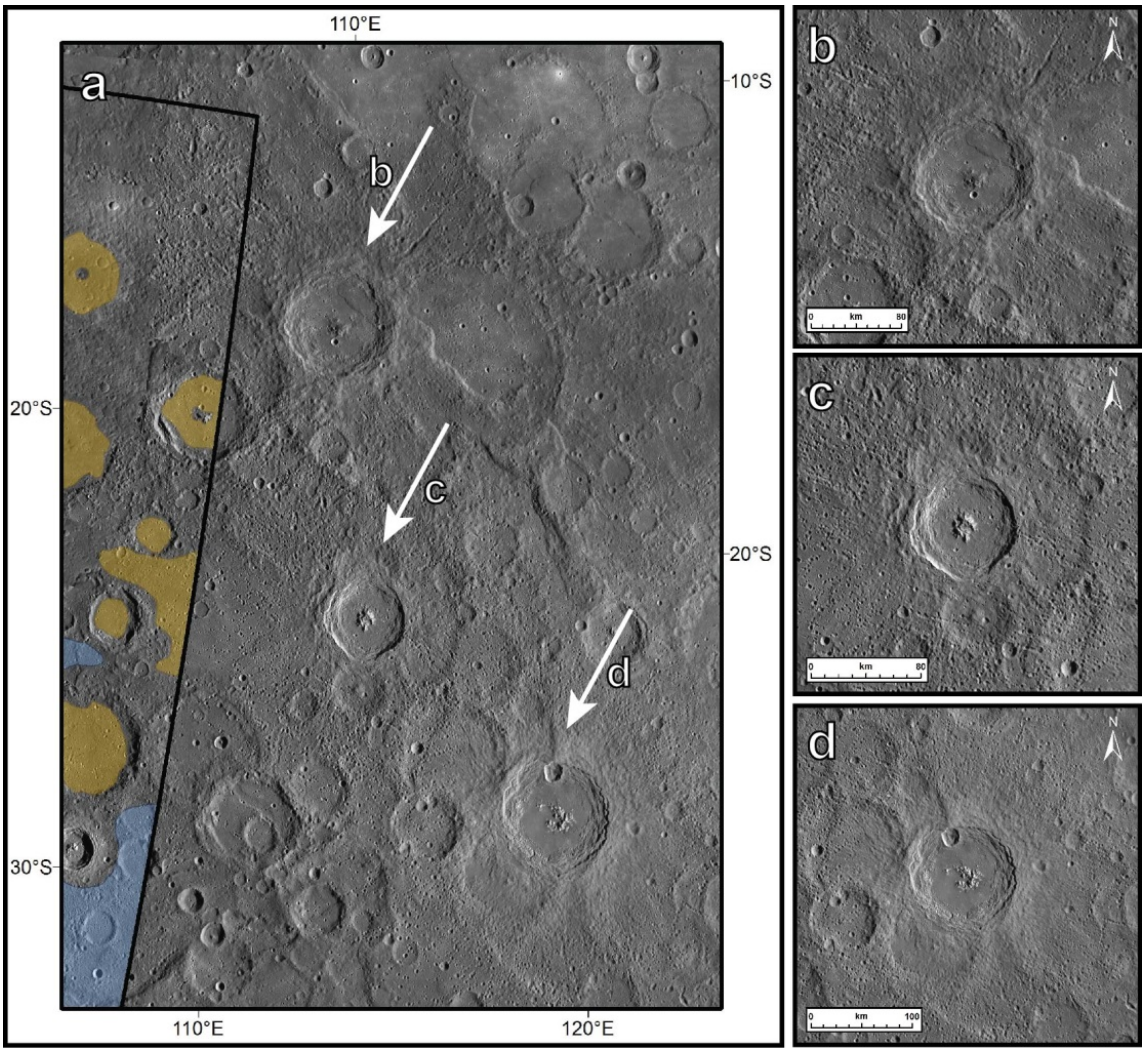

Figure 6.

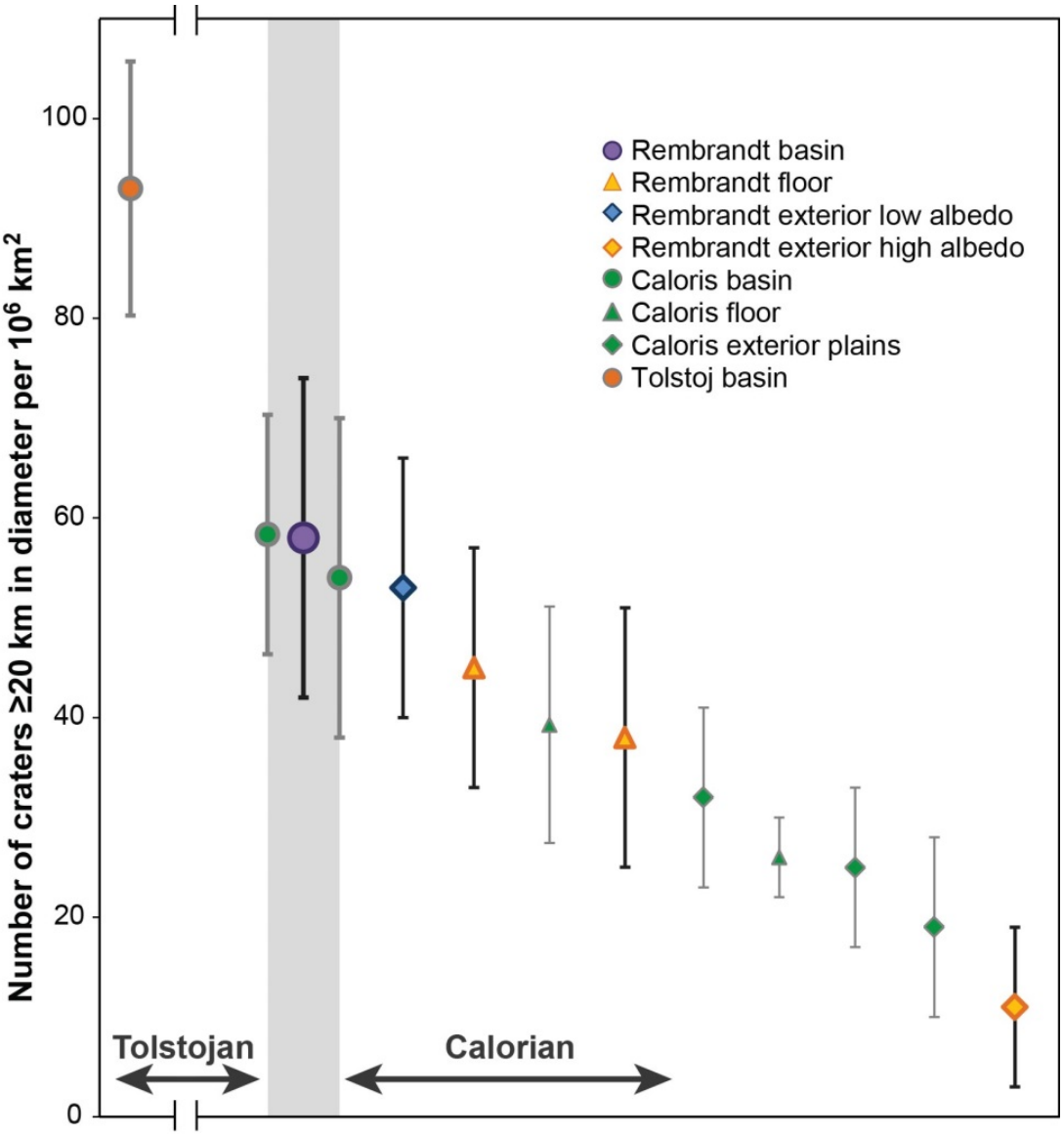
Number of craters ≥20 km in diameter per 10^6 km^2
100
80
60
40
20
0
Rembrandt basin
Rembrandt floor
Rembrandt exterior low albedo
Rembrandt exterior high albedo
Caloris basin
Caloris floor
Caloris exterior plains
Tolstoj basin
Tolstojan
Calorian

Figure 7.

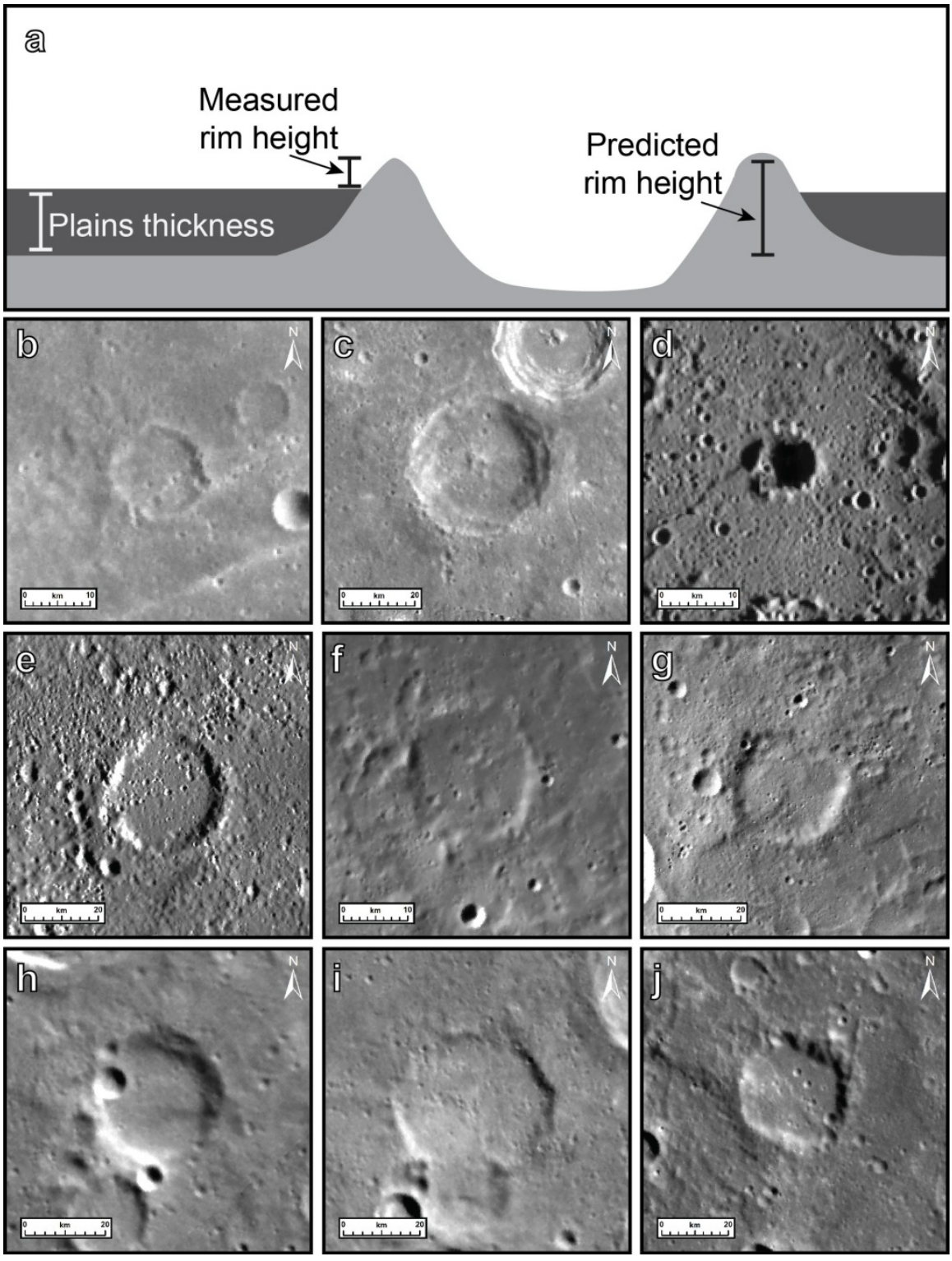
a
Measured
rim height
Predicted
rim height
Plains thickness
b
c
d
e
f
g
h
i
j
N
0 km 10
0 km 20

Figure 8.

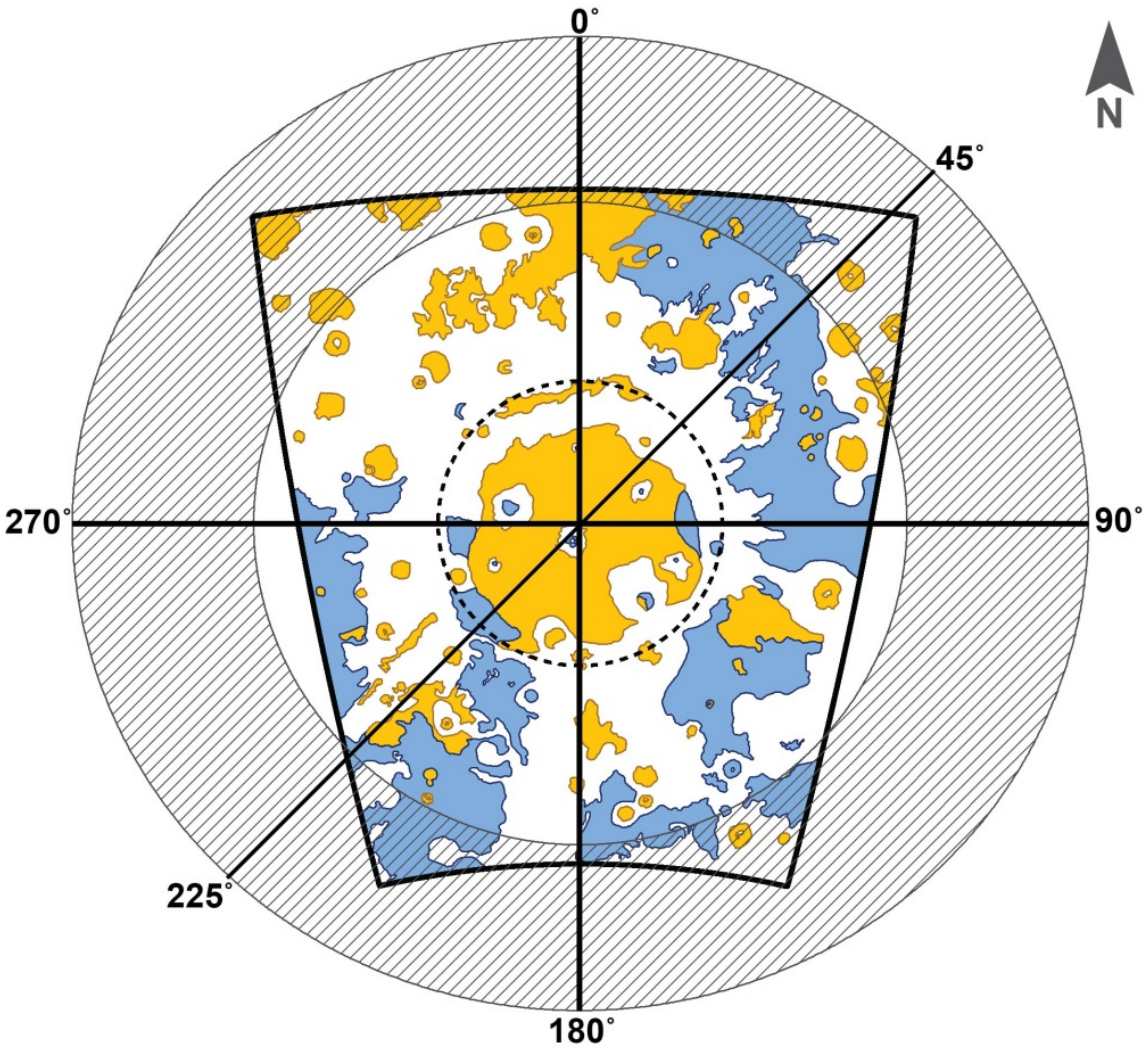

Figure 9.

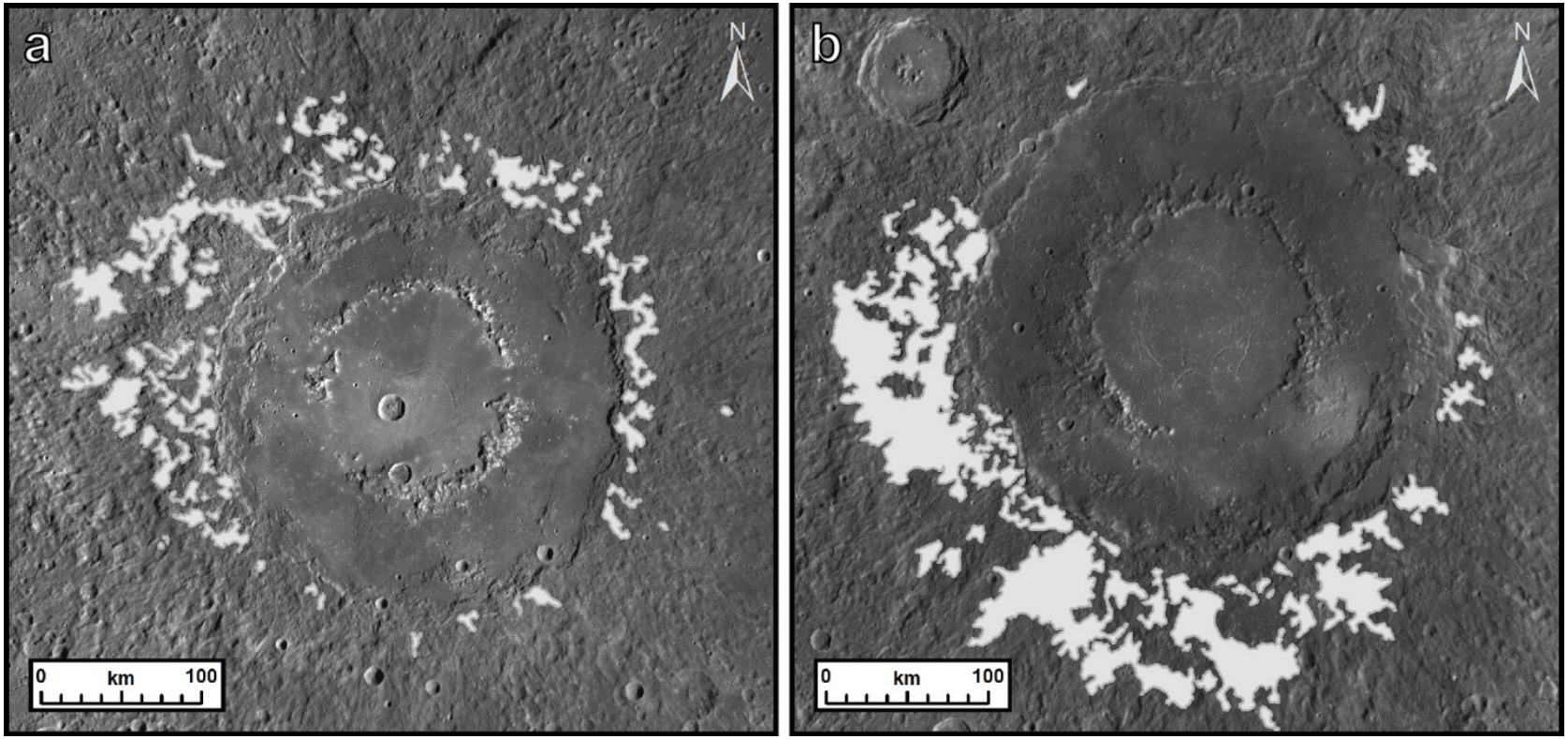

Figure 10.

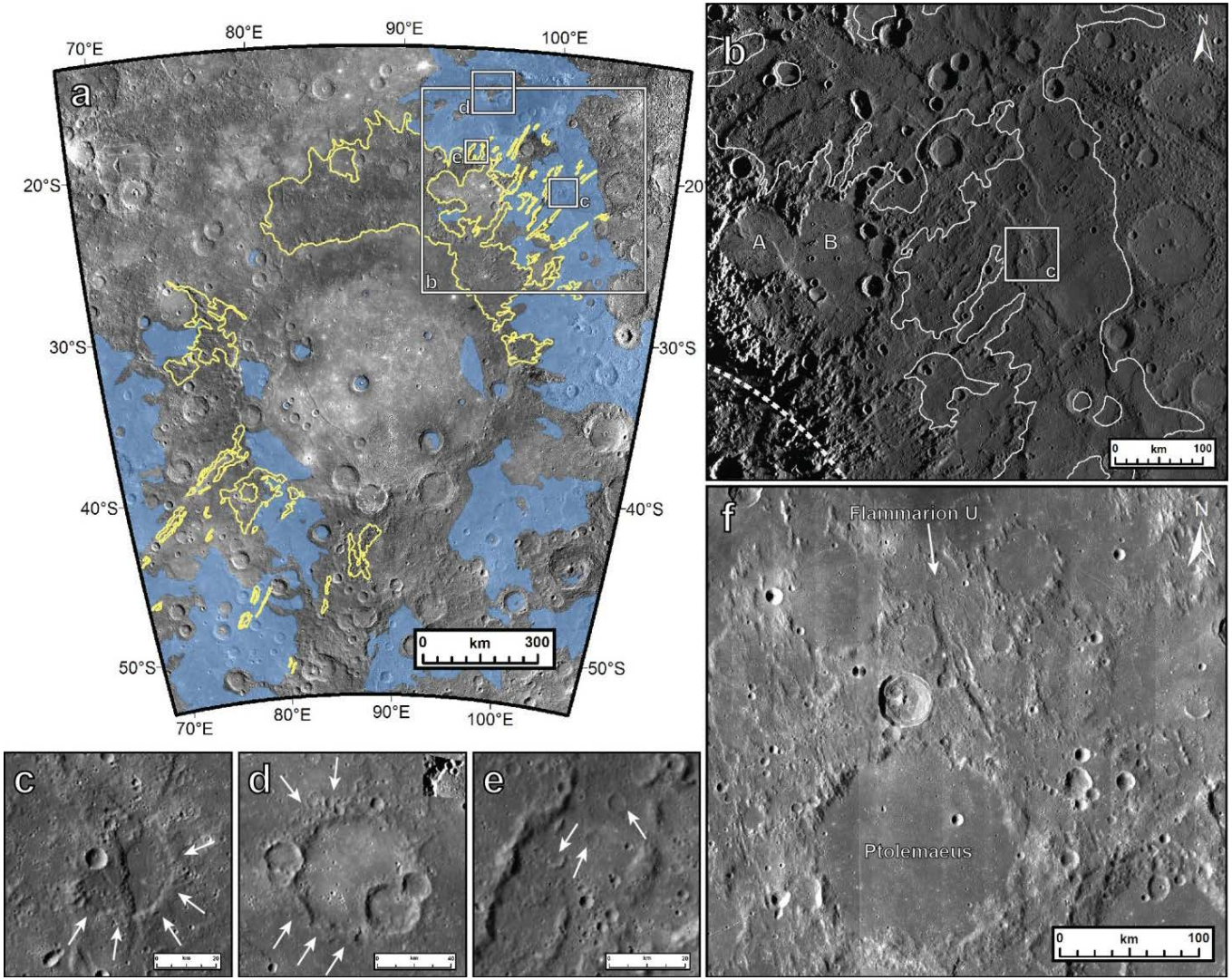
a
b
c
d
e
f
70°E
80°E
90°E
100°E
20°S
30°S
40°S
50°S
0 km 300
A
B
N
0 km 100
Flammarion U
Ptolemaeus

Figure 11.

Chapter 6:
Ancient volcanic deposits on the Moon and Mercury: A synthesis

Jennifer L. Whitten

Department of Geological Sciences, Brown University,
324 Brook St., Box 1846, Providence, RI 02912.

1. Introduction

This dissertation work has explored the best methods for identification and characterization of ancient volcanic deposits on the Moon and Mercury. On both planets, ancient volcanic deposits are obscured by more recent impact craters and their associated ejecta deposits. These early volcanics were emplaced at a time when the impact flux was much higher than today; in fact, the impact flux was substantially higher than when mare basalts and young smooth plains were being emplaced on the Moon and Mercury (Strom et al., 2005). Therefore, ancient volcanic deposits have been greatly modified either by superposed impact craters or by superposed basin ejecta deposits. Ancient volcanic deposits would have also been emplaced into heavily cratered topography that affected the distribution of the deposits (Chapter 1). It was critical to identify, map, and characterize ancient volcanic deposits (Chapter 2, 3, and 4) so that they can be differentiated from basin-produced smooth plains (see Chapter 2). Below I synthesize the work presented in individual chapters and discuss the geologic processes responsible for the emplacement of ancient volcanic deposits on the Moon and Mercury.

2. Ancient volcanism on the Moon – the cryptomaria

Lunar cryptomaria eruptions were controlled by a combination of crustal thickness and KREEP distribution, being emplaced in topographic lows with the most areally extensive deposits clustered around the nearside visible mare basalts.

The type and morphologic expression of early eruptions onto the surfaces of the Moon and Mercury were different (Fig. 1). Ancient volcanic deposits on the Moon, how

hidden and called cryptomaria, were restricted to within topographic lows (Fig. 2), especially within Pre-Nectarian and Nectarian aged impact basins. These ancient volcanic deposits have a range of ages, but the largest cryptomaria associated with impact basins are at least 3.7 Ga (Chapter 2). Despite a high impact flux during the emplacement of cryptomaria, many of these ancient volcanic deposits preserve a smooth texture even with superposed basin ejecta. Cryptomaria do not appear to be significantly larger or more voluminous than later basaltic eruptions onto the lunar nearside. Therefore, based on current observations of ancient volcanic deposits the higher heat flux during the early history of the Moon did not produce substantially larger volcanic eruptions. As the Moon began to cool, the size and flux of volcanic eruptions began to decrease, especially after 3.4 Ga (Fig. 1 in Chapter 2). While heat production was important for mantle melting, it appears that the crustal thickness of the Moon played a comparatively larger role in the distribution of surficial volcanic deposits.

There are several eruption barriers in place on the Moon that prevented basaltic melts from being emplaced on the lunar surface. The Lunar Magma Ocean (LMO) hypothesis predicts that after ~80% crystallization solidification of a molten Moon (e.g., Snyder et al., 1992) a plagioclase flotation crust formed. This plagioclase crust introduced a density barrier to the eruption of early mantle melts because of its low density compared with basaltic mantle melts. Exacerbating this problem is the fact that early basaltic mantle melts would have been relatively denser than younger melts. This is because the LMO mantle overturn (e.g., Hess and Parmentier, 1995) brought titanium-rich materials, such as ilmenite, down to depths consistent with the mare basalt source regions (250-640 km) (Grove and Krawczynski, 2009; Krawczynski and Grove, 2012).

Thus, titanium-rich materials were integrated into the mantle source region and incorporated into early melts because ilmenite and olivine are on the liquidus (Grove and Krawczynski, 2009; Krawczynski and Grove, 2012) and therefore would melt first. Later mantle melts from the same source region would contain less titanium because earlier mantle melts had depleted the region in ilmenite.

In order for the earliest dense magmas to erupt onto the low-density plagioclase crust, they need to experience an excess pressure capable of propagating the melt through the crust and onto the surface. Excess pressures may have been created by volume changes in the magma body by melt crystallization, gas exsolution, or a new injection of melt (Wilson and Head, 1981; Head and Wilson, 1992). Due to the more extreme density difference between the crust and mantle melts early in the Moon's history, and the lack of excess driving pressure, it is probable that many early mantle melts became stalled in the crust during eruption. As the plagioclase crust continued to trap mantle melts, these igneous deposits increased the average density of the crust, which aided in the eruption of later, lower density basaltic melts. However, the densification of the lunar crust was somewhat balanced by the impact bombardment of the crust. During the early history of the inner solar system the impact flux was at least an order of magnitude higher than it is today (e.g., Morbidelli et al., 2012); this bombardment fractured the anorthositic crust, increasing the porosity and lowering the lunar crustal density (Wieczorek et al., 2013).

Despite these difficulties, early mantle melts were able to propagate to the surface. Of all the ancient igneous rock types (Mg-suite, KREEP basalts, high-Al basalts, mare basalts; Chapter 3) the mare basalts appear to have been deposited in the most areally extensive eruptions and have been emplaced inside impact basins over their entire

eruptive history. The Mg-suite rocks are thought to have formed predominantly as igneous intrusions in the lunar crust. KREEP basalts are limited in space and time to the regions of the lunar mantle that developed a substantial KREEP-rich layer, thought to have formed during the last stages of LMO crystallization some time between 4.42 and 4.51 Ga (Nemchin et al., 2009; Elkins-Tanton et al., 2011). The concentration of KREEP materials on the nearside has led to the suggestion that the thinned nearside crust is a product of the melting induced by this high concentration of rare earth elements (Wieczorek and Phillips, 2000). Therefore, a combination of these variables (crustal thickness, KREEP, heat sources for mantle melting) is responsible for the pattern of basaltic deposits on the lunar surface.

Analysis of the eruptive possibilities on the lunar farside (Chapter 2) shows that a small basalt deposit is expected on the floor of the farside basin Mendeleev (325 km in diameter). Many, but not all of the farside basins are almost completely filled to the rim with high albedo plains. There is a discrepancy between the amount of fill and the ages of these basins; Mendeleev is younger than the Freundlich-Sharonov farside basin (Fassett et al., 2012), but has substantially more light plains fill (Fig. 13a vs. 14a in Chapter 2). Freundlich-Sharonov is almost twice as large as Mendeleev and also has small deposit of mare basalts in its interior (Lacus Luxuriae). The morphologically fresh crater Buys Ballot is superposed on the center of the Freundlich-Sharonov basin, itself filled mare basalt deposits which indicates relatively recent volcanic eruptions. Therefore, even at the current farside crustal thickness of ~45 km mare basalts were able to propagate through the crust and erupt onto the surface (Wieczorek et al., 2013). The presence of these young mare basalts suggests that mare basalts were capable of erupting into all of the farside

basins and perhaps lie just beneath the visible high albedo plains. Thus, ancient volcanic deposits may be more evenly distributed across the lunar surface than is presently appreciated, and due to current data limitations we are unable to observe these deposits.

3. Ancient volcanism on Mercury – the intercrater plains

The intercrater plains were probably emplaced as large-scale volcanic deposits akin to LIPs on Earth. Perhaps a small percent of the intercrater plains are composed of basin impact melt.

Mercury does not exhibit the same type of eruptive behavior as the Moon for its earliest volcanic deposits, the intercrater plains. Intercrater plains are a near-globally distributed deposit on Mercury that probably formed through a series of volcanic eruptions during the period of heavy bombardment (Chapter 4); the continuum in intercrater plains morphologies, in addition to crater size-frequency distributions, suggests that these deposits were emplaced over an extended period of time. These volcanic deposits were constantly being reworked by impact cratering to produce the characteristic intercrater plains texture observed today. Areally extensive volcanic plains deposits were being emplaced on the surface of Mercury and then quickly modified by impact craters and their associated ejecta deposits. Compared with the lunar cryptomaria, intercrater plains were more affected by impact gardening because the higher impact velocities on Mercury lead to more and larger secondary impact craters. Eventually, as Mercury began to cool, contractional stresses in the lithosphere produced an environment that was not conducive to large-scale volcanic eruptions, such as those observed within

and around Caloris (Fassett et al., 2009; Denevi et al., 2013) and in the northern volcanic plains (Head et al., 2011), and volcanic eruptions ceased.

Unlike the Moon, Mercury does not possess a low density plagioclase flotation crust (Nittler et al., 2011), because the low bulk concentration of FeO in a mercurian magma ocean (if one existed) would produce plagioclase denser than the residual liquid (Riner et al., 2009). Therefore, mantle melts on Mercury would not encounter a buoyancy barrier due to interaction with a low density plagioclase crust. In addition, the lavas on Mercury contain less Fe and Ti compared with volcanics on the Moon, suggesting the mantle melts on Mercury were less dense. The combination of relatively low-density mantle melts and a crustal density more similar to the mantle composition would have created an environment conducive to surface eruptions on Mercury.

Young volcanic deposits on Mercury are confined to topographic lows, especially within and adjacent to impact structures. In contrast, the intercrater plains, which are thought to be volcanic (Chapter 4), do not have the same topographic association. Currently the intercrater plains are located at a variety of different elevations (Fig. 2). However, Mercury has experienced substantial tectonic modification by lobate scarps and long-wavelength crustal folding (e.g., Zuber et al., 2012; Byrne et al., 2014) that destroyed the original elevation distribution of the intercrater plains making it difficult to deduce their initial geologic setting. Due to the close spatial association of volcanic smooth plains and impact basins, the emplacement of volcanic deposits on Mercury is probably related to impact events. Recent studies of the effect of large impact basins on the melting and convection in Mercury's mantle reveal that these impact events can induce sufficient melting to produce volcanic eruptions within the impact basins. Exterior

volcanic deposits can also be formed, but only from slow, large basin impact events (Roberts and Barnouin, 2012). Other than Caloris, there is only one other positively identified impact basin >1000 km in diameter on Mercury (Fassett et al., 2012), suggesting that this emplacement mechanism for volcanic plains may not have been prevalent across the surface of Mercury.

Based on the areal distribution of intercrater plains, these deposits probably formed as large-scale flood basalt eruptions and may be controlled by the same geologic processes that produce large igneous provinces (LIPs) on Earth. LIPs are massive volcanic deposits ($>10^5$ km^3) that have been erupted into a variety of tectonic environments on Earth and, thus, are not controlled by plate tectonics (Coffin and Eldholm, 1994). Instead, LIP formation is believed to be associated with mantle plumes. An initial large eruption of magma results when a mantle plume head intersects with a planetary crust. Subsequent smaller and longer-lived volcanic eruptions are believed to result from magmas transported through the mantle plume tail. The largest terrestrial LIP is the Ontong Java Plateau, which has an area of 4.88×10^6 km^2 and an estimated volume of $36–76\times10^6$ km^3 (Coffin and Eldholm, 1994). In order to produce such large-scale, long-lived volcanic eruptions there needs to be a thermal boundary layer within the planetary mantle or at the core-mantle boundary (Coffin and Eldholm, 1994 and references therein).

The heat production on Mercury at 4.0 Gyr due to radiogenic isotopes was four times larger compared with today (Peplowski et al., 2011). With this additional heat, ancient volcanic eruptions on Mercury had the potential to be gigantic. The added heat plus the relatively primitive, or unmelted, mercurian mantle may have provided the right

conditions for large-scale mantle melting. The large, but concentrated, young volcanic deposits (like the northern volcanic plains) are consistent with the size of volcanic deposits expected from mantle plume heads as they intersect a planetary surface. Thus, the potential for mantle plumes early in Mercury's history is also plausible. Though Mercury's mantle has been constrained to <400 km thick (Smith et al., 2012; Hauck et al., 2012), thermal evolution models suggest that mantle convection can develop and persist on Mercury for several billions years (Michel et al., 2013). Therefore, mantle plume production was possible. Several mantle plumes may have been responsible for the emplacement of the intercrater plains throughout much of Mercury's early history. Certainly the distribution of the intercrater plains is consistent with widespread voluminous volcanism predicted by these thermal models and could easily be the mercurian equivalent of terrestrial LIPs.

The intercrater plains may not all have been produced by volcanic processes; some portions of the intercrater plains could be basin impact melt deposits (Chapter 5). Impact melt production is greater on Mercury compared with the Moon, largely due to the higher average impact velocities (Le Feuvre and Wieczorek, 2008). Therefore, the largest impact basins have the potential produce substantial amounts of impact melt, a portion of which will be deposited exterior to the basin rim. Of the 87 identified and proposed impact basins on Mercury >300 km in diameter 46 are verified (Fig. 3) (Fassett et al., 2012). From Chapter 5, the furthest extent of impact melt around Rembrandt basin (~720 km in diameter) is approximately two basin radii from the rim crest. Assuming a linear relationship between basin diameter and total extent of impact melt, the total surface area of Mercury covered by impact melt is <71.5% (Fig. 3). Impact melt deposits

around smaller basins 250–300 km in diameter, such as Raditladi and Rachmaninoff, are not extensive enough to resurface large parts of the surface of Mercury. In fact, impact melt around these two basins occurs only as small discrete deposits within 0.5 basin radii of the rim crest (Fig. 10 in Chapter 5). This observation indicates that the areal extent of exterior impact melt deposits does not scale linearly with basin diameter on Mercury (as shown in Fig. 3). Therefore, only larger basins would be able to produce extensive exterior impact melt deposits that could cause regional resurfacing.

4. Outstanding questions

While the work presented in this dissertation has revealed important information about the distribution and influence of ancient volcanic deposits on the Moon and Mercury there are still many outstanding questions that can be addressed in the future. A few of the most interesting of these questions are outlined below:

Could some ancient volcanic deposits be dominated by Mg-rich silicate minerals?

Visible to near-infrared (VNIR) spectroscopy can only detect mineral absorption features caused by transition metals, the most prevalent one being iron. Magnesium is not a transition metal. Therefore, near-endmember Mg-rich minerals should not produce strong mineral absorption bands in the VNIR region of the electromagnetic spectrum. In addition, the Lunar Prospector gamma-ray Mg data are of low spatial resolution (5°/pixel; ~152 km/pixel). Mg-rich regions generally correlate with exposed mare basalts (Fig. 4). However, there are a few relatively high-Mg detections on the farside that are not necessarily correlated with mare basalts. If there were smaller Mg-rich regions within the farside highlands or along the boundary of the

nearside mare basalts the magnesium measurements could be “averaged out” due to the low spatial resolution of the dataset.

In order to develop identification techniques for Mg-rich ancient volcanic it is important to synthesize Mg-rich basalts and Mg-suite lithologies in the laboratory and measure their spectra, mineralogy, and elemental composition. With this information new instruments can be developed to specifically target unique mineralogic or compositional features of these rock types. For instance, variations in pyroxene composition (including differences in iron and magnesium) can be detected in the thermal infrared part of the electromagnetic spectrum (Hamilton, 2000). Unfortunately, the Diviner instrument, a thermal imaging spectrometer in orbit around the Moon, does not have the spectral resolution to make pyroxene identification straightforward. Instead of only measuring three wavelengths centered around Christiansen feature (~8 μm) on Diviner, a new instrument would need to be capable of measuring multiple wavelengths between 8–12 μm and 15–21 μm.

Do the Apollo extrusive KREEP basalt samples have any distinct spectral characteristics?

Laboratory VNIR spectral measurements of lunar samples have focused largely on volcanic materials that dominate the surface of the Moon: high- and low-Ti mare basalts. The shortage of publically accessible spectral information on different Mg-suite and KREEP basalt lithologies makes it difficult to search for these relatively rare rock types on planetary surfaces. Of the lunar samples having a KREEP basalt composition, the majority are actually interpreted to be impact melt deposits. Therefore, VNIR laboratory measurements of impact and extrusive KREEP basalts

are need in order to determine the differences between these two rock types in the hope that we may be able to develop criteria to distinguish them from one another remotely.

What is the distribution of basin ejecta (impact melt and secondary crater deposits) on Mercury?

The theory explaining the formation of high albedo smooth plains deposits was developed for the Moon after the Apollo 16 mission to the Descartes Highlands west of Nectaris basin (Oberbeck et al., 1974). Its application to Mercury is complicated by the intense modification of the surface by impact structures. Even relatively young impact basins on Mercury, such as Caloris, do not appear to preserve impact melt deposits. Impact melt ponds can be observed around craters several tens of kilometers in diameter (e.g., Beach et al., 2012), but these deposits become more difficult to map around impact basins. For mercurian impact craters <100 km in diameter most of the continuous ejecta deposit is piled up immediately adjacent to the crater rim and the ejected material extends no further than three crater radii away from the rim crest. The secondary crater field is also easily observed and occurs <5 crater radii from the rim (Gault et al., 1975). Again, these deposits are difficult to identify around impact basins on Mercury as most of them, especially the largest ones, have been heavily modified by superposed impacts. The distribution of secondary crater smooth plains deposits on Mercury needs to be mapped in detail to determine how basin formation and ejecta emplacement differ from the Moon and whether secondary craters on Mercury produce substantial smooth plains deposits that are capable of resurfacing large areas. If basin impact ejecta do cause substantial resurfacing, then less of the

surface of Mercury is composed of volcanic plains. Perhaps resurfacing via impact processes on Mercury was even more prevalent than on the Moon.

What is the mineralogy of the young volcanic deposits (smooth plains) on Mercury? How does the mineralogy vary between deposits and how does it compare with the intercrater plains?

The MESSENGER mission does not have an instrument suite capable of detecting small-scale mineralogical variations on the surface, although the average crustal composition and the composition of areally extensive deposits can be measured. Knowing how the mineralogy of volcanic deposits has evolved over time and how the deposits vary spatially is important for understanding mantle dynamics and the thermal and magmatic evolution of Mercury. Variations in VNIR properties are observed for young volcanics deposits as well as between these deposits and the intercrater plains (Izenberg et al., 2014). However, the relationship between these variations and differences in mineralogy is currently unclear. It is important to understand if observed mineralogical and compositional variations in the MESSENGER data are due to space weathering effects or actual compositional differences within and between volcanic deposits.

Are there mineralogical boundaries within the intercrater plains?

The MESSENGER X-ray spectrometer has observed a distinct region of high magnesium content within the intercrater plains. The low spatial resolution of the dataset prevents direct correlation between surface features and the high-Mg compositional measurements. If high-resolution spectroscopic measurements of the intercrater plains were made and mineralogical boundaries were detected, these

observations would provide evidence that the unit is composed of multiple deposits, possibly different volcanic flows. Mineralogical boundaries have been preserved on the Moon through billions of years of impact bombardment by the same impactor populations as Mercury (Strom et al., 2005). However (and unfortunately), the consequences of this impact flux on Mercury were more severe (e.g., higher impact velocities, more secondary craters, larger secondary craters) and may have mixed the regolith thoroughly enough to remove all evidence of mineralogically distinct lava flows.

5. Future directions

Where do we go from here? All of the work completed for this dissertation has been facilitated by various spacecraft in orbit around the Moon and Mercury. Many new discoveries have been made because of these orbital datasets, such as the existence of a new spinel-rich lithology on the Moon (e.g., Pieters et al., 2011) or hollows on Mercury (Blewett et al., 2011). However, in looking forward I believe it is time to consider landed missions to these two planetary bodies in order to understand better the geologic processes and their timing and stratigraphy. Of course landing on the surface of either the Moon or Mercury is taking a giant leap forward, both technologically and economically. Current attitudes are not focused on landed missions to either the Moon or Mercury. However, many pressing science questions can be addressed by doing rover-scale geology on these two planets.

Chapter 2 has provided information about where to look for ancient volcanic deposits on the Moon. Visible to near-infrared spectroscopic data indicate that the

mineralogy of cryptomaria is consistent with mare basalts (Chapter 3). Therefore, to understand better the temporal variations in mare basalts there are two outstanding landing sites: the cryptomare in (1) South Pole-Aitken basin (Fig. 5) and (2) Schiller-Zucchius basin (Fig. 6). Both regions of cryptomaria are far removed from the nearside mare basalts (and therefore may be less contaminated by these geologic materials due to impact ejecta) and would provide important information about the composition of basalts outside of the Procellarum KREEP Terrane (Jolliff et al., 2000).

For South Pole-Aitken basin, determining the absolute age of the basin formation event would provide a critical stratigraphic marker for lunar chronology in terms of the duration of the heavy bombardment and the frequency of impact events. A rover mission that could measure the age of both basin materials and cryptomare fill would be critical for understanding the relationship between basin formation and mare basalt emplacement (Whitten et al., 2011 and references therein). The combination of compositional measurements and age determinations would be extremely useful in addressing questions about the paucity of volcanic fill in South Pole-Aiken basin as well as its depth of excavation into the lunar crust. A rover mission to the center of the basin (Fig. 5a, white box) would be ideal because the rover would have access to both freshly exposed basaltic deposits and feldspathic basin materials (Fig. 5b). The landing site I propose (Fig. 5b, c) is also well within the range of Apollo basin ejecta deposits, meaning the regolith may also contain materials from that basin event that can be dated and their composition analyzed. The Apollo basin is superposed on South Pole-Aitken basin, meaning it has excavated even deeper into the lunar crust and may be able to provide important information on the composition of the lower crust.

Schiller-Zucchius basin, the second proposed landing site on the Moon, is located southeast of Orientale basin. The central part of the basin is filled with mare basalts that have a thin veneer of feldspathic ejecta from Orientale (Fig. 6a). By landing along a basin ring within Schiller-Zucchius (Fig. 6b, c) the age and composition of the basin, cryptomare, and the Orientale event could be ascertained. As with South Pole-Aitken basin, dating the basin event and the mare basalts will provide information on the temporal relationship between basin formation and mare basalt emplacement. Since Schiller-Zucchius is within the range of Orientale ejecta, basin soil samples may contain enough Orientale basin ejecta to also date the formation of Orientale. Sampling or measuring the ring materials at Schiller-Zucchius may provide information about the crustal composition at this location on the Moon. No pure anorthosite materials have been detected in the ring structure of Schiller-Zucchius (Ohtake et al., 2009; Donaldson Hanna et al., in revision) and it is unclear if this is because the basin ring structure does not excavate from a pure anorthosite layer or because space weathering has destroyed all rock outcrops. The proposed landing site in Schiller-Zucchius (Fig. 6b, c) is centered near a dark-halo impact crater and within 25 km of basin ring materials, both directly to the east and west. Measurements of the anorthosite crust and the basaltic materials at either South Pole-Aitken or Schiller-Zucchius will provide important constraints on models of the thermal and magmatic evolution of the Moon.

The work completed for this dissertation also provides vital information for selecting key landing sites to understand better the volcanic history of Mercury. If spacecraft technology is sophisticated enough to land a rover on the surface of Mercury and withstand the large temperature variations, on the order of ~600 K, I would propose

one of two landing sites: (1) the rim of the Caloris impact basin (Fig. 7) and (2) the edge of the northern volcanic plains (Fig. 8). Caloris is the largest, most well-preserved impact basin on Mercury and it shows distinct color differences between its exterior smooth plains (LBP), interior surface fill (HRP), and material underlying the surface fill (LRM). There is one location along the western edge of the basin (Fig. 7a, white box) where a small crater <5 km in diameter excavates LRM material from below the HRP (Fig. 7b). Within 50 km of this LRM crater there is a small fresh crater that only excavates HRP materials and both of these craters are within 50 km of basin rim massifs (Fig. 7c). A mission of this magnitude would be able to address several important questions about the surface composition of Mercury and the sequence of geologic units within and around Caloris basin. Currently, it is difficult to determine the mineralogy and diversity of volcanic deposits on Mercury. The MESSENGER Mercury Dual Imaging System (MDIS) collects multispectral data and the Mercury Atmospheric and Surface Composition Spectrometer (MASCS) makes hyperspectral measurements of the surface of Mercury, but only for wavelengths <1 μm. No spectral absorption features have been clearly observed to date. The MESSENGER X-ray and gamma ray instruments have revealed the surface composition of Mercury in greater detail than ever before. However, the spatial resolution of these instruments is poor enough that it is impossible to measure the composition of small regions on the surface. A rover equipped with near-infrared spectrometers or an x-ray diffraction instrument would be able to provide unprecedented mineralogic information about the surface composition of the LRM, HRP, and Caloris rim materials. Additionally, if these basin and volcanic materials could be radiometrically dated then, like the proposed lunar landing sites, they would provide information about

the temporal relationship between basin formation and emplacement of volcanic deposits and also provide a stratigraphic marker for the mercurian cratering chronology.

Another important volcanic deposit on Mercury that has been mentioned throughout this dissertation is the northern volcanic plains (Head et al., 2011). This massive deposit has the same MDIS color properties as the Caloris interior plains (i.e., HRP), but MASCS spectra indicate that Caloris and the northern volcanic plains are mineralogically different (Helbert et al., 2013). Landing a rover capable of making surface measurements at the boundary between the northern volcanic plains and the intercrater plains (Fig. 8a, white box) would allow compositional measurements of the young northern volcanic plains and also the intercrater plains geologic materials (Fig. 8b, c). The age of the northern volcanic plains could be ascertained, which would aid in constraining the thermal history of the planet. If the northern volcanic plains are younger than currently expected (~3.8 Ga; Strom et al., 2011) then the mantle had to have enough heat to melt such a large volume of mantle material and the planet could not be been in a dominantly contractional stress state. Measuring the composition of the intercrater plains materials along the edge of the northern volcanic plains would be able to provide a sense of what lithologies and other geologic materials compose the oldest regolith deposits on the planet.

It is important to note that the BepiColombo mission, set to launch in July 2016 and arrive at Mercury in 2024, will include a suite of instruments to measure the composition of Mercury, including the MErcury Radiometer and Thermal Imaging Spectrometer (MERTIS). MERTIS will image the surface at thermal wavelengths (7–14 μm) to measure the surface mineralogy with a spatial resolution of 500 m/pixel. The orbit

of the BepiColombo spacecrcaft is different from that of MESSENGER; BepiColombo will be inserted into polar orbit such that periapsis is located at the sunlit equator. Periapsis for the MESSENGER mission is near the north pole. The different orbit of BepiColombo will be able to provide a much higher resolution view of the equator and the southern hemisphere, which may spark more questions than answers about the geology of the innermost planet.

There is so much exciting science to come. Currently available orbital datasets have enabled the work presented in this dissertation, aimed at mapping the extent of early volcanism on the Moon and Mercury, and are still unveiling the mysteries of the terrestrial planets, giving rise to new scientific questions. Technological advances in spacecraft and instrument capabilities are going to propel science forward with higher resolution and faster measurements. Where will these new technologies take us? What new scientific questions will be generated from these data? We will have to wait and see!

References

Beach, M.J., Head, J.W., Ostrach, L.R., Robsinon, M.S., Denevi, B.W., Solomon, S.C., 2012. The influence of pre-existing topography on the distribution of impact melt on Mercury. Lunar Planet. Sci. Conf. 43, abstract 1335.

Blewett, D.T., Chabot, N.L., Denevi, B.W., Ernst, C.M., Head, J.W., Izenberg, N.R., Murchie, S.L., Solomon, S.C., Nittler, L.R., McCoy, T.J., Xiao, Z., Baker, D.M.H., Fassett, C.I., Braden, S.E., Oberst, J., Scholten, F., Preusker, F., Hurwitz, D.M., 2011. Hollows on Mercury: MESSENGER evidence for geologically recent volatile-related activity. Science 333, 1856–1859. doi:10.1126/science.1211681.

Byrne, P.K., Klimczak, C., Şengör, A.M.C., Solomon, S.C., Watters, T.R., Hauck II, S.A., 2014. Mercury's global contraction much greater than earlier estimates. Nature Geosci. online publication. doi:10.1038/NGEO2097.

Coffin, M.F., Eldholm, O., 1994. Large igneous provinces: Crustal structure, dimensions, and external consequences. Rev. Geophys. 32, 1–36.

Denevi, B.W., Ernst, C.M., Meyer, H.M., Robinson, M.S., Murchie, S.L., Whitten, J.L., Head, J.W., Watters, T.R., Solomon, S.C., Ostrach, L.R., Chapman, C.R., Byrne, P.K., Klimczak, C., Peplowski, P.N., 2013. The distribution and origin of smooth plains on Mercury. J. Geophys. Res. Planets 118, 891–907. doi:10.1002/jgre.20075.

Donaldson Hanna, K.L., Cheek, L.C., Pieters, C.M., Mustard, J.F., Greenhagen, B.T., Thomas, I.R., Bowles, N.E., 2014. Global assessment of pure crystalline

plagioclase across the Moon and implications for the evolution of the primary crust. J. Geophys. Res., in review.

Elkins-Tanton, L.T., Burgess, S., Yin, Q.-Z., 2011. The lunar magma ocean: Reconciling the solidification process with lunar petrology and geochronology. Earth Planet. Sci. Lett. 304, 326–336. doi:10.1016/j.epsl.2011.02.004.

Fassett, C.I., Head, J.W., Blewett, D.T., Chapman, C.R., Dickson, J.L., Murchie, S.L., Solomon, S.C., Watters, T.R., 2009. Caloris impact basin: Exterior geomorphology, stratigraphy, morphometry, radial sculpture, and smooth plains deposits. Earth Planet. Sci. Lett. 285, 297–308. doi:10.1016/j.epsl.2009.05.022.

Fassett, C.I., Kadish, S.J., Head, J.W., Solomon, S.C., Strom, R.G., 2011. The global population of large craters on Mercury and comparison with the Moon. Geophys. Res. Lett. 38, L10202. doi:10.1029/2011GL047294.

Fassett, C.I., Head, J.W., Kadish, S.J., Mazarico, E., Neumann, G.A., Smith, D.E., Zuber, M.T., 2012. Lunar impact basins: Stratigraphy, sequence and ages from superposed impact crater populations measured from Lunar Orbiter Laser Altimeter (LOLA) data. J. Geophys. Res. 117. doi:10.1029/2011JE003951.

Gault, D.E., Guest, J.E., Murray, J.B., Dzurisin, D., Malin, M.C., 1975. Some comparisons of impact craters on Mercury and the Moon. J. Geophys. Res. 80, 2444–2460.

Grove, T.L., Krawczynski, M.J., 2009. Lunar mare volcanism: Where did the magmas come from? Elements 5, 29–34. doi:10.2113/gselements.5.1.29.

Hamilton, V.E., 2000. Thermal infrared emission spectroscopy of the pyroxene mineral series. J. Geophys. Res. 105, 9701–9716.

Hauck II, S.A., Solomon, S.C., Margot, J.-L., Lemoine, F.G., Mazarico, E., Peale, S.J., Perry, M.E., Phillips, R.J., Smith, D.E., Zuber, M.T., 2012. Mercury's internal structure as constrained by MESSENGER observations. Lunar Planet Sci. 43, abstract 1170.

Head, J.W., Wilson, L., 1992. Lunar mare volcanism: Stratigraphy, eruption conditions, and the evolution of secondary crusts. Geochim. Cosmochim. Acta 56, 2155–2175.

Head, J.W., Chapman, C.R., Strom, R.G., Fassett, C.I., Denevi, B.W., Blewett, D.T., Ernst, C.M., Watters, T.R., Solomon, S.C., Murchie, S.L., Prockter, L.M., Chabot, N.L., Gillis-Davis, J.J., Whitten, J.L., Goudge, T.A., Baker, D.M.H., Hurwitz, D.M., Ostrach, L.R., Xiao, Z., Merline, W.J., Kerber, L., Dickson, J.L., Oberst, J., Byrne, P.K., Klimczak, C., Nittler, L.R., 2011. Flood volcanism in the northern high latitudes of Mercury revealed by MESSENGER. Science 333, 1853–1856. doi:10.1126/science.1211997.

Helbert, J., D'Amore, M., Head, J.W., Byrne, P.K., Holsclaw, G.M., Izenberg, N.R., McClintock, W.E., Solomon, S.C., 2013. A comparison of the spectral properties of the Caloris and Rembrandt impact basins. Lunar Planet. Sci. 44, abstract 1496.

Hess, P.C., Parmentier, E.M., 1995. A model for the thermal and chemical evolution of the Moon's interior: Implications for the onset of mare volcanism. Earth Planet. Sci. Lett. 134, 501–514.

Izenberg, N.R., Klima, R.L., Murchie, S.L., Blewett, D.T., Holsclaw, G.M., McClintock, W.E., Malaret, E., Mauceri, C., Vilas, F., Sprague, A.L., Helbert, J., Domingue, D., Head III, J.W., Goudge, T.A., Solomon, S.C., Hibbitts, C., Dyar, M.D., 2014. The

low-iron, reduced surface of Mercury as seen in spectral reflectance by MESSENGER. Icarus 228, 364–374. doi: 10.1016/j.icarus.2013.10.023.

Jolliff, B.L., Gillis, J.J., Haskin, L.A., Korotev, R.L., Wieczorek, M.A., 2000. Major lunar crustal terranes: Surface expressions and crust-mantle origins. J. Geophys. Res. 105, 4197–4216.

Krawczynski, M.J., Grove, T.L., 2012. Experimental investigation of the influence of oxygen fugacity on the source depths for high titanium lunar ultramafic magmas. Geochim. Cosmochim. Acta 79, 1–19. doi:10.1016/j.gca.2011.10.043.

Le Feuvre, M., Wieczorek, M.A., 2008. Nonuniform cratering of the terrestrial planets. Icarus 197, 291–306. doi:10.1016/j.icarus.2008.04.011.

Michel, N.C., Hauck II, S.A., Solomon, S.C., Phillips, R.J., Roberts, J.H., Zuber, M.T., 2013. Thermal evolution of Mercury as constrained by MESSENGER observations. J. Geophys. Res. Planets 118, 1033–1044. doi:10.1002/jgre.20049.

Morbidelli, A., Marchi, S., Bottke, W.F., Kring, D.A., 2012. A sawtooth-like timeline for the first billion years of lunar bombardment. Earth Planet. Sci. Lett. 355–356, 144–151. doi:10.1016/j.epsl.2012.07.037.

Nemchin, A., Timms, N., Pidgeon, R., Geisler, T., Reddy, S., Meyer, C., 2009. Timing of crystallization of the lunar magma ocean constrained by the oldest zircon. Nature Geosci. 2, 133−136. doi:10.1038/NGEO417.

Nittler, L.R., Starr, R.D., Weider, S.Z., McCoy, T.J., Boynton, W.V., Ebel, D.S., Ernst, C.M., Evans, L.G., Goldsten, J.O., Hamara, D.K., Lawrence, D.J., McNutt Jr., R.L., Schlemm II, C.E., Solomon, S.C., Sprague, A.L., 2011. The major element

composition of Mercury's surface from MESSENGER x-ray spectrometry. Science 333, 1847–1850. doi:10.1126/science.1211567.

Oberbeck, V.R., Morrison, R.H., Hörz, F., Quaide, W.L., Gault, D.E., 1974. Smooth plains and continuous deposits of craters and basins. Proc. Lunar Planet. Sci. Conf. 5, 111–136.

Ohtake, M., Matsunaga, T., Haruyama, J., Yokota, Y., Morota, T., Honda, C., Ogawa, Y., Torii, M., Miyamoto, H., Arai, T., Hirata, N., Iwaskaki, A., Nakamura, R., Hiroi, T., Sugihara, T., Takeda, H., Otake, H., Pieters, C.M., Saiki, K., Kitazato, K., Abe, M., Asada, N., Demura, H., Yamaguchi, Y., Sasaki, S., Kodama, S., Terazono, J., Shirao, M., Yamaji, A., Minami, S., Akiyama, H., Josset, J.-L., 2009. The global distribution of pure anorthosite on the Moon. Nature 461, 236–240. doi:10.1038/nature08317.

Peplowski, P.N., Evans, L.G., Hauck II, S.A., McCoy, T.J., Boynton, W.V., Gillis-Davis, J.J., Ebel, D.S., Goldsten, J.O., Hamara, D.K., Lawrence, D.J., McNutt Jr, R.L., Nittler, L.R., Solomon, S.C., Rhodes, E.A., Sprague, A.L., Starr, R.D., Stockstill-Cahill, K.R., 2011. Radioactive elements on Mercury's surface from MESSENGER: Implications for the planet's formation and evlution. Science 333, 1850–1852. doi:10.1126/science.1211576.

Pieters, C.M., Besse, S., Boardman, J., Buratti, B., Cheek, L., Clark, R.N., Combe, J.P., Dhingra, D., Goswami, J.N., Green, R.O., Head, J.W., Isaacson, P., Klima, R., Kramer, G., Lundeen, S., Malaret, E., McCord, T., Mustard, J., Nettles, J., Petrom N., Runyon, C., Staid, M., Sunshine, J., Taylor, L.A., Thaisen, K., Tompkins, S.,

Whitten, J., 2011. Mg-spinel lithology: A new rock type on the lunar farside. J. Geophys. Res. 116, E00G08. doi:10.1029/2010JE003727.

Riner, M.A., Lucey, P.G., Desch, S.J., McCubbin, F.M., 2009. Nature of opaque components on Mercury: Insights into a Mercurian magma ocean. Geophys. Res. Lett. 36, L02201. doi:10.1029/2008GL036128.

Roberts, J.H., Barnouin, O.S., 2012. The effect of the Caloris impact on the mantle dynamics and volcanism of Mercury. J. Geophys. Res. 117, E02007. doi:10.1029/2011JE003876.

Smith, D.E., Zuber, M.T., Phillips, R.J., Solomon, S.C., Hauck II, S.A., Lemoine, F.G., Mazarico, E., Neumann, G.A., Peale, S.J., Margot, J.-L., Johnson, C.L., Torrence, M.H., Perry, M.E., Rowlands, D.D., Goossens, S., Head, J.W., Taylor, A.H., 2012. Gravity field and internal structure of Mercury from MESSENGER. Science 336, 214–217. doi:10.1126/science.1218809.

Snyder, G.A., Taylor, L.A., Neal, C.R., 1992. A chemical model for generating the sources of mare basalts: Combined equilibrium and fractional crystallization of the lunar magmasphere. Geochim. Cosmochim. Acta 56, 3809–3823. doi: 10.1016/0016-7037(92)90172-F.

Spudis, P.D., 1978. Composition and origin of the Apennine Bench Formation. Proc. Lunar Planet. Sci. Conf. 9, 3379–3394.

Strom, R.G., Malhotra, R., Ito, T., Yoshida, F., Kring, D.A., 2005. The origin of planetary impactors in the inner solar system. Science 309, 1847–1850. doi:10.1126/science.1113544.

Strom, R.G., Banks, M.E., Chapman, C.R., Fassett, C.I., Forde, J.A., Head III, J.W., Merline, W.J., Prockter, L.M., Solomon, S.C., 2011. Mercury crater statistics from MESSENGER flybys: Implications for stratigraphy and resurfacing history. Planet. Space Sci. 59, 1960–1967. doi:10.1016/j.pss.2011.03.018.

Whitten, J.L., Head, J.W., Staid, M., Pieters, C.M., Mustard, J., Clark, R., Nettles, J., Klima, R.L., Taylor, L.A., 2011. Lunar mare deposits associated with the Orientale impact basin: New insights into mineralogy, history, mode of emplacement, and relation to Orientale Basin evolution from Moon Mineralogy Mapper (M^3) data from Chandrayaan-1. J. Geophys. Res. Planets 116. doi:10.1029/2010JE003736.

Wieczorek, M.A. and Phillips, R.J., 2000. The "Precellarum KREEP Terrane": Implications for mare volcanism and lunar evolution. J. Geophys. Res. 105, 20417–20430.

Wieczorek, M.A., Neumann, G.A., Nimmo, F., Kiefer, W.S., Talor, G.J., Melosh, H.J., Phillips, R.J., Solomon, S.C., Andrews-Hanna, J.C., Asmar, S.W., Konopliv, A.S., Lemoine, F.G., Smith, D.E., Watkins, M.M., Williams, J.G., Zuber, M.T., 2013. The crust of the Moon as seen by GRAIL. Science 339, 671–675. doi:10.1126/science.1231530.

Wilson, L., Head, J.W., 1981. Ascent and eruption of basaltic magma on the Earth and Moon. J. Geophys. Res. 86, 2971–3001.

Zuber, M.T., Smith, D.E., Phillips, R.J., Solomon, S.C., Neumann, G.A., Hauck, S.A., Peale, S.J., Barnouin, O.S., Head, J.W., Johnson, C.L., Lemoine, F.G., Mazarico, E., Sun, X., Torrence, M.H., Freed, A.M., Klimczak, C., Margot, J.-L., Oberst, J.,

Perry, M.E., McNutt Jr., R.L., Balcerski, J.A., Michel, N., Talpe, M.J., Yang, D., 2012. Topography of the northern hemisphere of Mercury from MESSENGER laser altimetry. Science 336, 217–220. doi:10.1126/science.1218805.

Figure Captions

Figure 1. Mapped volcanic deposits on the Moon (left) and Mercury (right). The entire surface of Mercury has yet to be mapped, therefore there are straight edges in the intercrater plains boundary that correspond the map boundaries. Dark grey features are young volcanic plains (mare basalts on the Moon and smooth plains on Mercury). Colored features denote ancient volcanic deposits. The two planetary bodies are scaled relative to one another. Numbers are the longitude for each row of images; all images have a latitude of 0°. Volcanic map units are superposed on a Lunar Orbiter Laser Altimeter 237 m/pixel hillshade and an MDIS stereo photogrammetry topographic model at 665 m/pixel.

Figure 2. Elevation frequency distributions for volcanic deposits on the Moon (left) and Mercury (right). On both planets the younger volcanic deposits (mare basalts and smooth plains, dark gray lines) are located at lower elevations. On Mercury, the intercrater plains have been substantially modified by lobate scarps and long-wavelength topographic folding due to global contraction. The gray rectangular regions denote the elevation range on both planets; the Moon has a much larger elevation range compared to Mercury. Lunar orbiter laser altimeter data at 237 m/pixel and stereo photogrammetry from MDIS at 665 m/pixel.

Figure 3. Maximum distribution of basin impact melt deposits on the eastern (top left) and western (top right) hemispheres of Mercury. The 46 confirmed basin rims are denoted by white circles and the impact melt deposits are shown as purple halos around

the basins, approximately one basin radius from the rim crest. Predicted basin impact melt deposits on the eastern hemisphere (bottom left) and western hemisphere (bottom right) of Mercury are compared with the distribution of mapped intercrater plains (light purple). It is clear that these maximum estimates of basin impact melt deposits cannot explain the current intercrater plains distribution. For many of the smaller basins the impact melt would only be expected on the basin rim as small areally discontinuous deposits (Fig. 10 in Chapter 5).

Figure 4. The distribution of magnesium across the nearside (top) and farside (bottom) of the Moon. Generally, the Mg-rich regions of the Moon correlated with the distribution of mare basalts (black outlines). The highest Mg (wt %) material is associated with the Imbrium basin. Lunar Prospector gamma ray spectrometer data (5°/pixel or ~152 km/pixel) superposed on a Lunar Orbiter Laser Altimeter 237 m/pixel hillshade.

Figure 5. Proposed landing site within the South Pole-Aitken basin for a hypothetical rover mission. (a) Overview image of the entire South Pole-Aitken basin (black oval denotes the basin rim). Cryptomaria (white outlines) are concentrated in the center of the basin. The white box denotes the location of parts (b) and (c). Lunar Reconnaissance Orbiter Camera 100 m/pixel mosaic. (b) View of the proposed landing site from the Moon Mineralogy Mapper color mosaic (R: 1 μm integrated band depth; G: 2 μm integrated band depth; B: 1489 nm reflectance). Yellow colors denote pyroxene-rich lithologies and blue indicates the presence of anorthosite. Cryptomare boundaries are outlined in white. (c) The proposed landing site contains fresh impact craters that

excavate both basalts (locations 1 and 2) and basin materials (location 3). Lunar Reconnaissance Orbiter Camera 100 m/pixel mosaic. Lambert azimuthal equal area projection centered on South Pole-Aitken basin. The white dashed circle is 50 km in diameter and represents the assumed distance that a modern rover would be able to traverse across the surface. Previous rovers, including Opportunity (2004-present) and Lunokhod 2 (1973), traveled a maximum of ~40 km over a period of ~10 years and <1 year, respectively.

Figure 6. Proposed landing site within the Schiller-Zucchius basin, located to the south of the Schiller-Schickard region. (a) Overview image of the entire Schiller-Schickard region, with cryptomare (white outlines) and Schiller-Zucchius (orange circle). The white box denotes the location of parts (b) and (c). Lunar Reconnaissance Orbiter Camera 100 m/pixel mosaic. (b) View of the proposed landing site along the rim of Schiller-Zucchius from the Moon Mineralogy Mapper color mosaic (R: 1 μm integrated band depth; G: 2 μm integrated band depth; B: 1489 nm reflectance). Yellow colors denote pyroxene-rich lithologies and blue indicates the presence of noritic anorthosite. Cryptomare boundaries are outlined in white. (c) The proposed landing site contains fresh dark-halo impact craters and basin rim (left edge of white dashed circle) and ring materials (right edge of white dashed circle). Lunar Reconnaissance Orbiter Camera 100 m/pixel mosaic. Lambert azimuthal equal area projection centered on mapped Schiller-Schickard cryptomare. The white dashed circle is 50 km in diameter and represents the assumed distance that a modern rover would be able to traverse across the surface.

Figure 7. Proposed landing site along the boundary of the Caloris impact basin. (a) Overview image of the basin, with the smooth interior plains indicated (black outline) to show the location of the basin rim. The white box denotes the location of parts (b) and (c). Mercury Dual Imaging System 250 m/pixel mosaic. (b) View of the proposed landing site along the edge of Caloris from the Mercury Dual Imaging System 665 m/pixel color mosaic (R: second principal component; G: first principal component; B: 430/1000 nm ratio). Tan to pink colors represent the HRP unit, which fills most of the basin interior. The <5 km diameter impact crater excavating LRM is indicated by a black arrow. An even smaller fresh crater (white to cyan) located along the right edge of the proposed landing site (white dashed circle) excavates HRP material. (c) The proposed landing site (white dashed circle) boarders the LRM ejecta deposits from a fresh crater (location 1), is close to Caloris basin massifs (location 2), and contains a fresh impact crater in HRP material (location 3). Mercury Dual Imaging System 250 m/pixel mosaic. Stereographic projection centered on Caloris basin.

Figure 8. Proposed landing site along the boundary of the northern volcanic plains on Mercury. (a) Overview image of the entire northern volcanic plains deposit (black outline). The white box denotes the location of parts (b) and (c). Mercury Dual Imaging System 250 m/pixel mosaic. (b) View of the proposed landing site along the edge of the northern volcanic plains from the Mercury Dual Imaging System 1 km/pixel color mosaic (R: second principal component; G: first principal component; B: 430/1000 nm ratio). Tan to pink colors represent the high-reflectance red plains (HRP). Intercrater plains typically have a grey to blue hue and can be composed on low-reflectance blue plains

(LBP) or low reflectance material (LRM). Fresh crater materials appear as white or cyan; a fresh impact crater is located at the top-center of the image frame. The ejecta from this crater is superposed on the smooth plains within the proposed landing site (white dashed circle). (c) The proposed landing site (white dashed circle) contains a fresh impact crater in HRP material, is close to the smooth plains/ intercrater plains boundary, and ejecta deposits from the fresh crater at the top-center of the image frame. Mercury Dual Imaging System 250 m/pixel mosaic. Stereographic projection centered on the north pole of Mercury.

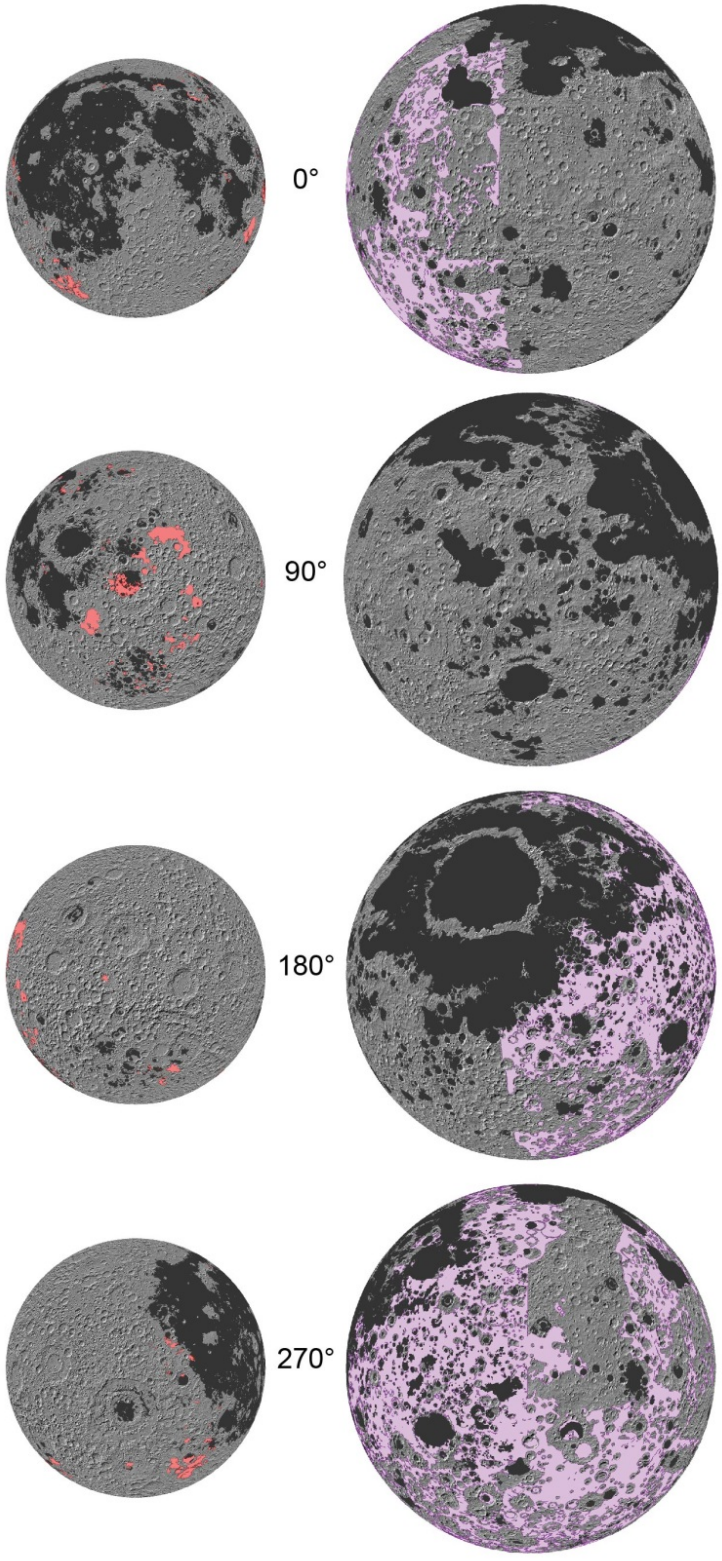

Figure 1.

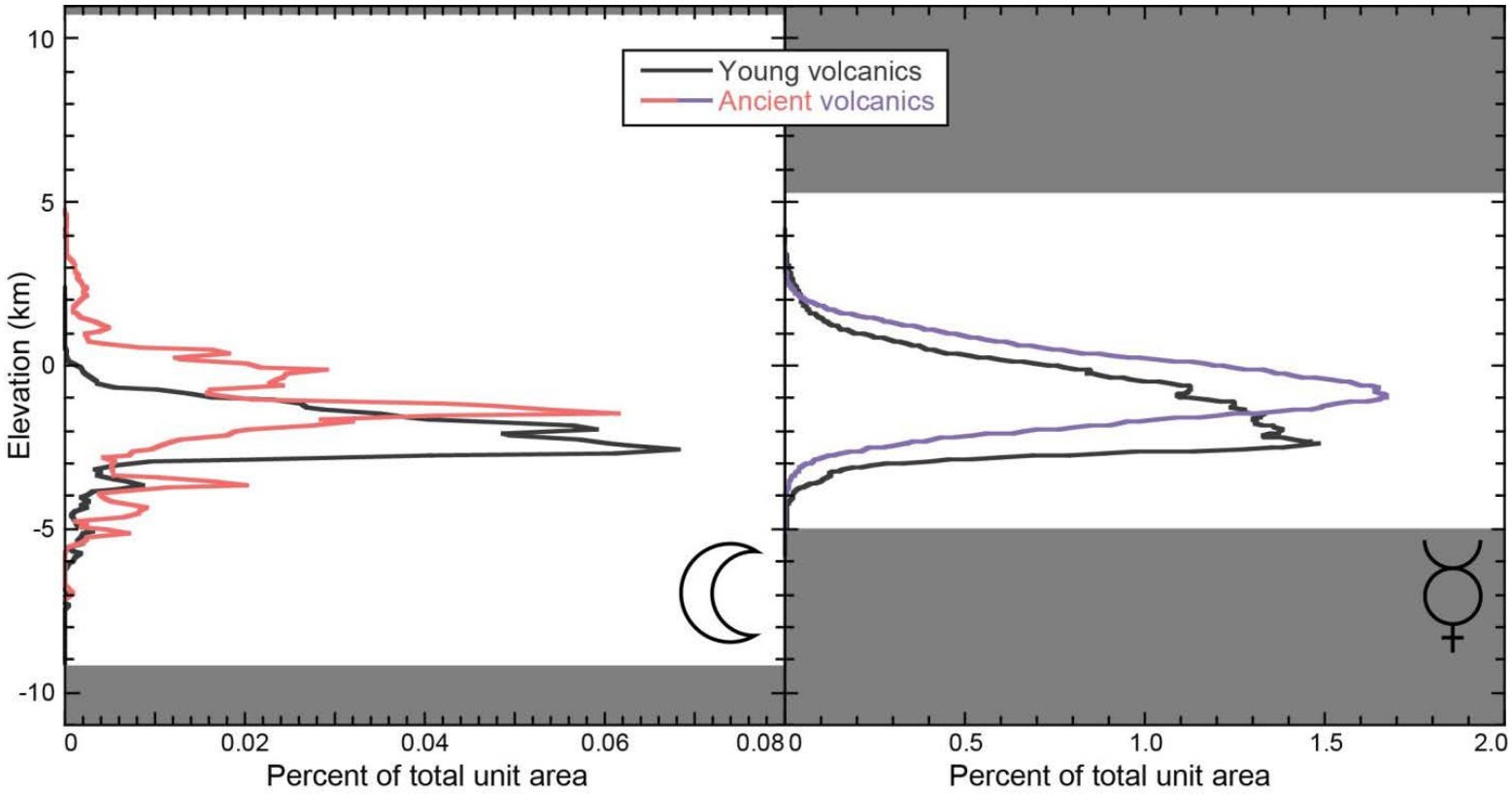
Young volcanics
Ancient volcanics
Elevation (km)
10
5
0
-5
-10
0
0.02
0.04
0.06
0.08
Percent of total unit area
0
0.5
1.0
1.5
2.0
Percent of total unit area

Figure 2.

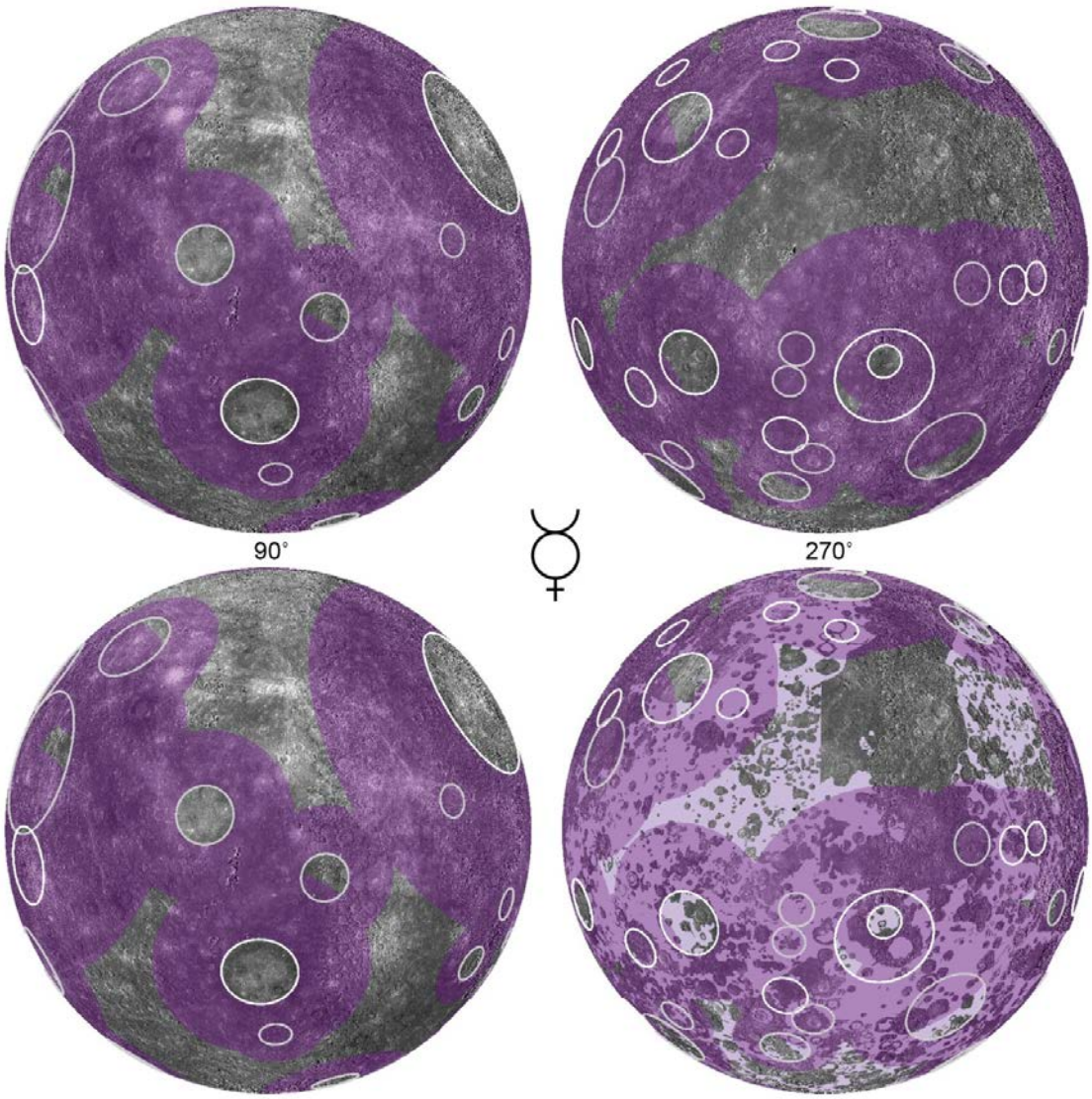

Figure 3.

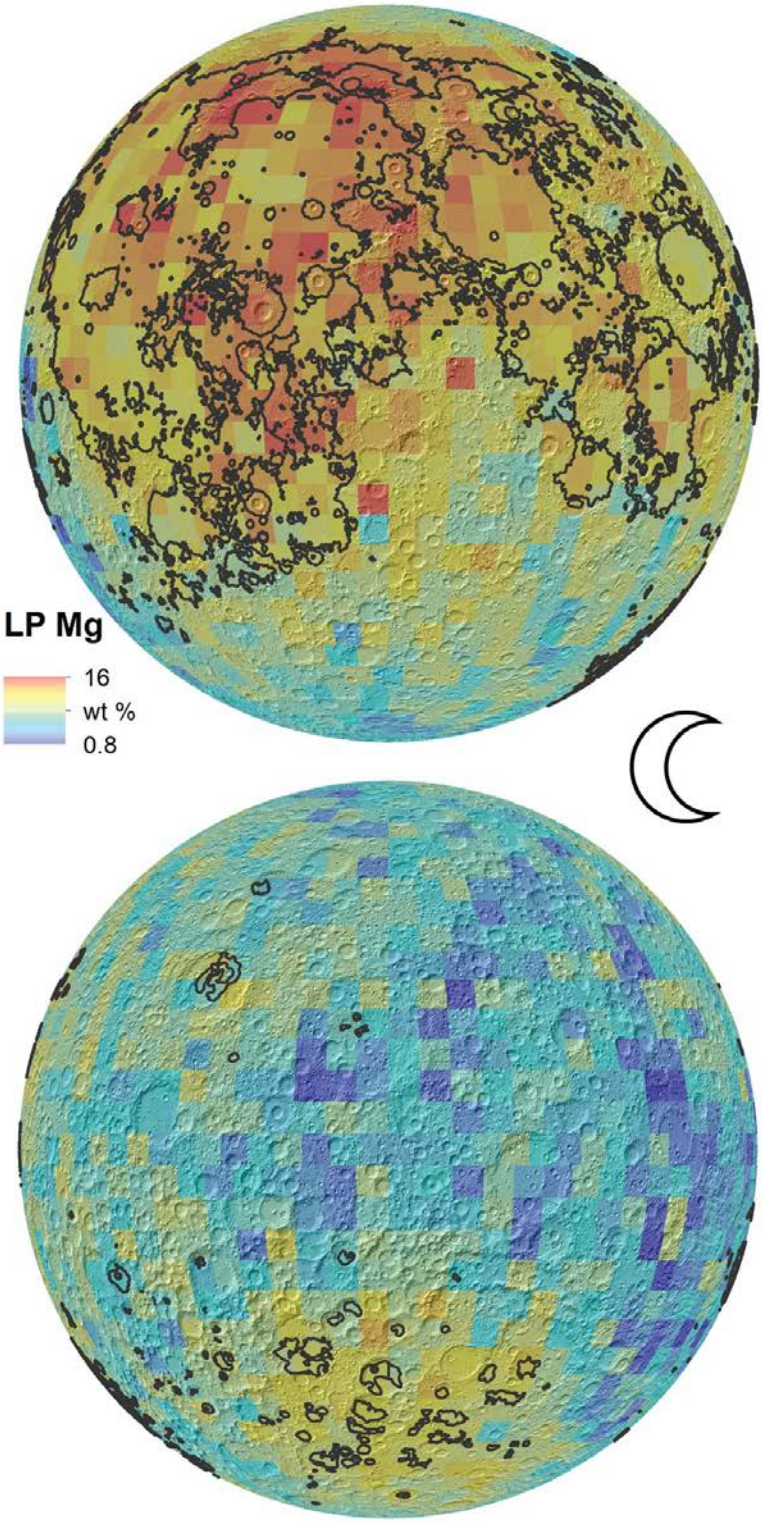

Figure 4.

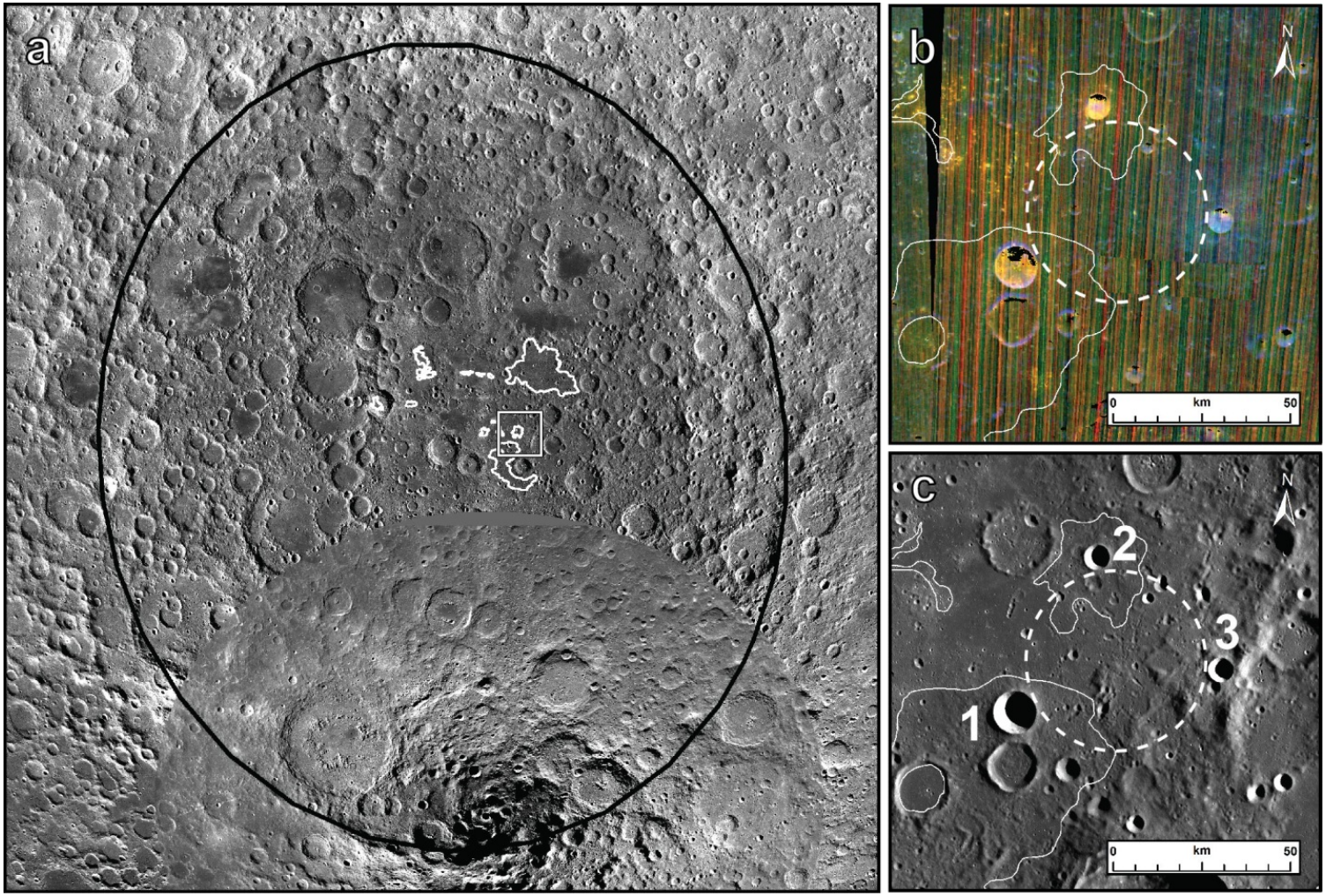

Figure 5.

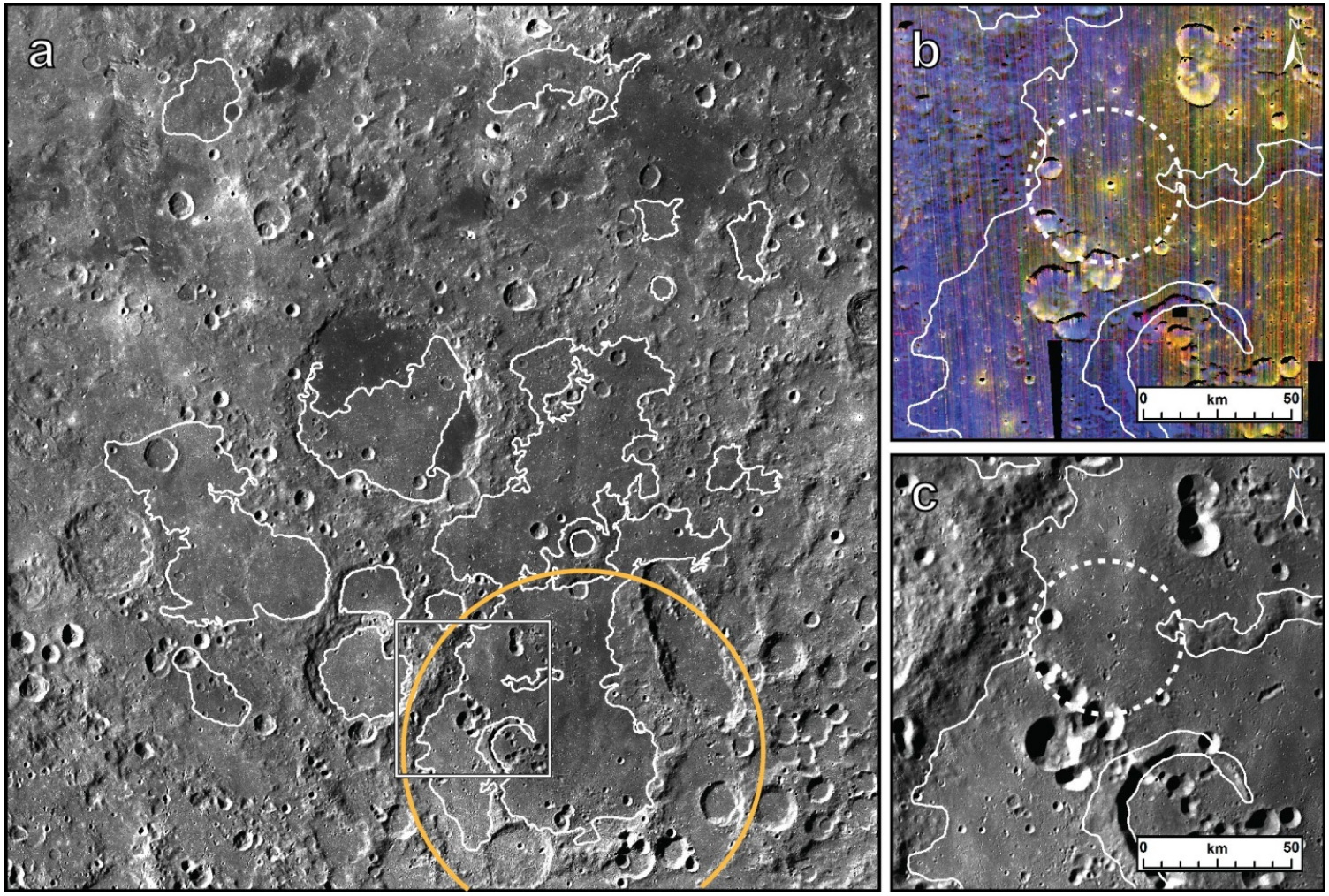

Figure 6.

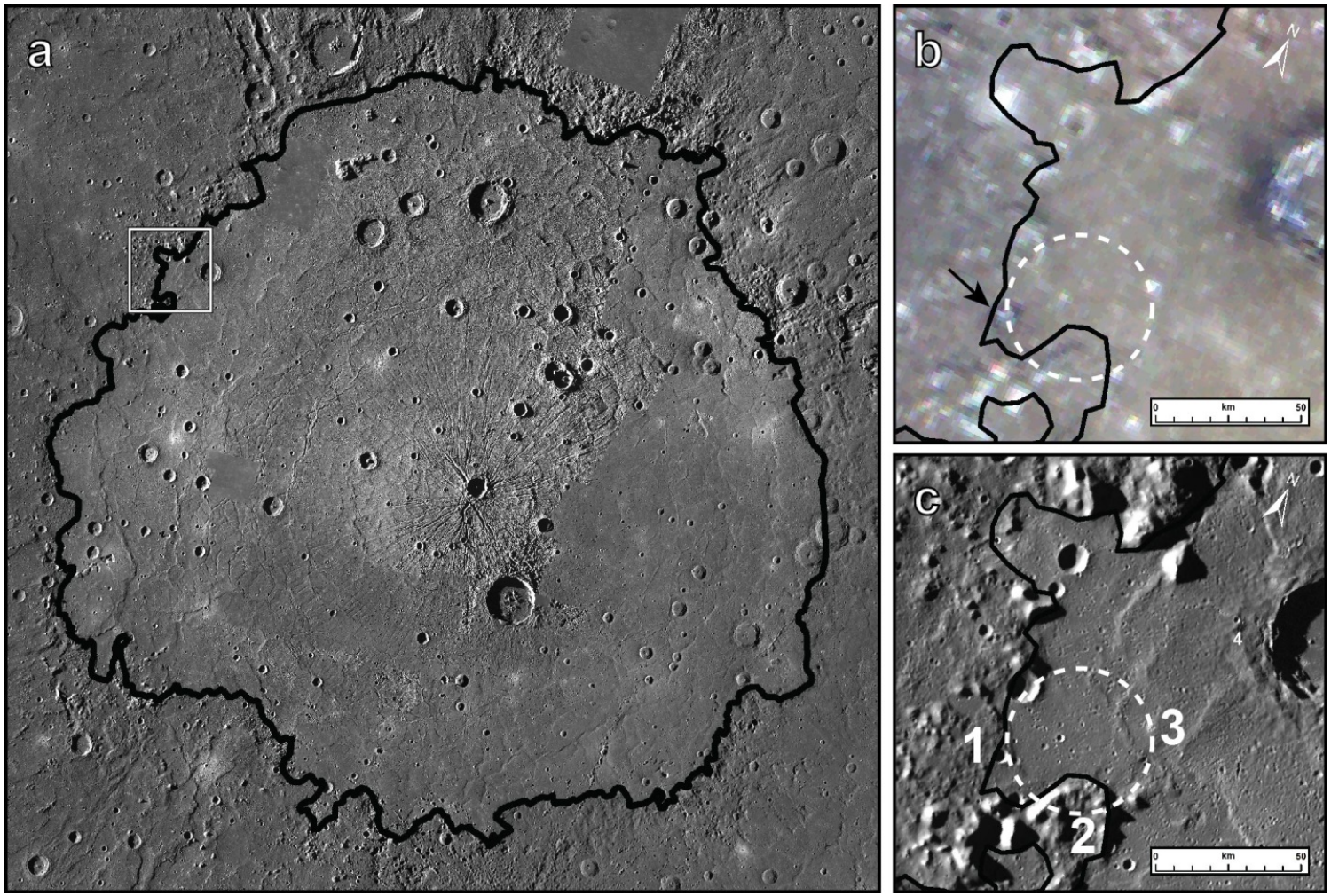

Figure 7.

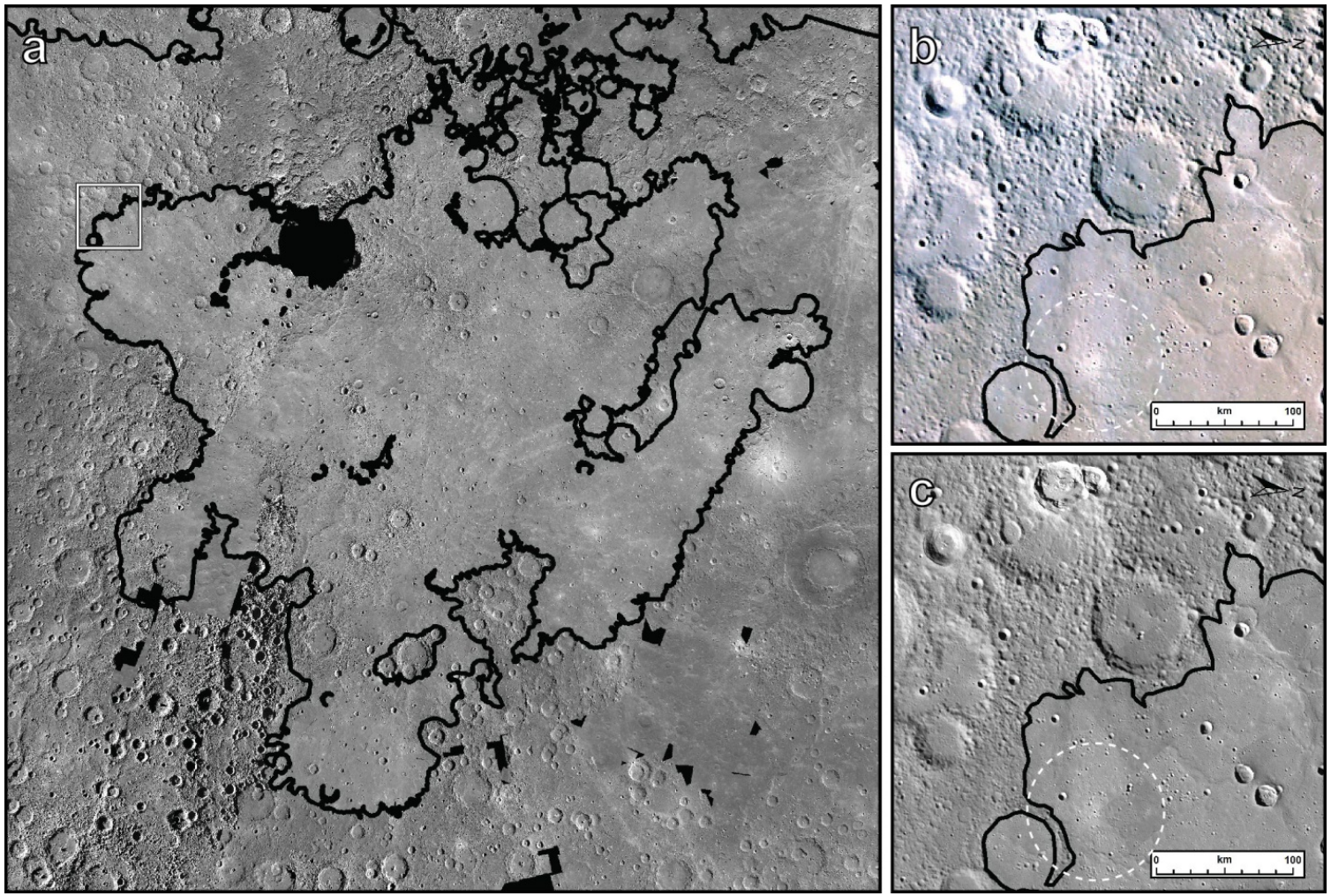

Figure 8.